GREEN'S FUNCTION SIMULATION METHOD FOR EARTH-AIR HEAT EXCHANGERS

by

Chantz Michael Denowh

A dissertation submitted in partial fulfillment
of the requirements for the degree

of

Doctor of Philosophy

in

Engineering

MONTANA STATE UNIVERSITY
Bozeman, Montana

January 2015

©COPYRIGHT

by

Chantz Michael Denowh

2015

All Rights Reserved

ACKNOWLEDGMENTS

I would like to dedicate this work to my parents, Michael and Debra Denowh. Throughout my life, Mom and Dad have encouraged me to follow my own path, and given me all the support I could ask for along the way. Sometimes this support would involve working on the ranch with Dad or participating in activities Mom saw as important. I remember questioning why I had to do all that at the time. Now looking back, I understand how important the childhood my parents provided has been for my success. I've also picked up my parent's personality traits along the way. I learned the importance of hard work, honesty, and integrity from my father. From my mother, I learned self-reliance, to take pride in my work, and to show compassionate for others. I will always be grateful and love them for providing me the foundation to complete this work and attain my doctorate. I would not have got this far without them.

TABLE OF CONTENTS

1. INTRODUCTION 1

2. BACKGROUND 9

EAHX Design and Construction 9
Soil Properties 11
Foundation Construction 11
Radon Collection in Earth-Air Heat Exchangers 13
Internal Pipe Flow 14
Entrance Regions and Boundary Layers 14
Pressure Drop and Friction Factor 16
Energy Balance and Log Mean Temperature Difference 18
Convective Correlations for Laminar and Turbulent Flow 20
Coefficient of Performance and Effectiveness 21
Heating and Cooling Degree Days 22

3. LITERATURE REVIEW 24

Soil Temperature Predictions 24
Analytical Earth-Air Heat Exchanger Models 30
Numerical Based Earth-Air Heat Exchange Models 35
Computer Simulation Programs and Efforts 40
Heat Transfer in Foundation Slabs 41

4. PREVIOUS RESEARCH AND MOTIVATION 46

5. EXPERIMENTAL DATA 49

Earth-Air Heat Exchanger Experimental Setup 49
REHAU® Montana Ecosmart House Project 49
Earth-Air Heat Exchanger Construction 50
Foundation Slab Construction 54
Data Acquisition Equipment 55
Experimental Data from the REHAU® Montana Ecosmart House Project 59
Experiment Description 59
Airflow Raw Data 60
Dew Points and Condensation 66
Soil Temperatures 67
Consequences of Soil Temperature Probe Locations. 73
Annual Under Yard and Under Slab Soil Temperatures. 74
Average Data Comparison 75
Coefficient of Performance 82
Experimental Errors and Recommendations 85

TABLE OF CONTENTS CONTINUED

Location Data for Simulation Models 86
Typical Meteorological Year 88
Soil Temperature and Moisture Data 89

6. EARTH-AIR HEAT EXCHANGER SIMULATION USING GREEN'S FUNCTIONS 90

Transient Conduction Solution Method 90
The Green's Function Method 92
Introduction to Green's Functions 92
Numbering System for Boundary and Initial Conditions 93
Green's Function Solution Equation 95
Numeric Integration and Time Variable Boundary Conditions 98
Space Variable Boundary Conditions 99
Example Green's Function Application 101
Characteristics of Green's Functions Specific to Earth-Air Heat Exchangers 104
Convective Green's Functions 104
Orthogonal Boundary Conditions 105
Long and Short-Time Green's Functions 105
Neglecting Pipe Wall Thermal Resistance 106
Temperature Effects on the Convective Heat Transfer Coefficient 110
Computer Simulation using the Base Solution Generation Technique 116
Time Refinement 120
Base Solution Generation 124
Numeric Integration 130
Accuracy Verification 133
Simulation Times and Integration Step Sizes 136

7. SOIL TEMPERATURE SIMULATIONS 140

Under Yard Green's Function Formulation 141
Base Solution Generation Optimization of Under Yard Formulation 144
Refined Time Step 145
Numeric Integration Time Interval Analysis 146
Data Block Size 151
Under Yard Soil Temperature Simulations 152
Location Based Experimental Results 152
NRCS and TMY Boundary Condition Comparison 157
Soil Simulation Application to Earth-Air Heat Exchangers 159
Soil Diffusivity Effects 161
Soil Simulation at REHAU® Montana Ecosmart House Project 162
Soil Temperature Simulation Using a Surface Flux 166

TABLE OF CONTENTS CONTINUED

Soil Heat Flux Estimated from Surface Soil Temperature 167
Shifting Surface Temperatures for Zero Initial Flux 169
Building a Surface Flux Function 171
Green's Function Formulation for Surface Flux Boundary Condition 172
Base Solution Optimization of Surface Flux 173
Soil Heat Flux Simulation Results 174

8. SOIL TEMPERATURES BELOW AN ON-GRADE SLAB 179

Under Slab Green's Function Solution Formulation 180
Surface Flux Boundary for Non-Radiant Slabs 181
Space Integration of an Infinite Medium 183
Surface Temperature Boundary for Radiant Slabs 186
Base Solution Generation Optimization 187
Time Refinement for Non-Radiant On-Grade Slabs 187
Time Refinement for Radiant On-Grade Slabs 190
Optimized Base Solution Generation 191
Foundation Heat Loss Boundary Condition 191
Heat Loss for Non-Radiant Slabs 191
Temperature Function for Radiant Slabs 194
Soil Temperature Distributions Below On-Grade Slabs 195
Standard Foundation Size for Comparative Simulations 195
Simulation Results for Non-Radiant Slabs 197
Non-Radiant Slab Errors and Unrealistic Results 201
Effect of Insulation Thickness 202
Soil Diffusivity in Non-Radiant Slabs 203
Simulation Results for Radiant Slabs 206
Soil Diffusivity in Radiant Slabs 209
Translation to Under Slab EAHX Simulation 211

9. UNDER YARD AND UNDER SLAB EARTH-AIR HEAT EXCHANGER SIMULATIONS 212

Green's Function Formulations for Soil Conduction 213
Basis of One-Dimensional Model 213
Initial Condition Functions 214
Earth-Air Heat Exchanger One-Dimensional Green's Function Formulations 216
Under Yard Formulation for the Above Earth-Air Heat Exchanger 216
Non-Radiant Under Slab Formulation for the Above Earth-Air Heat Exchanger 218

TABLE OF CONTENTS CONTINUED

Radiant Under Slab Formulation for Above the Earth-Air Heat Exchanger 219
Below Earth-Air Heat Exchanger Solution 219
Mathematical Nature of Convective Green Functions 220
Justification for Short Time Solutions 223
Application of the Above/Below Earth-Air Heat Exchanger Simulation 224
2-D ANSYS Validation of 1-D Green's Function Simulation 227
Finite Difference Method for Transient Conduction Along Earth-Air Heat Exchangers 232
Basis of the Finite Difference Method 232
Time and Length Sub-Section Analysis 236
Validation with Computation Fluid Dynamics 239
Transient Validation 242
Choice of Pipe Surface Temperature Location 246
Conclusion to Computation Fluid Dynamics Validation 247
Computational Time Advantages of Finite Difference Method 248
Example Optimization of Green's Function Finite Difference Method 249
Optimization Method 250
Optimization Results and Comparison 251
Other Optimization Applications 257

10. CONCLUSION 258

11. FUTURE WORK 261

REFERENCES CITED 263

APPENDICES 271

APPENDIX A Experimental Data 272
APPENDIX B Location Weather Data and Curve Fits 312
APPENDIX C Estimated Soil Surface Heat Flux 328
APPENDIX D Under Yard Soil Temperatures 337
APPENDIX E Periodic Foundation Heat Loss Functions 391
APPENDIX F Soil Temperature Distributions Below On-Grade Slabs 400
APPENDIX G Example Programs 431

LIST OF TABLES

Table Page

1. Soil properties at 77ºF from GLD geothermal design software [6] 12
2. Soil and rock thermal properties from ASHRAE Handbook [7] 13
3. Moody diagram ε/D values for drawn tubing at various diameter piping..... 18
4. Experimental test dates for the under yard and under slab EAHXs at the REHAU® Montana Ecosmart House Project. 60
5. Under yard max and min temperatures and max cooling/heating temperature differences during each experiment period 63
6. Under slab max and min temperatures and max cooling/heating temperature differences during each experiment period 63
7. Average air velocity (ft/min) for each EAHX experiment..... 64
8. Fifteen locations chosen for EAHX simulations with base 65ºF heating degree day (HDD) and cooling degree day (CDD) values [13] 87
9. Boundary notation for Green's Function numbering system [72] 94
10. Time and space variable boundary condition notation for Green's Function numbering system [72]..... 94
11. Space variable initial condition notation for Green's Function numbering system [72]..... 95
12. Conductivity values of three common EAHX materials (Btu/hr·ft·°F) [75-77] 107
13. Pipe wall thermal resistance percentage for PVC and k_{soil} = 0.08 Btu/hr·ft·°F..... 108
14. Pipe wall thermal resistance percentage for PVC and k_{soil} = 1.25 Btu/hr·ft·°F..... 109
15. Pipe wall thermal resistance percentage for HDPE and k_{soil} = 0.08 Btu/hr·ft·°F..... 109

LIST OF TABLES CONTINUED

Table Page

16. Pipe wall thermal resistance percentage for HDPE and k_{soil} = 1.25 Btu/hr·ft·°F 109

17. Difference between the 0°F and 100°F convective heat transfer coefficients using the Gnielinski correlation 115

18. Computation time required for example simulations based on integration interval size, data blocks one day in length with one minute time interval 137

19. Simulation times in minutes for integration interval and data block size combinations over a 370 to 730 day simulation, 10 day interval 139

20. Arrays size for integration interval and data block size combinations over a 370 to 730 day simulation, 10 day interval 139

21. Temperature differences with depth between a non-refined and refined time soil simulation (730 day simulation for Bozeman, MT with 0.0015 1/ft^2 GF threshold) 146

22. Computational times for a 730 day simulation using one, five, and ten day data blocks, and a 10 minute integration interval 151

23. Residual sum of squares analysis ($^oF^2$) between observed values and the NRCS soil surface, TMY, and TMY corrected BCs 158

24. Standard foundation construction material properties and dimensions 196

25. Boundary condition values for the soil surface and air temperature in 2-D ANSYS validation of the 1-D above/below Green's Function solution method 228

26. Boundary condition temperatures for validation of the simplified EAHX 240

27. Optimization results for the under yard earth-air heat exchangers 252

28. Optimization results for the non-radiant slab earth-air heat exchangers 252

LIST OF TABLES CONTINUED

Table Page

29. Optimization results for the radiant-slab earth-air heat exchangers..... 253

30. Averaged data results for UY-Exp 1, 3/31/2013 to 4/23/2013 (avg – average, temp – temperature, std dev– standard deviation) 291

31. Averaged data results for UY-Exp 2, 6/22/2013 to 7/9/2013 (avg – average, temp – temperature, std dev– standard deviation) 292

32. Averaged data results for UY-Exp 3, 12/20/2013 to 1/8/2014 (avg – average, temp – temperature, std dev– standard deviation) 293

33. Averaged data results for UY-Exp 4, 2/4/2014 to 2/27/2014 (avg – average, temp – temperature, std dev– standard deviation) 294

34. Averaged data results for US-Exp 1, 3/14/2013 to 3/31/2013 (avg – average, temp – temperature, std dev– standard deviation) 295

35. Averaged data results for US-Exp 2, 4/23/2013 to 5/8/2013 (avg – average, temp – temperature, std dev– standard deviation) 297

36. Averaged data results for US-Exp 3, 1/10/2014 to 2/2/2014 (avg – average, temp – temperature, std dev– standard deviation) 298

37. Averaged data results for US-Exp 4, 3/18/2014 to 4/13/2014 (avg – average, temp – temperature, std dev– standard deviation) 299

LIST OF FIGURES

Figure Page

1. Early example of a windcatcher and earth-air heat exchanger in ancient Persian/Arabic architecture [4] 2
2. Example of two pipe legs on an earth-air heat exchanger 10
3. Moody diagram for friction factor in a circular pipe - permission to copy granted under the GNU Free Documentation License [3] 17
4. REHAU® Montana Ecosmart House Project [67] 50
5. The under yard and under slab EAHXs located at the REHAU® Montana Ecosmart House Project in relation to the residence's footprint, also pictured is location of sump-pumps, booster fans, and soil temperature sensors 51
6. Inlet towers of the under yard and under slab EAHXs directed directly into mechanical room through the foundation 52
7. Under yard EAHX during construction 53
8. Under slab EAHX during construction 54
9. Early slab construction at REHAU® Montana Ecosmart House Project 55
10. Left – Under yard wireless temperature/RH sensor located at the outlet, Right – Under slab wireless temperature/RH sensor located at the outlet, also pictured are the PEXa tubes for soil temperatures 56
11. Under yard soil temperature sensor locations, sensors distanced 12 inches from pipe center 57
12. Under slab soil temperature sensor locations, sensors distanced 16 inches from pipe center 58
13. Left – National Instruments SCXI 1000 chassis, Right – National Instruments cRIO 9072 59
14. Under yard inlet air temperature, outlet air temperatures, and corresponding air velocity for UY-Exp 3 62

LIST OF FIGURES CONTINUED

Figure Page

15. Under slab inlet air temperature, outlet air temperatures, and corresponding air velocity for US-Exp 3 62

16. Under yard inlet, outlet air relative humidity for UY-Exp 3..... 65

17. Under slab inlet, outlet air relative humidity for US-Exp 3..... 65

18. Under yard inlet dry bulb air temperatures, pipe surface temperature, and outdoor dew point for UY-Exp 3..... 68

19. Under slab inlet dry bulb air temperatures, pipe surface temperature, and outdoor dew point for US-Exp 3 69

20. Under yard soil temperatures for UY-Exp 3 69

21. Under yard inlet dry bulb air temperature compared to changes in soil temperatures for UY-Exp 3 70

22. Under slab soil temperatures for US-Exp 3..... 72

23. Under slab inlet dry bulb air temperature compared to changes in soil temperatures for US-Exp 3..... 72

24. Basement radiant slab temperatures for US-Exp 3, these four sensors cover majority of US EAHX..... 73

25. Soil temperatures measured away from the EAHXs and RMEH foundation from June, 2013 to April, 2014..... 75

26. Under yard outlet vs. inlet averaged dry bulb air temperature and average pipe surface temperatures for UY-Exp 3, error bars represent standard deviation of averaged outlet temperature..... 78

27. Under slab outlet vs. inlet averaged dry bulb air temperature and average pipe surface temperatures for US-Exp 3, error bars represent standard deviation of averaged outlet temperature..... 79

28. Under yard averaged dry bulb air temperature outlet vs. inlet for four testing periods..... 79

LIST OF FIGURES CONTINUED

Figure Page

29. Under slab averaged dry bulb air temperature outlet vs. inlet for four testing periods 80

30. Under yard outlet vs. inlet averaged dry bulb air temperature and average pipe surface temperatures when available for all testing periods, error bars represent standard deviation of averaged outlet temperature 80

31. Under slab outlet vs. inlet averaged dry bulb air temperature and average pipe surface temperatures when available for all testing periods, error bars represent standard deviation of averaged outlet temperature 81

32. Under yard vs. under slab averaged dry bulb air temperature outlet for all testing periods 81

33. Coefficient of performance for the under yard EAHX based on inlet temperature for UY-Exp 3 83

34. Coefficient of performance for the under slab EAHX based on inlet temperature for US-Exp 3 84

35. Coefficient of performance for the under yard and under slab EAHX based on the averaged inlet and outlet temperatures for all testing periods 84

36. Fifteen locations chosen for EAHX simulations based on availability of soil and air temperature data 87

37. Example of space and time non-homogeneous boundary condition common in US EAHX simulation 91

38. Green's Function number system example, X12B14Y31B10T2 problem type 95

39. Space variable boundary conditions example (X22B00Y12Bx51T0 type) 101

40. Example Green's Function method setup – semi-infinite solid with constant surface temperature T_s and homogenous initial condition 102

LIST OF FIGURES CONTINUED

Figure Page

41. Thermal circuit for one-dimensional heat transfer between soil surface temperature and air convection inside the EAHX pipe 107

42. Heat transfer coefficient vs. dry bulb temperature for internal turbulent flow in an eight inch pipe for Gnielinski and Dittus-Boelter correlations 113

43. Heat transfer coefficient vs. dry bulb temperature for internal turbulent flow at 1000 FPM air velocity for Gnielinski and Dittus-Boelter correlations 114

44. Heat transfer coefficient vs. air temperature from the Gnielinski correlation at various air velocities in an eight inch pipe..... 114

45. Heat transfer coefficient vs. air temperature from the Gnielinski correlation for various pipe diameters at air velocity of 1000 FPM 115

46. Simplified trapezoidal rule integration example where the light dotted line is the product of the BC and GF graphed with respect to dummy time "τ" 118

47. Generalized diagram of programs and inputs in the Base Solution Generation technique..... 119

48. Values at different depths for the derivative of an G_{Y10} GF, Equation (55), with respect to the dummy time variable "τ" 121

49. Closer view of the G_{Y10} GF derivative in Equation (54), with respect to the dummy time variable "τ"..... 123

50. 1-D semi-infinite solid with constant surface temperature, temperature distribution represented by 6 x 1 grid for computer simulation..... 126

51. Example of three-dimensional data block used for calculating GF values..... 128

52. Example problem for verification of Base Solution Generation Technique, semi-infinite solid with constant surface temperature (Y10B1T0 problem type)..... 133

LIST OF FIGURES CONTINUED

Figure Page

53. Temperature distribution after 1095 days (3 years) using BSG technique compared the exact solution for Y10B1T0 problem type 135

54. Three year (1095 days) BSG solution using full simulation time and refined simulation time for GFs above $2.5 \cdot 10^{-4}$ $1/ft^2$ only or 906 days..... 136

55. Soil conduction problem setup for Green's Function method, Y10B-T1 problem type 141

56. Bozeman, Montana– Least-squares curve fit to observed soil surface temperatures using four term Fourier series..... 143

57. Bozeman, Montana – Least-squares curve fit to dry bulb air temperatures from a typical meteorological year (TMY) using four term Fourier series..... 144

58. Soil temperatures for the numerical integration time step comparison over one year time period in Bozeman, MT for a depth of one inch 147

59. Soil temperatures for the numerical integration time step comparison over one year time period in Bozeman, MT for a depth of five inches..... 148

60. Soil temperatures for the numerical integration time step comparison over one year time period in Bozeman, MT for a depth of 72 inches..... 149

61. Soil temperatures for the numerical integration time step comparison over one year time period in Columbus, OH for a depth of 72 inches..... 149

62. Soil temperatures for the numerical integration time step comparison over one year time period in Houston, TX for a depth of 72 inches..... 150

63. Closer inspection of numerical integration time step comparison from days 200 to 300 of a typical year for Bozeman, MT for a depth of 72 inches 150

64. Bozeman, Montana – 20 inch observed vs. simulated Green's Function soil temperatures – observed surface soil temperature boundary condition..... 155

LIST OF FIGURES CONTINUED

Figure Page

65. Bozeman, Montana – 40 inch observed vs. simulated Green's Function soil temperatures – observed surface soil temperature boundary condition 155

66. Bozeman, Montana – 20 inch observed vs. simulated Green's Function soil temperatures – typical meteorological year (TMY) and corrected TMY surface air temperature boundary conditions 156

67. Bozeman, Montana – 40 inch observed vs. simulated Green's Function soil temperatures – typical meteorological year (TMY) and corrected TMY surface air temperature boundary conditions 156

68. Residual sum of squares results ($^oF^2$) between observed values and the NRCS soil surface, TMY, and TMY corrected BCs at 40 inch depth 158

69. Bozeman, Montana – simulated Green's Function soil temperatures at various depths– observed surface soil temperature boundary condition 160

70. Bozeman, Montana – simulated Green's Function soil temperatures at various depths – corrected TMY surface air temperature boundary condition 161

71. Soil temperatures using diffusivity extremes for Bozeman at 6 feet (72 inches) 162

72. REHAU® Montana Ecosmart House Project observed surface soil temperature, missing data made up with NRCS soil temperature data 163

73. Surface soil temperatures and least-squares regression fit with a Fourier series at the REHAU® Montana Ecosmart House Project 164

74. Observed vs. simulated soil temperatures at 4ft depth for the REHAU® Montana Ecosmart House project using the Ecohouse surface temperature BC 165

75. Diffusivity calibration for the REHAU® Montana Ecosmart House soil simulations at 4ft depth 166

LIST OF FIGURES CONTINUED

Figure Page

76. Bozeman, Montana – Least squares curve fit to shifted soil temperature shifted forward 119 days using four term Fourier series 171

77. Bozeman, Montana – estimated soil surface heat flux function using the NRCS soil surface temperatures over a two year period starting on Julian day 119..... 172

78. Green's Function values for a semi-infinite medium with surface heat flux, problem type GY20..... 174

79. Amarillo, Texas – 20 inch observed vs. simulated soil temperatures using the surface flux boundary condition derived from both soil surface and air surface temperatures 176

80. Pine Bluff, Arkansas – 20 inch observed vs. simulated soil temperatures using the surface flux boundary condition derived from both soil surface and air surface temperatures 176

81. Columbus, Ohio – Least squares curve fit to shifted soil temperature shifted forward 102.8 days using four term Fourier series 178

82. Columbus, Ohio – estimated soil surface heat flux function using the NRCS soil surface temperatures over a two year period starting on Julian day 102.8..... 178

83. Heat flow paths from a below grade surface – courtesy of the 2009 ASHRAE Fundamentals, Chapter 18 Non-Residential Cooling and Heating Load Calculations [80] 179

84. Two-dimensional domain for under slab Green's Function soil formulation..... 181

85. Value of the space integration functions for ±20 feet from foundation center, slab is 20 feet in length..... 185

86. Green's Function values over one year for the flux based solution (G_{Y20}) on the positive soil boundary [Equation (73)], space integration included..... 189

LIST OF FIGURES CONTINUED

Figure Page

87. Green's Function values over one year for the flux based boundary (G_{Y20}) on the positive soil boundary [Equation (73)] and foundation slab [Equation (74)], space integration included 189

88. Green's Function values over one year for the temperature based solution (G_{Y10}) on the positive soil boundary [Equation (82)], space integration included 190

89. Left – heat loss factor h_s for no insulation on soil surface Right – Absolute value of $|h_p^1|$ and φ_p^1 [61] 194

90. Standard foundation construction and geometry for non-radiant on-grade slab simulations 196

91. Houston, Texas – soil temperature distribution for non-radiant slab at 180 days (top), 270 days (middle), and 360 days (bottom) starting from January 1st for a slab length of 40 feet 199

92. Bozeman, Montana– soil temperature distribution for non-radiant slab at 180 days (top), 270 days (middle), and 360 days (bottom) starting from January 1st for a slab length of 40 feet 200

93. Under slab temperature distribution for Bozeman, Montana on day 180 with the y-axis centered on the foundations edge instead of the foundation center 202

94. Soil temperature distributions under a non-radiant slab for Bozeman, Montana at day 270 using foundation insulation thicknesses of 2, 4, 6, 8 inches from top (2 in) to bottom (8 in) 204

95. Soil temperature distributions under a no-radiant slab for Bozeman, Montana at day 270 using soil diffusivity of 0.6, 0.8, 1.0, and 1.2 ft^2/day from top (0.6 ft^2/day) to bottom (1.2 ft^2/day) 205

96. Houston, Texas– soil temperature distribution for a radiant slab at 180 days (top), 270 days (middle), and 360 days (bottom) starting from January 1st for a slab length of 40 feet 207

97. Bozeman, Montana – soil temperature distribution for a radiant slab at 180 days (top), 270 days (middle), and 360 days (bottom) starting from January 1st for a slab length of 40 feet 208

LIST OF FIGURES CONTINUED

Figure Page

98. Soil temperature distributions under a radiant slab for Bozeman, Montana at day 270 using soil diffusivity of 0.6, 0.8, 1.0, and 1.2 ft^2/day from top (0.6 ft^2/day) to bottom (1.2 ft^2/day) 210

99. Basis of one-dimensional under yard and under slab EAHX split into two independent solution zones 212

100. Detailed representation of the 1-D "above/below EAHX" simulation setup for the under yard and under slabs locations 214

101. Piece-wise initial condition assembled from a previous temperature distribution for Bozeman, Montana on January 1st at 12:00 AM..... 216

102. Value of G_{Y31} GF over a simulation time of 20 days (τ axis is 20 days), domain depth is five feet 222

103. Value of G_{Y32} GF over a simulation time of 20 days (τ axis is 20 days), domain depth is five feet 222

104. Example soil temperature distribution for the under yard EAHX buried at a six foot depth after six hours of operation starting on July 1st at midnight..... 225

105. Example soil temperature distribution for the non-radiant under slab EAHX buried at a three foot depth after six hours of operation starting on July 1st at midnight 225

106. Example soil temperature distribution for the radiant under slab EAHX buried at a three foot depth after six hours of operation starting on July 1st at midnight 226

107. Domain size and boundary conditions in 2-D ANSYS validation of the 1-D above/below Green's Function solution method..... 228

108. Mesh sizing for the 2-D ANSYS validation of the 1-D above/below Green's Function solution method 229

109. Initial condition for the 2-D ANSYS validation of the 1-D above/below Green's Function solution method..... 230

LIST OF FIGURES CONTINUED

Figure Page

110. Results of 2-D ANSYS EAHX after six hours of operation using the domain and boundary conditions in Figure 107 and Table 25 231

111. Validation of the "above/below EAHX" Green's Function method with a 2-D transient finite element simulation over a six hour time frame 231

112. Green's Function finite difference method example 236

113. Air temperature along a 100 foot EAHX for time steps of 15 minutes to 60 minutes in 15 minute increments, and length steps of 0.25 feet to 4 feet in 0.25 foot increments located in Bozeman, MT from January 1st, 12:00 AM to 6:00 AM 237

114. Pipe surface temperature along a 100 foot EAHX for time steps of 15 minutes to 60 minutes in 15 minute increments, and length steps of 0.25 feet to 4 feet in 0.25 foot increments located in Bozeman, MT from January 1st, 12:00 AM to 6:00 AM 238

115. Air temperature along a 100 foot EAHX located in Bozeman, MT from January 1st, 12:00 AM to 6:00 AM for time steps ranging from 1 to 20 239

116. Simplifed EAHX for the computational fludi dynamics validation of the finite difference method and its assumptions (all dimensions in inches) 240

117. Polyhedral mesh for the finite difference method validation 241

118. Air temperatures along the simplified 50 foot EAHX one hour into the four hour transient validation, CFD results compared to the EAHX finite difference method using a 20 minute time step 242

119. Air temperatures along the simplified 50 foot EAHX two hours into the four hour transient validation, CFD results compared to the EAHX finite difference method using a 20 minute time step 243

120. Air temperatures along the simplified 50 foot EAHX three hours into the four hour transient validation, CFD results compared to the EAHX finite difference method using a 20 minute time step 243

LIST OF FIGURES CONTINUED

Figure Page

121. Air temperatures along the simplified 50 foot EAHX four hours into the four hour transient validation, CFD results compared to the EAHX finite difference method using a 20 minute time step 244

122. Soil temperatures at the midpoint of the simplified 50 foot EAHX two hours into the four hour transient simulation using the EAHX finite difference method with 20 minute time step, compared to the CFD soil temperatures 245

123. Soil temperatures at the midpoint of the simplified 50 foot EAHX four hours into the four hour transient simulation using the EAHX finite difference method with 20 minute time step, compared to the CFD soil temperatures 245

124. Comparison of pipe surface temperature during 5 and 20 minute time steps where the reference temperature is taken 1 inch and ½ inch from the pipe surface, two hours into the four hour CFD validation simulation 247

125. Optimization procedure based off the Newton-Raphson method 251

126. Optimized earth-air heat exchanger lengths for the under yard, non-radiant under slab, and radiant under slab installation locations 253

127. Total heat transfer in the optimized earth-air heat exchanger for the under yard, non-radiant under slab, and radiant under slab installation locations 254

128. Heat transfer per unit length in the optimized earth-air heat exchanger for the under yard, non-radiant under slab, and radiant under slab installation locations 254

129. Comparison of the under yard and non-radiant under slab air temperature and pipe surface temperature along the optimized earth-air heat exchanger length in Bozeman, Montana 256

130. Comparison of the under yard and non-radiant under slab air temperature and pipe surface temperature along the optimized earth-air heat exchanger length in Houston, Texas 256

LIST OF FIGURES CONTINUED

Figure Page

131. Dimensions of the under yard (UY) earth-air heat exchanger located at the REHAU® Montana Ecosmart House Project in Bozeman, Montana 273

132. Dimensions of the under slab (US) earth-air heat exchanger located at the REHAU® Montana Ecosmart House Project in Bozeman, Montana 273

133. Under yard inlet air temperature, outlet air temperatures, and corresponding air velocity for UY-Exp 1 274

134. Under yard inlet air temperature, outlet air temperatures, and corresponding air velocity for UY-Exp 2 274

135. Under yard inlet air temperature, outlet air temperatures, and corresponding air velocity for UY-Exp 4 275

136. Under slab inlet air temperature, outlet air temperatures, and corresponding air velocity for US-Exp 1 275

137. Under slab inlet air temperature, outlet air temperatures, and corresponding air velocity for US-Exp 2 276

138. Under slab inlet air temperature and outlet air temperatures for US-Exp 4 276

139. Under yard inlet, outlet air relative humidity for UY-Exp 1 277

140. Under yard inlet, outlet air relative humidity for UY-Exp 2 277

141. Under yard inlet, outlet air relative humidity for UY-Exp 4 278

142. Under slab inlet, outlet air relative humidity for US-Exp 1 278

143. Under slab inlet, outlet air relative humidity for US-Exp 2 279

144. Under slab inlet, outlet air relative humidity for US-Exp 4 279

145. Under yard inlet /outlet dry bulb temperatures and outdoor dew point for UY-Exp 1 280

LIST OF FIGURES CONTINUED

Figure Page

146. Under yard inlet /outlet dry bulb temperatures and outdoor dew point for UY-Exp 2 280

147. Under yard inlet dry bulb air temperatures, pipe surface temperature, and outdoor dew point for UY-Exp 4..... 281

148. Under slab inlet dry bulb air temperatures, pipe surface temperature, and outdoor dew point for US-Exp 1 281

149. Under slab inlet dry bulb air temperatures, pipe surface temperature, and outdoor dew point for US-Exp 2 282

150. Under slab inlet dry bulb air temperatures, pipe surface temperature, and outdoor dew point for US-Exp 4 282

151. Under yard soil temperatures for UY-Exp 4 283

152. Under yard inlet dry bulb air temperature compared to changes in soil temperatures for UY-Exp 4 283

153. Under slab soil temperatures for US-Exp 1..... 284

154. Under slab inlet dry bulb air temperature compared to changes in soil temperatures for US-Exp 1 284

155. Under slab soil temperatures for US-Exp 2..... 285

156. Under slab inlet dry bulb air temperature compared to changes in soil temperatures for US-Exp 2 285

157. Under slab soil temperatures for US-Exp 4..... 286

158. Under slab inlet dry bulb air temperature compared to changes in soil temperatures for US-Exp 4 286

159. Basement radiant slab temperatures for US-Exp 1, these four sensors cover majority of US EAHX 287

160. Basement radiant slab temperatures for US-Exp 2, these four sensors cover majority of US EAHX 287

LIST OF FIGURES CONTINUED

Figure Page

161. Basement radiant slab temperatures for US-Exp 4, these four sensors cover majority of US EAHX 288

162. Under yard outlet vs. inlet averaged dry bulb air temperature and average pipe surface temperatures for UY-Exp 1, 3/31/2013 to 4/23/2013 experiment, error bars represent standard deviation of averaged outlet temperature 288

163. Under yard outlet vs. inlet averaged dry bulb air temperature and average pipe surface temperatures for UY-Exp 2, 6/22/2013 to 7/9/2013 experiment, error bars represent standard deviation of averaged outlet temperature 289

164. Under yard outlet vs. inlet averaged dry bulb air temperature and average pipe surface temperatures for UY-Exp 4, 2/4/2014 to 2/27/2014 experiment, error bars represent standard deviation of averaged outlet temperature 289

165. Under slab outlet vs. inlet averaged dry bulb air temperature and average pipe surface temperatures for US-Exp 1, 3/14/2013 to 3/31/2013 experiment, error bars represent standard deviation of averaged outlet temperature 290

166. Under slab outlet vs. inlet averaged dry bulb air temperature and average pipe surface temperatures for US-Exp 2, 4/23/2013 to 5/8/2013 experiment, error bars represent standard deviation of averaged outlet temperature 290

167. Under slab outlet vs. inlet averaged dry bulb air temperature and average pipe surface temperatures for US-Exp 4, 3/18/2014 to 4/13/2014 experiment, error bars represent standard deviation of averaged outlet temperature 291

168. Coefficient of performance for the under yard EAHX based on inlet temperature for UY-Exp 1 301

169. Coefficient of performance for the under yard EAHX based on inlet temperature for UY-Exp 2 301

170. Coefficient of performance for the under yard EAHX based on inlet temperature for UY-Exp 4 302

LIST OF FIGURES CONTINUED

Figure Page

171. Coefficient of performance for the under slab EAHX based on inlet temperature for US-Exp 1 302

172. Coefficient of performance for the under slab EAHX based on inlet temperature for US-Exp 2 303

173. Coefficient of performance for the under slab EAHX based on inlet temperature for US-Exp 4 303

174. Albuquerque, New Mexico – observed ground temperatures at 20 inch and 40 inch depths (taken from Los Lunas PMC site outside of Albuquerque, NM) [71]..... 304

175. Amarillo, Texas – observed ground temperatures at 20 inch and 40 inch depths (taken from Bushland site outside of Amarillo, TX) [71] 304

176. Athens, Georgia – observed ground temperatures at 20 inch and 40 inch depths (taken from Watkinsville site outside of Athens, GA) [71] 305

177. Bozeman, Montana – observed ground temperatures at 20 inch and 40 inch depths (taken from Table Mountain site outside of Bozeman, MT) [71] 305

178. Columbus, Ohio – observed ground temperatures at 20 inch and 40 inch depths (taken from Moly Caren site outside of Columbus, OH) [71] 306

179. Houston, Texas – observed ground temperatures at 20 inch and 40 inch depths (taken from Prairie View #1 site outside of Houston, TX) [71]..... 306

180. Kansas City, Missouri – observed ground temperatures at 20 inch and 40 inch depths (taken from Powell Gardens site outside of Kansas City, MO) [71] 307

181. Las Vegas, Nevada – observed ground temperatures at 20 inch and 40 inch depths (taken from Pine Nut site outside of Las Vegas, NV) [71] 307

LIST OF FIGURES CONTINUED

Figure Page

182. Moses Lake, Washington – observed ground temperatures at 20 inch and 40 inch depths (taken from Lind site outside of Moses Lake, WA) [71] 308

183. Pine Bluff, Arkansas – observed ground temperatures at 20 inch and 40 inch depths (taken from UAPB Campus-PB site outside of Pine Bluff, AR) [71] 308

184. Saint Cloud, Minnesota – observed ground temperatures at 20 inch and 40 inch depths (taken from Crescent Lake site outside of Saint Cloud, MN) [71] 309

185. Salt Lake City, Utah – observed ground temperatures at 20 inch and 40 inch depths (taken from Grantsville site outside of Salt Lake City, UT) [71] 309

186. Sioux Falls, South Dakota – observed ground temperatures at 20 inch and 40 inch depths (taken from EROS Data Center site outside of Sioux Falls, SD) [71] 310

187. State College, Pennsylvania – observed ground temperatures at 20 inch and 40 inch depths (taken from EROS Data Center site outside of Sioux Falls, SD) [71] 310

188. Tallahassee, Florida – observed ground temperatures at 20 inch and 40 inch depths (taken from Wakulla site outside of Tallahassee, FL) [71] 311

189. Albuquerque, New Mexico – Least-squares curve fit to observed soil surface temperatures using four term Fourier series 313

190. Albuquerque, New Mexico – Least-squares curve fit to dry bulb air temperatures from a typical meteorological year (TMY) using four term Fourier series 313

191. Amarillo, Texas – Least-squares curve fit to observed soil surface temperatures using four term Fourier series 314

192. Amarillo, Texas – Least-squares curve fit to dry bulb air temperatures from a typical meteorological year (TMY) using four term Fourier series 314

LIST OF FIGURES CONTINUED

Figure Page

193. Athens, Georgia – Least-squares curve fit to observed soil surface temperatures using four term Fourier series 315

194. Athens, Georgia – Least-squares curve fit to dry bulb air temperatures from a typical meteorological year (TMY) using four term Fourier series 315

195. Bozeman, Montana– Least-squares curve fit to observed soil surface temperatures using four term Fourier series 316

196. Bozeman, Montana – Least-squares curve fit to dry bulb air temperatures from a typical meteorological year (TMY) using four term Fourier series 316

197. Columbus, Ohio – Least-squares curve fit to observed soil surface temperatures using four term Fourier series 317

198. Columbus, Ohio – Least-squares curve fit to dry bulb air temperatures from a typical meteorological year (TMY) using four term Fourier series 317

199. Houston, Texas – Least-squares curve fit to observed soil surface temperatures using four term Fourier series 318

200. Houston, Texas – Least-squares curve fit to dry bulb air temperatures from a typical meteorological year (TMY) using four term Fourier series 318

201. Figure 201: Kansas City, Missouri – Least-squares curve fit to observed soil surface temperatures using four term Fourier series 319

202. Kansas City, Missouri – Least-squares curve fit to dry bulb air temperatures from a typical meteorological year (TMY) using four term Fourier series 319

203. Las Vegas, Nevada – Least-squares curve fit to observed soil surface temperatures using four term Fourier series 320

204. Las Vegas, Nevada – Least-squares curve fit to dry bulb air temperatures from a typical meteorological year (TMY) using four term Fourier series 320

LIST OF FIGURES CONTINUED

Figure Page

205. Moses Lake, Washington – Least-squares curve fit to observed soil surface temperatures using four term Fourier series 321

206. Moses Lake, Washington – Least-squares curve fit to dry bulb air temperatures from a typical meteorological year (TMY) using four term Fourier series..... 321

207. Pine Bluff, Arkansas – Least-squares curve fit to observed soil surface temperatures using four term Fourier series 322

208. Pine Bluff, Arkansas – Least-squares curve fit to dry bulb air temperatures from a typical meteorological year (TMY) using four term Fourier series..... 322

209. Saint Cloud, Minnesota – Least-squares curve fit to observed soil surface temperatures using four term Fourier series 323

210. Saint Cloud, Minnesota – Least-squares curve fit to dry bulb air temperatures from a typical meteorological year (TMY) using four term Fourier series..... 323

211. Salt Lake City, Utah – Least-squares curve fit to observed soil surface temperatures using four term Fourier series 324

212. Salt Lake City, Utah – Least-squares curve fit to dry bulb air temperatures from a typical meteorological year (TMY) using four term Fourier series..... 324

213. Sioux Falls, South Dakota – Least-squares curve fit to observed soil surface temperatures using four term Fourier series 325

214. Sioux Falls, South Dakota – Least-squares curve fit to dry bulb air temperatures from a typical meteorological year (TMY) using four term Fourier series..... 325

215. State College, Pennsylvania – Least-squares curve fit to observed soil surface temperatures using four term Fourier series 326

216. State College, Pennsylvania – Least-squares curve fit to dry bulb air temperatures from a typical meteorological year (TMY) using four term Fourier series..... 326

LIST OF FIGURES CONTINUED

Figure Page

217. Tallahassee, Florida – Least-squares curve fit to observed soil surface temperatures using four term Fourier series 327

218. Tallahassee, Florida – Least-squares curve fit to dry bulb air temperatures from a typical meteorological year (TMY) using four term Fourier series..... 327

219. Albuquerque, New Mexico – estimated soil surface heat flux function using the NRCS soil surface temperatures over a two year period starting on Julian day 98.2 329

220. Amarillo, Texas – estimated soil surface heat flux function using the NRCS soil surface temperatures over a two year period starting on Julian day 111..... 329

221. Athens, Georgia – estimated soil surface heat flux function using the NRCS soil surface temperatures over a two year period starting on Julian day 109..... 330

222. Bozeman, Montana – estimated soil surface heat flux function using the NRCS soil surface temperatures over a two year period starting on Julian day 119..... 330

223. Columbus, Ohio – estimated soil surface heat flux function using the NRCS soil surface temperatures over a two year period starting on Julian day 102.4..... 331

224. Houston, Texas – estimated soil surface heat flux function using the NRCS soil surface temperatures over a two year period starting on Julian day 102.9..... 331

225. Kansas City, Missouri– estimated soil surface heat flux function using the NRCS soil surface temperatures over a two year period starting on Julian day 106.6..... 332

226. Las Vegas, Nevada – estimated soil surface heat flux function using the NRCS soil surface temperatures over a two year period starting on Julian day 109.6..... 332

LIST OF FIGURES CONTINUED

Figure Page

227. Moses Lake, Washington– estimated soil surface heat flux function using the NRCS soil surface temperatures over a two year period starting on Julian day 115.7 333

228. Pine Bluff, Arkansas – estimated soil surface heat flux function using the NRCS soil surface temperatures over a two year period starting on Julian day 108.6 333

229. St. Cloud, Minnesota – estimated soil surface heat flux function using the NRCS soil surface temperatures over a two year period starting on Julian day 124.5 334

230. Salt Lake City, Utah – estimated soil surface heat flux function using the NRCS soil surface temperatures over a two year period starting on Julian day 118.3 334

231. Sioux Falls, South Dakota– estimated soil surface heat flux function using the NRCS soil surface temperatures over a two year period starting on Julian day 117.2 335

232. State College, Pennsylvania – estimated soil surface heat flux function using the NRCS soil surface temperatures over a two year period starting on Julian day 114.7 335

233. Tallahassee, Florida – estimated soil surface heat flux function using the NRCS soil surface temperatures over a two year period starting on Julian day 93.3 336

234. Albuquerque, New Mexico – 20 inch observed vs. simulated Green's Function soil temperatures – observed surface soil temperature boundary condition 338

235. Albuquerque, New Mexico – 40 inch observed vs. simulated Green's Function soil temperatures – observed surface soil temperature boundary condition 338

236. Albuquerque, New Mexico – 20 inch observed vs. simulated Green's Function soil temperatures – typical meteorological year (TMY) and corrected TMY surface air temperature boundary conditions 339

LIST OF FIGURES CONTINUED

Figure Page

237. Albuquerque, New Mexico – 40 inch observed vs. simulated Green's Function soil temperatures – typical meteorological year (TMY) and corrected TMY surface air temperature boundary conditions 339

238. Albuquerque, New Mexico – simulated Green's Function soil temperatures at various depths– observed surface soil temperature boundary condition..... 340

239. Albuquerque, New Mexico – simulated Green's Function soil temperatures at various depths – corrected TMY surface air temperature boundary condition..... 340

240. Amarillo, Texas – 20 inch observed vs. simulated Green's Function soil temperatures – observed surface soil temperature boundary condition..... 341

241. Amarillo, Texas – 40 inch observed vs. simulated Green's Function soil temperatures – observed surface soil temperature boundary condition..... 341

242. Amarillo, Texas – 20 inch observed vs. simulated Green's Function soil temperatures – typical meteorological year (TMY) and corrected TMY surface air temperature boundary conditions 342

243. Amarillo, Texas – 40 inch observed vs. simulated Green's Function soil temperatures – typical meteorological year (TMY) and corrected TMY surface air temperature boundary conditions 342

244. Amarillo, Texas – simulated Green's Function soil temperatures at various depths– observed surface soil temperature boundary condition..... 343

245. Amarillo, Texas – simulated Green's Function soil temperatures at various depths – corrected TMY surface air temperature boundary condition..... 343

246. Athens, Georgia – 20 inch observed vs. simulated Green's Function soil temperatures – observed surface soil temperature boundary condition..... 344

LIST OF FIGURES CONTINUED

Figure Page

247. Athens, Georgia – 40 inch observed vs. simulated Green's Function soil temperatures – observed surface soil temperature boundary condition 344

248. Athens, Georgia – 20 inch observed vs. simulated Green's Function soil temperatures – typical meteorological year (TMY) and corrected TMY surface air temperature boundary conditions 345

249. Athens, Georgia – 40 inch observed vs. simulated Green's Function soil temperatures – typical meteorological year (TMY) and corrected TMY surface air temperature boundary conditions 345

250. Athens, Georgia – simulated Green's Function soil temperatures at various depths– observed surface soil temperature boundary condition 346

251. Athens, Georgia – simulated Green's Function soil temperatures at various depths – corrected TMY surface air temperature boundary condition 346

252. Columbus, Ohio – 20 inch observed vs. simulated Green's Function soil temperatures – observed surface soil temperature boundary condition 347

253. Columbus, Ohio – 40 inch observed vs. simulated Green's Function soil temperatures – observed surface soil temperature boundary condition 347

254. Columbus, Ohio – 20 inch observed vs. simulated Green's Function soil temperatures – typical meteorological year (TMY) and corrected TMY surface air temperature boundary conditions 348

255. Columbus, Ohio – 40 inch observed vs. simulated Green's Function soil temperatures – typical meteorological year (TMY) and corrected TMY surface air temperature boundary conditions 348

256. Columbus, Ohio – simulated Green's Function soil temperatures at various depths– observed surface soil temperature boundary condition 349

LIST OF FIGURES CONTINUED

Figure Page

257. Columbus, Ohio – simulated Green's Function soil temperatures at various depths – corrected TMY surface air temperature boundary condition 349

258. Houston, Texas – 20 inch observed vs. simulated Green's Function soil temperatures – observed surface soil temperature boundary condition 350

259. Houston, Texas – 40 inch observed vs. simulated Green's Function soil temperatures – observed surface soil temperature boundary condition 350

260. Houston, Texas – 20 inch observed vs. simulated Green's Function soil temperatures – typical meteorological year (TMY) and corrected TMY surface air temperature boundary conditions 351

261. Houston, Texas – 40 inch observed vs. simulated Green's Function soil temperatures – typical meteorological year (TMY) and corrected TMY surface air temperature boundary conditions 351

262. Houston, Texas – simulated Green's Function soil temperatures at various depths– observed surface soil temperature boundary condition 352

263. Houston, Texas – simulated Green's Function soil temperatures at various depths– corrected TMY surface air temperature boundary condition 352

264. Kansas City, Missouri – 20 inch observed vs. simulated Green's Function soil temperatures – observed surface soil temperature boundary condition 353

265. Kansas City, Missouri – 40 inch observed vs. simulated Green's Function soil temperatures – observed surface soil temperature boundary condition 353

266. Kansas City, Missouri – 20 inch observed vs. simulated Green's Function soil temperatures – typical meteorological year (TMY) and corrected TMY surface air temperature boundary conditions 354

LIST OF FIGURES CONTINUED

Figure Page

267. Kansas City, Missouri – 40 inch observed vs. simulated Green's Function soil temperatures – typical meteorological year (TMY) and corrected TMY surface air temperature boundary conditions..... 354

268. Kansas City, Missouri – simulated Green's Function soil temperatures at various depths– observed surface soil temperature boundary condition..... 355

269. Kansas City, Missouri – simulated Green's Function soil temperatures at various depths – corrected TMY surface air temperature boundary condition..... 355

270. Las Vegas, Nevada – 20 inch observed vs. simulated Green's Function soil temperatures – observed surface soil temperature boundary condition..... 356

271. Las Vegas, Nevada – 40 inch observed vs. simulated Green's Function soil temperatures – observed surface soil temperature boundary condition..... 356

272. Las Vegas, Nevada – 20 inch observed vs. simulated Green's Function soil temperatures – typical meteorological year (TMY) and corrected TMY surface air temperature boundary conditions..... 357

273. Las Vegas, Nevada – 40 inch observed vs. simulated Green's Function soil temperatures – typical meteorological year (TMY) and corrected TMY surface air temperature boundary conditions..... 357

274. Las Vegas, Nevada – simulated Green's Function soil temperatures at various depths– observed surface soil temperature boundary condition..... 358

275. Las Vegas, Nevada – simulated Green's Function soil temperatures at various depths – corrected TMY surface air temperature boundary condition..... 358

276. Moses Lake, Washington – 20 inch observed vs. simulated Green's Function soil temperatures – observed surface soil temperature boundary condition..... 359

LIST OF FIGURES CONTINUED

Figure Page

277. Moses Lake, Washington – 40 inch observed vs. simulated Green's Function soil temperatures – observed surface soil temperature boundary condition 359

278. Moses Lake, Washington – 20 inch observed vs. simulated Green's Function soil temperatures – typical meteorological year (TMY) and corrected TMY surface air temperature boundary conditions 360

279. Moses Lake, Washington – 40 inch observed vs. simulated Green's Function soil temperatures – typical meteorological year (TMY) and corrected TMY surface air temperature boundary conditions 360

280. Moses Lake, Washington – simulated Green's Function soil temperatures at various depths– observed surface soil temperature boundary condition 361

281. Moses Lake, Washington – simulated Green's Function soil temperatures at various depths – corrected TMY surface air temperature boundary condition 361

282. Pine Bluff, Arkansas – 20 inch observed vs. simulated Green's Function soil temperatures – observed surface soil temperature boundary condition 362

283. Pine Bluff, Arkansas – 40 inch observed vs. simulated Green's Function soil temperatures – observed surface soil temperature boundary condition 362

284. Pine Bluff, Arkansas – 20 inch observed vs. simulated Green's Function soil temperatures – typical meteorological year (TMY) and corrected TMY surface air temperature boundary conditions 363

285. Pine Bluff, Arkansas – 40 inch observed vs. simulated Green's Function soil temperatures – typical meteorological year (TMY) and corrected TMY surface air temperature boundary conditions 363

286. Pine Bluff, Arkansas – simulated Green's Function soil temperatures at various depths– observed surface soil temperature boundary condition 364

LIST OF FIGURES CONTINUED

Figure Page

287. Pine Bluff, Arkansas – simulated Green's Function soil temperatures at various depths – corrected TMY surface air temperature boundary condition 364

288. Saint Cloud, Minnesota – 20 inch observed vs. simulated Green's Function soil temperatures – observed surface soil temperature boundary condition 365

289. Saint Cloud, Minnesota – 40 inch observed vs. simulated Green's Function soil temperatures – observed surface soil temperature boundary condition 365

290. Saint Cloud, Minnesota – 20 inch observed vs. simulated Green's Function soil temperatures – typical meteorological year (TMY) and corrected TMY surface air temperature boundary conditions 366

291. Saint Cloud, Minnesota – 40 inch observed vs. simulated Green's Function soil temperatures – typical meteorological year (TMY) and corrected TMY surface air temperature boundary conditions 366

292. Saint Cloud, Minnesota – simulated Green's Function soil temperatures at various depths– observed surface soil temperature boundary condition 367

293. Saint Cloud, Minnesota – simulated Green's Function soil temperatures at various depths – corrected TMY surface air temperature boundary condition 367

294. Salt Lake City, Utah – 20 inch observed vs. simulated Green's Function soil temperatures – observed surface soil temperature boundary condition 368

295. Salt Lake City, Utah – 40 inch observed vs. simulated Green's Function soil temperatures – observed surface soil temperature boundary condition 368

296. Salt Lake City, Utah – 20 inch observed vs. simulated Green's Function soil temperatures – typical meteorological year (TMY) and corrected TMY surface air temperature boundary conditions 369

LIST OF FIGURES CONTINUED

Figure Page

297. Figure 297: Salt Lake City, Utah – 40 inch observed vs. simulated Green's Function soil temperatures – typical meteorological year (TMY) and corrected TMY surface air temperature boundary conditions 369

298. Salt Lake City, Utah – simulated Green's Function soil temperatures at various depths– observed surface soil temperature boundary condition 370

299. Salt Lake City, Utah – simulated Green's Function soil temperatures at various depths – corrected TMY surface air temperature boundary condition 370

300. Sioux Falls, South Dakota – 20 inch observed vs. simulated Green's Function soil temperatures – observed surface soil temperature boundary condition 371

301. Sioux Falls, South Dakota – 40 inch observed vs. simulated Green's Function soil temperatures – observed surface soil temperature boundary condition 371

302. Sioux Falls, South Dakota – 20 inch observed vs. simulated Green's Function soil temperatures – typical meteorological year (TMY) and corrected TMY surface air temperature boundary conditions 372

303. Figure 303: Sioux Falls, South Dakota – 40 inch observed vs. simulated Green's Function soil temperatures – typical meteorological year (TMY) and corrected TMY surface air temperature boundary conditions 372

304. Sioux Falls, South Dakota – simulated Green's Function soil temperatures at various depths– observed surface soil temperature boundary condition 373

305. Sioux Falls, South Dakota – simulated Green's Function soil temperatures at various depths – corrected TMY surface air temperature boundary condition 373

306. State College, Pennsylvania – 20 inch observed vs. simulated Green's Function soil temperatures – observed surface soil temperature boundary condition 374

LIST OF FIGURES CONTINUED

Figure Page

307. State College, Pennsylvania – 40 inch observed vs. simulated Green's Function soil temperatures – observed surface soil temperature boundary condition..... 374

308. State College, Pennsylvania – 20 inch observed vs. simulated Green's Function soil temperatures – typical meteorological year (TMY) and corrected TMY surface air temperature boundary conditions 375

309. State College, Pennsylvania – 40 inch observed vs. simulated Green's Function soil temperatures – typical meteorological year (TMY) and corrected TMY surface air temperature boundary conditions 375

310. State College, Pennsylvania – simulated Green's Function soil temperatures at various depths– observed surface soil temperature boundary condition..... 376

311. State College, Pennsylvania – simulated Green's Function soil temperatures at various depths – corrected TMY surface air temperature boundary condition..... 376

312. Tallahassee, Florida – 20 inch observed vs. simulated Green's Function soil temperatures – observed surface soil temperature boundary condition..... 377

313. Tallahassee, Florida – 40 inch observed vs. simulated Green's Function soil temperatures – observed surface soil temperature boundary condition..... 377

314. Tallahassee, Florida – 20 inch observed vs. simulated Green's Function soil temperatures – typical meteorological year (TMY) and corrected TMY surface air temperature boundary conditions..... 378

315. Tallahassee, Florida – 40 inch observed vs. simulated Green's Function soil temperatures – typical meteorological year (TMY) and corrected TMY surface air temperature boundary conditions..... 378

316. Tallahassee, Florida – simulated Green's Function soil temperatures at various depths– observed surface soil temperature boundary condition..... 379

LIST OF FIGURES CONTINUED

Figure Page

317. Tallahassee, Florida – simulated Green's Function soil temperatures at various depths – corrected TMY surface air temperature boundary condition 379

318. Observed vs. simulated soil temperatures at 2ft depth for the REHAU® Montana Ecosmart House project using the Ecohouse surface temperature BC 380

319. Observed vs. simulated soil temperatures at 6ft depth for the REHAU® Montana Ecosmart House project using the Ecohouse surface temperature BC 380

320. Observed vs. simulated soil temperatures at 2ft depth for the REHAU® Montana Ecosmart House project using the NRCS Table Mtn surface temperature BC 381

321. Observed vs. simulated soil temperatures at 6ft depth for the REHAU® Montana Ecosmart House project using the NRCS Table Mtn surface temperature BC 381

322. Diffusivity calibration for the REHAU® Montana Ecosmart House soil simulations at 2ft depth 382

323. Diffusivity calibration for the REHAU® Montana Ecosmart House soil simulations at 6ft depth 382

324. Albuquerque, New Mexico – 40 inch observed vs. simulated soil temperatures using the surface flux boundary condition derived from both soil surface and air surface temperatures 383

325. Amarillo, Texas – 40 inch observed vs. simulated soil temperatures using the surface flux boundary condition derived from both soil surface and air surface temperatures 383

326. Athens, Georgia – 40 inch observed vs. simulated soil temperatures using the surface flux boundary condition derived from both soil surface and air surface temperatures 384

327. Bozeman, Montana – 40 inch observed vs. simulated soil temperatures using the surface flux boundary condition derived from both soil surface and air surface temperatures 384

LIST OF FIGURES CONTINUED

Figure Page

328. Columbus, Ohio – 40 inch observed vs. simulated soil temperatures using the surface flux boundary condition derived from both soil surface and air surface temperatures 385

329. Houston, Texas – 40 inch observed vs. simulated soil temperatures using the surface flux boundary condition derived from both soil surface and air surface temperatures 385

330. Kansas City, Missouri – 40 inch observed vs. simulated soil temperatures using the surface flux boundary condition derived from both soil surface and air surface temperatures 386

331. Las Vegas, Nevada – 40 inch observed vs. simulated soil temperatures using the surface flux boundary condition derived from both soil surface and air surface temperatures 386

332. Moses Lake, Washington – 40 inch observed vs. simulated soil temperatures using the surface flux boundary condition derived from both soil surface and air surface temperatures 387

333. Pine Bluff, Arkansas – 40 inch observed vs. simulated soil temperatures using the surface flux boundary condition derived from both soil surface and air surface temperatures 387

334. St. Cloud, Minnesota – 40 inch observed vs. simulated soil temperatures using the surface flux boundary condition derived from both soil surface and air surface temperatures 388

335. Salt Lake City, Utah – 40 inch observed vs. simulated soil temperatures using the surface flux boundary condition derived from both soil surface and air surface temperatures 388

336. Sioux Falls, South Dakota – 40 inch observed vs. simulated soil temperatures using the surface flux boundary condition derived from both soil surface and air surface temperatures 389

337. State College, Pennsylvania – 40 inch observed vs. simulated soil temperatures using the surface flux boundary condition derived from both soil surface and air surface temperatures 389

LIST OF FIGURES CONTINUED

Figure Page

338. Tallahassee, Florida – 40 inch observed vs. simulated soil temperatures using the surface flux boundary condition derived from both soil surface and air surface temperatures 390

339. Albuquerque, New Mexico– example foundation heat loss function for 40 by 40 foot on grade slab..... 392

340. Amarillo, Texas– example foundation heat loss function for 40 by 40 foot on grade slab 392

341. Athens, Georgia– example foundation heat loss function for 40 by 40 foot on grade slab 393

342. Bozeman, Montana – example foundation heat loss function for 40 by 40 foot on grade slab 393

343. Columbus, Ohio – example foundation heat loss function for 40 by 40 foot on grade slab 394

344. Houston, Texas – example foundation heat loss function for 40 by 40 foot on grade slab 394

345. Kansas City, Missouri – example foundation heat loss function for 40 by 40 foot on grade slab 395

346. Las Vegas, Nevada – example foundation heat loss function for 40 by 40 foot on grade slab 395

347. Moses Lake, Washington – example foundation heat loss function for 40 by 40 foot on grade slab..... 396

348. Pine Bluff, Arkansas – example foundation heat loss function for 40 by 40 foot on grade slab 396

349. Saint Cloud, Minnesota – example foundation heat loss function for 40 by 40 foot on grade slab 397

350. Salt Lake City, Utah – example foundation heat loss function for 40 by 40 foot on grade slab 397

LIST OF FIGURES CONTINUED

Figure Page

351. Sioux Falls, South Dakota – example foundation heat loss function for 40 by 40 foot on grade slab..... 398

352. State College, Pennsylvania – example foundation heat loss function for 40 by 40 foot on grade slab..... 398

353. Tallahassee, Florida – example foundation heat loss function for 40 by 40 foot on grade slab 399

354. Albuquerque, New Mexico– soil temperature distribution for non-radiant slab at 180 days (top), 270 days (middle), and 360 days (bottom) starting from January 1st for a slab length of 40 feet..... 401

355. Amarillo, Texas – soil temperature distribution for non-radiant slab at 180 days (top), 270 days (middle), and 360 days (bottom) starting from January 1st for a slab length of 40 feet..... 402

356. Athens, Georgia – soil temperature distribution for non-radiant slab at 180 days (top), 270 days (middle), and 360 days (bottom) starting from January 1st for a slab length of 40 feet..... 403

357. Bozeman, Montana– soil temperature distribution for non-radiant slab at 180 days (top), 270 days (middle), and 360 days (bottom) starting from January 1st for a slab length of 40 feet..... 404

358. Columbus, Ohio – soil temperature distribution for non-radiant slab at 180 days (top), 270 days (middle), and 360 days (bottom) starting from January 1st for a slab length of 40 feet..... 405

359. Houston, Texas – soil temperature distribution for non-radiant slab at 180 days (top), 270 days (middle), and 360 days (bottom) starting from January 1st for a slab length of 40 feet..... 406

360. Kansas City, Missouri – soil temperature distribution for non-radiant slab at 180 days (top), 270 days (middle), and 360 days (bottom) starting from January 1st for a slab length of 40 feet..... 407

361. Las Vegas, Nevada – soil temperature distribution for non-radiant slab at 180 days (top), 270 days (middle), and 360 days (bottom) starting from January 1st for a slab length of 40 feet..... 408

LIST OF FIGURES CONTINUED

Figure Page

362. Moses Lake, Washington – soil temperature distribution for non-radiant slab at 180 days (top), 270 days (middle), and 360 days (bottom) starting from January 1st for a slab length of 40 feet..... 409

363. Pine Bluff, Arkansas – soil temperature distribution for non-radiant slab at 180 days (top), 270 days (middle), and 360 days (bottom) starting from January 1st for a slab length of 40 feet..... 410

364. Saint Cloud, Minnesota – soil temperature distribution for non-radiant slab at 180 days (top), 270 days (middle), and 360 days (bottom) starting from January 1st for a slab length of 40 feet..... 411

365. Salt Lake City, Utah – soil temperature distribution for non-radiant slab at 180 days (top), 270 days (middle), and 360 days (bottom) starting from January 1st for a slab length of 40 feet..... 412

366. Sioux Falls, South Dakota – soil temperature distribution for non-radiant slab at 180 days (top), 270 days (middle), and 360 days (bottom) starting from January 1st for a slab length of 40 feet..... 413

367. State College, Pennsylvania – soil temperature distribution for non-radiant slab at 180 days (top), 270 days (middle), and 360 days (bottom) starting from January 1st for a slab length of 40 feet..... 414

368. Tallahassee, Florida – soil temperature distribution for non-radiant slab at 180 days (top), 270 days (middle), and 360 days (bottom) starting from January 1st for a slab length of 40 feet..... 415

369. Albuquerque, New Mexico – soil temperature distribution for radiant slab at 180 days (top), 270 days (middle), and 360 days (bottom) starting from January 1st for a slab length of 40 feet..... 416

370. Amarillo, Texas – soil temperature distribution for radiant slab at 180 days (top), 270 days (middle), and 360 days (bottom) starting from January 1st for a slab length of 40 feet..... 417

371. Athens, Georgia – soil temperature distribution for radiant slab at 180 days (top), 270 days (middle), and 360 days (bottom) starting from January 1st for a slab length of 40 feet..... 418

LIST OF FIGURES CONTINUED

Figure Page

372. Bozeman, Montana – soil temperature distribution for radiant slab at 180 days (top), 270 days (middle), and 360 days (bottom) starting from January 1st for a slab length of 40 feet 419

373. Columbus, Ohio – soil temperature distribution for radiant slab at 180 days (top), 270 days (middle), and 360 days (bottom) starting from January 1st for a slab length of 40 feet 420

374. Houston, Texas – soil temperature distribution for radiant slab at 180 days (top), 270 days (middle), and 360 days (bottom) starting from January 1st for a slab length of 40 feet 421

375. Kansas City, Missouri – soil temperature distribution for radiant slab at 180 days (top), 270 days (middle), and 360 days (bottom) starting from January 1st for a slab length of 40 feet 422

376. Las Vegas, Nevada – soil temperature distribution for radiant slab at 180 days (top), 270 days (middle), and 360 days (bottom) starting from January 1st for a slab length of 40 feet 423

377. Moses Lake, Washington – soil temperature distribution for radiant slab at 180 days (top), 270 days (middle), and 360 days (bottom) starting from January 1st for a slab length of 40 feet 424

378. Pine Bluff, Arkansas – soil temperature distribution for radiant slab at 180 days (top), 270 days (middle), and 360 days (bottom) starting from January 1st for a slab length of 40 feet 425

379. Saint Cloud, Minnesota – soil temperature distribution for radiant slab at 180 days (top), 270 days (middle), and 360 days (bottom) starting from January 1st for a slab length of 40 feet 426

380. Salt Lake City, Utah – soil temperature distribution for radiant slab at 180 days (top), 270 days (middle), and 360 days (bottom) starting from January 1st for a slab length of 40 feet 427

381. Sioux Falls, South Dakota – soil temperature distribution for radiant slab at 180 days (top), 270 days (middle), and 360 days (bottom) starting from January 1st for a slab length of 40 feet 428

LIST OF FIGURES CONTINUED

Figure Page

382. State College, Pennsylvania – soil temperature distribution for radiant slab at 180 days (top), 270 days (middle), and 360 days (bottom) starting from January 1st for a slab length of 40 feet..... 429

383. Tallahassee, Florida – soil temperature distribution for radiant slab at 180 days (top), 270 days (middle), and 360 days (bottom) starting from January 1st for a slab length of 40 feet..... 430

NOMENCLATURE

T	temperature [°F,ºR]
t	time [sec, hr]
x, y	real space variables [in, ft]
x', y'	dummy space variables [in, ft]
τ	dummy time variable [sec, hr]
α	soil thermal diffusivity [in^2/sec, ft^2/day]
k	thermal conductivity [Btu/hr·ft·ºR, Btu/sec·in·ºR]
d	depth [in, ft]
ω	frequency [sec^{-1}, hr^{-1}]
f	friction factor [dimensionless]
p	pressure [psi]
θ	Julian date [days]
θ_{year}	annual period (365 days) [days]
θ_{lag}	time from January 1st to the day of minimum surface temperature [days]
h	convective heat transfer coefficient [Btu/sec·in^2·ºR , Btu/hr·ft^2·ºR]
$\bar{h}$	average convective heat transfer coefficient [Btu/sec·in^2·ºR, Btu/hr·ft^2·ºR]
ρ	density [lbm/in^3, lbm/ft^3]
$\dot{m}$	mass flow rate [lbm/sec]
q	heat transfer rate [Btu/hr]
$q"$	heat flux [Btu/hr·ft^2]
$C_{p,v}$	specific heat at constant pressure, volume [Btu/lbm·ºR]
u	air velocity (ft/s)
$\bar{u}$	mean air velocity (ft/s)
μ	dynamic viscosity [lbm/in·sec, lbm/ft·hr]
D	pipe diameter [in, ft]
$G(t)$	soil heat flux [Btu/hr·ft^2]
L	slab length [in, ft]
W	slab width [in, ft]
h_s	steady-state slab heat loss factor [dimensionless]
h_p^1	periodic slab heat loss factor [dimensionless]
ϕ_p^1	periodic slab heat loss phase angle [dimensionless]

Subscripts

a	air
amb	ambient
i	inlet
o	outlet
m	mean
s	surface
ss	steady-state

ABSTRACT

Earth-air heat exchangers (EAHXs), or earth-tubes, decrease building heating/cooling loads by pre-conditioning supply air in underground pipes. Air circulates underground to exchange heat with the surrounding soil before entering the building. The concept is fairly simple, but the field currently lacks fundamental information of the energy interactions in common EAHX installations. This identifies the need of a model framework inclusive of all EAHX design considerations, time-dependent climate conditions, and EAHX types to support the completion of this fundamental information. The EAHX types in this study include installations under locations free of structures (under yard) and under foundational slabs (under slab). This research develops the groundwork of this framework through a versatile model using the Green's Function method and numeric integration. The Green's Function method incorporates the majority of time-dependent heat transfer mechanisms surrounding EAHXs through long and short time solution components. The long time component calculates the initial soil temperature distribution in the under yard, non-radiant under slab, and radiant under slab installations. The under yard simulations were successfully validated using experimental soil temperature data from around the United States. The non-radiant under slab temperatures produced unrealistic results in some locations, but the novel Green's Function method in this location has significant potential for under slab EAHX applications. Results from the long time solution feed into the short time solution as a space-dependent initial condition. The short time solution uses a finite difference approach to calculate the heat transfer along the EAHX length. This method was validated using computation fluid dynamics with good agreement. The two components work together to quickly simulate a large number of EAHX installations. The research includes an example optimization procedure to demonstrate the framework's versatility. It successfully optimized the EAHX lengths for 95% effectiveness in cooling on the hottest day of the year in 15 locations around the United States.

INTRODUCTION

The U.S. Energy Information Administration predicts worldwide energy consumption will increase 56% by 2040. The majority of the increase will come from the non-Organized for Economic Cooperation and Development countries, such as India, China, and Russia, as their economies continue to grow [1]. Part of this energy growth is from building heating and cooling. As economic conditions continue to improve, the demand for comfortable buildings will also rise. Cheap ways to meet this power demand unfortunately result in the burning fossil fuels which contribute to climate change. This is why there is currently significant research and investment in energy efficiency measures to reduce current and future energy use in buildings. In fact, energy efficiency investment recently overtook investment in renewable energy [2]. One efficiency measure currently gaining renewed interest in reducing building heating and cooling loads is the earth-air heat exchanger (EAHX).

The use of relatively constant soil temperatures to condition indoor spaces is not a new concept, and has its roots in ancient Persia. Ancient Persian architecture commonly employed windcatchers to naturally ventilate buildings. They are still in use today. Windcatchers were also commonly joined to underground tunnels called qanats as seen in Figure 1. Qanats are larger tunnels meant to distribute a water supply to several buildings. The pressure difference across the windcatcher would cause air to be drawn from the surface through the qanat. This would use the cooler soil temperatures to condition the air before it was brought in the building [3]. Today modern ventilation systems apply the same principles for EAHXs. Air is preconditioned by circulation

through underground pipes in either an open or closed loop configuration. The soil captures or dissipates heat from the air flowing through the pipes before active heating or cooling begins. Earth-air heat exchangers come in several different cross-sectional areas and forms such as pipes, ducts, crawlspaces, and large tunnels. Two common types of EAHXs are installations under a space free of above structures, termed under yard (UY) in this research, and installations under a building's foundational slab, termed under slab (US) in this research.

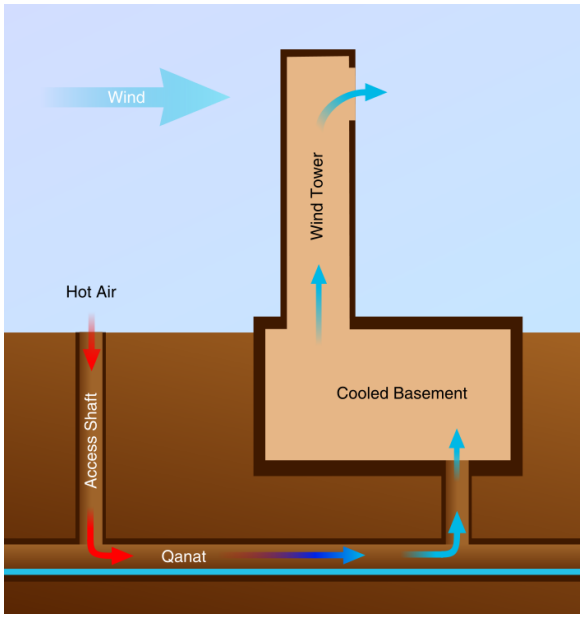


Figure 1: Early example of a windcatcher and earth-air heat exchanger in ancient Persian/Arabic architecture [4]

There are numerous benefits an EAHX can provide to a building and its occupants. The most obvious is increased energy efficiency of the building's mechanical equipment. This translates to lower operating expenses for the building and reduced emissions through less electrical or fuel consumption. Another less obvious benefit is

better air quality for the building's occupants. This is accomplished by bringing more outside air into the building at a lower energy cost. Buildings typically recirculate indoor air through the mechanical system to keep energy use low since conditioning outdoor air is more energy intensive. This recirculated indoor air is mixed with a small amount of outdoor air. The downside is this causes increases in carbon dioxide and volatile organic compound levels. This decreases occupant comfort, and in extreme cases can lead to sick building syndrome. Since an EAHX will pre-condition outdoor air, it is not as energy intensive to condition it and more can be brought into the building.

The renewed interest in EAHXs has come with increased research, but the status of currently available information is insufficient. Design information for architects and engineers is generalized and full of assumptions which lead to poor design decisions. The limited information has led to a history of unsatisfactory installations where systems demonstrate meager performance and unhealthy air quality due to condensation. Oddly, there are no design guides, standards, or codes dedicated to EAHXs. The field is in need of these guides and standards, but the fundamental information to base them on is currently not present. This fundamental information includes common design considerations such as EAHX length, air speed, duct diameter, burial depth, etc. But it must go beyond the basic design variables, and include other considerations such as the heat transfer differences of US EAHXs for radiant and non-radiant slabs, the performance between an UY and US EAHXs in the same climatic condition, or the performance results with respect to a location's time-dependent climate conditions to name a few. All

this fundamental information structured together will give the holistic view needed for EAHXs to take the next step in the industry.

Current research is making steps to fill in the fundamental EAHX information. There are a number of simple design methods in literature for basic engineering calculations. These are limited to steady-state analysis and are not as accurate since EAHXs are transient systems. Other studies solve the transient partial different equations for soil conduction and air convection/diffusion with numerical methods. These methods are highly accurate on a localized scale, but are limited to the number of heat transfer mechanisms they include. For example, a cylinder of soil around the EAHX is the domain boundary instead of the soil surface and deep soil. Other research uses finite element analysis (FEA) and computation fluid dynamic (CFD) simulations which have had great success. The only drawback is they are prohibitively time intensive to conduct the number of simulations in a fundamental study. One analytical study by Cucumo et al. [5] comes the closest to capturing the transient nature of EAHXs and the majority of heat transfer interactions. This model is only valid for UY EAHXs though. Its other limitation is it assumes a heat transfer distribution along the EAHX pipe, which may not be representative of the actual soil temperature distribution.

The studies above provide useful information, but individually these studies are not inclusive enough to cover all the fundamental information listed earlier in a single simulation model. A simulation model is essential because there are too many design iterations to cover with experimentation only. This identifies a need for a simulation method robust enough to include all design considerations in each type of EAHX

installation, and allow for input of time-dependent, climate specific weather conditions. This framework must accomplish all this and more while retaining a high level of accuracy and low computational time. The goal of the following research is to fill this need by developing the framework for this robust simulation method capable of supplying the fundamental information the industry lacks. The specific objectives are:

- Performing experimentation at a test residence with near identical UY and US EAHX for general observation and validation
- Develop a means to quickly calculate annual undisturbed soil temperature distributions in the UY and US installation locations
- Develop a finite difference scheme using pseudo-analytical relationships to determine to convective and conductive heat transfer along an EAHX
- Perform an example optimization with the above methods to demonstrate the effectiveness of the simulation framework

This framework is an extension of the analytical model developed by Cucumo et al. [5]. It will follow their basic setup, but expands the analytical approach to US EAHXs, includes more time-variable boundary conditions, and uses a finite difference approach for the heat transfer along the EAHX pipe.

The framework is split into two steps that are generally termed the long and short time solutions. The long time solution is the first step which establishes an UY or US soil temperature distribution. A pseudo-analytical approach solves for the distribution where numeric integration solves analytical integrals with no exact representation. The numerical integration can be quite time intensive for large US domains, which is not in

line with this research's goals. In response, the research developed a new method called the Base Solution Generation (BSG) technique that is capable of quickly performing large scale numerical integration. The soil temperature distribution from the long time solution provides the initial condition information for the following short time, finite difference approach to calculate heat transfer along the EAHX. The finite difference method splits the domain into two 1-D solutions for above and below the EAHX which combine at the end to form the total solution.

A powerful heat conduction solution technique called the Green's Function (GF) method captures all the time-dependent heat transfer mechanisms in the long and short time solutions. The GF method is very useful in EAHX simulations since it is capable of incorporating both time and space dependent boundary conditions and space dependent initial conditions in an analytical format. This is an attractive approach since the soil temperature, air temperature, foundation slab, and initial soil temperature are all dependent on time or space. The GF method is an analytical approach where the exact solution for the heat transfer system is written directly into integral form. This integral does not necessarily have an exact representation of elementary functions though; especially for the time dependent boundary conditions in EAHXs. This is why the EAHX simulations are pseudo-analytical because numeric integration is the only means to solve the GF integrals.

The GF method is advantageous in many respects, but it does have limitations. For example, the US installation type is limited to on-grade foundations. The GF method requires orthogonal boundary conditions, and odd shaped domains that include basements

are not possible. Along the same lines as orthogonal boundary conditions, the simulations are limited to 1-D heat transfer from the EAHX for simplicity. Later results show there are 2-D effects around the EAHX, but it does not significantly affect results. The EAHX is continuously on in the simulations. Intermittent operation is possible in the finite difference method, but not investigated in this research. Other limitations include only single circular pipe systems. Commonly, EAHX are set up in multiple pipe runs or labyrinths to maximize surface area and heat transfer. This research does not consider the changes in airflow through each of the multiple pipes and heat interactions between pipe legs. It is also possible to have square duct or large tunnel EAHXs, but the following is limited to only small diameter circular pipes (less than two feet). The final limitation outside the GF method has to do with internal convective flow inside the EAHX. This convection does not include the latent heat from mass (moisture) transfer.

Despite the limitations, the research successfully developed a model framework for a fundamental EAHXs study. Many of limitations discussed above can integrate into the current framework and are a subject of future work. Currently, the model can efficiently calculate the soil temperature distributions in the UY, non-radiant US, and radiant US locations (on-grade slabs only). The BSG technique significantly reduced the amount of time to calculation these distributions. The non-radiant US distributions did result in some unrealistic results for several locations, and requires future work to expand the solution method to three-dimensions. The finite difference method for transient heat transfer through the EAHX was also successful and validated with CFD simulations. It also takes far less computational time than CFD. The long and short time solutions

worked together to perform an example optimization of all three installation types in 15 locations around the United States. This example optimized the EAHX length to achieve 95% effectiveness with respect to the undisturbed soil temperature in cooling on the hottest day of the year in each location.

The example optimization is just one way to apply the model framework, and demonstrates the framework's versatility. The model's current state meets the research goals of developing a framework for an all-inclusive EAHX study. Future work can improve the framework to include such considerations as intermittent operation and latent heat transfer. This research has laid the groundwork for a robust EAHX simulation model capable of completing the fundamental information required to generate standards and design guidelines for EAHXs. The information will help the field improve the quality of EAHX designs, and in turn reduce emissions and building energy consumption.

BACKGROUND

EAHX Design and Construction

Earth-air heat exchangers are classified as any below grade air ducting such as pipes, rectangular ducts, crawlspaces, and large tunnels that exchange heat with the surrounding soil. As previously stated, this research is only concerned with small diameter (less than 2ft) circular pipe EAHXs. Earth-air heat exchangers are typically located in one of two areas: under a green space adjacent to a building or under the building's foundation itself. From this point on, EAHXs located under the green space will be referred to as under yard (UY), and under the foundation slab as under slab (US). Installation of EAHXs along a foundation's perimeter is also common, but is not considered in this research. Usually, EAHXs are split into multiple pipe legs to increase surface area and maximize heat transfer. These are also known as pipe labyrinths. Figure 2 is an example of an EAHX split into two pipe legs. Under slab EAHXs are attractive systems because they are cheaper to install during new construction when excavation is already taking place. Only a foot or two of additional excavation is required in this location and the excavator is already on-site. Compare this to an UY install needing six to eight feet of excavation and the cost savings are apparent.

There are several considerations to follow when designing or installing EAHXs to prevent standing water from collecting in the piping. Water is introduced into the system through rain at the inlet or condensation from the air during cooling and heating. Water mitigation strategies are important because standing water can lead to mold or microbial

growth in the EAHX. This is almost impossible to remove and can lead to abandonment of the system since it is extremely unhealthy. Luckily, it is easy to prevent. Earth-air heat exchangers should always be installed at a grade much like a septic system. This grade should drain any water to a drain or sump pump. The example EAHX shown in Figure 2 has such a drain under the two main pipe legs that leads to the sump pump at the right of the figure. Inlet towers should also have covers and filters. The covers prevent rain water from entering the pipe and the filters prevent food for microbe growth. It is also a good idea to construct an EAHX from piping specifically meant for that purpose. There are currently several companies that specialize in this piping and sell EAHXs in kits. Current EAHX pipes have silver linings along the internal surface to inhibit microbe growth. The pipe joints also use rubber gaskets for the joints since this is where water can infiltrate. Glued joints are also common and sufficient.



Figure 2: Example of two pipe legs on an earth-air heat exchanger

Soil Properties

Soil properties are difficult to anticipate based on location. They are highly variable and depend on soil composition and moisture content. Luckily, there is a fairly well understood range of common soil types. The classification of soil types comes in one of two ways. They are either generalized as heavy, light, dry, or damp as shown in Table 1 from the GLD geothermal design software from Thermal Dynamics®. The other type of classification is by clay and silt type soil with moisture content as shown in Table 2 from the ASHRAE Fundamentals Handbook. Both tables display similar results. The difficulty comes in classifying on-site soils as heavy, light, clay, or silt. This is where soil classification becomes subjective. Since the majority of soil types have relativity similar thermal properties, estimating an average value is typically acceptable.

Foundation Construction

The rate of heat loss or gain from a building to the soil will influence the performance of an under slab EAHX. The building to soil heat transfer depends on the building's foundation type. Basement, slab-on-grade, and crawlspaces are the three primary types of foundations. The insulation methods and moisture control strategies for each foundation type varies based on climate location, but several building energy codes recommend insulating foundations in climates with greater than 2500 heating degree days (base 65ºF). An uninsulated foundation can be responsible for up to 20% of buildings heat loss. Basement and slab-on-grade foundations are either insulated on the interior or exterior. Interior insulation is easier to inspect and install in most cases, but exposes the

foundation wall to freezing and thawing. Exterior insulation is also more continuous and limits thermal bridging. Moisture is controlled through subgrade drainage through a gravel base below the foundation slab. Above the gravel base, a vapor barrier keeps any moisture from diffusing through the concrete [8].

There are more design options for a crawlspace foundation. It can be unconditioned or semi-condition space below the building. An unconditioned space requires ventilation so moisture does not collect and degrade insulation performance. Typically, a moisture blocking ground cover is more effective that passive ventilation. Crawlspace ventilation can also increase building energy loses through the floor and require more insulation on walls, ducting, and piping. A semi-conditioned space offers advantages of requiring less insulation on ducting and piping. The insulation is also easier to install since it can be placed on the ground surface instead of between floor joists. Insulation can also be placed on the exterior of the building and crawlspace. Both types of crawlspace construction complicated predicting heat loss to the ground since the air temperature of the crawlspace is difficult to determine with any ventilation or conditioning [8].

Table 1: Soil properties at 77ºF from GLD geothermal design software [6]

Soil Type	k (Btu/hr·ft·ºF)	C_p (Btu/lb·ºF)	ρ (lb/ft^3)	α (ft^2/day)
Heavy, Damp	0.75	0.23	131	0.60
Heavy, Dry	0.50	0.20	125	0.48
Light, Damp	0.50	0.25	100	0.48
Light, Dry	0.20	0.20	90	0.26

Table 2: Soil and rock thermal properties from ASHRAE Handbook [7]

Soil Type (Percentage Water)	ρ (lb/ft^3)	k (Btu/hr·ft·°F)	α (ft^2/day)
Heavy Clay, 15%	120	0.8 - 1.1	0.45 - 0.65
Light Clay, 15%	80	0.4 - 0.6	0.35 - 0.50
Heavy Sand, 15%	120	1.6 - 2.2	0.9 - 1.2
Light Sand, 15%	80	0.6 - 1.2	0.5 - 1.0
Heavy Clay, 5%	120	0.6 - 0.8	0.5 - 0.65
Light Clay, 5%	80	0.3 - 0.5	0.35 - 0.6
Heavy Sand, 5%	120	1.2 - 1.9	1.0 - 1.5
Light Sand, 5%	80	0.5 - 1.1	0.6 - 1.3

Radon Collection in Earth-Air Heat Exchangers

A common concern in any residential building is radon gas. Radon is a radioactive gas created from the breakdown of uranium in rock, soil and water, and is a leading cause of lung cancer. Radon is drawn into buildings through cracks and gaps in foundations, and through the foundation materials themselves. Most conditioned buildings are negatively pressure, and this acts as the driving force for the infiltration and diffusion of radon from the foundation. There are several methods to prevent the majority of radon from entering a building if it is present. The most common method is active slab depressurization where air is drawn from the gravel layer below the slab. The presence of radon gas always requires testing since radon concentrations can vary with buildings directly next to each other [8, 9].

A concern with EAHX operation is that radon will diffuse through the underground piping material and mix with the incoming air. This is a valid concern and there is currently no research on the diffusion of radon into an EAHX air pipe or duct. Important information to consider is that typically radon infiltrates a building through

cracks and gaps. It will eventually diffuse through concrete, but concrete is also porous and not an impermeable barrier. Radon will also diffuse through EAHX piping materials such as PVC, but has much lower diffusion coefficient values than concrete. Radon is also unlikely to collect in an EAHX system when it is not operating since there is little pressure differential to drive the diffusion. Fresh air is continually brought through the EAHX system while operating resulting in diluted radon concentrations. Any planned site for an EAHX installation should test if radon gas is present and in what concentrations as part of the design process.

Internal Pipe Flow

Green's Functions are the primary tool for analyzing the conductive heat transfer in the soil surrounding the EAHX pipe. They cannot however calculate the convective heat transfer between the moving air and pipe wall, or the pressure drop through the underground piping. These calculations require turbulent internal flow correlations to calculate the convective heat transfer, and ultimately the EAHX's outlet air conditions. The following discussion is concentrated on circular pipes since similar relationships are available for other types and shapes of underground ducting.

Entrance Regions and Boundary Layers

Internal flows in all cross-sections are split into two regions: the entrance region and the fully developed region. The entrance region is a product of the no-slip condition for viscous flows. A boundary layer or shear layer begins to form at the entrance as the fluid contacts the wall. The boundary layer continues to grow until it merges and extends

over the entire cross-section. The flow is fully-developed at this point. The distance between the entrance and the fully-developed region is called the hydrodynamic entrance length. The flow velocity after the entrance length is purely axial and varies only in the axial coordinate [10, 11].

The hydrodynamic entrance length depends on the effective duct diameter and if the flow is laminar or turbulent. The transition between laminar and turbulent flow is determined by the Reynolds number shown in Equation (1). In fully developed flow for a circular pipe, the transition occurs at a Reynolds number of approximately 2,300. However, larger Reynolds numbers on the order of 10,000 are required for fully turbulent conditions for internal flow [10]. The velocity profile varies across the cross-section of the pipe so Equation (1) uses the cross-sections' mean fluid velocity. The entrance length in laminar flows can be approximated from Equation (2) [11]. There is no universal approximation for the turbulent entrance length, but it is known that it is generally independent of Reynolds number. Equation (3) gives a rough approximation for the turbulent entrance length [10].

$$Re_D = \frac{\rho u_m D}{\mu} \tag{1}$$

$$\left(L_{velocity}\right)_{laminar} \approx D(0.5 + 0.05Re_D) \tag{2}$$

$$10 \leq \left(\frac{L_{velocity}}{D}\right)_{turbulent} \leq 60 \tag{3}$$

Internal pipe flow also develops a thermal entrance region that is similar to the hydrodynamic entrance length. The thermal boundary layer forms as the air convectively

transfers heat with the pipe wall. Given enough length, thermally fully developed conditions are reached [10]. The length of the thermal boundary layer is dependent on Prandlt number in laminar flow. Atmospheric air experiences Prandlt numbers around 0.7, meaning the thermal boundary layer will develop before the hydrodynamic [12]. The length of the thermal boundary layer can be approximated using Equation (4). The turbulent flow thermal boundary layer is less a function of Pandlt number and harder to predict. Approximations such as Equation (5) are reported in literature [10].

$$\left(\frac{L_{thermal}}{D}\right)_{laminar} \approx 0.05 Re_D Pr \tag{4}$$

$$\left(\frac{L_{thermal}}{D}\right)_{turbulent} \approx 10 \tag{5}$$

Pressure Drop and Friction Factor

Analytical expressions to describe pressure drop in ducts are preferred, but turbulent flow is too complex for analytical expressions. Instead, the wall shear stress is non-dimensionalized using the dynamic pressure to yield the Darcy friction factor in Equation (6). The Darcy friction factor's usefulness is not apparent until viewed as the Moody diagram in Figure 3. Here the friction factor is experimentally related to the Reynolds Number, duct diameter, and duct surface roughness. Using these three parameters, the Moody diagram yields an estimated friction factor that is used in Equation (7) to calculate the pressure drop through the duct. This is a quick and simple way to calculate pressure drop in a fully developed, turbulent circular duct [10, 11]. Determining the pressure drop using friction factors is not limited to turbulent flow.

Laminar flow friction can also be read off the Moody diagram, or calculated directly using Equation (8).

$$f = \frac{8\tau_w}{\rho \bar{u}^2} = \frac{-\left(dp/dx\right) D}{\rho\, \bar{u}^2/2} \tag{6}$$

$$\Delta p = f \frac{\rho\, \bar{u}^2/2}{2D} (x_2 - x_1) \tag{7}$$

$$f = \frac{64}{Re_D} \tag{8}$$

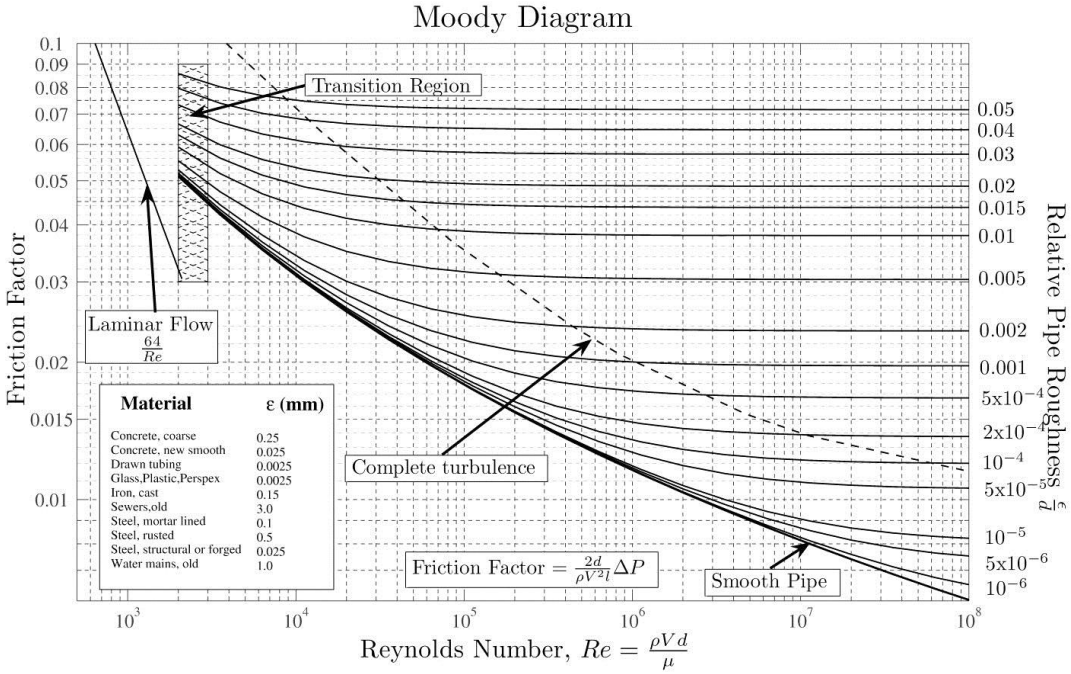


Figure 3: Moody diagram for friction factor in a circular pipe - permission to copy granted under the GNU Free Documentation License [3]

Reading friction factors off the Moody diagram is not always convenient; especially in computer programming. Equation (9) is a curve fit for friction factor along the smooth pipe line of the Moody diagram. This is a convenient way to calculate turbulent flow friction factors, but only for smooth pipes. A smooth pipe is defined as having an almost zero value when dividing the surface roughness by the duct diameter. Earth-air heat exchanger pipes are typically 6 to 12 inches in diameter and made of plastics (such as PVC, HDPE, etc.). This type of piping falls under the category of "drawn pipe," and according to Figure 3 has a roughness factor 0.0025 mm (9.843E-05 inches). Table 3 calculates the surface roughness to diameter value for several of drawn pipe sizes. The results are small, and from Figure 3 their friction factor values are along the smooth pipe line until Reynolds number values of 10^6 to 10^7. Equation (9) is a fair approximation of friction factor below these Reynolds numbers [10, 11].

Table 3: Moody diagram ε/D values for drawn tubing at various diameter piping

Pipe Diameter (inches)	Roughness Factor (mm)	Roughness Factor (inches)	ε/D
6.0	0.0025	9.843E-05	1.641E-05
8.0	0.0025	9.843E-05	1.230E-05
10.0	0.0025	9.843E-05	9.843E-06
12.0	0.0025	9.843E-05	8.203E-06

$$f = (0.790 * ln(Re_D) - 1.64)^{-2} \quad (9)$$

Energy Balance and Log
Mean Temperature Difference

An energy balance can be applied to internal flow in a pipe since the fluid is completely enclosed. This results in a general expression for the inlet and outlet

temperatures, and rate of convective heat transfer shown in Equation (10). This expression is valid no matter the internal flow conditions or thermal boundary conditions.

$$q_{conv} = \dot{m} C_P \left(T_{m,out} - T_{m,in}\right) \tag{10}$$

The two types of boundary conditions common in internal flow are a constant heat flux and constant surface temperature. The latter boundary condition is common for EAHXs since it is possible to predict the soil temperature around the EAHX pipe. Through integration, it is possible to derive Equation (11) which relates the averaged convective heat transfer coefficient, flow rate, pipe dimensions, pipe surface temperature, and inlet/outlet temperatures. The temperature difference along the pipe is averaged using the log mean temperature difference in Equation (12) since the fluid temperature follows an exponential decay as it travels through the pipe. The log mean temperature difference is used in Equation (10) in place of the normal temperature difference to yield Equation (13) which is the convective heat transfer for internal flow with constant surface temperature boundary condition [10].

$$\frac{\Delta T_{out}}{\Delta T_{in}} = \frac{T_s - T_{m,out}}{T_s - T_{m,in}} = exp\left(-\bar{h}\frac{PL}{\dot{m}C_P}\right) \tag{11}$$

$$\Delta T_{lm} = \frac{\Delta T_{out} - \Delta T_{in}}{ln\left(\Delta T_{out}/\Delta T_{in}\right)} \tag{12}$$

$$q_{conv} = \bar{h} A_s \Delta T_{lm} \tag{13}$$

Convective Correlations for
Laminar and Turbulent Flow

The use of Equation (11) requires convection heat transfer coefficients which are calculated from the Nusselt number in Equation (14). Laminar Nusselt numbers and convection coefficients can be derived theoretically or empirically. A detailed mathematical explanation on laminar convection coefficient derivation for incompressible, constant property fluid is available from multiple sources [10, 12] and is not discussed in this section. Two important results from this derivation are for the constant heat flux and constant surface temperature boundary conditions shown in Equation (15) and Equation (16) respectively.

$$Nu = \frac{hD}{k} \tag{14}$$

$$Nu_D = 4.36 \quad q"_s = constant \tag{15}$$

$$Nu_D = 3.66 \quad T_s = constant \tag{16}$$

Turbulent flow is much more complex than laminar and requires the use of empirical correlations. A classical equation for fully developed (hydrodynamically and thermally) turbulent flow in a circular pipe is the Dittus-Boelter equation, Equation (17). This equation is accurate for $L/D \geq 10$, $Re \geq 10{,}000$, and $0.6 \leq Pr \leq 160$. While the Dittus-Boelter equation is generally considered accurate, errors as large as 25% are observed in literature. Error is reduced by using Equation (18) proposed by Gnielinski [10]. The "f" in the equation refers to the friction factor from which is found on the

Moody diagram or calculated from Equation (9). Equation (18) is valid over $3{,}000 \leq Re \leq 5*10^6$ and $0.5 \leq Pr \leq 2000$. The lower limit of Reynolds number indicates it is also valid in the transitional region.

$$Nu_D = 0.23 Re_D^{4/5} Pr^n \quad n = 0.4\ heating \quad n = 0.3\ cooling \tag{17}$$

$$Nu_D = \frac{\left(f/8\right)(Re_D - 1000)Pr}{1 + 12.7\left(f/8\right)^{1/2}(Pr^{2/3} - 1)} \tag{18}$$

Coefficient of Performance and Effectiveness

A convenient way to measure the performance of an EAHX is through the coefficient of performance (COP). A general definition of COP from the ASHRAE fundamentals is the amount of energy removed/added during a cycle or process divided by the required energy input to operate the cycle [13]. For EAHX, the amount of energy removed/added during the cycle is the convective heat transfer rate between the air and surrounding soil. Fan energy is the only energy input to operate the EAHX (cycle). In other words, the COP says how many units of energy are extracted or rejected per unit of energy input to run the EAHX. A high COP indicates a high efficiency. Equation (19) is the general equation for the EAHX COP. Equation (10) calculates the convective heat transfer (Q_{conv}) in Btu/hr. The fan power input is calculated from fan curves or direct on-site measurements. For this research, a positive COP represents heating of the airstream,

and a negative COP cools the air stream. The negative values do not mean the EAHX is underperforming. It is only signifies the EAHX is in cooling mode.

$$COP = \frac{q_{conv}}{W_{fan}} \tag{19}$$

Another means to measure EAHX performance is through heat transfer effectiveness. Effectiveness is a simple method that compares the actual change in air temperature to maximum possible change as seen in Equation (20). In the case of EAHXs, the maximum possible change in temperature is with respect to the undisturbed soil temperature at the same depth. This is based off the idea that if the EAHX was infinitely long, the air temperature would eventually reach equilibrium with the surrounding soil.

$$eff = \frac{T_{out} - T_{in}}{T_{und,soil} - T_{in}} \tag{20}$$

Heating and Cooling Degree Days

The degree-day method is primarily for building energy analysis. It can estimate the energy consumption of HVAC equipment by multiplying different values of outdoor temperature by the corresponding number of hours. The method provides a simple estimate of annual loads, and concisely characterizes a climate's severity [13]. In this research, this last characteristic is the main concern since numerous locations are compared and contrasted. The number of heating degree days (HDDs) and cooling degree days (CDDs) allows for climate and building load comparison between locations.

For example, high numbers of both HDDs and CDDs indicates a location that goes through drastic temperature swings in winter and summer. Another example commonly seen is a location with a high number of HDDs and hardly any CDDs. This indicates a location with harsh winters and low cooling requirements in the summer.

The degree-day method starts with the balance point temperature in Equation (21). In heating, this is defined as the value of the outdoor temperature at which the total heat loss is equal to the heat gain from the sun, occupants, lights, plug loads, and other energy sources for the specified value of indoor temperature. This indoor temperature can vary and is typically 65ºF to 45ºF. "K_{tot}" is the total heat loss coefficient for the building. It is possible the equation for HHDs and CDDs using the balance point temperature and integrating the rate of energy consumption by the heating/cooling system. The resulting two equations are shown in Equation (22) and Equation (23). Equation (22) indicates heating in the building is only needed when the outdoor temperature is below the balance point temperature. The opposite is true for the CDDs where the balance point temperature is below the outdoor temperature. For more information on the degree day method, see the ASHRAE Fundamentals [13]

$$T_{balance} = T_{inside} - \frac{q_{gain}}{K_{total}} \tag{21}$$

$$HDD(T_{balance}) = (1day) \sum_{days} (T_{balance} - T_{outside})^{+} \tag{22}$$

$$CDD(T_{balance}) = (1day) \sum_{days} (T_{outside} - T_{balance})^{+} \tag{23}$$

LITERATURE REVIEW

Literature associated with earth-air heat exchangers (EAHXs), also known as earth tubes, is loosely classified into analytical and numerical models for under yard (UY) installations. Soil temperature prediction is a heavily studied area for analytical models since it has a considerable influence on design. These studies either directly incorporate a previously established soil prediction method or use a close variation. One difficulty in analytic methods is coupling the conductive and convective heat transfer between the soil and air passing through the EAHX. Coupling the two heat transfer modes is easier with numerical models. The numerical models are commonly quasi-numerical since they incorporate some analytical components. Currently missing the field are studies on under slab (US) EAHXs. This is a common installation type, but there is no information on how it differs from the UY install. Foundation heat loss and soil temperatures below a foundation slab are important factors for US installations. The following discusses there two topics since current literature reviews them in detail.

Soil Temperature Predictions

Soil temperatures in areas free of above structures experience smaller periodic fluctuations daily, and a large sinusoidal fluctuation annually. Daily fluctuations occur near the surface and are not of interest for EAHXs. The larger annual fluctuations of interest occur at a much lower depth. The annual fluctuation is sinusoidal in shape and caused by the periodic nature of annual air temperatures and/or solar radiation. A third effect on the soil temperature is latent heat transfer of moisture transport through the soil.

Soil models begin with the atmospheric air temperature, and then include solar radiation and moisture transport to increase accuracy. There are two approaches for predicting the annual soil temperatures present in literature. They both solve the Fourier heat equation shown in Equation (24), but differ on boundary condition (BC) application. The first uses the annual air temperature and/or solar radiation as a time-dependent BC. The second develops an energy balance including all possible thermal effects for the BC.

$$\nabla^2 T = \frac{1}{\alpha}\frac{\partial T}{\partial t} \tag{24}$$

The classical method of predicting soil temperatures is the Carslaw and Jaeger solution for a semi-infinite solid with a harmonic surface temperature in the form of Equation (25). This solution is the building block of other simplified solutions because it is possible to represent the annual sinusoidal air temperature with Equation (25). The solution proceeds from the fundamental solution for this problem type in Equation (26). Equation (26) represents a temperature wave of wave number κ and wavelength λ. Equation (27) is found from solving Equation (26) with Fourier transforms and Equation (25) acting as the temperature wave. Equation (27) uses the same coefficients as the harmonic surface function. The Carslaw and Jaeger solution fits well to experimental data, and many studies use it or a similar form for soil predictions [14].

$$\phi(t) = A_0 + A_1 \cos(\omega t - \epsilon_1) + A_2 \cos(\omega t - \epsilon_2) + \cdots \tag{25}$$

$$(y, t) = Ae^{-\kappa y} \cos(\omega t - \kappa x - \epsilon) \tag{26}$$

$$T(y,t) = A_o + \sum_{n=1}^{\infty} A_n e^{\left(-y\sqrt{\frac{n\omega}{2\alpha}}\right)} \cos\left[n\omega t - \varepsilon_n - y\left(\frac{n\omega}{2\alpha}\right)^{1/2}\right] \quad (27)$$

A simplification to the Carslaw-Jaeger solution is presented by Nofziger and Wu. The simplification comes from re-arranging Equation (27) specifically for predicting soil temperatures. Equation (27) is a general solution for any semi-infinite solid. Several weather and time constants replace the harmonic coefficients and eliminates the infinite series to result in Equation (28). An annual mean surface temperature, $T_{m,s}$, and a surface temperature amplitude, A_s are the weather constants that depend on location. The time constants are "θ" for the Julian date (days), and "θ_{lag}" for the time from January 1st to the day of the minimum surface temperature (days). Equation (29) calculates the surface temperature amplitude where T_{max} and T_{min} are the daily maximum and minimum surface temperatures respectively [15].

$$T(y,t) = T_{m,s} + A_s e^{-y\sqrt{2\pi/\theta_{year}\alpha}} sin\left[\frac{2\pi(\theta - \theta_{lag})}{\theta_{year}} - y\sqrt{\frac{2\pi}{\theta_{year}\alpha}} - \frac{\pi}{2}\right] \quad (28)$$

$$A_s = \frac{1}{2} average\left(\sum_{m=1}^{365} \frac{T_{max} + T_{min}}{2}\right) \quad (29)$$

Calculations for the surface temperature and surface temperature amplitude in Equation (28) use either the annual air or soil surface temperatures. Nofziger and Wu found that using air temperatures consistently underestimated the soil temperatures. Their observations conclude better results are obtained by increasing the maximum and minimum air temperatures by 3.5 °F (2 °C) before calculating the means surface

temperature and surface temperature amplitude. The best agreement between the predicted and observed soil comes from the soil surface conditions [15]. Two other similar studies also identified accurate predictions using the soil surface to calculate climatic constants. The studies use soil temperature data measured in Athens, Greece from 1917 to 1990, and a Carslaw-Jaeger based equation for the simulation [16, 17].

The ASHRAE HVAC Systems and Equipment Handbook reports a similar equation for soil temperatures under the District Heating and Cooling chapter. The only difference is a change to the phase lag inside the sine function. The ASHRAE equation requires no preliminary calculations since the mean temperature and surface temperature amplitude are listed in a Regional Climatic Constants table [18]. This creates an easy to use equation as long as the climatic constants table is available. The purpose of the ASHRAE equations is to estimate heat loss from district heating and cooling hydronic systems. There is no mention of EAHXs, but the equations still apply. The handbook does comment that the equation cannot account for freezing, thawing, or evaporation of moisture in the soil [7].

The ASHRAE handbook also includes equations for estimating soil diffusivity and effective thickness of soil surface covers. The diffusivity calculation in Equation (30) is a function of soil moisture content "w", soil density "ρ_s", soil thermal conductivity "k_s" and specific heat of the soil and water. This equation is meaningful because it relates moisture to diffusivity. The ASHRAE handbook's heat loss from the district piping depends on the type of soil surface cover. Equation (31) is a correction factor that adds a fictitious soil layer to account for this extra resistance where "h" is the convective heat

transfer coefficient at the surface. The effective thickness "δ" is included in the length of the thermal resistance calculation [7]

$$\alpha = \frac{24k_s}{\rho_s[C_s + C_w(w/100)]} \tag{30}$$

$$\delta = \frac{k_s}{h} \tag{31}$$

An early study uses an energy balance to develop what it terms the solair temperature BC. The solair temperature is a combination of convection and radiation on the soil surface as seen in Equation (32) where $\alpha_0 = 0.9$, "S" is the solar intensity (Btu/hr·ft^2), "ε" is the emissivity, and $\Delta R = 20$ Btu/hr·ft^2. This equation is familiar because without the radiation terms it is a convective BC. The solution proceeds much in the same way as previous Carslaw-Jaeger boundary value problems. A Fourier series is fit to the periodic solair temperature which acts as the BC for the semi-infinite solution. The model results are not exceptional due to generalizations of the convective heat transfer coefficient, absorption, and emissivity. These values change with time, but the model uses constant values [19].

$$-k_s\left(\frac{\partial T}{\partial y}\right) = h[T_{atm} - T_s] + \alpha_0 S - \varepsilon \Delta R \tag{32}$$

A later publication expands the solair temperature BC by adding the latent heat flux due to evaporation. The energy balance also includes convection at the surface, solar radiation, and long-wave radiation. This study differs from the previous by using the

energy balance to first calculate the soil surface temperature instead of a BC in the boundary value problem. A Fourier series is fit to the calculated surface temperatures, and the solution proceeds in the same manner as the Carslaw-Jaeger solution. The model agrees well with yearlong experimental results. This is partly due to a large amount of historical experimental data that calibrated the convective and radiation constants. It is unclear if this model works well in other locations without extensive calibration. This study finishes with a sensitivity analysis between wind speed, absorptivity, evaporation fraction, and relative humidity [20].

Several studies also predict soil temperatures with numeric models. Rajeev, Chan, and Kodikara discretized two diffusion equations for heat and moisture transport in GEO-SLOPE International 2010 to model heat and moisture movement in soil over a 20 year period. The study determined how years of drought could affect underground infrastructure. Two sites near Melbourne Australia provided the experimental data for model validation. The numerical results were generally in good agreement with field measurements [21]. Another numerical study by Qin, Hiller, Jiang, and Bao is specific to cold-region soil temperatures. They use the numerical model to identify the freeze/thaw interface in an upper boundary layer. The authors compare the upper boundary model to a temperature only boundary. They found it as a more accurate prediction of soil temperature [22].

Analytical Earth-Air Heat Exchanger Models

Tzaferis and De Paepe classify the analytical models for EAHX systems into two groups. The algorithms of the first group calculate the convective heat transfer from the circulating air to the pipe, and then the conductive heat transfer from the pipe to the surrounding soil. The second group calculates only the convective heat transfer from the circulating air to the pipe. The first classification group requires the additional inputs of soil thermal characteristics and the undisturbed soil temperature during system operation [23]. The convective model complexity in both groups increases with inclusion of mass transfer. The two classification groups hold true for the majority of EAHX analytic literature. Other studies increase complexity by coupling the convective and conductive heat transfer through the convective boundary condition or an energy balance. Others assume no atmospheric surface effects and develop models for local heat transfer around the EAHX pipe. Optimization and economic aspects are also analyzed through use of the above models. The following literature review of analytical algorithms starts with the convective heat transfer only classification and moves forward to models of increasing complexity.

The convection only models require three inputs: the geometrical characteristics of the system, thermal characteristics of the pipe, and temperature of the pipe surface [23]. The last input is typically found using a previously discussed soil temperature model. Muehleisen published a simple design algorithm to calculate the length of tubing, heat transfer effectiveness, pressure drop, fan power, and mean monthly temperature of outlet air. The algorithm implementation only requires a computer spreadsheet. The

algorithm has built in inputs for pipe surface roughness that factors into Nusselt number calculations. An equation and tabulated values from the British Standard Institution similar to the ASHRAE method estimates the pipe surface temperature. Muehleisen compared this algorithm to other simplified models and found that neglecting the tube and soil thermal resistance results in a much smaller length for the same amount of heat transfer. This was due to the overall heat transfer coefficient being much smaller when including the soil and pipe wall [24].

De Paepe and Janssens published a method for preliminary EAHX design checks. The authors note a majority of current algorithms are too complex for the target audience of EAHX designers. Their algorithm uses a simple log mean temperature difference to calculate the convective heat transfer rate. The Nusselt number for the convective heat transfer coefficient is found by the Glielinski correlation for smooth pipes [10]. No calculation for soil temperature is given in the publication. It simply states that soil temperatures are practically constant throughout the year at depths of 6 to 12 feet. Design effectiveness is determined by a dimensionless number called the "Number of Heat Transfer Units" which is a function of mass flow rate, surface area, and convective coefficient. The optimal design choice based on building ventilation requirements is found by a ratio of heat transfer units to pressure drop and tube length [25].

Pfafferott compared EAHX designs in three locations through a simplified coefficient of performance (COP) calculation. The COP expression in Equation (33) is a ratio of the useful heating and cooling energy gain through the EAHX to the fan input power. The energy gain was found using the energy balance in Equation (10) which

requires the EAHX outlet temperature. Equation (11) calculates the outlet temperature with the soil temperature as the pipe surface temperature. Recall Equation (11) is the energy balance result for internal pipe flow with a constant surface temperature. A soil temperature model similar to Equation (28) predicts the soil temperatures at pipe depth. Each of the three experimental sites uses a typical fan efficiency of 70%. This leads to COP values of 29, 88, and 380 for the three locations. The COP of 380 results from a combination of large pipe diameter and low air speed [26].

$$COP = \frac{\sum_{useful}(q_{heat} + q_{cool})}{\sum_{useful}(\Delta p \cdot u)} \tag{33}$$

A convective only study by Krarti and Kreider increases complexity by considering heat input from the surrounding soil in an air flow energy conservation equation. The authors accomplish this by treating the soil surrounding the pipe as an insulative layer. The U-value of this layer depended on the convective heat transfer coefficient, air temperature, and undisturbed soil temperature. The undisturbed soil temperature was found using an equation similar to Nofziger [15]. This method then solves the conservation of energy equation to find the mean temperature variation along the EAHX at any hour of the day. The model was verified against experimental data with relatively good agreement. A parametric study also analyzes the influence of air flow rate and pipe diameter on the EAHX's cooling effect [27].

A good example of repurposing existing underground infrastructure as an EAHX was studied by Sodha et al. Two hospital buildings near Delhi, India were originally connected by one kilometer long maintenance tunnel. The tunnel varied in cross section

from 3ft by 3ft to 12ft x 15ft. The building owners found the tunnel could double as an EAHX for cooling. Wet and dry bulb temperatures were monitored along the tunnel to validate an analytical model for heat and mass transfer. The mass transfer model uses simplified equations meant for environmental engineering. It is unclear if these relationships were accurate for the air tunnel since only air temperature is reported in the results. The air temperature had a satisfactory match with observed values [28].

The process of coupling convective and conductive heat transfer is difficult analytically, and typically requires numerical methods. Hollmuller presents an algorithm that couples the radial form of Fourier's heat equation with the air energy conservation. The two are linked though the convective air/soil heat exchange (Robin or 3rd type BC). The Dittus-Boelter correlation estimates the convective heat transfer coefficient. This model is simplified to a radial solution by ignoring the upper surface exposed to atmospheric air. Instead, a radial isothermal or adiabatic BC is placed in the soil a specified distance away from the EAHX pipe. Solving the three differential equations for this boundary value setup is not trivial. The authors verified the model with experimental results, and conclude EAHXs have potential phase-shifting of inlet air temperatures that have not been previously exploited [29].

Analytical models to this point either use undisturbed soil temperatures for the convective BC, or couple the pipe and surrounding soil without accounting for heat from the upper free surface. Cucumo, Montoro, and Vulcano incorporate the upper surface and convective heat transfer to the soil in a 1-D transient analytical model using Green's Functions. A 1-D plate models the domain between the surface and EAHX with time-

dependent BCs on each surface. The soil surface accounts for daily and yearly fluctuations in air temperature and solar radiation. The convective fluid temperature on the EAHX boundary depends on inlet atmospheric air. A second domain below the EAHX is modeled as a 1-D semi-infinite medium with the previously mentioned convective BC. This way the model accounts for conduction above and below the EAHX. The boundary value problem also uses the undisturbed soil temperature as a space-variable IC. The BCs and IC create a complex boundary value problem that requires the Green's Function method. Finding the pipe surface temperature is the point of the conduction analysis [5]. The surface temperature acts as a BC for a power series heat and mass transfer convective solution presented by Boulama et al. [30]. This Green's Function algorithm is one of the most comprehensive soil conduction solutions present in literature.

A different approach to EAHX analytical models is a building wide energy balance. A series of publications by the Ghosal et al. evaluated the useful energy input from the EAHX to a passive greenhouse. This included an energy balance for heat loss/gains through the walls and roof of the greenhouse. This allowed the authors to determine when the EAHX was aiding the passive goal by adding/removing useful energy. Yearlong data logging validated the energy balance model with fair agreement. They concluded a 7-8°C rise and 5-6 °C reduction of greenhouse temperature for the winter and summer respectively [31-33]. A similar study changes a building's cooling balance point temperature based on EAHX contributions. A building's balance point temperature is part of the cooling degree hour calculations. The author's goal was to

develop an algorithm for implementation in building simulation codes such as DOE and TRNSYS [34]. The code calculated outlet temperatures and heat transfer rate from the EAHX using a previously published algorithm by the same authors [35].

The analytical models and algorithms discussed to this point are 1-D and only analyze a single pipe system. EAHXs are commonly installed with multiple parallel pipe legs. Sodha, Mahajan, and Sawhney analyzed the thermal performance of an EAHX system using anywhere from 1 to 30 parallel pipes. The heating and cooling potential in Equation (34) and Equation (35) respectively characterized the thermal performance where "d" is the number of days. The potentials sum the meaningful heat additions during the operational period and report the value in kilowatt hours. The positive sign above the temperature brackets indicates the calculation uses only positive temperature differences [36]. The authors use a separate model by Claesson and Dunand to calculate the pipe surface temperature for any number of parallel pipes in the two equations [37].

$$HP = \sum_{j=1}^{N} \frac{\dot{m}_{a,j} C_a \left(T_{ao,j} - T_{amb}\right)^{+} (24d)}{1000} \tag{34}$$

$$CP = \sum_{j=1}^{N} \frac{\dot{m}_{a,j} C_a \left(T_{amb} - T_{ao,j}\right)^{+} (24d)}{1000} \tag{35}$$

Numerical Based Earth-Air Heat Exchange Models

Analytical EAHX models with simpler mathematical equations are convenient for fast preliminary design checks, but neglect important heat transfer mechanisms which

decreases accuracy. Model fidelity increases with inclusion of more boundary conditions and transport phenomenon, but the required mathematical knowledge is rarely present outside of academia. Numerical models offer the advantage of simplifying complex mathematics into finite element methods or pre-packed software. The coupling of convective and conductive heat transfer, which is so difficult analytically, is much easier numerically. They also offer the means to calculate the simultaneous heat and mass transfer of the air inside the EAHX pipe. The main disadvantage is numerical methods are typically very time intensive.

Pre-packaged computational fluid dynamics (CFD) software is the easiest way to setup a numerical simulation. Zhang and Haghighat applied CFD to explain the fluid flow dynamics in a large earth-air heat exchange tunnel. They discovered that common analytical relationships in literature are not accurate for larger tunnels. The CFD analysis revealed reverse airflow in the top portion of the duct and temperature stratification through the entire duct height. A second observation was the simulation's sensitivity to convective heat transfer coefficients. They compared seven empirical correlations from pervious literature and found all seven were considerable smaller than experimental values for large air tunnels. The authors developed a local convective heat transfer coefficient for each surface of the air tunnel which significantly increased simulation accuracy [38].

Computational fluid dynamics is a useful tool for EAHX convective flow solutions, but has a large computational workload. A group of researchers from Xihua University in China developed a numerical algorithm using explicit and implicit finite

difference methods. Their goal was to predict air temperature and humidity delivered to an underground mine through a large air tunnel. The rock surround the tunnel was model with a 1-D radial transient explicit heat conduction model. The tunnel length was divided into N number of segments for a 1-D implicit transient convection model. The convection model included heat and mass transfer. A sequential computing algorithm couples the convective and conductive models. The convective heat and mass transfer solves first and calculates the heat flux through the rock-air interface. The heat flux then inputs into the conduction model to solve for heat propagation through the rock. The time interval is increased and the process repeats. The experimental values match well with the simulation. Some error occurred with the mass transfer which the authors contributed to a poor empirical correlation for the mass transfer coefficient. The authors also note the computational time was 15 minutes on a standard personal computer. This was for 11 nodes in both the radial and axial directions [39].

Implicit finite difference schemes are also useful to solve simultaneous heat and mass transfer into the soil from the circulating air as shown in a model developed by Kumar and Kaushik. Their model accounts for the natural thermal stratification of the soil, soil surface conditions, and latent/sensible heat. The coupled heat and mass transfer equations were developed in a previous study by Ahmed for agricultural purposes [40]. The boundary conditions incorporate energy balance equations for heat transferred into the pipe from the soil, but the study is unclear on how soil surface conditions fit into the formation. The predicted results match very well to the experimental data with errors below 4%. The authors conclude the reduction in error is only possible by including

mass transfer in the airstream, and the progressive heating of the soil around the EAHX pipe [41].

Hollmuller and Lachal also used an explicit numerical model to solve sensible and latent heat transfer in an EAHX. The model uses a more simplified form of latent heat transfer called the Lewis approach from the ASHRAE Fundamentals [13]. Experimental data from a greenhouse validated the sensible heat, but the latent heat transfer was not as accurate. The authors attribute this to water droplets entering the EAHX from the greenhouse while the air circulated. This study is unique in that the authors also performed a heating/cooling potential and economic analysis for three EAHX installations connected to one building. They found all three configurations were capable of reducing energy use when compared to traditional sources [42].

A more involved transient implicit numerical model was presented by Mihalakakou et al. Unique to this model is it includes a complete mathematical model of the moisture migration through the soil with temperature. The latent heat of moisture transport is a difficult phenomenon to model accurately. The authors were successful though and validated simulation values with an extensive set of experimental data [43]. Mihalakakou used this numerical model in two separate publications. The first was for validation of EAHX heating potential using a neural network estimation. Artificial neural networks try to simulate the function and structure of biological neurons. The neural network and a backpropagation algorithm allowed the author to successful estimate outlet air temperatures [44]. The second publication investigated the influence of bare soil and short grass cover on the EAHX heating potential. The bare soil surface

was found to increase system heating capacity. The above model was programmed into the TRNSYS simulation environment for a parametric study on pipe length, pipe radius, air velocity, and soil depth [45].

The studies thus far assume the EAHX is continuously operating for simplicity. This is not true however since buildings are not continuously drawing in outside air. Stevens analyzes the consequences of intermittent EAHX operation though a numerical finite-difference analysis in a single round pipe. The model was 1-D and did not account for mass transfer. Stopping and starting the fluid flow at a specified time interval accomplished the intermittent operation. The author concluded the average intermittent cycle heat transfer was lower than continuous operation. Also, the instantaneous heat transfer was higher during the active part of each intermittent cycle. In total, the study simulated 180 test combinations to characterize the dimensionless convective heat transfer coefficient, diffusivity, and intermittence factor. The author formed empirical correlations for intermittent heat transfer from the 180 combinations. The correlations predicted heat transfer rate within 20% for 95% of the data and within 10% for 70% of the data [46].

Soil shading and soil surface covers are two factors affecting heat transfer from the surface that few models take into account. A study by Trzaki and Zawada includes both in a numerical mesh. This is accomplished by calculating whether a particular mesh subdivision element is blocked from radiation based on environmental geometry, and the time moment solar altitude and azimuth angles. This allows the model to account for the EAHX location relative to surrounding structures. The convective heat transfer to the

soil from the EAHX is based on the enthalpy of the entering air and the air-ground energy transfer balance. This includes the pipe wall thermal resistance, but not mass transfer. The 2-D numerical model is also able to analyze the effects of parallel pipes. The study ends with the best practices to increase heat exchange efficiency. The authors conclude it is not possible for a general optimization due to the multiplicity and interdependence of the design variables. Each new design requires an independent optimization based on a series of simulations accounting for construction and operating conditions [47].

Computer Simulation Programs and Efforts

A unique approach by Bojic et al. couples an EAHX simulation program with a building energy simulation. The purpose was to determine building energy reductions and cost savings associated with EAHX design iterations. The soil-EAHX mathematical model calculates energy exchange by splitting the soil into layers. The program solves the layers in a step-wise manner from the surface past the EAHX pipe. Convection and solar radiation are considered at the soil surface. The convective heat transfer coefficient was found experimentally and inputs into the program as a fitted equation. The soil model does not account for moisture propagation. The coupling of the EAHX and building allowed the authors to observe how EAHX design choices affect the building energy balance [48].

Other studies have incorporated EAHX models into building simulation programs. Ho Lee and Strand investigated the implementation of an EAHX into the EnergyPlus program. EnergyPlus is a robust building simulation tool developed by the U.S. Department of Energy. They added the rate of heat transfer from the EAHX into the

heat balance calculation framework. A simpler analytical model for soil temperature calculates the pipe surface temperature, and empirical convective correlations calculate heat transfer rate from the soil to the EAHX [49]. A similar effort was made by Lee in a Master's Thesis for the development, verification, and implementation of an EAHX heat transfer model into EnergyPlus [50]. Benkert et al. developed a standalone calculation tool for EAHX optimization for use in building simulation tools. The program was called Graphical Design of Earth Heat Exchangers or GAEA. This tool also utilizes analytical equations for fast design calculations [51].

Heat Transfer in Foundation Slabs

Simulating heat transfer between a building's foundation and the surrounding soil is a difficult heat transfer problem due to the large number of parameters and assumptions. One-dimensional, steady-state solutions are typically only appropriate for rough heating load calculations. Higher levels of accuracy require two or three dimensional transient conductive and convective heat transfer. This is further complicated by the inclusion of building edges since this is where the majority of heat transferred from a building occurs [8]. Edge calculations are complex mathematically due to the indoor and outdoor boundary conditions meeting at the same point for slab-on-grade foundations. A below grade slab or basement creates a non-orthogonal domain that few analytical methods can solve. Other complications include inhomogeneous soil, moisture migration, groundwater flow, freezing/thawing, and influence of surrounding

buildings [52]. The difficult heat transfer analysis is why the majority of models use advanced mathematics or numerical methods.

The ASHRAE Fundamentals presents one of the few approximate methods for calculated below grade steady-state heat loss. It assumes steady-state heat loss will follow prescribed paths to the surface. These paths are dependent on indoor temperature, outdoor temperature, and a floor U-factor. The below three equations describe the heat loss of a basement slab. The heat loss "q" (Btu/hr) in Equation (36) is equal to the floor area times a value called the heating load factor "HF" (Btu·hr/m^2). The heat load factor in Equation (37) is a function of the below grade space air temperature "t_{in}", mean annual air temperature "$T_{m,s}$", and the soil surface temperature amplitude "A_s" which is shown in Equation (29). The last term "$U_{avg,bf}$" is the average U-factor for a below grade surface calculated from Equation (38) where "w_b" is the shortest basement width, "z_f" is the floor depth below grade, and "R_{other}" is the total thermal resistance of the wall assembly. No comments are made to how accurate the follow equations, but they are meant for design purposes only [13].

$$q = A \cdot HF \tag{36}$$

$$HF = U_{avg}\left(t_{in} - T_{m,s} + A_s\right) \tag{37}$$

$$U_{avg,bf} = \frac{2k_{soil}}{\pi w_b}\left[ln\left(\frac{w_b}{2} + \frac{z_f}{2} + \frac{k_{soil}R_{other}}{\pi}\right) - ln\left(\frac{z_f}{2} + \frac{k_{soil}R_{other}}{\pi}\right)\right] \tag{38}$$

Krarti et al. has performed a large body of work on foundation heat loss using an analytical solution they term the interzone temperature profile estimation (ITPE)

technique. The technique splits the building/soil domain into several zones where it is easier to solve the heat conduction equations. The heat conduction zones are coupled together through symmetry and heat flux continuity at each boundary. This produces a system of Fourier coefficient equations that are solved with Gauss-Jordan elimination. The number of coefficient equation depends on the number of specified zones. The final temperature distributions for each zone are found by substituting in the coefficient values. The Fourier coefficient calculation is not trivial, but does result in a highly accurate method. Several studies use this technique in different foundation configurations for both steady-state and periodic heat loss [53-57]. Krarti and Choi also present a successful simplification of the ITPE technique that is within 10% of the building heat loss when compared to the full ITPE technique [58].

Other analytical methods include a study by Delsante, Stokes, and Walsh who calculate heat loss into a two and three dimensional semi-infinite solid using Fourier transforms. The end result is a solution for the 3-D heat flow into the soil underneath a rectangular slab. They represent the surface temperature boundary condition as a harmonic function. They found the heat flow is 1-D perpendicular to the slab if the harmonics frequency is one day [59]. Kusuda and Bean present a comparison of three foundation heat loss methods, one of which uses Green's Functions called the Lachenbruch Solution. The Lachenbruch Solution is formulated around the heat loss of a radiant slab-on-grade foundation into a 3-D semi-infinite medium. From the resulting soil temperature distribution, the authors found a large temperature gradient exists near the floor edge during winter, and summer heat transfer is practically one-dimensional

[60]. The Lachenbruch Solution is important because it establishes a Green's Functions precedent in foundation heat loss formulations.

Hagentoft and Claesson present a set of papers that balance mathematical complexity with accuracy. They split the heat flow into a steady-state, periodic, and pure temperature step. The total time dependent heat loss is found by solving the three parts separately and then superimposing them together. The formulation uses dimensional analysis throughout the process to reduce the number of parameters. An innovative concept by the authors is to combine the foundation assembly and materials into an equivalent insulation thickness. In other words, the foundation is treated as a fictitious soil layer that has the same thermal resistance as the foundation. This reduces the number of parameters describing the foundation assembly to one value. This process is repeated for other parameters and graphed for various insulation and foundation thicknesses. The three parts of the time-dependent heat loss are found by inserting parameter values read off the graphs. This greatly simplifies an otherwise complex analytical analysis [52, 61, 62].

Numerical methods for calculating foundation heat loss are much more common in literature since it is easier to represent the non-orthogonal domain and foundation construction. Researches from the Tohoku University in Japan present detailed experimental results from five years of measurements at a semi-underground test house. The experiments give an excellent indication of heat flow paths around the building's foundation which they were able to replicate with a simple 2-D finite element model [63]. A later study by different authors uses the same test house data to verify a 3-D finite

element simulation. Their results were in better agreement with experimental values than the previous 2-D simulation [64]. Zhong and Braun present another study for slab-on-grade that assumes 1-D heat flow paths from the foundation to the ambient and deep soil. Their purpose was to develop correlations for a more general application method meant for hourly simulations using transient 2-D finite element models. A convective boundary represents the inside slab surface, and a solair temperature derived from the typical meteorological year represents the soil surface. The authors conclude the method results in accurate hourly heat flux predictions for building simulations [65]

Weitzmann et al. present another 2-D transient model that is simplified by using a characteristic dimension shown below in Equation (39). The characteristic dimension "CD" is equal to the floor area divided by half the foundation perimeter. This parameter simplifies the true 3-D heat flow from a foundation to two-dimensions by extending the actual foundation width to the value of the characteristic dimension. Heat loss from a foundation is by its nature 3-D, so any simplification to two-dimensions will have inherent errors. The intent of the characteristic dimension is to reduce those errors by applying a width that is more representative of the three dimensions. The authors specifically applied this parameter to a slab-on-grade heated floor. The model was validated with good agreement against temperature measurements throughout the foundation and soil [66].

$$CD = \frac{A}{1/2\,P} \tag{39}$$

PREVIOUS RESEARCH AND MOTIVATION

The review of current literature and information in the field of earth-air heat exchangers (EAHXs) reveals essential research in several areas. Soil temperature prediction in areas free of structures is well documented, and in many cases easy to implement. There also exist many steady-state analytical EAHX design calculations that are good for basic engineering assessments. More complex models perform well at coupling the soil conduction with heat and mass transfer in the EAHX. These models are both analytical and numerical. While they have high accuracy, the mathematical degree of difficulty is at the academic level, and they are limited to certain EAHX design types. The above mentioned models are effective at simulating certain aspects of EAHXs. A few of the more advanced concepts can even take into account intermittent operation and heat transfer between multiple parallel legs (labyrinth systems).

This information is important to the field, but it is not much help to architects and engineers outside of academia who are trying to construction high performance homes. It is unrealistic to expect them to pick up a model out of literature with advanced mathematics or numerical methods, and start designing EAHX systems. Unfortunately, this is really the only avenue for the design information they need since there are currently no other resources. For example, there is no information on the pros/cons of installing an under slab EAHX in a hot/humid climate such as Houston, Texas, or the expected BTU's per foot from an under yard EAHX in a northern climate like Bozeman, Montana. These are just two examples of many that portray basic, fundamental information regarding EAHXs as a system that is currently missing from the field.

This fundamental information would be present in EAHX design standards or guidelines, but these currently do not exist. Earth-air heat exchangers are not a new technology, so the question becomes why has this not been done yet? Part of the reason is a simulation model currently does not exist to conduct the number of extensive studies required to form this basic information. None of the previous discussed models in literature are up to the task for a variety of reasons. Some are too simplified such as the steady state models. Others have high levels of accuracy, but are concentrated on a specific heat transfer mechanism or a certain set of conditions.

The absence of a model and framework inclusive to all EAHX design considerations needed in a fundamental study provides the motivation for this research. This research approaches EAHXs on systems level that combines all design parameters and energy transfer into one interlinked problem. The end result is a model framework that encompasses the majority of EAHXs simulations needed in fundamental research. The framework must be versatile enough to incorporate other design attributes not included in now through future work. The hope is this framework will give academia and industry the tools to provide much needed information to the rest of the field.

This research is split into five chapters which each represent a piece of the model framework. The first chapter covers experimental data a test residence with near identical under yard and under slab EAHXs. This provides the basis for a comparative study between two installation types, and experimental data for model validation. The next chapter develops the backbone of the model using the Green's Function method. This method is capable of incorporating most of the heat transfer mechanisms and time-

dependent weather conditions EAHX experience. This process however requires numerical integration which can be time intensive. In response, a new simulation technique was developed to speed the simulation process. The next two chapters then apply this process to predict the under yard and under slab soil temperatures. This proves out the Green's Function method and lays the groundwork for a novel method of calculating under slab soil temperatures. These soil temperature models then feed information into the last chapter which simulates EAHX operation with a finite difference approach. The finite method calculates heat transfer along the EAHX for any set of operating conditions.

EXPERIMENTAL DATA

Earth-Air Heat Exchanger Experimental Setup

REHAU® Montana Ecosmart House Project

There are few instrumented earth-air heat exchanger (EAHX) systems in the United States. This research has access to both an under yard (UY) and under slab (US) EAHX at the REHAU® Montana Ecosmart House Project (RMEH) located in Bozeman, Montana. The RMEH, pictured in Figure 4, is a collaborative effort between industry and academia to expand knowledge regarding environmental and human sustainability. The residence incorporates a series of available, affordable, energy-efficient, and sustainable building products in an integrated design approach to determine which combination optimizes energy consumption, comfort, and life-cycle costs. The RMEH also addresses human sustainability by incorporating designs that allow for disabilities and aging-in-place [67].

The energy-efficient and sustainable systems include geothermal, solar thermal, a heat recovery ventilator, thermal heat sink, thermochromic windows, electronically controlled pumps, insulated concrete forms, structurally insulated panels, radiant heating/cooling, and of course two EAHXs. The residence's mechanical system is controlled via web-based software. The software is capable of recording data through the control sensors, but lacks the large-scale instrumentation for research. A data acquisition system separate from the control system was also installed to extensively monitor the energy systems and building envelope. There are over 250 sensors spread throughout the

residence for long term monitoring. The data acquisition program stores daily data files for all sensors. This allows researchers to test any system or product while simultaneously monitoring effects throughout the house and provides a complete picture of energy use in the residence.



Figure 4: REHAU® Montana Ecosmart House Project [67]

Earth-Air Heat Exchanger Construction

The purpose behind installing both an UY and US EAHX in the same residence was to conduct a comparative study between the two systems under the same set of experimental conditions. The EAHXs orientations' relative to the residence foot print is shown in Figure 5. Separate inlet towers for both systems are located just outside the foundation which flow directly into the mechanical room after dropping under-ground as pictured in Figure 6. The reason both systems first flow into the mechanical room is for control purposes. The inlets are directed through a series of ducts and dampers capable

system isolation or bypass. Since air flows into the mechanical room before entering the EAHXs, dry bulb temperatures were increased 10°F to 15°F between the outdoors and the actual inlet during the coldest parts of testing.

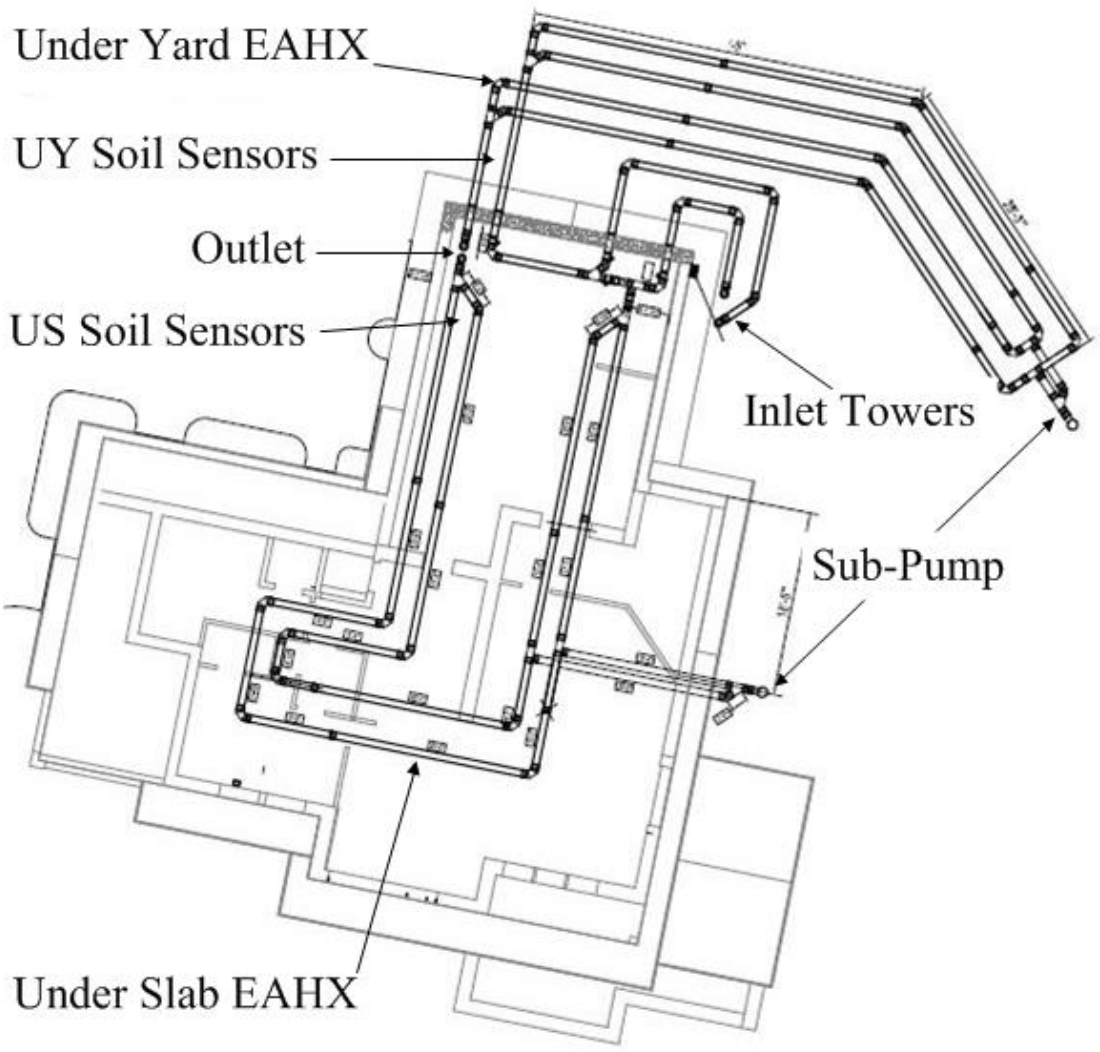


Figure 5: The under yard and under slab EAHXs located at the REHAU® Montana Ecosmart House Project in relation to the residence's footprint, also pictured is location of sump-pumps, booster fans, and soil temperature sensors



Figure 6: Inlet towers of the under yard and under slab EAHXs directed directly into mechanical room through the foundation

A direct comparison between the two EAHXs is possible because they have near identical construction. The piping (or ducting) is eight inch diameter polyvinyl chloride (PVC) with a 0.20 inch wall thickness. It is manufactured using a specialized extrusion process that adheres a 0.05 inch thick internal silver lining. This gives the pipe wall a total thickens of 0.25 inches. The silver lining's purpose is to inhibit microbial or mold growth. Each system has a total buried length of 350 feet and is installed at an angle to drain condensed water to separate sub-pumps as seen in Figure 5. The outlet of both systems is equipped with a 327 watt Fantech model FKD 8XL booster fan. The booster fan typically achieves an air velocity between 900 and 1100 feet per minute. The booster fans typically operate at 150 watts and 160 watts for the UY and US respectively. The fan curves for the Fantech booster fan are available online [68]. Dimensioned

mechanical drawings of both EAHXs are available in Figure 131 and Figure 132 of APPENDIX A.

The only differences that keep these systems from being completely identical are orientation and installation depth. Figure 5 gives an idea of how the orientation differs, but it is clearly seen in Figure 7 and Figure 8. The UY system in Figure 7 requires a wye and a 90 degree elbow to split flow into two parallel legs, while the US system in Figure 8 only requires one wye. This orientation difference, while small, will slightly change flow characteristics and convective heat transfer rates. The installation depth from the surface is also different in both systems. The UY EAHX is between 6 feet and 7 feet below the surface depending on landscape slope. The US EAHX is 50 inches below the basement slab measured from the slab surface. The basement slab varies in depth from approximately 9 feet to the ground surface depending on sloping landscape



Figure 7: Under yard EAHX during construction



Figure 8: Under slab EAHX during construction

Foundation Slab Construction

Heat loss through the foundation slab is important when analyzing or simulating below slab soil temperatures. The heat loss rate is dependent on construction and material types. The slab at the RMEH consists of four inches of concrete embedded with PEXa piping for radiant heating/cooling. Below the concrete slab is two inches of sprayed urethane foam, four to six inches of gravel, then native soil from the gravel to the EAHX. This places the pipe centerline 40 to 38 inches below the gravel, or 36 to 34 inches from the gravel to the pipe surface. Figure 9 is a good example of the slab construction before installation of the urethane foam. The US EAHX is currently below the layer of gravel in the figure. The US installation trench in Figure 8 was backfilled to the top with native soil, and then covered with the gravel shown.



Figure 9: Early slab construction at REHAU® Montana Ecosmart House Project

Data Acquisition Equipment

The air temperature and humidity at the inlet and outlet of both systems is monitored by Banner SureCross DX80 wireless sensors. The wireless sensors are placed as close to the inlet and outlet of the EAHXs as possible as seen in Figure 10 to minimize heat transfer with the mechanical room. The outlet sensors do no measure any heat gain from the booster fans sine the sensors are located four feet upstream of the fans. Air velocity is measured with a Dwyer Series AVU Air Velocity Transmitter which is moved from system to system between tests. The air volumetric flow rate is a function of the air velocity, duct cross-sectional area, and current air density. The RMEH also has a Davis Vantage Pro weather station located in the back yard to monitors outdoor temperature, relative humidity, barometric pressure, dew point, and wind speed/direction.



Figure 10: Left – Under yard wireless temperature/RH sensor located at the outlet, Right – Under slab wireless temperature/RH sensor located at the outlet, also pictured are the PEXa tubes for soil temperatures

Each EAHX system includes two soil temperature and one pipe surface temperature probe located near the outlets. The two locations are labeled in Figure 5. Micro Control Systems T100 thermistors spaced 12 inches apart from the pipe center monitor the soil temperatures in the UY system as shown in Figure 11. Three crosslinked polyethylene (PEXa) radiant tubes provide access to the US soil. These are spaced 16 inches apart from the pipe center as seen in Figure 12. The PEXa tubes are imbedded in the slab and come out inside the mechanical room. They are show near the floor in Figure 10. The tubes contain a type-T thermocouple and are sealed with spray foam.

The sensor locations are labeled as pipe surface, between pipes, and along pipes. The between pipes is between the two pipe legs, and the alongside probe has only soil past its location. Undisturbed soil temperatures away from the EAHXs and foundation are also measured by type-T thermocouples from just below the sod (surface) to a depth of six feet in two foot increments.

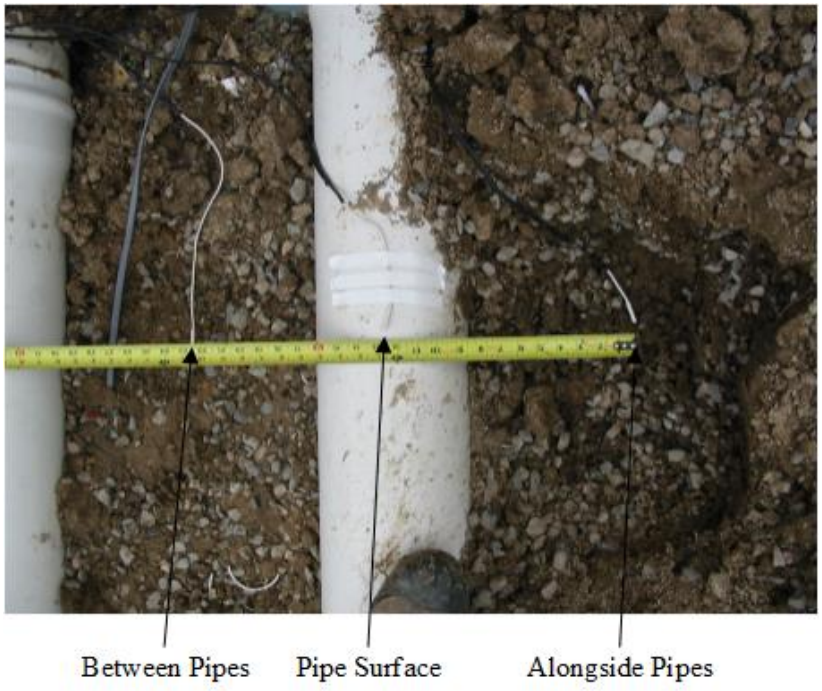


Figure 11: Under yard soil temperature sensor locations, sensors distanced 12 inches from pipe center



Figure 12: Under slab soil temperature sensor locations, sensors distanced 16 inches from pipe center

All data acquisition sensors are monitored by a central desktop computer using LabVIEW 2011 software. Three data acquisition units (DAQs) monitor the 250+ sensors. The main DAQ is a National Instruments (NI) SCXI-1000 chassis, pictured on the left in Figure 13, with four SCXI 1303 thermocouple cards, two SCXI 1300 general purpose voltage cards, and one SCXI 1308 current input card. A NI cRIO 9072 stand-alone DAQ, picture on the right in Figure 13, monitors thermocouples and voltages in the mechanical room. The cRIO is positioned in the mechanical room for convenience since there is no more room for wires around the main SCXI chassis. The third DAQ is an Agilent 34970A which only monitors the three under yard soil temperature thermistors (Figure 11).

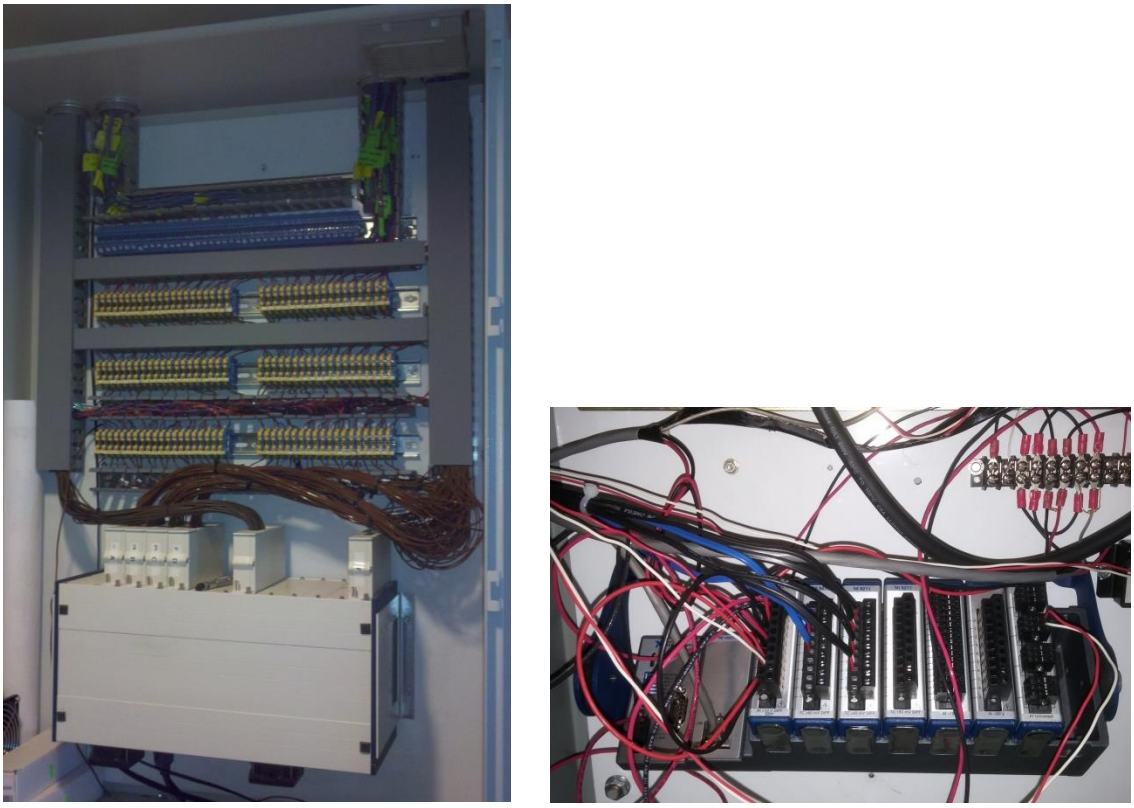


Figure 13: Left – National Instruments SCXI 1000 chassis, Right – National Instruments cRIO 9072

Experimental Data from the REHAU® Montana Ecosmart House Project

Experiment Description

The EAHX tested consisted of four separate 20 to 30 day experiments on each EAHX over the course of one year. Continuously conducting experiments throughout the year was not possible due to other research occurring at the RMEH. The EAHX experiments did not run during these times so they would not interfere with other experiments. This resulted in two blocks of testing. The first was from March 14th, 2013 to June 22nd, 2013, and the second from December 20th, 2013 to April 13th of 2014.

Table 4 summarizes the experiment dates of each EAHX and gives each experiment an identifying abbreviation.

The experimental procedure was fairly simple. The EAHX of interest was isolated from the other systems with dampers. Only the booster fan was activated to provide airflow. The booster fans were continuously on during the testing period. It is much easier to validate simulations with the continuously on approach and does not require writing multiple control algorithms. Soil temperatures for UY-Exp 1 and UY-Exp 2 were not recorded because the Agilent DAQ used to monitor the UY sensors was not added to the data acquisition system until UY-Exp 3 and UY-Exp 4. Air velocity data for US-Exp 4 was also not recorded due to an unnoticed connection error.

Table 4: Experimental test dates for the under yard and under slab EAHXs at the REHAU® Montana Ecosmart House Project.

Under Yard			Under Slab		
Identifier	Start	End	Identifier	Start	End
UY-Exp 1	03/31/2013	04/23/2013	US-Exp 1	03/14/2013	03/31/2013
UY-Exp 2	06/22/2013	07/09/2013	US-Exp 2	04/23/2013	05/08/2013
UY-Exp 3	12/20/2013	01/08/2014	US-Exp 3	01/10/2014	02/02/2014
UY-Exp 4	02/04/2014	02/27/2014	US-Exp 4	03/18/2014	04/13/2014

Airflow Raw Data

Figure 14 through Figure 17 displays the temperature and relative humidity (RH) raw data for the airside inlet and outlet for UY-Exp 3 and US-Exp 3. These two experiments are highlighted because they occur in similar outdoor conditions, and it was the first time the UY soil temperatures were recorded. Similar figures for the other testing periods are found in Figure 133 through Figure 144 of APPENDIX A. All the

figures mentioned display raw data sampled on an hourly basis. The first interesting observation in Figure 14 and Figure 15 is daily temperature fluctuations with the time of day; especially in Figure 14. These diurnal fluctuations are more pronounced in experiments 1 and 2 during the summer months (see Figure 133, Figure 134, Figure 136, and Figure 137). Another interesting result is the outlet temperatures vary only slightly with inlet temperature. This by itself is not that surprising, but it does reveal information on the EAHXs' design. An over-designed EAHX would cause the air to always equilibrate with the surrounding soil before the outlet. This is not happening since the outlet is changing. It is not under designed either since there are no large fluctuations in outlet temperature.

Table 5 and Table 6 provide a summary of max/min temperatures for each experiment, and the max/min temperature difference for heating and cooling. The two tables give an idea of the heating and cooling potential of the two EAHXs. Important to note is that the max/min temperatures did not necessarily happen at the same time as the max/min temperature difference. UY-Exp 2 has the highest cooling temperature difference of approximately 21ºF, but also encounters higher inlet temperatures. In heating, both systems produced an approximate 33 ºF temperature difference during UY-Exp 4 and US-Exp 3. It is clear from the results that the two EAHX systems are easily capable of producing 20ºF to 30ºF air temperature swings. The following sections show these temperature differences are not constant throughout the experiments, and changes in soil temperature around the EAHX happen relatively quickly.

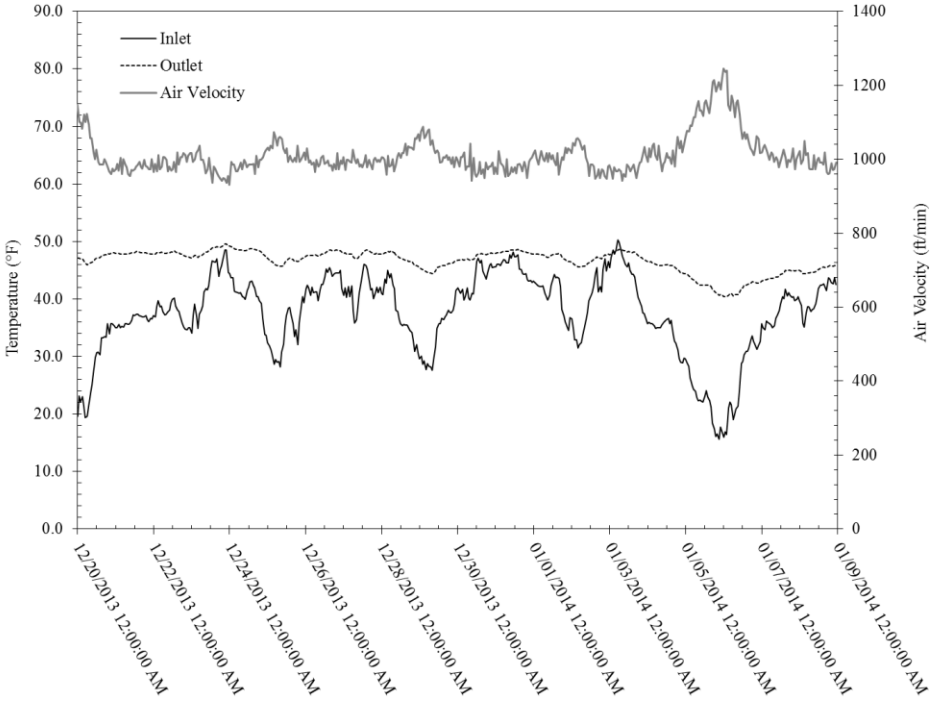


Figure 14: Under yard inlet air temperature, outlet air temperatures, and corresponding air velocity for UY-Exp 3

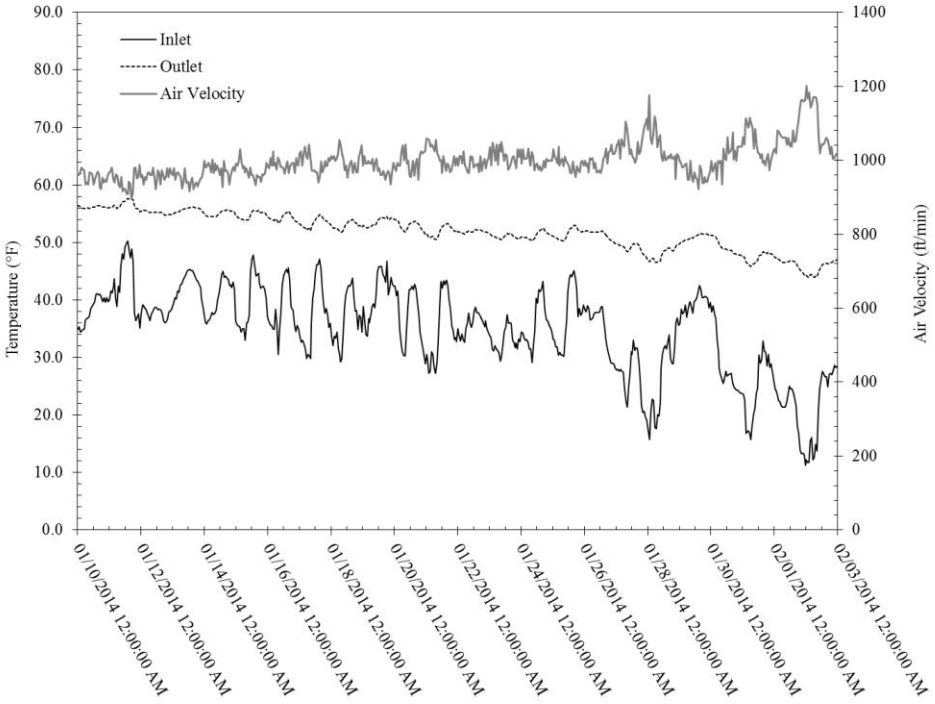


Figure 15: Under slab inlet air temperature, outlet air temperatures, and corresponding air velocity for US-Exp 3

Table 5: Under yard max and min temperatures and max cooling/heating temperature differences during each experiment period

Identifier	Min Inlet Temp	Max Inlet Temp	Max Cooling Temp Diff	Max Heating Temp Diff
UY-Exp 1	32.85	68.95	18.10	9.80
UY-Exp 2	49.35	83.65	20.90	3.10
UY-Exp 3	15.65	50.25	1.80	27.40
UY-Exp 4	2.35	50.25	5.10	33.70

Table 6: Under slab max and min temperatures and max cooling/heating temperature differences during each experiment period

Identifier	Min Inlet Temp	Max Inlet Temp	Max Cooling Temp Diff	Max Heating Temp Diff
US-Exp 1	23.05	57.65	3.30	24.80
US-Exp 2	28.95	72.35	11.00	22.20
US-Exp 3	11.25	50.25	N/A	32.90
US-Exp 4	25.25	71.15	14.40	23.60

An important piece of information to note from Figure 14 and Figure 15 is the air velocity does not remain constant through the entire testing period. There are several occasions, such as in Figure 134 (UY-Exp 2) and Figure 137 (US-Exp 2), where flow is all but cut off even though the booster fan does not modulate. The separation of the control and data acquisition systems causes the flow fluctuations. The REHAU® Company administers the control system, which has proven difficult to work with for the research team. It is important to note though that the average air velocity during each test is relatively the same as shown in Table 7. The same average velocity increases confidence in making direct comparisons between experiments. Note, the lower air velocities of US-Exp1 (Figure 136) were not included in the averaged air velocities.

Table 7: Average air velocity (ft/min) for each EAHX experiment

Identifier	Avg Air Velocity (ft/min)	Identifier	Avg Air Velocity (ft/min)
UY-Exp 1	1050	US-Exp 1	1027
UY-Exp 2	1053	US-Exp 2	1011
UY-Exp 3	1011	US-Exp 3	999
UY-Exp 4	1090	US-Exp 4	N/A

The air velocity also dramatically increases on several occasions with the decrease in air temperature. The best example is in Figure 14 between Jan-5 and Jan-7, but smaller increases are also observed in Figure 15. It is not uncommon to see increases in air velocity with decrease in air temperature, and can be accounted for through published correction factors. A fan is a constant volume mechanism. It will pump a specific volume of air at a given rotational speed and static pressure independent of air density [69]. While a fan is considered constant volume, cooler (denser or heavier) air is more difficult to move and requires more energy. Typically this energy increase causes the fan to run at a higher RPM and increases air velocity. This is likely the case with the booster fans on both EAHXs.

The relative humidity (RH) in Figure 16 and Figure 17 correctly tracks the increases or decreases in dry bulb temperature. Figure 139 through Figure 144 in APPENDIX A displays the same RH data for the other experiments. For example, inlet dry bulb temperatures in US-Exp 3 (Figure 15) are always lower than the outlet. Accordingly in Figure 17, the inlet relative humidity is always higher than the outlet. There are also several occasions in other experiments where the inlet temperature goes above or below the outlet, and the relative humidity shadows the same path. Figure 133

and Figure 139 clearly display this behavior in two locations where the inlet temperature drops below the outlet and the inlet relative humidity rises above the outlet.

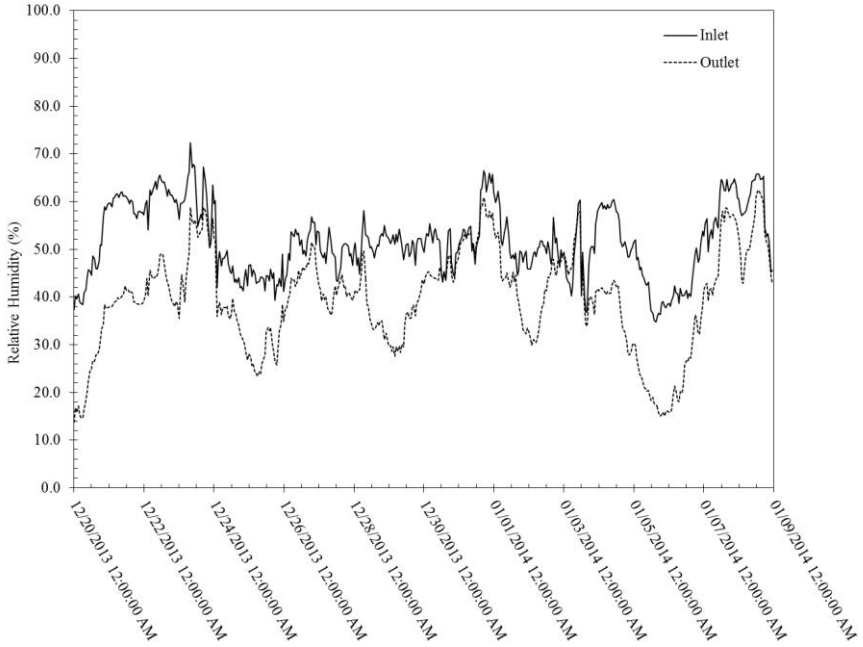


Figure 16: Under yard inlet, outlet air relative humidity for UY-Exp 3

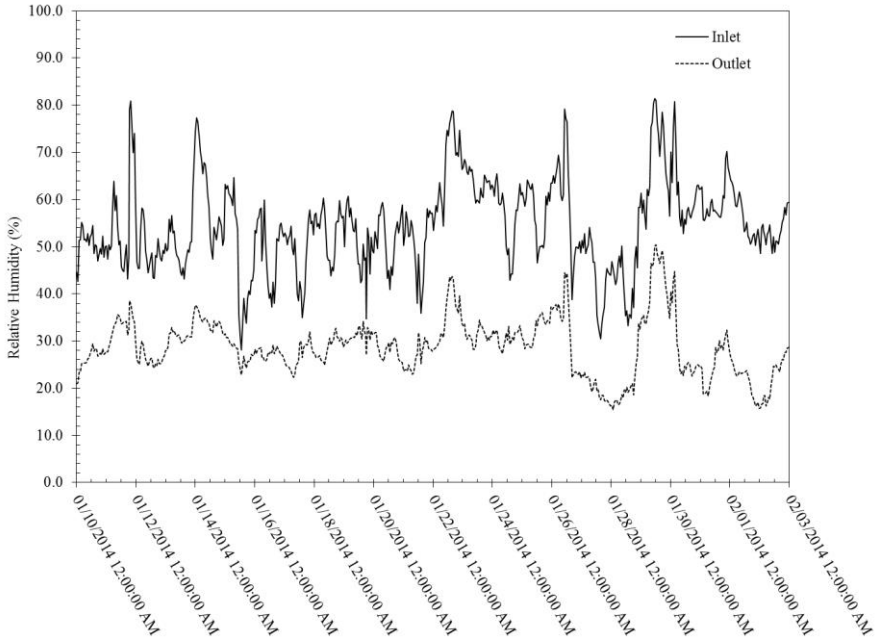


Figure 17: Under slab inlet, outlet air relative humidity for US-Exp 3

Dew Points and Condensation

Condensation mitigation is an important component in EAHX design, but physically measuring condensation in the EAHX piping is challenging. Instead, the experiments determine if condensation occurs by measuring dew points with the outside weather station. The comparison of dew points, air inlet temperatures, and pipe surface temperatures determines if condensation has occurred. Air conditions in Bozeman, Montana are typically very dry during both the summer and winter. This is evident in the low dew point temperatures in Figure 18 and Figure 19 for UY-Exp 3 and US-Exp 3 respectively. Condensation occurs on the pipe surface first, and the pipe surface temperature is approximately 10ºF from the dew points in Figure 18 and Figure 19. The same is observed in the other experiments in Figure 147 through Figure 150. This is not the best way to determine the presence of condensation since the pipe surface temperatures are on the EAHX outlets, but it is the best the current experimental setup can offer.

The soil temperatures for UY-Exp 1 and UY-Exp 2 (Figure 145 and Figure 146) are not available, and instead the outlet air temperature is compared to the dew point. UY-Exp 2 in Figure 146 is the only experiment where condensation occurred as indicated by a lower outlet than dew point temperature. This happens five times during the experiment for short periods; easily less than half a day total. In conclusion, latent heat transfer from condensation was not a major factor during the eight experiments. It only occurred during one experiment and for a short period of time. It is an important

consideration for the design of EAHXs in more humid areas, but not for the atmospheric conditions in Bozeman, Montana.

Soil Temperatures

Soil temperature changes around the UY EAHX reveal several important observations. The first is that an EAHX undergoes transient conduction. This is obvious from UY-Exp 3 in Figure 20 where the alongside pipe temperature sensor experiences a 15ºF temperature difference over the test period (see Figure 11 and Figure 12 for description of sensor locations). The soil surrounding the pipe also loses heat quickly. The alongside pipe temperature drops around 5ºF in the first day due to the cooler inlet temperatures. There is also a temperature lag between the pipe surface and alongside pipe sensor in Figure 20. Several times the pipe surface temperature increases or decrease, and there is a small time delay before the alongside pipe location trends in the same direction.

Figure 21, which includes inlet temperatures, gives a better picture of temperature lag. For example, on December 28th the inlet air drops quickly to around 25ºF. The pipe surface and alongside pipe sensors start at the same temperature and decrease together. On December 29th, the temperature rapidly increases. The pipe surface temperature immediately responds to this increase. The alongside pipe sensor has a small temperature lag and begins increasing less than half a day later. UY-Exp 4 in Figure 151 and Figure 152 exhibit the same trends. The soil temperatures in Figure 20 and Figure 151 both gradually decrease with time as well creating an overall decrease in performance during

extended exposure to lower temperatures. It is assumed higher temperatures will have the same effect, although no data for higher temperatures is available.

The final observation from the UY soil temperatures in Figure 20 and Figure 151 is the thermal short circuiting between the inlet and outlet pipes. The between pipes temperature sensor is at the midpoint of the inlet and outlet of the UY EAHX (see Figure 11). At this location, cool air from the inlet is passing next to warmed air that has already traveled the length of the EAHX. The warm outlet air is adding heat the soil while the cool inlet air is removing it. This creates the thermal short circuit and is why the between pipe sensor in both figures is sensing a much warmer temperature. Placing the inlet and outlet together like this is a design flaw in the UY EAHX, but luckily it only happens over a small distance. This does not happen in the US EAHX since the inlet and outlet are spread apart.

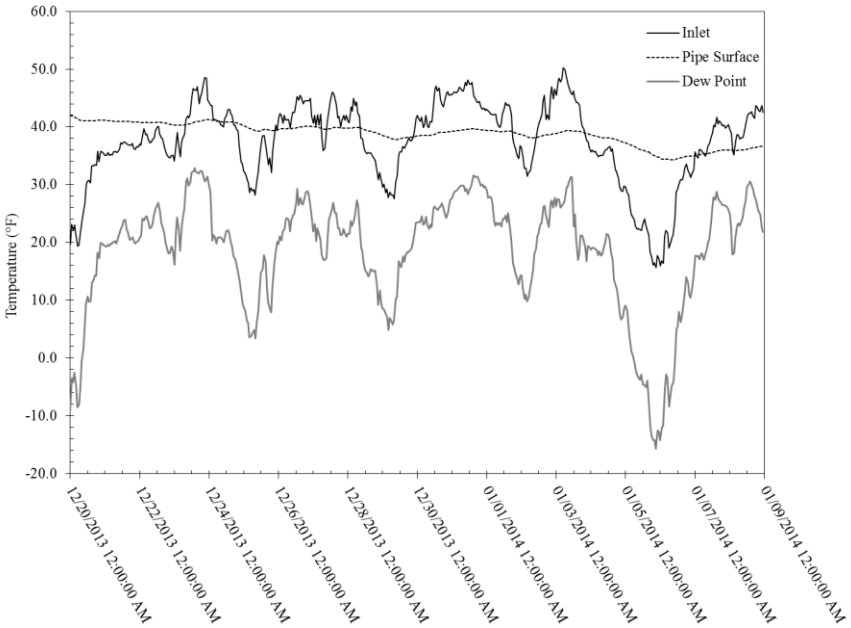


Figure 18: Under yard inlet dry bulb air temperatures, pipe surface temperature, and outdoor dew point for UY-Exp 3

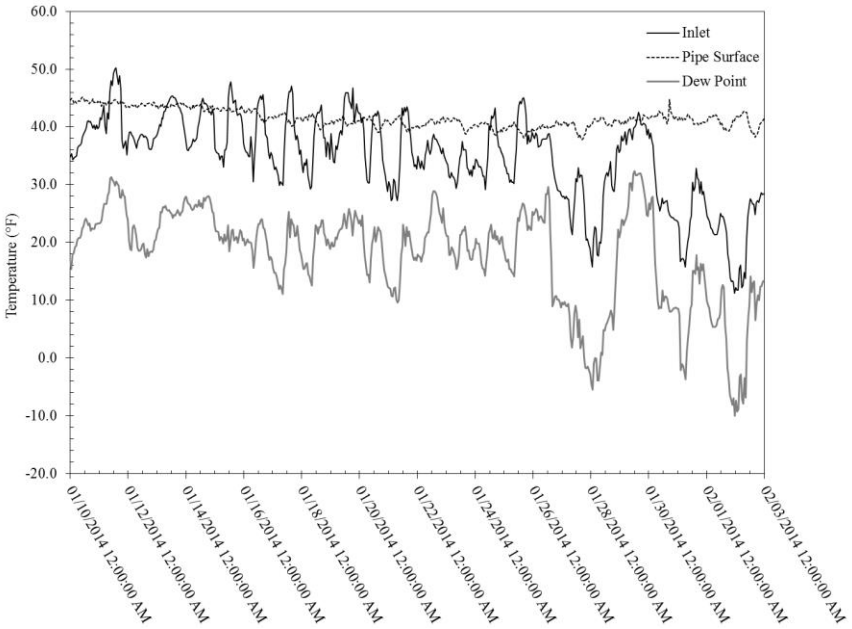


Figure 19: Under slab inlet dry bulb air temperatures, pipe surface temperature, and outdoor dew point for US-Exp 3

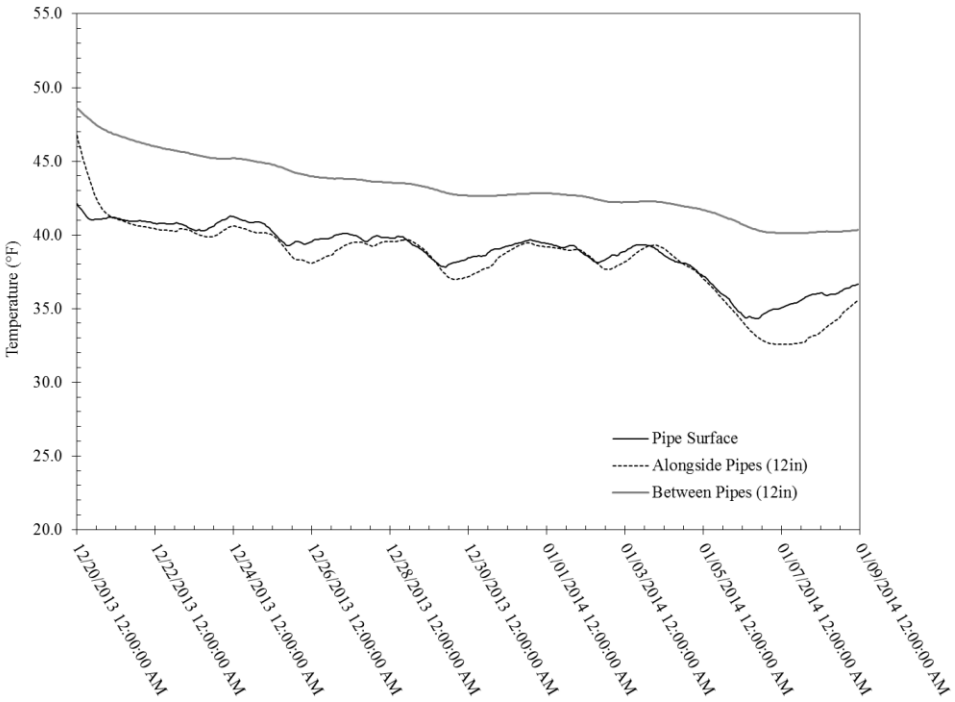


Figure 20: Under yard soil temperatures for UY-Exp 3

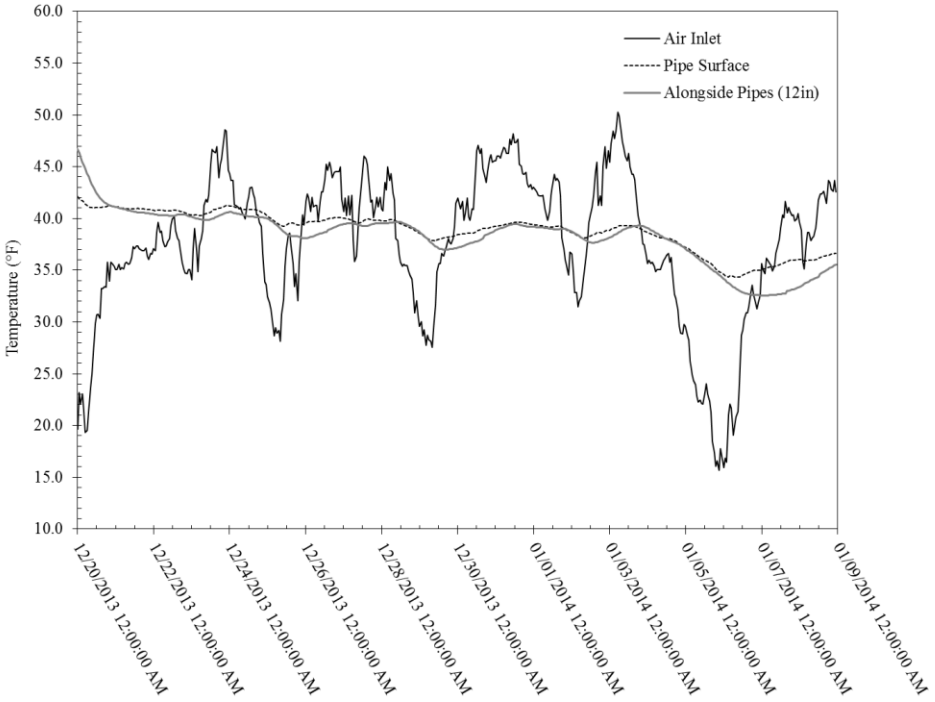


Figure 21: Under yard inlet dry bulb air temperature compared to changes in soil temperatures for UY-Exp 3

Soil temperatures in the US location behave quite differently than the UY. The radiant slabs were actively heating and cooling the RMEH during almost all the experiments. This is evident in Figure 22 where the three soil temperatures vary erratically, but always in the same direction. The irregular temperature is from drift in the radiant slabs. The radiant slabs are not kept at a constant temperature and vary with room requirements. The US soil dependence on slab temperature is further evident in Figure 23 and Figure 24. The last five days of US-Exp 3 show decrease in inlet air temperature (Figure 23) while the pipe surface and alongside pipe temperatures slightly increase. The reason for the slight increase is shown in Figure 24 where the mechanical room slab temperature also slightly increases. Figure 153 through Figure 161 display the same soil temperature behavior for the other three experiments. One feature Figure 22

lacks is a significant decrease in soil temperature due to cooler inlet air, such as those observed in Figure 20. These variations probably occur at the inlet of the US EAHX, but recall the temperature sensors for each system are located at the outlets. The UY inlet and outlet are also right next to each other.

US-Exp 4 encounters an unusual spike in soil temperature in Figure 157 with a simultaneous decrease in rec room slab temperatures in Figure 161. This is counter-intuitive and was first attributed to sensor malfunction. The actual cause was an open outside door in the rec room that was not noticed for around a week. It was unusually cold during this time in March as well, and the rec room staying around 40ºF. The radiant floor was constantly on as high as it could go during this time, but could not meet room requirements. The slab sensors, located near the slab surface, recorded cooler temperatures due to the low ambient in the room. At the same time, the soil saw a drastic increase in temperature from the radiant slabs running constantly on high.

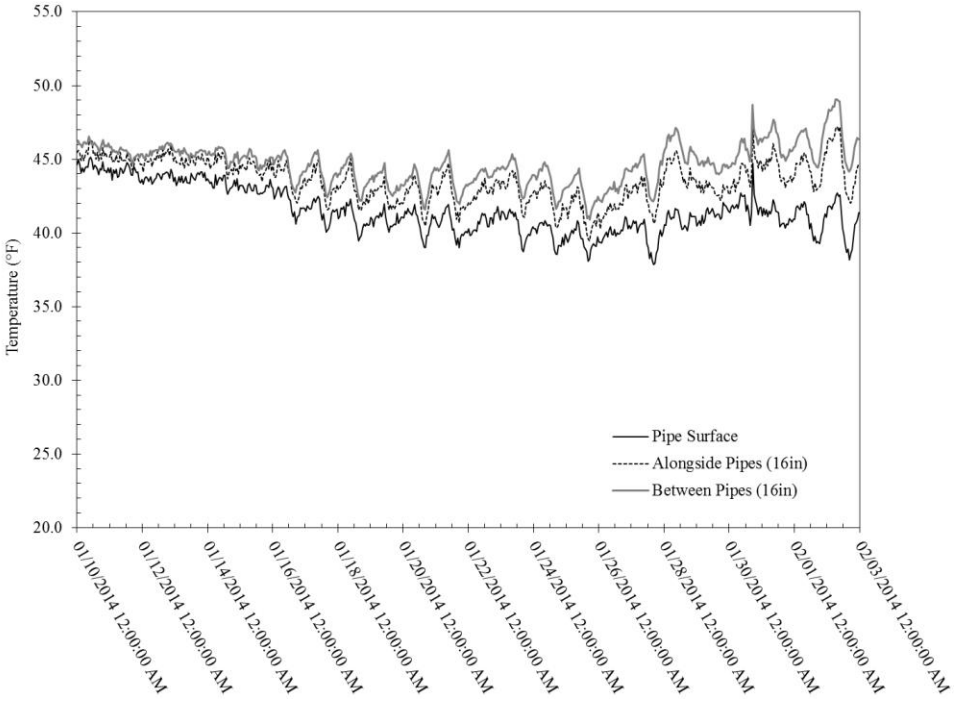


Figure 22: Under slab soil temperatures for US-Exp 3

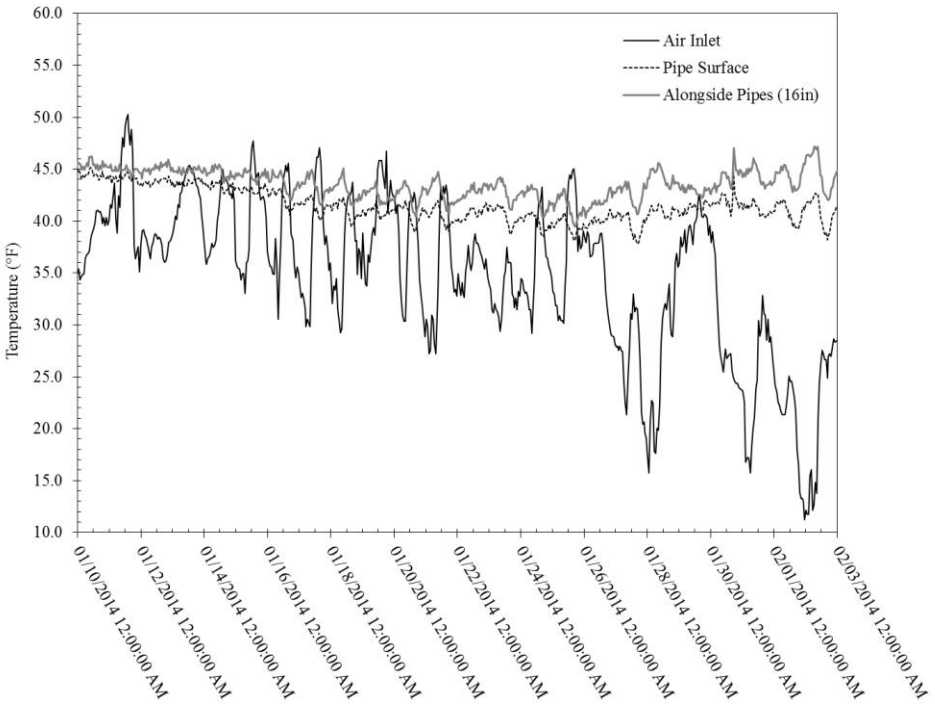


Figure 23: Under slab inlet dry bulb air temperature compared to changes in soil temperatures for US-Exp 3

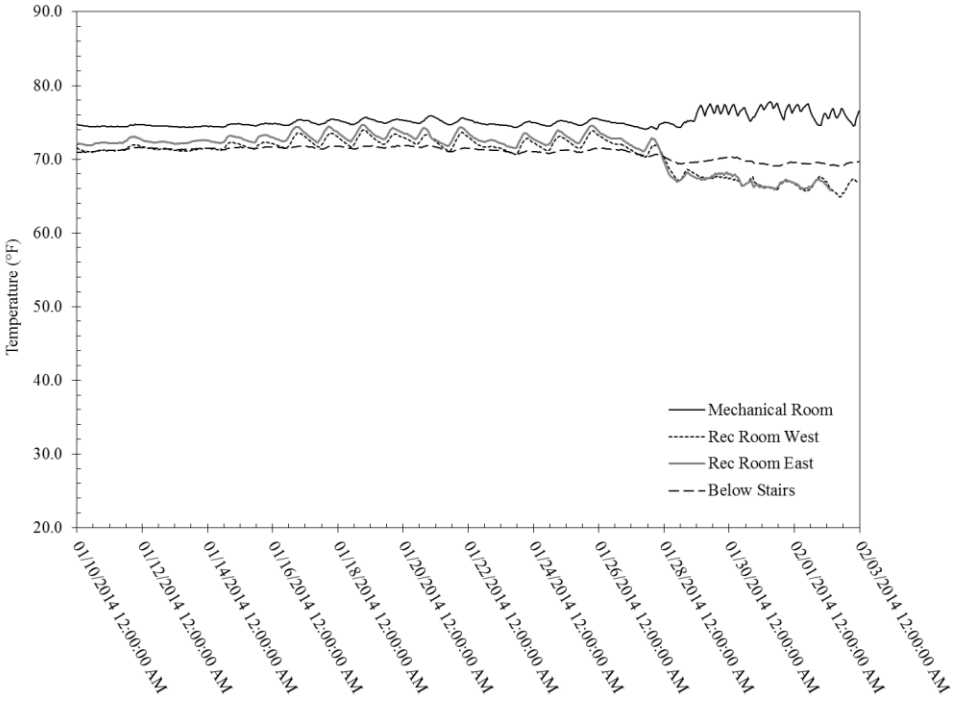


Figure 24: Basement radiant slab temperatures for US-Exp 3, these four sensors cover majority of US EAHX

Consequences of Soil Temperature Probe Locations. The placement of the soil temperature probes on the EAHX occurred very early on in the construction of the RMEH. Only a few Montana State University undergraduate students were involved with the project at this time, not including the author. It is fortunate the contractors on-site at the time had the foresight to include soil temperature probes, but they should not have been located at the EAHX outlets. A well designed EAHX is nearly 100% effective and will cause the inlet air temperature to reach equilibrium with the surrounding soil by the outlet. Air temperature equilibrium though means no potential to drive the conductive heat transfer in the soil. This is why the US soil temperatures in Figure 22 never change with the inlet air temperature. The air passing through the EAHX has already reached equilibrium with the soil by the outlet. The other US experiments in

Figure 153 through Figure 161 exhibit the same. The UY system displays some soil heat transfer in Figure 20 and Figure 151 for UY-Exp 4 due to the close proximity of the inlet and outlet pipes.

The sensor placement does not bode well for s. The US soil temperature data is completely useless for validation purposes since it lacks any soil conduction from the EAHX. There is some hope for the UY location since the between pipes sensor is next to the inlet. The problem here is the influence of the outlet air creates a complex heat transfer situation that is difficult to predict. One hope was to recreate UY-Exp 3 and UY-Exp 4 in the ANSYS finite element software. Then this ANSYS model could validate other UY simulations. Unfortunately, all attempts were unsuccessful. This is primarily due to the UY sensor's close proximity to the building's foundation (see Figure 5). The foundation adds unknown heat transfer mechanisms that were not possible to account for the in finite element model. Validation in later chapters will instead rely on general finite element and computational fluid dynamic simulations.

Annual Under Yard and Under Slab Soil Temperatures. Temperature probes at the surface, 2ft, 4ft, and 6ft depths recorded soil temperatures away from the EAHXs and house from June 2013 to April 2014. The soil temperatures, displayed in Figure 25, follow the typical sinusoidal temperature lag with depth observed in most locations free of structures. The purpose of this figure is to understand how the soil behaves in undisturbed conditions. This information is useful for predicting general EAHX performance at different depths and validates later soil temperature simulations.

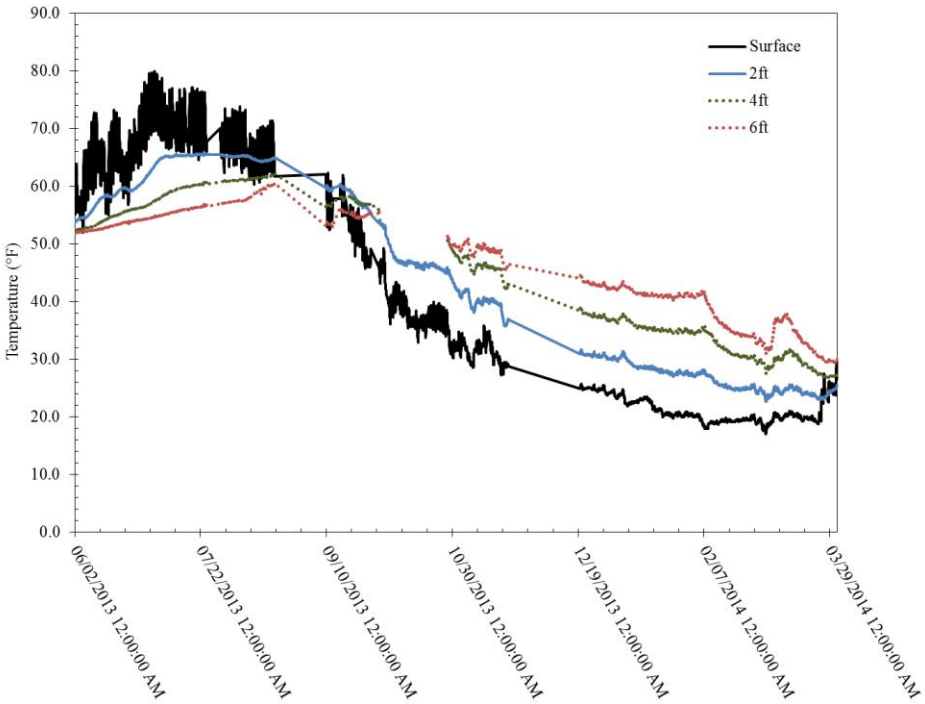


Figure 25: Soil temperatures measured away from the EAHXs and RMEH foundation from June, 2013 to April, 2014

Average Data Comparison

Experimental results covered thus far represent raw data. Raw data is useful, but not when simply trying to determine what outlet air temperature to expect from a given inlet temperature. Averaging common data based on inlet temperature better visualizes this information. The result is one averaged outlet temperature per inlet temperature. A computer program completed the outlet air temperature and soil temperature averaging (when available) based on inlet temperature for all eight experiments. The four experiments for each system were also averaged together into an overall data comparison. Before evaluating the averaged data, it is first necessary to review the computer program used to produce the results.

The following figures average the inlet and outlet temperatures, but the outlet temperatures are essentially the dependent variable. The computer program starts by scanning the inlet temperatures over a desired time period. When the inlet temperature falls inside a specified window around a whole number, it records the inlet and outlet temperatures. The program averages the outlet and inlet after the scan is complete. The temperature window for this study was plus/minus 0.25ºF. The following example better describes the averaging method. If the current whole number inlet temperature is 20ºF, the program records any inlet temperature from 19.75ºF to 20.25ºF along with its corresponding outlet temperature in two arrays. The program then averages the arrays when the scan is complete. This is done for each whole number for which the data extends. The program also calculates other values including average relative humidity, average soil temperature, average velocity, standard deviations, etc. Table 30 through Table 37 at the end of APPENDIX A displays the averaged data results for all eight experiments.

Figure 26 and Figure 27 display the averaged data results with the averaged soil temperatures for UY-Exp 3 and US-Exp 3 respectively. Figure 162 through Figure 167 are similar figures for the other six experiments. Note that in these figures the inlet temperature is on the x-axis, and the corresponding outlet temperature is on the y-axis. The UY soil temperatures in Figure 26 and Figure 164 both increase with increasing outlet temperature. The US soil temperatures in Figure 27 and Figure 165 through Figure 167 remain relatively constant for each inlet value due to sensor placement at the outlet.

Standard deviation increases for the mid-range data points as expected since these values average a large number of data points as seen in the tables of APPENDIX A.

Figure 28 includes averaged data for each individual experiment for the UY location. It is clear that each experiment yielded slightly different results over the same inlet temperatures. This is expected at the temperature extremes as it was already observed the soil temperature around the UY EAHX pipe is dependent on inlet air temperatures. Inlet air between 40ºF and 60 ºF is closer to the ambient soil temperature, but there is still outlet air temperature difference between experiments. This is attributed to two variables. The first is that UY soil temperatures vary throughout the year, and some tests are more than six months apart. The second reason is heat depletion of the soil. UY-Exp 3 and UY-Exp 4 took place around a month apart. From Figure 28, UY-Exp 3 produced consistently higher outlet temperatures than UY-Exp 4. UY-Exp 3 had already depleted the heat from the surround soil prior to UY-Exp 4. The month between the two experiments was not enough for this soil to regain the lost heat and resulted in lower outlet temperatures. This is another example of the transient nature of EAHXs.

The averaged data for the US experiments lie relatively close together as shown in Figure 29. The experiments that were six months apart yield close to the same outlet temperatures. More importantly is similarity between the US-Exp 3 and US-Exp 4. The cooler inlet temperatures during this testing period did not significantly drop the soil temperatures as in the UY experiments. This suggests the slab was losing a significant amount of heat to the soil since heat was replenished in the short time between the two

experiments. This raises the possibility that an US EAHX can draw significant amounts of heat from the foundation slab.

Figure 30 and Figure 31 averages together all the experimental data for each system. The standard deviation for each outlet temperature is much higher in the UY location than the US as expected. Figure 32 displays a side by side comparison of the averaged results for both systems, and it is the best example of how the heat transfer differs in the UY and US installations. The US EAHX clearly produces higher outlet temperatures than the UY for inlet temperatures below 60ºF. Above 60ºF, results are inconclusive due to a lack of data. Weather in Bozeman, Montana is relatively mild, but can reach over 100ºF. The US experiments were not operation during any high temperatures unfortunately.

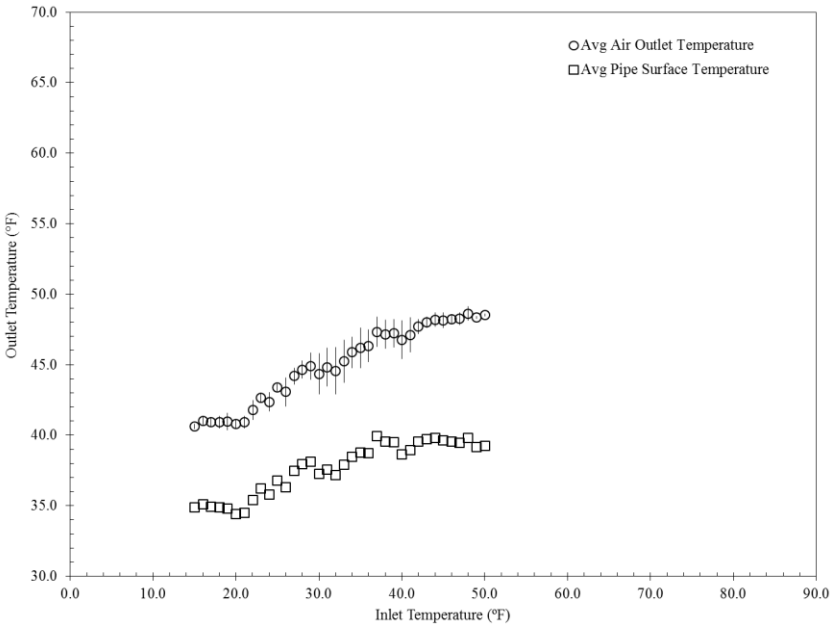


Figure 26: Under yard outlet vs. inlet averaged dry bulb air temperature and average pipe surface temperatures for UY-Exp 3, error bars represent standard deviation of averaged outlet temperature

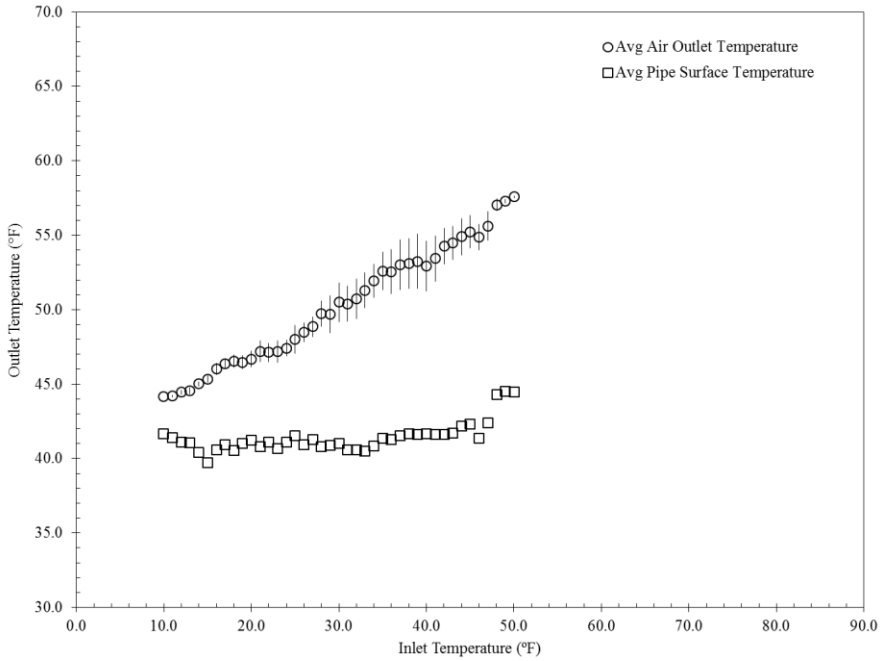


Figure 27: Under slab outlet vs. inlet averaged dry bulb air temperature and average pipe surface temperatures for US-Exp 3, error bars represent standard deviation of averaged outlet temperature

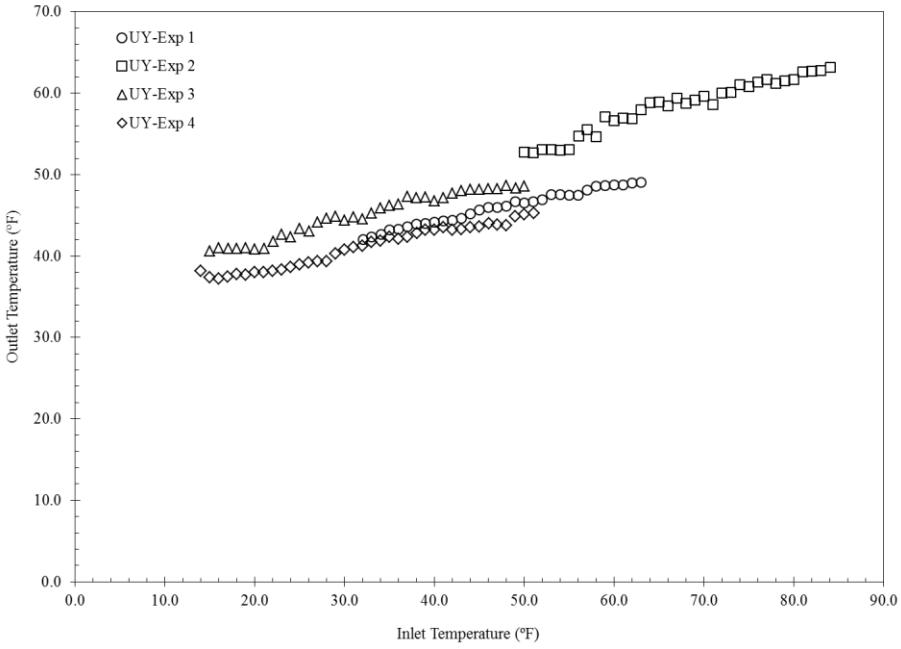


Figure 28: Under yard averaged dry bulb air temperature outlet vs. inlet for four testing periods

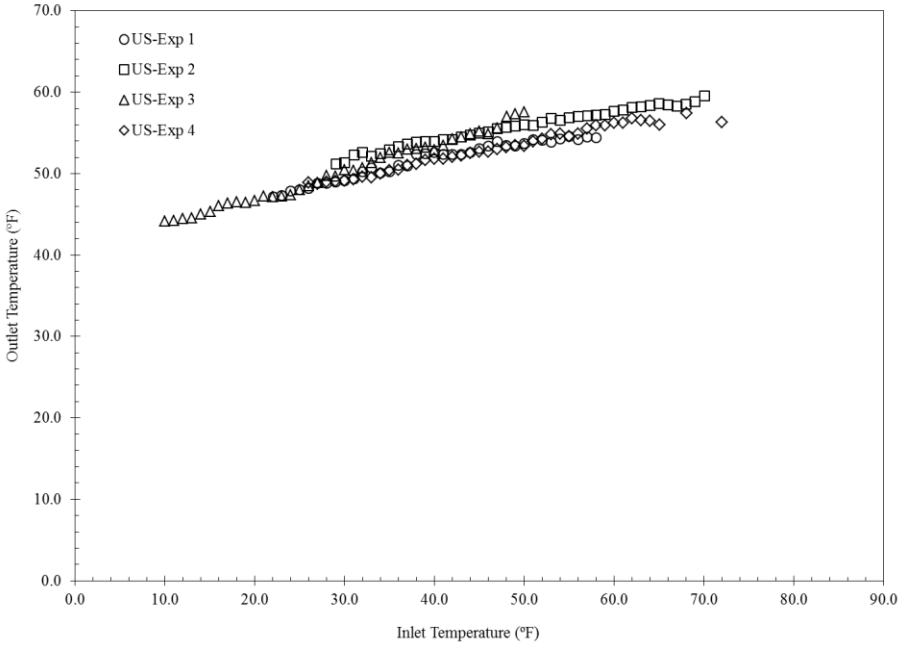


Figure 29: Under slab averaged dry bulb air temperature outlet vs. inlet for four testing periods

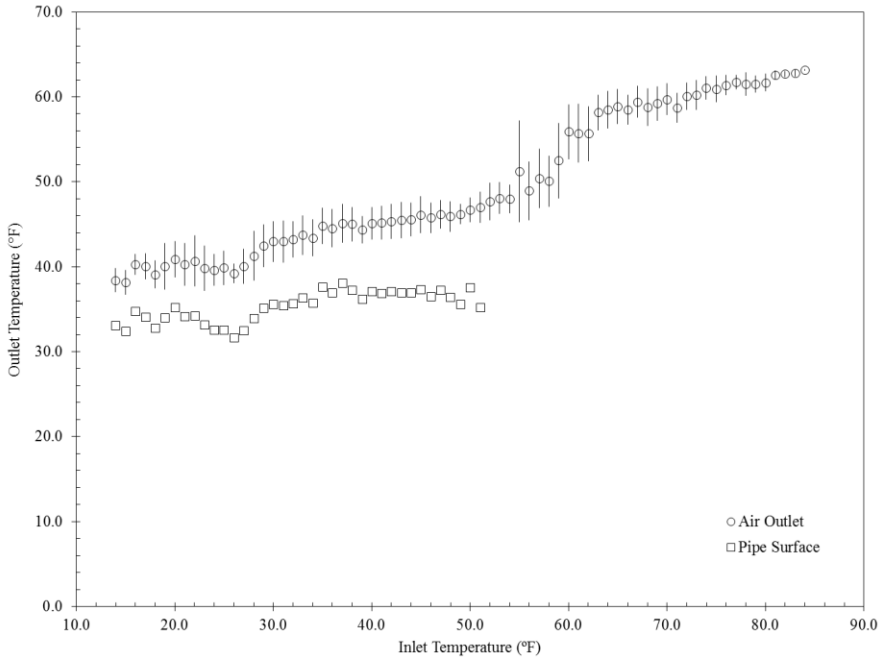


Figure 30: Under yard outlet vs. inlet averaged dry bulb air temperature and average pipe surface temperatures when available for all testing periods, error bars represent standard deviation of averaged outlet temperature

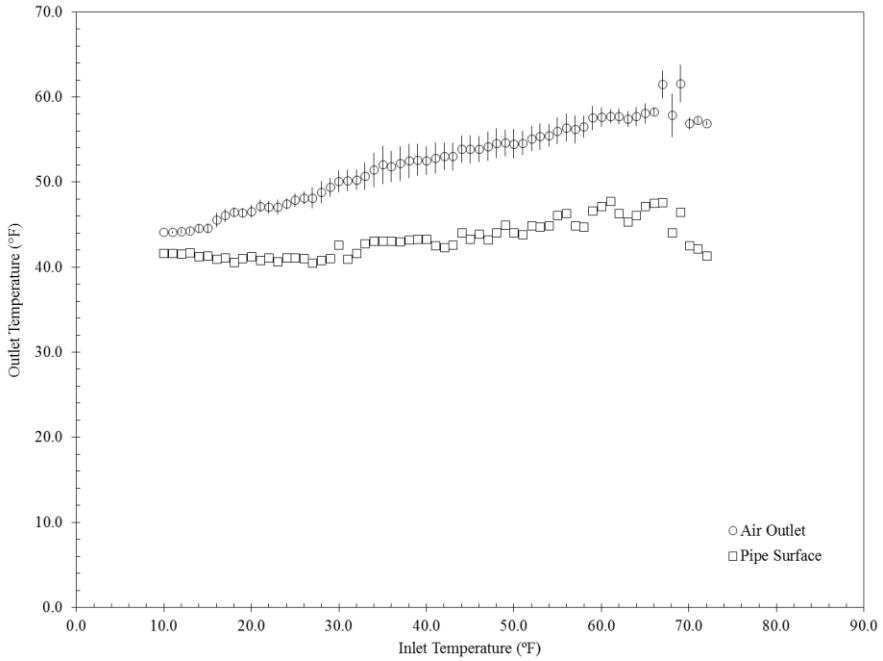


Figure 31: Under slab outlet vs. inlet averaged dry bulb air temperature and average pipe surface temperatures when available for all testing periods, error bars represent standard deviation of averaged outlet temperature

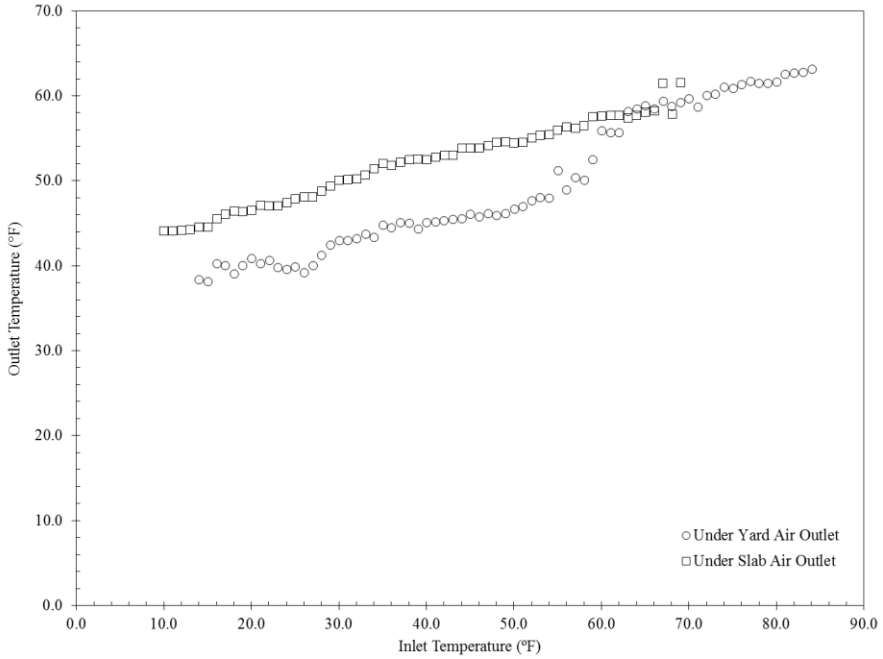


Figure 32: Under yard vs. under slab averaged dry bulb air temperature outlet for all testing periods

Coefficient of Performance

The coefficient of performance (COP) is a useful method of measuring the energy efficiency or effectiveness of the EAHXs. The COP is simply the energy extraction or rejection from the EAHX divided by the energy input as shown in Equation (19). Basically, this is the ratio of energy extraction or rejected to the energy input. The positive COP values indicate the EAHX is in heating mode, and the negative that the EAHX is cooling the airstream. The data for the inlet temperature, outlet temperature, and air velocity come from the averaged data comparisons in the previous section. Mass flow rate requires the air density which is found with the average temperature between the inlet and outlet.

This section highlights the results for UY-Exp 3 and US-Exp 3 in Figure 33 and Figure 34 respectively. Coefficient of performance results for the other six experiments are in Figure 168 through Figure 173 of APPENDIX A. UY-Exp 3 and US-Exp 3 took place between January and February so the EAHXs are mainly in heating mode. The COP values give no indication of leveling off in both figures and reach values as high as 25 to 30. This indicates extremely good performance in heating mode during the coldest parts of the year. That performance drops considerably though for the shoulder seasons when then air temperatures are between 40ºF and 60ºF. In cooling mode, the highest COP value recorded was approximately 17 in UY-Exp 2 in Figure 169 at an inlet air temperature of 80ºF.

Figure 35 displays the COP values for the averaged inlet and outlet temperatures over all the testing periods. This is the same data that is displayed in Figure 32. This

provides a clear picture of which EAHX performs better for the Bozeman, Montana location. In heating mode, the US EAHX clearly outperforms the UY at all temperatures up 45ºF. An interesting observation from this figure is that the UY EAHX switches into cooling mode at 45ºF. The US EAHX does not switch over until 56ºF. This implies that the UY EAHX is not providing any heating benefit for temperatures between 45ºF and 55ºF. In fact, it is actually working against the mechanical systems and further cooling the air. This information is hard to notice in Figure 32 for just the general air temperatures. This highlights the importance of considering control strategies for EAHXs. It is not always beneficial to operate an EAHX throughout the year. There are some air and soil temperatures that will work against the other mechanical systems.

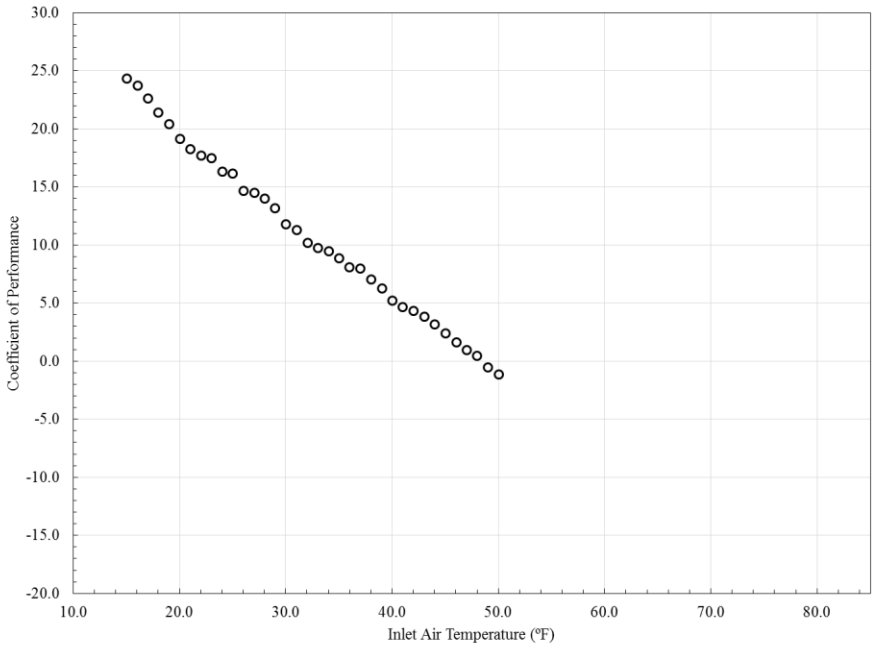


Figure 33: Coefficient of performance for the under yard EAHX based on inlet temperature for UY-Exp 3

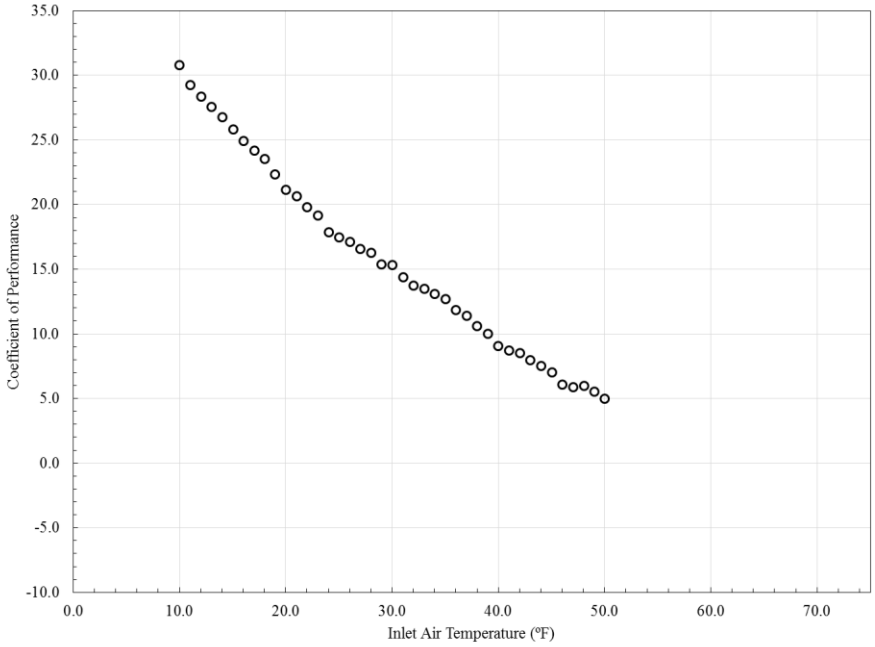


Figure 34: Coefficient of performance for the under slab EAHX based on inlet temperature for US-Exp 3

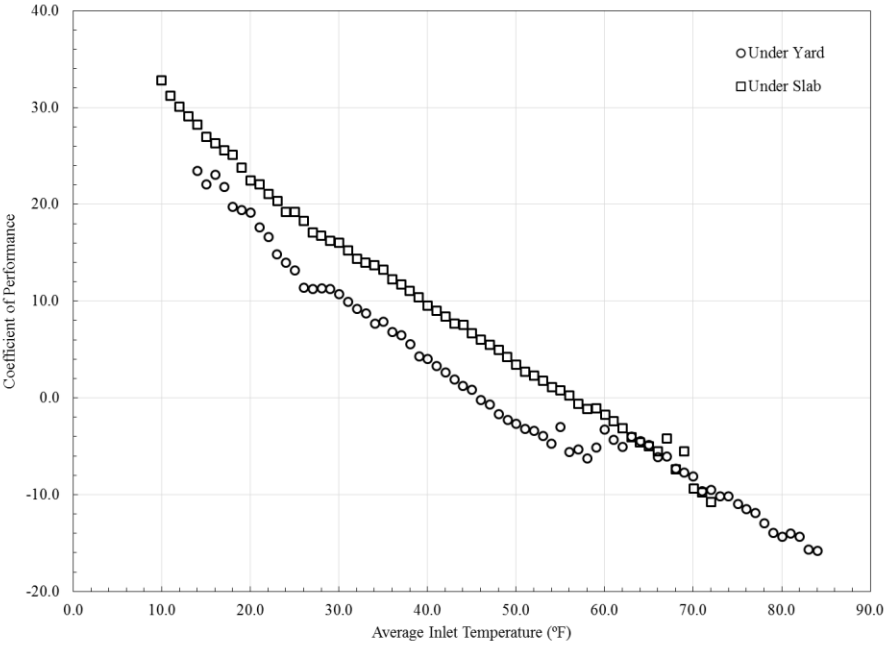


Figure 35: Coefficient of performance for the under yard and under slab EAHX based on the averaged inlet and outlet temperatures for all testing periods

Experimental Errors and Recommendations

The main causes of experimental errors at the RMEH are poor placement of soil temperature sensors and control system complications. A previous section in this chapter already discusses the poor placement of the soil temperature sensors. The control system caused problems during the experiments by executing seemingly random control algorithms. This occurred several times even after manually overriding the controls. The RMEH controls have always been a black box for the research team, and attempting to decipher or change the control algorithms was not an option do to time constraints. A good example of the control system influencing an experiment is in US-Exp 2 in Figure 137. On multiple occasions the control system closed dampers to the US EAHX cutting off air flow. Other examples include changing radiant slab temperatures during experiments or activating the heat recovery ventilator. The EAHX experiments were fortunate to capture and account for the errors caused by the control system with other data acquisition sensors.

The experimental errors discussed above are unfortunate, but they are useful lessons for design of future experiments. A future EAHX should be approximately 300-350 feet in length of six or eight inch pipe. It should also have optional single or multiple leg operation. Multiple leg operation is commonly seen in the field, but it is difficult to model since air flow through each leg can vary. Leg isolation would allow for experiments for modeling and actual operation. Next, the soil surrounding the EAHX requires many more sensors place vertically and horizontally along the entire length. This will allow for a better representation of soil temperatures for modeling. Spacing of

such sensors should be between 25-50 feet. Air temperature and humidity monitoring along the length at the same locations as the soil sensors would also be beneficial. Finally, connecting the EAHX to some kind of psychrometric chamber would allow for the simulation of air conditions for locations all around the world. This would be especially useful for modeling latent heat transfer.

Location Data for Simulation Models

An EAHX comprehensive study requires operational analysis in all types of climatic conditions. It is not feasible to conduct physical experiments like those at the REHAH® Montana Ecosmart House Project in multiple locations. Instead, this research conducts simulations in locations all around the United States based on available soil and air temperature data. Soil and air temperature data is available online from several sources and takes the place of physical experiments. Fifteen locations, including Bozeman, Montana, were selected based on the availability of weather and soil data. An effort was also made to diversify climate zones. Soil data close to major cities or airports was the determining factor on location choice. The locations are pictures below in Figure 36 courtesy of Google® Earth. Table 8 also lists the locations with corresponding heating and cooling degree day data. The study is limited to the United States due to difficulty in locating soil temperature data for other parts of the world.

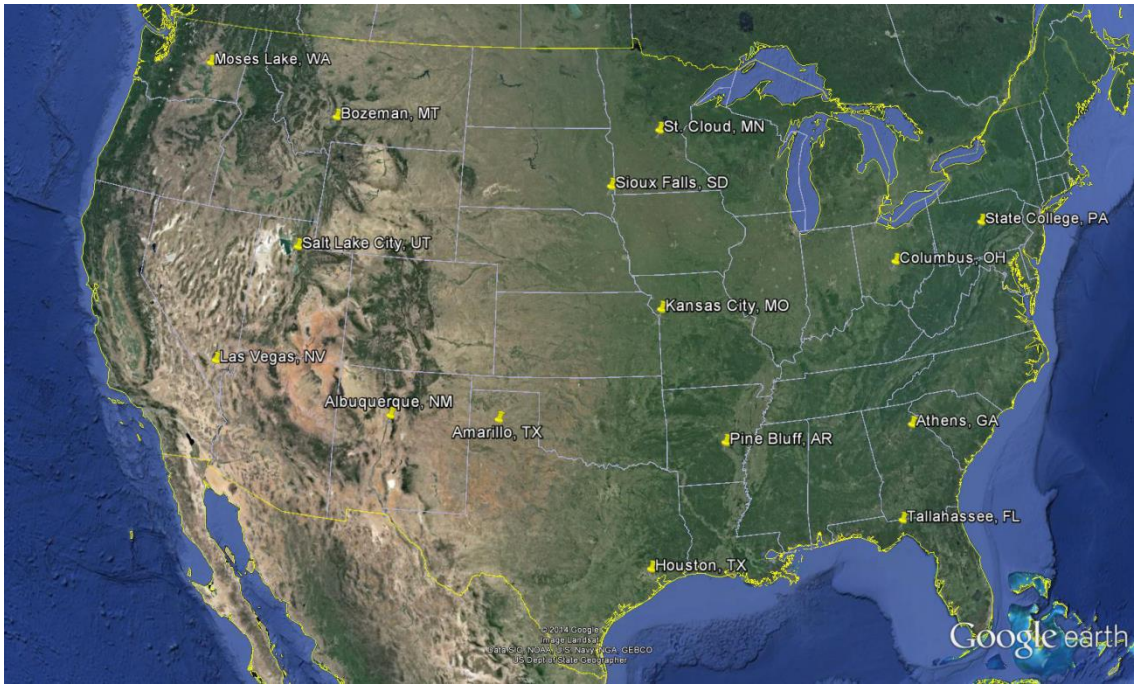


Figure 36: Fifteen locations chosen for EAHX simulations based on availability of soil and air temperature data

Table 8: Fifteen locations chosen for EAHX simulations with base 65ºF heating degree day (HDD) and cooling degree day (CDD) values [13]

Location	HDD	CDD
Albuquerque, New Mexico	4069	1348
Amarillo, Texas	4198	1369
Athens, Georgia	2762	1789
Bozeman, Montana	8372	212
Columbus, Ohio	5322	971
Houston, Texas	1414	3001
Kansas City, Missouri	5104	1356
Las Vegas, Nevada	2105	3348
Moses Lake, Washington		
Pine Bluff, Arkansas	2655	2236
Saint Cloud, Minnesota	8520	473
Salt Lake City, Utah	5521	1193
Sioux Falls, South Dakota	7524	753
State College, Pennsylvania		
Tallahassee, Florida	1534	2563

Typical Meteorological Year

Simulation of EAHXs requires yearly atmospheric air data. Atmospheric data is available from the National Oceanic and Atmospheric Administration (NOAA) for hundreds of locations around the world. Averaging several years of atmospheric data from NOAA is acceptable, but takes time to compile. A faster and more accurate means is to use the Typical Meteorological Year (TMY) compiled by the National Renewable Energy Laboratory (NREL). NREL derives the TMY files from the 1961-1990 and 1991-2005 National Solar Radiation Database archives. The data sets include hourly atmospheric and solar radiation values. They are specifically meant for use in computer simulation programs and do not represent extreme conditions (not mean for worst-case scenarios) [70]. This research uses the TMY3 data files for atmospheric conditions.

The primary value of interest for the EAHX simulations is dry bulb temperature, since it can calculate soil temperatures and convective heat transfer through the EAHX. Dry bulb air temperatures from the TMY files for all 15 locations listed in Table 8 are found in APPENDIX B. Inputting the raw hourly values from the TMY data files is acceptable for a simulation program, but also includes drastic shifts in temperature over short times. Fitting a function to the TMY data with a least-squares regression (LSR) is a better approach. A Fourier series is an appropriate function for the fit since yearly temperatures vary sinusoidally. APPENDIX B also includes a graphical representation of the Fourier LSR fits and the corresponding fit equations.

Soil Temperature and Moisture Data

Soil temperature and moisture data is available for a limited number of locations around the United Sates from the National Resource Conservation Service (NRCS), which is part of the U.S. Department of Agriculture [71]. Yearly data is available in daily or hourly intervals. There are no pre-averaged data files as is with the TMY data sets, so data for the last five years was averaged. The monitoring sites are typically located on farms outside major cities. The fifteen locations in Table 8 had a TMY data file and a NRCS soil monitoring station in close proximity. Figure 174 though Figure 188 in APPENDIX A includes observed soil temperatures at 20 and 40 inches. Forty inches was the maximum sensor depth on all monitoring stations. The soil surface temperatures are fit with the same Fourier LSR as the TMY files. They are also displayed graphically in APPENDIX B.

EARTH-AIR HEAT EXCHANGER SIMULATION USING GREEN'S FUNCTIONS

Transient Conduction Solution Method

Experimental data from the REHAU® Montana Ecosmart House Project clearly indicates transient soil conduction during under yard (UY) and under slab (US) operation. The best example is UY-Exp 3 in Figure 20 where soil temperatures drop more than 10ºF during the first 72 hours of the experiment. Soil temperature surrounding the earth-air heat exchanger (EAHX) pipe directly effects the performance, and it is also challenging to calculate and forecast. The simplest simulation approach calculates the soil temperature once and assumes it always remains constant. This is a common practice in several simulation models from literature, but is inaccurate since the soil really requires a transient conduction approach. Using packaged finite element analysis (FEA) software is one option, but is computationally intensive for extended time EAHX solutions. This leaves analytical methods which yield much faster results.

Equation (40) is the general form of Fourier's heat equation which describes all heat conduction. The first step to solve this equation is the application of boundary and initial conditions (BC and ICs). Boundary conditions for EAHXs include one or more of the following: soil surface, slab surface, far field soil temperature, convection, and symmetry planes. These boundaries are commonly non-homogeneous (not equal to zero), and vary arbitrarily with space and/or time. An example of a non-homogeneous space/time boundary condition is the edge of a basement slab next to the soil surface as

pictured in Figure 37. The slab is a constant temperature while the soil surface temperature varies with the time of year. The space dependency is from having two different temperature values on the same boundary. The space dependency takes this problem from 1-D to 2-D which adds additional complexity. Initial conditions are also commonly non-homogeneous and vary with soil depth.

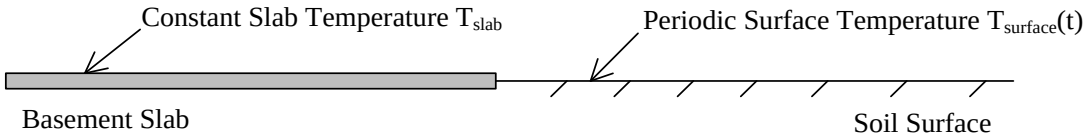


Figure 37: Example of space and time non-homogeneous boundary condition common in US EAHX simulation

$$\frac{\partial^2 T}{\partial \vec{r}^2} + \frac{1}{k} g(\vec{r}, t) = \frac{1}{\alpha} \frac{\partial T}{\partial t} \tag{40}$$

It is extremely difficult to solve Equation (40) with non-homogeneous, time/space dependent boundary and initial conditions using common heat conduction methods such as separation of variables or Laplace transforms. Instead, this research uses a powerful technique in heat conduction known as the Green's Function (GF) method. Green's Functions handle time/space variable BCs, generation terms, and space variable ICs with ease. Expressions for temperature distributions around the EAHX pipe are directly written into integral form. The only drawback is few of these integrals reduce to explicit expressions, but all can be solved with numeric integration. The purpose of the following chapter is to describe the GF method and how it applies to EAHXs.

The Green's Function Method

Introduction to Green's Functions

A simple description of a GF is that it is the most basic solution to a differential equation with homogeneous boundary conditions (BCs). The same GF for a given geometry and set of homogeneous BCs is a building block for the temperature distribution resulting from time/space variable boundary conditions, space variable initial conditions, and time/space variable energy generation [72]. Different homogeneous boundary conditions and geometry combinations result in different GF forms. Many geometry and boundary condition combinations are already solved and tabulated. Deriving a GF is unnecessary, and in many problems the solution in integral form is written directly from the tables. The integral form is either solved explicitly or with numerical integration. Two or three dimensional solutions are also possible by multiplication of one-dimensional building blocks. Any combination of the one-dimensional building blocks is possible as long as the problem is linear, the body is homogeneous, and the geometry is orthogonal (orthogonal in that the boundary is located where only one coordinate is constant) [72].

English mathematician George Green (1773-1841) first developed Green's Functions. They are included in many classical and modern heat conduction texts. Several texts rigorously cover the mathematical basis used to develop the GF method which is beyond the scope of this work. Please see Carslaw and Jeager [14], Beck [72], and Butkovskii [73] for mathematical basis and details. The texts also cover derivation of individual GFs based on geometry and boundary types. Individual GFs resemble heat

conduction solutions from other methods since many are derived using separation of variables and Laplace transforms. These texts also include many tabulated Green's Functions for Cartesian, cylindrical, and spherical coordinates along with useful integrals. This research uses the tables provided by Beck et al [72].

Numbering System for Boundary and Initial Conditions

A standardized numbering system for GFs is useful in two ways. First, it organizes GF tables in a logical way. The second is it classifies problem types and indicates the appropriate GFs. The numbering system devised by Beck et al. [72] includes notation for boundary types, BCs, and ICs. The four primary types of boundaries are in Table 9. Green's Functions for thin-film boundaries exist, but are not listed. The different function types for the time and space BCs are listed in Table 10. The homogeneous boundary is represented by B0, or the function of time that equals zero. The different types of space variable ICs are shown in Table 11. A GF exists for all basic geometry (semi-infinite medium, plate, cylinder, etc.) and boundary combinations listed in Table 9 where applicable. The boundary and initial conditions act as multipliers on the GF building blocks. The elementary functions listed in Table 10 result in integrals with explicit formulas.

A two-dimensional example in Figure 38 best illustrates the numbering system. The first vertical boundary is a constant temperature, and the second is a heat flux that changes exponentially with time. The top horizontal boundary is a homogeneous temperature, and the bottom boundary is convective with a constant fluid temperature.

The IC is a linear function with respect to the x-coordinate. The correct numbering designation is X12B14Y31B10T2. The X12 indicates the first boundary in the x-direction is of type 1, a temperature, and the second boundary is type 2, or a heat flux. The following B14 specifies the first temperature boundary as a constant with time while the second boundary is an exponential function with time (see Table 10). The same procedure repeats in the y-direction. The final T2 indicates the IC from Table 11. The boundary and initial condition notation is not only a convenient way to classify problems, it also specifies to use G_{X12} and G_{Y31} GFs.

Table 9: Boundary notation for Green's Function numbering system [72]

Notation	Boundary
0	No Physical Boundary (Infinite)
1	Temperature
2	Heat Flux
3	Convection

Table 10: Time and space variable boundary condition notation for Green's Function numbering system [72]

Notation	Time Variable	Notation	Space Variable
B-	Arbitrary f(t)	Bx-	Arbitrary f(x)
B0	$f(t) = 0$		
B1	$f(t) = C$		
B2	$f(t) = Ct$	Bx2	$f(x) = Cx$
B3	$f(t) = Ct^P$	Bx3	$f(x) = Cx^P$
B4	$f(t) = \exp(-at)$	Bx4	$f(x) = \exp(-ax)$
B5	Step changes in f(t)	Bx5	Step changes in f(x)
B6	$\sin(\omega t + E)$, $\cos(\omega t + E)$	Bx6	$\sin(\omega x + E)$, $\cos(\omega x + E)$

Table 11: Space variable initial condition notation for Green's Function numbering system [72]

Notation	Space variable initial condition
T-	Arbitrary F(r)
T0	F(r) = 0
T1	F(r) = C
T2	F(r) = Cr
T3	$F(r) = Cr^P$
T4	F(r) = exp(-ar)
T5	Step changes in F(r)
T6	sin(ωr + E), cos(ωr + E)
T7	Dirac delta function

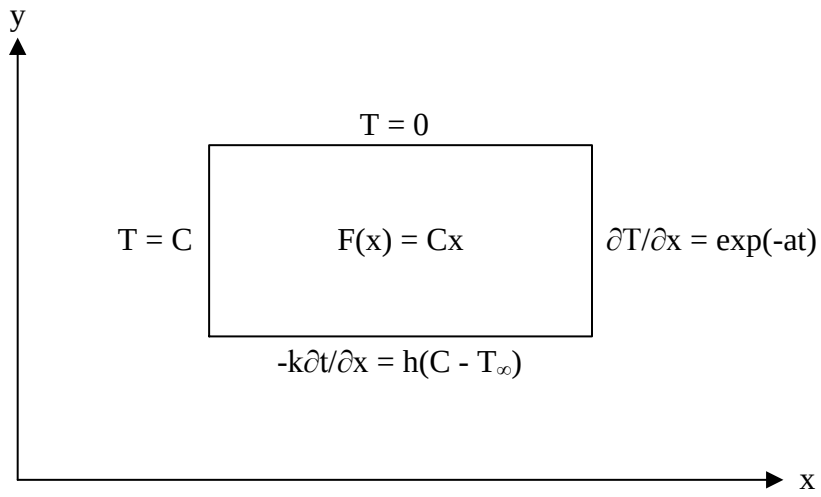


Figure 38: Green's Function number system example, X12B14Y31B10T2 problem type

Green's Function Solution Equation

A geometry and set of BCs are directly written into the integral form temperature distribution by following a systematic procedure. This procedure starts with the general from of the Green's Function Solution Equation (GFSE) in Equation (41). The space and time temperature distribution, $T(\vec{r}, t)$, in Equation (41) is a combination of three separate temperature distribution terms resulting from the initial condition, internal generation,

and the boundary conditions. These individual distributions sum to the combined temperature distribution. The summations in Equation (41) account for different BCs in each space dimension. The $G(\vec{r},t|\vec{r}',\tau)$ represents the Green's Function for that specific geometry and boundary combination. For example, the GF for a semi-finite solid (geometry) with constant surface temperature is slightly different than the GF for a semi-infinite solid with a constant surface heat flux. Note the separation of 1st kind BCs from the other kinds. Temperature (1st kind) BCs require a GF derivative, which are also listed in the GF tables.

$$T(\vec{r},t) = T_{IC}(\vec{r},t) + T_{gen}(\vec{r},t) + T_{BC}(\vec{r},t)$$

$$T_{IC}(\vec{r},t) = \int_R G(\vec{r},t|\vec{r}',0) * F(\vec{r})\ dv'$$

$$T_{gen}(\vec{r},t) = \int_{\tau=0}^{t}\int_R \frac{\alpha}{k} G(\vec{r},t|\vec{r}',\tau) * g(\vec{r},\tau)\ dv'd\tau$$

boundary conditions of the 2nd-5th kinds

$$T_{BC}(\vec{r},t) = \alpha \int_{\tau=0}^{t} \sum_{i=1}^{s} \int_{S_j} \frac{f_i(\vec{r}',\tau)}{k_i}\ G(\vec{r},t|\vec{r}',\tau)\ ds_i'd\tau \qquad (41)$$

boundary conditions of the 1st kind only

$$T_{BC}(\vec{r},t) = -\alpha \int_{\tau=0}^{t} \sum_{j=1}^{s} \int_{S_j} f_j(\vec{r}_j,\tau) \left.\frac{dG}{dn_j'}\right|_{\vec{r}'=\vec{r}_j'} ds_i'd\tau$$

Application of the GFSE is easily demonstrated by considering an infinite, one-dimensional body initially at temperature F(x) and internal generation g(x,t). This is an X00T2Gt-x- problem type. Equation (42) describes the time dependent temperature distribution for this problem, which includes a generation and initial condition term.

Equation (43) is the GF for an infinite solid found using the GF tables. This is the simplest form of any Green's Function and is also called the fundamental heat conduction solution. The fundamental solution also has an explicit integral involving error functions when integrating with respect to time. Other GF forms will often closely resemble the fundamental solution; especially for semi-infinite solids.

$$\frac{\partial^2 T}{\partial x^2} + \frac{1}{k} g(x,t) = \frac{1}{\alpha}\frac{\partial T}{\partial t} \quad -\infty \le x \le \infty \quad T(x,0) = F(x) \tag{42}$$

$$G_{X00}(x,t|x',\tau) = \frac{1}{[4\pi\alpha(t-\tau)]^{1/2}} \exp\left[\frac{(x-x')^2}{4\alpha(t-\tau)}\right] \quad t-\tau \ge 0 \tag{43}$$

The solution to the problem definition in Equation (42) is written directly into integral form using the GFSE. Equation (41) is first simplified by recognizing the problem is one-dimensional. The temperature contribution from $T_{BC}(\vec{r},t)$ is set to zero since there are no boundaries or BCs. The simplifications result in Equation (44) where $G_{X00}(x,t|x',\tau)$ is the fundamental GF solution in Equation (43). This is the exact solution in integral form, or also known as the integral form temperature distribution. Equation (44) simplifies to Equation (45) when the initial condition is set to a constant temperature, T_1, the generation term is set equal to zero, and Equation (43) is substituted in for the GF. This is now an X00T1 problem type. Integral tables, symbolic math software, or numeric integration can all solve this integral. An important aspect to notice when inserting Equation (43) into the IC contribution is tau (τ) equals zero, which considerably simplifies the equation. This example is fairly simple, but illustrates the ease of writing a heat conduction problem directly into integral form.

$$T(x,t) = \int_{x'=-\infty}^{\infty} G_{X00}(x,t|x',0)F(x')dx' + \int_{\tau=0}^{t}\int_{x'=-\infty}^{\infty} \frac{\alpha}{k} G_{X00}(x,t|x',\tau)g(\vec{r},\tau)dx'd\tau \quad (44)$$

$$T(x,t) = T_1 \int_{x'=-\infty}^{\infty} \frac{1}{[4\pi\alpha t]^{1/2}} \exp\left[\frac{(x-x')^2}{4\alpha t}\right] dx' \quad (45)$$

Numeric Integration and Time
Variable Boundary Conditions

The BCs for EAHX simulations are commonly functions of time. The soil surface temperature, convection in the EAHX pipe, and slab temperature or heat flux all represent boundaries that change with climatic conditions. A time variable, non-homogeneous BC is relatively straightforward to include in the GFSE. As an example, consider the annual soil surface temperature boundary is represented by the four term Fourier series in Equation (46). Later chapters show this equation fits well to annual soil and air temperatures using a least squares regression analysis. This temperature BC inserts into the GFSE by simply replacing the $f_j(\vec{r}_j,\tau)$ in Equation (41) with Equation (46) for BCs of the first kind (time variable "t" to the dummy time variable "τ"). The difficulty of a time variable BC comes when attempting to determine an explicit expression for the integral, which is a product of a Fourier series and GF derivative as shown in Equation (47). The integral in Equation (47), or close variations to it, commonly form in EAHX simulations. The equation has no obvious explicit integral of elementary function and solving requires numeric integration.

$$f_i(t) = a_0 + a_1\cos(t\omega) + b_1\sin(t\omega) + a_2\cos(2t\omega) + b_2\sin(2t\omega) \quad (46)$$

$$T(y,t) = -\alpha \int_{\tau=0}^{t} [a_0 + a_1 \cos(t\omega) + b_1 \sin(t\omega) + a_2 \cos(2t\omega) + b_2 \sin(2t\omega)] \left[\frac{y}{\{4\pi[\alpha(t-\tau)]^3\}^{1/2}} exp\left(-\frac{y^2}{4\alpha(t-\tau)} \right) \right] d\tau \quad (47)$$

There are many numeric integration schemes, but the extended trapezoid rule is sufficient for integrals encountered in EAHXs simulations. Equation (48) and Equation (49) represent the trapezoid rule where "N" is the number of interval points, "f_N" is the function value at each point, and "O" is the error term [74]. The extended trapezoid rule offers other advantages besides simplicity. The number of integration intervals can be doubled while using the results from previous calculations. This is a powerful property when coupled with an algorithm to determine when the maximum desired accuracy is reached [14, 72].

$$\int_{\tau_0}^{\tau_{N-1}} f(\tau) d\tau = h \left[\frac{1}{2} f_0 + f_1 + f_2 + \cdots f_{N-2} + \frac{1}{2} f_{N-1} \right] + O\left(\frac{(b-a)^3 f''}{N^2} \right) \quad (48)$$

$$h = \frac{\tau_{N-1} - \tau_0}{N-1} \quad (49)$$

Space Variable Boundary Conditions

A space variable BC occurs in situations like Figure 37 where the basement slab and soil surface are on the same orthogonal boundary. The type of space varying function along the boundary dictates how the integration proceeds. The boundaries for EAHXs change in a step-wise manner between two or more time dependent functions. In other words, the soil surface boundary in Figure 37 has its own temperature function,

$T_{surface}(t)$, which is the same over the whole soil surface. The soil temperature $T_{surface}(t)$ stops at the slab edge, and a step-wise change occurs to the constant slab temperature T_{slab}. The step-wise change in this example splits the BC temperature contribution, $T_{BC}(\vec{r}, t)$, from Equation (41) into two integrals. Three time dependent step-wise functions would split into three integrals. Integration over a boundary automatically requires a two-dimensional domain and a two-dimensional GF. The procedure is better illustrated by the following example.

The two-dimensional slab in Figure 39 is insulated on all boundaries expect for a space variable boundary along the top. This is a step-wise boundary between two temperature conditions simulating a concrete slab and the outside surface soil temperatures. The geometry, BC, and IC numbering identification is X22B00Y12Bx51T0. The identification is long, but signifies the use of a two-dimensional G_{X22Y21} GF. A G_{X22Y21} GF is the product of the tabulated G_{X22} and G_{Y21} Green's Functions. The GFSE in Equation (41) reduces to Equation (50) since the initial condition and all the boundaries are homogeneous except the 1st kind top boundary. Equation (51) results from Equation (50) after inserting the GFs, temperature functions, and limits of integration. Notice the space integration limits. Contributions from each BC are limited over the space they occupy. This does not mean temperatures from the slab will not contribute past length "b" and vice versa for the soil surface. The contributions are only much smaller due to the space integration. The partial derivative is with respect to the G_{Y21} Green's Function only since it is a function of the dummy y' variable. The same is true for the space integration with respect to the dummy x' variable

only involving the G_{X22} Green's Function. The partial derivatives could be moved outside the space integrals for further simplification.

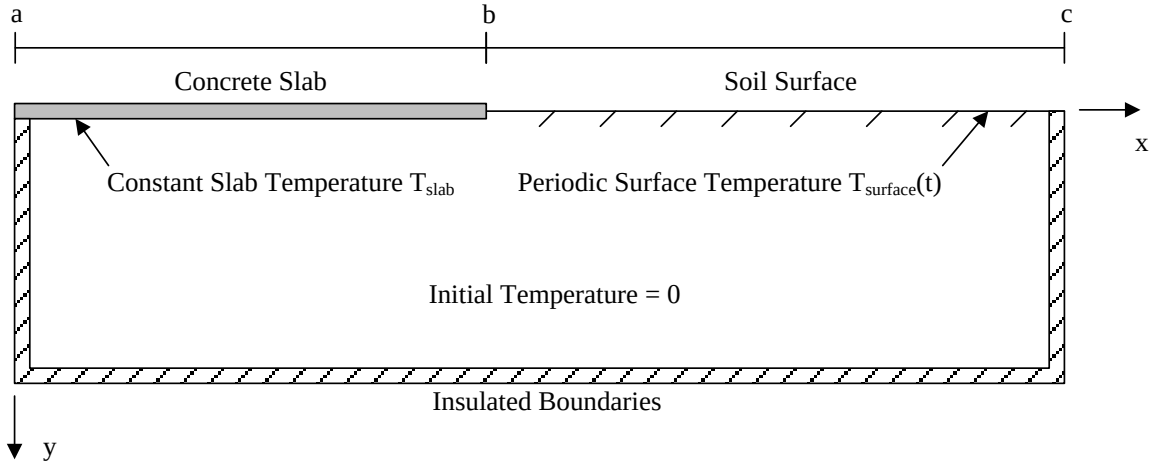


Figure 39: Space variable boundary conditions example (X22B00Y12Bx51T0 type)

$$\mathrm{T(x,y,t)} = T_{1st\,BC}(x,y,t) = -\alpha \int_{\tau=0}^{t} \sum_{j=1}^{s} \int_{S_j} f_j(\vec{r}_j,\tau) \left.\frac{dG}{dn_j'}\right|_{\vec{r}'=\vec{r}_j'} ds_i' d\tau \qquad (50)$$

$$\begin{aligned}\mathrm{T(x,y,t)} = -\alpha \int_{\tau=0}^{t} \Bigg[& \int_{a}^{b} T_{slab} \frac{\partial G_{Y12}(y,t|y',\tau)}{\partial y'} G_{X22}(x,t|x',\tau) dx' \\ & + \int_{b}^{c} T_{surface}(\tau) \frac{\partial G_{Y12}(y,t|y',\tau)}{\partial y'} G_{X22}(x,t|x',\tau) dx' \Bigg] d\tau \end{aligned} \qquad (51)$$

Example Green's Function Application

The following example demonstrates the GF solution process start to finish. Consider the semi-infinite solid with constant surface temperature and homogeneous initial condition (initially at zero temperature) in Figure 40. A common method for solving this problem is a similarity variable and results in the explicit temperature distribution expression shown in Equation (52) [10]. The integral temperature

distribution developed from the GF method yields the same results even though the derivation methods are completely different.

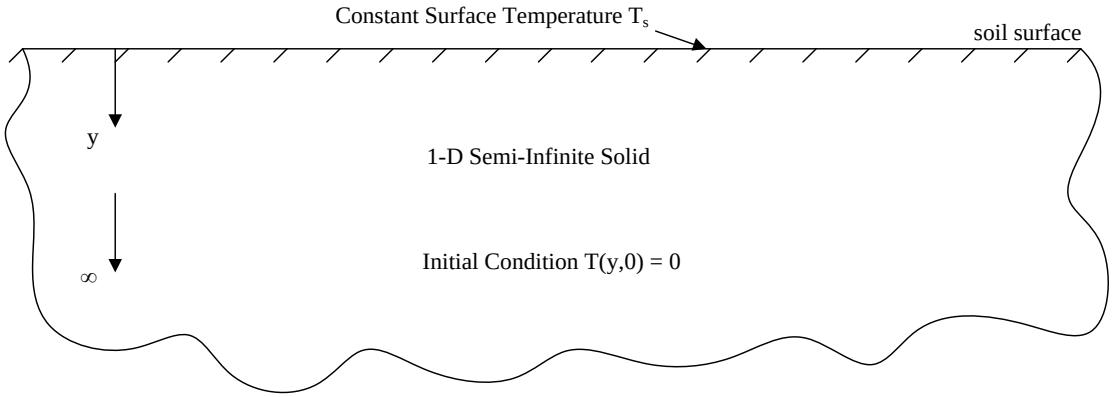


Figure 40: Example Green's Function method setup – semi-infinite solid with constant surface temperature T_s and homogenous initial condition

$$T(y,t) = T_s + (T_{initial} - T_s) \cdot erf\left(\frac{y}{2\sqrt{\alpha t}}\right) \tag{52}$$

The GF method always starts with simplifying the GFSE in Equation (41). The first simplification comes from recognizing the problem is one-dimensional. The summations drop out and the space variable changes to "y". Next, the initial condition, $F(\vec{r})$, is homogeneous (equal to zero) and there is no heat generation. This causes the $T_{in}(\vec{r},t)$ and $T_g(\vec{r},t)$ to drop out. The BC is of the first kind (specified temperature), so only the second term of $T_{BC}(\vec{r},t)$ is not equal to zero. This eliminates all the terms of the GFSE except one. Equation (53) below is the resulting simplified GFSE. The next step is to find the Green's Function derivative, $\partial G(y,t|y',\tau)/\partial y$, for a semi-infinite solid with a constant temperature boundary in a published table. The numbering system

designation for this problem is Y10 which implies a $G_{Y10}(\vec{r},t|\vec{r}',\tau)$ GF. The table published by Beck et al. [72] has this GF in the form of Equation (54).

$$T(y,t) = -\alpha \int_{\tau=0}^{t} f(\tau) \left. \frac{dG_{Y10}(y,t|y',\tau)}{dy} \right|_{y'=0} d\tau \tag{53}$$

$$\frac{\partial G_{Y10}(y,t|y',\tau)}{\partial y'} = \frac{\mathrm{y}}{\{4\pi[\alpha(t-\tau)]^3\}^{1/2}} \exp\left[-\frac{(y-y')^2}{4\alpha(t-\tau)}\right] \tag{54}$$

Equation (54) further simplifies by noticing the BC is located at y = 0. This causes the dummy space variable "y'" to equal zero. The only integration left in Equation (53) is with respect to the dummy time variable "τ". The f(τ) in Equation (53) is the BC which equals the constant surface temperature "T_s". The surface temperature moves outside the integral since it is a constant. It would remain inside the integral if it was a function of time. Equation (55) is the final equation after simplifications and substitutions. The remaining terms inside the integral are similar to the fundamental Green's Function solution. The integral in Equation (55) has an explicit formula found in integration tables and yields Equation (56). This equation is the same as the exact solution found using a similarity variable in Equation (52) after some rearrangement.

$$T(y,t) = \alpha T_s \int_{\tau=0}^{t} \frac{\mathrm{y}}{\{4\pi[\alpha(t-\tau)]^3\}^{1/2}} \exp\left[-\frac{(\mathrm{y})^2}{4\alpha(t-\tau)}\right] d\tau \tag{55}$$

$$T(y,t) = T_s erfc\left[\frac{y}{(4\alpha t)^{1/2}}\right] \tag{56}$$

Characteristics of Green's Functions Specific to Earth-Air Heat Exchangers

Convective Green's Functions

The Green's Function (GF) method is effective for EAHX simulations, but it cannot account for all design variables or heat transfer mechanisms. Knowing its limitations will save time and increase accuracy during simulation development. The first significant drawback is the inability to simultaneously solve the soil heat conduction and internal convective flow inside the EAHX pipe. This is a problem for any analytical heat transfer simulation using more than one heat transfer mode. A technique to get around the limitation is step-wise solving each heat transfer mode over short periods. A short time temperature result from one mode is an input into the BC for the other mode. The procedure is pseudo-numerical using analytical equations. This research later utilizes a similar process.

Convective BCs mimic the heat transfer from the air passing through the EAHX pipe to the soil. Equation (57) is the general form of a convective BC, also known as a Robin or 3rd kind BC, where "k" is the soil thermal conductivity, "T_∞" is the air temperature, and "h" is the convective heat transfer coefficient. Air temperature variations due to climatic conditions create the time dependency in EAHX convective BCs. The air convective coefficient "h" and air velocity are also dependent on temperature. This implies the convective coefficient should also vary with time, but it is not allowed in the GF formulation. A convective coefficient is allowed to vary with position, but must remain constant in time [72].

$$-k\frac{\partial T(x,y,t)}{\partial x}+h(y)\cdot T(x,y,t)=h(y)\cdot T_{\infty}(y,t) \tag{57}$$

Orthogonal Boundary Conditions

The primary advantage of the GF method is its ability to handle space/time variable boundary conditions. An important note though is values may change with space and time along an orthogonal boundary, but the boundary type must remain the same. For example, representing the concrete slab in Figure 37 with a heat flux boundary is more appropriate than a temperature boundary in a non-radiant slab. This is not possible though if the soil surface boundary remains a specified temperature. In other words, a 1st and 2nd kind BC cannot be on the same orthogonal boundary using the standard GF method. A specialized technique called the Galerkin-Based Integral Method may be used in the case of non-orthogonal bodies, but is not investigated in this research [72].

Long and Short-Time Green's Functions

Laplace transforms and separation of variables are the two common methods of deriving GFs. The same GF for a geometry and boundary type combination is often derived with both methods. This leads to two, sometimes more, forms of the same GF. This applies to all geometries except infinite and semi-infinite mediums with 1st and 2nd kind BCs. Which form of the GF to use depends on diffusivity, domain length, and time of interest for the simulation in question. Time of interest is the primary factor, and the forms are often called long and short-time GFs. Dimensionless Equation (58) determines

the threshold between long and short time GFs in almost all cases. The "value" variable changes between GFs, but typically ranges from 0.1 to 0.01. Large values of Equation (58) required the large-time GFs and vice versa for the short-time GFs.

$$\frac{\alpha(t-\tau)}{L^2} \leq value \tag{58}$$

Separation of variables yields long-time GFs which contain infinite trigonometric series. Long-time GFs are easier to manipulate and integrate than their short-time counter parts derived using Laplace transforms [72]. Boundary conditions of the 1st and 2nd kinds typically only have two or three GF forms for all geometries. Convective BCs, or BCs of the 3rd kind, have multiple forms. Appropriately selecting a 3rd kind BC greatly increases accuracy, but is difficult for EAHX simulations. Equation (58) is often close to the threshold due to low soil diffusivities and long-time values. The result is neither the long or short-time solutions provide satisfactory results. Numeric integration is advantageous in this situation because the GF form can change partway through the calculations. The EAHX simulation programs calculate Equation (58) for each step and automatically switch between GF forms. This practice takes advantage of both long and short-time GFs to increase solution accuracy.

Neglecting Pipe Wall Thermal Resistance

Neglecting the pipe wall thermal resistance is a common assumption in literature for the EAHX's convective flow, but few to no studies report its validity. The assumption indicates the pipe wall is thin, and convective heat transfer occurs directly

between the soil and air passing through the pipe. In other words, the soil temperature at the outer pipe wall is the surface temperature in the convective heat transfer boundary condition. One way to evaluate potential errors with this assumption is to find the pipe wall's contribution to the overall thermal resistance.

Figure 41 is a 1-D thermal circuit representing resistance between the soil surface and the inside of the EAHX pipe. The thermal circuit assumes a known soil surface temperature and ignores atmospheric convection. The convective heat transfer coefficient inside the EAHX pipe is a constant 3.0 Btu/hr·ft^2·°F, which is typical for EAHX air temperatures and velocities. Variables in Figure 41 include soil length "L_{soil}", pipe wall thickness "L_{pipe}", soil thermal conductivity "k_{soil}", and pipe thermal conductivity "k_{pipe}". Common soil thermal conductivities are listed in Table 1 and Table 2, and range from 0.08 to 1.25 Btu/hr·ft^2·°F. Calculations use the full range to account for all soil types. PVC, HDPE, and steel are common EAHX pipe materials, and Table 12 displays their respective thermal conductivities.

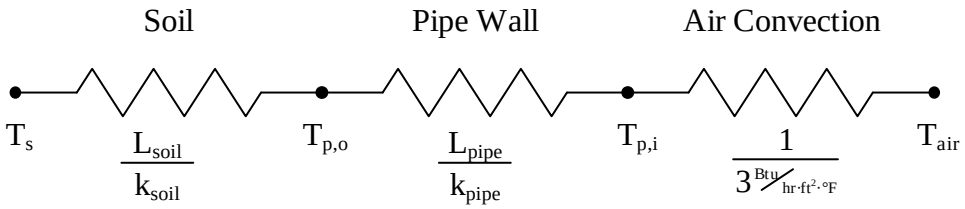


Figure 41: Thermal circuit for one-dimensional heat transfer between soil surface temperature and air convection inside the EAHX pipe

Table 12: Conductivity values of three common EAHX materials (Btu/hr·ft·°F) [75-77]

PVC	0.1083
HDPE	0.2708
Steel	25.4

Overall thermal resistance based on Figure 41 was calculated for each material type, three wall thicknesses, and at the extremes of soil conductivity for depths of one to eight feet. Table 13 through Table 16 summarizes the percentage the pipe wall contributes to the overall resistance in each instance. PVC has the lowest thermal conductivity which generates high pipe wall contributions. The low conductivity soil in Table 13 keeps the contribution below three percent. Higher conductivity soil in Table 14 pushes the contribution above 25% for shallow depths. Under slab installation depths of three feet are possible, but depths greater than four feet are recommended where contributions are below ten percent. HDPE pipe shares similar behavior in Table 15 and Table 16, but its maximum contribution is 12% due to its lower conductivity value. The 12% occurs at a 1ft depth where installation is not recommended. More realistic installation depths have a percent contribution below four percent. The steel pipe results are not included because their values were all practically zero due to its high conductivity.

Table 13: Pipe wall thermal resistance percentage for PVC and k_{soil} = 0.08 Btu/hr·ft·°F

Soil Depth (ft)	Wall Thickness (in)		
	0.25	0.375	0.5
1	1.5%	2.2%	2.9%
2	0.8%	1.1%	1.5%
3	0.5%	0.8%	1.0%
4	0.4%	0.6%	0.8%
5	0.3%	0.5%	0.6%
6	0.3%	0.4%	0.5%
7	0.2%	0.3%	0.4%
8	0.2%	0.3%	0.4%

Table 14: Pipe wall thermal resistance percentage for PVC and k_{soil} = 1.25 Btu/hr·ft·°F

Soil Depth (ft)	Wall Thickness (in)		
	0.25	0.375	0.5
1	14.5%	20.3%	25.3%
2	9.0%	13.0%	16.6%
3	6.6%	9.5%	12.3%
4	5.2%	7.5%	9.8%
5	4.3%	6.2%	8.2%
6	3.6%	5.3%	7.0%
7	3.1%	4.6%	6.1%
8	2.8%	4.1%	5.4%

Table 15: Pipe wall thermal resistance percentage for HDPE and k_{soil} = 0.08 Btu/hr·ft·°F

Soil Depth (ft)	Wall Thickness (in)		
	0.25	0.375	0.5
1	0.6%	0.9%	1.2%
2	0.3%	0.5%	0.6%
3	0.2%	0.3%	0.4%
4	0.2%	0.2%	0.3%
5	0.1%	0.2%	0.2%
6	0.1%	0.2%	0.2%
7	0.1%	0.1%	0.2%
8	0.1%	0.1%	0.2%

Table 16: Pipe wall thermal resistance percentage for HDPE and k_{soil} = 1.25 Btu/hr·ft·°F

Soil Depth (ft)	Wall Thickness (in)		
	0.25	0.375	0.5
1	6.4%	9.2%	12.0%
2	3.8%	5.6%	7.4%
3	2.7%	4.1%	5.3%
4	2.1%	3.2%	4.2%
5	1.7%	2.6%	3.4%
6	1.5%	2.2%	2.9%
7	1.3%	1.9%	2.5%
8	1.1%	1.7%	2.2%

Low percentages indicate a small change in temperature through the pipe wall, but the magnitude is dependent on the heat transfer rate through the thermal circuit. The percentage results are misleading in this way. The important information is the pipe wall is under 10% of the total thermal resistance in the worst case scenario for under yard installation depths. Ten percent is pushing the acceptable engineering error, but sandy, high moisture content soil (k_{soil} = 0.08 Btu/hr·ft·°F) with thick walled pipe is not commonly encountered. The thin-wall assumption in US installations though is pushing the limits of engineering error since these can be at depths of three feet or less. The assumption is still valid for US EAHXs, but it is important to remember the thin wall assumption is present when analyzing results.

Temperature Effects on the Convective Heat Transfer Coefficient

The convective heat transfer coefficient (CHTC) is shared between the soil conduction and air convection equations. An accurate CHTC is crucial for EAHX simulations since a slight change directly affects the heat transfer rate between the air and soil. Unfortunately, CHTCs depend on air temperature and velocity. Velocities are typically constant in EAHXs, but air temperatures change with outdoor conditions. The GF method requires a constant CHTC for the entire simulation since it cannot contain change with time (only with space). Constant properties and an averaged CHTC are also common assumptions in internal convective heat transfer. Without this assumption, the mathematical difficulty in the convective momentum and energy equations significantly increases and only specialized cases have solutions. Successful EAHX simulations

require understanding how the CHTC changes with air temperature, and if a constant value generates acceptable simulation results.

Potential ranges of CHTCs were calculated using the Dittus-Boelter and Gnielinski Nusselt number correlations based on typical EAHX design and operation. See Equation (17) and Equation (18) respectively for the Dittus-Boelter and Gnielinksi equations respectively. Literature contends that both yield satisfactory results, but the Gnielinski correlation is generally considered the more accurate with observed errors around ten percent [10]. The Gnielinski correlation is a function of friction factor though, which requires a Moody diagram while the Dittus-Boelter is strictly a calculation. This section compares the two correlations since the Dittus-Boelter is easier to calculate. The correlations calculate the air flow's Nusselt number, which is a function of Prandlt and Reynolds numbers. Prandlt and Reynolds numbers are functions of air temperature, pipe diameter, and air velocity. Figure 42 through Figure 45 investigate how the expected range of these three variables affect the resulting CHTC.

Figure 42 is the CHTC for temperatures from 0ºF to 100ºF in an eight inch pipe for air velocities of 600 FPM and 1200 FPM. Figure 43 is similar, but compares 6 and 12 inch pipe diameters at 1000 FPM. The air velocity range in Figure 42 shows a significant change in CHTC for both correlations. The reduction in CHTC with increasing air temperature is less noticeable, but still creates a 0.25 to 0.5 Btu/hr·ft^2·ºF change. Pipe diameter in Figure 43 has a much smaller effect. Moving from a 6 to 12 inch pipe decrease the CHTC by around 0.5 Btu/hr·ft^2·ºF. A surprising result is the discrepancy between correlations. There is a 0.25-0.75 Btu/hr·ft^2·ºF difference in both figures. The

Gnielinski correlation also consistently estimates a lower value. The two correlations were expected to be closer together even knowing the Gnielinski is generally considered more accurate. The Dittus-Boelter correlation is not as accurate as first hoped, and the clear choice for EAHX simulations is the Gnielinski correlation.

The Gnielinski correlation may be the preferred method for Nusselt number calculations, but it is still a function of Darcy fiction factor. It is not feasible to read friction factors off the Moody diagram in Figure 3 for each simulation. A curve fit to the smooth pipe line of the Moody diagram does exist in the form of Equation (9) though. Earth-air heat exchangers constructed from PVC, HDPE, or steel meet the smooth pipe requirement for Reynolds numbers below 10^7. The Gnielinski correlation is now a feasible option since most EAHXs meet the Reynolds number limit. Figure 44 and Figure 45 present a more in-depth investigation of the Gnielinski correlation. The significant effect of air velocity is again demonstrated in Figure 44 by an approximate 1.6 Btu/hr·ft^2·ºF change in CHTC between 600 and 1200 FPM. Pipe diameter is less influential with a 0.5 Btu/hr·ft^2·ºF change in CHTC from 6 to 12 inches in Figure 45.

Air velocity and diameter obviously contribute to CHTC in Figure 44 and Figure 45, but these variables remain constant during simulations. Air temperature is the troublesome variable. Table 17 gives some insight by listing the difference between CHTCs at 0ºF and 100ºF for all feasible situations. High velocities and smaller diameters have differences ranging from 0.6 to 0.88 Btu/hr·ft^2·ºF. The lower extreme for large diameter pipes and slower flow have 0.32 to 0.4 Btu/hr·ft^2·ºF for a 100ºF temperature difference. The average of all CHTC differences in the table is 0.59 Btu/hr·ft^2·ºF. Table

17 implies a large change in CHTC with temperature, but it is important to remember this is for a 100ºF temperature change. A temperature swing this large is unrealistic for EAHXs. Swings in the experimental data are below 30 ºF. The change in CHTC lowers to an average 0.21 Btu/hr·ft^2·ºF for all situations using a 30ºF temperature difference (60ºF and 30ºF data used for this average). This is a more realistic value for the change in a CHTC during EAHX operation. This change in CHTC is large enough that it cannot be neglected, but not large enough to drastically change heat transfer results. A constant value for the EAHX simulations is acceptable.

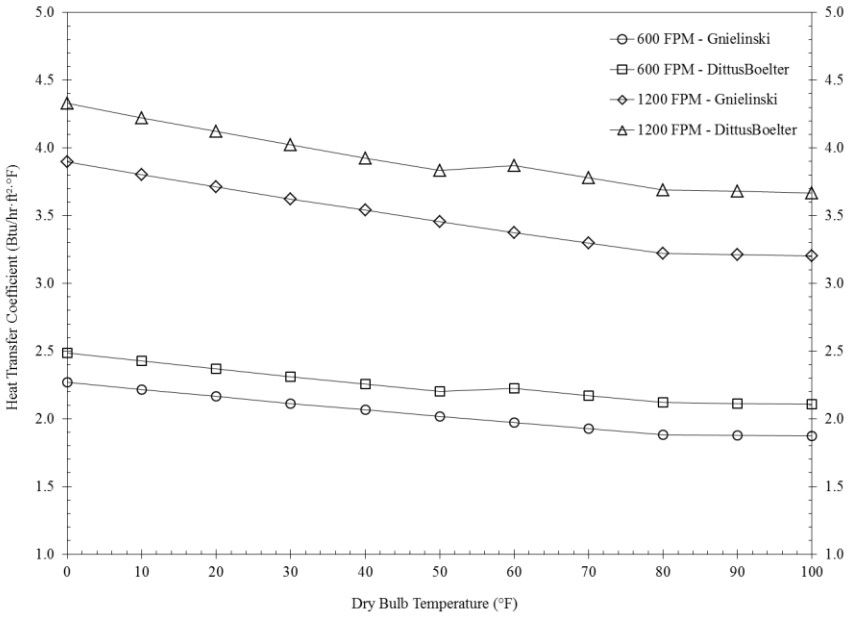


Figure 42: Heat transfer coefficient vs. dry bulb temperature for internal turbulent flow in an eight inch pipe for Gnielinski and Dittus-Boelter correlations

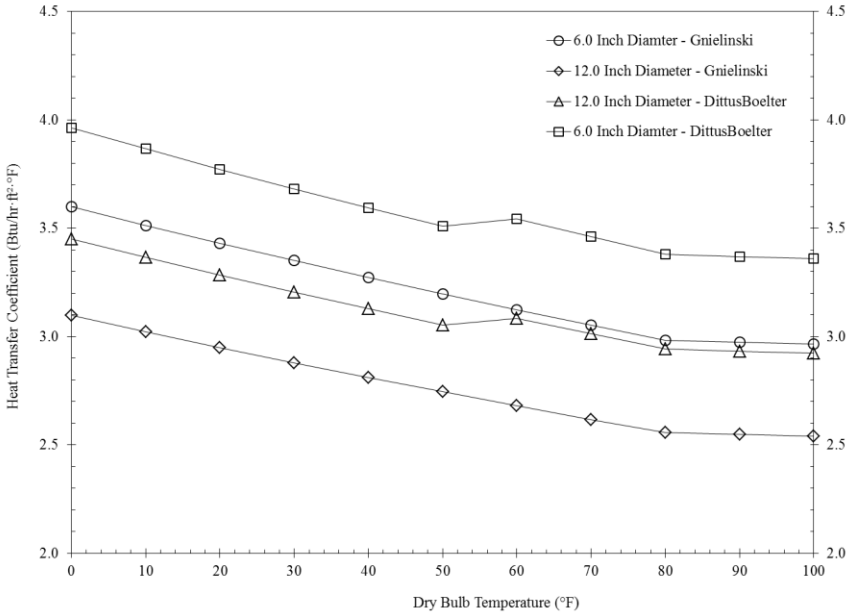


Figure 43: Heat transfer coefficient vs. dry bulb temperature for internal turbulent flow at 1000 FPM air velocity for Gnielinski and Dittus-Boelter correlations

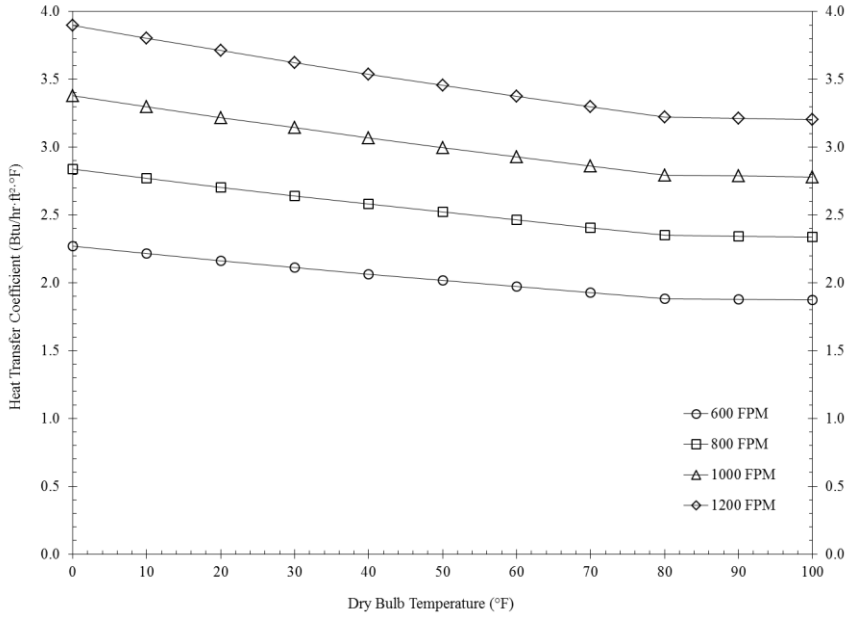


Figure 44: Heat transfer coefficient vs. air temperature from the Gnielinski correlation at various air velocities in an eight inch pipe

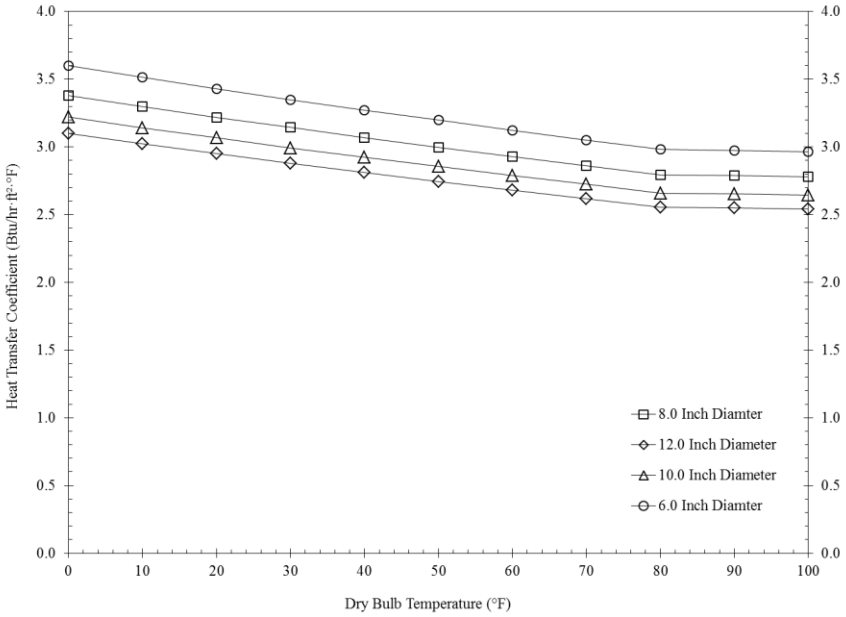


Figure 45: Heat transfer coefficient vs. air temperature from the Gnielinski correlation for various pipe diameters at air velocity of 1000 FPM

Table 17: Difference between the 0°F and 100°F convective heat transfer coefficients using the Gnielinski correlation

Air Velocity (FPM)	Pipe Diameter (inches)			
	6	8	10	12
500	0.37	0.34	0.33	0.32
600	0.42	0.40	0.38	0.37
700	0.48	0.45	0.43	0.42
800	0.53	0.50	0.48	0.46
900	0.58	0.55	0.53	0.51
1000	0.63	0.60	0.58	0.56
1100	0.68	0.65	0.62	0.60
1200	0.73	0.70	0.67	0.65
1300	0.78	0.74	0.72	0.69
1400	0.83	0.79	0.76	0.74
1500	0.88	0.84	0.81	0.78

Computer Simulation using the Base Solution Generation Technique

Green's Function integrals in EAHX simulations require numeric integration as previously discussed. The product of a time dependent BC and GF generally has no explicit formula of elementary functions. Numeric integration by the extended trapezoid rule is an accurate substitute to exact symbolic integration. Numerical integration calculates each temperature point in the domain individually for each time specified. This is a problem though when long-time EAHX simulations require hundreds of temperature points over large domains for visualizing soil temperature distributions. This process is computationally expensive for yearlong simulations using small time intervals (1 minute to 5 minute). The motivation for using the GF method is the efficient analysis of EAHXs in multiple climatic conditions. The computational time required for numeric integration in large domains and times is not efficient, and requires a new method.

This section presents a technique to bypass the hundreds of individual numeric integrations called Base Solution Generation (BSG) technique. The BSG technique takes advantage of the systematic way the GF method assembles integral solutions, and the separation of BCs from the GFs. Equation (59) represents the generalized temperature distribution from a non-homogeneous BC where the time dependent BC is multiplied by the time dependent GF inside the integral. Symbolic integration with respect to dummy time is not possible for this multiplication as already mentioned. It is possible though to pre-calculate GFs based on time and space values. GFs over large space domains are then multiplied by non-homogeneous BCs corresponding to the same dummy time. One

BC value is the same for all GF domain points. In this way, numeric integration occurs for all domain points simultaneously, and provides an easy means to incorporate the time-dependent BC.

$$T_{b.c.}(\vec{r},t) = \int_{\tau=0}^{t} [BC\ f(\tau)] * [Green's\ Function]\ d\tau \tag{59}$$

A simple example better illustrates the BSG methodology. The light dotted line in Figure 46 is the BC and GF product in Equation (59) plotted with respect to time. The temperature distribution at time 5 is the total area under this curve. The trapezoid rule is the process of splitting the area under the curve into multiple trapezoids. The solid lines in Figure 46 form the numeric integration trapezoids. Points f_0 through f_5 are values of Equation (59) that form the trapezoid edges. The first step in calculating the area of each trapezoid is to calculate the six edge points. These are the same "f" values as seen in the general form of the extended trapezoid rule in Equation (48). Equation (48) distributes the common variables to all trapezoids, like the width of each interval, out of the equation. The resulting integration process is the summation of each edge point ("f" values). The BSG technique follows this same procedure of summing edge values, except this is done simultaneously for all domain points. The first pre-calculated GFs are multiplied by a single BC value (corresponding to the same dummy time "τ") to find f_5. The process repeats for the next pre-calculated GFs to find f_4, and f_4 is added to f_5. The process repeats for each trapezoid edge point. This completes the summation in Equation (48). The "f" value sum is then multiplied by the common variables to yield the final temperature distribution.

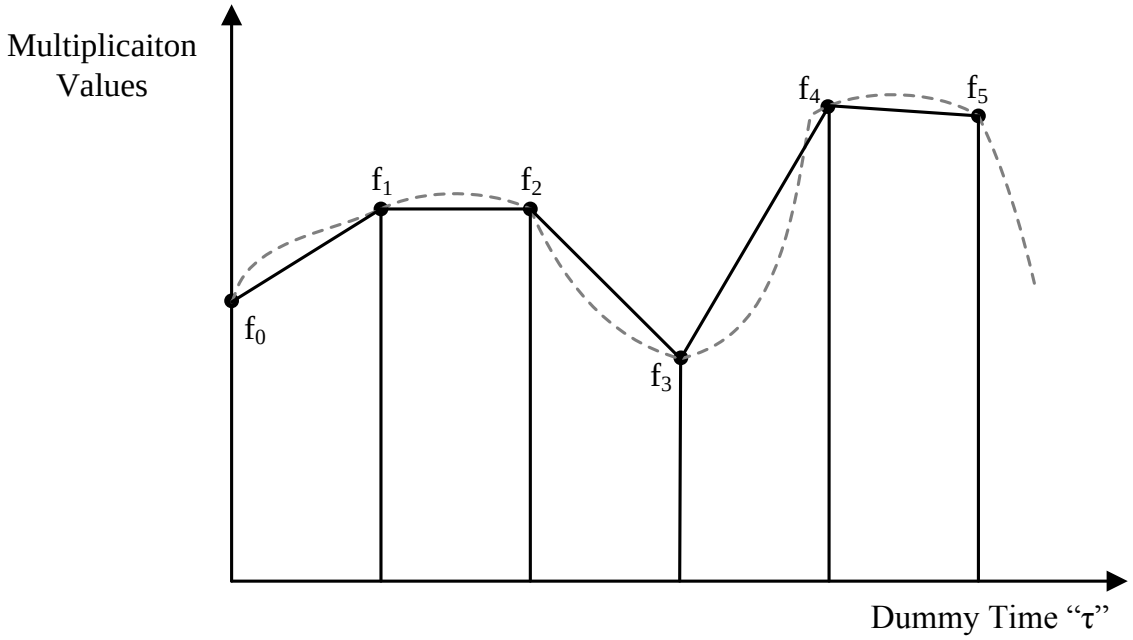


Figure 46: Simplified trapezoidal rule integration example where the light dotted line is the product of the BC and GF graphed with respect to dummy time "τ"

The BSG technique is organized into the Time Refinement, Base Solution Generation (BSG), and Numeric Integration programs. The BSG program forms a pre-calculated GF database which the Numeric Integration program accesses. Figure 47 is a general flow diagram illustrating program operation. The three primary programs are square boxes, and circles are outputs/inputs. Initial inputs for a simulation are the domain size, the maximum simulation time, time integration interval, material properties, and convective coefficients if applicable. The BSG program calculates the pre-calculated GF database from this information. Time Refinement is an optional program designed to reduce computation workload. It determines a refined solution time based on domain inputs. The refined solution time is an input for the BSG and Numeric Integration. The Numeric Integration runs last. The inputs are climatic conditions, end simulation time,

and integration interval. The climatic conditions are transformed into time dependent BC functions. The BSG program is the operational key, and the technique assumes its name. Following is a description of each program and how the three work together to efficiently produce an accurate temperature distribution. The example GF application started earlier in Figure 40 continues through this discussion to help explain the operation of each program.

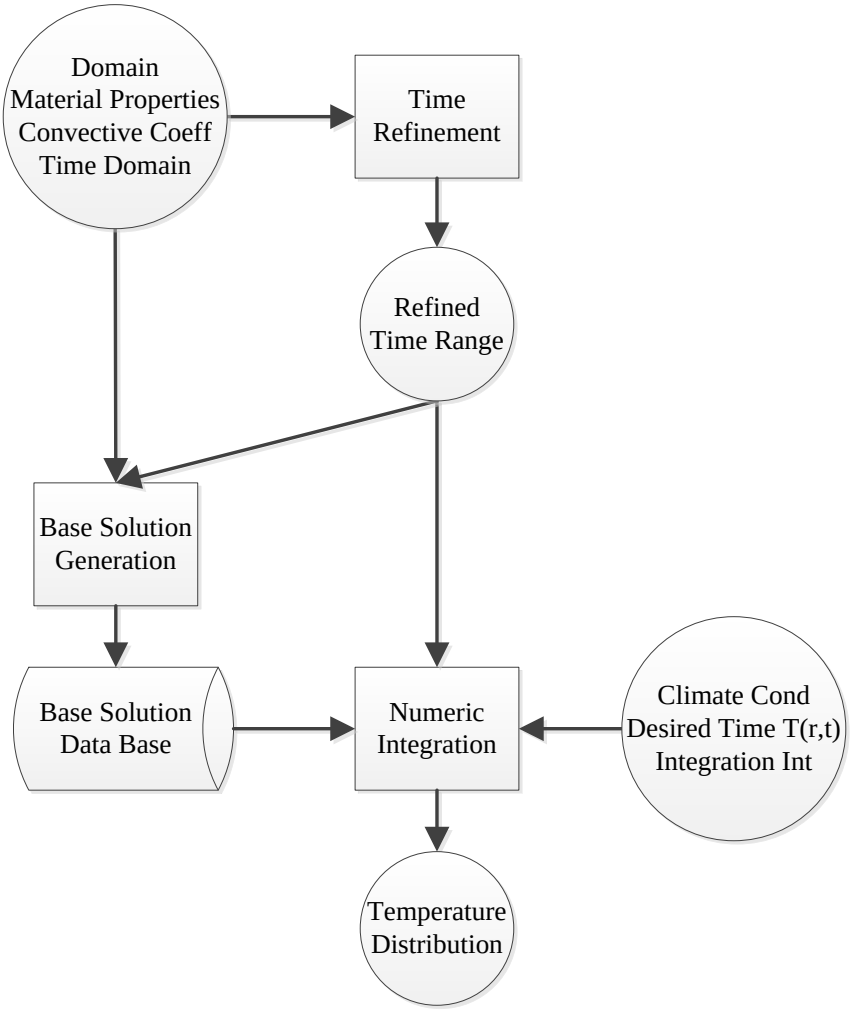


Figure 47: Generalized diagram of programs and inputs in the Base Solution Generation technique

Time Refinement

The only optional program is the Time Refinement. It reduces computation time in the other two programs by only generating and integrating solutions over a relevant time period. Earth-air heat exchanger simulations extend over large periods of time (several years). Green's Function values for some boundary types and geometry combinations are very small at large times. This is especially true for convective BCs. Physically this is intuitive. Recent boundary temperatures will inherently have a greater influence on the end temperature distribution than boundary temperatures from several days ago. Another way to think of it is the numeric integration trapezoids are much larger for recent times (a few days) than for times several days or years in the past. Equation (59) expresses the reduction in trapezoid size by significantly reducing the GF value inside the integral since the BC is mathematically independent.

An example is a better representation of diminishing GF values over large times. Consider the semi-infinite solid with constant temperature boundary condition in Figure 40. Equation (55) is the integral form temperature distribution to the problem setup in Figure 40 where the constant temperature BC is outside the integral. Numeric integration of Equation (55) yields the temperature distribution. In other words, the temperature distribution is the area under the curve produced by the G_{Y10} GF in Equation (54) multiplied by the constant surface temperature "T_s". This implies plotting the curve from Equation (54) will indicate which dummy time values contribute to the numeric integration, and which go to zero.

Figure 48 is a plot of Equation (55) with respect to dummy time "τ" from zero to the time of interest "t" at several different depths. The time of interest is five years (1825 days), and the soil's diffusivity is 0.6 ft^2/day. Time "t", diffusivity "α", and depth from the surface of interest "y" are now constant variables in Equation (55). The only variable left in Equation (55) is the dummy time "τ" which is integrated from zero to the time of interest "t". Figure 48 clearly shows the GF values going to practically zero for values of "τ" less than 800 days for all depths. The 12ft depth has the highest GF values, but they are less 10^{-4} 1/ft^2 for day 300 and less, and less than 10^{-3} 1/ft^2 until day 1500 out of 1825. These observations suggest an 1825 day simulation only needs 325 days of numeric integration. The last 325 days are the only times the integration contributes a meaningful value to the temperature distribution. There are five times fewer calculations with the Time Refinement program than without.

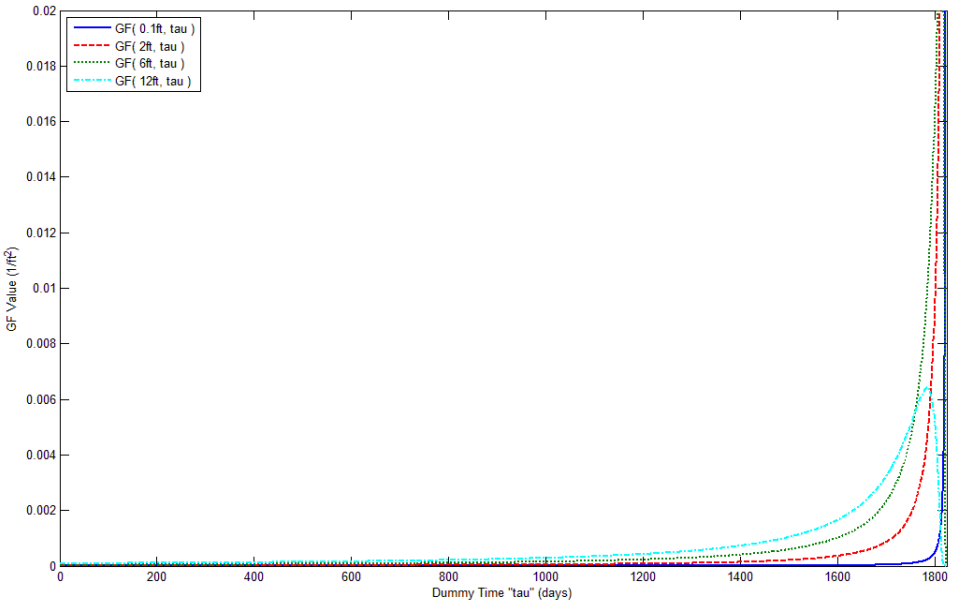


Figure 48: Values at different depths for the derivative of an G_{Y10} GF, Equation (55), with respect to the dummy time variable "τ"

A closer examination of Equation (55) when dummy time "τ" approaches the time of interest "t" demonstrates several interesting GF characteristics. Figure 49 is a smaller time window of the same plot in Figure 48. The first interesting observation is all GF values go to infinity at dummy time equal to the specified time. A closer look at Equation (55) reveals a (t-τ) multiplier in the GFs denominator. The denominator approaches zero as the dummy time "τ" reaches the upper limit of integration "t". This extremely small denominator causes the GF to go to infinity. This is the reason GFs do not behave well mathematically near the upper integration limits.

The second observation is GF values increase with depth except for the 12ft depth. The 12ft depth reaches a maximum value around 1775 days. The GF then decreases in value between 1775 and 1825 days. This is an example of the heat wave analogy. The surface temperature induces a heat wave to flow downward from the surface. The 12ft depth plot suggests the heat wave has not reached this depth yet for all times after approximately 1775 days. The BC temperature has little to no effect at this depth when the dummy time approaches the actual time limit. The 0.1ft depth plot on the other hand contributes to the temperature distribution only for dummy times near the limit of integration. This signifies that BC values for the last 25 to 30 days determine the final soil temperatures at a 0.1ft depth. This is intuitive since the soil temperature near the surface should be equal to the recent surface temperature.

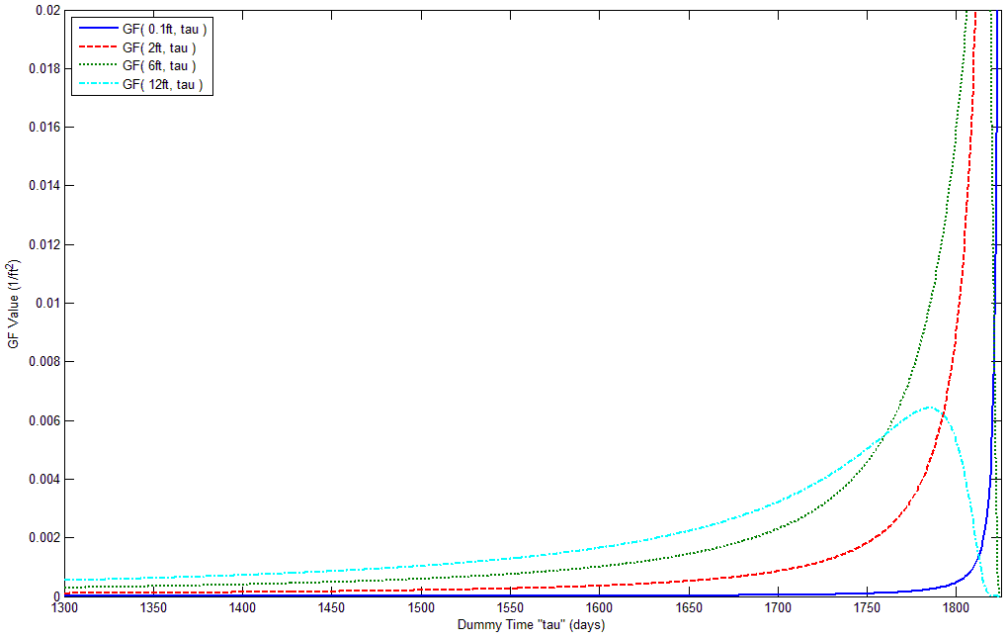


Figure 49: Closer view of the G_{Y10} GF derivative in Equation (54), with respect to the dummy time variable "τ"

The Time Refinement program does this same analysis based on the domain size, time range, material properties, and convective heat transfer coefficient if applicable. The below pseudo code outlines the program operation. The while-loop calculates the GF value based on the current dummy time. The maximum GF in the domain is compared to the minimum specified value. If the maximum GF is below the minimum specified value, the while-loop repeats and increases "τ" by one day. This continues until one point in the domain is above the minimum value. When this occurs, the program outputs the current dummy time as the "refined time" variable. "Refined time" is then an input into the next two programs as shown in Figure 47. Example code of the above program is available in APPENDIX G.

```
SET     desire minimum GF value

SET     dummy time to zero

WHILE   calculated GF value ≤ desired minimum GF value

        calculate GF values for all domain coordinates

        find the maximum calculated GF in the domain,
        this is the new calculated GF value

        add one day to the dummy time used in the GF
        calculation

REPEAT
END WHILE

OUTPUT refined time that desired minimum GF value
       occurs
```

Base Solution Generation

Base Solution Generation (BSG) is the next program in Figure 47. The BSG program builds a database of pre-calculated GFs based on (t-τ) time values and spatial coordinates. The material properties and convective coefficients remain constant for each database set. The program takes advantage of numeric integration only occurring in the time domain for EAHX GF integrals. Again, consider Equation (59). The product of a time dependent BC and GF is inside the time integral. The BC function changes with climatic conditions, convective heat transfer coefficient, slab heat loss, or any number of design variables. The one constant is the GF. The GF is dependent on geometry and boundary types only. A 1-D soil temperature simulation in Bozeman, Montana and Houston, Texas use the same G_{Y10} GF. This suggests a database of pre-calculated GFs

covers hundreds of simulations. The common GF shared between simulations is the basis of the BSG technique.

Green's Functions are symbolized by $G(\vec{r}', t|\vec{r}', t)$ where the $\vec{r}$ is up to three-dimensional. EAHX simulations are one or two-dimensional. The integral in Equation (59) is then at most a function of six variables including the dummy variables. The two dummy space variables are equal to zero or a constant. This leaves the real time "t", dummy time "τ", and real space variables "x" and "y". These four variables determine the base solutions. The time numeric integration does not affect the real space variables. The input domain specifies the grid size and spacing. The grid represents the temperature distribution, and each gird point is a calculated temperature. The space variables remain constant at each grid point during the base solution generation. In terms of programing, the grid is a 2-D array representing spatial coordinates. The 2-D array becomes a vector for 1-D simulations.

The above information is applied to the continued example for a 1-D semi-infinite solid with constant surface temperature. Figure 50 is the same problem setup as this earlier example, but a grid represents temperature points of interest. The grid physically represents the calculated temperature T(y,t) at six different depths ranging from the surface to 120 inches. The grid inputs into the computer simulation as a 6 x 1 array. Other variables save the physical spacing between grid points and total depth. The BSG program calculates the GF inside the integral of Equation (59) for each grid point in Figure 50. Equation (55) is the GF integral for this particular problem, and the depth "y"

is the only variable that changes between grid points. The real time and dummy time remain constant until the following step.

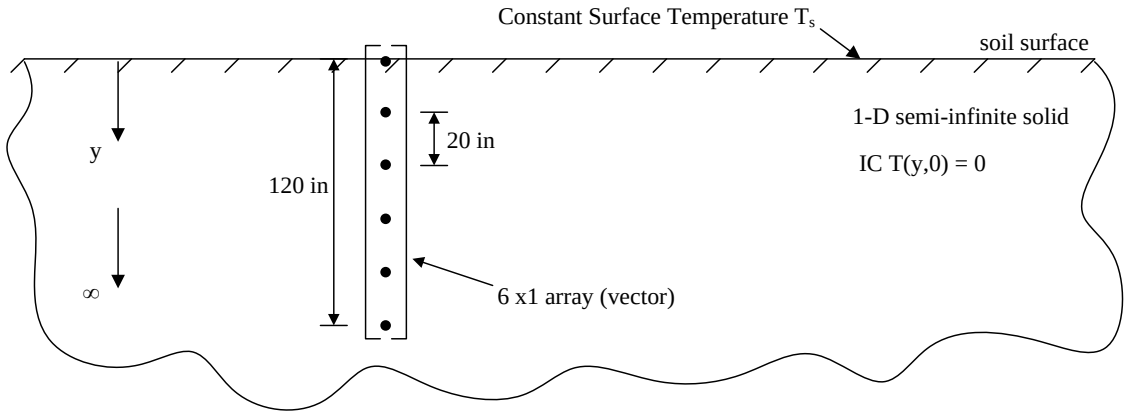


Figure 50: 1-D semi-infinite solid with constant surface temperature, temperature distribution represented by 6 x 1 grid for computer simulation

The space grid established in the previous step acts as a temperature location placeholder. The BSG program calculates the GF at each grid point for the same time value. Changing the time is the next step which creates the next grid of values. It is easier from this point on to think of the two time variables, "t" and "τ", as a single time (t-τ). For example, (t-τ) is equal to 50 days instead of "t" is equal to 100 days and "τ" is equal to 50 days. The following Numeric Integration program also treats the two times as a single variable. The purpose of treating the two times as one variable is database versatility. The database must cover all possible numeric integration times. The Numeric Integration program takes data for a 50 day and 100 day simulation from the same database. The 100 day simulation uses the same GF values as the 50 day simulation depending on the (t-τ) value. The only difference between the simulations is the BC multiplier. The 100 day simulation does not use the same first 50 days of BC

values. The Numeric Integration program must match the correct GF array with its BC multiplier based on the dummy time. The easiest way to ensure this happens is a $(t-\tau)$ organized database.

A third dimension accounts for $(t-\tau)$ values in the previously established 2-D space array. The result is a 3-D data block containing GF values at each space coordinate and $(t-\tau)$ time. Figure 51 is a graphical example of this data block organization. The first two dimensions define space coordinates that are representative of physical locations in the domain. The third dimension is time values at each space coordinate. The time values start at time "t" (or $\tau = 0$), and continue until $(t-\tau) = 0$. The data blocks are the only output from the Base Solution Generation program, which save to the database. Data blocks are split into intervals to decrease file size. They can be any size, but small enough for a computer simulation to quickly open and close. The size is also dependent on the numeric integration interval. As an example, the BSG program creates a five day database with a 10 minute time interval and one day data blocks for the grid in Figure 50. The database will have 5 data blocks, and each data block is a 6 x 1 x 144 array. The third array dimension is for the $(t-\tau)$ times.

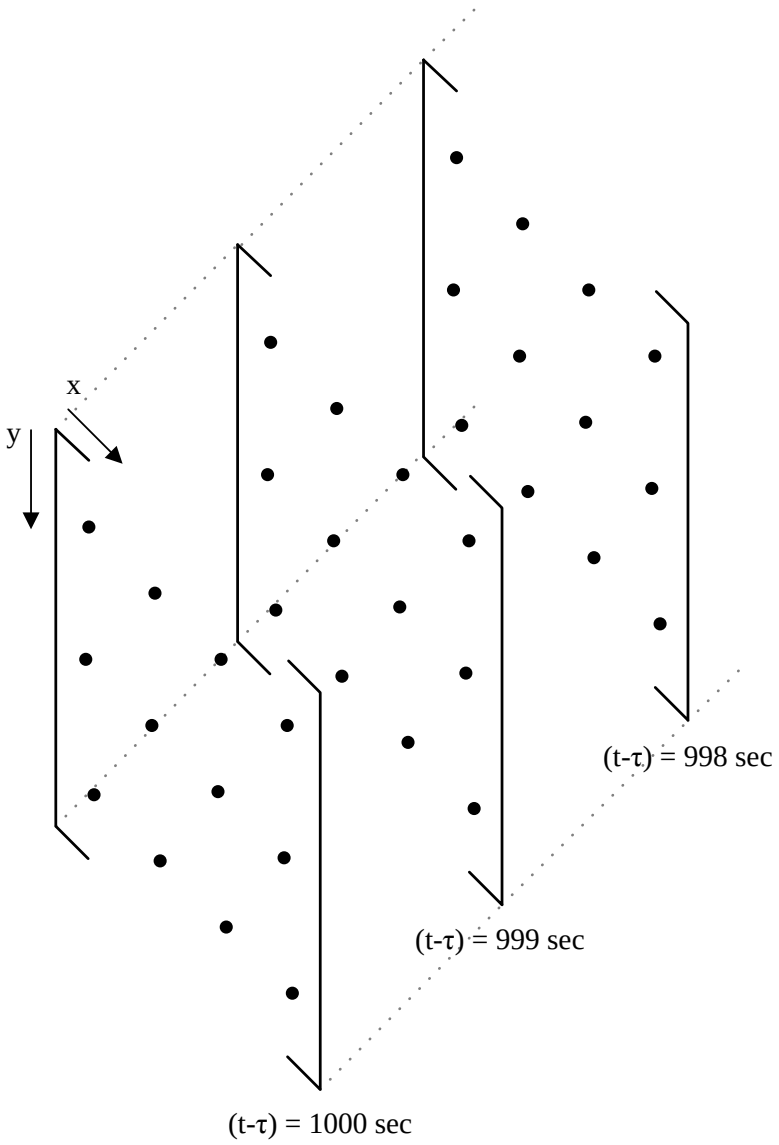


Figure 51: Example of three-dimensional data block used for calculating GF values

The below pseudo-code summarizes the BSG program. The main for-loop progresses through all (t-τ) times. The dummy time increases by the numeric integration time interval in each for-loop iteration. The third program input is the maximum time for any simulation. This variable limits the database size. A maximum time of five years extends the (t-τ) time to five years for example. It is then possible to execute any

simulation for a time of less than or equal to five years with this database. This is the variable the Refined Time program resets. If the maximum time requested is greater than the "refined time" output, the BSG program will consume computational time by generating useless data blocks. The refined time resets the maximum time so it generates only meaningful data blocks.

The first if-else statement saves full data blocks in the database, then re-initializes a new data block. The program only saves full data blocks. The second if-else statement determines if (t-τ) is equal to zero since a separate GF calculation executes with a close to zero (t-τ) value. All GFs are undefined at time equal zero. Green's Function calculations primarily occur under the else of this if-else statement. This step inserts calculated GF values into the data blocks. The end result is a database of GF values for all points in the space domain at all the time intervals specified. The database is now ready to pass information into the Numeric Integration program. Example code of this program is available in APPENDIX G.

```
SET    material and convection values

SET    limits on space domain

SET    maximum time for any simulation or refined time
       input

INIT   3-d data block to store GF values

FOR    values of τ starting at zero to maximum
       specified time

       IF     the data block is full of GF values

              SAVE   data block with time limits in
                     filename
```

```
            INIT   new blank data block for GFs

        ELSE
            nothing
        END IF

        IF     τ is equal to the maximum time specified

            calculate the zero time GF for all
            points in the space domain

            SAVE zero time GF array

        ELSE

            calculate GF values for all points in the
            space domain

            insert values of GF into 3rd dimension of
            data block array corresponding to current
            (t-τ) value

        ENDIF

        increase τ by desired interval amount

    REPEAT
    END FOR
```

Numeric Integration

The Numeric Integration program executes last to calculate the domain temperature distribution. Inputs shown in Figure 47 include the refined time, data block arrays from the database, climate conditions, and the numeric integration time interval. The output is the final temperature distribution. The program numerically integrates by adding the trapezoid edge points as described in Figure 46. The edge points are the product of the BC and GF inside the integral of Equation (59). A time dependent BC function is generated from the climatic condition input. The edge points, or "f" values in

Equation (48), calculate simultaneously for all space domain points at each interval time. This happens by extracting the appropriate GF array from the database and multiplying the array by the BC value at that time. This is the product of an array and constant. This calculates one edge point for all locations in the space domain. The current results add to the previous, and the process is repeated. The outcome is the simultaneous trapezoidal rule integration for all points in the domain, without calculating complex GF equations.

The pseudo-code below demonstrates program execution. The desired simulation time is the upper limit of integration in Equation (55). The refined time variable changes the upper integration limit if it is less than the input time. This limits the numeric integration to GFs that contribute meaningful values. This step significantly reduces the number of integrations. The numeric integration time interval specifies the trapezoid size. Smaller intervals increase accuracy and computation time. Any time interval is possible as long as it is a multiple of the database interval. For example, a minute interval in the database allows the numeric integration to use a one, two, five, ten, or even sixty minute interval for integration. The flexibility supports a balance of accuracy and computation speed.

Two for-loops working together provide this flexibility. The first loop loads a data block from the database each time it iterates. The time interval determines the second for-loop's step size. It extracts the appropriate GF array from the data block and multiplies it with the BC. The multiplication result is added to the previous values and sums the trapezoid edge points. Finishing the main for loop does not finish the integration. The zero time GF and BC are added to the summation outside the loop. The

summation is then multiplied by the appropriate constants to yield the final temperature distribution. Example code of this program is available in APPENDIX G.

```
      SET    desired time for temperature distribution or
             refined time input

      SET    numeric integration time interval

      LOAD   climate conditions for specified location

      FOR    values of (t-τ) starting at the desired
             temperature distribution time to zero time

             LOAD   data block specified by current (t-τ)
                    value

             FOR    time at start of data block to time at
                    end of data block

                    extract 2-D array from data block for
                    current τ value

                    multiply extracted GF array values by BC
                    value at the same τ time value

                    add multiplied values to previously
                    multiplied values (this is the addition
                    of trapezoids)

                    increase τ by time interval

             REPEAT
             END FOR

             decrease (t-τ) by data block size so next will
      load

      REPEAT
      END FOR

multiply zero time BC and zero time data block
```

```
add to previously multiplied values from for loop to
account for zero time GFs

multiply numeric integration result by integration
constants to yield temperature distribution
```

Accuracy Verification

This section verifies the accuracy and practicality of the Base Solution Generation (BSG) technique by continuing the example problem from earlier in the chapter. Figure 52 and Equation (60) repeat the example problem and the GF integral respectively for convenience. The derivation of Equation (60) is discussed earlier in the chapter. As a reminder, Equation (60) is the exact solution in integral form. Equation (52) is also an exact solution to this problem setup that is derived in literature using a similarity variable. A comparison of the similarity variable solution and numeric integration verifies the accuracy of the BSG technique.

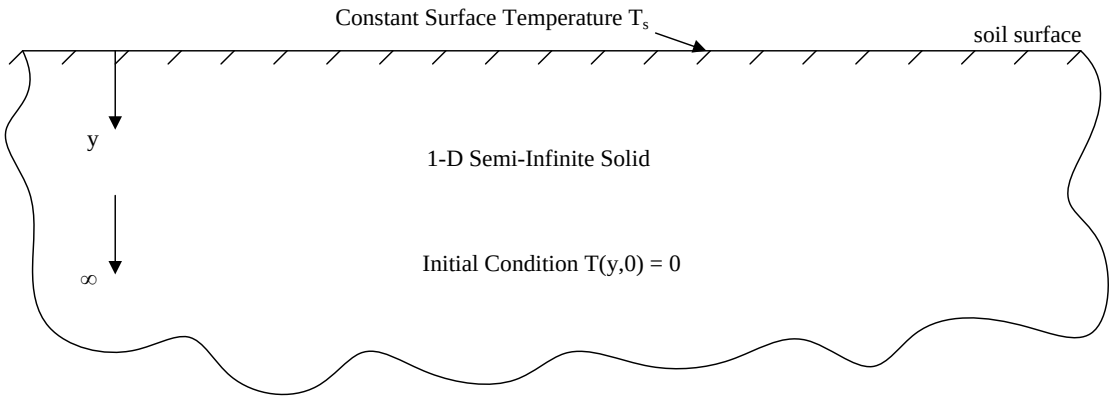


Figure 52: Example problem for verification of Base Solution Generation Technique, semi-infinite solid with constant surface temperature (Y10B1T0 problem type)

$$T(y,t) = \alpha T_s \int_{\tau=0}^{t} \frac{\mathrm{y}}{\{4\pi[\alpha(t-\tau)]^3\}^{1/2}} \exp\left[-\frac{(\mathrm{y})^2}{4\alpha(t-\tau)}\right] d\tau \qquad (60)$$

The input domain for the accuracy verification is from the surface to a 144 inch depth with two inch spacing. This establishes a grid of 73 points counting the surface. The domain inputs into the Refined Time and BSG program as a 73 x 1 array. Soil properties are a diffusivity of 0.60 ft^2/day and conductivity of 0.75 Btu/hr·ft·ºF. The surface is a constant temperature of 100ºF, and the domain is initially at zero temperature. The time domain input into the Refined Time and BSG program is 1095 days (3 years). The integration time step for the BSG program is one minute with one day data blocks. These settings create data blocks that are 73 x 1 x 1440 in size. There are 1440 minutes in one day. The threshold value in the Time Refinement program is 0.0025 1/ft^2. Times resulting in GF values less than the threshold are thrown out. Examination of Figure 49 led to this choice. The exact solution from the similarity variable in Equation (52) uses the same material, domain, and time variables.

The Numeric Integration program calculated the temperature distribution seen in Figure 53 at day 1095. The program uses data blocks generated by the BSG program, and a five minute integration time step. Figure 53 did not use the optional "refined time" input, and instead numerically integrated for all 1825 days. Note the BSG program generated data blocks with a minute time step, but the Numeric Integration program can use any time step that is a multiple of one minute. The exact solution from the similarity variable is the solid black line in Figure 53. It is evident the two solutions are exactly the same for all practical purpose. The maximum percent error between the two is 0.07%. The negligible percent error proves numeric integration by the BSG technique is an accurate heat conduction analysis method.

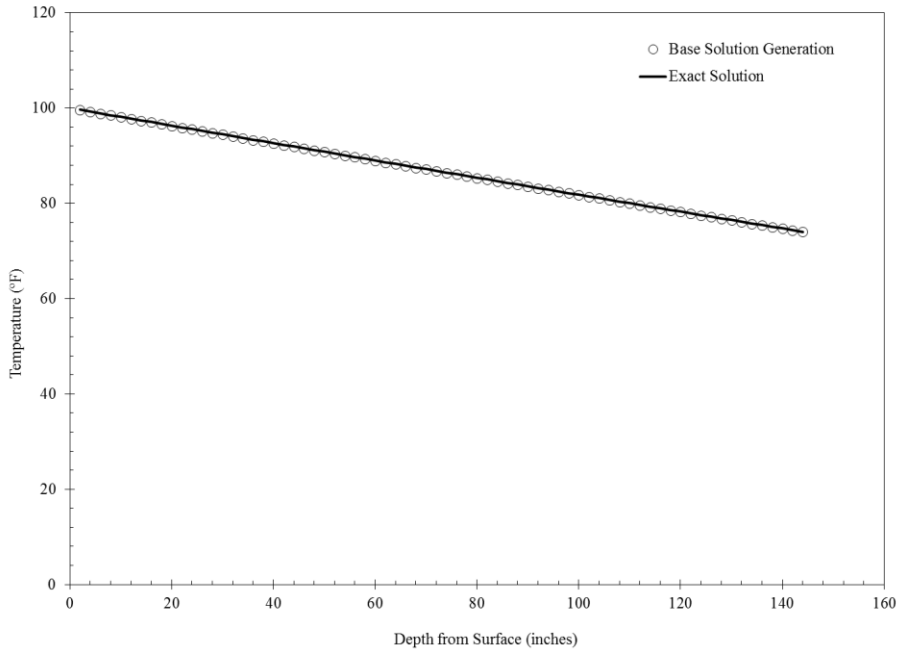


Figure 53: Temperature distribution after 1095 days (3 years) using BSG technique compared the exact solution for Y10B1T0 problem type

The simulation above did not use the Refined Time program's output. Figure 54 investigates accuracy reductions from limiting the numeric integration to GF values above of 0.0025 $1/ft^2$. The dotted time is the refined time simulation. The two numeric integrations are similar for shallow depths, but diverge as depth increases. Increasing depths generate higher GF values for extended time GFs. The higher GF values also stay around the same value as time increases. The shallower are practically zero at high time values while these deeper GFs remain relatively constant. This is clearly seen in Figure 48. The Refined Time program throws out the higher values and more information is lost than the shallower GFs. This is why the two lines in Figure 54 are diverging. The computation time is cut in half though by integrating over 906 days instead of 1825. The

Refined Time program balances computation time and accuracy depending on depth of interest.

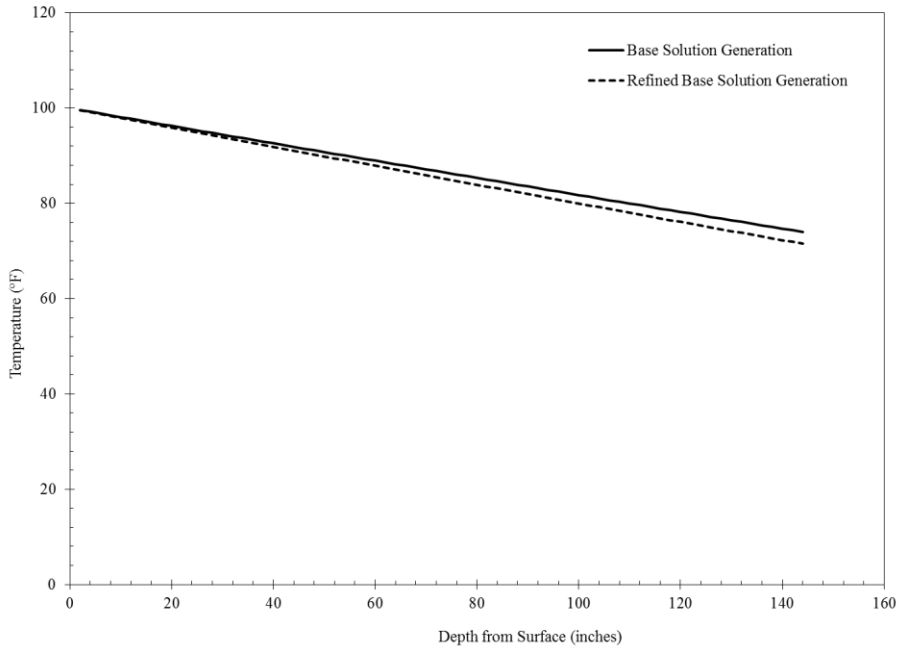


Figure 54: Three year (1095 days) BSG solution using full simulation time and refined simulation time for GFs above $2.5 \cdot 10^{-4}$ $1/ft^2$ only or 906 days

Simulation Times
and Integration Step Sizes

The computational time to complete the numeric integration changes with time interval and data block size combinations. This section examines different combinations to see how the computation times change in the BSG technique. The Matlab® 2012b simulation environment performed the calculations on a 64 bit Windows 7 desktop computer with an Intel® Core™ i7-4770 @ 3.4 GHz processor and 16.0 GB of RAM. Table 18 is the time in seconds the above computer took to finish the same 1095 day simulation in Figure 52 using time intervals from 1 to 60 minutes. The accuracy of each

simulation was surprisingly the same for depths below six inches. The accuracy of large integration intervals in this simulation is due to the constant BC values. This is a trait not shared in time-dependent BC simulations. The one minute interval simulation took the longest at 18.1 seconds as expected. The simulation times decrease until the 10 minute interval after which they relativity hold constant. This is counter-intuitive considering numeric integration by the trapezoidal rule. Doubling the time interval leads to half as many calculations and presumably half the simulation time. This is not true with the BSG technique due to the pre-calculated data block structure.

The Numeric Integration program must open and close data block arrays from the BSG database. Accessing the database is the simulation time limitation, not the integration interval. The 60 minute time step is still theoretically the fastest, but the computer spends the majority of its time manipulating the 1095 data blocks. Matlab's® built-in trapezoidal integration only takes 7.3 seconds to finish the same simulation with a one minute interval by contrast. This is much faster than the BSG technique and further reinforces the high computational workload for data block manipulation. It also suggests BSG simulations times could be reduced by changing data block sizes.

Table 18: Computation time required for example simulations based on integration interval size, data blocks one day in length with one minute time interval

Integration Time Interval (min)	Computational Time (sec)
1	18.1
2	15.54
5	14.26
10	13.67
20	13.56
60	13.27

A new simulation investigates the role data block size contributes to computation time. The new simulation expands the previous example problem to two dimensions over an annual basis. The annual basis investigates annual changes in soil temperatures by executing 36 separate simulations from 370 to 730 days (10 day interval). This way it is possible to analyze temperature changes throughout the year and is more representative of an EAHX simulation. The 2-D domain is 24 feet wide by 12 feet deep in 2 inch increment and inputs into the computer as a 73 x 145 array. The simulation investigates six integration intervals and data block size combinations. The data block interval is either one minute or five minutes, and the block sizes were one, five, and ten days. The Numeric Integration program used a 5 minute integration interval for all simulations.

The computational times from the six annual simulations in Table 19 reveal the BSG technique's efficiency is strongly dependent on the data block time interval. The five minute block is between 4.1 and 4.3 times faster than the one minute blocks. Recall, all six simulations use a five minute integration interval in the Numeric Integration program. The data block array size for each simulation in Table 20 obviously contributes to the time reduction, but is not the only factor. The five minute, five day block takes the same amount of time as the five minute, ten day block even though it is twice the size. The five minute, ten day block opens 73 files while the five minute, five day block opens 146. This represents a balance point between opening a data block and manipulating it in the Numeric Integration program. The five minute, ten day block takes longer to open, but makes up that time during the integration. The one minute data blocks are simply too large for the computer program to efficiently open and close.

The Matlab® built-in trapezoidal algorithm also takes much longer to finish the above simulation at 60.1 minutes. The Matlab® algorithm was much faster than the BSG technique for the previous 1-D simulation, but its simulation time steadily increases with domain size. The built-in algorithms integrate one point at a time, and simulation time is linearly related to the number of domain points. The BSG technique on the other hand relies on array multiplication, and experience smaller increases in simulation time with domain size. The end result is the BSG technique is 3.3 times faster than built-in algorithms for the simulation described above. Computational times are subject to the type of simulation and computer hardware.

Table 19: Simulation times in minutes for integration interval and data block size combinations over a 370 to 730 day simulation, 10 day interval

Data Block Interval	Data Block Size		
	1 Day	5 Day	10 Day
1 Minute	78.1	75.2	76.8
5 Minute	19.1	17.9	17.9

Table 20: Arrays size for integration interval and data block size combinations over a 370 to 730 day simulation, 10 day interval

Data Block Interval	Data Block Size		
	1 Day	5 Day	10 Day
1 Minute	73x145x1440	73x145x7200	73x145x14400
5 Minute	73x145x288	73x145x1440	73x145x2880

SOIL TEMPERATURE SIMULATIONS

Earth-air heat exchanger (EAHX) simulations rely heavily on the soil surface boundary condition (BC). Its accurate representation is essential since it is a primary factor for determining soil temperatures around the EAHX pipe. Soil surface temperatures are the best option to represent this boundary, but are not available in all locations. Atmospheric air data is more common for locations all around the world. Fluid air temperature implies a convective BC. This is a problem though due to highly variable wind speeds, and in turn convective heat transfer coefficients. A time-variable or annually averaged coefficient is too unpredictable and likely to generate significant errors. Treating the atmospheric air as a constant temperature at the surface significantly simplifies the simulations, but is not as precise as the actual soil surface temperature.

The purpose of this chapter is to determine if soil surface temperature and heat flux boundary conditions will yield acceptable results in soil conduction simulations before moving onto EAHX simulations. The chapter also investigates several other soil simulation factors such as soil properties and integration techniques. The analysis uses 15 locations listed in Table 8 to evaluate effects of diverse climatic zones. Annual soil temperature data is available near all 15 locations from the National Resource Conservations Service (NRCS). The data includes the surface, 20, and 40 inch depths. Typical Meteorological Year (TMY) data files including a historically averaged dry bulb air temperature are also available at these locations. The observed data for simulation validation is the 20 and 40 inch NRCS soil temperatures in Figure 174 to Figure 188 of APPENDIX A.

Under Yard Green's Function Formulation

The semi-infinite solid is a common means to model soil conduction from a surface boundary. Figure 55 outlines the boundary value problem for this simulation, which is an Y10B-T1 problem type. This is similar to the example in the previous chapter except the initial condition is a non-homogenous constant temperature "T_m". Simplification of the Green's Function Solution Equation (GFSE) in Equation (41) leads to Equation (61). The first term in Equation (61) is the initial condition (IC) contribution. Notice it contains a space integration from zero to infinity with respect to the dummy space variable. The second term is the contribution from the time-dependent surface temperature BC. Note the surface temperature, "$T_s(\tau)$", is a function of the dummy time variable. Equation (54) is the expression for the Green's Function (GF) derivative in the second term. Equation (62) is the G_{Y10} Green's Function (GF) for the IC space integration. This space integration appears difficult, but has a tabulated explicit representation. Equation (63) is the final form for the Base Solution Generation (BSG) technique after integration and inserting the GFs. The simulation still lacks an initial condition value, material properties, and a surface temperature function.

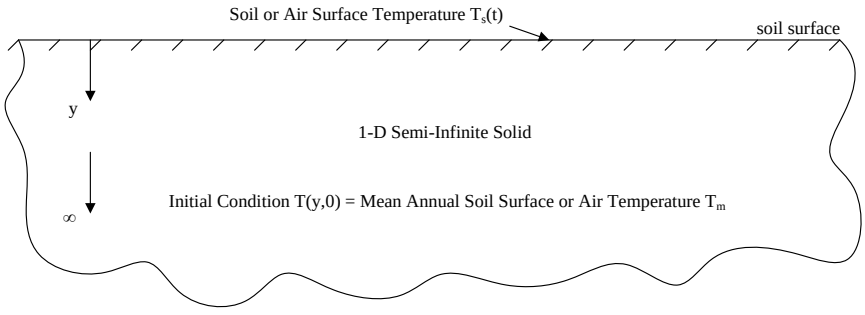


Figure 55: Soil conduction problem setup for Green's Function method, Y10B-T1 problem type

$$T(y,t) = \int_{y'=0}^{\infty} T_m G_{Y10}(y,t|y',\tau)dy' - \int_{\tau=0}^{t} \alpha T_s(\tau) \frac{\partial G_{Y10}}{\partial y'} d\tau \tag{61}$$

$$G_{Y10}(y,t|y',\tau) = \frac{1}{[4\pi\alpha(t-\tau)]^{1/2}} \left[exp\left(-\frac{(y-y\prime)^2}{4\alpha(t-\tau)}\right) - exp\left(-\frac{(y+y\prime)^2}{4\alpha(t-\tau)}\right)\right] \tag{62}$$

$$T(y,t) = T_m erf\left(\frac{y}{[4\alpha t]^{1/2}}\right) + \alpha \int_{\tau=0}^{t} T_s(\tau) \frac{y}{\{4\pi[\alpha(t-\tau)]^3\}^{1/2}} exp\left(-\frac{y^2}{4\alpha(t-\tau)}\right) d\tau \tag{63}$$

The non-homogeneous IC is meant as an approximate starting point to speed convergence to a realistic solution. Otherwise, it may take several years of calculations before the soil develops a periodic temperature distribution. The mean annual soil surface or air temperature is a logical choice for the "T_m" value. Soil temperatures approximately fluctuate around the mean annual atmospheric temperature according to past literature. Literature also recommends a diffusivity of 0.6 ft^2/day when soil type is unknown. An approximate diffusivity is the only option since there is no location based diffusivity data available, and physical measurement is not practical [7, 15].

A least squares regression (LSR) fit with a Fourier series in the form of Equation (46) describes the time-dependent surface BC "$T_s(t)$". A Fourier series fit is appropriate because the near surface soil and air temperatures are sinusoidal by nature. This is shown by the red dots in Figure 56 and Figure 57. Figure 56 is the soil surface temperature from the NRCS Table Mountain site near Bozeman, Montana. Figure 57 is the dry bulb air temperatures from the Bozeman TMY data file. The Fourier series fits represented by the black lines in the figures appear the same shape. The differences are only noticeable

through the fitted line's equation below the figures. The soil surface's mean annual temperature is 2ºF warmer than the air (this is the a_0 term) and has higher temperatures at the colder extremes. A previous study in literature encountered a similar mean temperature difference and recommends a 2ºC (3.6ºF) correction factor to air temperatures [15]. The following soil simulations test the correction factor by comparing unaltered TMY air temperatures and TMY air temperatures increased by 3.6ºF. The increased temperatures are known as the corrected TMY data files. Weather data and fits for all 15 locations in Table 8 are in Figure 189 through Figure 218 of APPENDIX B.

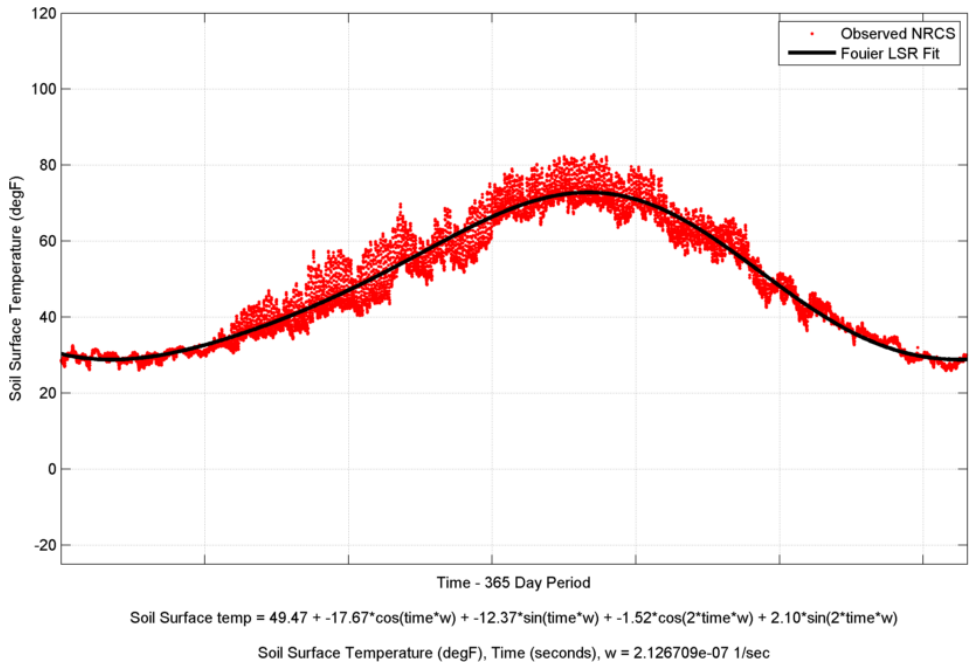


Figure 56: Bozeman, Montana– Least-squares curve fit to observed soil surface temperatures using four term Fourier series

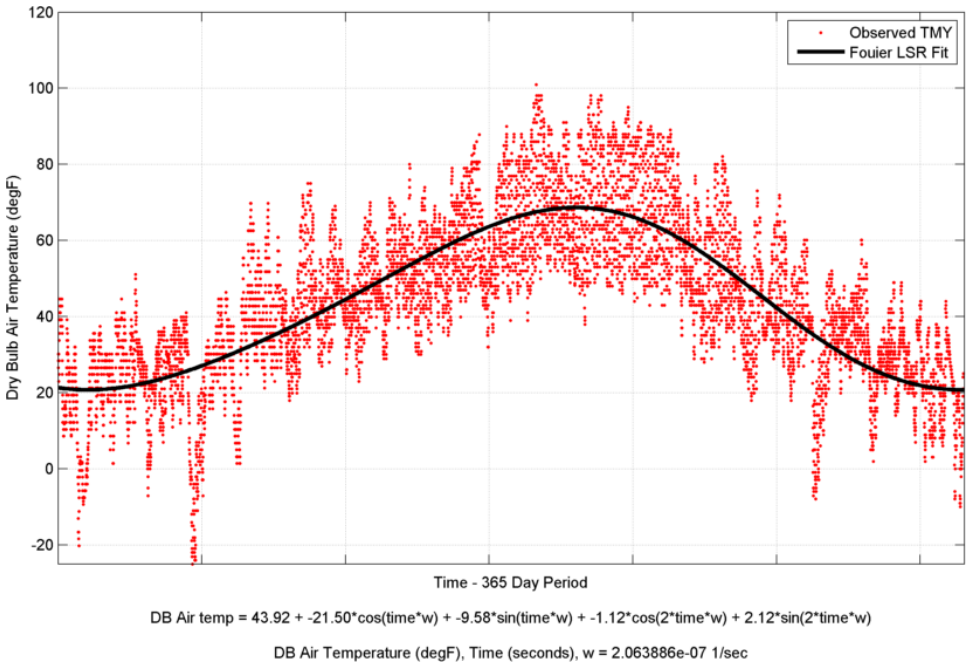


Figure 57: Bozeman, Montana – Least-squares curve fit to dry bulb air temperatures from a typical meteorological year (TMY) using four term Fourier series

Base Solution Generation
Optimization of Under Yard Formulation

The purpose of this section is to perform an example optimization of the BSG technique using the UY soil temperature formulation. Base Solution Generation optimizations occur in other parts of this research, but are not discussed in detail. The space domain for this example is 1-D and extends from the surface to eight feet in two inch increments. The initial time of interest is three years. The Time Refinement program uses this information to determine possible computational reductions by limiting the time domain. The BSG program then calculates a preliminary database using a one minute integration interval and one day data blocks. Two analyses from this preliminary database will optimize program execution. A numeric integration time interval analysis

finds an appropriate time interval size for this boundary value problem. The appropriate time interval leads to data block size selection. Test simulations determine the most computationally efficient combination, and the optimization is complete. The time interval analysis compares three locations from Table 8 to ensure uniform behavior between various climatic conditions. The locations are Bozeman, Montana, Houston, Texas, and Columbus, Ohio. The time refinement and data block optimization use only Bozeman, Montana for its analyses since they are not dependent on BC values.

Refined Time Step

The only difference between Equation (63) and the example GF application from the previous chapter in Equation (55) is the addition of an IC. The GF derivatives in the time integrations are the same, which implies Figure 48 and Figure 49 are valid representations of the GF derivative over extended times. The figures help determine a practical GF threshold of 0.0015 $1/ft^2$ for a 1-D domain extending to a depth of eight feet. The Time Refinement program determines this threshold is reached when $(t-\tau)$ equals 268 days. In other words, the only GF values that contribute to the final temperature distribution (above the threshold), occur 268 days from the end simulation time. The next step is to verify the reduction in accuracy from this threshold value is within acceptable limits.

A 730 day soil simulation for Bozeman, Montana accomplishes the accuracy verification. The first simulation uses the full 730 days in the Numeric Integration program with a one minute integration interval. The simulation takes 13.69 seconds to complete on the pre-described computer. The numeric integration using the 268 day

input from the Time Refinement program takes 6.51 seconds. The simulation time is reduced by half with small increases in computational error. Table 21 summarizes the difference in temperature between the non-refined and refined time numeric integrations. The refined-time values for four and six feet are approximately 0.5ºF lower than the non-refined integration. The maximum difference is 0.74ºF at eight feet. These are acceptable errors for the domain of interest.

Table 21: Temperature differences with depth between a non-refined and refined time soil simulation (730 day simulation for Bozeman, MT with 0.0015 $1/ft^2$ GF threshold)

Depth (ft)	Temperature Difference (ºF)
2.0	0.20
4.0	0.40
6.0	0.58
8.0	0.74

Numeric Integration Time Interval Analysis

The time interval analysis ascertains the largest possible integration interval that still retains a high level of fidelity in the soil simulation. A larger time step significantly reduces the number of calculations and computational workload. The analysis covers Bozeman, Montana, Houston, Texas, and Columbus, Ohio to check the effect of BC values. The Numeric Integration program executes the soil temperature simulation using integration intervals of 1, 5, 10, 20, and 60 minutes. The simulation executes every 5 days from 365 to 730 days (74 separate calculations) to characterize the annual soil temperatures and does not use the Time Refinement program. The primary depth of

interest is six feet, but the simulation calculates all depths to eight feet in one inch increments.

Figure 58 and Figure 59 evaluate the surface accuracy for each integration interval. Green's functions for Semi-infinite solids are not mathematically well behaved near the surface boundary, and Figure 58 shows that capturing the temperature changes in the soil surface requires smaller integration intervals. Fortunately discrepancy between interval sizes rapidly decreases with depth as seen in Figure 59. Here the soil temperatures at five inches generally converge to the same value except for the 60 minute time step. Soil temperatures past five inches follow the same trend and are relatively the same. Domains of interest five inches or less will require a minute time step, but generally EAHX installation is at depths of four feet and greater.

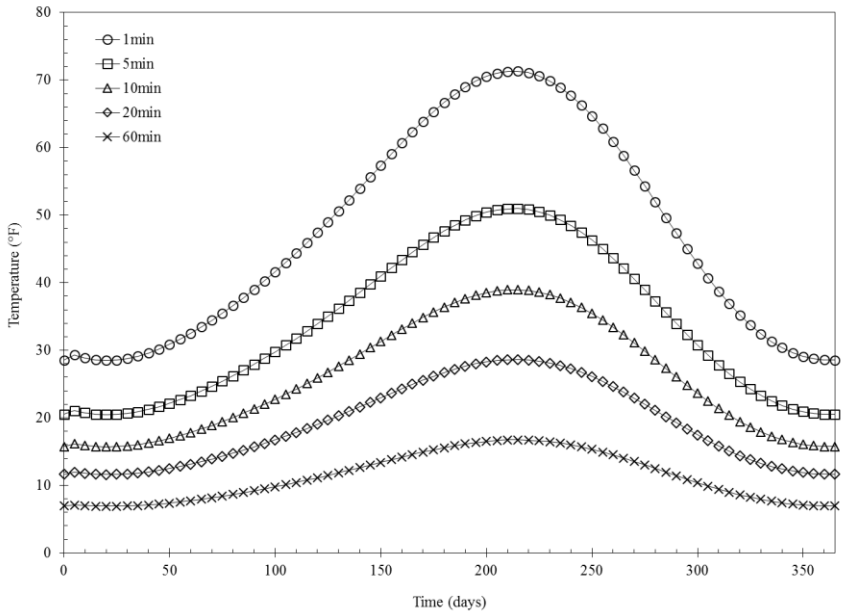


Figure 58: Soil temperatures for the numerical integration time step comparison over one year time period in Bozeman, MT for a depth of one inch

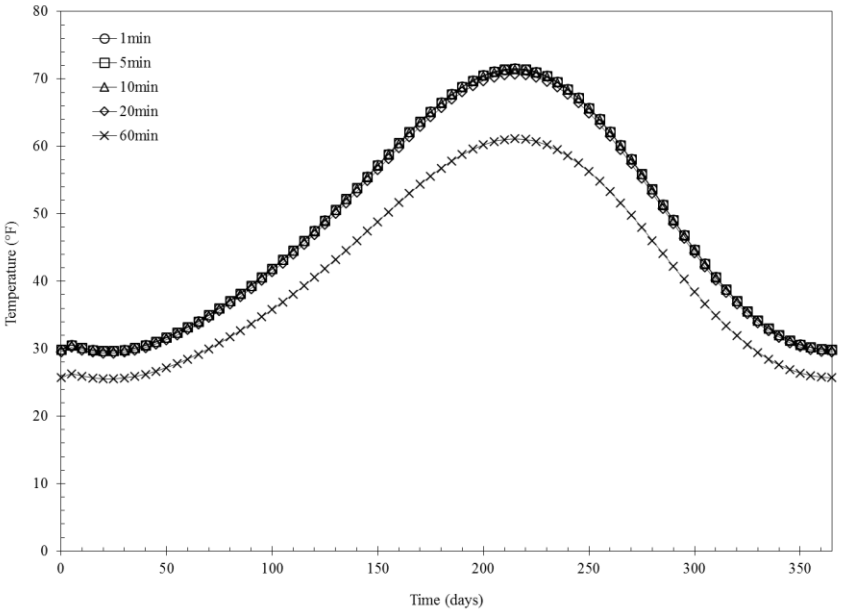


Figure 59: Soil temperatures for the numerical integration time step comparison over one year time period in Bozeman, MT for a depth of five inches

The 72 inch soil temperatures for each of the three locations in Figure 60 through Figure 62 are in good agreement. The only visibly difference is in the 60 minute interval. The divergence between each time step is not clear until enlarging the figures. Figure 63 is a zoomed in view of Figure 60 from day 200 to 300. This shows a clear separation between each time interval. Temperatures decrease with increasing time interval indicating the larger time steps are not capturing as much information as the smaller. The 60 minute interval in Figure 63 is a full degree different from the others and not a suitable choice. The 1, 5, and 10 minute intervals are practically the same, and throughout the year there is a less than 0.3ºF difference between the 1 and 10 minute interval. The optimal integration interval is 10 minutes since it retains a high level of fidelity and significantly reduces the number of calculations in the Numeric Integration program.

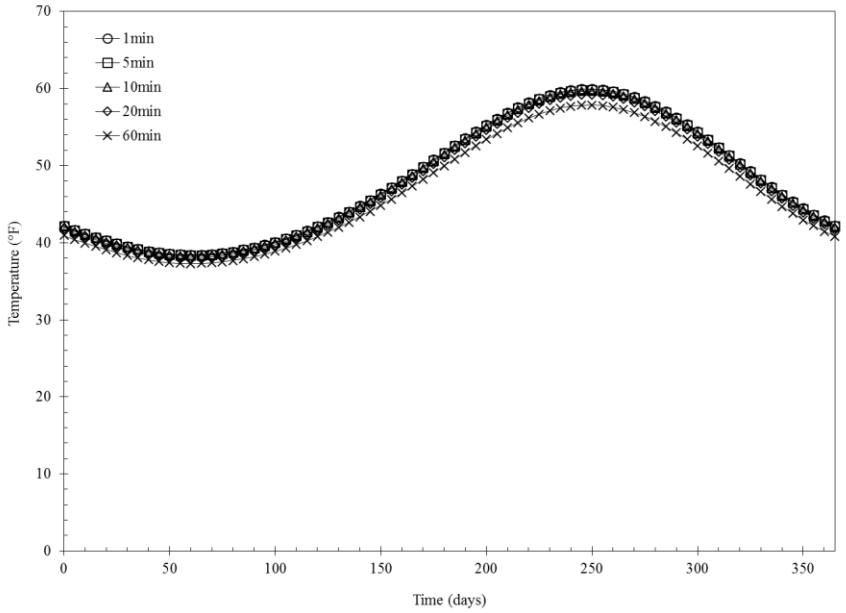


Figure 60: Soil temperatures for the numerical integration time step comparison over one year time period in Bozeman, MT for a depth of 72 inches

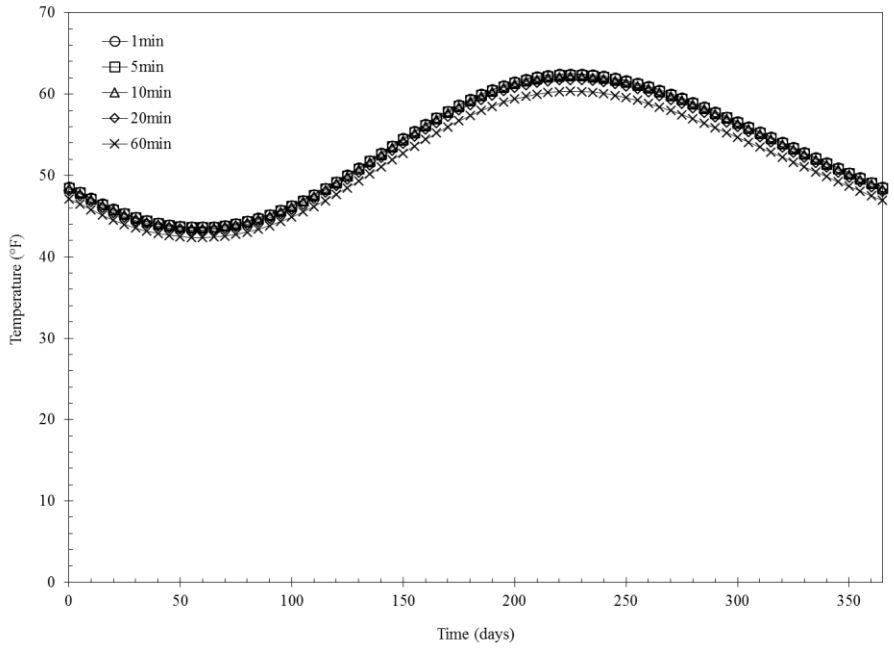


Figure 61: Soil temperatures for the numerical integration time step comparison over one year time period in Columbus, OH for a depth of 72 inches

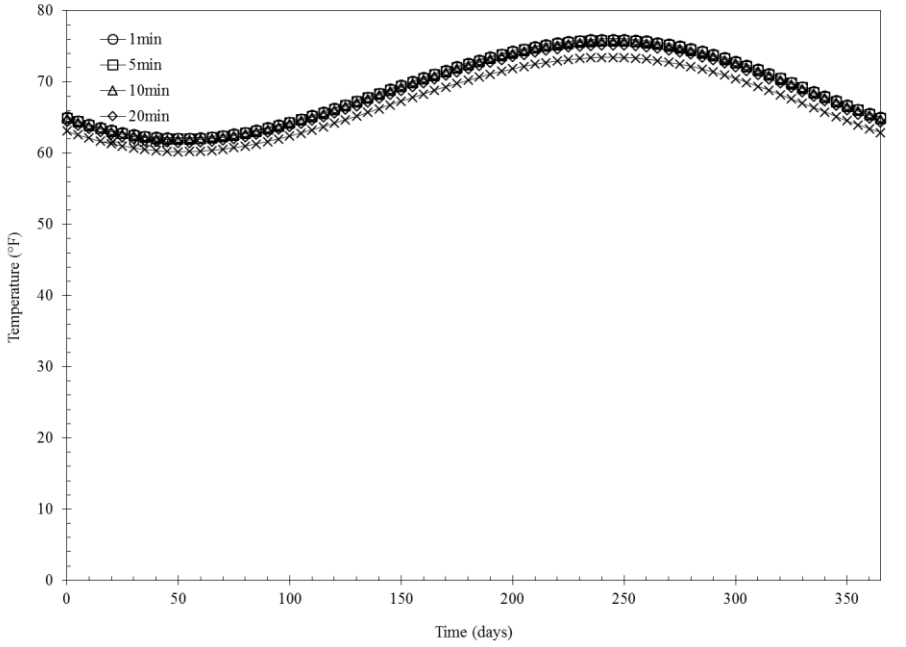


Figure 62: Soil temperatures for the numerical integration time step comparison over one year time period in Houston, TX for a depth of 72 inches

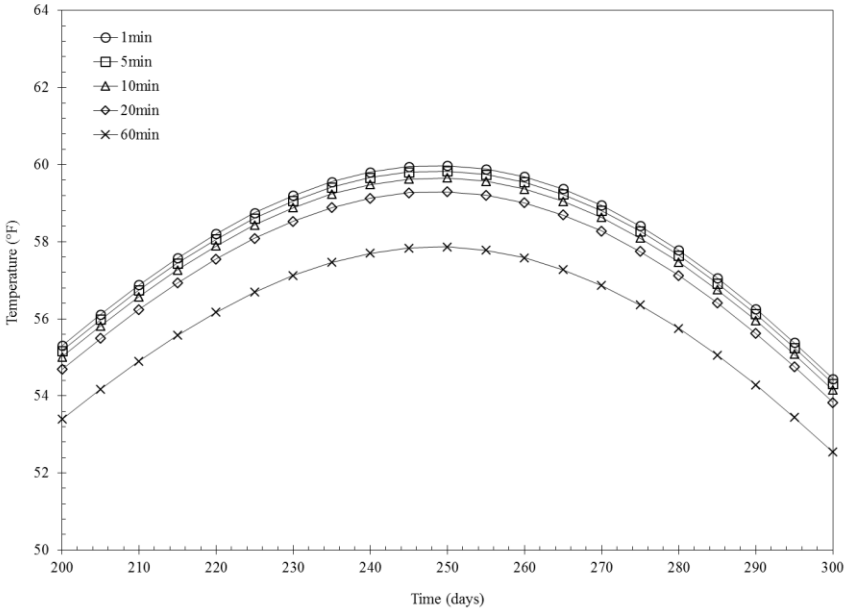


Figure 63: Closer inspection of numerical integration time step comparison from days 200 to 300 of a typical year for Bozeman, MT for a depth of 72 inches

Data Block Size

The final step in the BSG optimization identifies a computationally efficient data blocks size to pair with the ten minute integration interval. This process uses the same 730 day simulation for a 1-D domain extending to eight feet and does not use time refinement. The BSG program creates databases for one, five, and ten day data blocks. Data blocks greater than 10 days were not considered because simulation times are limited to multiples of the data block size. Table 22 summarizes the computation times for each interval and data block pair. The one day data blocks took on average 5.72 seconds to finish the simulation while the five and ten took around 3.0 seconds. By contrast, the same simulation using one minute time interval and one day data blocks takes 13.69 seconds. A ten second reduction in simulation time may not seem like much, but the savings add up when running several hundred simulations. Some accuracy is lost by using the 10 minute interval, but the error is acceptable for soil temperatures. The optimal combination is the ten minute interval and five day data block. Little computational time is saved by moving to a 10 day block, and a five day block allows greater simulation flexibility.

Table 22: Computational times for a 730 day simulation using one, five, and ten day data blocks, and a 10 minute integration interval

Data Block Size	Simulation Times (sec)			Average (sec)
1 Day	5.75	5.68	5.73	5.72
5 Day	3.09	3.06	3.04	3.06
10 Day	2.92	2.92	2.91	2.92

Under Yard Soil Temperature Simulations

Location Based Experimental Results

The following soil temperature simulations solve the boundary value problem in Figure 55 using the optimized BSG technique. This chapter highlights the Bozeman, Montana location, and APPENDIX Dincludes results for all locations in Table 8. Each location simulates the surface boundary with the NRCS soil surface temperatures, the TMY dry bulb air temperatures, and a 2ºC (3.6ºF) corrected TMY temperatures. The soil surface and air dry bulb data fits are listed in APPENDIX B. The non-homogeneous IC is equal to the mean soil or air temperature depending on BC type. All locations use a $0.6 ft^2$/day diffusivity as recommended by previous studies. Experimental data at 20 and 40 inch depths from the NRCS sites validates the soil simulations. Forty inches is as deep as the monitoring sites extend. The same sites provide the soil surface temperature BC.

Figure 64 and Figure 65 are the simulated vs. observed soil temperatures at 20 and 40 inches respectively using the NRCS BC in Bozeman, Montana. The predictions very closely match the observed data. This is also true for the other 14 locations in APPENDIX D. The soil surface is much more accurate than the TMY air temperatures even with the correction factor. The strong correlation is expected since the surface BC and observed data come from the same monitoring site. The important observation from these results is the validity of the diffusivity assumption. All locations have satisfactory results from an assumed diffusivity of 0.6 ft^2/day. Soil types are not the same in each location, but this value captures a majority of soil types. It is now not necessary to

calculate or measure soil diffusivity at a planned EAHX site. An assumed 0.6 ft^2/day is close enough for design and simulation purposes.

The same simulations using the TMY and TMY corrected dry bulb air temperature BCs do not match the observed data as closely. Figure 66 and Figure 67 are the Bozeman, Montana simulations at 20 and 40 inches respectively. Both figures follow the sinusoidal soil temperature path and peak at the correct summer month temperatures. The simulation has some difficulty though during winter months with cooler air temperatures. Other locations in Table 8 with heating degree days over 7000 like Bozeman, Montana experience the same errors. For example, the predicted temperatures for St. Cloud, Minnesota (HDD 8520) in Figure 290 and Figure 291, and Sioux Fall, South Dakota (HDD 7524) in Figure 302 and Figure 303 also do not match the observed data in the winter months. The NRCS soil surface BC on the other hand is still accurate in these locations.

The winter deviations are due to effects outside of the GF heat conduction formulation. This is proven by the high level of accuracy in locations with lower HHDs. Take Houston, Texas (HDD 1414) for example in Figure 260 and Figure 261. The TMY and corrected TMY BCs both closely match the observed data at 20 and 40 inches. The same trend is true in other locations such as Athens, Georgia (HHD 2762) in Figure 248 to Figure 249 and Pine Bluff, Arkansas (HHD 2655) in Figure 284 to Figure 285. The TMY BCs are fairly accurate until air temperatures drop below 32ºF. In Bozeman, Montana for example, the soil surface temperatures in Figure 56 never fall below 32ºF; even though the air temperatures are below freezing as seen in Figure 57. Literature

identifies several factors that contribute to the soil's resistance to freezing. These include the latent heat of moisture changing phases, and snow cover and/or vegetation acting as an insulative barrier. The same studies present methods to compensate for these effects, but are currently not necessary. The soil surface temperature BC already provides a high fidelity model.

The only location where the TMY results were nowhere near the observed soil data was Las Vegas, Nevada in Figure 272 and Figure 273. The cause in this instance has to do with elevation differences between the NRCS and TMY measurement sites. Recall the NRCS sites are typically outside of major cities. The NRCS Pine Nut soil measurement site is located in the mountains outside of Las Vegas at an elevation of 6770 feet. The TMY atmospheric data comes from McCarran International Airport at an elevation of 2181 feet. A 4589 foot elevation difference will significantly affect annual climate conditions. Elevation differences are one drawback of using NRCS testing sites outside of major metropolitan areas. The soil simulation using the TMY BCs are most likely correct for the Las Vegas elevation based on other sites with similar number of cooling degreed days.

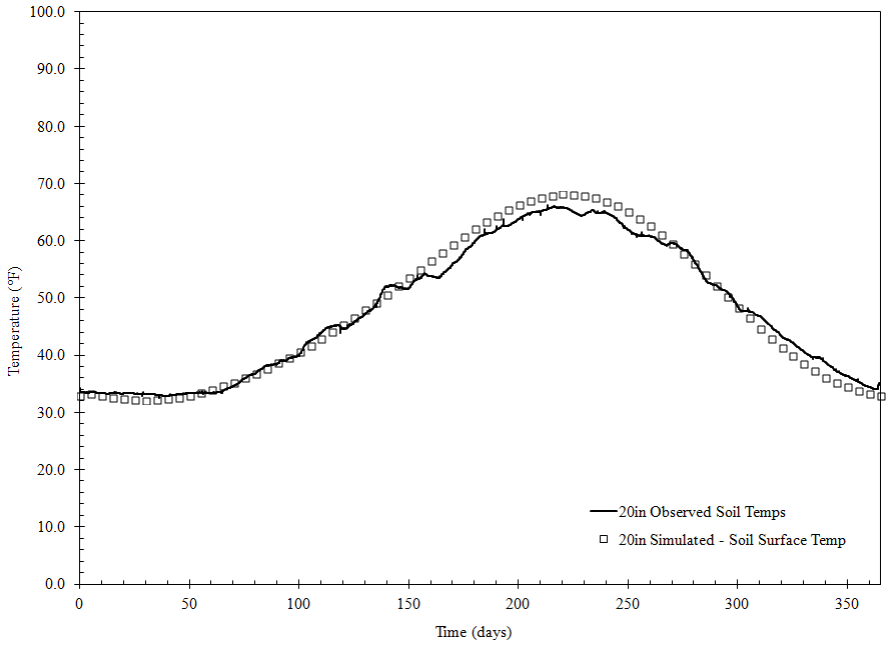


Figure 64: Bozeman, Montana – 20 inch observed vs. simulated Green's Function soil temperatures – observed surface soil temperature boundary condition

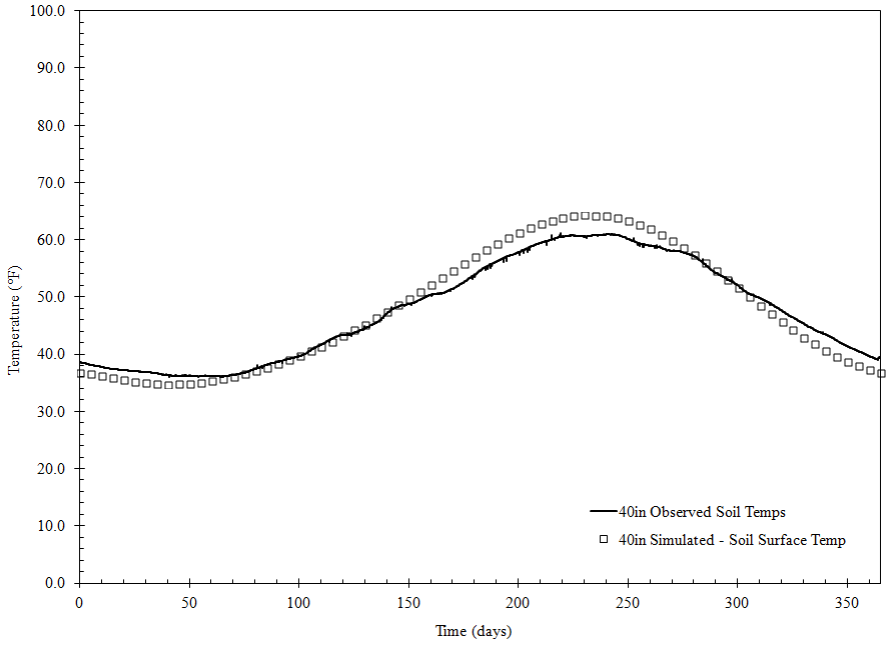


Figure 65: Bozeman, Montana – 40 inch observed vs. simulated Green's Function soil temperatures – observed surface soil temperature boundary condition

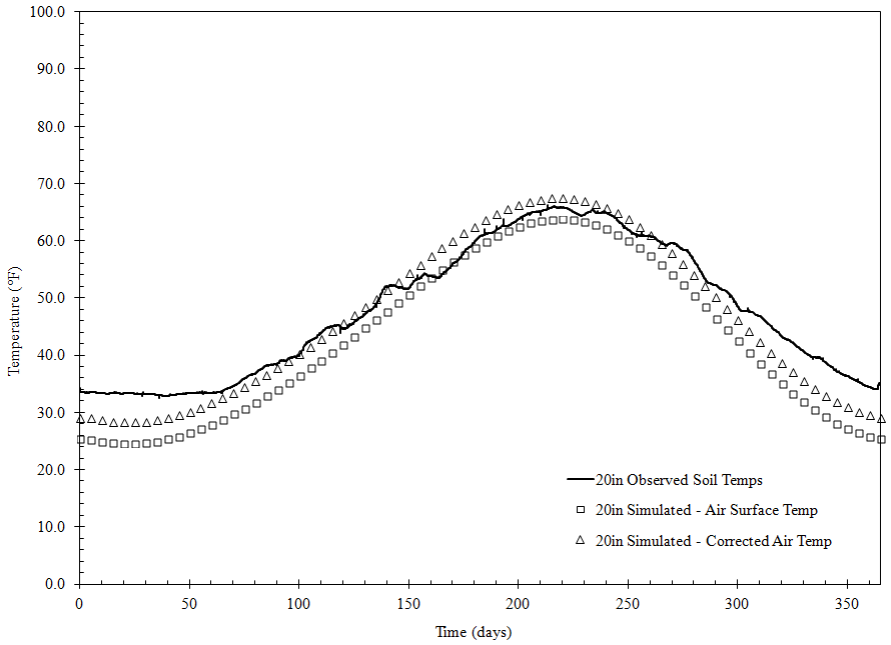


Figure 66: Bozeman, Montana – 20 inch observed vs. simulated Green's Function soil temperatures – typical meteorological year (TMY) and corrected TMY surface air temperature boundary conditions

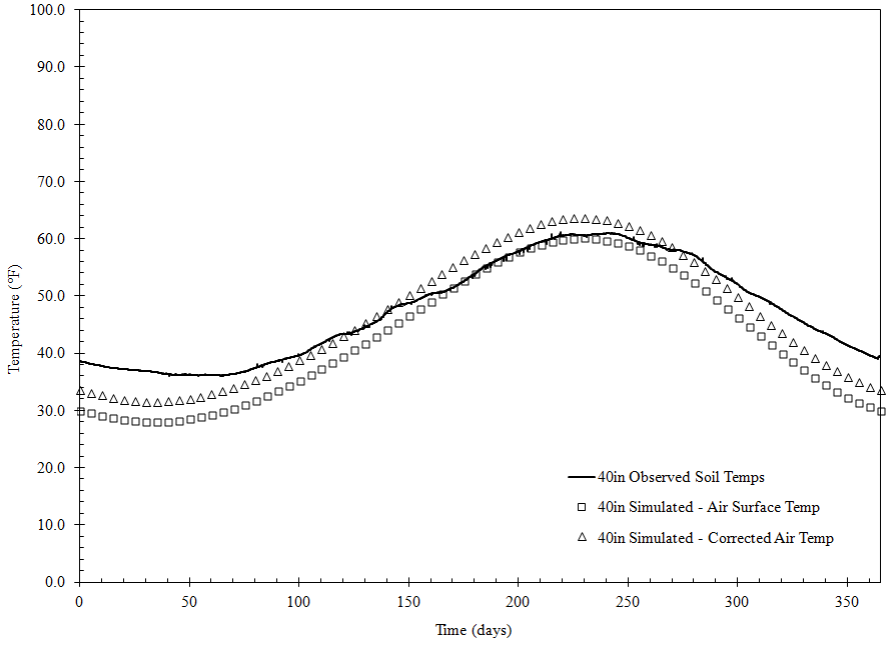


Figure 67: Bozeman, Montana – 40 inch observed vs. simulated Green's Function soil temperatures – typical meteorological year (TMY) and corrected TMY surface air temperature boundary conditions

NRCS and TMY
Boundary Condition Comparison

The NRCS soil surface BC is clearly the most accurate of the three for simulating soil temperatures. Visually there is no clear advantage in most locations of correcting the TMY BC by 2ºC. A Residual Sum of Squares (RSS) analysis is a better indication of which of the two BCs lies closer to the observed values. Table 23 lists the RSS results for each BC at 20 and 40 inch depths. Figure 68 is a graphical representation of the RSS at the 40 inch depth. The RSS for Las Vegas in Table 23 is over 20,000 $^{o}F^{2}$ due to the previously discussed elevation difference and was not included in Figure 68. The NRCS soil surface in blue has low RSS values for all locations except Salt Lake City, Utah. The TMY RSS values are the most inaccurate by a large margin, and the corrected TMY BC is a clear improvement in all locations except State College, Pennsylvania. State College's TMY BCs are still fairly close with difference of only 154 $^{o}F^{2}$. The TMY BC with correction factor offers a clear improvement to the soil simulations using atmospheric air temperatures and is recommended when soil surface data is not available.

Table 23: Residual sum of squares analysis ($^oF^2$) between observed values and the NRCS soil surface, TMY, and TMY corrected BCs

Location	Soil 20in	Soil 40in	Air 20in	Air 40in	Air Corr. 20in	Air Corr. 40in
Albuquerque, NM	294	121	2840	2746	630	571
Amarillo, TX	83	42	797	729	310	198
Athens, GA	155	189	928	840	312	236
Bozeman, MT	231	337	2365	2349	781	841
Columbus, OH	360	241	1438	1019	702	550
Houston, TX	69	64	238	182	537	524
Kansas City, MO	179	65	3293	2085	1236	535
Las Vegas, NV	726	524	12795	12838	20592	20689
Moses Lake, WA	314	567	675	854	829	567
Pine Bluff, AR	61	59	1446	875	564	268
Saint Cloud, MN	61	142	7145	5196	5126	2989
Salt Lake City, UT	1139	2047	1244	2518	687	1091
Sioux Falls, SD	74	103	3099	1798	2427	1702
State College, PA	1255	239	1681	386	308	540
Tallahassee, FL	93	60	608	387	204	256

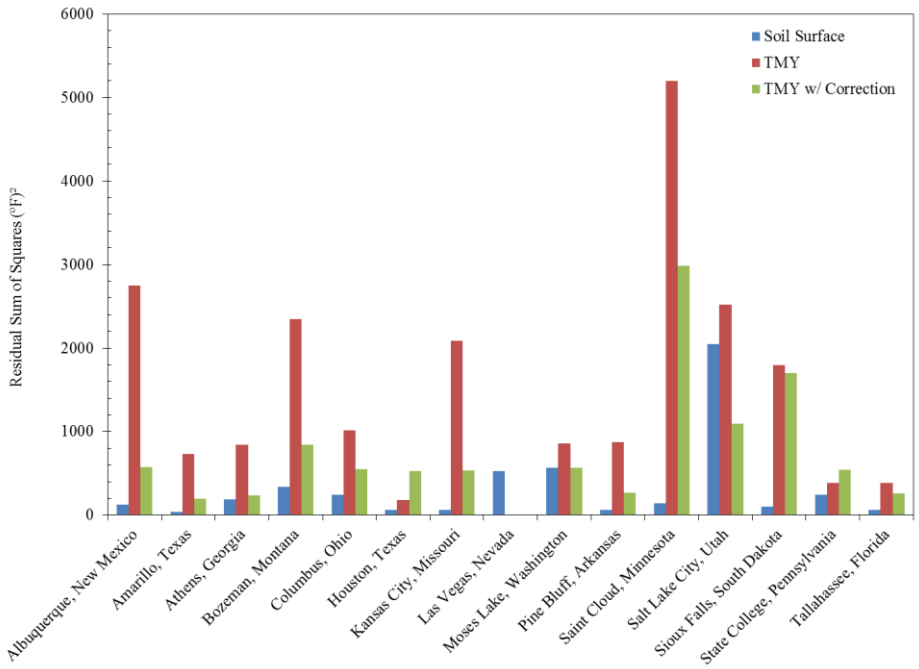


Figure 68: Residual sum of squares results ($^oF^2$) between observed values and the NRCS soil surface, TMY, and TMY corrected BCs at 40 inch depth

Soil Simulation Application
to Earth-Air Heat Exchangers

Experimental data is only available for a maximum depth of 40 inches, but EAHX are typically installed four feet or more below grade. Figure 69 and Figure 70 are the simulated soil temperatures for 2, 4, 6, 8, and 10 feet in Bozeman, Montana. Figure 69 uses the soil surface BC, and Figure 70 the TMY corrected BC. Similar figures for the other 14 locations are found in APPENDIX D. The two figures are similar in shape, and the only difference is lower winter temperatures with the TMY BC. The "heat wave" traveling from the warm surface is clearly visible in the temperature lag between depths. The 10 foot depth is the last to plateau from the warmer summer temperatures at day 275 (middle of October). The soil temperatures at all depths fluctuate around the same mean temperature which is surprisingly close to the mean atmospheric air temperature. It is a common belief that soil temperatures remain constant after a certain depth. The fluctuation amplitude is decreasing with depth, but there is still a several degree fluctuation at 10 feet.

An EAHX installed six to eight feet below grade for Bozeman (8372 HHDs) experiences prolonged higher soil temperatures in the early winter months due to the temperature lag through the soil. In other words, the soil at a six to eight foot depth does not start to cool from atmospheric conditions until approximately day 300, or the start of November, from Figure 69. Average air temperature at this time is already at 30°F [13] and significant energy extraction from the soil is possible. The temperature lag has a negative effect at the end of winter though since it takes 60 to 90 days for the soil to begin to warm again. The cooling months of June through August in Bozeman, days

150-250, have soil temperatures around 50°F, and would provide excellent cooling during the day.

Bozeman, Montana is a heating dominated climate. An EAHX behaves differently in a cooling dominated climate such as Athens, Georgia (2762 CDDs, 1789 HHDs). Figure 250 and Figure 251 are the soil temperatures for Athens. The two figures show the same temperature trends as Bozeman, just with a higher yearly average surface temperature and fluctuation amplitude. Athens in July and August (days 182-243) have higher soil temperatures around 70 °F at eight feet, but this is still lower than the average atmospheric temperature during this time of 80°F [13]. The short heating season in Athens would see considerable energy savings though since the soil has hardly cooled. In January at eight feet, the soil is still around 65 °F and the average design temperature is 44°F [13].

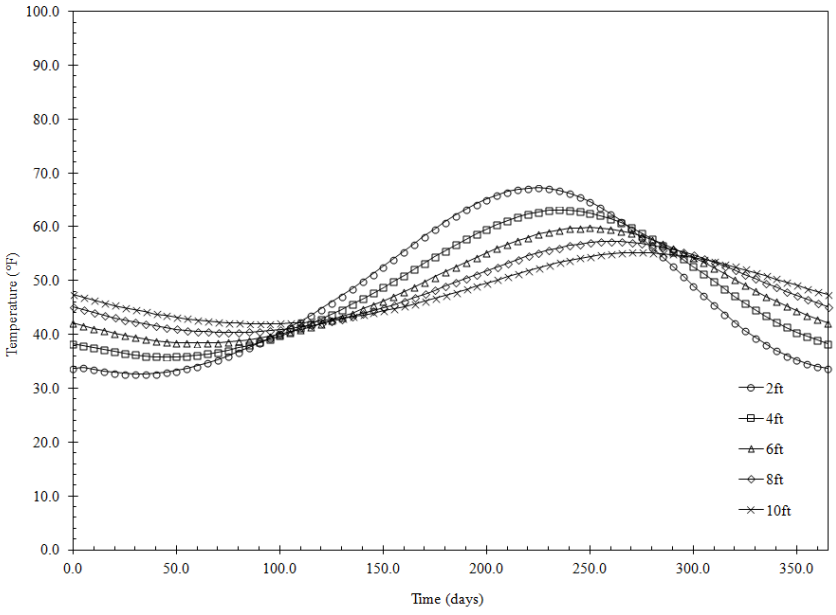


Figure 69: Bozeman, Montana – simulated Green's Function soil temperatures at various depths– observed surface soil temperature boundary condition

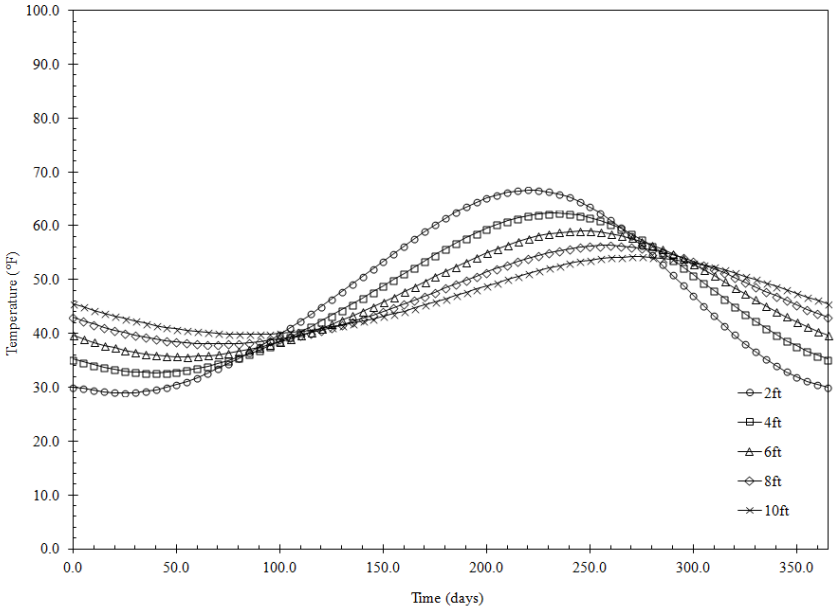


Figure 70: Bozeman, Montana – simulated Green's Function soil temperatures at various depths – corrected TMY surface air temperature boundary condition

Soil Diffusivity Effects

All soil simulations to this point use an assumed diffusivity of 0.6 ft^2/day. Soils are known to have a much larger range though. Table 1 and Table 2 list soil properties which range from 0.26 to 1.5 ft^2/day. The strong correlation between the NRCS observed and simulated soil temperatures show higher diffusivities are not as common near the surface. The references for the above tables are meant for vertical geothermal ground loops and are not necessarily surface soil values. Table 1 is more representative of near surface soils, and has a diffusivity range from about 0.30 and 0.75 ft^2/day. Figure 71 examines the effect these two diffusivity extremes have on the previous soil simulation for Bozeman, Montana at 6ft (72 inch) depth. The fluctuation amplitude is lower for the smaller diffusivity since it limits heat flow through the soil. This also results in a higher mean annual temperature. The temperature lag is also around 25 to 50 days more than

the higher diffusivity limit. This means it takes another 25 to 50 days for temperatures to start increasing from the warmer surface, and the same time to start decreasing from cooler surface temperatures. It is possible to calibrate soil models with this information if the predicted values do not match the observed, but is not needed in previous simulations.

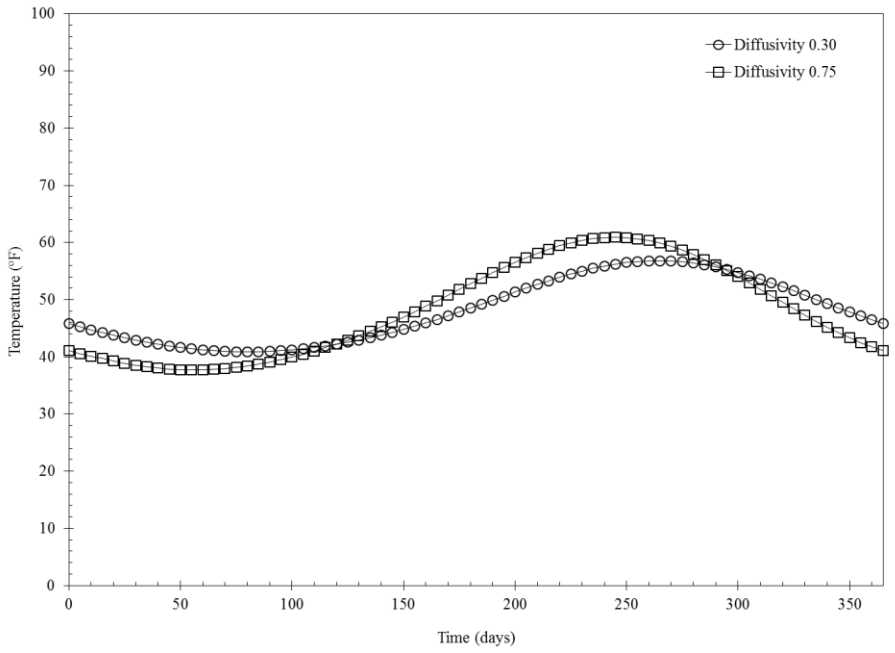


Figure 71: Soil temperatures using diffusivity extremes for Bozeman at 6 feet (72 inches)

Soil Simulation at REHAU®
Montana Ecosmart House Project

The experimental data from the REHAU® Montana Ecosmart House Project includes soil temperature data from the surface to six feet in two foot increments. This provides another means to verify the GF soil temperature simulation with on-site data. Figure 25 in the EXPERIMENTAL DATA chapter displays the soil temperatures from the RMEH. The surface temperature values in this figure are repeated in Figure 72.

Since data for half the year is missing, the NRCS soil surface temperatures from Bozeman, Montana fill in the gaps. This makes it possible to fit a Fourier series to the data for an annual soil temperature simulation. The result is a surface temperature and LSR fit shown in Figure 73.

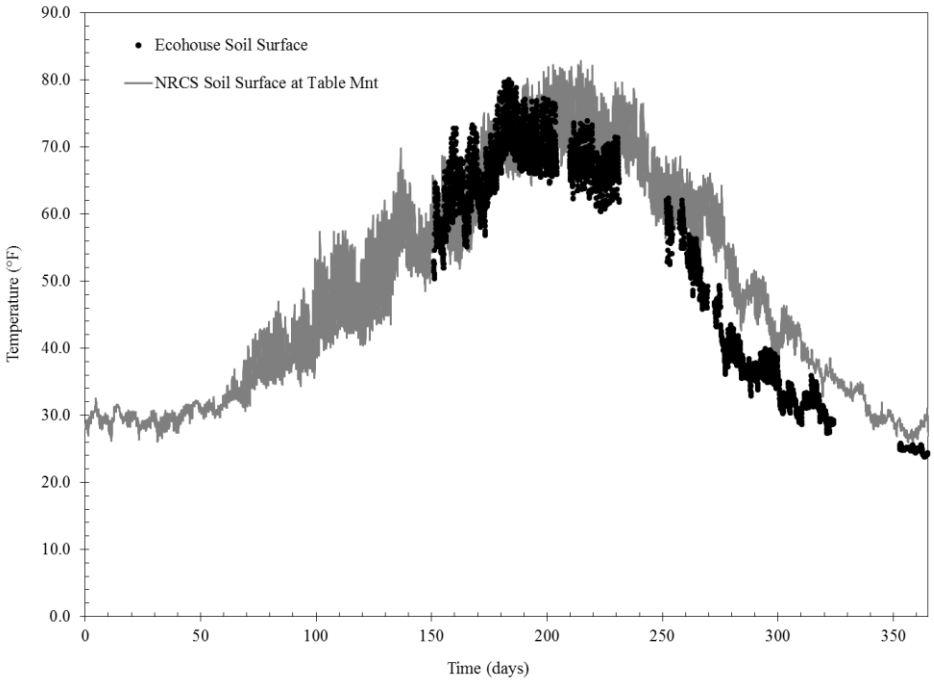


Figure 72: REHAU® Montana Ecosmart House Project observed surface soil temperature, missing data made up with NRCS soil temperature data

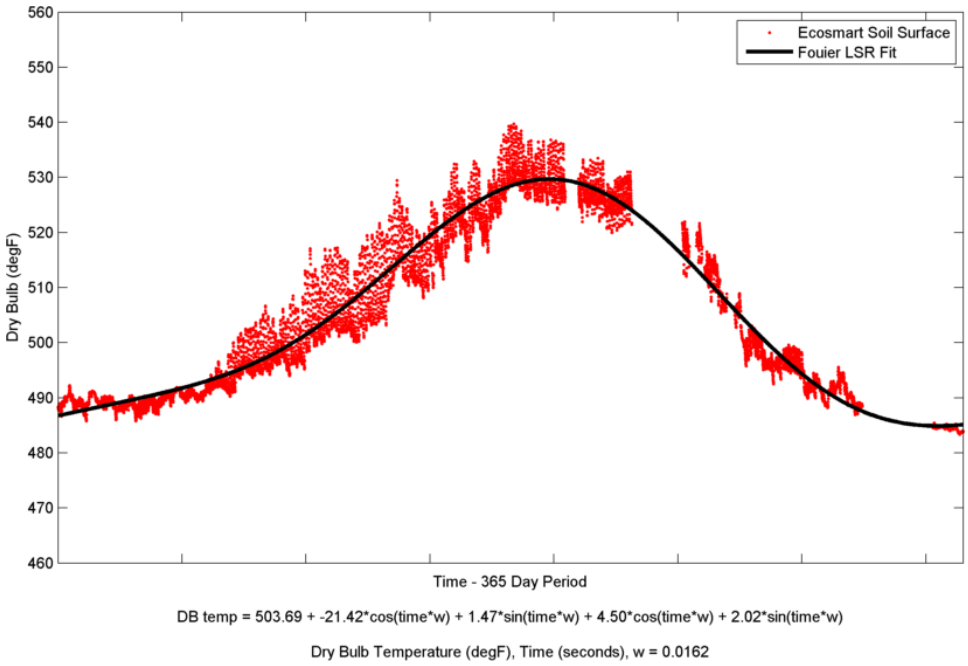


Figure 73: Surface soil temperatures and least-squares regression fit with a Fourier series at the REHAU® Montana Ecosmart House Project

The results from the RMEH soil temperature simulation in Figure 74 show the simulation values are several degrees lower the observed values. This figure is at a four foot depth. The other depths have similar results where the simulation is consistently lower than the observed. One source for this error could be the soil diffusivity. These temperature sensors are located in an irrigated area which could increase soil diffusivity through the increased moisture content. Figure 75 completes the same simulation with four different diffusivities covering a range from 0.30 to 0.75 ft^2/day. None of the new simulations match both the summer and winter soil temperatures. This suggests the soil diffusivity is not the problem. The lower soil temperatures at all simulation depths suggests the NRCS data that filled in the first half of the year's soil surface temperatures is too low in temperature. The actual surface temperature during this time at the RMEH

was likely higher; especially in the first few months. The surface temperatures from this time take several months to reach depths of four and six feet due to the temperature lag. Higher surface temperatures in the first few months translate to higher temperatures at the four foot depth in the summer months.

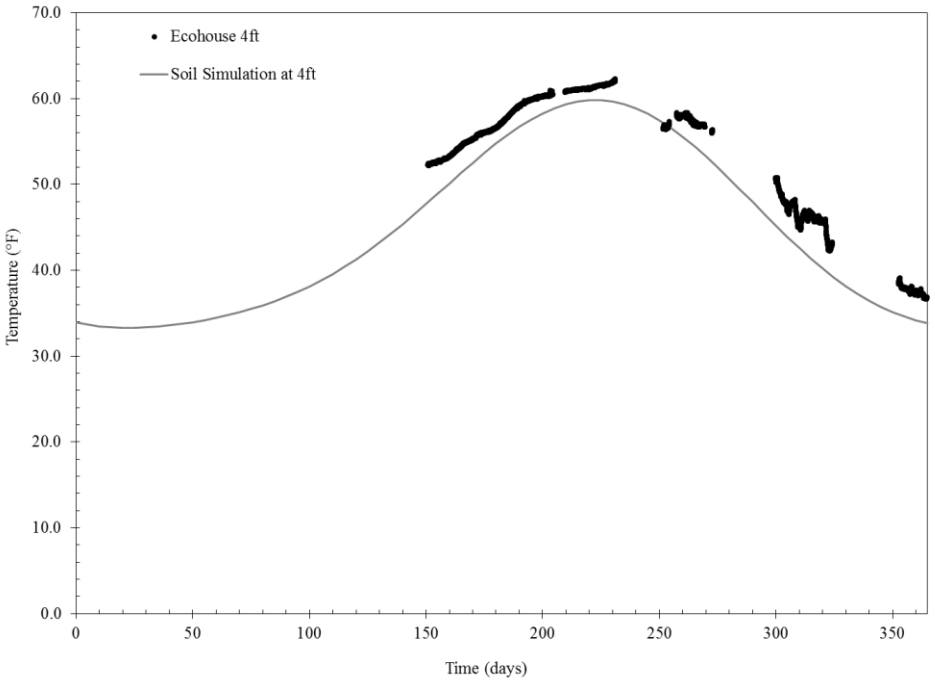


Figure 74: Observed vs. simulated soil temperatures at 4ft depth for the REHAU® Montana Ecosmart House project using the Ecohouse surface temperature BC

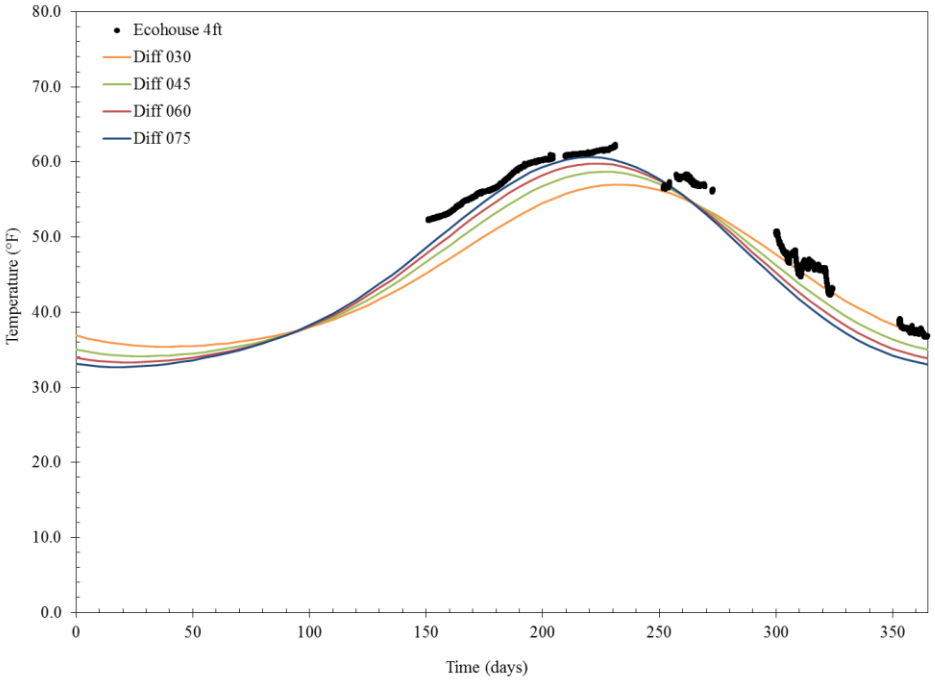


Figure 75: Diffusivity calibration for the REHAU® Montana Ecosmart House soil simulations at 4ft depth

Soil Temperature Simulation Using a Surface Flux

The previous sections demonstrate the feasibility of simulating soil temperatures using a time-dependent temperature boundary condition (BC). A surface temperature BC is not always a possible choice though when simulating an EAHX system. In particular, the slab in the under slab (US) EAHX is more accurately represented as a flux type boundary for most situations. Slab temperatures, or soil temperatures just below a slab, are difficult to predict since slab heat loss is dependent on indoor temperature, slab construction, slab dimensions, outdoor temperature, and other factors. The only time this is not true is for a radiant heating/cooling slab which is assumed to be at a constant temperature. Since the slab loses heat to the soil surface, any simulation to find the

temperature distribution below a slab must also include the soil surface to act as a heat source/sink. This becomes a problem for the Green's Function (GFs) method due to the orthogonal boundary condition requirement.

The most practical way to model the slab to soil thermal interaction is with the slab as a heat flux boundary and the soil as a temperature boundary. Recall though that GFs must have orthogonal BCs. In other words, any one boundary must have the same type of boundary condition. This BC can change with both space and time, but it must of one type. The only choices than are modeling both the slab and the soil surface as a temperature or flux boundary. As already stated, modeling a foundation slab as a temperature is not accurate in most situations, unless it is a radiant slab. To cover design situations other than radiant slabs, a method by Wang and Bras [78] is introduced to estimate a soil surface flux from the previously established soil surface and air temperatures. The remainder of this chapter establishes a feasible method of representing the soil surface as a time-dependent heat flux function for use in simulating below foundation slab temperature distributions.

Soil Heat Flux Estimated from Surface Soil Temperature

The method by Wang and Bras uses soil surface temperatures and soil properties to estimate a corresponding surface heat flux. The authors' purpose was to develop a simple method to replace more complex algorithms and expensive testing equipment that are prone to errors. While originally meant for use on a daily time scale, it is applied on an annual basis here which presents several challenges. The following section covers the

basics of this method, but does not go into detailed derivations. For a more detailed treatment, please see Wang and Bras article in the Journal of Hydrology [78].

Wang and Bras solve Fourier's heat equation, Equation (24), using a field of mathematics known as fractional calculus. Before moving onto the formulation, a brief introduction to fractional calculus is helpful. Fractional calculus investigates taking the differential operator, d/dx, to the power of real and complex numbers. For example, the primary relationship in this formulation is Equation (64). The function "f(t)" is differentiated with respect to "t" where the differential is to the power of some value "β" that is between 0 and 1. The result is the integration of the function with respect to the dummy variable "s" multiplied by the gamma function. This is just one example where "β" is a fractional real number. It could also be an integer or complex number. A more detailed description of fractional calculus is beyond the scope of this work except for a few relationships required to describe the soil heat flux estimation formulations [78, 79].

$$\frac{d^{\beta} f(t)}{dt^{\beta}} = \frac{1}{\Gamma(1-\beta)} \frac{d}{dt} \int_0^t \frac{f(s)}{(t-s)^{\beta}} ds \tag{64}$$

The boundary conditions for this differential equation include the deep soil at some temperature "T_0", and a function "f(t)" describing the surface temperature with time. The initial condition (IC) is a uniform temperature throughout the domain at the same deep soil temperature "T_0". Through several mathematical operations the authors develop Equation (65) where "G(t)" is the soil heat flux, "T_s(s)" is the soil surface temperature function, and "t" is the time from some starting point. Important to note is that the time derivative from Equation (64) was moved inside the integral in Equation

(65). This is an important simplification for this derivation, and is only possible by having zero heat flux on the soil surface at the start of the integration (time zero). The only time there is zero heat flux at the surface boundary is when the surface temperature is equal to the uniform initial condition temperature. This implies the starting time is not arbitrary and must be chosen at a specific time of the year. The choice of starting time on an annual basis is the first time in the year when the surface temperature is equal to the mean annual surface temperature. From previous literature and models, it is well established the mean annual soil surface temperature is representative of the deep soil temperature. The deep soil temperature is also equal to the uniform IC. This implies Equation (65) requires a time shift in the surface temperature function so that the temperature at time zero is equal to the IC.

$$G(t) = \sqrt{\frac{k_{soil}\rho_{soil}C_{p,soil}}{\pi}}\int_0^t \frac{dT_s(s)}{\sqrt{t-s}}ds \tag{65}$$

Shifting Surface Temperatures for Zero Initial Flux Previous sections have already shown a four term Fourier series can represent the soil surface and air temperature for any location (see Figure 189 through Figure 218 in APPENDIX B). The surface temperature function "$T_s(s)$" in Equation (65) uses these previously established Fourier series. The form of the Fourier series is shown in Equation (46) and repeated below in Equation (66) for convenience with "t" replaced with the dummy variable "s". Before performing the integration, recall the function's starting time is shifted to a time

when the surface temperature is equal to the mean annual surface temperature (also the initial condition).

The following study accomplishes this by programmatically calculating values of the surface function starting at time zero until a time when the function equals the mean annual surface temperature. This time then becomes time zero. The soil surface or air temperature data is then re-arranged to start at this time, and the data from January 1st to the new time zero is appended to the shifted data. A new Fourier series is fit to the shifted data and is the "$T_s(s)$" in Equation (65). For example, see the shifted temperature data in Figure 76 for Bozeman, Montana. The original data that starts on January 1st is shown in Figure 195 of APPENDIX B for comparison. The annual soil surface temperature in Bozeman is 48.2 ºF. This temperature occurs on Julian day 119 or April 29th. The data is then shifted so this day is the new time zero, and a new Fourier series is fitted to that data. This satisfies the BC requirement for Equation (65).

$$T_g(s) = a_0 + a_1 \cos(s\omega) + b_1 \sin(s\omega) + a_2 \cos(2s\omega) + b_2 \sin(2s\omega) \qquad (66)$$

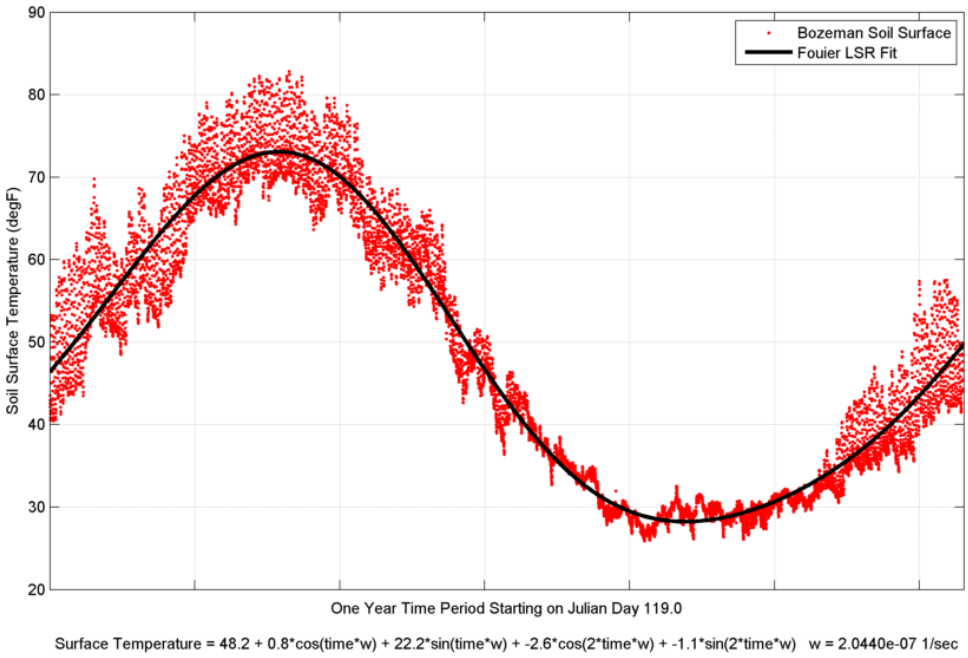


Figure 76: Bozeman, Montana – Least squares curve fit to shifted soil temperature shifted forward 119 days using four term Fourier series

Building a Surface Flux Function The appropriately shifted Fourier series is next differentiated in Equation (65). The resulting integral is a differentiated Fourier series divided by the square root of the integration variable. No explicit representation for this integral was found in integration tables or by mathematical programs. This leaves numeric integration. The end goal of this process is to develop a function to describe the soil surface as a heat flux. Since an explicit relationship for this function cannot be found due to the complex integral, a function is built instead. Numeric integration determines the heat flux every 10 days for two years. The result is a sinusoidal surface flux that is fit with another Fourier series. This final Fourier series is the surface flux function for use in the GF solution method. This process created Figure 77 which uses the surface temperature function from Figure 76. Note that the function extends over two years and

started at Julian date 119 or April 29th. For surface flux functions for all 15 locations based on the NRCS soil surface temperatures, see Figure 219 through Figure 233 in APPENDIX C. This step completes the process of estimating an annual soil surface flux function from the soil surface temperatures for the GF method.

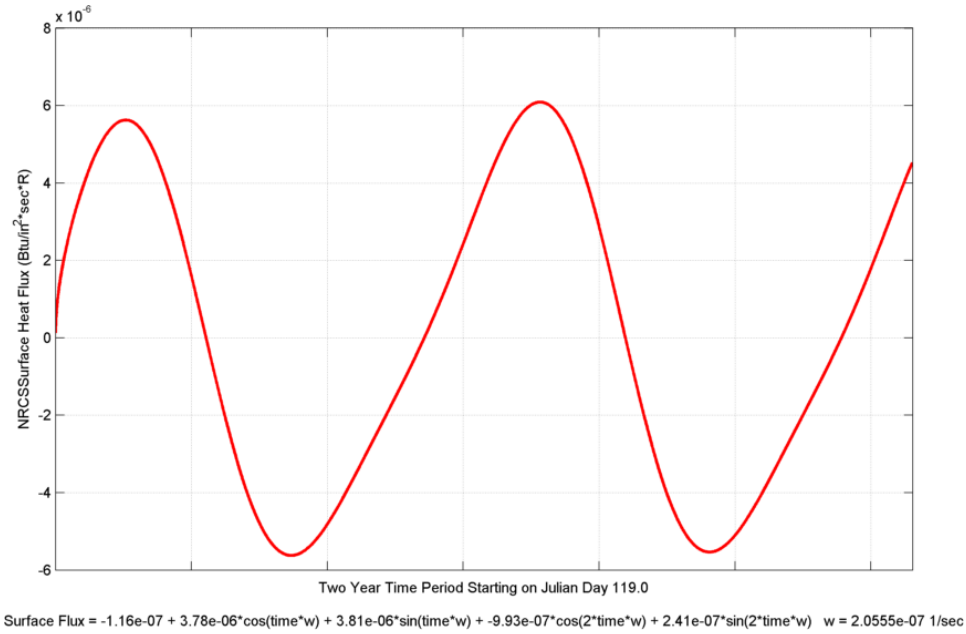


Figure 77: Bozeman, Montana – estimated soil surface heat flux function using the NRCS soil surface temperatures over a two year period starting on Julian day 119

Green's Function Formulation for
Surface Flux Boundary Condition

The GFs problem type for a surface boundary flux into a semi-infinite medium is a Y20B-T1. This has a similar problem setup as shown in Figure 55 except that the surface temperature function is now a surface flux function. The Green's Function Solution Equation (GFSE) in Equation (41) is reduced to Equation (67) where Equation (68) is the G_{Y20} GF for a semi-infinite medium with surface heat flux. Other variables in Equation (67) include the surface flux function "$q''(\tau)$" which is a Fourier series in the

form of Equation (66), and the mean annual surface temperature "T_m" which acts as the initial condition. Since the initial condition is a constant, it is removed from the space integration of the G_{Y20} GF. The space integration of G_{Y20} from zero to infinity with respect to the dummy space variable is equal to one. This simplifies Equation (67) down to Equation (69) which is the final form for numeric integration.

$$T(y,t) = \int_{y'=0}^{\infty} T_m G_{Y20}(y,t|y',0)dy' + \frac{\alpha}{k_s}\int_{\tau=0}^{t} q''(\tau)G_{Y20}(y,t|y',\tau)d\tau \quad (67)$$

$$G_{Y20}(y,t|y',\tau) = \frac{1}{[4\pi\alpha(t-\tau)]^{\frac{1}{2}}}\left\{exp\left[\frac{-(y-y')^2}{4\alpha(t-\tau)}\right] + exp\left[\frac{-(y+y')^2}{4\alpha(t-\tau)}\right]\right\} \quad (68)$$

$$T(y,t) = T_m + \frac{\alpha}{k_s}\int_{\tau=0}^{t} q''(\tau)G_{Y20}(y,t|y',\tau)d\tau \quad (69)$$

Base Solution Optimization of Surface Flux The surface flux optimization for the Base Solution Generation technique follows the same procedure outlined previously with the surface temperature boundary. The optimization process for this simulation is not repeated since the simulations are almost identical. The previous results for integration step size and data block size both apply for this simulation type. The only difference between the two is in the time refinement. The GF values in the previous constant surface temperature (G_{Y10} problem type) quickly approached zero as the time range increases as seen in Figure 48. For a surface flux (G_{Y20} problem type), the extended time GF values remain relatively constant as seen in Figure 78. Figure 78 indicates all numeric integration values are relevant for a surface flux BC. This intuitively makes

sense as well. If a heat flux is constantly applied to one side of an insulated domain, that domain's temperature is continually increases due to the flux for all times. The lack of a time refinement option will increase computation times in the BSG method due to longer numeric integration time frames.

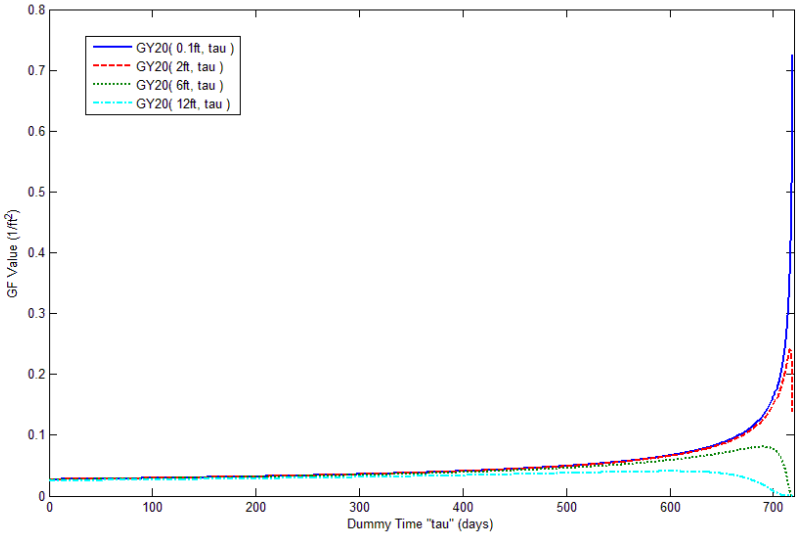


Figure 78: Green's Function values for a semi-infinite medium with surface heat flux, problem type GY20

Soil Heat Flux Simulation Results

The fidelity of simulating soil temperatures using the above estimated surface heat flux functions was evaluated at 20 and 40 inch depths over a 365 day period at all 15 locations of interest. This validation is similar to the previous surface temperature BC validation. The flux functions were estimated from both the soil surface and air temperatures from the NRCS and TMY data files respectively. This was done to determine if air temperatures are a feasible replacement to soil surface temperatures. Soil properties for the simulations were a thermal diffusivity of 0.6 ft^2/day, and a thermal

conductivity of 0.75 Btu/hr·ft·ºF. The purpose of this validation is to ensure the flux functions are an accurate representation of soil surface heat transfer.

The simulations produced mixed results as shown in Figure 324 through Figure 338 in APPENDIX D for all 15 locations at the 40 inch depth. This section discusses examples for the 20 inch depth. Other 20 inch depth figures are not included since they follow similar trends to the 40 inch depths. Some locations, particularly those with a high number of heating degree days, fit the experimental data very well. For example, see Figure 79 for Amarillo, Texas where the NCRS and TMY flux fits produce good agreement with experimental data. Other locations such as Pine Bluff, Arkansas in Figure 80 are not as accurate. The NRCS soil temperature data in this case is follows the correct trend, but is out of phase. The TMY heat flux function though is not accurate at all. There are several other locations, including Columbus, Ohio, Las Vegas, Nevada, and St. Cloud Minnesota to name a few also display a poor fit with the TMY flux function. The poor results are not solely due to poor input data, but the flux function creation process.

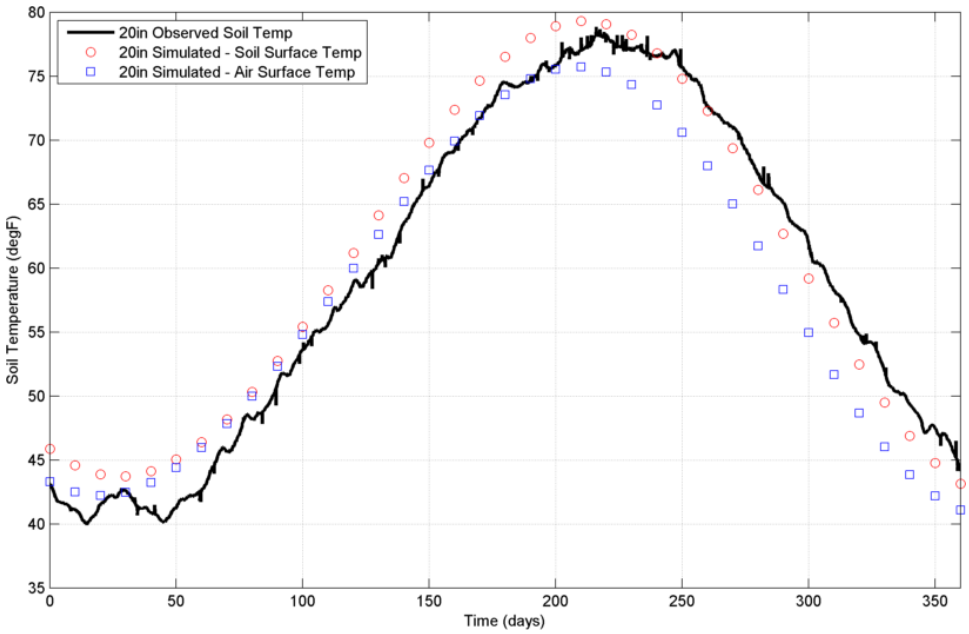


Figure 79: Amarillo, Texas – 20 inch observed vs. simulated soil temperatures using the surface flux boundary condition derived from both soil surface and air surface temperatures

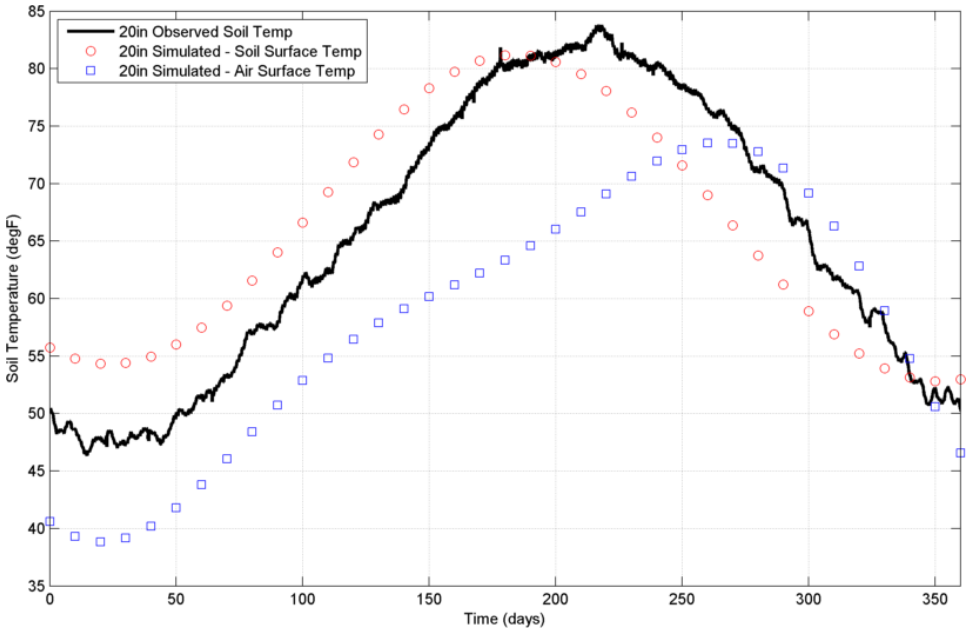


Figure 80: Pine Bluff, Arkansas – 20 inch observed vs. simulated soil temperatures using the surface flux boundary condition derived from both soil surface and air surface temperatures

Deriving the flux function uses three separate four term Fourier series least-squares regression curve fits. In most cases, the four term Fourier series is far more than is needed to have a good fit. This research uses the four term series because some TMY data files require the extra two terms to fit irregularities in the data. The computerized curve fits is the mechanism that introduces error in the TMY flux functions. Take the shifted temperature curve fit for Columbus, Ohio in Figure 81 for example. Notice how the curve fit ends at a higher temperature than it started at, and the steep slope of the line shows no sign of leveling back out to lower temperatures. Behavior like this causes the errors in the TMY flux functions. It is most pronounced in the Columbus, Ohio case. If this function is extended beyond 365 days, the temperature increases to unrealistic levels. Increasing the number of terms in the Fourier series will not change this outcome since it is due to the trend in the data. The effects beyond 365 days are easy to see in Figure 82 which displays the flux function resulting from this temperature fit.

The non-uniform start and end of the TMY data is due to the data files being 20 year averages of temperatures. This mismatch in the start and end of the data files is seen in other locations as well. In addition to these errors, the TMY surface flux functions did not in general yield acceptable results in the soil temperature simulations. The NRCS flux functions were not excellent in all locations, but will work for the purpose of provided a heat source/sink for the under foundation temperature simulation. The 2-D US simulations in the next chapter will only make use of the NRCS flux functions.

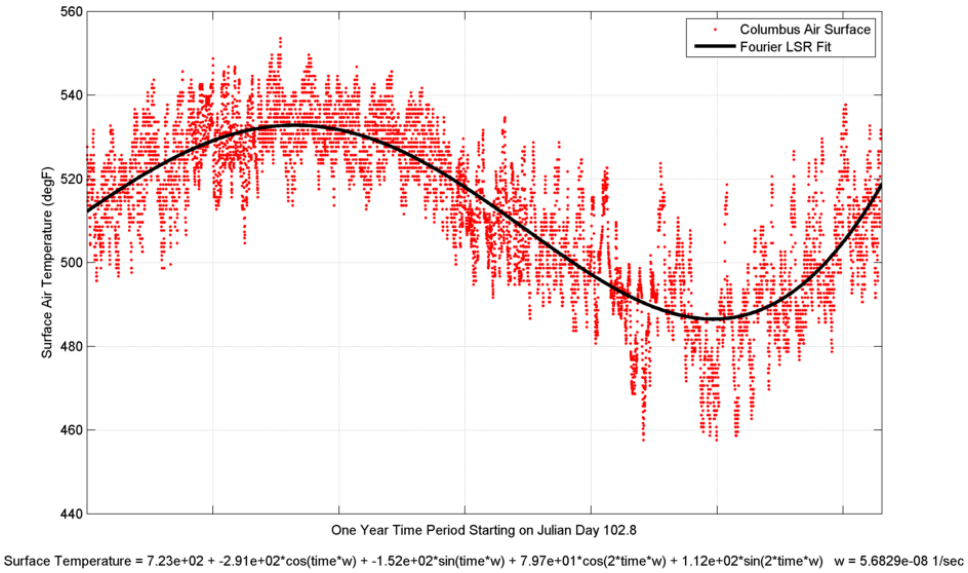


Figure 81: Columbus, Ohio – Least squares curve fit to shifted soil temperature shifted forward 102.8 days using four term Fourier series

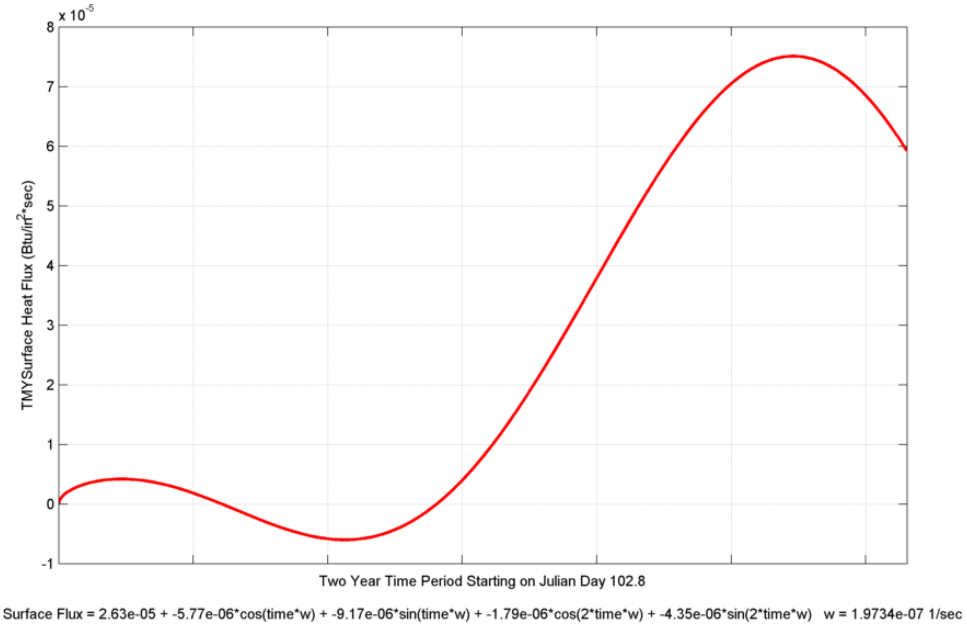


Figure 82: Columbus, Ohio – estimated soil surface heat flux function using the NRCS soil surface temperatures over a two year period starting on Julian day 102.8

SOIL TEMPERATURES BELOW AN ON-GRADE SLAB

The previous chapter reviewed the Green's Function (GF) method for simulating soil temperatures at any time of the year based on surface temperatures or estimated fluxes. This information is essential to the under yard (UY) simulation and will act as the initial condition (IC) in future EAHX simulations. This IC creates a much more realistic temperature domain for the transient conduction solution. The under slab (US) simulation requires a similar initial soil temperature distribution, but calculating that distribution is complicated by several factors. Heat loss/gain from a basement slab or basement walls flows toward the outdoor soil surface. Figure 83 from the 2009 ASHRAE Fundamentals is a good representation of the paths heat takes as it flows from the foundation to the surface. This implies an under slab soil temperature simulation must include the soil surface as well, and a 3-D transient conduction simulation to account for all possible heat paths to the surface.

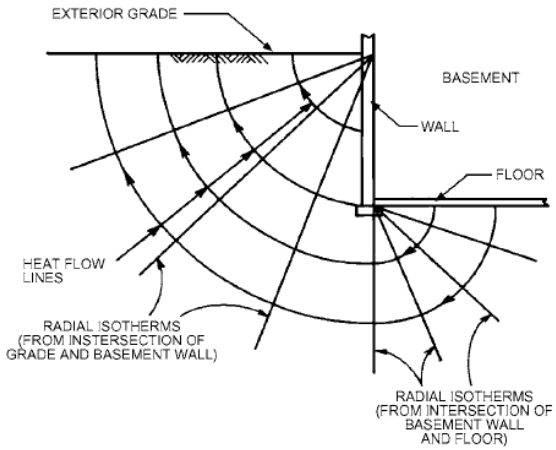


Figure 83: Heat flow paths from a below grade surface – courtesy of the 2009 ASHRAE Fundamentals, Chapter 18 Non-Residential Cooling and Heating Load Calculations [80]

This research reduces the transient heat conduction to a 2-D domain for simplicity. Literature on slab heat loss agrees the problem is 3-D, but many studies successfully simplify the domain to two dimensions [54, 56, 57, 63, 65]. This simplified domain is appropriate for the current purpose of calculating an initial condition. A heat loss (flux) boundary best models a non-radiant slab while a constant temperature boundary suits a radiant heating/cooling slab. The following formulation considers both slab types for slab-on-grade foundations to cover all building types. The limitation to slab-on-grade foundations is due to Green's Functions (GF) requiring orthogonal boundary conditions (BCs). Galerkin based GFs are one option for non-orthogonal BCs, but is not investigated in this research. The following chapter discusses the 2-D GF solution, its application to non-radiant and radiant slabs, calculation of an appropriate slab heat loss function, and how these results are translated to the US EAHX simulations.

Under Slab Green's Function Solution Formulation

The domain for the US soil temperatures distribution is a 2-D semi-infinite solid pictured in Figure 84. It is a semi-infinite solid in the y-direction, and an infinite solid along the x-direction. The foundation slab is centered at the origin, and the surface soil extends from the slab edge to an infinite distance. The distance between the y-axis and the foundation edge is half the slab length. Notice the slab and soil surface are either modeled as a time-dependent temperature (BC 1st kind) or a heat flux (BC 2^{nd} kind). The BC type must be consistent across the entire boundary. In other words, if the slab is a heat flux BC, then the soil surface must also be a heat flux BC. The time-dependent

functions split the surface into three sections. Each section acts as an independent boundary condition in the Green's Function solution equation (GFSE). Contributions from each BC are compensated across the whole domain by space integration along the x-direction. The domain is also symmetrical across the y-axis. This symmetry plane reduces the number of calculations later on in the numerical integration.

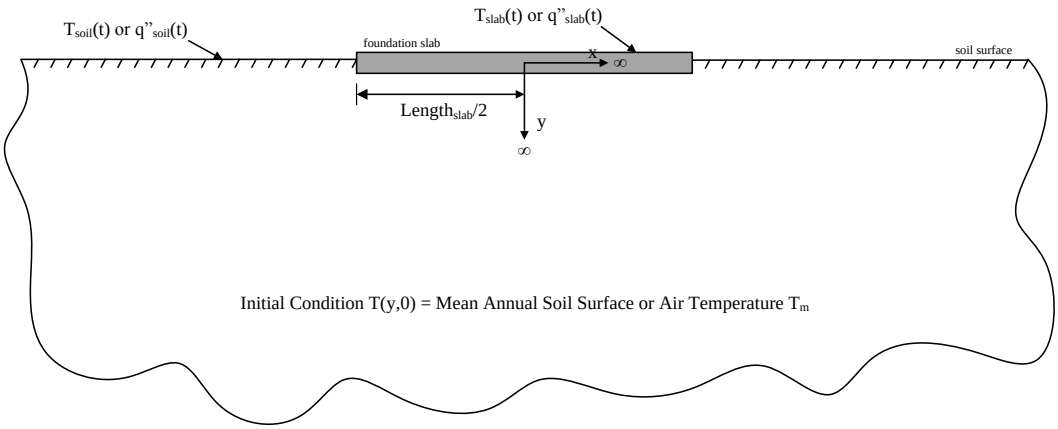


Figure 84: Two-dimensional domain for under slab Green's Function soil formulation

Surface Flux
Boundary for Non-Radiant Slabs

The surface flux (BC 2nd kind) is appropriate for EAHX installed under non-radiant foundation slabs. A temperature BC is not a feasible option for this foundation type since common foundations include an assembly of concrete, insulation, vapor barriers, and gravel. Prediction of the soil surface temperature through these layers is difficult. That is why literature commonly models heat flow out of basement as an averaged heat rate for use in load calculations. The GF problem type designation for this setup is X00Y20B-x5T1. This designates a two dimensional GF with no boundary in the x-direction, a semi-infinite boundary in the y-direction, an arbitrary time boundary

condition with step-wise changes in the space x-coordinate, and a constant initial condition. From this designation, the Green's Function solution equation (GFSE) can systematically be written into Equation (70) through Equation (74). The GFs are left in their symbolic form to keep the solution compact, but see Equation (68) in the previous chapter for the G_{Y20} GF and Equation (43) for the G_{X00} GF in the EARTH-AIR HEAT EXCHANGER SIMULATION USING GREEN'S FUNCTIONS chapter.

$$T(x,y,t) = T_{IC} + T_{NegSoil} + T_{PosSoil} + T_{Slab} \tag{70}$$

$$T_{IC} = \int_{y'=0}^{\infty}\int_{x'=-\infty}^{\infty} T_0 G_{X00}(x,t|x',0)G_{Y20}(y,t|y',0)dx'dy' \tag{71}$$

$$T_{NegSoil} = \frac{\alpha}{k_s}\int_{\tau=0}^{t}\int_{x'=-\infty}^{-L_{slab}/2} q''_{soil}(\tau)G_{X00}(x,t|x',\tau)G_{Y20}(y,t|0,\tau)dx'd\tau \tag{72}$$

$$T_{PosSoil} = \frac{\alpha}{k_s}\int_{\tau=0}^{t}\int_{x'=L_{slab}/2}^{\infty} q''_{soil}(\tau)G_{X00}(x,t|x',\tau)G_{Y20}(y,t|0,\tau)\,dx'd\tau \tag{73}$$

$$T_{Slab} = \frac{\alpha}{k_s}\int_{\tau=0}^{t}\int_{x'=-L_{slab}/2}^{L_{slab}/2} q''_{slab}(\tau)G_{X00}(x,t|x',\tau)G_{Y20}(y,t|0,\tau)\,dx'd\tau \tag{74}$$

Equation (70) breaks the solution into four temperature distributions that add to produce the final result. The first distribution results from the IC contribution. The IC is the same mean annual surface temperature as in the previous UY soil temperature simulations. It can be pulled out of the integrations since it is a constant. Solving the initial condition requires two space integrations, which are found in the GF table by Beck et al. [72] and are quite simple. The integrations in each direction are equal to one as

seen in Equation (75) and Equation (76), and only the constant "T_0" is left for the IC contribution. The other three BC contributions are split by the step-wise space integration in the x-direction. The first integration in Equation (72) is for the soil surface on the negative side of the x-axis. Notice the limits of the space integration are from negative infinity to the foundation slab edge. The positive soil contribution in Equation (73) has similar limits. Equation (74) is the contribution across the slab as seen in its limits of integration. The space integration limits the contribution of any one boundary condition across the space domain. Some interesting results fall out of the space integration and are worth a closer examination.

$$\int_{x'=-\infty}^{\infty} G_{X00}(x,t|x',\tau)dx' = 1 \tag{75}$$

$$\int_{y=0}^{\infty} G_{Y20}(y,t|y',\tau)dy = 1 \tag{76}$$

Space Integration of an Infinite Medium

This section briefly covers the space integration of an infinite medium. For more information on applying space variable BCs to the GFSE, see the earlier discussion in the EARTH-AIR HEAT EXCHANGER SIMULATION USING GREEN'S FUNCTIONS chapter. The three previously mentioned space integrations can be isolated from the time integration since the G_{Y20} GF and the boundary function, q''(τ) or T(τ), are not functions of the x-direction dummy space variable. The integrations are then performed separately, but must still be included inside the time integral since they are still a function of the dummy time. These integrals have exact solutions as seen in Equation (77) through

Equation (79). This considerably simplifies Equation (72) through Equation (74) and leaves only the time integrals. The time integration now has three expressions multiplied together that are all functions of the dummy time. Exact integration of this product is not trivial, and requires numeric integration.

$$\int_{x'=-\infty}^{-L_{slab}/2} G_{X00}(x,t|x',\tau)dx' = \frac{1}{2} erfc\left[\frac{x + {L_{slab}}/{2}}{[4\alpha(t-\tau)]^{1/2}}\right] \tag{77}$$

$$\int_{x'=L_{slab}/2}^{\infty} G_{X00}(x,t|x',\tau)dx' = 1 - \frac{1}{2} erfc\left[\frac{x - {L_{slab}}/{2}}{[4\alpha(t-\tau)]^{1/2}}\right] \tag{78}$$

$$\int_{x'=-L_{slab}/2}^{L_{slab}/2} G_{X00}(x,t|x',\tau)dx' = \frac{1}{2}\left\{erfc\left[\frac{x - L_{slab}/2}{[4\alpha(t-\tau)]^{1/2}}\right] - erfc\left[\frac{x + L_{slab}/2}{[4\alpha(t-\tau)]^{1/2}}\right]\right\} \tag{79}$$

One way to picture the above three integrations is as "contribution multipliers" that influence the BCs contribution at a given x-location. This is true since they are the only part of the equations that contain the x-direction space variable. These "contribution multipliers" have an interesting result when graphed with respect to the x-coordinate in Figure 85. Figure 85 is the value of the three above equations as the x-coordinate changes from -20ft to 20ft for a 20 foot slab. In other words, the slab extends for 10 feet on either side of the origin which leave 10 feet of soil surface on either side. The time in the denominator of all three equations is set to 180 days. The negative soil function,

Equation (77), and the positive soil function, Equation (78), are at a maximum at the negative and positive end of the domain respectively. They then decrease as the move away from their limits of integration. Mathematically, this translates to the minimization of the temperature distributions from those boundary conditions as the current x-location of interest moves away from that boundary. The slab function, Equation (79), has the same behavior of decreasing in value as the x-coordinate moves past the foundation edges. The interesting part is at any x-location, the three functions sum to one. This is why they are termed "contribution multipliers" since they determine the temperature distribution contribution across the x-coordinate.

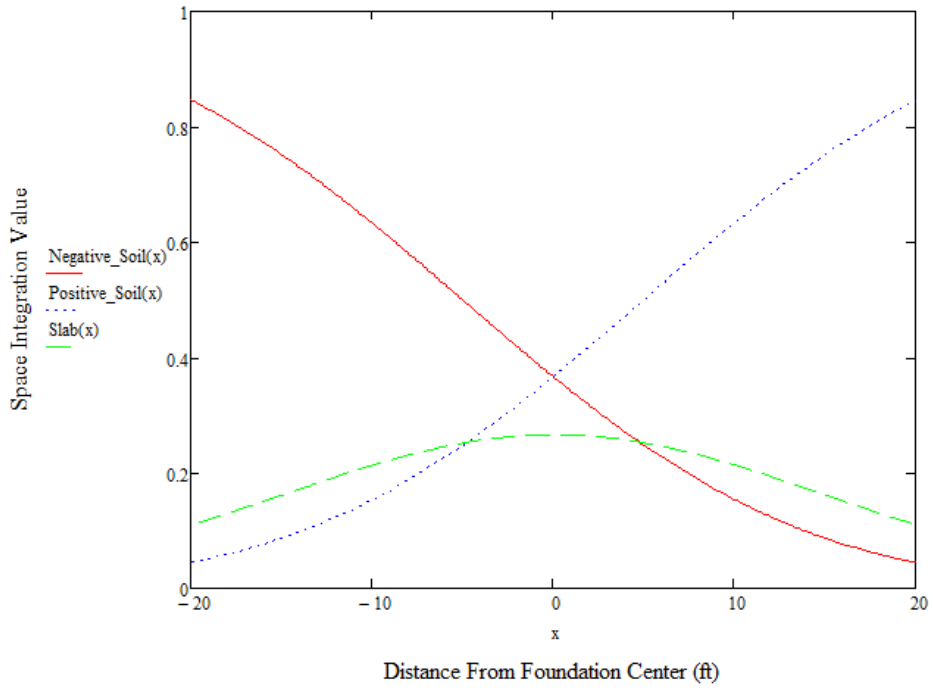


Figure 85: Value of the space integration functions for ±20 feet from foundation center, slab is 20 feet in length

Surface Temperature
Boundary for Radiant Slabs

Radiant slabs hold nearly a constant temperature during the heating and cooling seasons. The constant temperature makes it possible to assume the bottom of the foundation slab is also at this temperature. Realistically, the radiant slab is changing temperature to meet room requirements and to stay above the air's dew point. An assumed constant value is sufficient though for this soil temperature simulation. A similar study by Lachenbruch also uses GFs in a 3-D foundation heat loss simulation for radiant floors and assumes the constant temperature BCs [60]. The formulation for the temperature BCs is very similar to the previous flux surface condition. The problem type is now an X00Y10B-x5T1. Equation (70) is again the general solution for this problem type. The initial condition in this situation reduces to Equation (80) instead of one. Equation (81) through Equation (83) use the same space integration in the x-direction as the previous flux boundary condition. The G_{Y10} derivative is shown in Equation (54) of the EARTH-AIR HEAT EXCHANGER SIMULATION USING GREEN'S FUNCTIONS chapter.

$$T_{IC} = T_0 erf\left\{\frac{y}{[4\alpha t]^{1/2}}\right\} \tag{80}$$

$$T_{NegSoil} = \alpha \int_{\tau=0}^{t} \int_{x'=-\infty}^{-L_{slab}/2} T_{soil}(\tau) G_{X00}(x,t|x',\tau) \left(\left.\frac{\partial G_{Y10}}{\partial y'}\right|_{y'=0}\right) dx' d\tau \tag{81}$$

$$T_{PosSoil} = \alpha \int_{\tau=0}^{t} \int_{x'=L_{slab}/2}^{\infty} T_{soil}(\tau) G_{X00}(x,t|x',\tau) \left(\left.\frac{\partial G_{Y10}}{\partial y'}\right|_{y'=0}\right) dx' d\tau \tag{82}$$

$$T_{Slab} = \alpha \int_{\tau=0}^{t} \int_{x'=-L_{slab}/2}^{L_{slab}/2} T_{slab}(\tau) G_{X00}(x, t|x', \tau) \left(\frac{\partial G_{Y10}}{\partial y'}\bigg|_{y'=0} \right) dx' d\tau \qquad (83)$$

Base Solution Generation Optimization

Simulating soil temperatures below an on-grade foundation is an ideal application for the Base Solution Generation (BSG) technique. The domains of interest are large due to the size of a typical building's footprint. Point by point numeric integration using the trapezoidal rule is computationally intensive for the hundreds of locations needed to create a meaningful temperature distribution. The BSG method on the other hand already has the data saved in an array which is multiplied by a constant BC value. The result is a far lower computational workload and faster result generation. The follow sections optimize the BSG technique for the flux and temperature based BCs to minimize simulation run-time.

Time Refinement for Non-Radiant On-Grade Slabs

This section investigates opportunities to reduce the size of the base solution database for non-radiant slabs. A standard foundation length of 20 feet and a soil diffusivity of 0.6 ft^2/day are assumed. The calculated GF values also include the space integration multiplier for the x-coordinate. Figure 86 analyses the effect depth has on the base solution value. Notice all the data lines are for an x-location of 180 inches. This is 60 inches past the edge of the foundation slab. The soil boundary condition on the negative side of the x-axis is a mirror image of the positive. As expected, the shallower depths have larger base solution contributions as the dummy time nears the end

simulation time. The base solution values at small dummy time values do not go to zero as with the G_{Y10} GF in the previous chapter. They stay relatively constant from approximately zero to 180 days. A similar trend is seen in Figure 87 which investigates x-locations near the surface for Equation (73) and Equation (74). The space integration multipliers were expected to significantly reduce the values in Figure 87, but they are still high enough to include in the numeric integration.

Figure 86 and Figure 87 show a time-refinement is not possible with a flux type BC. Physically, this is a valid conclusion. A heat flux, even though it is time-dependent, continually adds or removes energy from the domain. This energy builds up in the domain over time if it is not removed by another BC. The energy buildup results in continued temperature increase or decrease. The potential for energy buildup is why it is necessary to account for all time points over the time integration interval. Lack of time refinement causes increases in computation storage space, and a higher computational workload to generate the base solutions and higher numeric integration run times. Even with these time increases, the BSG technique is still a faster solution method than point by point numeric integration. The speed of the base solution generation and the base solution integration can always be increased limiting the window of interest under the foundation slab.

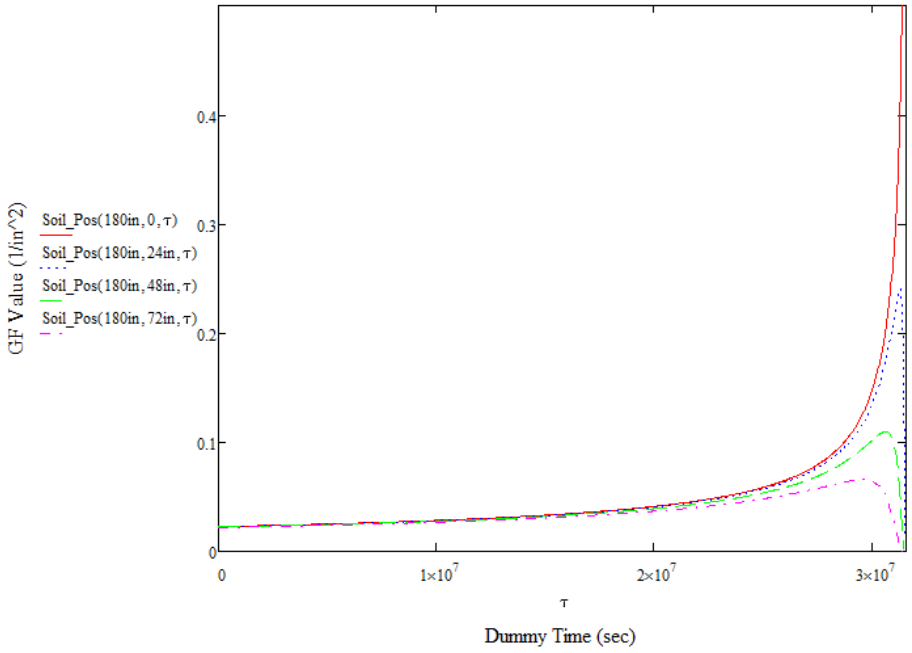


Figure 86: Green's Function values over one year for the flux based solution (G_{Y20}) on the positive soil boundary [Equation (73)], space integration included

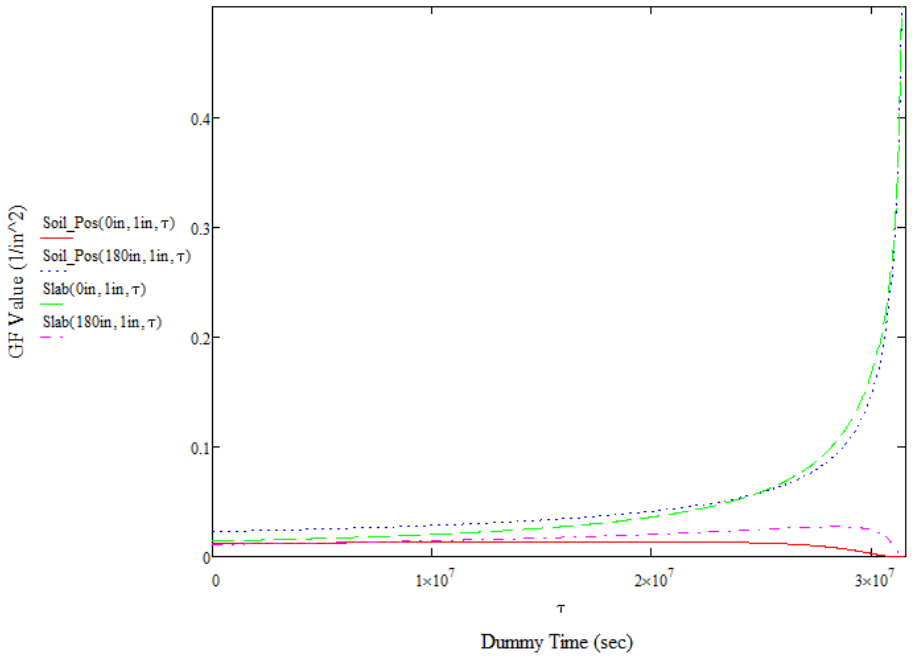


Figure 87: Green's Function values over one year for the flux based boundary (G_{Y20}) on the positive soil boundary [Equation (73)] and foundation slab [Equation (74)], space integration included

Time Refinement for Radiant On-Grade Slabs

Radiant on-grade slab simulations use temperature BCs for the soil surface and foundation slab. These GFs and space integration multiplies do result in small enough base solutions values that time refinement is possible as seen in Figure 88. Dummy time τ values at approximately $2 \cdot 10^7$ seconds, or 230 days, first start to generate base solution values that are large enough to contribute to the final temperature distribution. This implies significant computation storage and time can be achieved by including a time refinement in the BSG technique. Figure 88 suggests a value of 10^{-5} for a GF value cutoff. Note, values similar to the locations in Figure 87 were not included in this discussion since their values were all below 10^{-5} $1/in^2$.

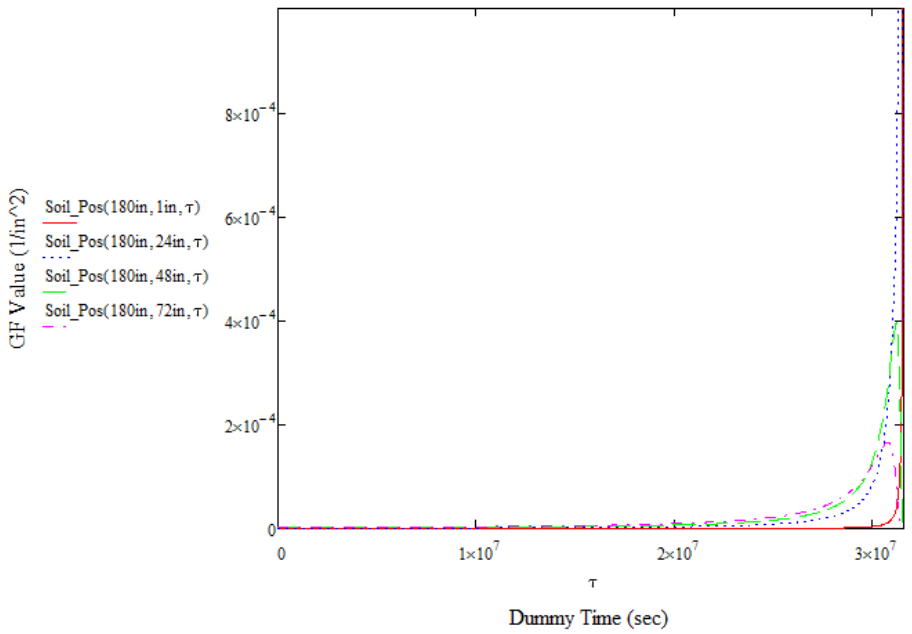


Figure 88: Green's Function values over one year for the temperature based solution (G_{Y10}) on the positive soil boundary [Equation (82)], space integration included

Optimized Base Solution Generation

The BSG optimization follows the same procedure outlined in the SOIL TEMPERATURE SIMULATION chapter. The details of this optimization are not included here, but result in the use of a five minute time step for the numeric integration, and a two day data block for the base solution database. The domain for this optimization was 40 feet by 10 feet with 6 inch spacing which results in an 81 by 20 array, or 1620 data points in the temperature distribution. A 360 day simulation takes approximately 60 seconds using the above parameters and computer described earlier. The foundation slabs are also symmetric along the foundation centerline. A full simulation only requires half the foundation and surrounding soil.

Foundation Heat Loss Boundary Condition

Heat Loss for Non-Radiant Slabs

The only information missing from the above formulation is a time-dependent function describing the heat loss from the foundation slab. A non-radiant slab requires a heat flux boundary as already discussed. There are several methods to determine this heat loss with varying levels of complexity and accuracy. The Hagentoft method balances both. The Hagentoft method produces a periodic function of foundation heat loss that is dependent on outdoor temperature and foundation construction. Following is a brief description of the method developed by Hagentoft for slab-on-grade foundations. For more information on this and below grade foundations, see the following references [52, 61, 81].

Hagentoft breaks the heat loss from a foundation into three parts: steady-state, periodic, and step changes. The step change can capture daily extreme temperature fluctuations, but is not needed here. This results in Equation (84) for the time dependent slab heat loss rate. The heat flux is found by dividing the rate by the slab area. The outdoor and indoor temperatures dictate the heat flow through the foundation to the soil surface outside the building. These heat transfer process are broken down and simplified through superposition and dimensional analysis. Dimensional analysis also reduces the number of individual parameters that can affect the heat transfer. The soil is assumed to be homogeneous with constant thermal properties. The heat transfer is purely conduction into a semi-infinite medium.

$$q_{HeatLoss}(t) = q_{SteadyState} + q_{Periodic}(t) \tag{84}$$

An important example of parameter reduction is the equivalent insulation thickness in Equation (85). Foundations are construction of several different materials. The equivalent insulation thickness reduces the thermal conductivities and thicknesses of these materials into one length parameter. This equivalent length represents the length of soil that would have the same thermal resistance as the foundation materials. This is calculated by adding together the thermal resistance of each material in the foundation. This value is then multiplied by the soil thermal conductivity so only a length is left. Related to the equivalent insulation thickness is the thermal penetration depth in Equation (86). The penetration depth is a way to describe the depth a thermal event will reach over a specified time. That specified time is called the periodic time, "t_p". This time is

arbitrary and can range from hours to a year. The greater the time, the larger the penetration depth and the "further" a thermal event will penetrate into the soil.

$$d = k_{soil}\left(\frac{d_i}{k_i} + \cdots\right) \tag{85}$$

$$d_p = \sqrt{\frac{\alpha t_p}{\pi}} \tag{86}$$

Other parameter reductions simplify the foundation geometry and relate insulation thicknesses to steady-state and periodic heat loss. The author assumes it is possible to tabulate heat transfer characteristics based on soil type and foundation construction. This leads to the calculation of parameters that can describe the expected heat transfer of most simple foundation types for any soil properties. The tabulated values require numerical solutions in most cases, but result in the two plots of Figure 89. The plot on the left tabulates a heat loss factor based on the equivalent insulation thickness and slab geometry. This heat loss factor, "h_s", is part of the steady-state heat loss in Equation (87). The plot on the right determines two time damping values , the periodic slab heat loss factor "$h_p{}^1$" and the periodic slab heat loss phase angle "$\varphi_p{}^1$", also based on the equivalent insulation thickness and penetration depth for the periodic heat loss in Equation (88). The sinusoidal function that represents the outdoor temperature in Equation (89) determines the other variables in Equation (88). The one user defined variable in Equation (89) is the periodic time," t_p", which is equal to one year. Equation

(89) requires a least-squares regression fit and is not as accurate in some locations as the four term Fourier series from earlier chapters.

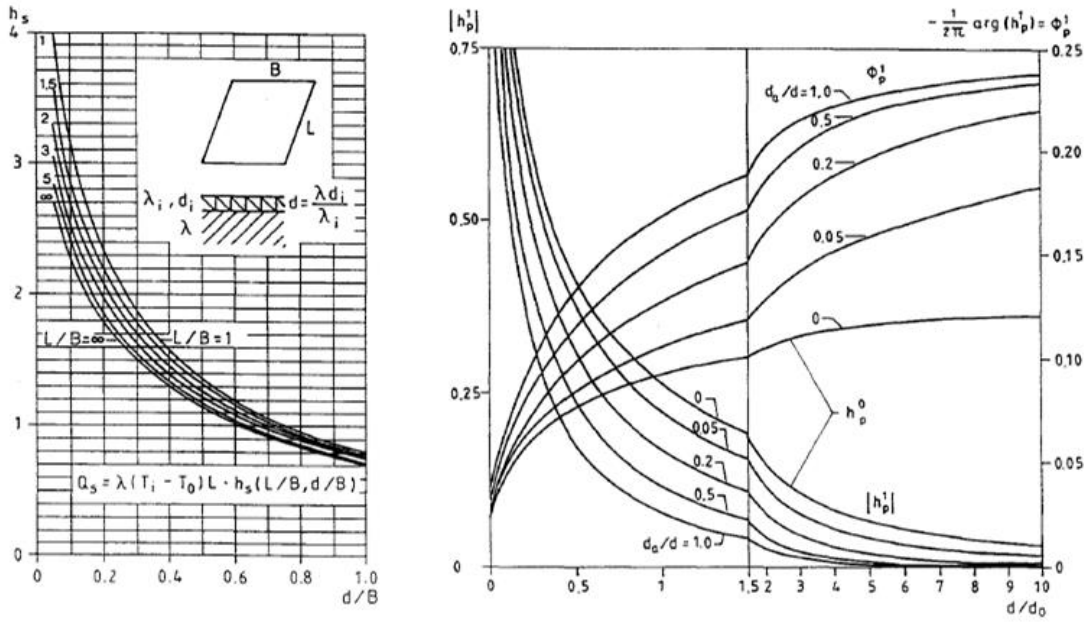


Figure 89: Left – heat loss factor h_s for no insulation on soil surface Right –Absolute value of $|h_p^1|$ and φ_p^1 [61]

$$q_{SteadyState} = k_s(T_{in} - T_{out})L_f h_s \tag{87}$$

$$q_{Periodic}(t) = -(2L_f + 2W_f)k_s|h_p^1|sin\left[2\pi\left({}^{t}/_{t_p} - \phi_p^1\right) + \phi_1\right] \tag{88}$$

$$T_{OutTemp}(t) = T_0 + T_1 sin\left(\frac{2\pi t}{t_p} + \phi_1\right) \tag{89}$$

Temperature Function for Radiant Slabs

Radiant slabs are typically between 75ºF and 80ºF for heating, and 60ºF to 65ºF for cooling. The set-point for radiant slabs in cooling mode will change with indoor humidity. The control strategy is to prevent the slabs from falling below the air's dew

point and forming condensation. Fine-tuned prediction of annual slab temperature is beyond the scope of this study, and the simulations use a simple temperature step function for heating and cooling. The months of October through March are considered the heating season, and the slab is set at a constant 80ºF. The cooling season is the months of April through September, and the slab set-point is a constant 65ºF. The shoulder seasons will see the slab in heating and cooling mode on the same day, but this daily variation is not considered in the simulations.

Soil Temperature Distributions Below On-Grade Slabs

The following sections use the above GFs formulation, slab heat flux functions, and soil surface flux estimations from the previous chapter to simulate soil temperature distributions below on-grade slabs. This includes simulations for all 15 locations in Table 8 to investigate different climate conditions. Simulation times of interest are 180, 270, and 360 days starting from January 1st. All simulations use a standard sized foundation geometry and construction. This section also investigates the role of insulation thickness and soil diffusivity. This section highlights the results for the Bozeman, Montana and Houston, Texas locations.

Standard Foundation Size for Comparative Simulations

Figure 90 is the standard geometry and construction for the 15 location comparative study. The standard rectangular slab is constructed of three materials: concrete, insulation, and gravel. A foundation commonly includes a vapor barrier as

well, but it is neglected since it is very thin. Table 24 lists the thickness of each material along with its respective thermal conductivity. Note the indoor air temperature is a constant 70ºF. The insulation thickness is the only variable in Table 24 that will vary in the following simulations since it is anticipated to have a significant effect on slab heat loss. The other thicknesses and thermal conductivities have smaller effects, but it is not feasible to investigate each one separately. The soil thermal diffusivity is a constant 0.6 ft^2/day for all simulations except those specifically investigating effects of soil diffusivity. Figure 339 through Figure 353 in APPENDIX Edisplay the annual slab heat flux functions for all 15 locations using the Hagentoft method for this foundation construction.

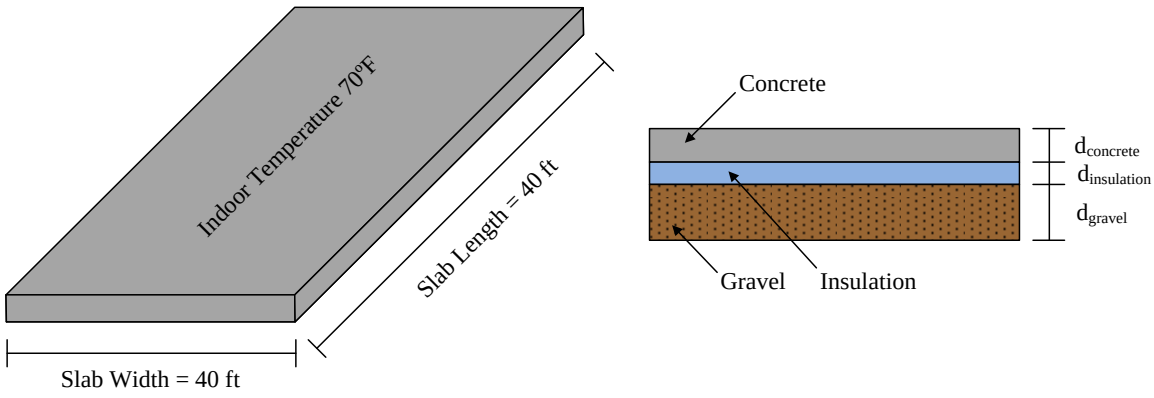


Figure 90: Standard foundation construction and geometry for non-radiant on-grade slab simulations

Table 24: Standard foundation construction material properties and dimensions

Material	Thickness (inch)	Thermal Conductivity (Btu/hr·ft·ºF)	Source
Concrete	6	0.982	[66]
Insulation	2	0.023	[66]
Gravel	6	0.404	[66]
Soil	-	0.750	[82]

Simulation Results for Non-Radiant Slabs

The simulation results from Houston, Texas and Bozeman, Montana are highlighted in this section to represent cooling and heating dominated locations. See Table 8 for heating and cooling degree day comparisons. Figure 91 is the distribution in Houston, Texas after 180, 270, and 360 days starting on January 1st. The three figure time lapse indicates the soil temperatures below the foundation are dynamic and range from 74ºF to 68ºF over half a year. The slab also has an insulative effect in heating and cooling. In the top contour of Figure 91, the higher outdoor temperatures only penetrate a few feet below the slab The same is observed in the bottom contour for day 360 where the under slab soil remains warmer than the surrounding soil.

An interesting feature of the middle contour of Figure 91 is the "bubbled" effect of the soil temperatures several feet away from the foundation. The 77ºF isotherm is the best example of this where the soil from approximately 1½ feet to 8 feet is at 77ºF. This seems counter-intuitive, but is observed in another similar study of soil temperatures for non-radiant slabs [64]. The nature of the slab heat loss, or more specifically the slab heat flux function, is one explanation for this effect. From Figure 344, the slab has a negative heat flux from day 180 to 270 (heat is flowing into the slab). This in effect pulls heat from the soil surrounding the foundation which the temperature isotherms illustrate by moving towards the foundation. This is realistic since the soil temperatures away from the slab are much warmer than under the slab at this time due to the previously discussed slab insulation effect. The deeper, warmer soil temperatures then want to flow towards the cooler soil under the slab.

The isotherms have returned to a more uniform distribution by day 360. An interesting feature is the soil temperatures under the slab are much warmer on day 360 than day 270, even though outdoor temperatures are colder (Figure 200). The foundation heat loss function in Figure 344 increases around day 240 and does not become positive until day 300. This leaves 60 days of positive heat flux under the foundation, which is likely not enough to cause the increase in temperature. A second additive effect is the "bubbled" heat wave from the deeper and warmer soil reaching the foundation. The "bubbled" heat wave is moving towards the foundation at day 270, and by day 360 it is adding heat to the soil directly under the foundation. This effect is also observed in the similar study already mentioned where the soil was 2.7ºF higher on day 365 than day 205 [64].

The heating dominated climate of Bozeman, Montana has very different temperature distributions in Figure 92. The first observation is the soil temperatures away from the slab at day 180 are much higher than the soil temperatures free of structures in Figure 69. The soil surface flux estimation for Bozeman in Figure 327 did result in higher than normal soil temperatures around day 180. The slab heat loss function for Bozeman in Figure 342 is also positive for the entire year. This is one reason the "bubbled" effect at day 270 observed in Houston, Texas is in the opposite direction in Bozeman on day 270. Too much heat is added to the domain during this time and results in unrealistic soil temperatures. Other locations with a higher number of heating degree days have similar results of unrealistically high below slab temperatures. Figure 354 through Figure 368 in APPENDIX F display the results for the other 13 locations.

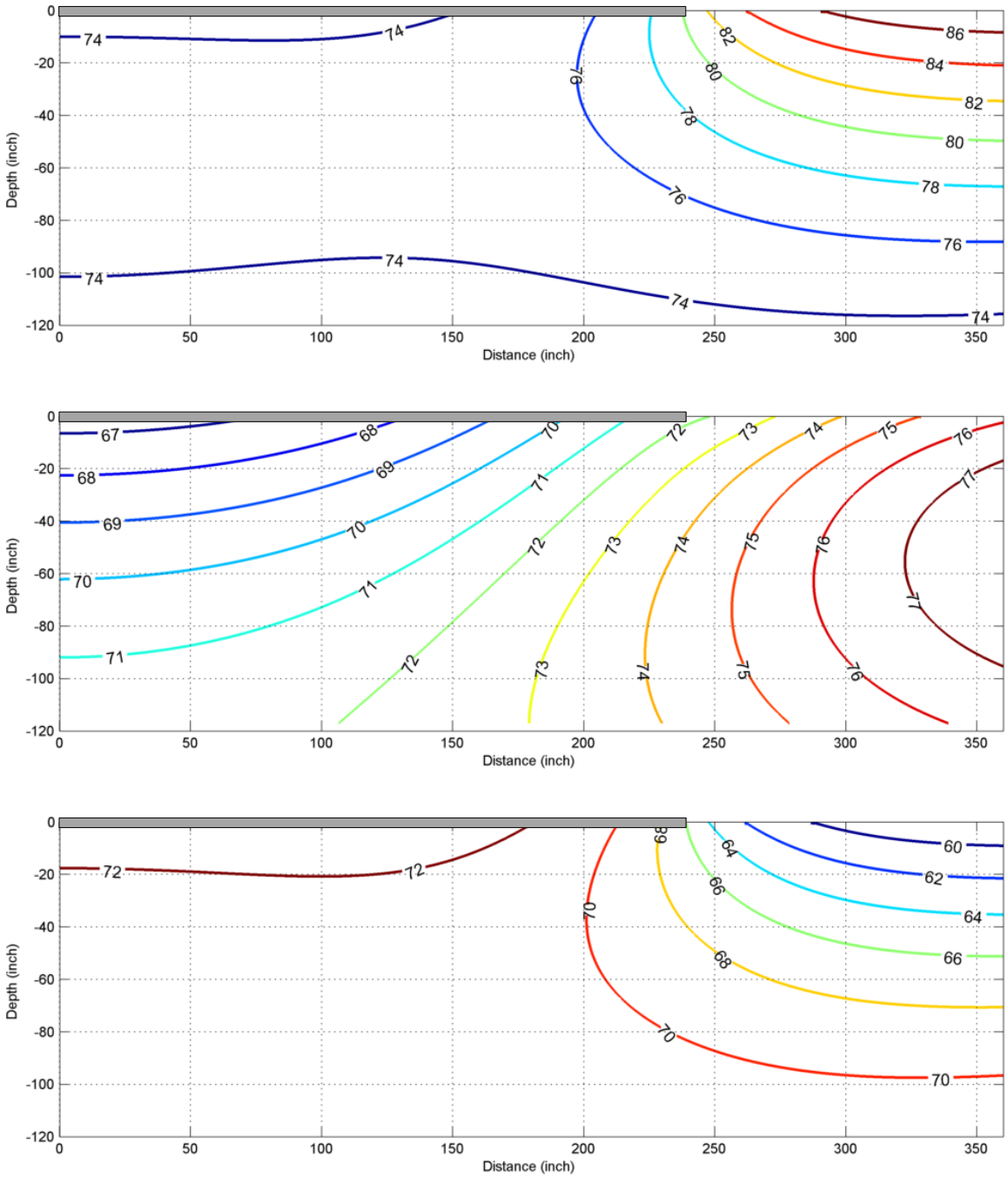


Figure 91: Houston, Texas – soil temperature distribution for non-radiant slab at 180 days (top), 270 days (middle), and 360 days (bottom) starting from January 1st for a slab length of 40 feet

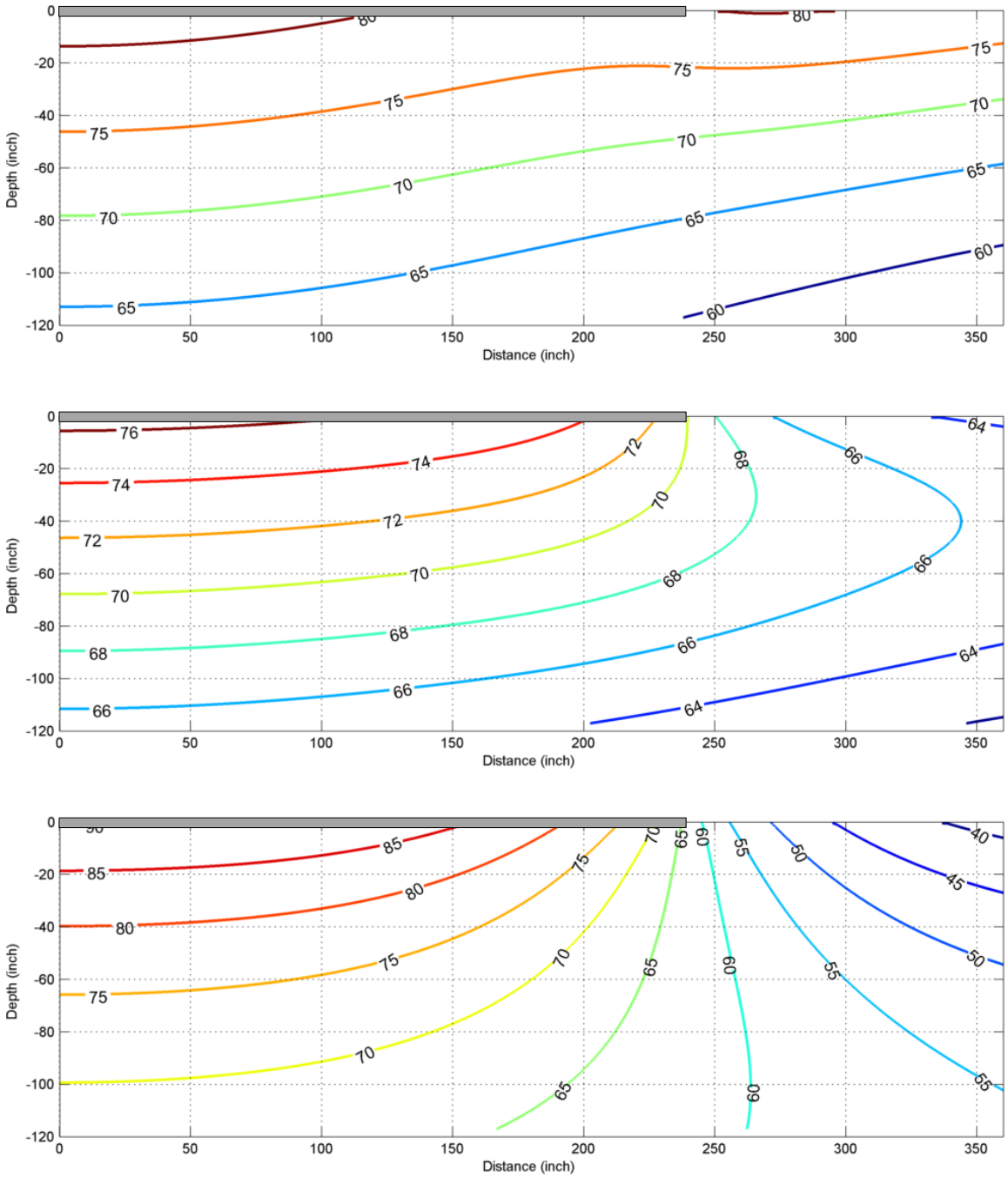


Figure 92: Bozeman, Montana– soil temperature distribution for non-radiant slab at 180 days (top), 270 days (middle), and 360 days (bottom) starting from January 1st for a slab length of 40 feet

Non-Radiant Slab Errors and Unrealistic Results. Previous studies in literature agree slab heat loss is a three dimensional problem, and simplification to two dimensions generates a certain amount of error. For example, the foundation heat loss function from Hagentoft's method uses superposition, dimensional analysis, and tabulated values to simplify truly three dimensional heat losses. The 2-D GF solution in this chapter is applying a BC developed for three dimensions, and this is one variable that causes the unrealistically high soil temperatures.

An early attempt to model below slab temperatures with GFs illustrates the effects of ignoring the third dimension. Figure 93 is an attempt at the 180 day temperature distribution for Bozeman Montana. It uses the same GF formulation already discussed, except it centers the y-axis on the slabs edge instead of the center. This essentially allows the slab to extend to infinity in the negative x-direction. This results in the temperature isotherms trending downwards under the foundation instead of leveling out and trending back toward the surface. This is due to the infinite heat addition of the slab in the negative x-direction. The same is occurring in the 2-D GF solutions in Figure 91 and Figure 92 in the slab width direction (z-direction). The infinite slab width in this case is contributing too much heat from the foundation slab. The consequence is the slab having a higher than normal contribution to the soil when compared to a realistic systems.

A third dimension also allows the soil surface heat flux to remove more heat from under the slab during the winter months. The slab in Figure 91 and Figure 92 is a 3-D, 40 by 40 foot square, but the system is not perfectly symmetric, and soil temperatures will be lower in winter than with the current two-dimensional solution. This becomes even

more important in long and narrow slabs where the heat loss over the slab width (z-direction) will have a far more significant contribution. It is possible to extend the current GF solution to three dimensions. It is not trivial, but does follow the same systematic GF procedure. The BSG technique is not currently set-up to handle a three dimensional problem, and is anticipated to cause the BSG database to become prohibitively large. The scope of this work is to develop an EAHX simulation using GFs. A 3-D under slab soil temperature simulation is outside this scope and is future work for a separate study.

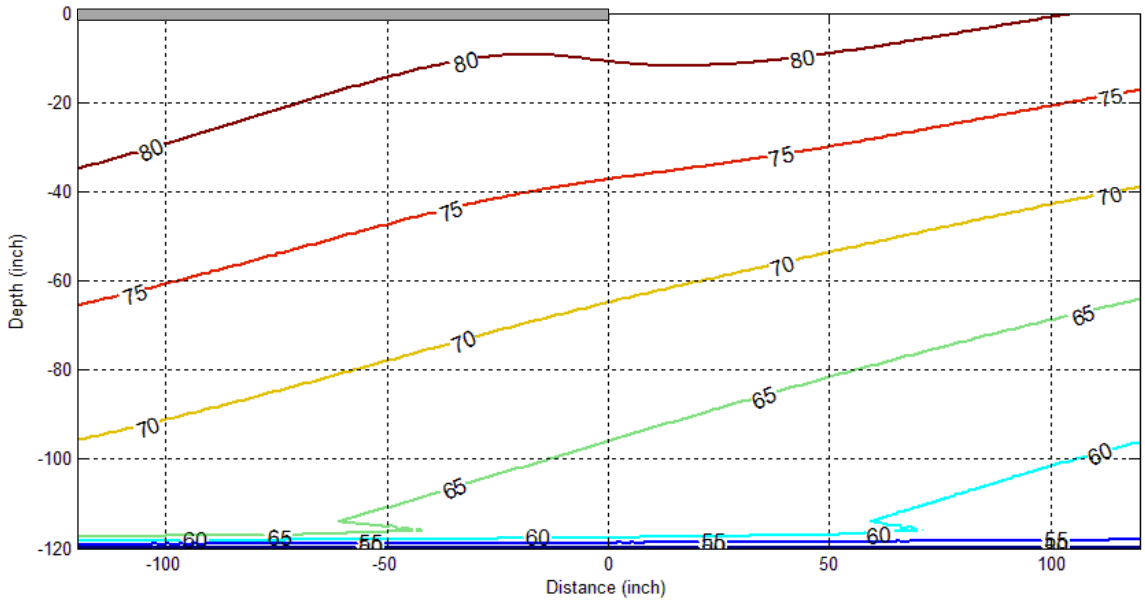


Figure 93: Under slab temperature distribution for Bozeman, Montana on day 180 with the y-axis centered on the foundations edge instead of the foundation center

Effect of Insulation Thickness. Figure 94 investigates the effect insulation thickness has on slab heat loss, and the resulting temperature distribution for Bozeman, Montana at day 270 using the typical foundation in Figure 90. The only variable in Table

24 that changes is the insulation thickness. From the top to bottom contours, the insulation thickness is 2, 4, 6, and 8 inches. The resulting four contours show the insulation thickness does matter since the temperatures directly under the foundation range from 75ºF to 55ºF. An insulation thickness of greater than four inches is highly unlikely in a typical foundation construction, unless it is being designed specifically for an under slab EAHX. These results provide the first indication that the slab insulation will play a crucial role in EAHX operation. For example, a significant amount of insulation in climates with a higher number of cooling degree days like Bozeman, Montana is not necessarily beneficial. Heat loss from the slab is less, but so are the under slab soil temperatures. This results in poor EAHX performance during the heating season.

Soil Diffusivity in Non-Radiant Slabs. Figure 95 examines how soil diffusivity affects the under slab temperature distribution. Again, this set of simulations use the same foundation construction parameters. Note the soil thermal conductivity is a constant 0.75 Btu/hr·ft·ºF. Soil temperatures directly below the foundation increase by approximately 2ºF with each 0.2 ft^2/day increase in diffusivity. The same is true for the soil temperatures under the exposed surface soil. The shape of all four contours is almost the same though. The higher diffusivities result in a faster rate of heat input by the flux boundary conditions into a domain initially at a uniform temperature. The initial uniform temperature is likely why the temperature isotherms are the same shape.

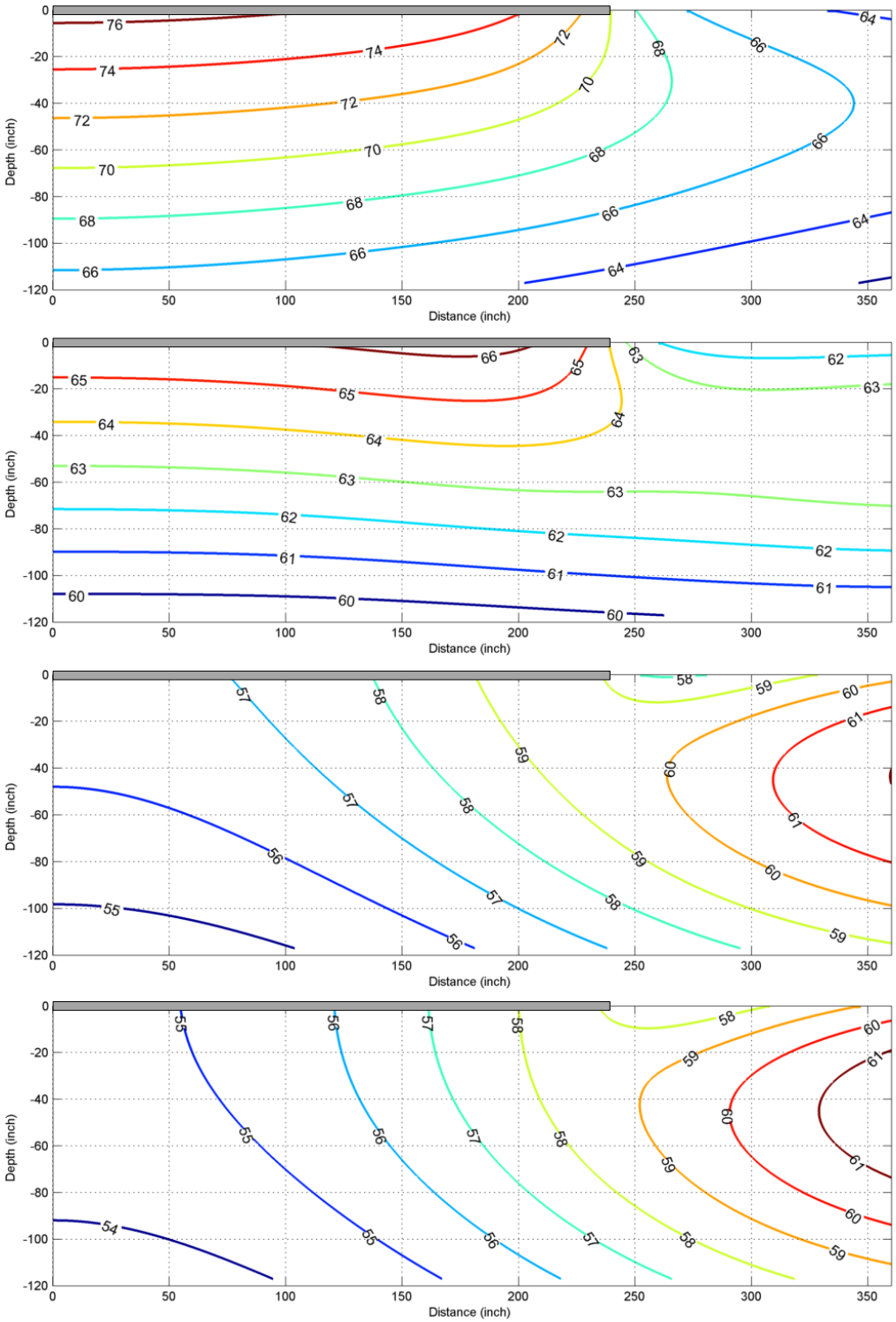


Figure 94: Soil temperature distributions under a non-radiant slab for Bozeman, Montana at day 270 using foundation insulation thicknesses of 2, 4, 6, 8 inches from top (2 in) to bottom (8 in)

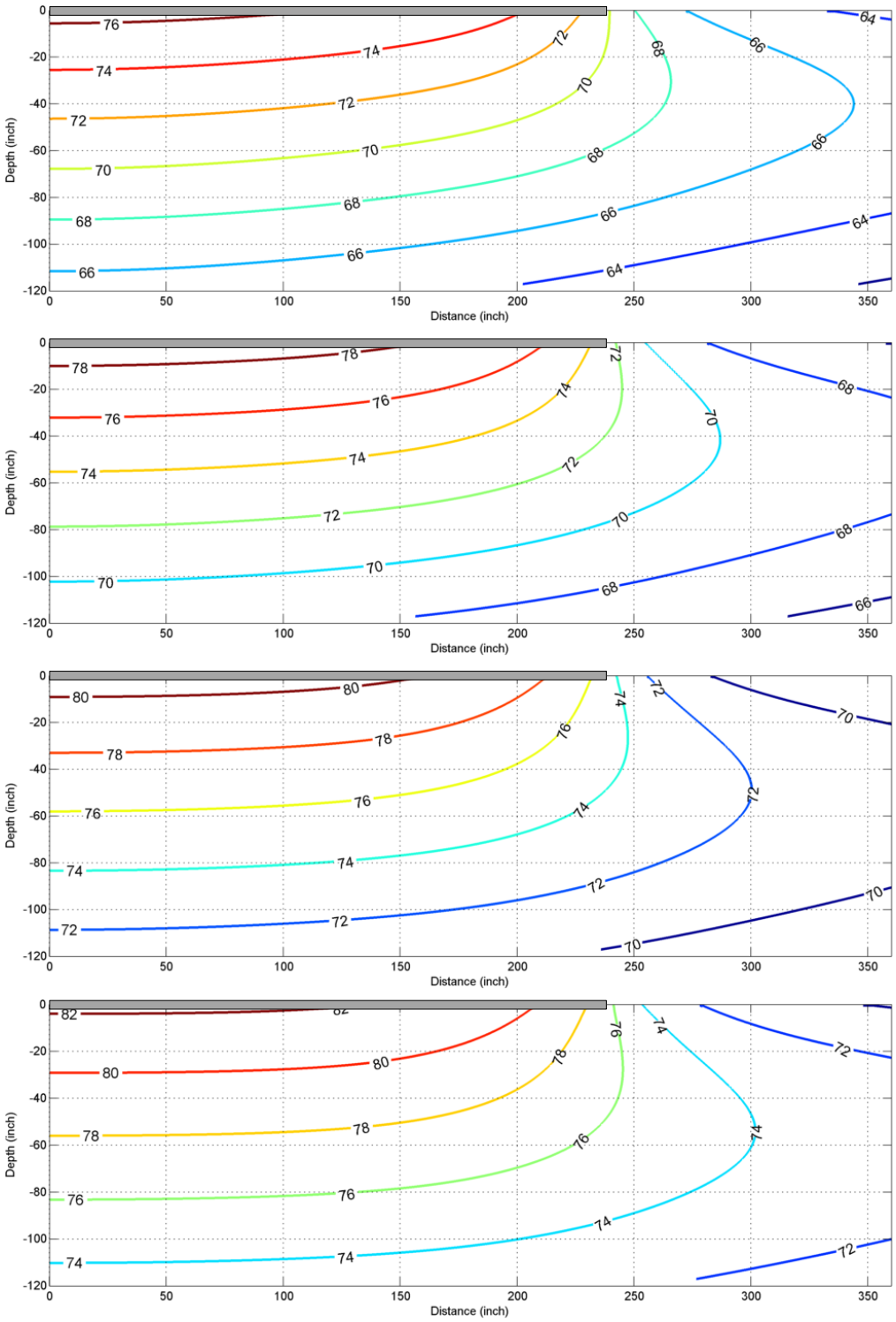


Figure 95: Soil temperature distributions under a no-radiant slab for Bozeman, Montana at day 270 using soil diffusivity of 0.6, 0.8, 1.0, and 1.2 ft^2/day from top (0.6 ft^2/day) to bottom (1.2 ft^2/day)

Simulation Results for Radiant Slabs

Figure 96 and Figure 97 are the radiant slab soil temperature distributions for Houston, Texas, and Bozeman, Montana respectively. Figure 369 through Figure 383 in APPENDIX F display the results for the other 13 locations. These are much different than the non-radiant distributions in Figure 91 and Figure 92. The main difference occurs at the foundation edges where there are high concentrations of temperature isotherms. A separate study for radiant on-grade slabs confirms this observation [53]. The isotherms in non-radiant slabs are more spread-out by the foundation edge, and the soil is at consistently higher temperatures. Previous simulations in the SOIL TEMPERATURE SIMULATION chapter indicate the surface temperature boundary condition is a more accurate than the heat flux boundary. This is further evidence that the non-radiant slab heat flux boundary conditions are adding too much heat to the soil domain over time.

The simulation results indicate the soil temperature directly below a radiant slab is highly dependent on the slab temperature. The slab set points of 80ºF and 65ºF for heating and cooling respectively may not be as accurate due to not considering foundation insulation, but the soil's dependence on this set point is still apparent. For example, the radiant slab in the top and middle contours for Houston in Figure 96 is still in cooling mode. The soil 10 feet from the foundation center and up to four feet below the slab is close to the cooling set point of 65ºF. It is not until closer to the foundation edge that the surface influences the soil temperatures. This is an important observation for under slab EAHXs installed near radiant slabs since the EAHX pipe surface temperature will be near the radiant slab set point.

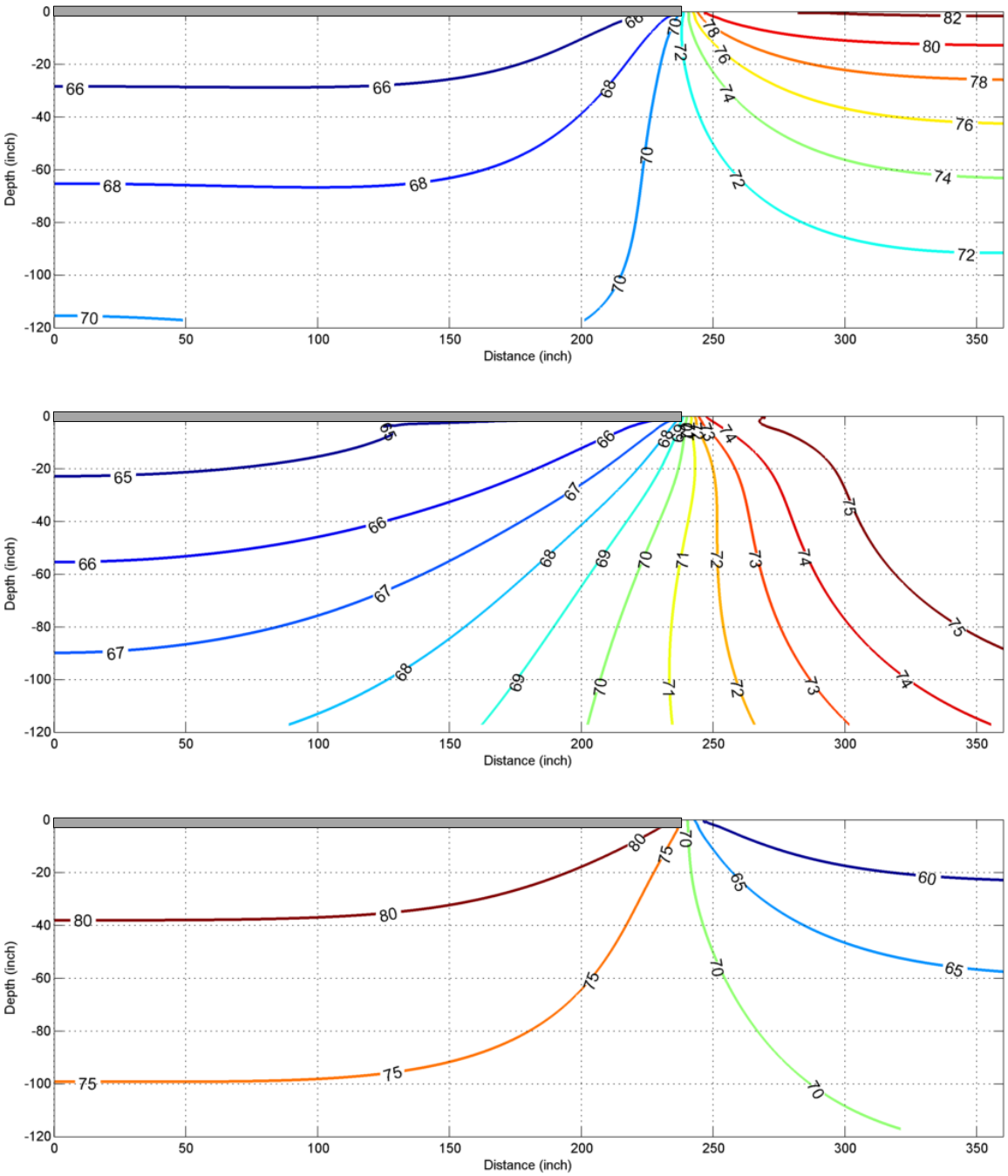


Figure 96: Houston, Texas– soil temperature distribution for a radiant slab at 180 days (top), 270 days (middle), and 360 days (bottom) starting from January 1st for a slab length of 40 feet

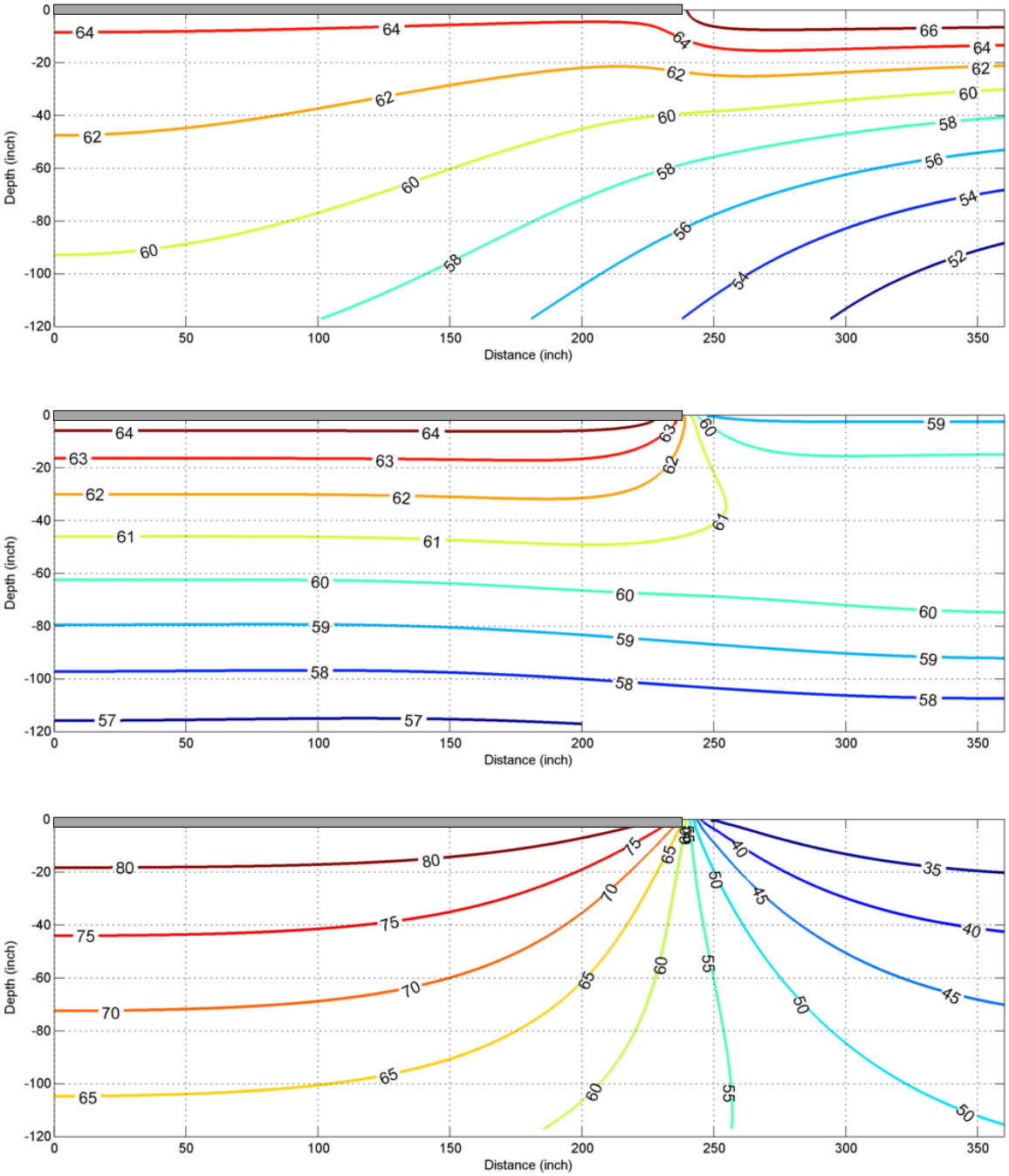


Figure 97: Bozeman, Montana – soil temperature distribution for a radiant slab at 180 days (top), 270 days (middle), and 360 days (bottom) starting from January 1st for a slab length of 40 feet

Soil Diffusivity in Radiant Slabs. Increasing the soil diffusivity in the radiant slab simulation has little effect on the soil temperature distribution as shown in Figure 98 for Bozeman, Montana on day 270. The contour plots are almost identical except for at the soil surface and depths greater than eight feet (96 inches). Part of the reason why the profiles are near identical is the small temperature difference between the slab set point and soil surface. The similar temperatures do not provide the potential to drive heat transfer under the foundation. This observation was validated by performing the same simulation at day 360 instead of day 270 (not pictured). This resulted in a more notable temperature difference at depths below eight feet where the higher temperatures from the radiant slab had traveled further into the soil. The diffusivity effects are still much less noticeable than in the non-radiant slabs.

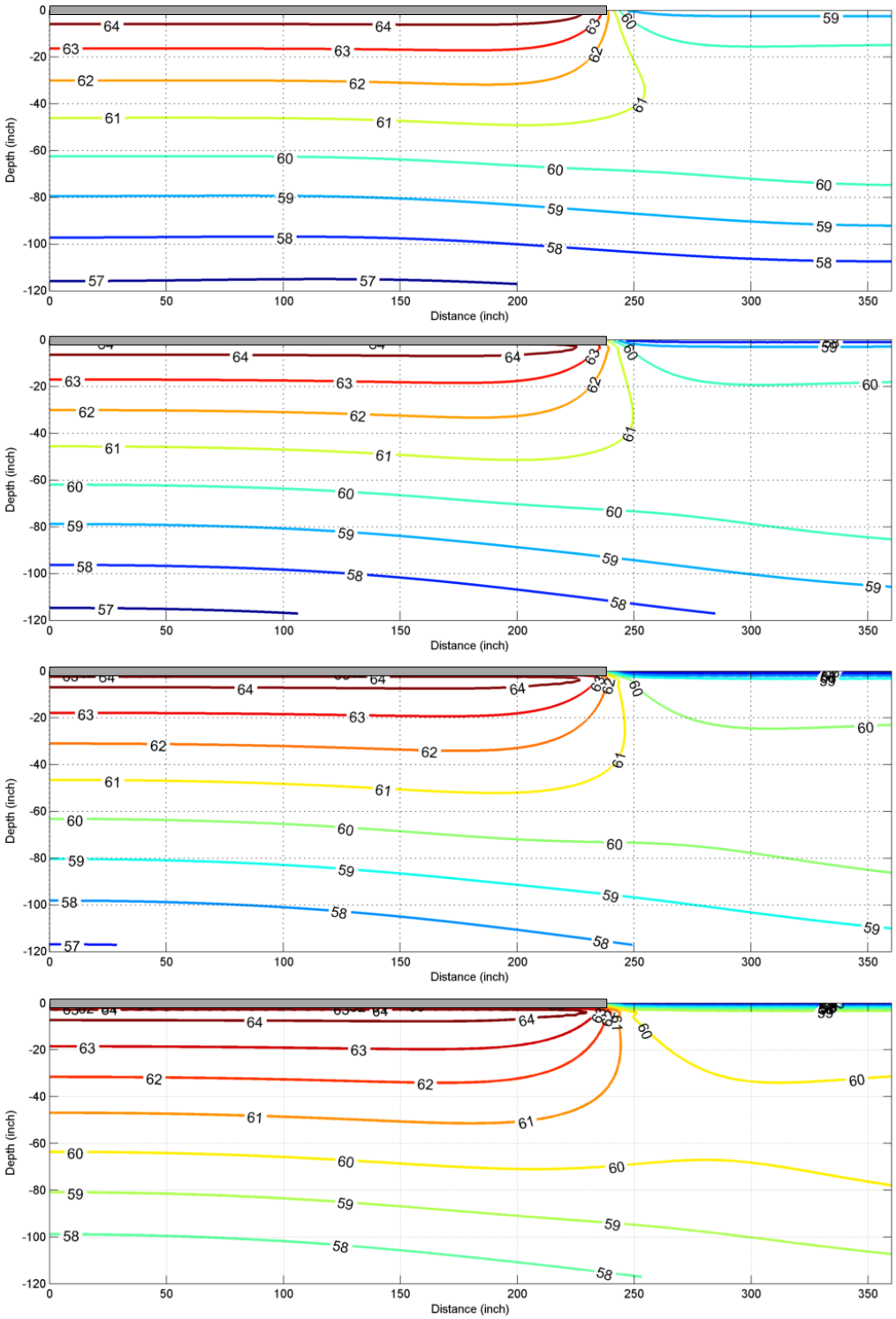


Figure 98: Soil temperature distributions under a radiant slab for Bozeman, Montana at day 270 using soil diffusivity of 0.6, 0.8, 1.0, and 1.2 ft^2/day from top (0.6 ft^2/day) to bottom (1.2 ft^2/day)

Translation to Under Slab EAHX Simulation

The under slab soil temperature simulation developed in this chapter is useful in two ways. The first is that it provides design level information on soil temperatures below a foundation. Preliminary design calculations can use just the soil temperatures to gain insight on how an EAHX will perform based on soil temperatures. For example, a designer can decide if excavating another foot of soil is beneficial to the EAHX, or the consequences of adding another inch of insulation. The second purpose of this simulation is to provide an initial condition to the EAHX simulation in the next chapter. It is clear early on in the next chapter that the simulation accuracy strongly depends on the soil's initial temperatures. The computationally efficient for the under slab temperature distribution discussed in this chapter is the first step in the overall EAHX simulation

UNDER YARD AND UNDER SLAB

EARTH-AIR HEAT EXCHANGER SIMULATIONS

The Green's Function (GF) method has proven useful in finding soil temperatures in locations free of structures and beneath on-grade foundations slabs. It is next applied to describe the conductive and convective heat transfer between the soil surrounding the earth-air heat exchanger (EAHX), and the air traveling through it. This simulation follows the method developed by Cucumo et al. [5] who were the first to apply the GFs to EAHXs. Their formulation was purely analytical where a 1-D domain, such as the one picture in Figure 99, is split into two separate solutions. The first solution is a 1-D plate that represents the distance between the soil or slab surface and the EAHX pipe. The second solution is a 1-D semi-infinite solid that extends from the EAHX downwards. The two boundaries of the EAHX are convective boundary conditions (BCs). The simulation assumes 1-D heat transfer, and there is not heat transfer in the axial direction. The two separate solutions for soil temperature combine at the end to yield a total temperature distribution.

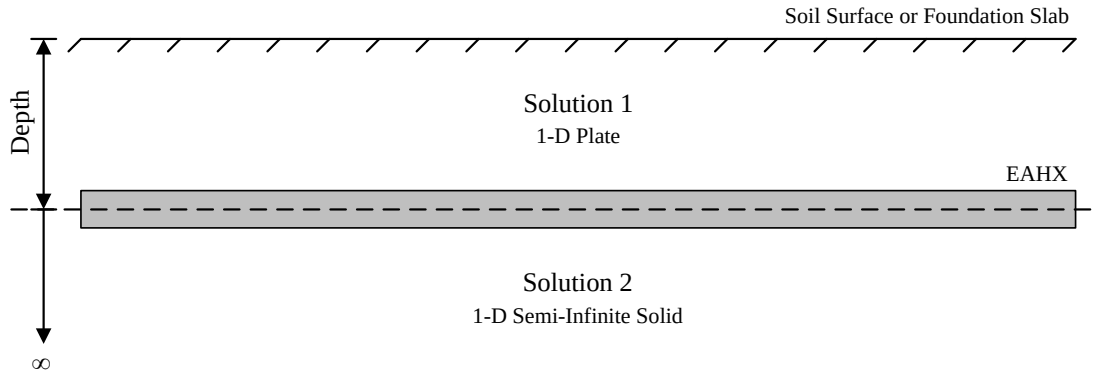


Figure 99: Basis of one-dimensional under yard and under slab EAHX split into two independent solution zones

The following extends the work by Cucumo et al. in two ways. The first is to apply the method of splitting an EAHX into two solutions to the under slab location. This will provide needed information on a type of installation that is not present in literature with limitations. It is possible to determine the soil temperature around the inlet of the EAHX because the inlet conditions are known. The fluid air temperature past the inlet though is more difficult to determine because the air is heating or cooling. Without knowing the air temperature, it is not possible to find the soil temperatures past the inlet. One option is to assume an outlet temperature and a temperature distribution along the EAHX pipe, but these assumptions are not ideal. The second extension to the previous work is a numerical finite-difference scheme to couple the GF soil conduction to convective internal flow. This will allow analysis of the changing air and soil temperature along the entire length of the EAHX.

Green's Function Formulations for Soil Conduction

Basis of One-Dimensional Model

Figure 100 is a more detailed representation of the domain and boundary conditions for the "above/below EAHX" soil conduction model. This figure is the same for the under yard (UY) and under slab (US) simulations since only the surface boundary type changes. The time-dependent outdoor air temperature enters the EAHX at some average air velocity. This average air velocity and inlet temperature determines the convective heat transfer coefficient (CHTC) through the Gnielinski correlation in Equation (18). The CHTC coefficient is a constant and cannot vary with time in the GF

method. The CHTC and inlet air temperature complete the convective BC. This is then combined with the time-dependent surface temperature, periodic slab heat flux, or periodic slab temperature to complete the boundaries of the 1-D plate for the "above EAHX" solution. The 1-D semi-infinite solid for the "below EAHX" solution uses the same convective BC. Since this is a 1-D model, the air temperature passing through the EAHX pipe is constant. Without the finite difference approach, the temperature distribution is only really valid at the EAHX inlet.

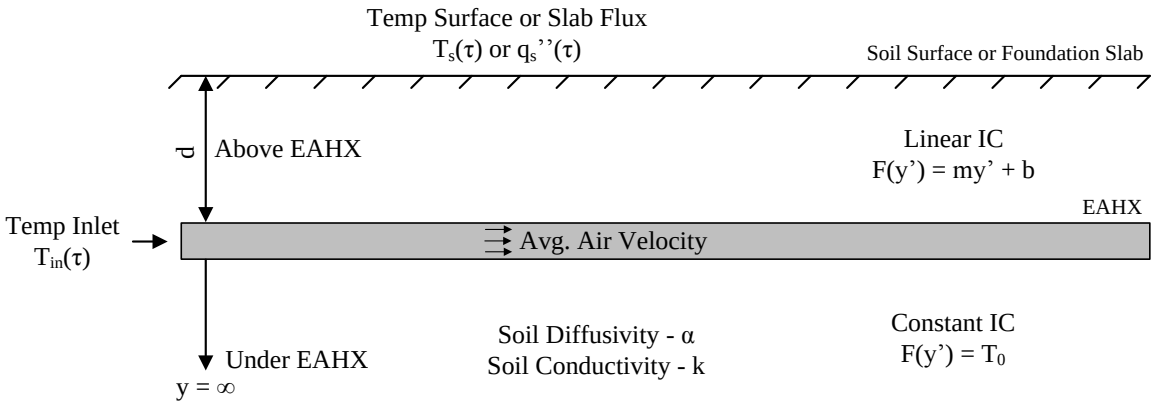


Figure 100: Detailed representation of the 1-D "above/below EAHX" simulation setup for the under yard and under slabs locations

Initial Condition Functions. The initial temperature profile above and below the EAHX can be a complex curve depending on time of the year and if the EAHX was previously operating. The IC contribution from the Green's Function solution equation (GFSE) requires this complex curve in a function form to complete a space integration over the domain. For example, take Equation (90) which is the IC contribution for the "under EAHX" solution. In this equation, the G_{Y31} GF is multiplied by some function "F(y')" describing the IC temperature distribution. This product is integrated with

respect to the space coordinates over the entire domain. It is not always possible or practical to attempt a curve fit to produce the initial function in this research. Instead, the integration program creates a piece-wise estimation of the function based on the initial soil temperature distribution. The soil temperature simulations in the SOIL TEMPERATURE SIMULATION and SOIL TEMPERATURES BELOW AN ON-GRADE chapters determine this distribution for undisturbed soil, or previous simulation values if the EAHX has operated previously. This piece-wise IC requires numeric integration to solve the integral.

The trapezoid rule completes the space integration in Equation (90). This splits the integral from y'=0 to the depth "d" into a number of small increments. If increments of the same size are applied to a pre-determined initial temperature distribution, they can be split into step-wise values. For example, say the soil temperature at a depth of 10 inches to 11 inches is 50ºF. If the numeric integration splits each inch into ten sections, then the ten sections from 10 to 11 inches are all 50ºF. This is done programmatically for all the trapezoid increments. The result is an initial temperature distribution that looks like Figure 101 which is the piece-wise IC for a simulation starting on January 1st at 12:00 AM in Bozeman, Montana. A close examination reveals a step progression in temperature at each inch in depth. This step-wise process can estimate any curve above or below the EAHX to complete the IC contribution integral.

$$T_{IC}(y,t) = \int_{y'=0}^{d} G_{Y31}(y,t|y',0) * F(y') \; dy' \tag{90}$$

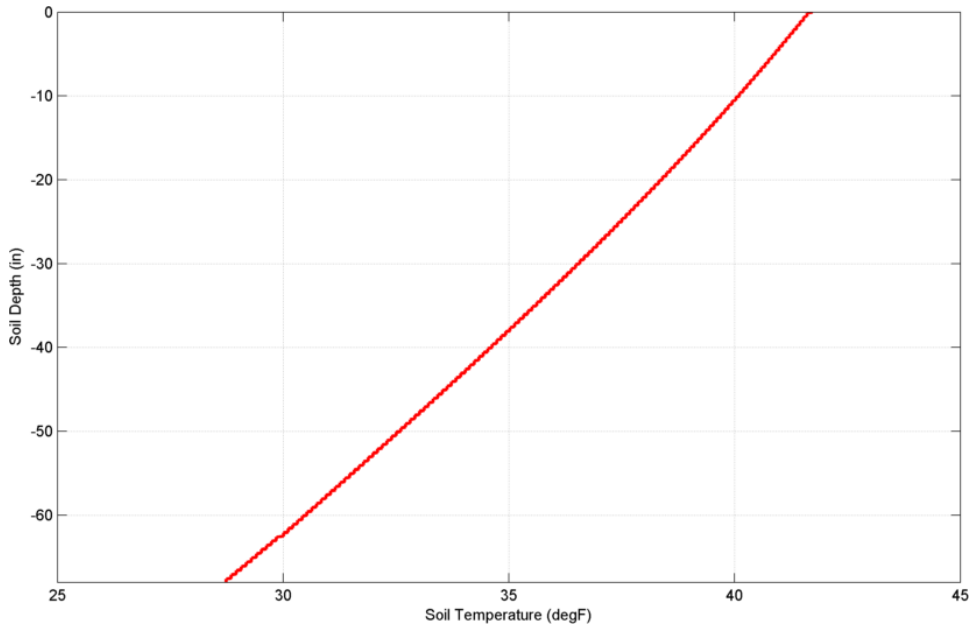


Figure 101: Piece-wise initial condition assembled from a previous temperature distribution for Bozeman, Montana on January 1st at 12:00 AM

Earth-Air Heat Exchanger One-Dimensional Green's Function Formulations

Under Yard Formulation for the Above Earth-Air Heat Exchanger. The UY GFSE for the "above EAHX" is shown in Equation (91). It uses a G_{Y31} Green's Function and its derivative. See Table 9 for the GF number system. The GF and its derivative have short and long time representations, whose use depends on domain and time properties. For this GF type, the short times are for values of $\alpha(t-\tau)/L^2$ less than or equal to 0.022. Equation (92) and Equation (93) are the short and long time convective GFs respectively. The infinite series in Equation (93) typically converges after eight terms. The surface temperature boundary uses the G_{Y31} derivative for short and long times in Equation (94) and Equation (95) respectively. Note that these two equations were evaluated at the depth "d". The long time convective GFs are quite complex since they require Eigen

value approximations (β_m). Again, a specific set of conditions for the time and space domain determines the appropriate approximation. For the EAHX domain size and time frame, Equation (96), Equation (97), and Equation (98) together form the Eigen function approximation. The BSG technique in the SOIL TEMPERATURE SIMULATION chapter determines the step-wise IC values.

$$T(y,t) = \int_{y'=0}^{d} F(y')G_{Y31}(y,t|y',0)dy' + \int_{\tau=0}^{t} \frac{\alpha h T_{\infty}(\tau)}{k} G_{Y31}(y,t|0,\tau)d\tau - \int_{\tau=0}^{t} \alpha T_s(\tau) \frac{\partial G_{Y31}(y,t|d,\tau)}{\partial y'} d\tau \quad (91)$$

$$G_{Y31}(y,t|y,\tau) = \frac{1}{[4\pi\alpha(t-\tau)]^{\frac{1}{2}}} \left\{ exp\left[\frac{-(y-y')^2}{4\alpha(t-\tau)}\right] + exp\left[\frac{-(y+y')^2}{4\alpha(t-\tau)}\right] - exp\left[\frac{-(2d-y-y')^2}{4\alpha(t-\tau)}\right] \right\} - \frac{h}{k} exp\left[\frac{h(y+y')}{k} + \frac{h^2\alpha(t-\tau)}{k^2}\right] \quad (92)$$

$$G_{Y31}(y,t|y',\tau) = \frac{2}{d} \sum_{m=1}^{\infty} e^{\frac{-\beta_m^2 \alpha(t-\tau)}{d^2}} \frac{(\beta_m^2 + B^2) sin\left[\beta_m\left(1-\frac{y}{d}\right)\right] sin\left[\beta_m\left(1-\frac{y'}{d}\right)\right]}{\beta_m^2 + B^2 + B} \quad (93)$$

$$\frac{\partial G_{Y31}(y,t|d,\tau)}{\partial y'} = \frac{d-y}{[4\pi\{\alpha(t-\tau)\}^3]^{\frac{1}{2}}} exp\left[\frac{(d-y)^2}{4\alpha(t-\tau)}\right] \quad (94)$$

$$\frac{\partial G_{Y31}(y,t|d,\tau)}{\partial y'} = \frac{2}{d^2} \sum_{m=0}^{\infty} e^{\frac{-\beta_m^2 \alpha(t-\tau)}{d^2}} \frac{\beta_m(\beta_m^2 + B^2) sin\left[\beta_m\left(1-\frac{y}{d}\right)\right]}{\beta_m^2 + B^2 + B} \quad (95)$$

$$\beta_m \approx m\pi - \left(A + \frac{3m\pi}{2B}\right)^{1/3} + \left(A - \frac{3m\pi}{2B}\right)^{1/3} \quad (96)$$

$$B = \frac{h \cdot d}{k} \tag{97}$$

$$A \approx \left[\left(\frac{3m\pi}{2B}\right)^2 + \left(1 + \frac{1}{B}\right)\right]^{1/2} \tag{98}$$

Non-Radiant Under Slab Formulation
for the Above Earth-Air Heat Exchanger. The non-radiant US GFSE for the "above EAHX" is shown in Equation (99). This is similar to the UY GFSE except for using a G_{Y32} GF and a periodic heat flux for the surface condition. It also has a short and long time GF representation in Equation (100) and Equation (101) respectively. The short/long time split is the same as the G_{Y31} GF at a $\alpha(t-\tau)/L^2$ value of less than or equal to 0.022. Equation (102) is the Eigen value approximation. The time-dependent slab heat flux function uses the same method and foundation construction described in the SOIL TEMPERATURES BELOW AN ON-GRADE chapter. The 2-D slab on-grade GF method from the this same chapter also determines the values for the step-wise IC. These values are from the vertical temperature distribution directly under the center of the foundation. Accuracy in this method can be improved by including the horizontal location of the EAHX inlet with respect to the foundation, but is not considered at this time.

$$\begin{aligned} T(y,t) = \int_{y'=0}^{d} F(y') G_{Y32}(y,t|y',0)dy' + \int_{\tau=0}^{t} \frac{\alpha h T_\infty(\tau)}{k} G_{Y32}(y,t|0,\tau)d\tau \\ + \int_{\tau=0}^{t} \frac{\alpha q_s''(\tau)}{k} G_{Y32}(y,t|d,\tau)d\tau \end{aligned} \tag{99}$$

$$G_{Y32}(y,t|y',\tau) = \frac{1}{[4\pi\alpha(t-\tau)]^{\frac{1}{2}}}\left\{exp\left[\frac{-(y-y')^2}{4\alpha(t-\tau)}\right] + exp\left[\frac{-(y+y')^2}{4\alpha(t-\tau)}\right] - exp\left[\frac{-(2d-y-y')^2}{4\alpha(t-\tau)}\right]\right\} - \frac{h}{k}exp\left[\frac{h(y+y')}{k} + \frac{h^2\alpha(t-\tau)}{k^2}\right] \cdot erfc\left[\frac{y+y'}{[4\pi\alpha(t-\tau)]^{\frac{1}{2}}} + \frac{h}{k}[\alpha(t-\tau)]^{1/2}\right] \quad (100)$$

$$G_{Y32}(y,t|y',\tau) = \frac{2}{d}\sum_{m=1}^{\infty} e^{\frac{-\beta_m^2\alpha(t-\tau)}{d^2}} \frac{(\beta_m^2 + B^2)cos\left[\beta_m\left(1-\frac{y}{d}\right)\right]cos\left[\beta_m\left(1-\frac{y'}{d}\right)\right]}{\beta_m^2 + B^2 + B} \quad (101)$$

$$\beta_m \approx \frac{(2m-1)\pi B}{2(B+1)}\left\{1 + \frac{[(2m-1)\pi]^2}{12(B+1)^3 + [(2m-1)\pi]^2(2B-1)}\right\} \quad (102)$$

Radiant Under Slab Formulation for Above the Earth-Air Heat Exchanger. The radiant under slab GF formulation for above the EAHX is identical to the under yard except in the surface temperature function. The G_{Y31} GF still applies since the model assumes a temperature boundary for the radiant slab. The radiant slab surface temperature uses the same set points as described in the SOIL TEMPERATURES BELOW AN ON-GRADE chapter. The step-wise IC function is also found using the 2-D soil temperature distribution from the same chapter.

Below Earth-Air Heat Exchanger Solution. The soil conduction solution for below the EAHX is the same for all three "above EAHX" simulations. Equation (103) is the GFSE for the convective surface boundary. This uses a G_{Y30} GF which is shown in Equation (104). The y-axis in this equation is shifted so that y=0 is at the bottom of the

EAHX pipe. The piece-wise IC is especially useful for below the EAHX since soil temperatures become constant around 10 to 15 feet depending on location. It is difficult to fit a function to the soil temperatures as they level off. The upper limit of the space integration in Equation (103) is infinity, but a depth of 20 feet is typically enough to complete the numerical integration. Past 20 feet the exponentials in Equation (104) become practically zero.

$$T(y,t) = \int_{y'=0}^{\infty} F(y') G_{Y30}(y,t|y',0)dy' + \int_{\tau=0}^{t} \frac{\alpha h T_{\infty}(\tau)}{k} G_{Y30}(y,t|0,\tau)d\tau \quad (103)$$

$$\begin{aligned} G_{Y30}(y,t|y,\tau) = {} & \frac{1}{[4\pi\alpha(t-\tau)]^{\frac{1}{2}}}\left\{exp\left[\frac{-(y-y')^2}{4\alpha(t-\tau)}\right] + exp\left[\frac{-(y+y')^2}{4\alpha(t-\tau)}\right]\right\} \\ & -\frac{h}{k} exp\left[\frac{h(y+y')}{k} + \frac{h^2\alpha(t-\tau)}{k^2}\right] \\ & \cdot erfc\left[\frac{y+y'}{[4\pi\alpha(t-\tau)]^{\frac{1}{2}}} + \frac{h}{k}[\alpha(t-\tau)]^{1/2}\right] \end{aligned} \quad (104)$$

Mathematical Nature of
Convective Green Functions

Green's Functions with convective boundaries are different from other GFs in that their values decrease quickly as the difference between the time and dummy time (t-τ) increases. To illustrate this, Figure 102 and Figure 103 graph the G_{Y31} (under yard) and G_{Y32} (under slab) GFs evaluated at y'=0 respectively at several depths. The depth "d" in these two equations is five feet, so the last trace represents the temperature at the soil or slab boundary. The G_{Y31} GF values in Figure 102 decrease to practically zero after a (t-τ) value of 15 days. In other words, any boundary condition contribution 15 days before the

end simulation time is negligible. The same is observed in Figure 103 for the G_{Y32} GF where the values fall very quickly and then level off to an almost constant value.

These results illustrate an interesting observation. The convective BC only affects the soil temperatures surrounding the EAHX on a short period of time near the end of the simulation. This is counter-intuitive since an easy assumption to make is that continually passing cold air through the EAHX will deplete the heat in the soil around the EAHX, and vice versa for warm air. Following this assumption for continually cold air, the soil is thermally depleted and it will take extended amounts of time to warm the soil again with warmer air. Another way to picture this is the soil has a heat transfer history. The mathematical nature of convective GFs says differently though. Figure 102 and Figure 103 indicate there is no heat transfer history for the convective boundary past 20 days in both instances. It is important to note that this is for the convective boundary only. The second boundary, temperature or heat flux, does add significant value past 20 days which is accounted for in the IC.

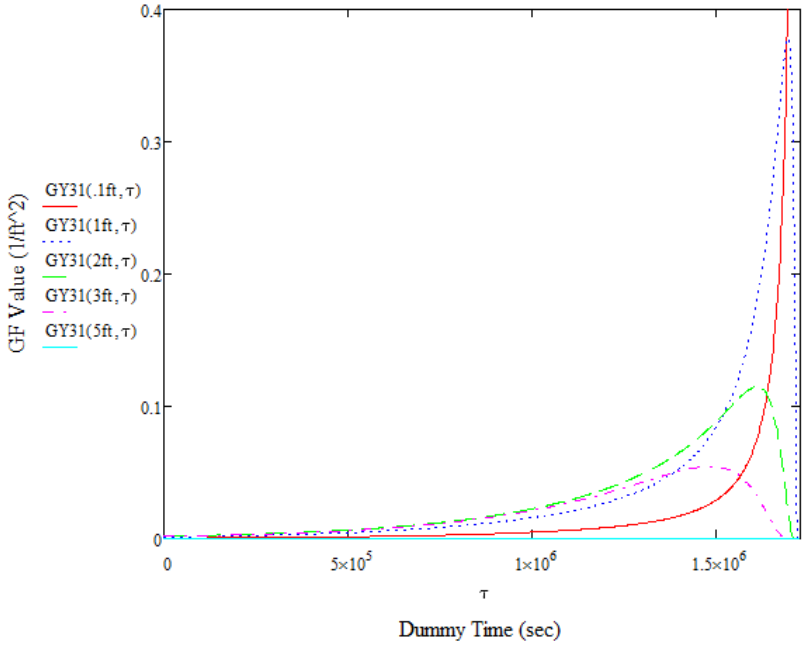


Figure 102: Value of G_{Y31} GF over a simulation time of 20 days (τ axis is 20 days), domain depth is five feet

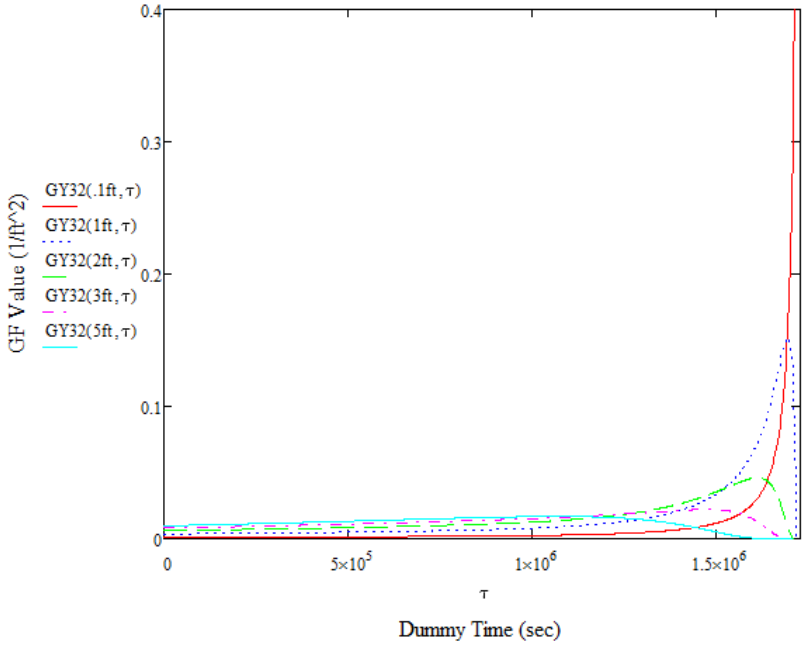


Figure 103: Value of G_{Y32} GF over a simulation time of 20 days (τ axis is 20 days), domain depth is five feet

Justification for Short Time Solutions

Simulation times for the "above/below EAHX" simulations are greatly reduced by starting with an IC temperature distribution determined by the BSG technique. The convective boundary in the "above/below EAHX" simulations does not contribute to the soil conduction until approximately the last 20 days. The top surface boundary does contribute for a much longer time. This is also the same boundary and boundary values as the soil temperature solutions found with the BSG technique. This suggests the BSG technique can be used to execute the long time portion of a simulation up to the start time of interest. Then the combined 1-D simulations with convective BCs executes over shorter time frames to find the transient soil conduction of the EAHX. For example, an UY three day simulation starting on July 1st would execute by using the BSG technique to find the soil temperatures on July 1st. This temperature distribution passes into the "above/below EAHX" convective simulation as an IC. The "above/below EAHX" then calculates the three days to find the final temperature distribution around the EAHX.

Another reason for small time solutions (less than a few days) is large simulation times for the non-radiant slab solution results in non-realistic temperature values. This is due to the nature of the G_{Y32} GF in the IC equation. Specially, the exponential multiplier in Equation (101) that includes the time "t" very quickly goes to zero as time increases. This is typically not an issue except for the two EAHX boundary conditions. The convective boundary condition does not extend very far into the soil due to the low diffusivity. On the other side, the heat flux from the foundation slab is so small that it

adds very little to the soil domain. This results in soil at the center of the domain having extremely small temperatures where the IC should be making a contribution.

Application of the Above/Below Earth-Air Heat Exchanger Simulation

This section displays three example applications of the "above/below EAHX" method to demonstrate its effectiveness and expected outputs. The three examples are for the UY, non-radiant US, and radiant US in Figure 104, Figure 105, and Figure 106 respectively. The EAHX is all three examples have operated for six continuous hours starting at midnight on July 1st in Bozeman, Montana. The typical meteorological year (TMY) data files provide the hourly inlet air temperatures. This implies the inlet air only changes temperature at the start of each hour. The soil diffusivity and thermal conductivity is 0.6 ft^2/day and 0.75 Btu/hr·ft·^{o}F respectively. The EAHX is eight inches in diameter. It is buried six feet under the surface in the UY simulation, and three feet below the foundation slab in the US simulation. The US simulations use the previous established foundation construction in Figure 90. The non-radiant US simulations also use the previous established periodic foundation heat loss and soils surface flux functions.

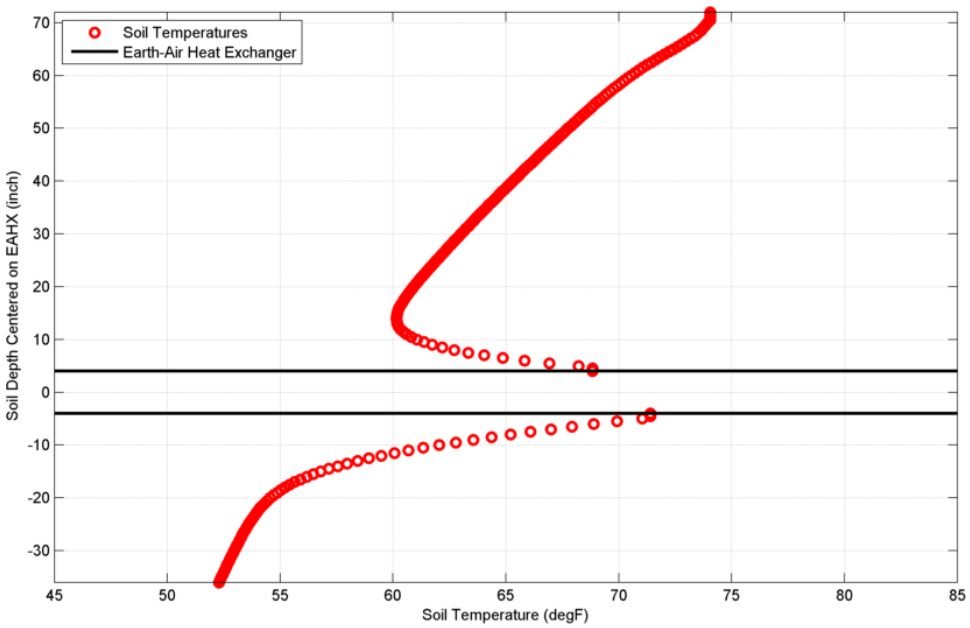


Figure 104: Example soil temperature distribution for the under yard EAHX buried at a six foot depth after six hours of operation starting on July 1st at midnight

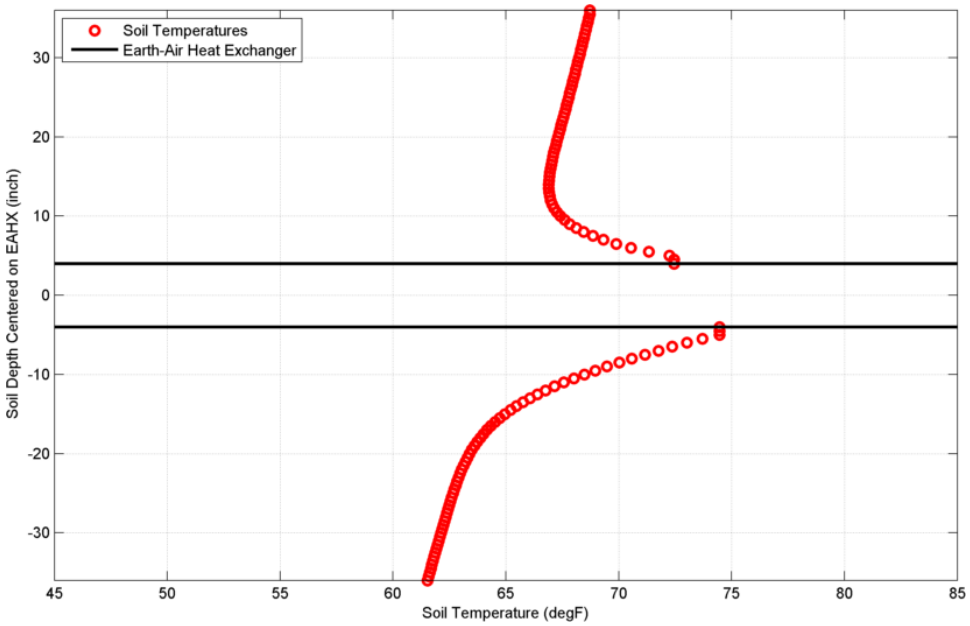


Figure 105: Example soil temperature distribution for the non-radiant under slab EAHX buried at a three foot depth after six hours of operation starting on July 1st at midnight

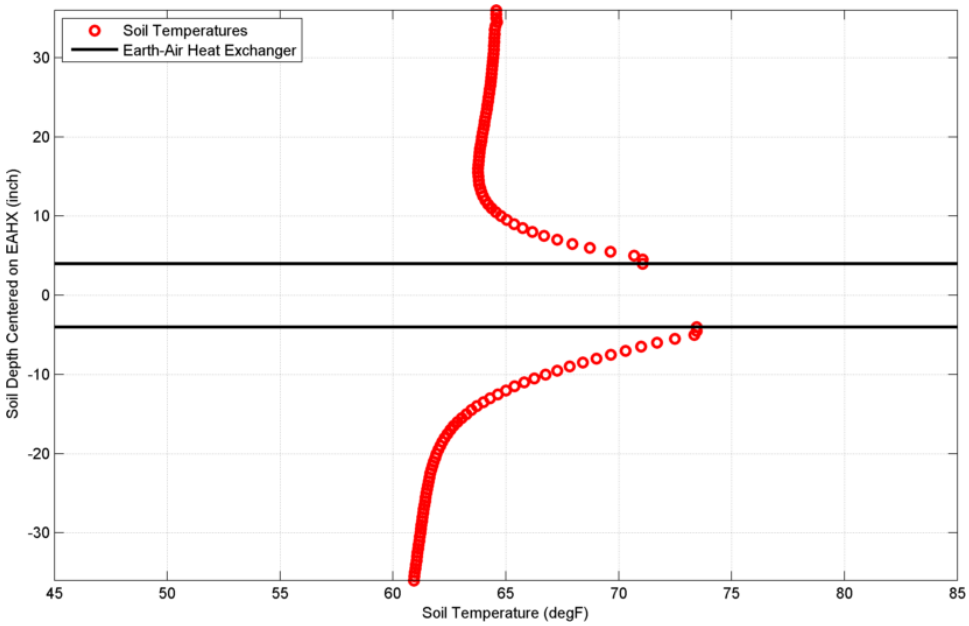


Figure 106: Example soil temperature distribution for the radiant under slab EAHX buried at a three foot depth after six hours of operation starting on July 1st at midnight

The three examples above again reveal the transient nature of EAHX operation. The soil immediately around the EAHX experiences temperature increases of 10-15ºF after the six hours of operation. The inlet air temperature in Bozeman, Montana for these examples was an average 74.7ºF. In all three figures, the bottom pipe surface temperature is 1-1½ºF higher than the top surface. This is not a cause for concern though since this within an acceptable soil temperature increase for eight inches. Soil outside the EAHX disturbance zone forms a straight line from the surface to the deep soil in all three figures. This lends confidence that the combination of two 1-D solutions is correct. The soil disturbances around the EAHX extend approximately a foot above the EAHX, and 1½ feet below. This is as far as the heat reached in the six hours of operation due to the soil's low thermal conductivity and diffusivity. In conclusion, these simulations indicate

other common models in literature are inaccurate. These models assume a constant pipe surface temperature, but this is not true after a few hours of operation.

2-D ANSYS Validation of 1-D Green's Function Simulation

A potential source of error in the 1-D "above/below EAHX" simulations is neglecting the lateral heat transfer from the sides of the EAHX pipe. In other words, the out of plane heat transfer has the potential to influence the soil temperatures above and below the EAHX. The 1-D simulation really only includes half the heat transfer from the EAHX pipe. The other half is exchanged laterally from the pipe. Note this is not the axial soil conduction along the length of the pipe. The effects of axial conduction are ignored in all the analysis of this chapter. The purpose of this section is to determine if the lateral heat transfer adversely effects above and below soil temperature distribution through a 2-D transient finite element simulation.

The ANSYS simulation environment performs the 2-D transient thermal finite element simulation. Figure 107 is the domain and boundary condition setup for the 2-D finite element model. The soil is a 20 by 13 foot rectangle with a thermal conductivity of 0.75 Btu/hr·ft·ºF and diffusivity of 0.6 ft^2/day. Centered horizontally in the soil is an eight inch diameter EAHX. This EAHX is six feet below the surface. The soil then extends another seven feet below the EAHX. The simulation time is six hours and starts at midnight on January 1st in Bozeman, Montana. This soil surface and air temperature during the six hours depends on data from the NRCS and TMY data files. Each hour uses a constant temperature from these data files. The soil surface uses the NRCS soil

temperatures, and the convective EAHX boundary the TMY air temperatures. The convective heat transfer coefficient in the EAHX is a constant 3 Btu/hr·ft^2·ºF. Table 25 outlines the soil surface and air temperature data for each hour of the simulation. The vertical boundaries are both thermally insulated. The bottom boundary represents the deep soil temperature which is 56.5ºF for this time of the year in Bozeman, Montana.

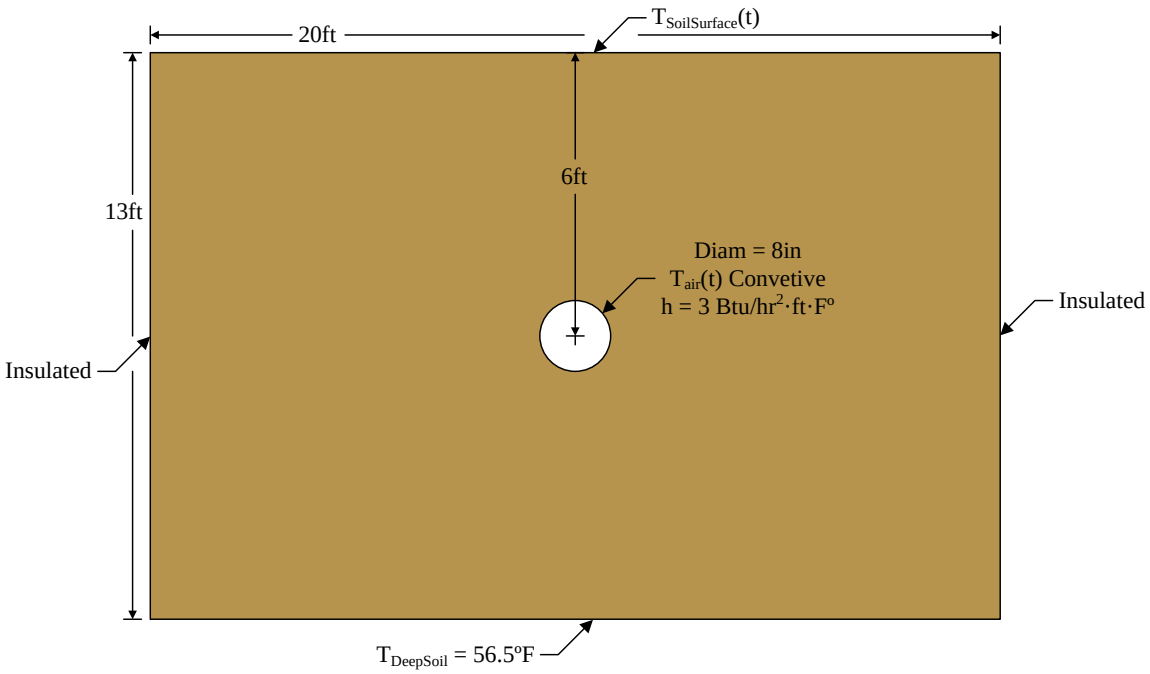


Figure 107: Domain size and boundary conditions in 2-D ANSYS validation of the 1-D above/below Green's Function solution method

Table 25: Boundary condition values for the soil surface and air temperature in 2-D ANSYS validation of the 1-D above/below Green's Function solution method

Time (hrs)	1	2	3	4	5	6
Soil Surface	28.8	28.7	28.6	28.5	28.4	28.3
Outdoor Air	30.3	28.5	26.7	30.3	23.1	23.1

Figure 108 displays the mesh for the finite element model. There is a high concentration of elements around the EAHX and near the soil surface. The majority of

HT occurs in these two locations. The simulation is only six hours long so heat will not transfer very far from the EAHX. Figure 109 depicts the initial condition for the transient simulation, and represents the January 1st undisturbed soil temperatures in Bozeman, Montana. The initial condition is important because the vertical temperature gradients also affect the heat transfer around the pipe. The IC is not completely accurate for the undisturbed soil temperatures since ANSYS required a linear temperature change with depth.

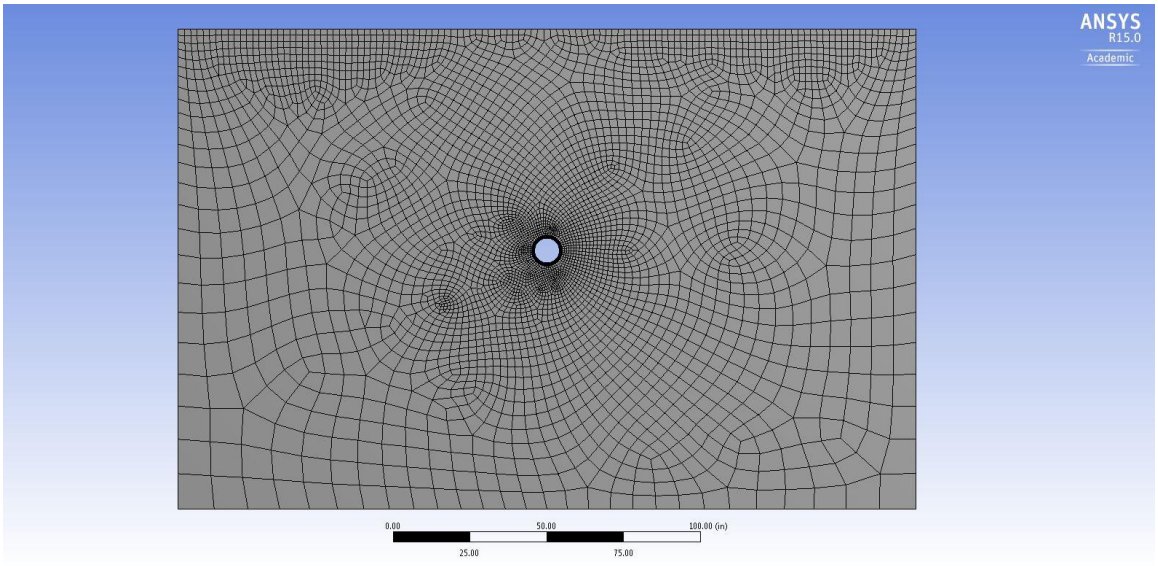


Figure 108: Mesh sizing for the 2-D ANSYS validation of the 1-D above/below Green's Function solution method

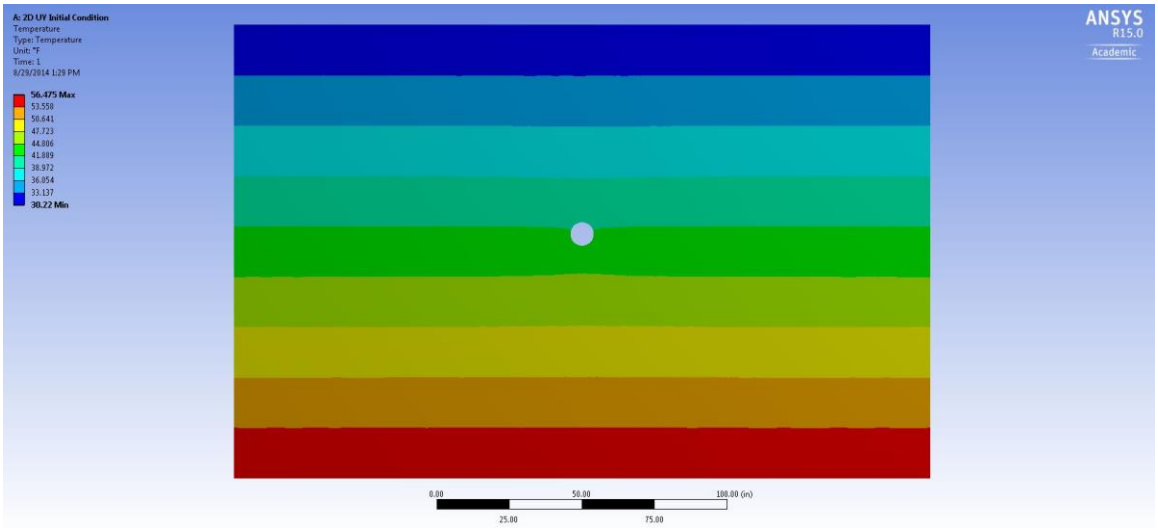


Figure 109: Initial condition for the 2-D ANSYS validation of the 1-D above/below Green's Function solution method

Figure 110 is a contour plot of the soil temperatures around the EAHX pipe after six hours of transient simulation. As shown, the temperature disturbance after the six hours extends less than a foot from the pipe. Vertical soil temperatures from the surface to a depth of 13 feet through the center of the EAHX were exported from ANSYS. This information is compared to the "above/below EAHX" GF method using the same boundary and initial conditions as described above. The results in Figure 111 show a noticeable difference between the ANSYS and GF simulations near the EAHX pipe. This difference is strongest in the above soil. The first few inches above the EAHX have temperature differences of approximately 2ºF. This difference significantly decreases as distance from the pipe increases. This indicates definite contribution from the lateral soil heat transfer. It is important to be aware of this contribution and decrease of accuracy in the GF method, but it is not significant enough to cease using the1-D GF method.

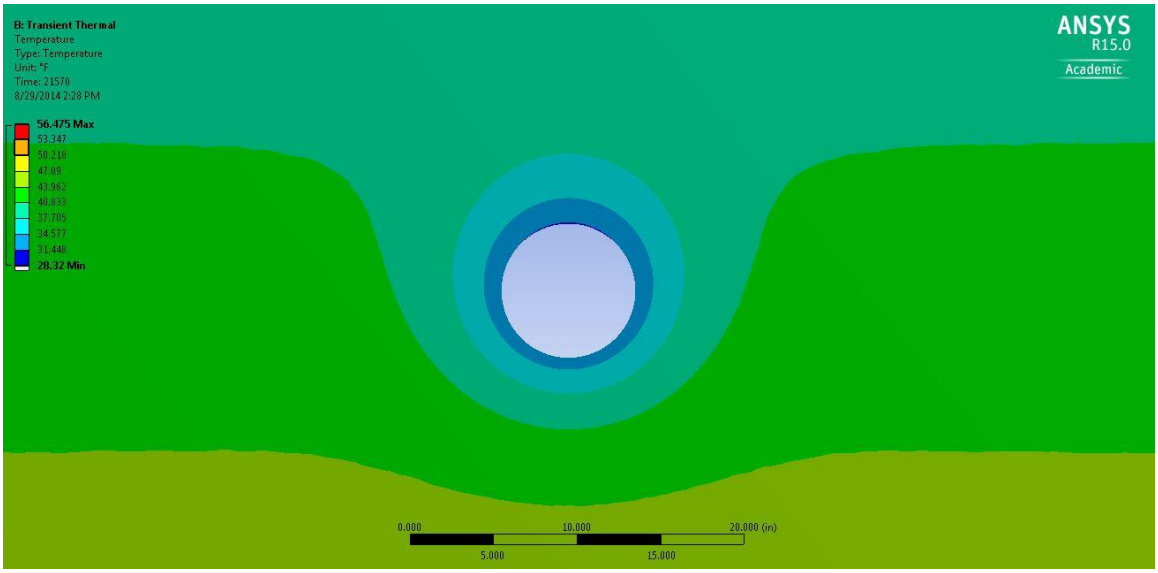


Figure 110: Results of 2-D ANSYS EAHX after six hours of operation using the domain and boundary conditions in Figure 107 and Table 25

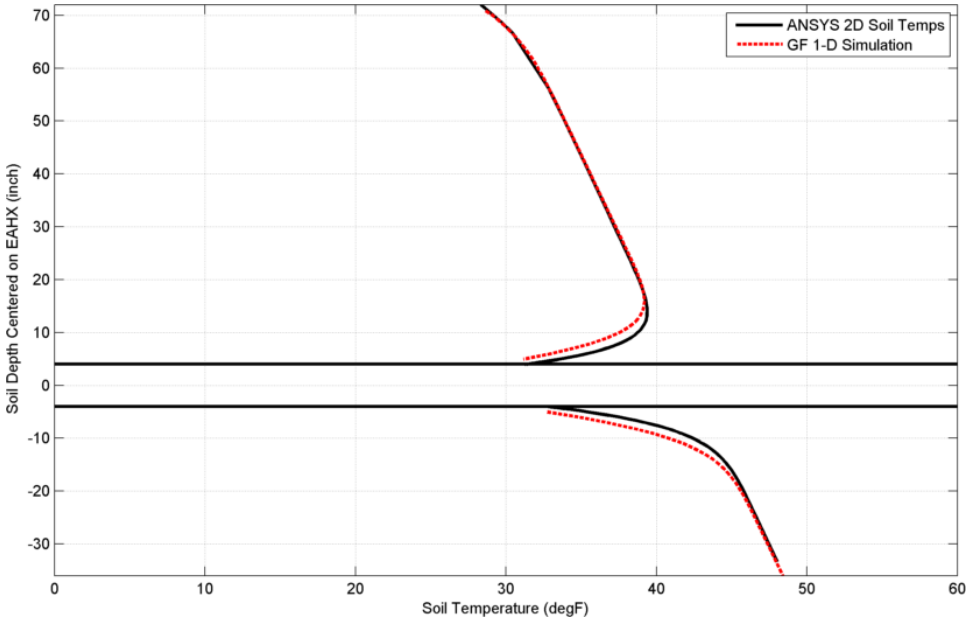


Figure 111: Validation of the "above/below EAHX" Green's Function method with a 2-D transient finite element simulation over a six hour time frame

Finite Difference Method for Transient Conduction Along Earth-Air Heat Exchangers

The "above/below" EAHX simulations from the previous section are only representative of the soil near the EAHX entrance. This is due to using the current outdoor temperature as the inlet temperature into the EAHX. It is possible to use this one air temperature to find the convective heat transfer through the entire EAHX length, but would be a worst case design scenario. In actuality, the pipe surface temperature along the EAHX is not constant. The next step to expand the "above/below" EAHX method is a finite difference approach that couples with convective internal flow. The remainder of this chapter proposes a finite difference approach to quickly and accurately determine the soil temperature distribution and air temperatures along the EAHX pipe.

Basis of the Finite Difference Method

The proposed GF finite difference method is similar to other finite difference methods in that it breaks up the EAHX pipe and surrounding soil into smaller length and time sub-sections that solve in a step-wise process. It is different in that the fundamental partial differential equations are not explicitly discretized. The finite difference process splits the soil and air into two heat transfer zones that are coupled through the pipe surface temperature. The first process determines the soil conduction surrounding the EAHX pipe. This is done with the "above/below EAHX" method outlined in the previous section. The pipe surface temperature from the first step then transfers to the second zone to find the convective heat transfer of the air flowing through the EAHX pipe. This is done using the Nusselt Number correlations for turbulent internal flow. The

Nusselt Number is found with the Gnielinski correlation in Equation (18). The method assumes a constant pipe surface temperature to solve the energy balance over each length sub-section. Integration of the energy balance yields Equation (11) to solve for the air outlet temperature from each length sub-section.

An example best illustrates the solution procedure. Figure 112 displays the first three time steps in the finite difference method. Note Figure 112 is only displaying the soil above the EAHX. The soil below the EAHX follows the same process, but is left out currently to simplify the figure. The first step breaks the length of the EAHX into sub-sections of length ΔL. This is similar to creating finite difference nodes along the EAHX. The pipe length in Figure 112 is split into six sections labeled at the bottom of the figure. The length sub-sections represent individual 1-D columns of soil that solve in step-wise process. These soil columns are independent of each other, and no axial heat transfer takes place. A time step is also chosen at this point. The time step represents the time range in the GF soil conduction solution. The convective internal flow in Equation (11) is time independent. For simplicity in this example, the time step is one.

The simulation requires a soil initial condition from the surface to a depth of 20 feet before the finite difference solution can proceed. This is found using the GF soil temperature methods as outlined in the "above/below EAHX" simulation section. The initial condition is represented at $\Delta t = 1$ in Figure 112 by the dashed lines running from the surface to the EAHX pipe. The lines increase in temperature as they move from left to right. For example, a vertical line represents the soil is all the same temperature. The current lines represent a colder temperature at the surface that increases with depth. So

the example in Figure 112 takes place during the heating season. Each soil column separated by the vertical dotted lines creates individual figures similar to Figure 104 through Figure 106. The soil temperature lines at $\Delta t = 1$ in Figure 112 are all the same angle because this represents the initial soil temperature condition.

The GF finite difference method is now ready to proceed. At the start of $\Delta t = 1$, outdoor air enters the EAHX at some temperature T_{in}. Typical Meteorological Year (TMY) for a specific location and time determines the T_{in} inlet temperature. The "above/below EAHX" GF method then calculates the heat transfer from the inlet air to the soil in section 1 during the duration of time step Δt. This results in a new soil temperature distribution around the EAHX that is saved as a data file. The new temperature distribution in section 1 does not appear in Figure 112 until the next time step, $\Delta t = 2$. After the "above/below EAHX" soil conduction completes its integration for the first time range, the finite difference method records the soil temperature in proximity to the EAHX (typically at half an inch). This is assumed to be a close representation of the actual pipe surface temperature. The pipe surface temperature is then transferred to the coupled convective internal flow heat transfer solution.

The next step determines the temperature T_1 coming out of length section 1. Equation (11) is solved for T_{out} based on the inlet temperature T_{in}, and the pipe surface temperature passed down from the previous step. The outlet temperature T_1 from section is now the new inlet temperature into length section 2. The same process described above repeats for section 2, 3, and so on until section 6 where air exits the EAHX at

outlet temperature T_{out}. Note that this is all occurring during the first time step. The simulation integrates the entire length before moving onto the next time step.

The key to the GF finite difference method is the passing of initial condition information from one time step to the other. At the start of time step $\Delta t = 2$, the soil temperature distributions from the previous time step load into the next GF soil conduction simulations as initial conditions. This would not be possible without representing the temperature distributions as piece-wise functions like the example in Figure 101. This allows for numeric integration to solve the space integration in Equation (91), Equation (99), and Equation (103). Notice in the second time step that the initial conditions in section 1 and 2 are now showing temperature decreases around the EAHX. The finite difference approach repeats at the second time step with a new inlet temperature T_{in}. This time though, the pipe surface temperature in section 1 and 2 will be lower than the previous step. The resulting soil temperature distributions in the second time step then pass to the third as ICs. The time steps keep repeating until Δt equals the final simulation time. This finite difference approach allows for a more accurate soil temperature distribution along the axial EAHX axis, and a more accurate outlet temperature with time.

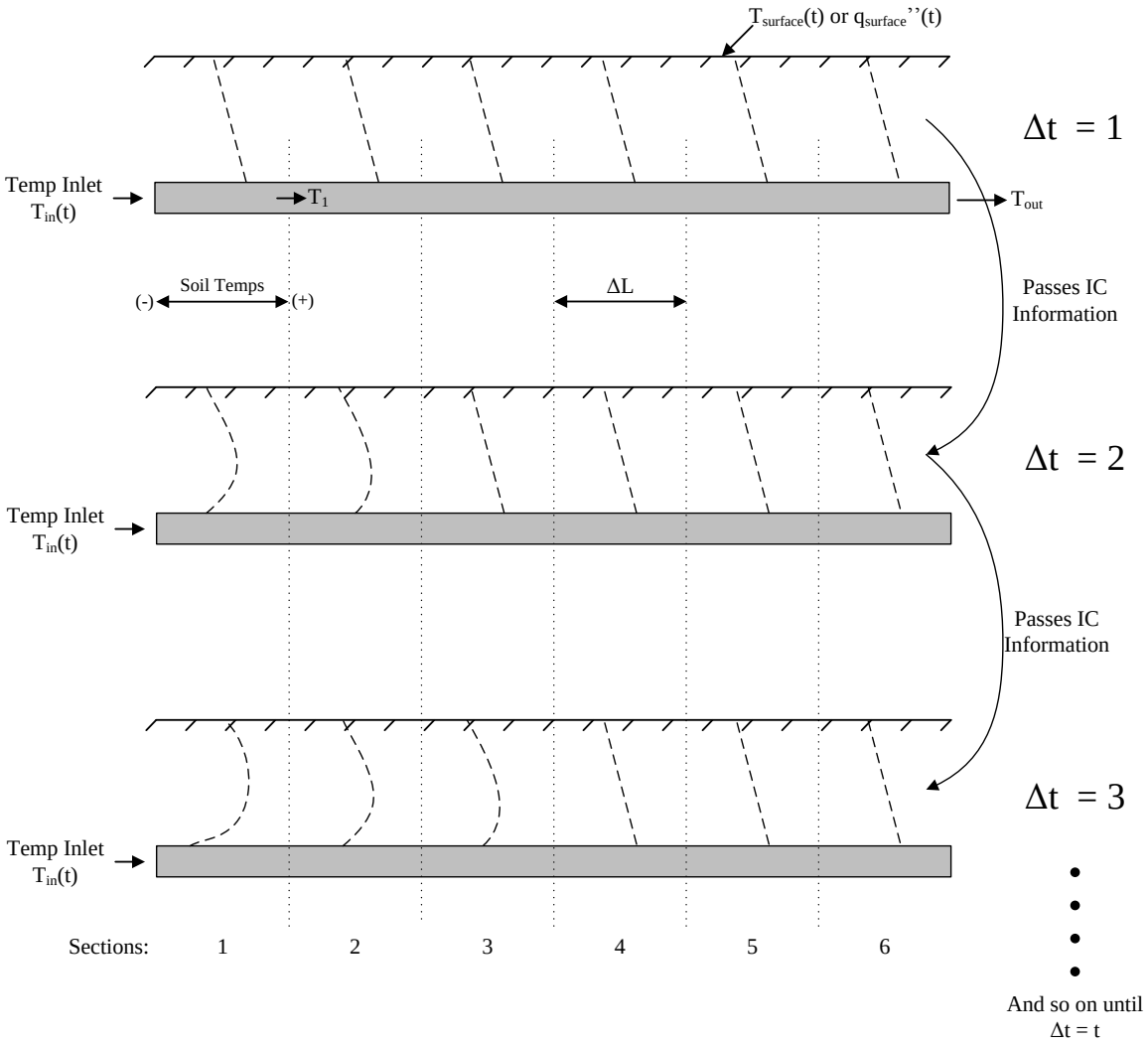


Figure 112: Green's Function finite difference method example

Time and Length Sub-Section Analysis

Two unknowns from the above finite difference approach are the size of the length sections and time steps. Both factors will impact the soil conduction and air convection. Figure 113 is the simulation results for air temperature along the EAHX pipe, and Figure 114 is the pipe surface temperature along the EAHX. Note the x-axis in both figures represents the axial distance from the inlet to outlet of the EAHX. The two

figures are not meant to show individual trends, but rather how groups of variables behave. These simulations use a 100 foot UY EAHX in Bozeman, Montana running from midnight to 6:00 AM. There are 64 individual simulations in each figure; one for each combination of 15, 30, 45, and 60 minute time steps and length sections from 0.25ft to 4ft in 0.25 foot increments.

Four separate groups are clearly visible. The groups are easier to see in Figure 114 for the pipe surface temperature which has four even splits. The four groups represent the four time steps of 15, 30, 45, and 60 minutes. The length increment has little effect on the solution results since all the length simulations for the same time step group together. The more influential variable is the time step. Figure 113 though shows these four time steps group relatively close together for the air temperature along the EAHX with only a degree difference between the 15 and 60 minute time steps at the outlet.

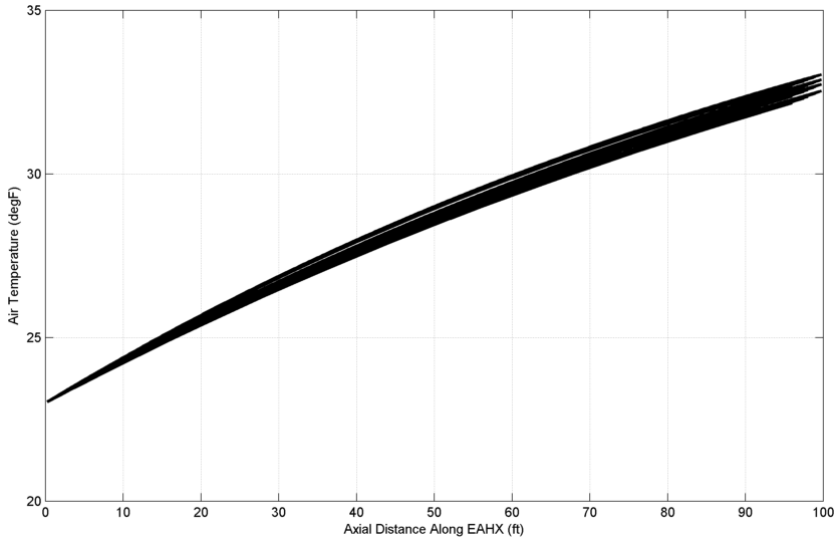


Figure 113: Air temperature along a 100 foot EAHX for time steps of 15 minutes to 60 minutes in 15 minute increments, and length steps of 0.25 feet to 4 feet in 0.25 foot increments located in Bozeman, MT from January 1st, 12:00 AM to 6:00 AM

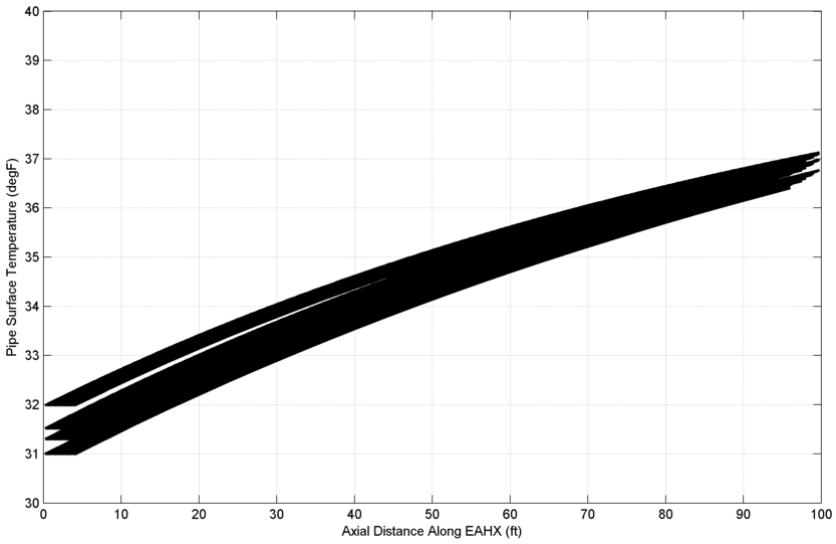


Figure 114: Pipe surface temperature along a 100 foot EAHX for time steps of 15 minutes to 60 minutes in 15 minute increments, and length steps of 0.25 feet to 4 feet in 0.25 foot increments located in Bozeman, MT from January 1st, 12:00 AM to 6:00 AM

Since time steps are the most influential variable in the finite difference method, the next round of simulations investigates time steps of less than 20 minutes. The results are surprising as shown in Figure 115. A plausible assumption is the one minute time step would have the best resolution and accuracy. Actually, it has an unrealistic result since the pipe surface temperature at the start of the simulation is less than 42°F. Time steps of two and three minutes are also further away from where the rest of the time step results converge. In Figure 115, the 10, 15, and 20 minute time step traces are overlaid. This suggests that the proposed finite difference method experience errors with time steps of five minutes or less. The evaluation of the pipe surface temperature, or more specifically the location in the soil domain where the pipe surface temperature is evaluated, causes the small time step errors. The following section investigates pipe surface evaluation locations, and its effect on accuracy during a computational fluid dynamics validation.

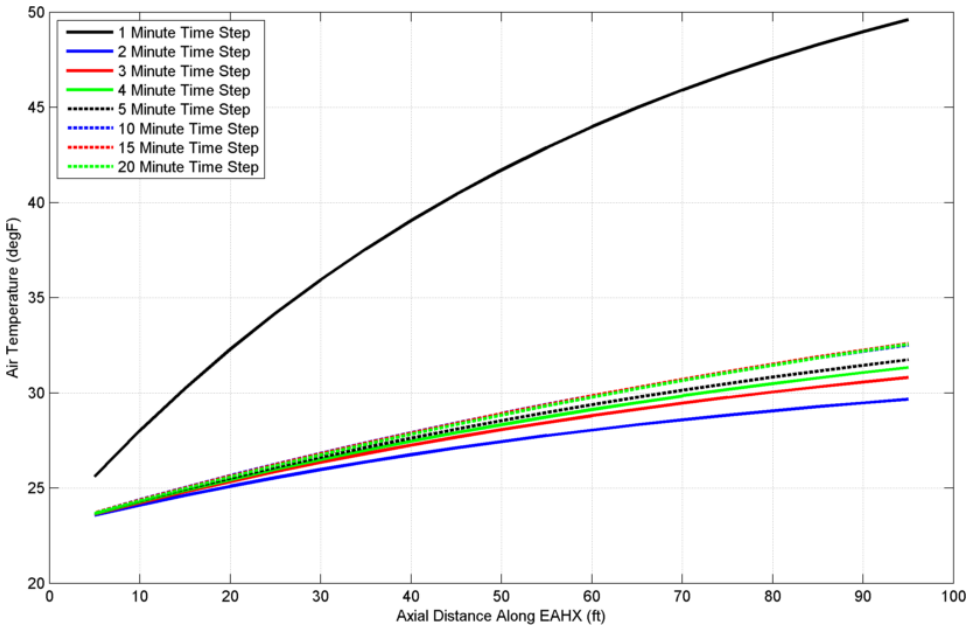


Figure 115: Air temperature along a 100 foot EAHX located in Bozeman, MT from January 1st, 12:00 AM to 6:00 AM for time steps ranging from 1 to 20

Validation with Computation Fluid Dynamics

This section validates the finite difference method and its assumptions with computation fluid dynamics (CFD) software before its use in an EAHX application. The CFD model in CD-adapco's Star-CCM+ software uses coupled convection and conduction to simulate heat transfer to the soil. Figure 116 is the simplified model setup for this validation. It consists of a soil cylinder eight feet in diameter and 50 feet long. In the center of this cylinder is an eight inch diameter hole that represents the EAHX. The outside surface of the soil cylinder is kept at a constant 60ºF. The ends of the cylinder are both thermally insulated. Air enters the EAHX portion at a speed of 1000 ft/min. The air is at a constant 30ºF for the first two hours of the test, and 0ºF for the following two hours. The boundary conditions for each hour are summarized in Table 26. The transient simulation is four hours long in total. Average air and pipe surface temperatures are

taken every five feet along the cylinder. The EAHX finite difference method replicates this simplified EAHX by using the above UY formulation above and below the EAHX. This in essence creates a plane wall that has a length of eight feet, and an EAHX running through the middle.

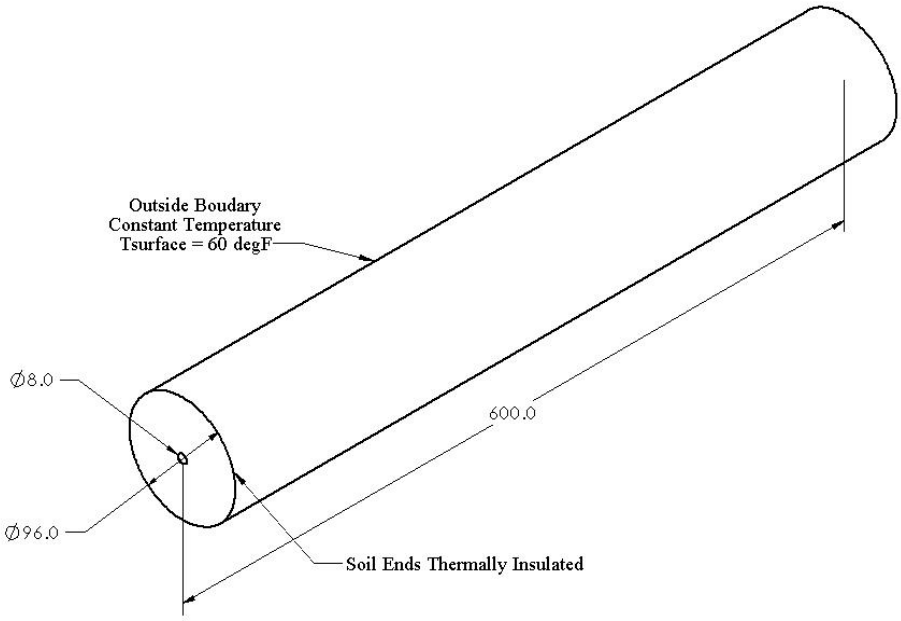


Figure 116: Simplifed EAHX for the computational fludi dynamics validation of the finite difference method and its assumptions (all dimensions in inches)

Table 26: Boundary condition temperatures for validation of the simplified EAHX

Hour	1	2	3	4
Air Inlet	30	30	0	0
Soil Surface	60	60	60	60

Figure 117 displays the mesh for this simulation model from Star-CCM+. The mesh was kept rather coarse at the air-soil interface to help speed the results of the transient simulation. This mesh at the boundary is not fine enough to exactly capture the

viscous boundary layer along the pipe wall, which defines the convective heat transfer coefficient (CHTC). The Star-CCM+ software estimates the boundary layer in a coarse mesh through an All Y+ model. In short, Y+ is a measure of the distance between the wall and the centroid of the first adjacent cell, evaluated as a function of the velocity field [83]. In other words, it is a good measure of how well the CFD software estimates the boundary layer. The All Y+ model requires a Y+ value greater than 30 and less than 60, but values up to 200 to 300 are also acceptable. The average Y+ for this model is 62.5 which is just outside the high bounds. To verify the All Y+ is still accurate, a Low Y+ steady-state model was conducted using the same simulation setup. This resulted in an average Y+ value of 1.9. This model produced almost the exact same results as the All Y+ steady-state model (less than 0.1ºF difference in air temperature). In conclusion, the All Y+ model with a coarse mesh accurately estimates the boundary layer and CHTC.

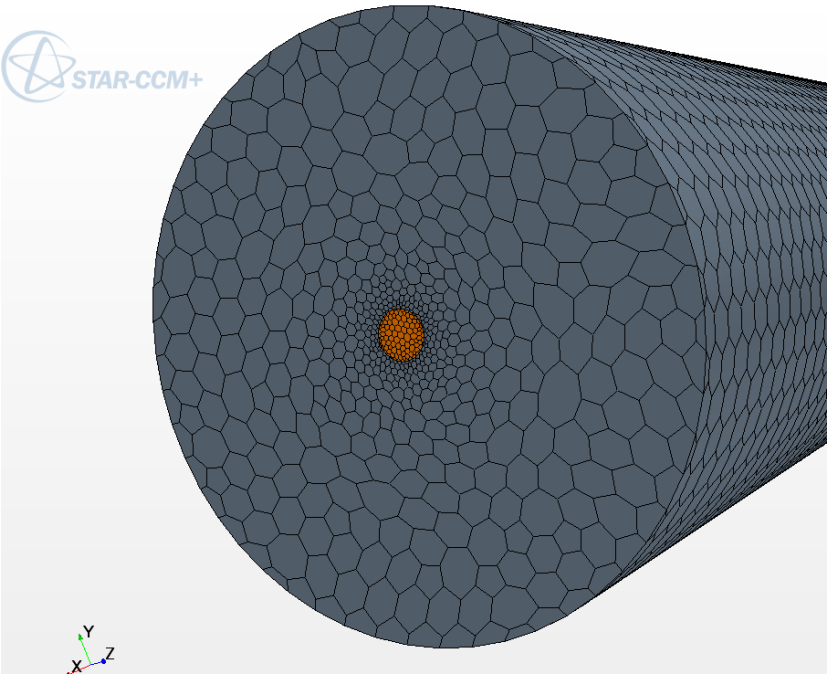


Figure 117: Polyhedral mesh for the finite difference method validation

Transient Validation. There is good agreement between the transient CFD results and the GF finite difference method. Figure 118 through Figure 121 show the comparison between the two simulations for air temperatures along the 50 foot EAHX at hours one, two, three, and four of the simulation. The results are very close at each five foot increment along the EAHX. The true test of the GF finite difference method is at the end of hour two when the inlet air temperature changes from 30ºF to 0ºF (see Table 26). Figure 120 is the air temperatures at the end of hour three, and the GF finite difference method correctly adjusts to the change in inlet temperature. These results confirm the power of passing piece-wise initial conditions between solution time iterations (see Figure 112). These ICs can become quite complex looking functions, but these results prove it is accurate to break the functions into small segments for the numerical integration.

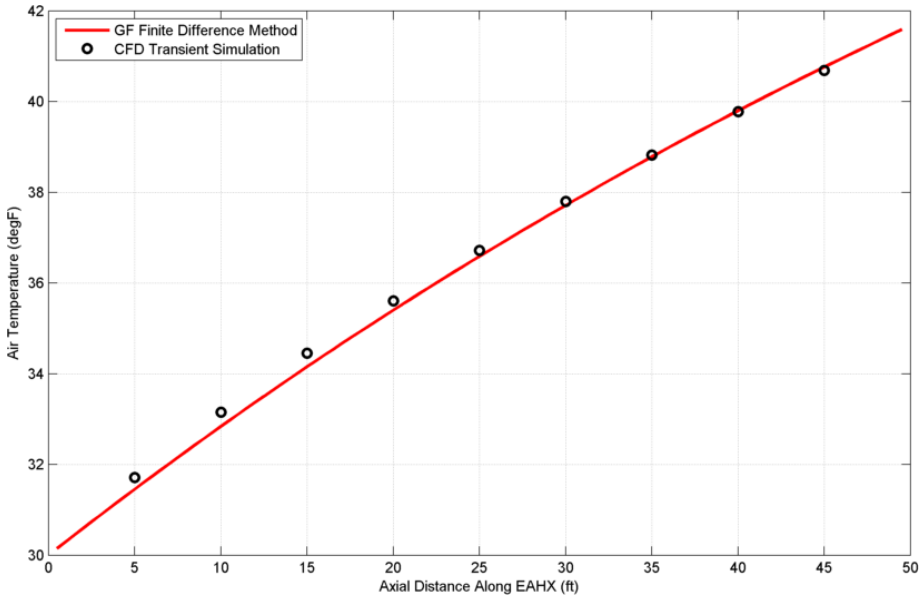


Figure 118: Air temperatures along the simplified 50 foot EAHX one hour into the four hour transient validation, CFD results compared to the EAHX finite difference method using a 20 minute time step

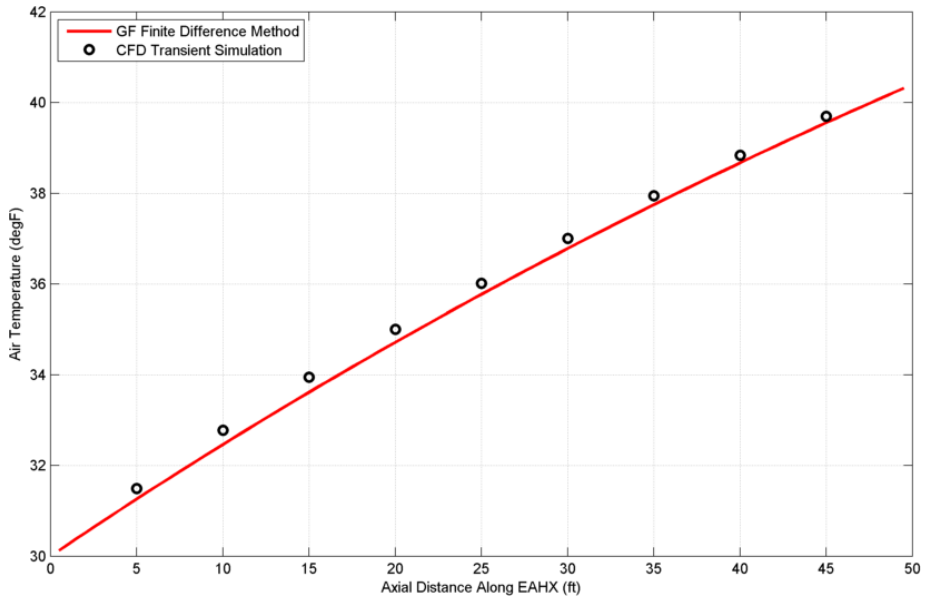


Figure 119: Air temperatures along the simplified 50 foot EAHX two hours into the four hour transient validation, CFD results compared to the EAHX finite difference method using a 20 minute time step

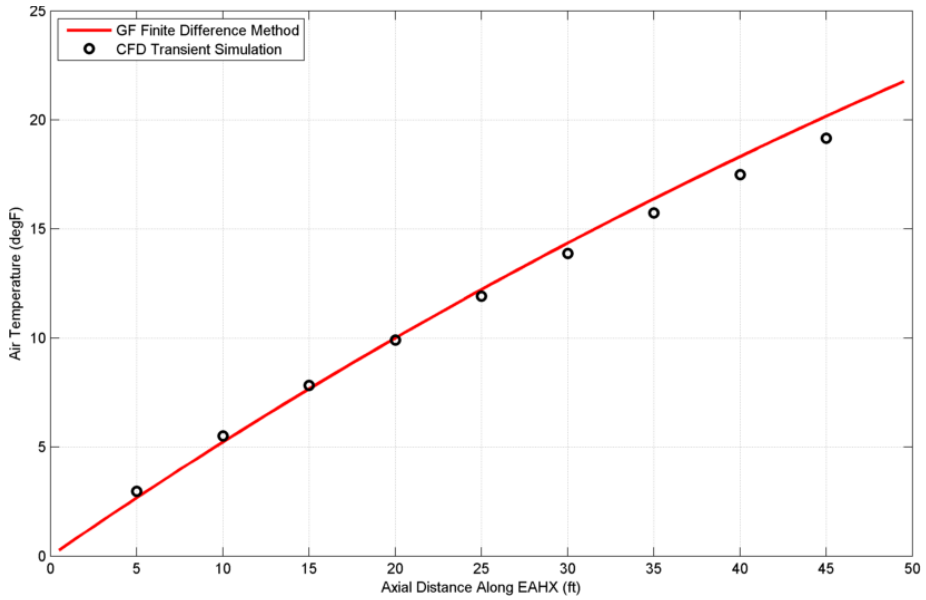


Figure 120: Air temperatures along the simplified 50 foot EAHX three hours into the four hour transient validation, CFD results compared to the EAHX finite difference method using a 20 minute time step

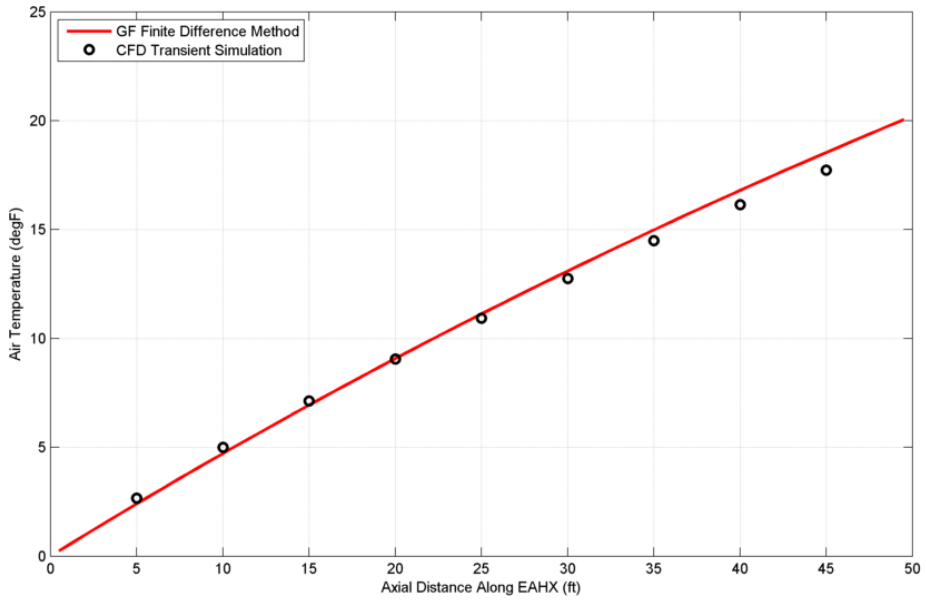


Figure 121: Air temperatures along the simplified 50 foot EAHX four hours into the four hour transient validation, CFD results compared to the EAHX finite difference method using a 20 minute time step

The air temperatures passing through the EAHX pipe have good agreement with the CFD model, but it is also important to verify the soil conduction surrounding the EAHX is in good agreement as well. Figure 122 and Figure 123 investigate this at the end of hours two and four at the midpoint of the 50 foot EAHX. The results again are in very close agreement. Notice in Figure 122 the last data point before the pipe surface forms a vertical line. The GF method cannot evaluate the pipe surface temperature, so the simulation uses the temperature ½ inch from the pipe surface instead. The 20 minute iteration time step for the finite difference method and the ½ inch reference location for the pipe surface temperature are a combination that work well for common soil and air thermal properties. The combination of these two values was not arbitrarily chosen. A different reference location, such as one inch, will require a larger iteration time step.

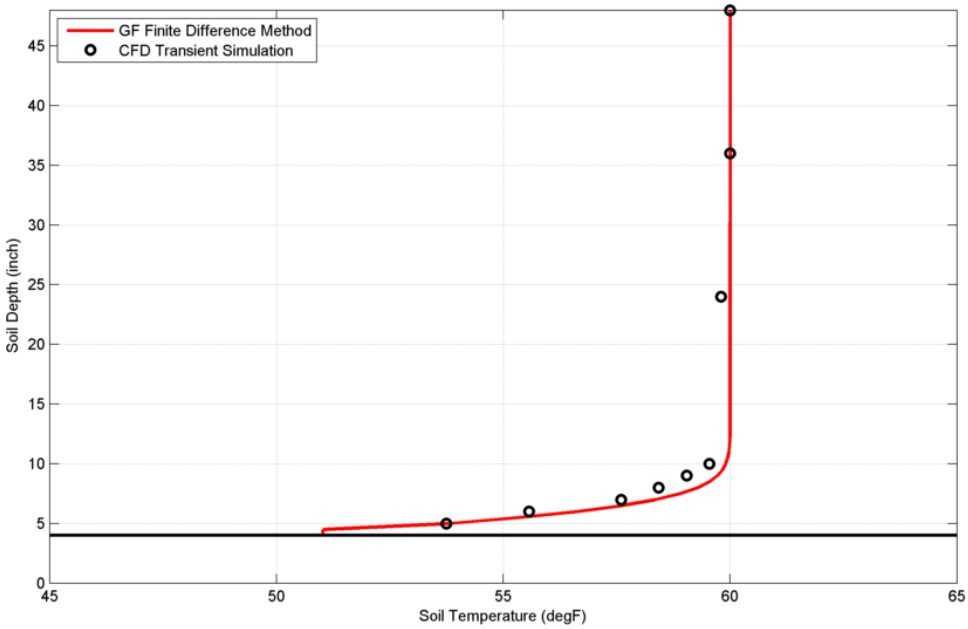


Figure 122: Soil temperatures at the midpoint of the simplified 50 foot EAHX two hours into the four hour transient simulation using the EAHX finite difference method with 20 minute time step, compared to the CFD soil temperatures

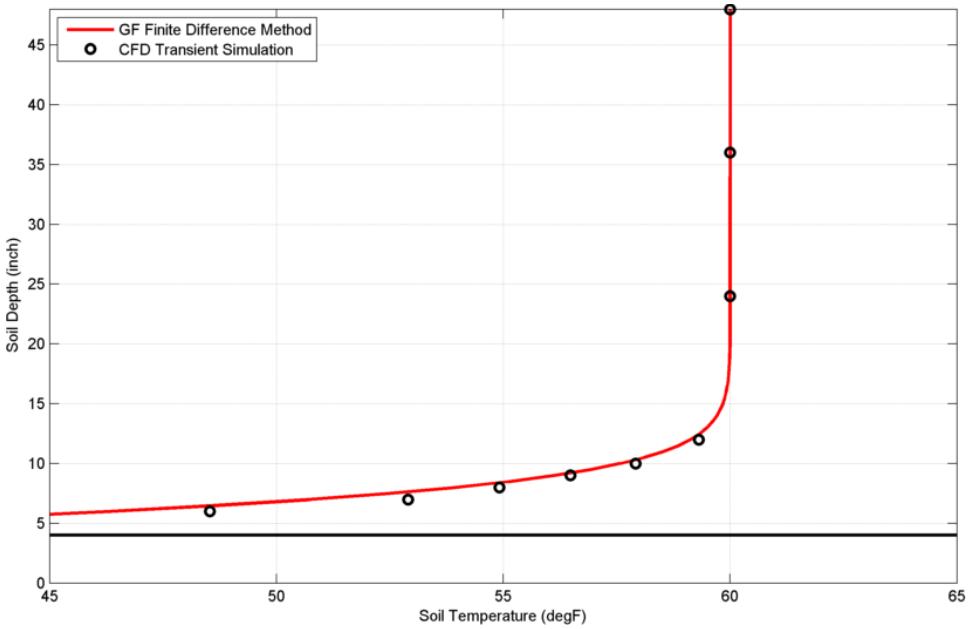


Figure 123: Soil temperatures at the midpoint of the simplified 50 foot EAHX four hours into the four hour transient simulation using the EAHX finite difference method with 20 minute time step, compared to the CFD soil temperatures

Choice of Pipe Surface Temperature Location. The GF finite difference method determines the pipe surface temperature after the soil conduction iteration at a reference position in the soil. This reference position is typically less than an inch from the EAHX pipe. Recall that GFs are not mathematically well behaved near boundaries, and in some cases not defined on the boundary itself. This is why using soil temperatures of less than half an inch yield unrealistic pipe surface temperatures. One important consequence of this reference location is that the time frame for the soil conduction iteration must be long enough for the heat transfer to reach that location. If the time step for the iteration is too short, the soil at the reference location will never change temperature.

Figure 124 shows the resulting pipe surface temperature two hours into the four hour CFD simulation using a 5 minute and 20 minute time steps at a reference distance of 1 and ½ inch. The pipe surface temperature at 1 inch and 5 minute time step has not changed after two hours of operation. This indicates the heat transfer from the air does not reach one inch into the soil after the five minute time step. This causes consistently higher pipe surface temperatures in the convective flow calculation as well. This is evident in Figure 115 where the smaller time steps have unrealistically high air temperatures. The air temperatures are so high because the pipe surface never cools during the simulation. The combination of the 20 minute time step with the one inch reference location still produces results that are too high. This implies there is a relationship between reference location, time step size, soil thermal properties, and air convection rates. For the current research, the ½ inch reference location and 20 minute

time step is acceptable, but further understanding this relationship is a point of future research.

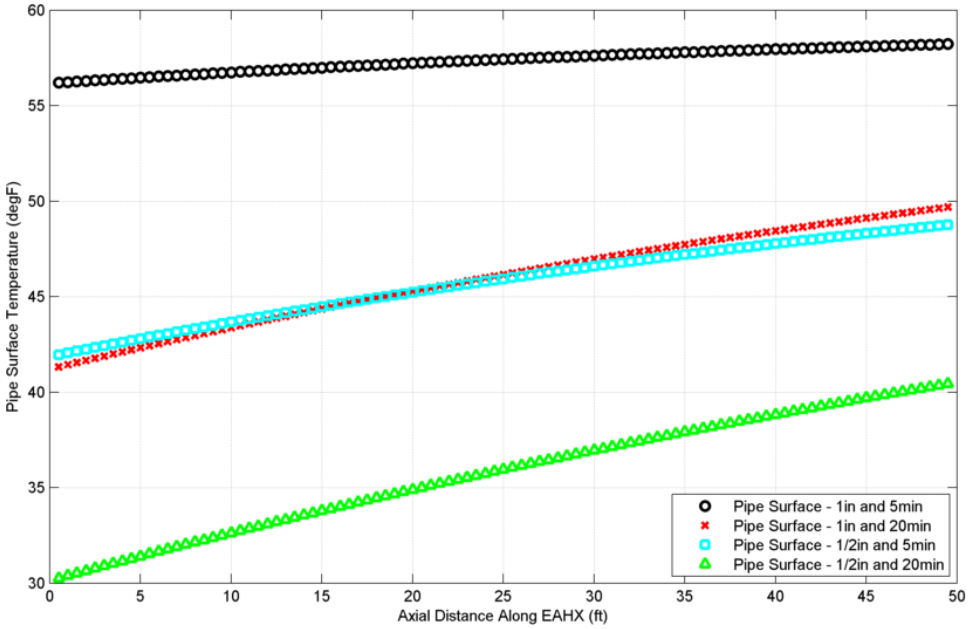


Figure 124: Comparison of pipe surface temperature during 5 and 20 minute time steps where the reference temperature is taken 1 inch and ½ inch from the pipe surface, two hours into the four hour CFD validation simulation

Conclusion to Computation Fluid Dynamics Validation. The above CFD simulation successfully validates of the GF finite difference method using the simplified EAHX setup in Figure 116. The agreement between the two models is very good, and the CFD model is deemed to be of high accuracy using the Star-CCM+ software's All Y+ model. An iteration time step and pipe surface temperature reference location of 20 minutes and ½ inches provides the most accurate results for the soil to air heat transfer. The following GF finite difference simulations in this research use these two values. These two values are subject to change in different EAHX situations, but are sufficient

for the limited realistic range of soil thermal properties, EAHX dimensions, and air thermal/flow properties.

Computational Time

Advantages of Finite Difference Method

The finite difference method uses a combination of GF solutions with convective internal flow correlations. This same problem could be solved using a more traditional finite difference method, which discretizes the fundamental partial differential equations, or with CFD as in the previous validation. Several authors use these approaches in literature. Each of the three approaches has its advantages. Traditional finite difference and CFD are more accurate that the GF finite difference method, but are far more computationally intensive. The main reason for this comes from how the GF finite difference method's determines its initial condition.

The GF finite difference method starts by solving for the initial soil temperatures using the Base Solution Generation technique. The Base Solution Generation technique uses a database of pre-calculated values to integrate several hundred day simulations over the course of minutes. A more traditional finite difference method or CFD would take an extended amount time (hours to days) to complete this same hundred day simulation. This is where the GF finite difference method has its main advantage. Even without the initial condition calculation, the GF finite difference method is still faster in its calculations that the other two methods. For example, the previous CFD validation used a 50 foot EAHX that considered the soil conduction for approximately four feet in each direction. This CFD simulation used a coarse mesh but still took between 36-48 hours to

complete. In comparison, the GF finite difference was able to complete the same simulation in approximately 15 minutes on the same computer. A traditional finite difference method simulation was not completed in this research, but it is also expected to take longer than the GF finite difference method. The GF method has a clear advantage in computation time without a noticeable decrease in accuracy.

Example Optimization of Green's Function Finite Difference Method

An optimization example best demonstrates the power of the finite difference Green's Function method. This optimization is meant to demonstrate the utility of the GF finite difference method; other optimizations are possible. In this example, a program optimizes the length of the EAHXs so the system is 95% efficient with respect to the undisturbed soil temperature according to Equation (20). This optimization is for cooling purpose only, and it takes place on the warmest day of the year in all 15 locations of interest. The optimization program performs the same analysis in the UY, non-radiant US, and radiant US installations. This leads to the best installation type (UY vs. US) for cooling purposes in all 15 locations. The EAHX in this program is eight inches in diameter and has an air velocity of 1000 ft/min. The soil uses a diffusivity of 0.6 ft^2/day and conductivity 0.75 Btu/hr·ft·ºF. The EAHX operates for two hours continuously before calculating the effectiveness. The EAHX inlet air temperature comes from the warmest day according to the TMY data files at the times of 12:00 PM to 2:00 PM. The UY simulations use the NRCS data files at the same time for the soil surface temperature.

The optimization uses the warmest part of the year for a worst case design scenario in cooling. Naturally though with different weather conditions in each location a comparison is difficult. For example, in Bozeman, Montana the air temperature is not as high as in Houston, Texas in the summer, and it should have a smaller EAHX length. Different installation types (UY vs. US) in the same location also may have deceiving length results. To aid in the comparison, the optimization also calculates the total heat transfer (Btu/hr), and the heat transfer per unit length of EAHX pipe (Btu/hr·ft). The convective energy balance in Equation (10) calculates the total heat transfer based on inlet and outlet temperatures. This information is also useful for designers who are probably most interested in the heat transfer per unit length.

Optimization Method

The optimization is based off the Newton-Raphson method for finding function roots. The Newton-Raphson extends a tangent from an initial guess, and where the tangent crosses the x-axis is an improved estimate of the actual root. This process repeats until it reaches the acceptable amount of error [84]. The proposed optimization method is similar, except the tangent forms from two initial length guesses spaced five feet apart as shown in Figure 125. A line formed from the effectiveness values at these two lengths calculates a new length based on the intercept at 95% effectiveness. Five feet is added to the new length and the process repeats until it brackets the 95%.

This method is efficient because the effectiveness change with length in all locations and for each EAHX type will look similar to Figure 125. The effectiveness starts at a zero and then increases almost linearly until it starts to level off to 100 %

effectiveness. Since this line is near linear, the two initial guesses at L_1 and L_1 plus five feet form a straight line that nearly intercepts the correct length and leads to a fast convergence. The current optimizations reached 95±0.1% effectiveness in four iterations (eight simulations total).

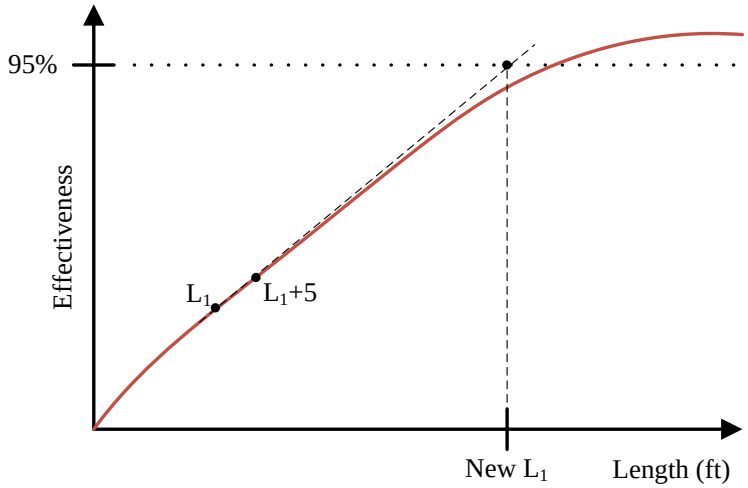


Figure 125: Optimization procedure based off the Newton-Raphson method

Optimization Results and Comparison

Table 27, Table 28, and Table 29 list the results of the optimization for the UY, non-radiant US, and radiant US respectively. All optimization effectiveness were within plus/minus 0.1% of 95%. The heat transfer and heat transfer per unit length are all negative since the air is cooling. The results are easier to visualize in Figure 126, Figure 127, and Figure 128. Figure 126 is the EAHX length results for all 15 locations and three installation types. Figure 127 and Figure 128 are similar except for displaying the total heat transfer and heat transfer per unit length respectively.

Table 27: Optimization results for the under yard earth-air heat exchangers

Location	Length (ft)	Heat Transfer (Btu/hr)	Heat Transfer per Unit Length (Btu/hr·ft)
Albuquerque, NM	205	-7431.6	-36.3
Amarillo, TX	194	-6412.6	-33.1
Athens, GA	189	-5651.3	-29.9
Bozeman, MT	222	-9804.8	-44.2
Columbus, OH	238	-12560.3	-52.8
Houston, TX	170	-4416.5	-26.0
Kansas City, MO	177	-4877.2	-27.6
Las Vegas, NV	238	-12475.5	-52.4
Moses Lake, WA	210	-7545.1	-35.9
Pine Bluff, AR	178	-4503.2	-25.3
Saint Cloud, MN	224	-10094.6	-45.1
Salt Lake City, UT	223	-9260.6	-41.5
Sioux Falls, SD	201	-6544.5	-32.6
State College, PA	-	-	-
Tallahassee, FL	197	-6691.6	-34.0

Table 28: Optimization results for the non-radiant slab earth-air heat exchangers

Location	Length (ft)	Heat Transfer (Btu/hr)	Heat Transfer per Unit Length (Btu/hr·ft)
Albuquerque, NM	221	-9117.2	-41.3
Amarillo, TX	207	-7437.1	-35.9
Athens, GA	212	-7429.2	-35.0
Bozeman, MT	214	-8105.8	-37.9
Columbus, OH	227	-9749.6	-42.9
Houston, TX	214	-7801.0	-36.5
Kansas City, MO	168	-4004.6	-23.8
Las Vegas, NV	243	-12942.2	-53.3
Moses Lake, WA	221	-8646.8	-39.1
Pine Bluff, AR	209	-6837.9	-32.7
Saint Cloud, MN	202	-6762.7	-33.5
Salt Lake City, UT	228	-9771.1	-42.9
Sioux Falls, SD	187	-5059.0	-27.1
State College, PA	176	-4373.5	-24.8
Tallahassee, FL	229	-10065.2	-44.0

Table 29: Optimization results for the radiant-slab earth-air heat exchangers

Location	Length (ft)	Heat Transfer (Btu/hr)	Heat Transfer per Unit Length (Btu/hr·ft)
Albuquerque, NM	211	-9089.5	-43.1
Amarillo, TX	199	-7605.2	-38.2
Athens, GA	199	-7255.5	-36.5
Bozeman, MT	213	-8925.1	-41.9
Columbus, OH	222	-10248.4	-46.2
Houston, TX	199	-7411.4	-37.2
Kansas City, MO	161	-4220.1	-26.2
Las Vegas, NV	239	-13454.1	-56.3
Moses Lake, WA	216	-9151.5	-42.4
Pine Bluff, AR	196	-6693.5	-34.2
Saint Cloud, MN	204	-7675.2	-37.6
Salt Lake City, UT	223	-10222.1	-45.8
Sioux Falls, SD	189	-5854.6	-31.0
State College, PA	177	-5075.6	-28.7
Tallahassee, FL	216	-9698.7	-44.9

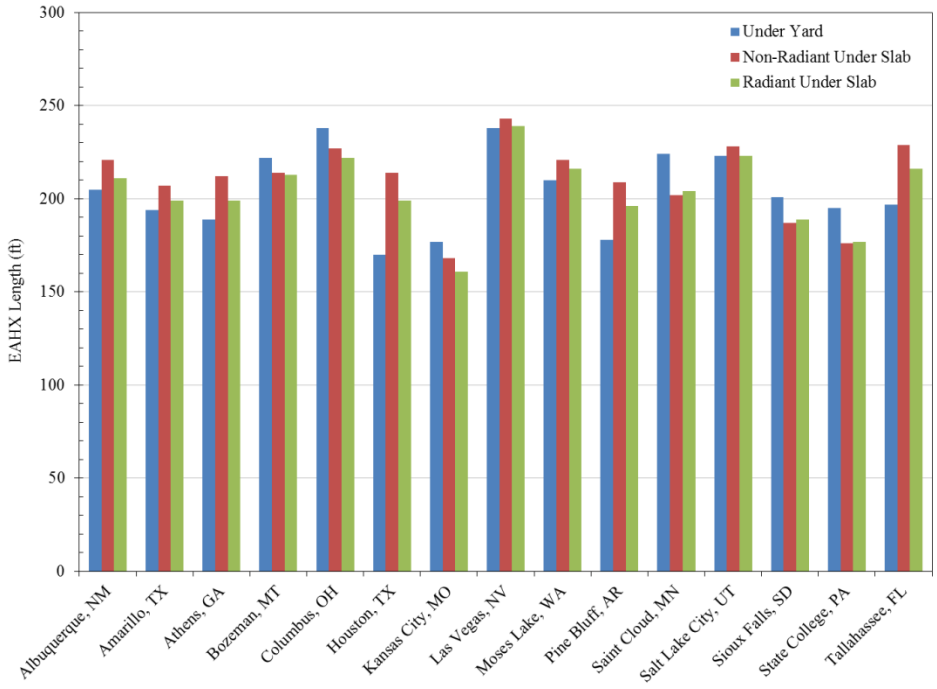


Figure 126: Optimized earth-air heat exchanger lengths for the under yard, non-radiant under slab, and radiant under slab installation locations

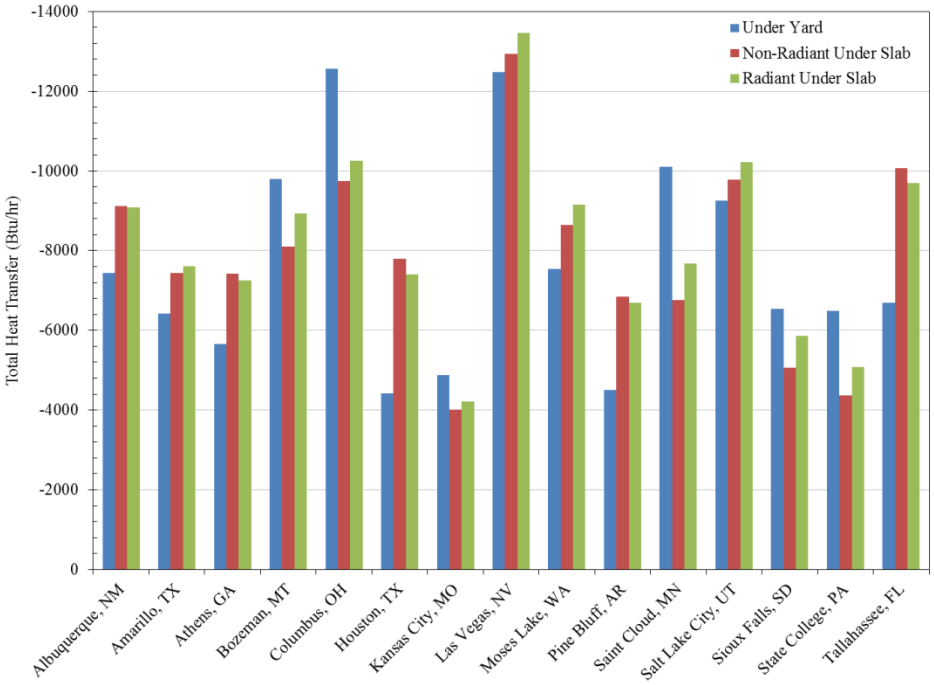


Figure 127: Total heat transfer in the optimized earth-air heat exchanger for the under yard, non-radiant under slab, and radiant under slab installation locations

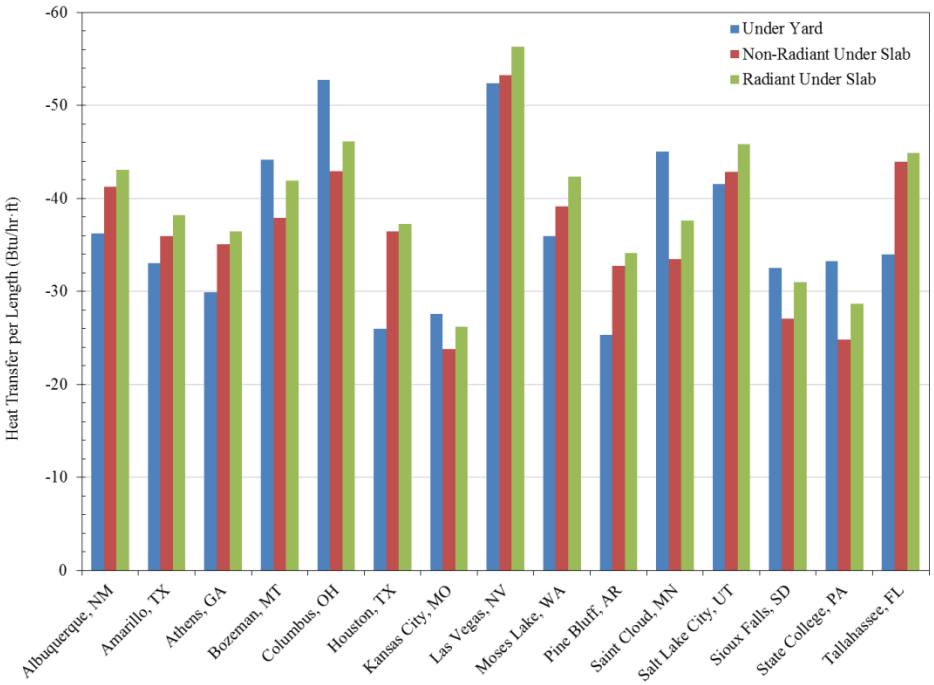


Figure 128: Heat transfer per unit length in the optimized earth-air heat exchanger for the under yard, non-radiant under slab, and radiant under slab installation locations

The results in the above figures reveal some interesting observations. The locations with a high number of heating degree days (HDDs), such as Albuquerque, New Mexico, Amarillo, Texas, Athens, Georgia, etc., call for shorter EAHX lengths in the UY location (Figure 126). The shorter lengths are not necessarily better though since the UY total heat transfer and heat transfer per unit length are less than the US installations. This is surprising because it was originally believed that a foundation slab would prevent the soil from losing heat to the surface during summer. Following this logic, the soil under the slab would always be at a higher temperature than the UY soil. This is not the case, and the opposite is true. The UY EAHX is the best choice in locations with a high number of heating degree days (HDDs), such as Bozeman, Montana, Columbus, Ohio, Kansas City, etc. The UY EAHX provides the highest total heat transfer and heat transfer per unit length in these instances.

Figure 129 explains why the UY EAHX is a better installation choice in locations with a high number of HDDs (Bozeman, Montana) when optimizing for cooling. This figure compares the air and pipe surface temperatures along the EAHX for the UY and non-radiant US installations in Bozeman, Montana. Both instances reach 95% effectiveness, but it is clear from the pipe surface temperature the UY has a much lower soil temperature than the US at this time of year. Recall the simulations take place during the hottest day in summer. The lower UY soil temperature allows for a higher total heat transfer over the longer length. Figure 130 is the same comparison for Houston, Texas which has a high number of CDDs. The US pipe surface temperature is this case is lower than the UY which yields a higher total heat transfer for cooling.

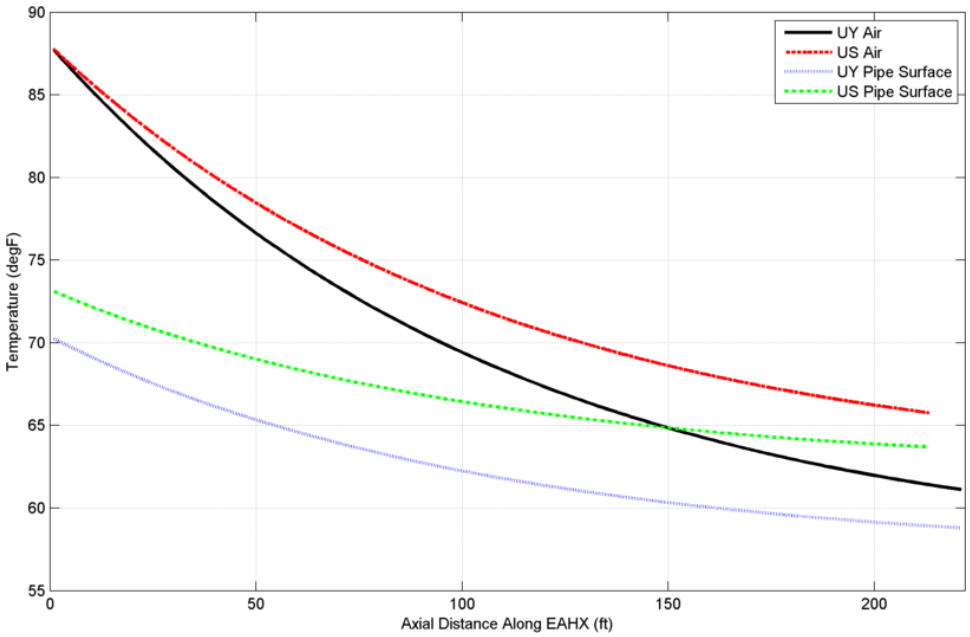


Figure 129: Comparison of the under yard and non-radiant under slab air temperature and pipe surface temperature along the optimized earth-air heat exchanger length in Bozeman, Montana

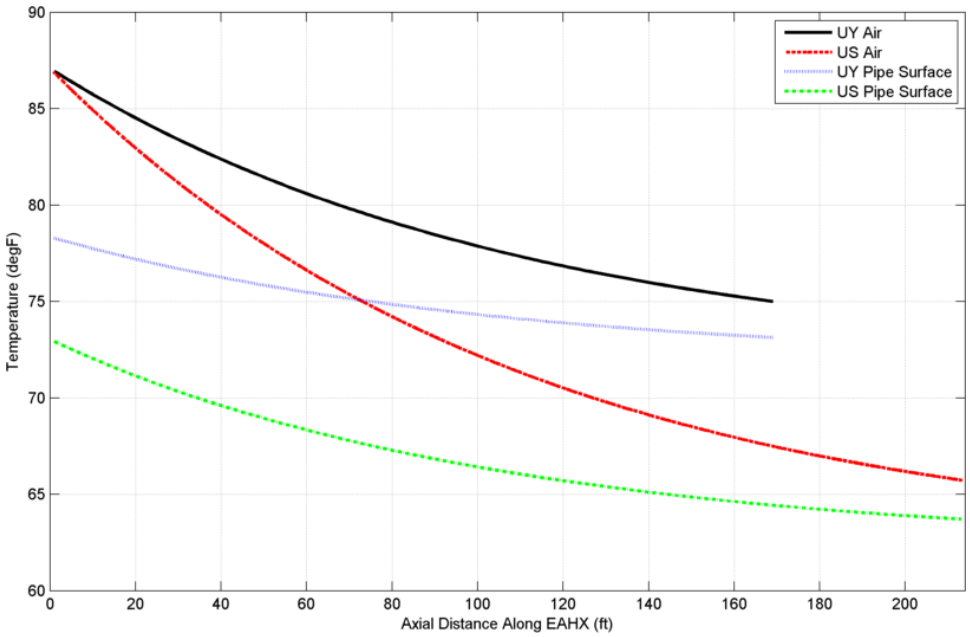


Figure 130: Comparison of the under yard and non-radiant under slab air temperature and pipe surface temperature along the optimized earth-air heat exchanger length in Houston, Texas

The foundation slab in a sense insulates the under slab soil, and causes the lower soil temperatures in locations with high CDDs values (Houston, Texas). The building is being actively cooled during the summer. This causes a low foundational heat loss, and in some cases a negative heat loss (heat flowing into building) as in Houston, Texas in Figure 344. The low or negative heat flow and the slab insulating the soil from the atmospheric air combine to cause low under slab temperatures. This is seen in Figure 91, which is the below slab soil temperature distribution for day 180, 270, and 360 for Houston, Texas. Day 180 and 270 have lower soil temperatures under the foundation than in the yard. Figures for the other locations in APPENDIX F with a high number of CDDs display similar results.

Other Optimization Applications

The above optimization for cooling is just one example of how the GF finite difference method for EAHXs is a powerful tool. A number of other optimizations are possible. The above process could be repeated for heating optimization. In a single location, the EAHX pipe diameter or air velocity can be optimized to maximize heat transfer. The same EAHX can be operated at different times in the year to understand how its performance will change. There are numerous possibilities which make this tool very exciting for future research.

CONCLUSION

This research set out to develop a robust model framework that was inclusive of all earth-air heat exchanger (EAHX) installations and design considerations. This framework would provide the means to conduct a fundamental study of EAHXs to aid in the generation of EAHX standards and design guides. The fundamental information includes common design parameters, heat transfer mechanisms in all installation types, effects of various climatic conditions, etc. There is currently no model available in the field that encompasses all these areas. Finite element analysis (FEA) and computation fluid dynamics (CFD) are one means to conduct this study, but they are far too time-intensive. For these reasons, this research expanded the work by Cucumo et al. [5] and pursued a quasi-analytical approach using the Green's Function (GF) method. This successfully resulted in a framework consisting of a long time solution to determine the UY or US initial temperature distribution. This distribution acts as an initial condition in the short time, finite difference method that calculates the heat transfer along the EAHX. The two solutions working together can quickly analyze most types of EAHXs, and has the potential for expansion past its current limitations.

The first step in an under yard (UY) or under slab (US) EAHX simulation determines the initial soil temperature distribution. This is the long time solution. These simulations are on an annual basis and cover long time ranges (several hundred days). To speed the numerical integration of large time ranges and space domains, this research developed a new method called the Base Solution Generation (BSG) technique. This method was well validated in the UY soils. The non-radiant US soil temperatures were found using

the GF method and flux based boundary conditions (BCs). This is a new approach for finding below slab temperatures since the majority of current literature is concerned with slab heat loss only. The non-radiant US method produced unrealistic results in some instances, but it is a promising and novel method for calculating the US soil temperatures. The long time soil temperature distributions act as the initial condition (IC) for the following short time finite difference method.

The short time finite difference method completes the goal of developing a transient model framework to find convective and conductive heat transfer along the EAHX. The mathematical nature of the GFs reveal that only recent air temperatures at the convective boundary condition (BC) affect the soil. In other words, the convective BC does not develop a heat transfer history that depends on air or soil temperatures several days in the past. The opposite surface boundary, whether the soil surface or foundation slab, does have this history. This is why it is appropriate to use the long time solutions as an IC in the finite difference method since these are the same boundaries. This method was validated with a CFD which was highly time intensive to finish (12 to 36 hours depending on simulation). The finite difference method on the other hand completed the same simulation in less than 15 minutes.

The long and short time solutions working together make it possible to include the majority of heat transfer mechanisms and design considerations for the UY, non-radiant US, and radiant US installation types. This model also functions in any geographical location, and can include time-dependent air and soil conditions. This is made possible by the two quasi-analytical GF solutions working together to quickly solve extended time

simulations over large domains. This model is not valid for all types of EAHXs or their operating conditions though, but it does however lay a framework for the inclusion of other factors through future work.

There are a number of impacts this research will have on the current field. First, it will provide a much needed model for US EAHXs that is currently not present in literature. Associated with the US EAHXs is a novel way to determine US slab soil temperatures using flux based BCs. It also identified that not all installation types (UY vs. US) are the same for a given location, and one is advantageous over the other. These are just a few impacts of many that represent fundamental EAHX information missing from the field. The most important impact comes in the form of an all-inclusive model framework covering the myriad of design variables and choices that can fill in this fundamental information. This framework is the first step. Through continued research, this method and framework will develop into the tool the industry needs to create standards and design guidelines for the improved utilization of earth-air heat exchangers.

FUTURE WORK

The non-radiant under slab (US) soil temperature distribution in some locations did not produce realistic results. As previously discussed, this is primarily attributed to a 2-D Green's Function (GF) solution instead of using three-dimensions. Foundation heat loss is really a 3-D problem, and by not including the third dimension the foundation slab adds too much heat to the soil domain. The solution to this is a 3-D GF solution with another space variable boundary condition (BC) in the third coordinate axis. This would also allow the foundation width to become a variable in the formulation. A 3-D GFs solution is not trivial, but follows the same systematic procedure. The Base Solution Generation (BSG) technique is not set up for three-dimensions. It currently uses the 3rd array dimension to store time values, but programs like Matlab® are set up for four-dimensional arrays.

Another area for improvement is the inclusion of latent heat transfer in the convective solution. The current finite difference method only considers sensible heat transfer. There can be significant energy associated with latent heat in the air-water vapor mixture; especially in humid climates. One advantage with the finite difference method is the pipe wall in the sub-sections is a constant temperature. This simplifies the boundary conditions enough that an analytical solution for the simultaneous heat and mass transfer ispossible. For example, Ghiaasiaan reports an analytical heat and mass transfer solution for internal laminar flow in a circular pipe with constant surface temperature [12]. Typically earth-air heat exchanger (EAHX) flow is turbulent though.

An exciting development that comes with the piece-wise initial condition (IC) in the finite difference method is the potential for intermittent operation. The EAHXs in this research operated as continuously on. But in reality, EAHXs only operated when required by the building. There are not many EAHX models in literature that allow for intermittent operation (only one found in literature review). The piece-wise IC allows for the input of any kind of IC temperature distribution into the GF method. This implies the finite difference method can transition between two types of Green's Function solution equations. It can start with a convective boundary for the EAHX to simulate the "on" condition. After several minutes or hours of operation, this boundary can switch to an insulated boundary (completely different GF solution). The temperature distribution from the last step of the convective finite difference method inputs into the insulated GF solution as the initial condition. The EAHX is now in the "off" position with the insulted boundary. These two solutions can interchange to simulate intermittent operation.

The combination of long and short time solutions has an abundance of variables. It is currently unknown which variables are the most important in the simulation. In other words, which EAHX design considerations have the greatest effect on the simulation? A sensitivity analysis is a tool that can answer this question. A sensitivity analysis is the study of stimulus and response to a system. The system is treated as a black box with only inputs and outputs. The inputs are adjusted in a systematic way to find variations in the outputs. It is a good way to determine the influential parameters in a system [85]. A sensitivity analysis might help simplify the simulation framework by eliminating parameters that are of little importance.

REFERENCES CITED

[1] U. S. E. I. Administration. (2013, November 11). *EIA Projects World Energy Consumption Will Increase 56% by 2040*. Available: http://www.eia.gov/todayinenergy/detail.cfm?id=12251

[2] L. Downing. (2014, November 11). *Efficiency Worth More Than Renewables at $310 Billion, IEA Says*. Available: http://www.bloomberg.com/news/2014-10-08/efficiency-worth-more-than-renewables-at-310-billion-iea-says.html

[3] S. Beck and R. Collins, "Moody diagram," in *wikipedia.org*, Moody_diagram.jpg, Ed., ed. University of Sheffield, 2008.

[4] Wikipedia. (2014, November 11). *Windcatcher*. Available: http://en.wikipedia.org/wiki/Windcatcher

[5] M. Cucumo, S. Cucumo, L. Montoro, and A. Vulcano, "A one-dimensional transient analytical model for earth-to-air heat exchangers, taking into account condensation phenomena and thermal perturbation from the upper free surface as well as around the buried pipes," *International Journal of Heat and Mass Transfer*, vol. 51, Feb 2008.

[6] T. Dynamics, "Ground Loop Design," R. Edition, Ed., ed, 2013.

[7] ASHRAE, *2012 ASHRAE Handbook - HVAC Systems and Equipment (Chapter 12)*: American Society of Heating, Refrigerating, and Air-Conditioning Engineers, 2012.

[8] ASHRAE, *2007 ASHRAE Handbook - Heating, Ventilating, and Air-Conditioning Applications*: American Society of Heating, Refrigeration, and Air-conditioning Engineers, Inc, 2007.

[9] U. S. E. P. Agency, "Consumer's Guide to Radon Reduction: How to Fix Your Home," ed. www.epa.gov/radon, 2013.

[10] F. P. Incropera, D. P. Dewitt, T. L. Bergman, and A. S. Lavine, *Introduction to Heat Transfer*, 5th ed.: John Wiley & Sons, 2007.

[11] F. M. White, *Viscous Fluid Flow*, 3rd ed. New York, New York: McGraw-Hill, 2006.

[12] S. M. Ghiaasiaan, "Convective Heat and Mass Transfer," ed: Cambridge University Press, 2011.

[13] ASHRAE, "ASHRAE 2012 Handbook - Fundamentals," ed: ASHRAE, 2012.

[14] H. S. Carslaw and J. C. Jaeger, *Conduction of Heat in Solids*: Oxford University Press, 1959.

[15] D. L. Nofziger and J. Wu. (2003, June 18). *Soil Temperature Variations With Time and Depth*. Available: http://soilphysics.okstate.edu/software/SoilTemperature/document.pdf

[16] G. Mihalakakou, M. Santamouris, and D. Asimakopoulos, "MODELING THE EARTH TEMPERATURE USING MULTIYEAR MEASUREMENTS," *Energy and Buildings,* vol. 19, pp. 1-9, 1992.

[17] C. P. Jacovides, G. Mihalakakou, M. Santamouris, and J. O. Lewis, "On the ground temperature profile for passive cooling applications in buildings," *Solar Energy,* vol. 57, pp. 167-175, Sep 1996.

[18] U. S. A. C. R. R. a. E. Laboratory, "Regional climatic constants for Equation 6 of the Corps of Engineers Guide Spec 02695," ed. Hanover, NH, 1996.

[19] A. K. Khatry, M. S. Sodha, and M. A. S. Malik, "PERIODIC VARIATION OF GROUND TEMPERATURE WITH DEPTH," *Solar Energy,* vol. 20, pp. 425-427, 1978.

[20] G. Mihalakakou, M. Santamouris, J. O. Lewis, and D. N. Asimakopoulos, "On the application of the energy balance equation to predict ground temperature profiles," *Solar Energy,* vol. 60, pp. 181-190, Mar-Apr 1997.

[21] P. Rajeev, D. Chan, and J. Kodikara, "Ground-atmosphere interaction modelling for long-term prediction of soil moisture and temperature," *Canadian Geotechnical Journal,* vol. 49, pp. 1059-1073, Sep 2012.

[22] Y. H. Qin, J. E. Hiller, G. S. Jiang, and T. Bao, "Sensitivity of thermal parameters affecting cold-region ground-temperature predictions," *Environmental Earth Sciences,* vol. 68, pp. 1757-1772, Mar 2013.

[23] A. Tzaferis, D. Liparakis, M. Santamouris, and A. Argiriou, "ANALYSIS OF THE ACCURACY AND SENSITIVITY OF 8 MODELS TO PREDICT THE PERFORMANCE OF EARTH-TO-AIR HEAT-EXCHANGERS," *Energy and Buildings,* vol. 18, 1992 1992.

[24] R. T. Muehleisen, "Simple Design Tools for Earth-Air Heat Exchangers," in *Fifth National Conference of IBPSA-USA*, Madison, Wisconsin, 2012.

[25] M. De Paepe and A. Janssens, "Thermo-hydraulic design of earth-air heat exchangers," *Energy and Buildings,* vol. 35, pp. 389-397, May 2003.

[26] J. Pfafferott, "Evaluation of earth-to-air heat exchangers with a standardised method to calculate energy efficiency," *Energy and Buildings*, vol. 35, Nov 2003.

[27] M. Krarti and J. F. Kreider, "Analytical model for heat transfer in an underground air tunnel," *Energy Conversion and Management,* vol. 37, pp. 1561-1574, Oct 1996.

[28] M. S. Sodha, A. K. Sharma, S. P. Singh, N. K. Bansal, and A. Kumar, "EVALUATION OF AN EARTH AIR TUNNEL SYSTEM FOR COOLING HEATING OF A HOSPITAL COMPLEX," *Building and Environment,* vol. 20, 1985 1985.

[29] P. Hollmuller, "Analytical characterisation of amplitude-dampening and phase-shifting in air/soil heat-exchangers," *International Journal of Heat and Mass Transfer,* vol. 46, pp. 4303-4317, Oct 2003.

[30] K. Boulama, N. Galanis, and J. Orfi, "Heat and mass transfer between gas and liquid streams in direct contact," *International Journal of Heat and Mass Transfer,* vol. 47, pp. 3669-3681, Aug 2004.

[31] M. K. Ghosal, G. N. Tiwari, N. S. L. Srivastava, and M. S. Sodha, "Thermal modelling and experimental validation of ground temperature distribution in greenhouse," *International Journal of Energy Research,* vol. 28, pp. 45-63, Jan 2004.

[32] M. K. Ghosal, G. N. Tiwari, D. K. Das, and K. P. Pandey, "Modeling and comparative thermal performance of ground air collector and earth air heat exchanger for heating of greenhouse," *Energy and Buildings,* vol. 37, Jun 2005.

[33] M. K. Ghosal and G. N. Tiwari, "Modeling and parametric studies for thermal performance of an earth to air heat exchanger integrated with a greenhouse," *Energy Conversion and Management,* vol. 47, Aug 2006.

[34] M. Santamouris, G. Mihalakakou, A. Argiriou, and D. N. Asimakopoulos, "ON THE PERFORMANCE OF BUILDINGS COUPLED WITH EARTH TO AIR HEAT-EXCHANGERS," *Solar Energy,* vol. 54, Jun 1995.

[35] G. Mihalakakou, M. Santamouris, and D. Asimakopoulos, "Modelling the thermal performance of earth-to-air heat exchangers," *Solar energy,* vol. 53, pp. 301-305, 01/01 1994.

[36] M. S. Sodha, U. Mahajan, and R. L. Sawhney, "THERMAL PERFORMANCE OF A PARALLEL EARTH AIR-PIPES SYSTEM," *International Journal of Energy Research,* vol. 18, pp. 437-447, Jun 1994.

[37] J. Claesson, "HEAT EXTRACTION FROM THE GROUND BY HORIZONTAL PIPES. A MATHEMATICAL ANALYSIS," ed, 1983.

[38] J. Zhang and F. Haghighat, "Simulation of Earth-To-Air heat Exchangers in Hybrid Ventilation Systems," presented at the Ninth International IBPSA Conference, Montreal, Canada, 2005.

[39] H. Su, X.-B. Liu, L. Ji, and J.-Y. Mu, "A numerical model of a deeply buried air-earth-tunnel heat exchanger," *Energy and Buildings*, vol. 48, May 2012.

[40] A. E.-S. Ahmed, "Simulation of Simultaneous Heat and Moisture Transfer in Soils Heated by Buried Pipes," Department of Agricultural Engineering, Ohio State University, 1980.

[41] R. Kumar, S. Ramesh, and S. C. Kaushik, "Performance evaluation and energy conservation potential of earth-air-tunnel system coupled with non-air-conditioned building," *Building and Environment*, vol. 38, pp. 807-813, Jun 2003.

[42] P. Hollmuller and B. Lachal, "Cooling and preheating with buried pipe systems: monitoring, simulation and economic aspects," *Energy and Buildings*, vol. 33, pp. 509-518, May 2001.

[43] G. Mihalakakou, M. Santamouris, and D. Asimakopoulos, "MODELING THE THERMAL PERFORMANCE OF EARTH-TO-AIR HEAT-EXCHANGERS," *Solar Energy*, vol. 53, Sep 1994.

[44] G. Mihalakakou, "On the heating potential of a single buried pipe using deterministic and intelligent techniques," *Renewable Energy*, vol. 28, pp. 917-927, May 2003.

[45] G. Mihalakakou, J. O. Lewis, and M. Santamouris, "The influence of different ground covers on the heating potential of earth-to-air heat exchangers," *Renewable Energy*, vol. 7, pp. 33-46, Jan 1996.

[46] J. W. Stevens, "Coupled conduction and intermittent convective heat transfer from a buried pipe," *Heat Transfer Engineering*, vol. 23, pp. 34-43, Jul-Aug 2002.

[47] A. Trzaski and B. Zawada, "The influence of environmental and geometrical factors on air-ground tube heat exchanger energy efficiency," *Building and Environment*, vol. 46, Jul 2011.

[48] M. Bojic, N. Trifunovic, G. Papadakis, and S. Kyritsis, "Numerical simulation, technical and economic evaluation of air-to-earth heat exchanger coupled to a building," *Energy*, vol. 22, pp. 1151-1158, Dec 1997.

[49] H. K. Lee and R. K. Strand, "Title," unpublished|.

[50] E. Lee, "Development, Verification, and Implementation of a Horizontal Buried Pipe ground Heat Transfer Model in EnergyPlus," Masters of Science, Oklahoma State university, Stillwater, OK, 2008.

[51] S. Benkert, F. D. Heidt, and D. Scholer, "Title," unpublished|.

[52] J. Claesson and C. E. Hagentoft, "HEAT-LOSS TO THE GROUND FROM A BUILDING .1. GENERAL-THEORY," *Building and Environment*, vol. 26, pp. 195-208, 1991.

[53] P. Chuangchid and M. Krarti, "Foundation heat loss from heated concrete slab-on-grade floors," *Building and Environment*, vol. 36, pp. 637-655, Jun 2001.

[54] M. Krarti, D. E. Claridge, and J. F. Kreider, "ITPE TECHNIQUE APPLICATIONS TO TIME-VARYING TWO-DIMENSIONAL GROUND-COUPLING PROBLEMS," *International Journal of Heat and Mass Transfer*, vol. 31, pp. 1899-1911, Sep 1988.

[55] S. H. Choi and M. Krarti, "Slab heat loss calculation with non-uniform inside air temperature profiles," *Energy Conversion and Management*, vol. 37, pp. 1435-1444, Sep 1996.

[56] M. Krarti, "STEADY-STATE HEAT-TRANSFER FROM HORIZONTALLY INSULATED SLABS," *International Journal of Heat and Mass Transfer*, vol. 36, pp. 2135-2145, May 1993.

[57] M. Krarti, "TIME-VARYING HEAT-TRANSFER FROM HORIZONTALLY INSULATED SLAB-ON-GRADE FLOORS," *Building and Environment*, vol. 29, pp. 63-71, Jan 1994.

[58] M. Krarti, S. H. Choi, and Ashrae, "Simplified method for foundation heat loss calculation," *Ashrae Transactions 1996, Vol 102, Pt 1*, vol. 102, pp. 140-152, 1996.

[59] A. E. Delsante, A. N. Stokes, and P. J. Walsh, "APPLICATION OF FOURIER-TRANSFORMS TO PERIODIC HEAT-FLOW INTO THE GROUND UNDER A BUILDING," *International Journal of Heat and Mass Transfer*, vol. 26, pp. 121-132, 1983 1983.

[60] T. Kusuda and J. Bean, "SIMPLIFIED METHODS FOR DETERMINING SEASONAL HEAT-LOSS FROM UNINSULATED SLAB-ON-GRADE

FLOORS," *Ashrae Journal-American Society of Heating Refrigerating and Air-Conditioning Engineers,* vol. 25, pp. 63-64, 1983.

[61] C. E. Hagentoft and J. Claesson, "HEAT-LOSS TO THE GROUND FROM A BUILDING .2. SLAB ON THE GROUND," *Building and Environment,* vol. 26, pp. 395-403, 1991.

[62] C. E. Hagentoft, "Periodic heat loss ford an edge insulated slab: Part II - A mixed boundary value problem," *Building and Environment,* vol. 37, pp. 27-34, Jan 2002.

[63] H. Yoshino, S. Matsumoto, M. Nagatomo, and T. Sakanishi, "5-YEAR MEASUREMENTS OF THERMAL PERFORMANCE FOR A SEMIUNDERGROUND TEST HOUSE," *Tunnelling and Underground Space Technology,* vol. 7, pp. 339-346, Oct 1992.

[64] S. W. Rees, H. R. Thomas, and Z. Zhou, "A numerical and experimental investigation of three-dimensional ground heat transfer," *Building Services Engineering Research & Technology,* vol. 27, pp. 195-208, 2006 2006.

[65] Z. Zhong and J. E. Braun, "A simple method for estimating transient heat transfer in slab-on-ground floors," *Building and Environment,* vol. 42, pp. 1071-1080, Mar 2007.

[66] P. Weitzmann, J. Kragh, P. Roots, and S. Svendsen, "Modelling floor heating systems using a validated two-dimensional ground-coupled numerical model," *Building and Environment,* vol. 40, pp. 153-163, Feb 2005.

[67] R. Academy, "Sustainable Building Technology - REHAU Montana Ecosmart House," ed: REHAU North America, 2014.

[68] Fantech. (May 12). *FKD 8 XL 230 V Diagram*. Available: http://www.fantech.net/FKD-8-XL-230V_enus-42576.aspx

[69] H. Bierwirth, "It's About Air: A Compendium of Pratical Information for those in the HVAC Business," ed. Tulsa, Oklahoma: AAON Corporation, 2000.

[70] N. R. E. Laboratory. (December 17). *National Solar Radiation Data Base, 1991-2005 Update: Typical Meteorological Year 3*. Available: http://rredc.nrel.gov/solar/old_data/nsrdb/1991-2005/tmy3/

[71] U. NRCS. (2013, June 18). *Soil Climate Analysis Network (SCAN)*. Available: http://www.wcc.nrcs.usda.gov/scan/

[72] J. V. Beck, K. D. Cole, A. Haji-Sheikh, and B. Litkouhi, "Heat Conduction Using Green's Functions," ed: Hemisphere Publishing, 1992.

[73] A. G. Butkovskii, *Green's Functions and Transfer Functions Handbook*: Ellis Horwood, 1982.

[74] W. H. Press, S. A. Teukolsky, W. T. Vetterling, and B. P. Flannery, *Numerical Recipes: The Art of Scientific Computing*, 3rd ed. New York, NY: Cambridge University Press, 2007.

[75] P. Plastics. (March 4, 2014). *Thermal Properties of Plastic Materials*. Available: http://www.professionalplastics.com/professionalplastics/ThermalPropertiesofPlasticMaterials.pdf

[76] P. International. (March 4, 2014). *Material Properties*. Available: http://www.plasticsintl.com/sortable_materials.php?display=thermal

[77] *Marks' Standard Handbook for Mechanical Engineers*, 11th ed.: MrGraw-Hill, 2007.

[78] J. Wang and R. L. Bras, "Ground heat flux estimated from surface soil temperature," *Journal of Hydrology*, vol. 216, pp. 214-226, Mar 22 1999.

[79] S. Das, *Functional Fractional Calculus*: Springer-Verlag Berlin Heidelberg, 2011.

[80] ASHRAE, "ASHRAE 2009 Handbook - Fundamentals," ed: ASHRAE, 2009.

[81] C.-E. Hagentoft, "Heat Loss to the Ground from a Building. Slab on the Ground and Cellar," Lund Institute of Technology, Sweden, 1988.

[82] ASHRAE, "Methods for Determining Soil and Rock Formation Thermal Properties from Field Tests," in *ASHRAE 1118-TRP*, ed.

[83] T. S. P.-. CD-adapco. (October 18). *How can I graphically check the validity of my turbulence wall treatment model?*

[84] S. C. Chapra, *Applied Numerical Methods with Matlab*: McGraw-Hill.

[85] (2010). *Encyclopedia of Research Design*.

APPENDICES

APPENDIX A

EXPERIMENTAL DATA

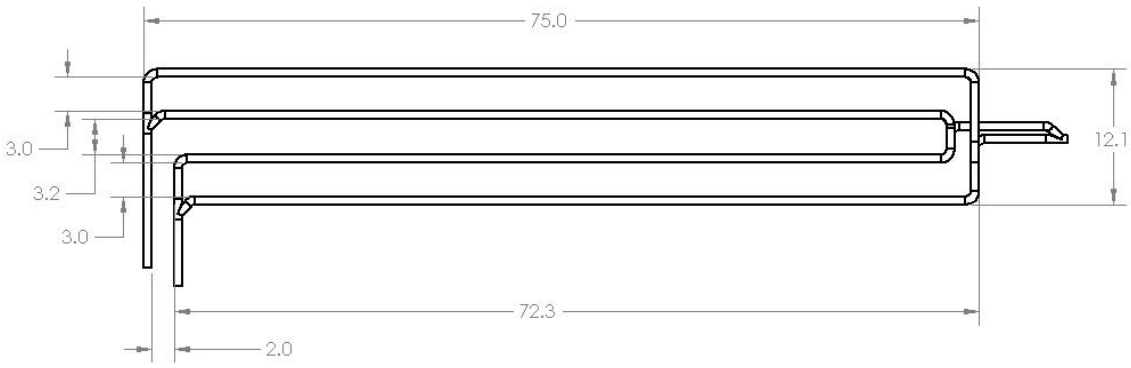


Figure 131: Dimensions of the under yard (UY) earth-air heat exchanger located at the REHAU® Montana Ecosmart House Project in Bozeman, Montana

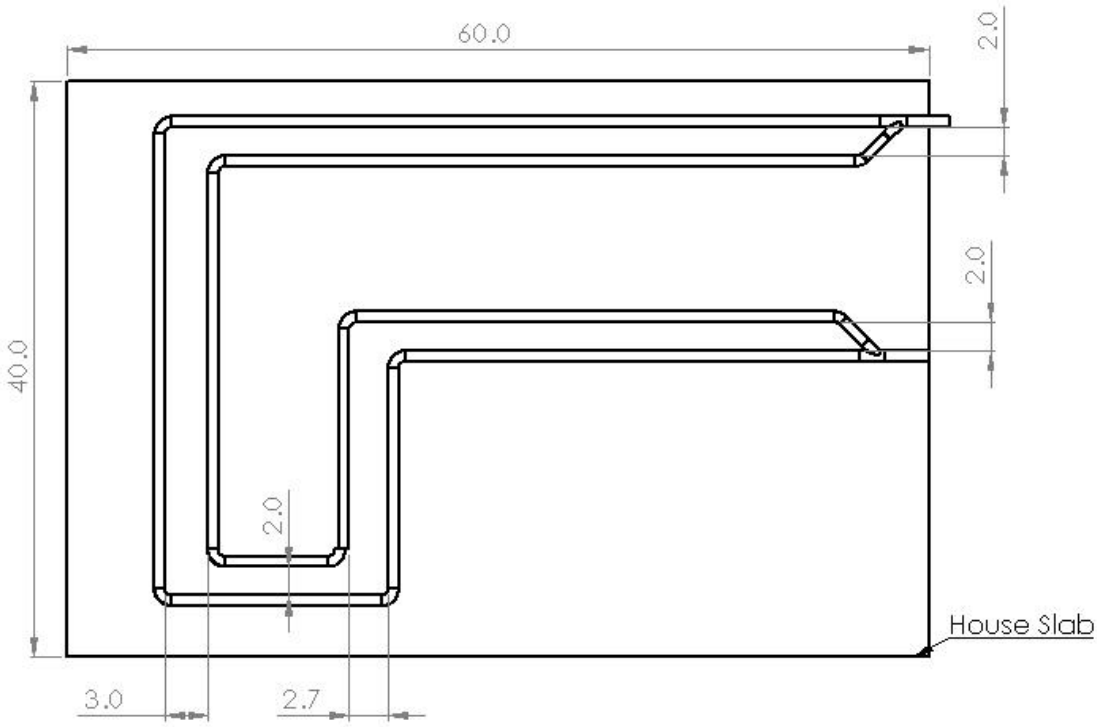


Figure 132: Dimensions of the under slab (US) earth-air heat exchanger located at the REHAU® Montana Ecosmart House Project in Bozeman, Montana

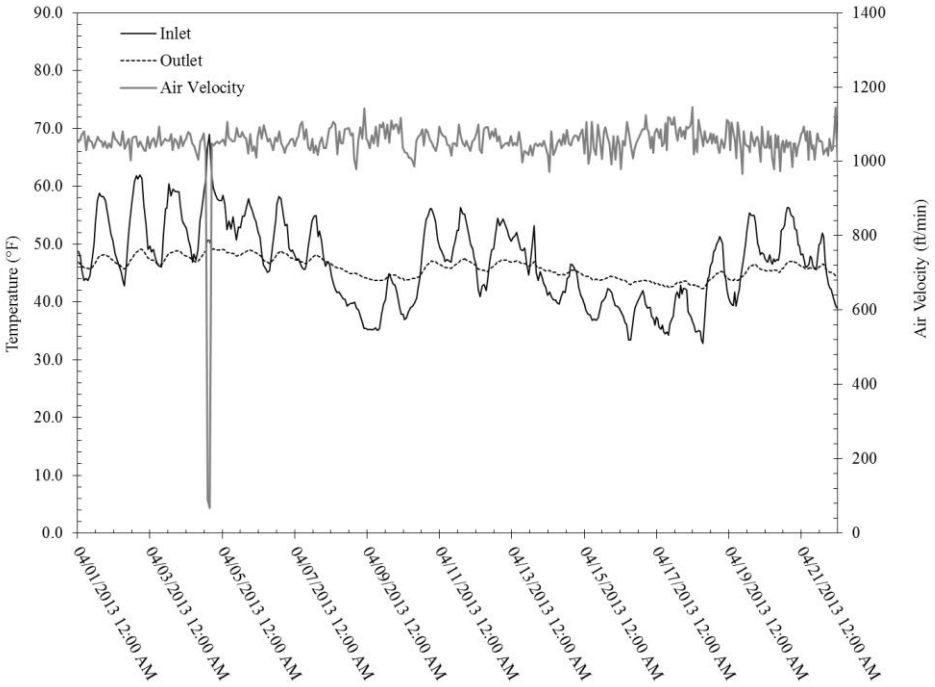


Figure 133: Under yard inlet air temperature, outlet air temperatures, and corresponding air velocity for UY-Exp 1

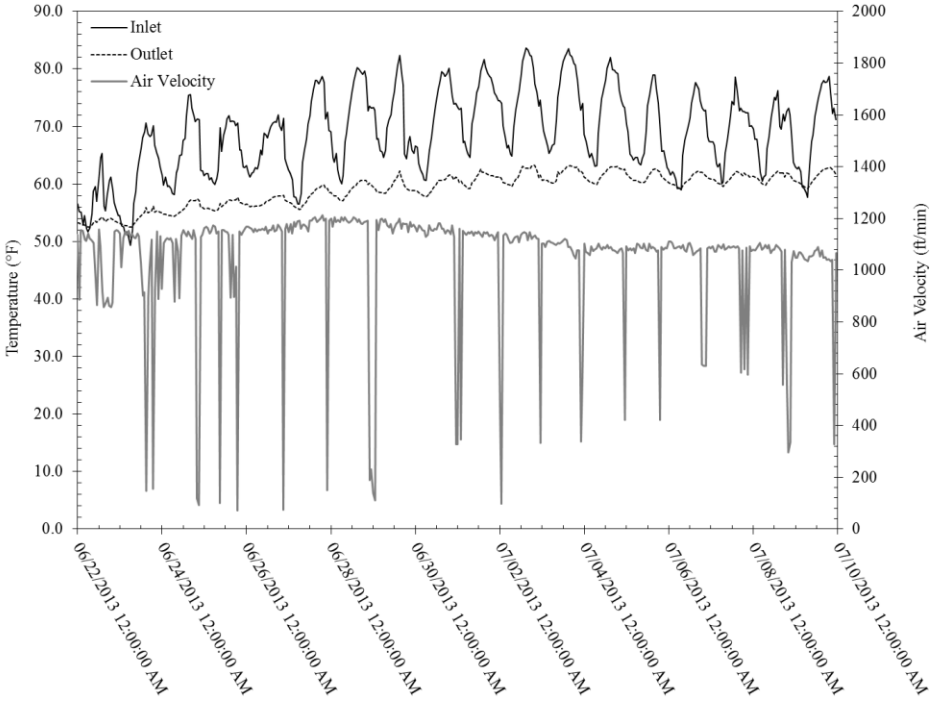


Figure 134: Under yard inlet air temperature, outlet air temperatures, and corresponding air velocity for UY-Exp 2

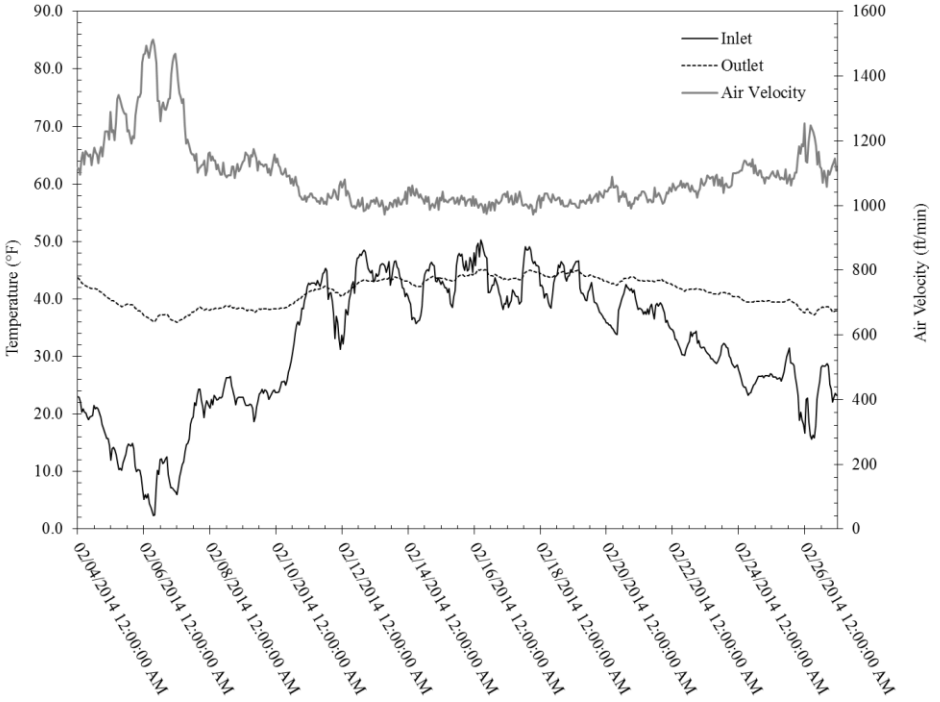


Figure 135: Under yard inlet air temperature, outlet air temperatures, and corresponding air velocity for UY-Exp 4

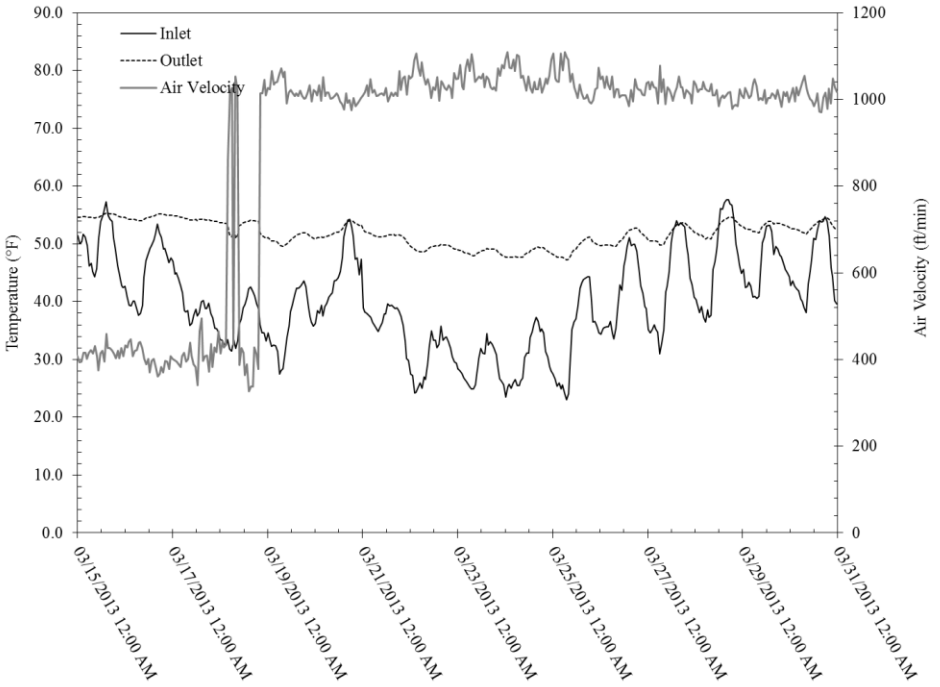


Figure 136: Under slab inlet air temperature, outlet air temperatures, and corresponding air velocity for US-Exp 1

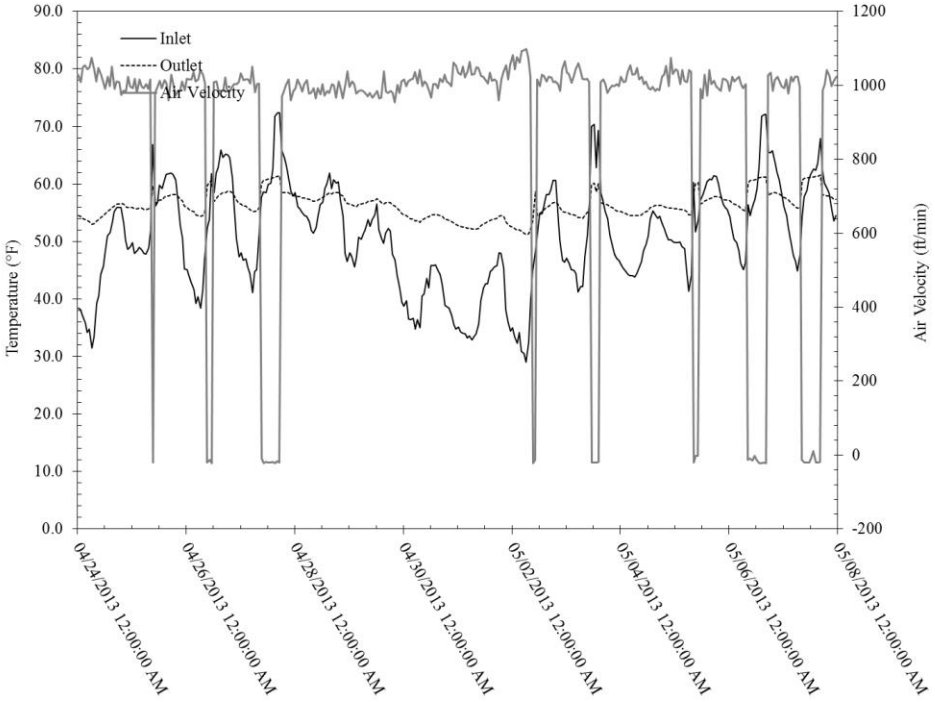


Figure 137: Under slab inlet air temperature, outlet air temperatures, and corresponding air velocity for US-Exp 2

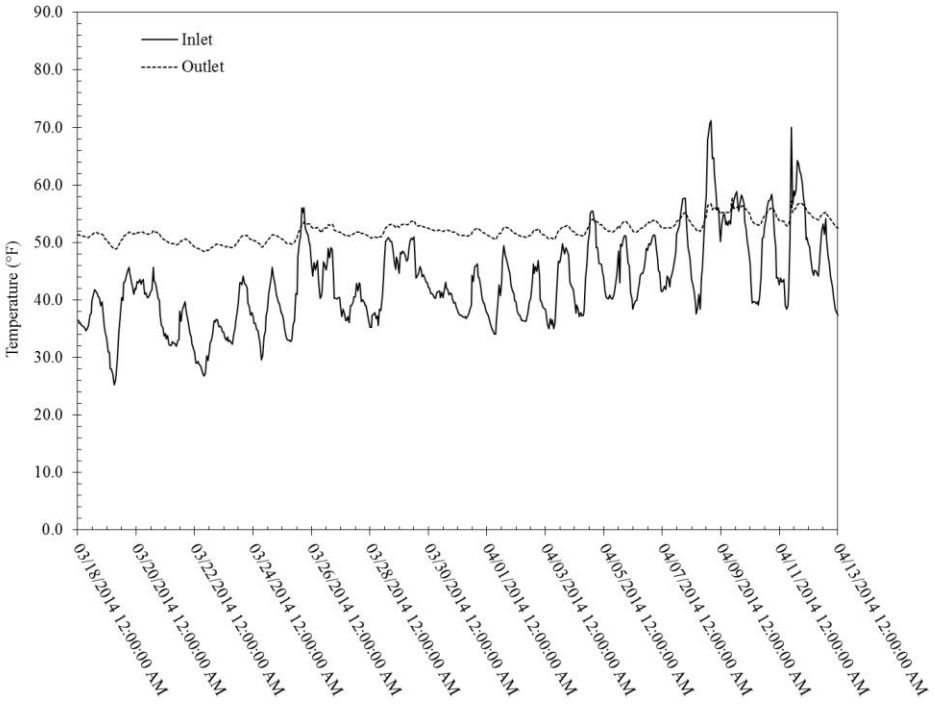


Figure 138: Under slab inlet air temperature and outlet air temperatures for US-Exp 4

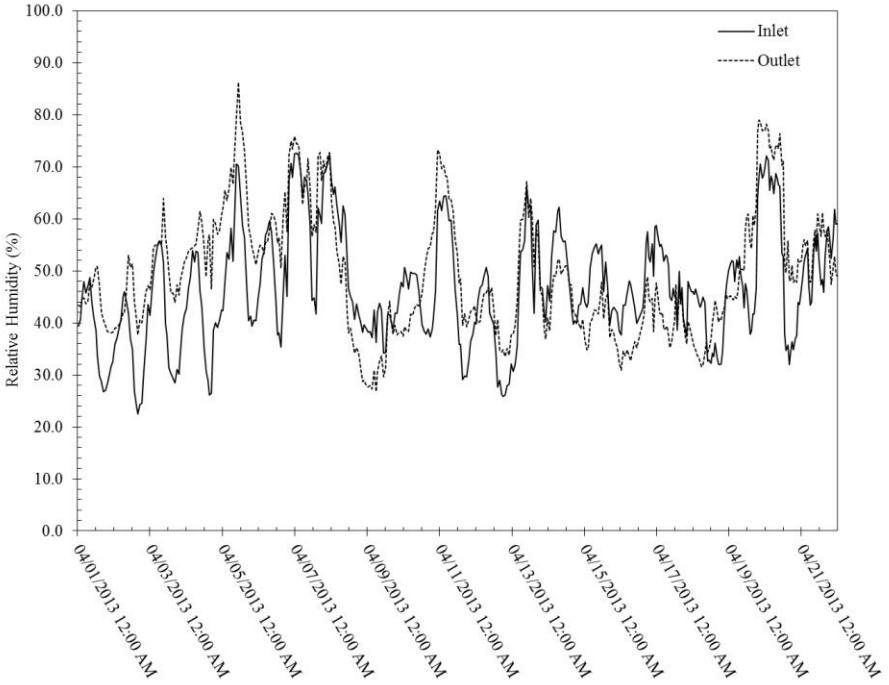


Figure 139: Under yard inlet, outlet air relative humidity for UY-Exp 1

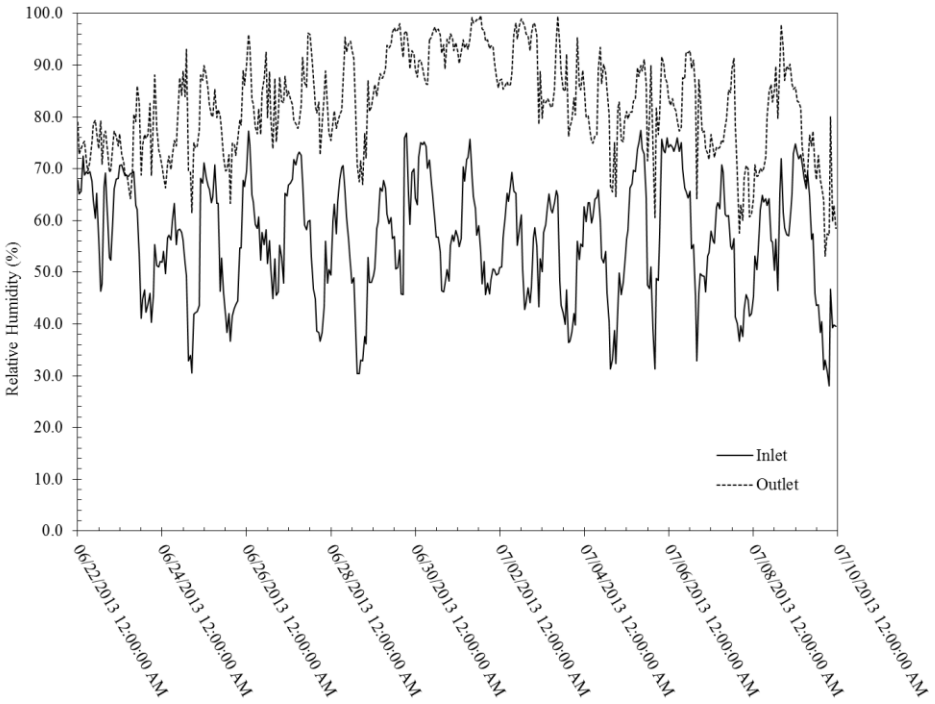


Figure 140: Under yard inlet, outlet air relative humidity for UY-Exp 2

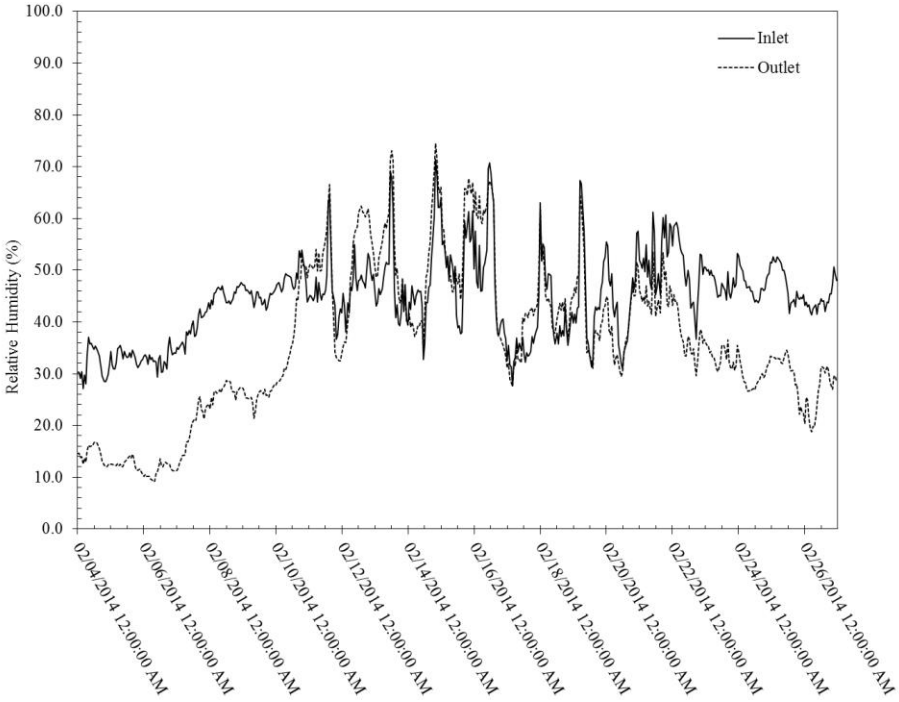


Figure 141: Under yard inlet, outlet air relative humidity for UY-Exp 4

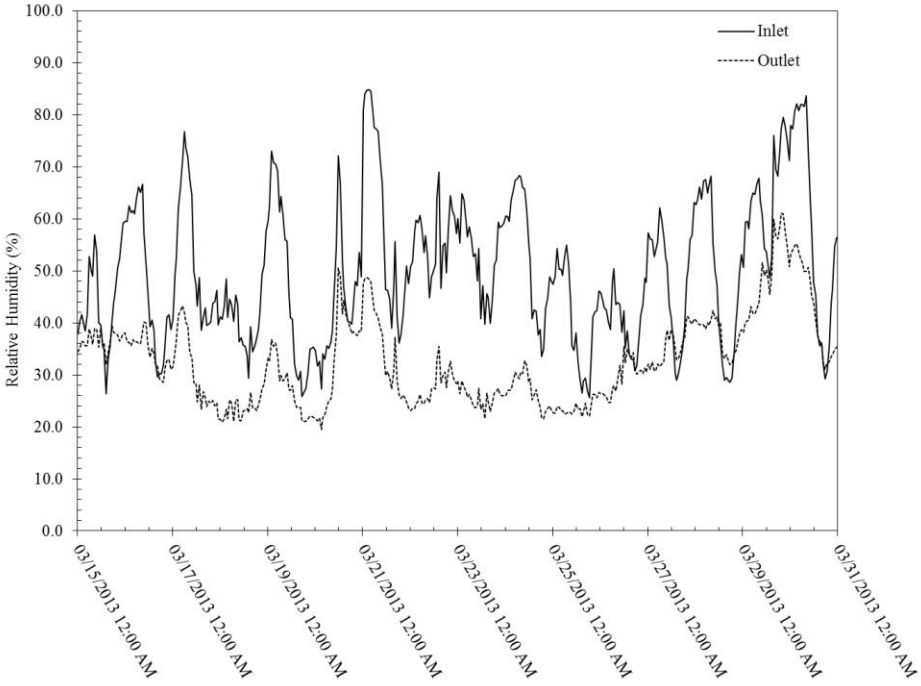


Figure 142: Under slab inlet, outlet air relative humidity for US-Exp 1

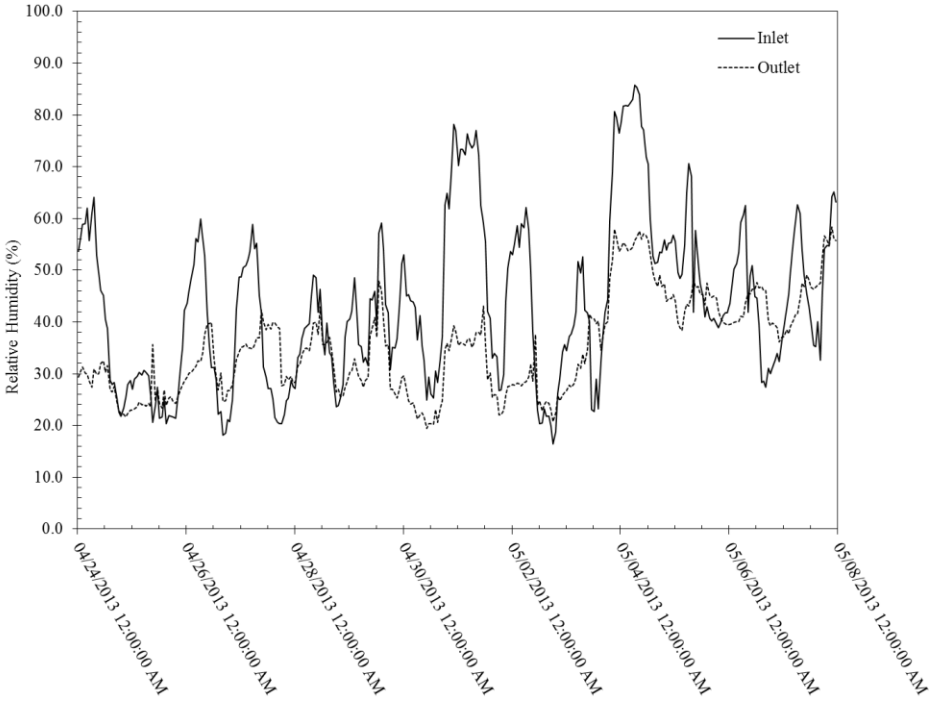


Figure 143: Under slab inlet, outlet air relative humidity for US-Exp 2

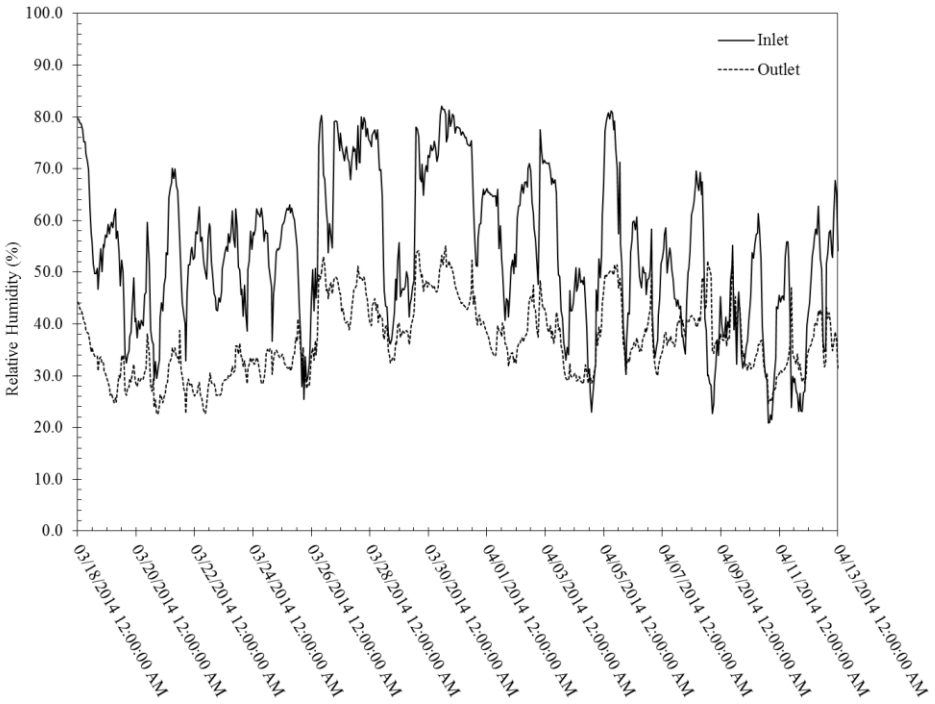


Figure 144: Under slab inlet, outlet air relative humidity for US-Exp 4

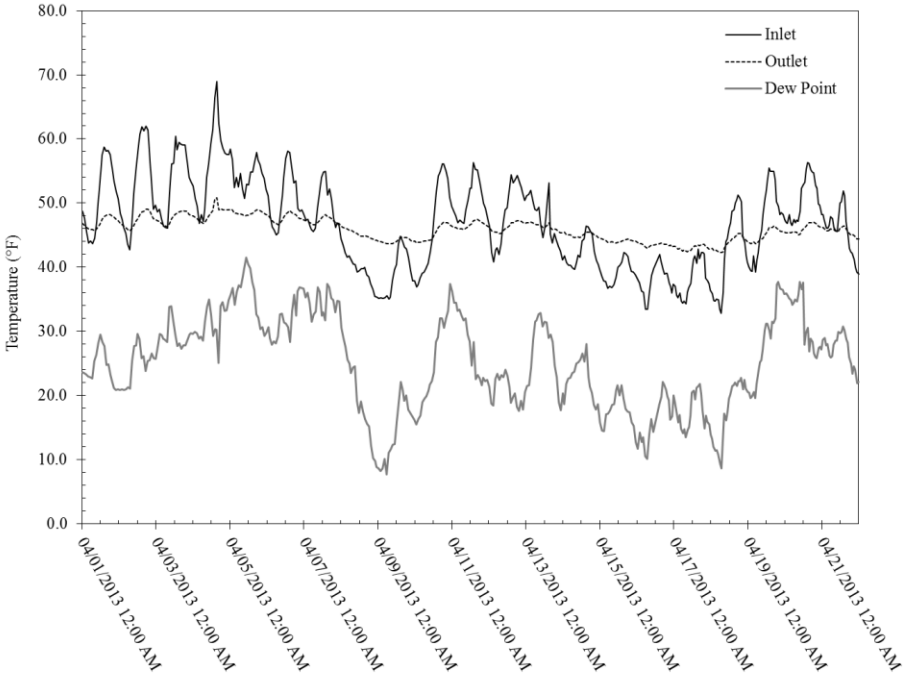


Figure 145: Under yard inlet /outlet dry bulb temperatures and outdoor dew point for UY-Exp 1

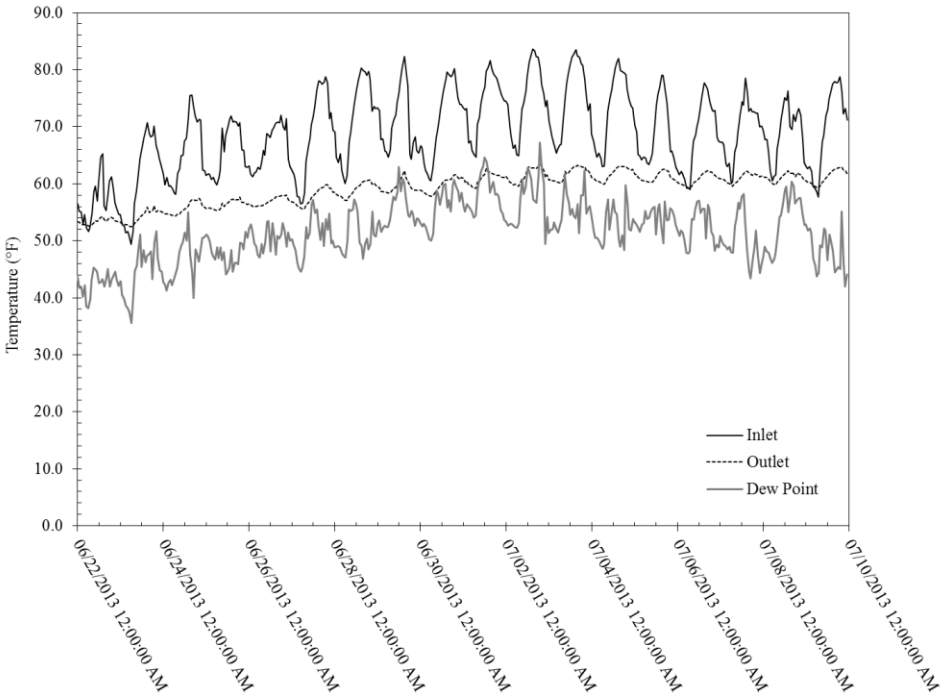


Figure 146: Under yard inlet /outlet dry bulb temperatures and outdoor dew point for UY-Exp 2

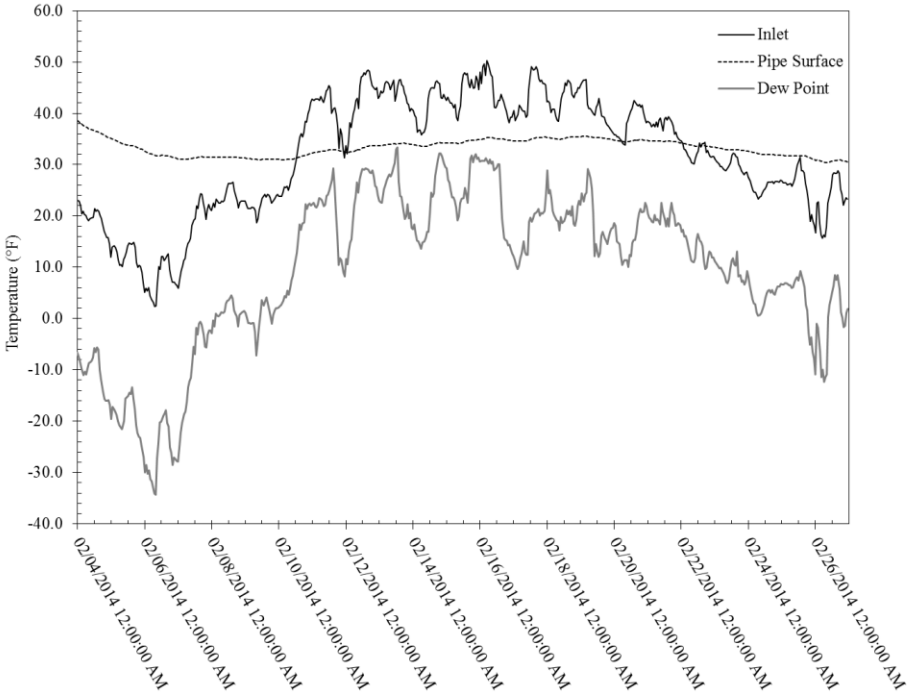


Figure 147: Under yard inlet dry bulb air temperatures, pipe surface temperature, and outdoor dew point for UY-Exp 4

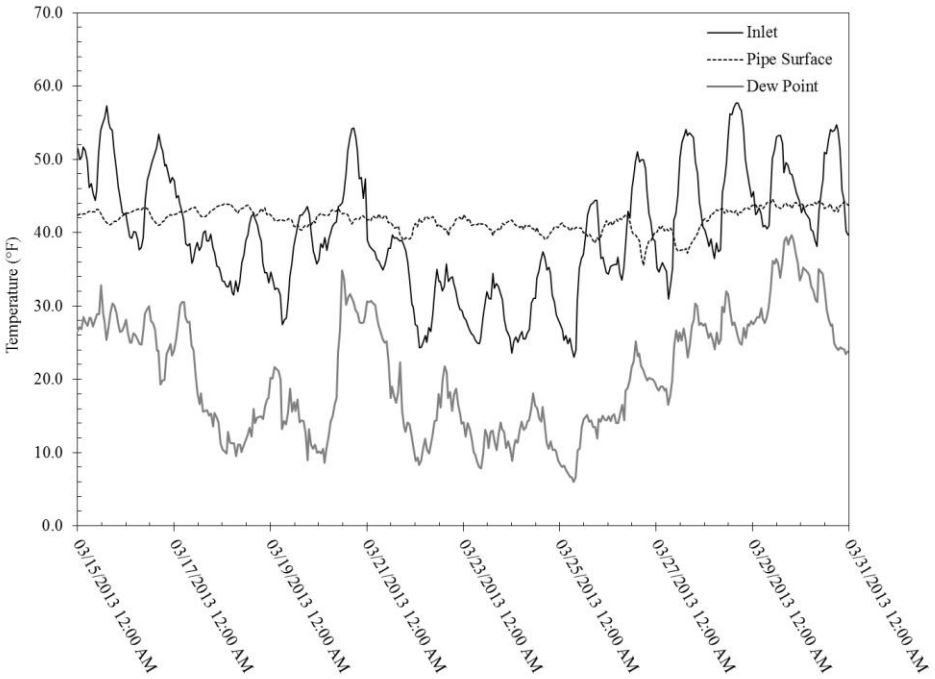


Figure 148: Under slab inlet dry bulb air temperatures, pipe surface temperature, and outdoor dew point for US-Exp 1

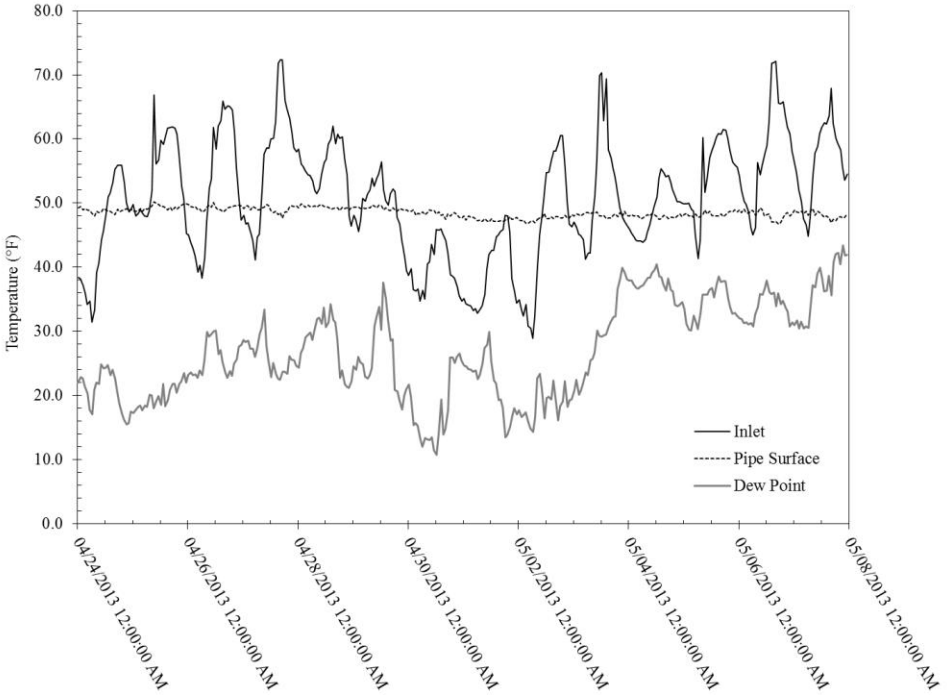


Figure 149: Under slab inlet dry bulb air temperatures, pipe surface temperature, and outdoor dew point for US-Exp 2

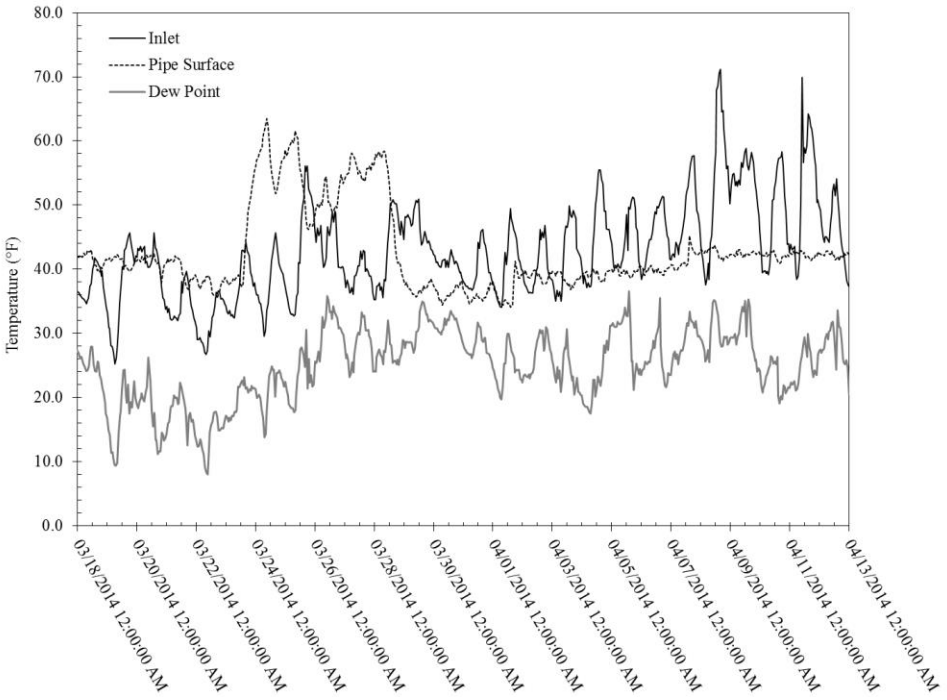


Figure 150: Under slab inlet dry bulb air temperatures, pipe surface temperature, and outdoor dew point for US-Exp 4

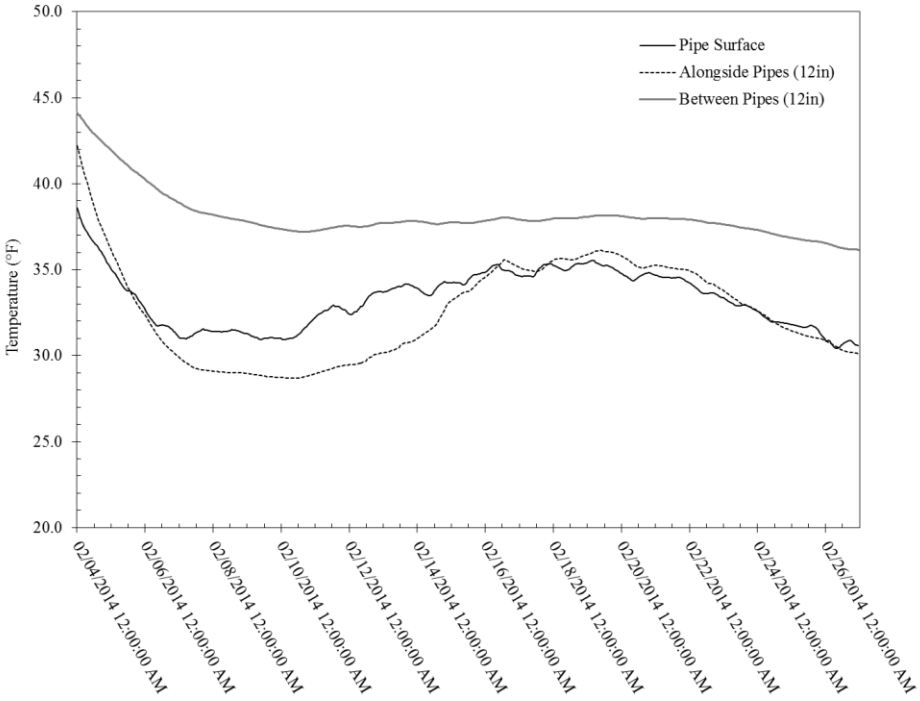


Figure 151: Under yard soil temperatures for UY-Exp 4

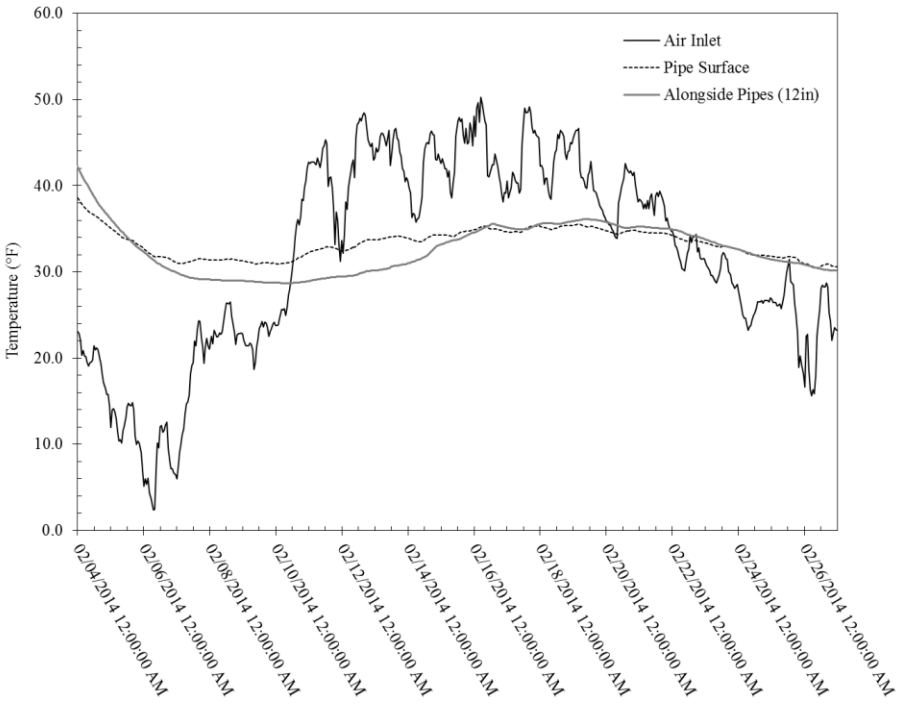


Figure 152: Under yard inlet dry bulb air temperature compared to changes in soil temperatures for UY-Exp 4

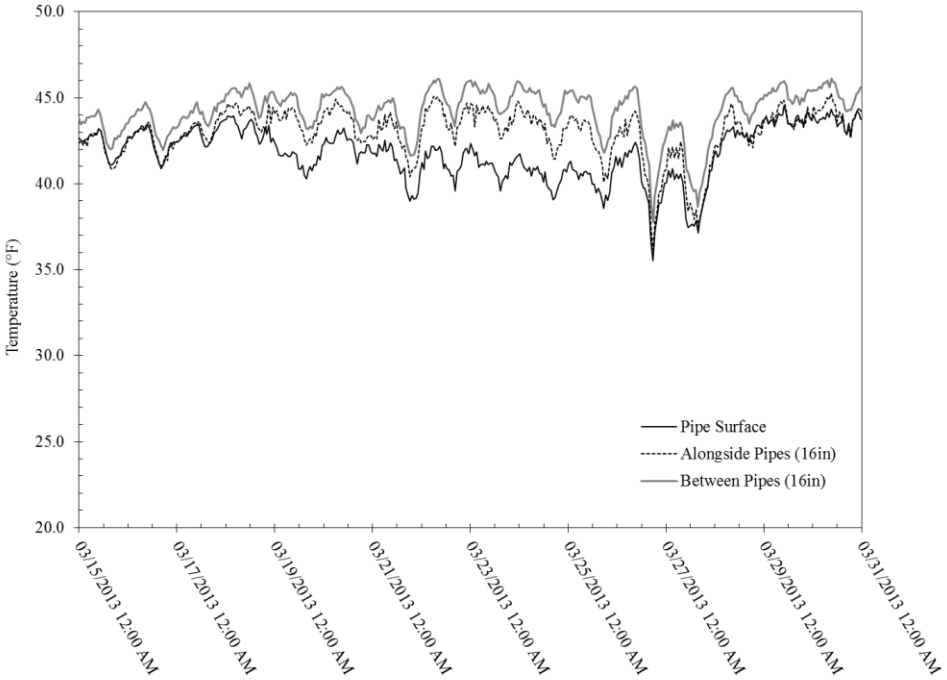


Figure 153: Under slab soil temperatures for US-Exp 1

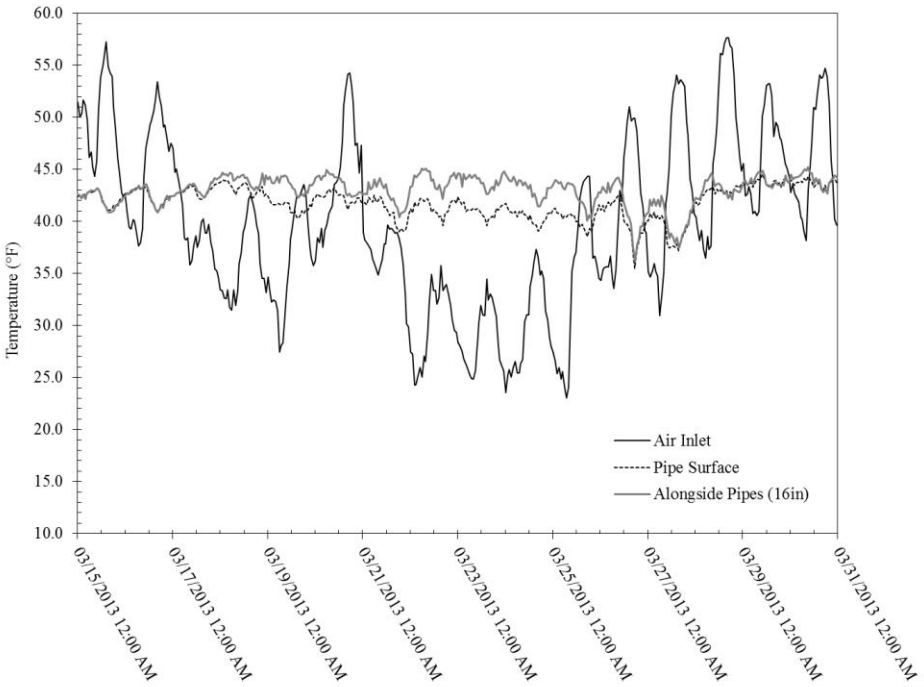


Figure 154: Under slab inlet dry bulb air temperature compared to changes in soil temperatures for US-Exp 1

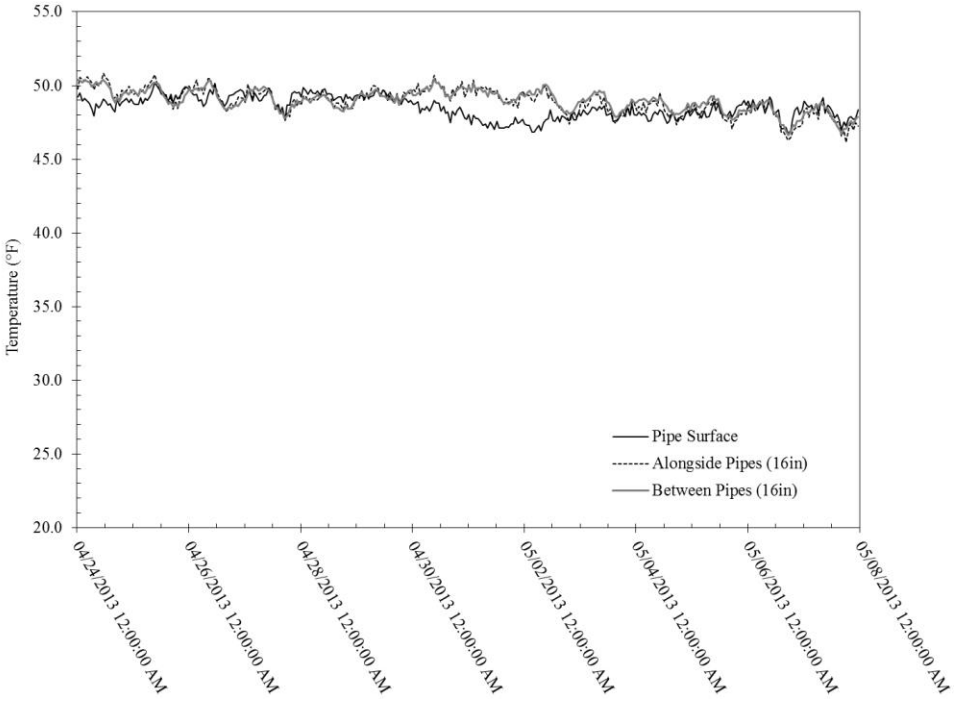


Figure 155: Under slab soil temperatures for US-Exp 2

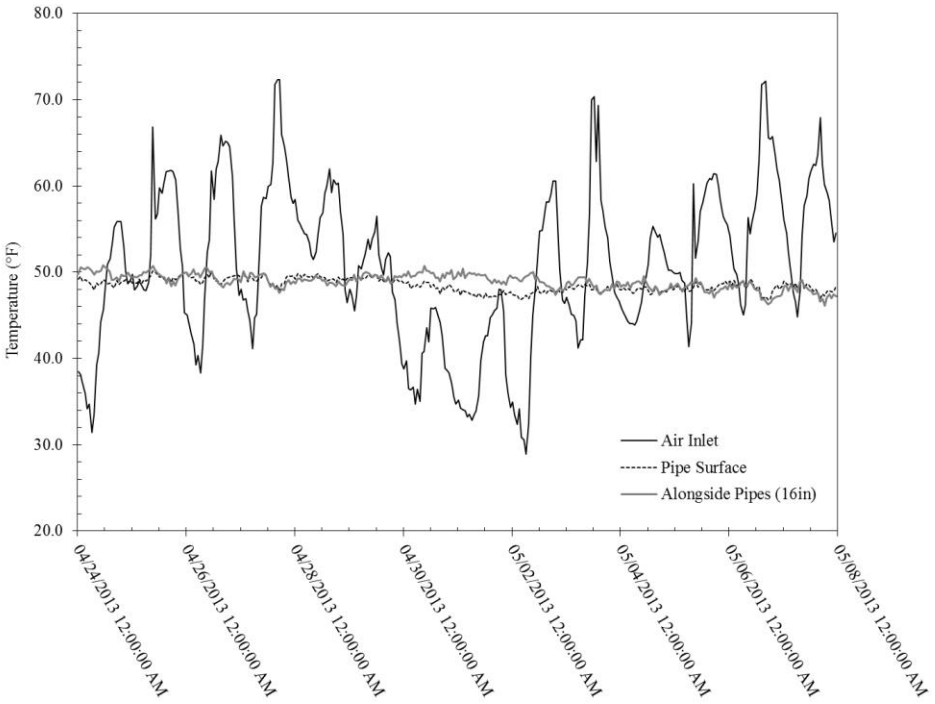


Figure 156: Under slab inlet dry bulb air temperature compared to changes in soil temperatures for US-Exp 2

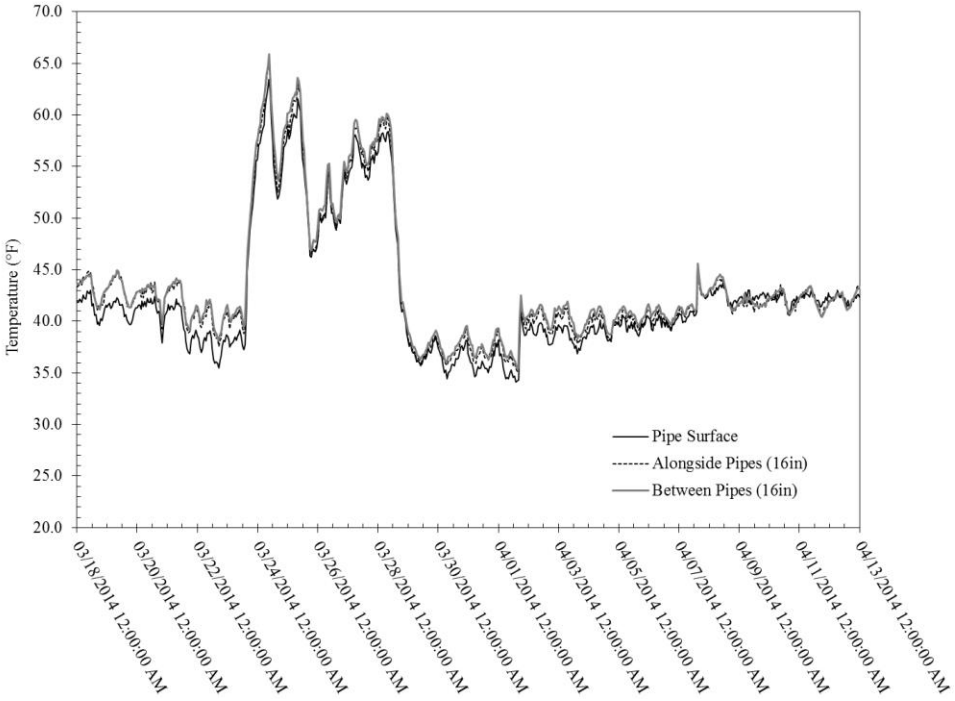


Figure 157: Under slab soil temperatures for US-Exp 4

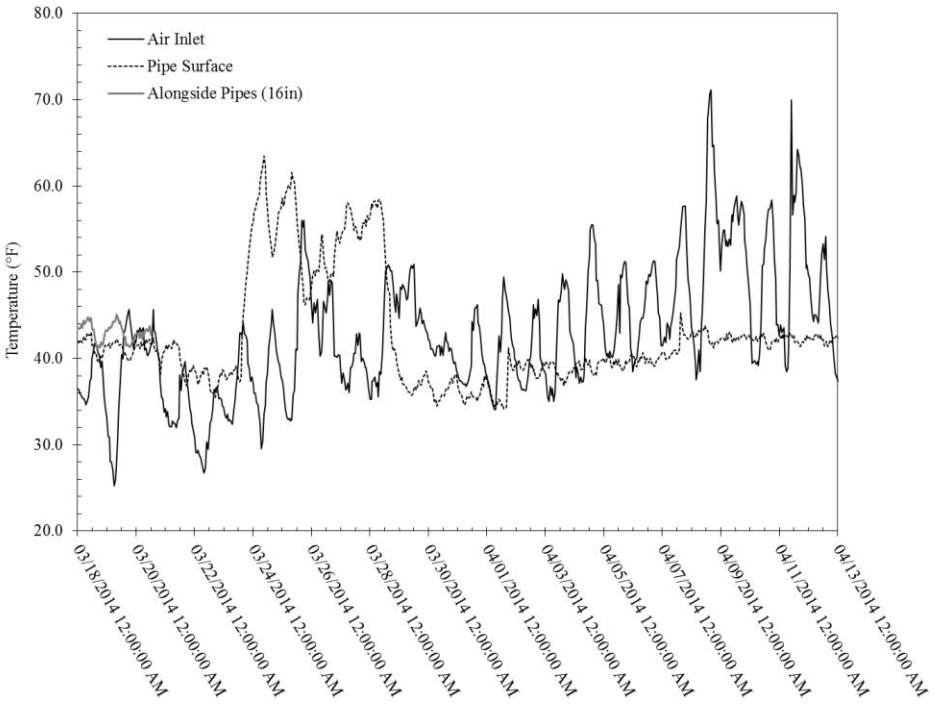


Figure 158: Under slab inlet dry bulb air temperature compared to changes in soil temperatures for US-Exp 4

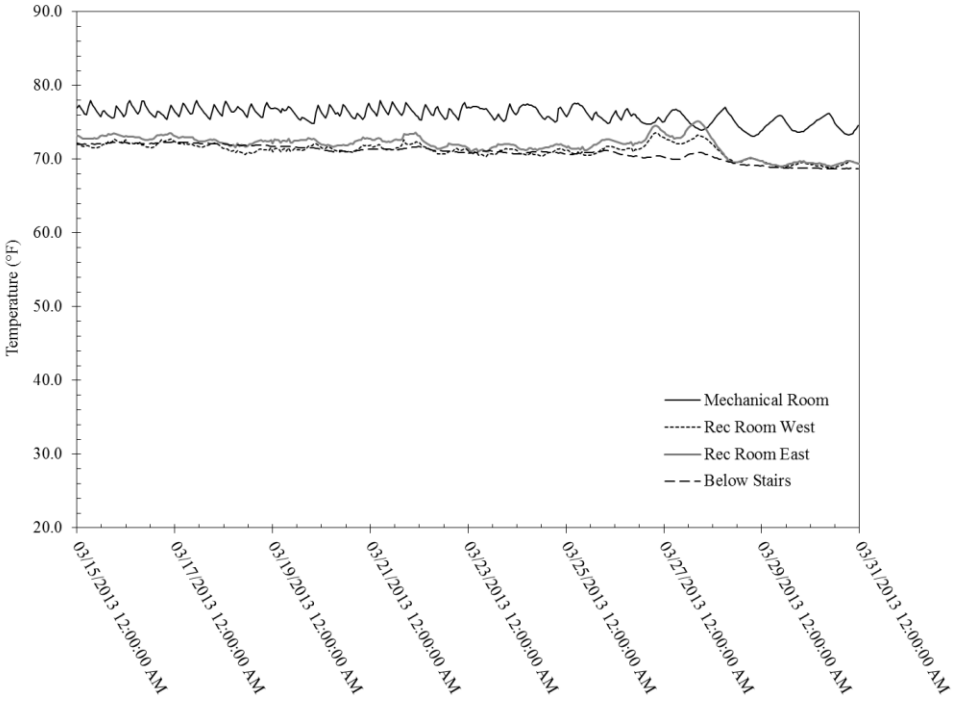


Figure 159: Basement radiant slab temperatures for US-Exp 1, these four sensors cover majority of US EAHX

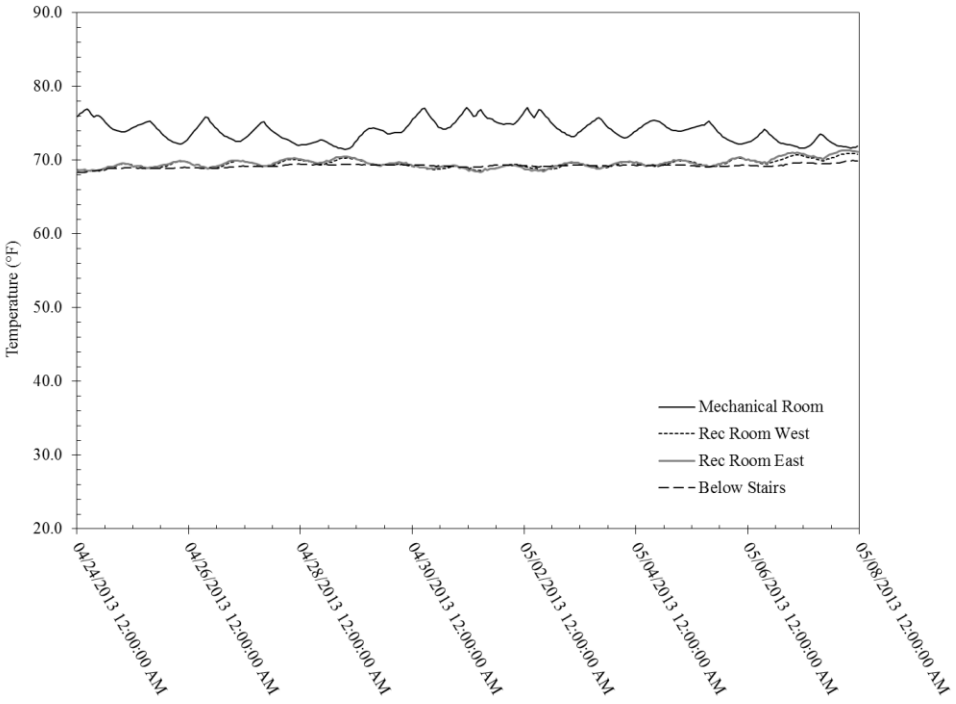


Figure 160: Basement radiant slab temperatures for US-Exp 2, these four sensors cover majority of US EAHX

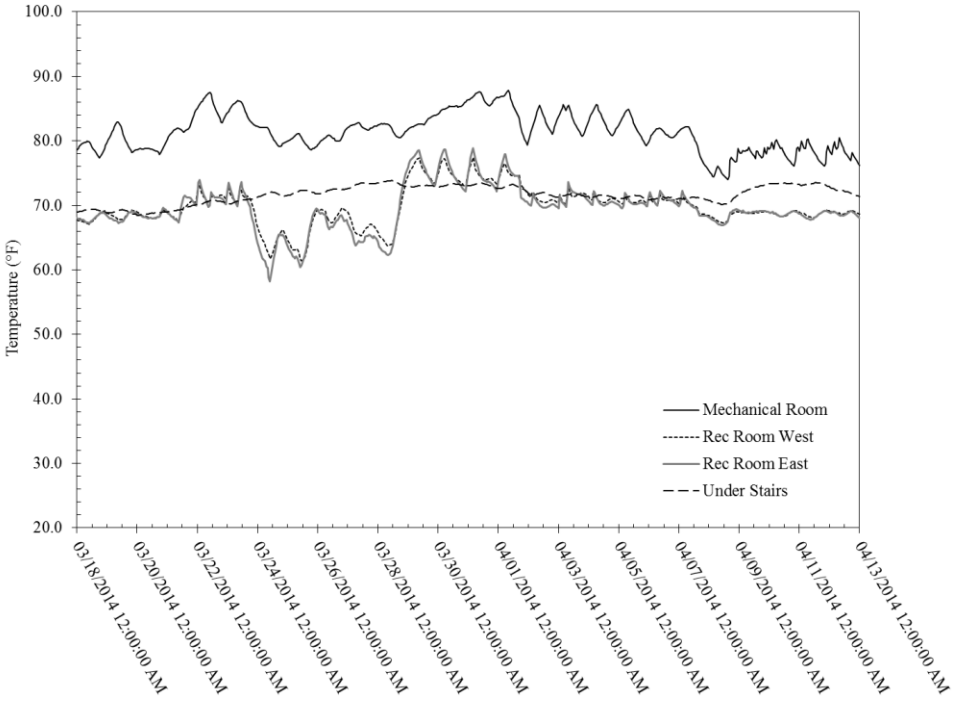


Figure 161: Basement radiant slab temperatures for US-Exp 4, these four sensors cover majority of US EAHX

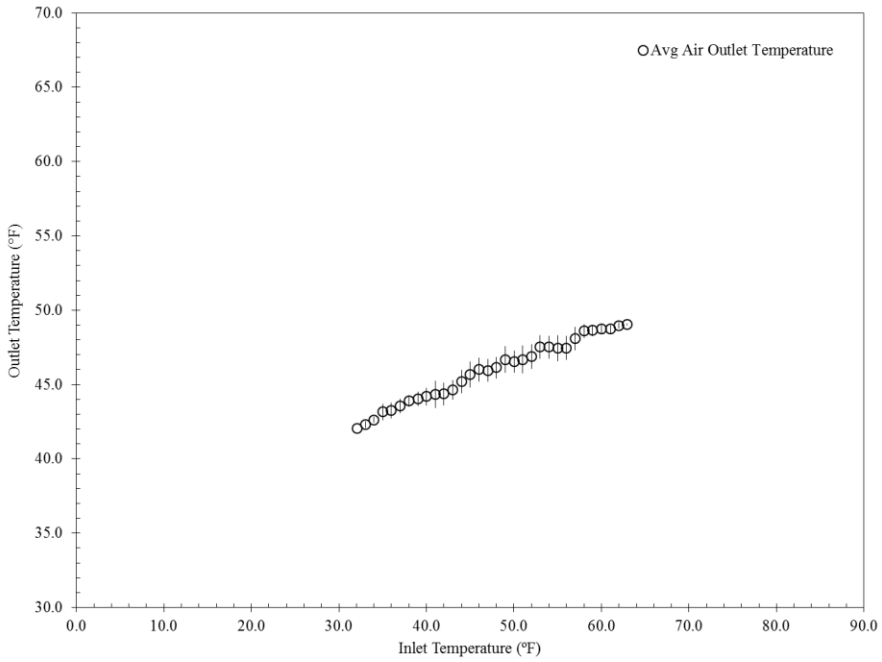


Figure 162: Under yard outlet vs. inlet averaged dry bulb air temperature and average pipe surface temperatures for UY-Exp 1, 3/31/2013 to 4/23/2013 experiment, error bars represent standard deviation of averaged outlet temperature

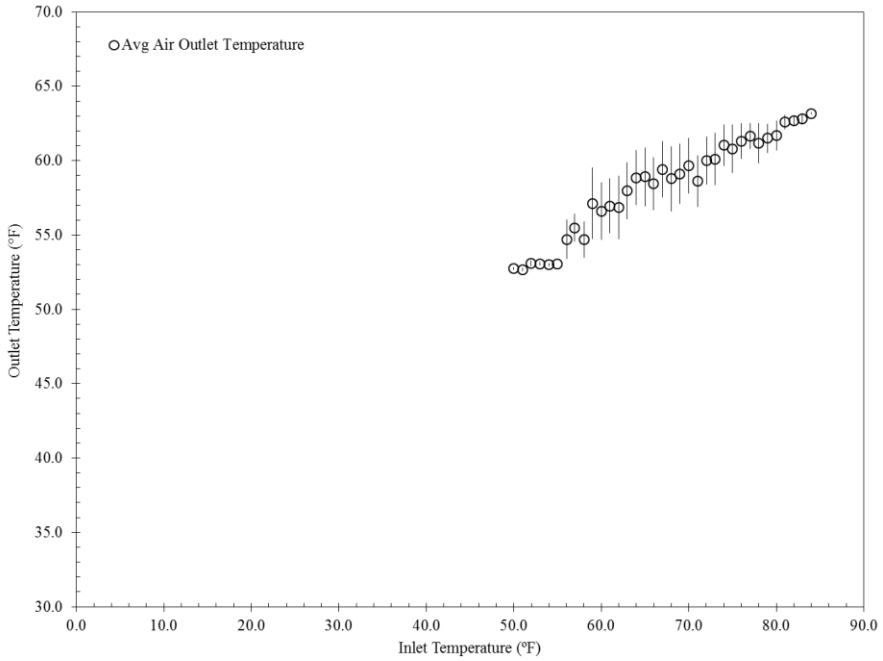


Figure 163: Under yard outlet vs. inlet averaged dry bulb air temperature and average pipe surface temperatures for UY-Exp 2, 6/22/2013 to 7/9/2013 experiment, error bars represent standard deviation of averaged outlet temperature

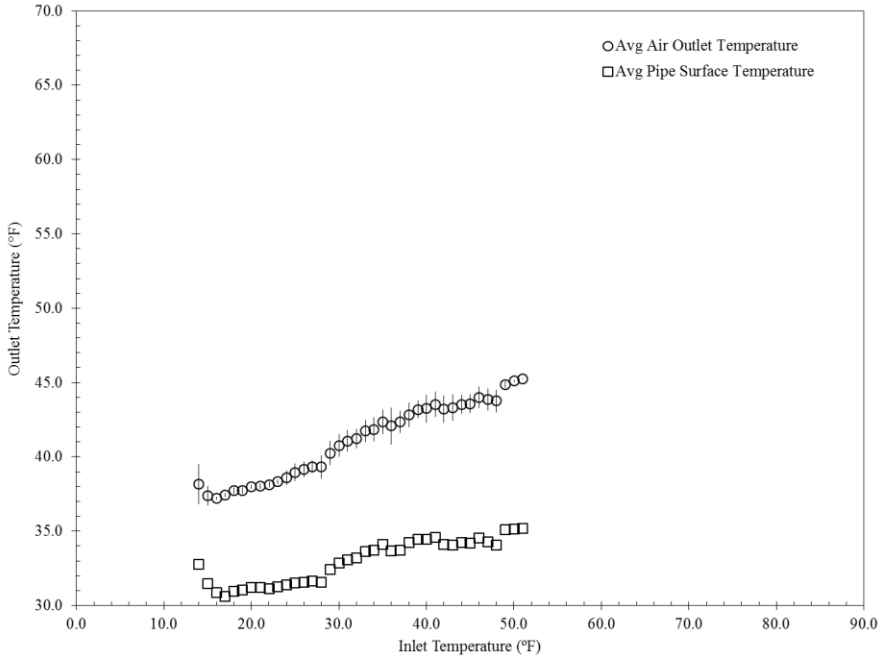


Figure 164: Under yard outlet vs. inlet averaged dry bulb air temperature and average pipe surface temperatures for UY-Exp 4, 2/4/2014 to 2/27/2014 experiment, error bars represent standard deviation of averaged outlet temperature

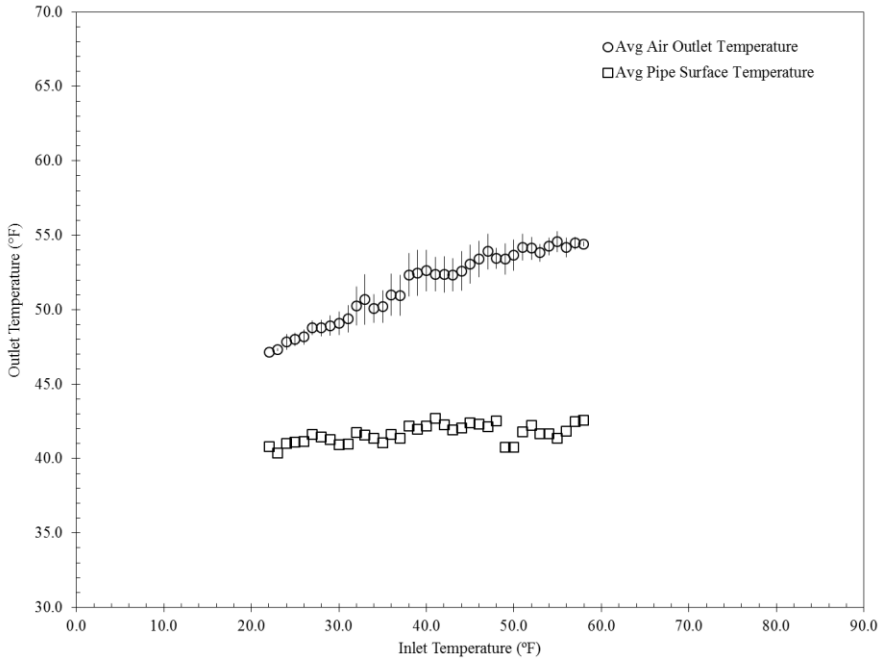


Figure 165: Under slab outlet vs. inlet averaged dry bulb air temperature and average pipe surface temperatures for US-Exp 1, 3/14/2013 to 3/31/2013 experiment, error bars represent standard deviation of averaged outlet temperature

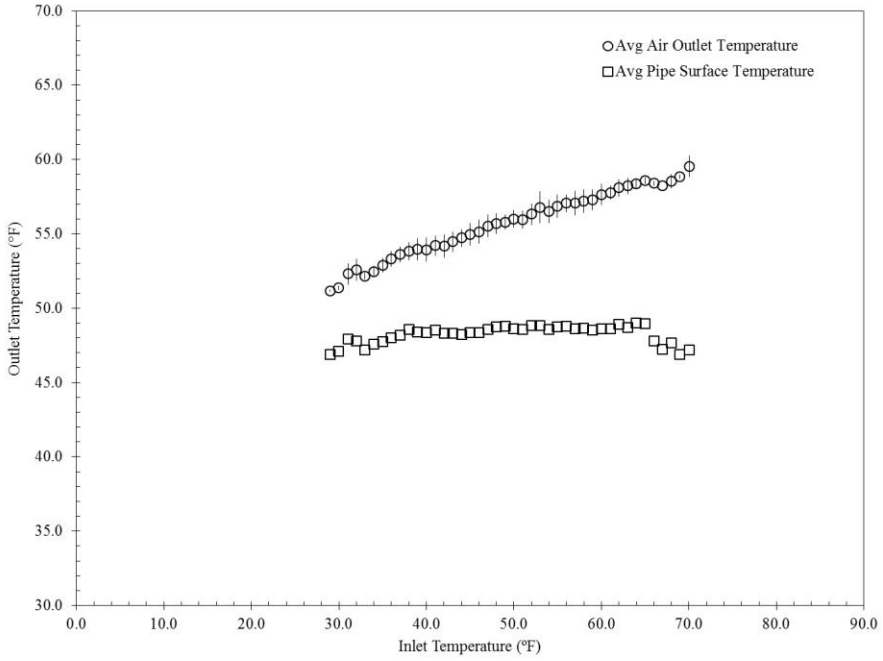


Figure 166: Under slab outlet vs. inlet averaged dry bulb air temperature and average pipe surface temperatures for US-Exp 2, 4/23/2013 to 5/8/2013 experiment, error bars represent standard deviation of averaged outlet temperature

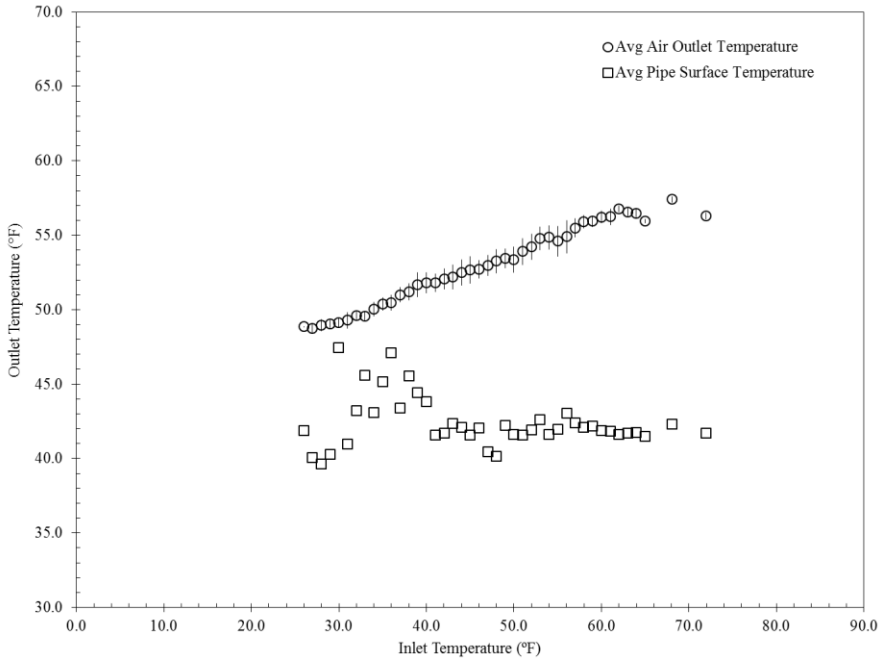


Figure 167: Under slab outlet vs. inlet averaged dry bulb air temperature and average pipe surface temperatures for US-Exp 4, 3/18/2014 to 4/13/2014 experiment, error bars represent standard deviation of averaged outlet temperature

Table 30: Averaged data results for UY-Exp 1, 3/31/2013 to 4/23/2013 (avg – average, temp – temperature, std dev– standard deviation)

#Data Points	Avg Inlet Temp	Avg Outlet Temp	Max Temp	Min Temp	Temp Std Dev	Avg Velocity
5	32.05	42.05	42.05	42.05	0.00	1140
77	33.01	42.31	42.95	42.05	0.20	1083
306	34.02	42.63	43.15	42.35	0.20	1069
944	34.99	43.17	43.95	42.25	0.54	1061
708	35.98	43.25	44.45	42.25	0.52	1071
1541	37.01	43.56	44.65	42.45	0.48	1067
844	38.01	43.89	44.75	42.65	0.37	1056
2237	39.01	44.03	45.15	42.65	0.48	1065
1410	40.00	44.19	45.55	42.75	0.59	1057
1140	40.99	44.33	45.85	42.95	0.91	1067
1626	42.00	44.36	45.95	43.05	0.76	1064
1396	43.01	44.65	46.15	43.25	0.64	1063
1651	44.00	45.20	46.45	43.35	0.79	1063

558	44.99	45.67	47.15	43.55	0.86	1054
1623	46.01	46.00	47.25	43.85	0.78	1066
2139	47.00	45.95	47.55	43.95	0.77	1050
1363	47.99	46.13	47.65	44.15	0.70	1059
1407	49.01	46.69	47.75	44.45	0.88	1053
1052	50.01	46.55	48.05	44.65	0.73	1050
1422	51.00	46.68	48.15	44.95	0.94	1052
1087	52.00	46.90	48.35	45.15	0.82	1044
1269	52.99	47.52	48.45	45.45	0.77	1058
1141	53.99	47.52	48.75	45.65	0.77	1047
1206	55.01	47.43	48.75	45.85	0.86	1053
987	55.99	47.45	48.85	45.95	0.80	1046
634	56.99	48.09	48.95	46.15	0.77	1057
940	58.00	48.59	49.05	47.55	0.45	1050
721	59.00	48.65	49.05	47.65	0.37	1056
72	60.01	48.74	49.15	47.95	0.30	1044
225	61.01	48.72	49.15	48.15	0.26	1049
230	62.01	48.96	49.25	48.45	0.20	1048
11	62.96	49.04	49.05	48.95	0.03	1051

Table 31: Averaged data results for UY-Exp 2, 6/22/2013 to 7/9/2013 (avg – average, temp – temperature, std dev– standard deviation)

#Data Points	Avg Inlet Temp	Avg Outlet Temp	Max Temp	Min Temp	Temp Std Dev	Avg Velocity
37	64.93	52.74	52.85	52.65	0.10	865
107	67.06	52.68	52.85	52.55	0.11	1011
142	68.09	53.07	53.15	52.55	0.17	880
89	73.02	53.06	53.15	52.75	0.11	1031
36	74.05	52.99	53.15	52.95	0.08	922
21	77.33	53.05	53.05	53.05	0.00	858
23	78.41	54.71	55.65	52.95	1.31	1150
131	78.53	55.49	55.95	53.05	0.92	1163
135	78.85	54.68	56.15	53.25	1.21	988
503	76.36	57.12	59.45	53.35	2.40	1046
450	78.66	56.61	59.75	53.55	1.93	1087
1196	79.22	56.95	60.25	53.75	1.84	1120
1493	81.49	56.85	60.35	53.75	2.11	1107

1152	82.34	57.98	60.55	53.95	1.89	1127
868	85.85	58.86	60.75	53.85	1.84	1106
1313	83.81	58.92	61.05	54.25	1.97	1089
1707	83.32	58.47	61.25	54.25	1.77	1123
1280	82.27	59.41	61.45	54.45	1.87	1101
2265	81.13	58.77	61.45	54.75	2.19	1092
725	83.06	59.12	61.65	54.95	2.01	1092
1211	79.17	59.65	61.95	55.05	1.87	1102
1207	80.65	58.62	61.95	55.35	1.72	1095
1068	85.12	60.02	62.05	56.05	1.59	1116
732	80.46	60.11	62.35	56.25	1.77	1116
1064	84.78	61.03	62.45	56.45	1.39	1110
934	86.76	60.80	62.65	56.75	1.64	1108
695	86.82	61.32	62.75	58.35	1.20	1120
871	86.14	61.66	62.95	58.65	0.87	1110
1098	87.15	61.17	63.55	58.95	1.33	1137
990	87.95	61.50	63.85	59.65	0.97	1141
696	83.87	61.70	63.45	59.85	1.01	1125
534	90.19	62.59	63.45	61.25	0.48	1097
346	84.75	62.70	63.15	61.65	0.33	1073
235	89.22	62.81	63.25	62.05	0.37	1123
37	87.24	63.17	63.25	63.05	0.06	1102

Table 32: Averaged data results for UY-Exp 3, 12/20/2013 to 1/8/2014 (avg – average, temp – temperature, std dev– standard deviation)

#Data Points	Avg Inlet Temp	Avg Outlet Temp	Max Temp	Min Temp	Temp Std Dev	Soil Temp Avg	Soil Temp Range	Avg Velocity
17	15.00	40.63	40.75	40.35	0.17	34.86	0.38	1188
47	16.01	41.02	41.35	40.25	0.28	35.08	1.01	1188
49	17.02	40.92	41.55	40.35	0.36	34.93	1.10	1186
72	18.00	40.93	41.65	40.35	0.41	34.87	1.14	1170
177	18.98	40.97	41.85	40.35	0.59	34.78	1.21	1166
110	20.01	40.80	41.95	40.55	0.30	34.42	1.29	1156
156	21.02	40.93	42.15	40.55	0.43	34.49	1.34	1153
413	22.02	41.79	42.65	40.75	0.70	35.42	1.99	1129
246	22.99	42.66	42.95	40.85	0.33	36.24	2.24	1125
529	24.00	42.37	43.25	41.05	0.65	35.80	2.40	1125

199	24.99	43.39	43.55	41.25	0.28	36.78	2.53	1114
32	26.03	43.08	43.65	41.35	1.01	36.31	2.61	1089
184	27.02	44.19	44.75	41.55	0.59	37.46	3.79	1074
371	28.01	44.64	45.95	41.65	0.62	37.96	5.18	1072
933	28.98	44.89	46.15	41.75	0.95	38.12	5.35	1057
758	30.00	44.35	46.45	41.95	1.43	37.26	5.40	1050
419	31.00	44.82	46.55	42.35	1.37	37.57	5.28	1043
682	32.01	44.57	47.05	42.55	1.65	37.17	5.50	1038
458	33.00	45.26	47.15	42.75	1.51	37.90	5.45	1022
555	34.01	45.88	47.55	42.95	1.10	38.46	5.49	1025
2575	35.00	46.19	47.95	43.15	1.42	38.75	6.10	1018
2028	35.99	46.34	48.05	43.35	1.16	38.72	5.81	1002
2308	37.00	47.32	48.15	43.75	1.06	39.92	5.56	994
1435	38.00	47.16	48.15	43.85	1.01	39.53	5.36	992
958	39.02	47.23	48.25	44.05	0.99	39.51	5.30	987
2159	40.00	46.77	48.45	44.25	1.35	38.66	5.35	1000
2450	40.99	47.12	48.75	44.45	1.24	38.94	5.46	987
2410	42.00	47.70	48.95	44.85	0.53	39.56	5.38	988
2065	43.01	48.02	48.95	46.85	0.39	39.73	2.73	994
1443	43.99	48.20	49.25	46.95	0.49	39.78	2.78	976
1545	44.99	48.15	49.35	47.15	0.54	39.62	2.78	983
1186	46.01	48.23	49.45	47.35	0.35	39.56	2.64	973
1053	47.00	48.28	49.45	47.55	0.44	39.46	2.61	971
500	47.99	48.62	49.65	47.85	0.50	39.78	2.36	973
88	49.02	48.35	48.55	48.15	0.10	39.17	0.28	966
175	50.02	48.54	48.65	48.35	0.08	39.24	0.11	973

Table 33: Averaged data results for UY-Exp 4, 2/4/2014 to 2/27/2014 (avg – average, temp – temperature, std dev– standard deviation)

#Data Points	Avg Inlet Temp	Avg Outlet Temp	Max Temp	Min Temp	Temp Std Dev	Soil Temp Avg	Soil Temp Range	Avg Velocity
6	33.99	38.15	39.65	36.95	1.34	32.75	3.93	1195
115	37.49	37.38	39.15	37.05	0.64	31.46	2.64	1186
12	39.84	37.21	37.35	37.15	0.08	30.85	0.76	1190
23	43.31	37.44	37.65	37.25	0.12	30.61	0.75	1185
176	42.78	37.74	38.15	37.35	0.22	30.96	0.88	1174
385	42.03	37.72	38.45	37.45	0.21	31.05	0.94	1168

237	43.15	37.98	38.55	37.65	0.13	31.21	1.08	1163
707	42.32	38.03	38.65	37.65	0.17	31.23	1.09	1157
746	43.73	38.13	38.65	37.75	0.18	31.13	1.08	1127
1719	46.20	38.31	38.75	37.85	0.17	31.26	1.10	1115
1510	44.46	38.60	39.55	37.95	0.49	31.38	1.72	1128
753	46.62	38.94	39.95	38.05	0.58	31.50	1.87	1124
1465	47.98	39.14	40.15	38.25	0.52	31.56	1.96	1093
791	48.62	39.34	40.25	38.45	0.41	31.66	1.89	1093
696	46.21	39.32	40.55	38.45	0.77	31.54	2.06	1099
1063	46.74	40.25	40.85	38.55	0.81	32.42	2.18	1070
716	48.64	40.76	41.55	38.95	0.77	32.83	2.57	1073
710	48.97	41.07	41.85	39.25	0.70	33.05	2.64	1074
451	48.89	41.21	41.95	39.25	0.65	33.19	2.69	1055
573	53.74	41.74	42.45	39.45	0.73	33.61	2.84	1053
908	44.54	41.84	42.65	39.75	0.80	33.70	3.15	1056
910	50.74	42.35	42.95	39.75	0.82	34.10	3.23	1055
1200	51.67	42.07	43.35	39.75	1.25	33.69	3.36	1036
964	47.05	42.35	43.45	40.05	0.73	33.74	3.24	1035
892	49.66	42.84	43.55	40.15	0.83	34.25	3.33	1026
1820	45.04	43.19	43.85	40.35	0.57	34.45	3.44	1023
1216	42.02	43.24	44.05	40.35	0.91	34.43	3.55	1027
2188	49.61	43.54	44.55	40.75	0.82	34.56	3.58	1014
1866	47.34	43.21	44.75	40.95	0.90	34.10	3.66	1016
1887	53.55	43.31	44.85	41.25	0.89	34.05	3.33	1019
1513	43.79	43.52	44.85	41.95	0.63	34.24	2.84	1011
1098	49.29	43.58	44.95	42.15	0.61	34.17	2.75	1011
1821	45.78	44.01	44.95	42.45	0.71	34.53	2.59	1002
782	46.82	43.85	44.95	42.55	0.74	34.26	2.21	1004
695	46.42	43.75	45.05	43.05	0.75	34.05	2.03	1005
604	39.98	44.86	45.25	44.45	0.20	35.10	0.40	999
121	46.47	45.09	45.25	44.95	0.08	35.14	0.17	1004
59	43.98	45.25	45.25	45.15	0.02	35.19	0.03	996

Table 34: Averaged data results for US-Exp 1, 3/14/2013 to 3/31/2013 (avg – average, temp – temperature, std dev– standard deviation)

#Data Points	Avg Inlet Temp	Avg Outlet Temp	Max Temp	Min Temp	Temp Std Dev	Soil Temp Avg	Soil Temp Range	Avg Velocity

1	22.05	47.15	47.15	47.15	0.00	40.81	0.00	1105
64	23.00	47.31	47.55	47.25	0.07	40.38	1.08	1083
199	24.01	47.83	49.05	47.35	0.53	41.02	2.22	1092
643	24.99	48.01	49.35	47.35	0.43	41.09	2.39	1084
1029	25.98	48.16	49.65	47.45	0.51	41.16	2.32	1063
533	26.99	48.78	49.75	47.55	0.48	41.60	2.39	1056
660	27.99	48.77	49.95	47.65	0.55	41.46	2.44	1064
301	29.00	48.93	50.15	47.75	0.68	41.27	2.93	1058
255	29.99	49.09	50.45	47.85	0.77	40.91	3.71	1038
330	31.02	49.39	51.35	47.95	0.91	40.97	4.96	1040
722	32.01	50.25	53.65	48.15	1.29	41.74	4.93	990
727	32.99	50.68	53.65	48.25	1.68	41.58	5.49	886
710	33.99	50.09	53.75	48.35	0.95	41.37	5.08	995
859	35.01	50.21	54.15	48.55	1.06	41.04	5.31	1001
1453	35.99	51.01	54.25	48.65	1.40	41.61	5.46	929
523	36.99	50.96	54.25	48.85	1.36	41.36	5.40	933
1101	38.00	52.33	54.45	49.15	1.45	42.17	5.97	810
950	38.99	52.46	54.55	49.25	1.53	41.95	5.57	765
1003	39.99	52.62	54.65	49.55	1.37	42.16	5.47	774
875	40.99	52.38	54.65	49.75	1.15	42.69	5.85	863
872	42.02	52.38	54.65	49.75	1.21	42.26	6.49	888
1139	42.99	52.34	54.65	49.95	1.10	41.91	6.76	920
378	44.02	52.59	54.85	50.35	1.32	42.06	7.22	895
853	45.01	53.05	54.85	50.85	1.30	42.38	7.18	823
488	45.98	53.41	54.85	50.95	1.21	42.30	7.47	760
433	47.02	53.90	54.95	51.25	1.19	42.12	7.34	652
581	48.00	53.46	54.95	51.45	0.68	42.50	7.42	917
524	48.99	53.41	55.05	51.65	1.04	40.74	9.34	832
547	49.99	53.67	55.15	51.95	1.04	40.76	9.87	771
567	51.00	54.20	55.15	52.25	0.89	41.80	7.31	652
396	52.00	54.12	55.15	52.45	0.76	42.20	7.34	780
493	52.99	53.82	55.15	52.65	0.58	41.64	7.06	932
626	54.00	54.25	55.25	52.95	0.58	41.67	7.48	867
233	54.98	54.57	55.25	53.05	0.71	41.36	7.23	641
113	56.01	54.18	55.25	53.25	0.64	41.85	6.73	884
398	57.02	54.47	55.25	53.45	0.40	42.47	2.17	937
107	57.98	54.41	54.55	53.95	0.15	42.58	1.10	1004

Table 35: Averaged data results for US-Exp 2, 4/23/2013 to 5/8/2013 (avg – average, temp – temperature, std dev– standard deviation)

#Data Points	Avg Inlet Temp	Avg Outlet Temp	Max Temp	Min Temp	Temp Std Dev	Soil Temp Avg	Soil Temp Range	Avg Velocity
70	29.02	51.17	51.35	51.15	0.06	46.89	0.93	1098
110	29.99	51.37	51.65	51.15	0.12	47.08	1.15	1081
103	31.03	52.31	53.05	51.25	0.73	47.93	2.48	1061
33	31.99	52.57	53.25	51.35	0.74	47.81	2.27	1060
312	32.99	52.15	53.35	51.45	0.23	47.20	2.20	1049
812	34.01	52.48	53.55	51.45	0.35	47.58	2.68	1045
411	35.01	52.88	53.75	51.55	0.48	47.76	2.84	1052
434	35.99	53.31	53.95	51.75	0.52	48.00	3.08	1032
358	36.99	53.63	54.25	51.85	0.51	48.18	2.87	1018
168	37.98	53.83	54.55	51.95	0.60	48.55	3.06	1025
337	39.00	53.97	54.75	52.15	0.73	48.39	2.80	1018
336	39.98	53.94	55.05	52.25	0.81	48.37	2.51	1016
431	40.99	54.21	55.25	52.35	0.67	48.52	2.84	1025
415	42.02	54.18	55.45	52.45	0.77	48.30	2.85	1018
525	43.00	54.47	55.55	52.65	0.67	48.31	2.92	1015
1493	44.01	54.72	56.15	52.75	0.58	48.24	3.06	1031
1380	45.00	54.98	56.45	52.95	0.74	48.36	3.39	1012
970	45.99	55.14	56.65	53.05	0.80	48.36	3.22	1016
650	47.01	55.52	56.95	53.95	0.76	48.58	3.26	1019
1394	48.00	55.70	57.15	54.25	0.69	48.74	3.23	1003
1285	48.99	55.79	57.25	54.65	0.50	48.76	2.39	1007
752	50.00	56.01	57.35	54.35	0.57	48.62	2.36	1007
521	51.00	55.94	57.45	54.35	0.62	48.56	2.51	1001
661	52.01	56.32	59.65	54.35	0.70	48.84	2.81	995
505	53.00	56.79	60.15	54.55	1.07	48.85	2.57	942
992	54.01	56.52	57.85	54.65	0.77	48.56	3.08	998
878	54.98	56.85	57.95	54.85	0.77	48.74	3.08	996
932	56.01	57.05	60.75	55.25	0.56	48.76	2.90	997
576	57.02	57.07	60.55	55.35	0.83	48.59	3.06	991
505	57.99	57.20	58.25	55.65	0.79	48.66	2.81	998
473	59.01	57.28	60.65	55.75	0.70	48.54	2.79	998
734	60.01	57.64	58.45	56.35	0.71	48.61	2.80	998
830	61.01	57.78	60.95	56.75	0.45	48.59	2.96	1001
425	61.99	58.09	61.25	56.95	0.59	48.91	3.09	976

176	63.00	58.22	61.35	57.15	0.53	48.70	3.23	979
176	63.99	58.39	58.75	57.85	0.31	49.00	2.47	1006
646	65.00	58.57	61.05	56.95	0.21	48.98	2.32	996
266	65.98	58.40	58.75	58.05	0.15	47.81	2.62	983
1	66.95	58.25	58.25	58.25	0.00	47.23	0.00	980
6	67.98	58.53	59.35	57.85	0.48	47.67	3.10	990
2	68.95	58.85	58.95	58.75	0.14	46.89	0.15	993
6	70.03	59.55	60.45	58.85	0.72	47.18	0.43	906

Table 36: Averaged data results for US-Exp 3, 1/10/2014 to 2/2/2014 (avg – average, temp – temperature, std dev– standard deviation)

#Data Points	Avg Inlet Temp	Avg Outlet Temp	Max Temp	Min Temp	Temp Std Dev	Soil Temp Avg	Soil Temp Range	Avg Velocity
2	9.95	44.15	44.15	44.15	0.00	41.64	0.02	1198
7	10.99	44.19	44.25	44.15	0.05	41.41	0.53	1175
69	12.01	44.45	44.75	44.25	0.15	41.08	1.43	1167
147	12.98	44.56	44.95	44.25	0.22	41.05	1.93	1167
108	14.01	45.01	45.25	44.35	0.16	40.41	1.95	1156
34	15.02	45.34	45.45	44.65	0.22	39.73	2.04	1142
134	16.00	46.02	46.65	45.45	0.40	40.56	2.88	1115
252	17.01	46.35	47.25	45.55	0.35	40.91	2.89	1108
425	18.00	46.54	47.35	45.65	0.43	40.55	3.53	1111
198	18.98	46.46	47.55	46.05	0.45	41.00	3.82	1097
325	19.99	46.68	48.25	46.15	0.55	41.24	4.19	1069
407	21.00	47.20	48.35	46.35	0.70	40.80	3.84	1066
415	22.00	47.13	48.55	46.45	0.63	41.10	4.23	1065
413	23.02	47.19	48.75	46.55	0.74	40.65	3.71	1072
1285	24.01	47.42	48.95	46.65	0.56	41.09	6.78	1035
217	24.99	48.01	49.05	46.75	0.95	41.54	4.76	1031
414	25.99	48.48	49.25	47.05	0.66	40.92	5.15	1035
541	26.99	48.86	50.85	47.05	0.68	41.25	4.64	1031
877	27.99	49.73	51.55	47.15	0.86	40.79	4.72	1022
945	29.01	49.68	52.15	47.45	1.25	40.88	4.77	1015
890	29.99	50.50	52.45	47.55	1.32	41.00	4.57	1022
1734	31.01	50.39	53.35	47.75	1.18	40.58	5.47	1016
1230	32.02	50.73	53.55	48.15	1.34	40.59	5.65	1007
1648	32.99	51.30	53.75	48.25	1.19	40.51	5.28	1011

1381	34.01	51.94	55.45	49.05	1.11	40.82	5.52	1005
1879	35.01	52.60	55.45	49.15	1.27	41.36	5.59	993
3826	35.99	52.55	55.75	49.25	1.49	41.26	5.90	989
2003	37.00	53.02	56.25	49.25	1.69	41.54	5.99	984
3420	37.98	53.10	56.45	49.65	1.67	41.67	6.57	973
2075	38.99	53.24	56.75	50.15	1.83	41.61	6.05	971
1621	39.98	52.92	56.95	50.65	1.69	41.64	6.45	970
1180	41.00	53.44	56.95	50.85	1.53	41.62	6.24	971
1961	42.01	54.27	57.05	51.45	1.21	41.60	6.66	969
1913	42.99	54.48	57.25	51.95	1.13	41.70	6.69	967
1374	44.01	54.91	57.25	52.15	1.23	42.18	6.75	965
1794	45.02	55.24	56.45	52.35	1.09	42.29	6.64	958
571	45.98	54.88	56.95	53.85	0.85	41.36	5.17	956
389	47.02	55.62	57.45	54.25	0.96	42.40	5.05	955
236	48.02	57.04	57.55	54.55	0.41	44.29	4.33	929
100	48.99	57.31	57.65	57.15	0.13	44.50	1.23	937
113	50.00	57.58	57.65	57.45	0.06	44.45	1.01	923

Table 37: Averaged data results for US-Exp 4, 3/18/2014 to 4/13/2014 (avg – average, temp – temperature, std dev– standard deviation)

#Data Points	Avg Inlet Temp	Avg Outlet Temp	Max Temp	Min Temp	Temp Std Dev	Soil Temp Avg	Soil Temp Range
100	25.97	48.85	49.05	48.75	0.04	41.89	1.06
507	26.99	48.74	49.25	48.35	0.32	40.07	4.71
201	27.98	48.96	49.55	48.35	0.40	39.62	5.14
509	29.00	49.04	49.75	48.45	0.27	40.26	25.22
281	29.99	49.12	49.85	48.55	0.31	47.42	24.72
332	31.01	49.29	50.15	48.65	0.53	40.97	26.36
715	32.01	49.61	50.25	48.85	0.25	43.22	26.88
1126	32.99	49.55	50.45	48.95	0.33	45.58	28.05
1059	34.00	50.02	50.65	49.05	0.48	43.09	29.44
1085	35.01	50.39	51.05	49.25	0.43	45.17	29.00
1741	36.00	50.47	51.15	49.35	0.51	47.08	29.28
2494	37.00	51.01	53.15	49.55	0.52	43.41	29.46
2104	37.99	51.20	53.25	49.85	0.58	45.56	26.19
1851	38.99	51.67	53.65	49.95	0.81	44.43	25.15
3099	39.99	51.80	53.85	50.05	0.68	43.80	24.84

2722	40.99	51.81	54.05	50.25	0.60	41.57	24.25
2317	42.01	52.06	54.15	50.35	0.69	41.70	22.93
3487	42.99	52.18	54.55	50.55	0.82	42.35	22.88
1732	44.01	52.50	54.55	50.75	0.87	42.07	22.92
2795	45.00	52.67	54.75	50.85	0.90	41.56	21.19
1455	45.98	52.71	54.85	50.95	0.62	42.06	20.36
1136	47.01	52.97	54.95	51.35	0.70	40.43	21.46
1647	48.00	53.26	55.15	51.65	0.80	40.14	20.91
1318	48.99	53.46	55.25	51.75	0.64	42.23	19.98
1147	49.99	53.36	55.65	51.95	0.85	41.63	19.90
1143	50.99	53.92	55.75	52.35	0.89	41.57	16.57
893	52.00	54.22	55.95	52.45	0.88	41.94	14.26
652	53.00	54.80	56.05	52.65	0.78	42.61	12.84
650	54.01	54.86	56.05	52.75	0.80	41.60	13.14
437	54.99	54.59	56.15	52.85	1.01	41.97	12.63
511	56.01	54.90	56.35	53.05	1.10	43.05	12.05
453	57.01	55.48	56.45	54.25	0.63	42.41	4.52
652	57.98	55.92	56.55	54.45	0.42	42.11	3.19
122	59.00	55.94	56.65	54.55	0.37	42.19	2.44
154	60.02	56.23	56.75	54.65	0.42	41.89	1.74
81	61.00	56.25	56.85	54.75	0.53	41.81	2.50
209	61.99	56.76	56.95	55.85	0.22	41.61	1.52
147	63.00	56.56	56.95	56.05	0.29	41.70	1.71
103	63.98	56.45	56.75	55.45	0.33	41.73	1.26
175	65.02	55.96	56.15	55.55	0.13	41.47	1.98
2	68.05	57.40	57.55	57.25	0.21	42.33	0.47
2	71.95	56.30	56.45	56.15	0.21	41.70	0.35

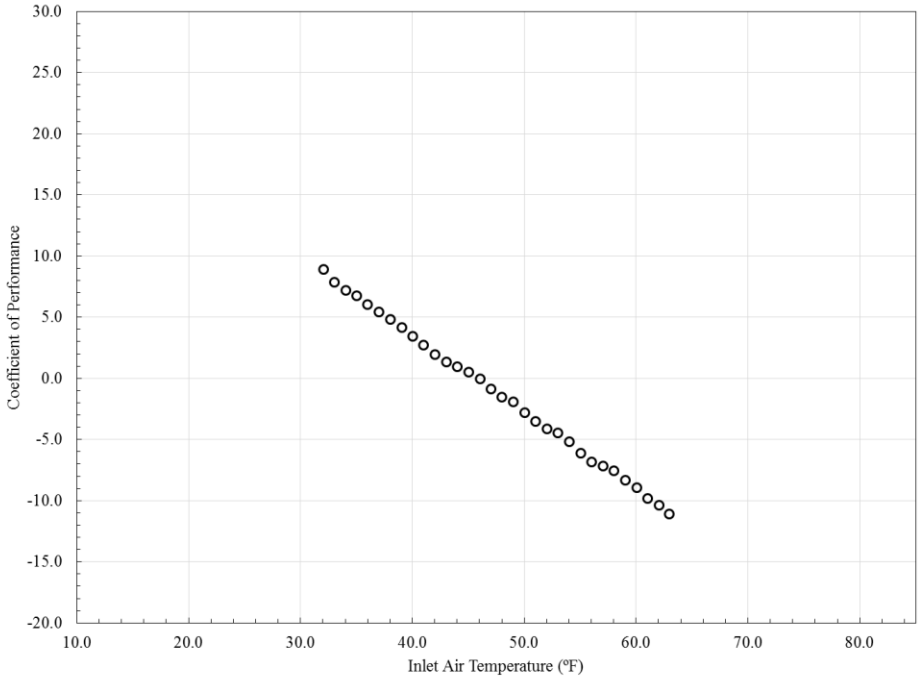


Figure 168: Coefficient of performance for the under yard EAHX based on inlet temperature for UY-Exp 1

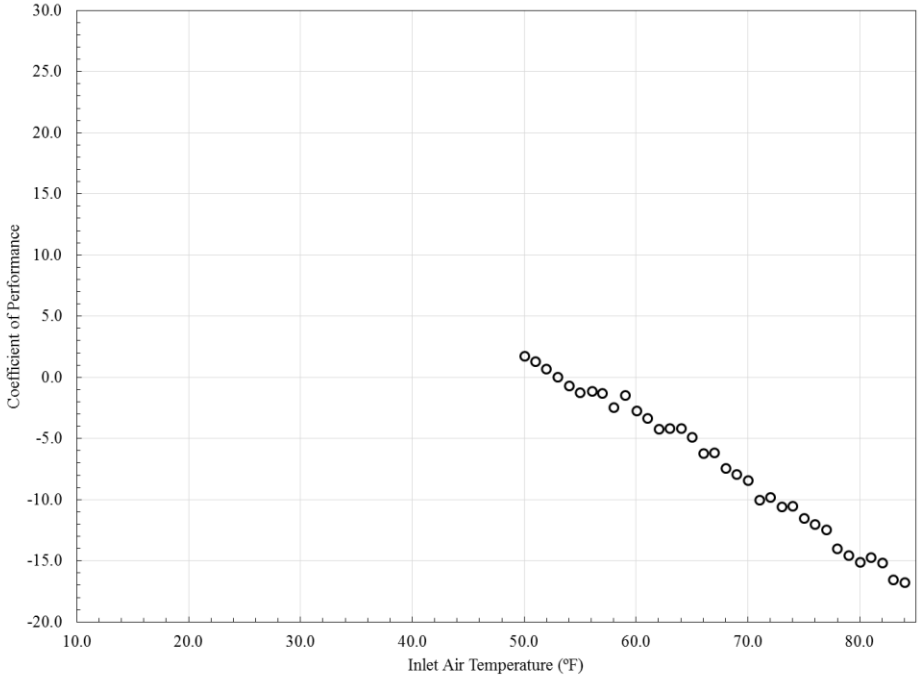


Figure 169: Coefficient of performance for the under yard EAHX based on inlet temperature for UY-Exp 2

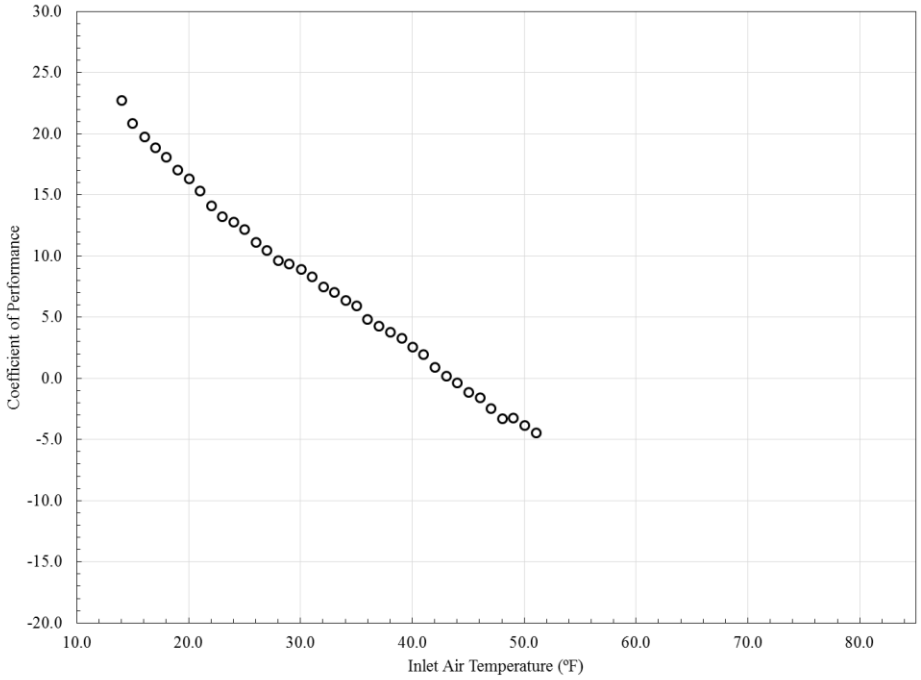


Figure 170: Coefficient of performance for the under yard EAHX based on inlet temperature for UY-Exp 4

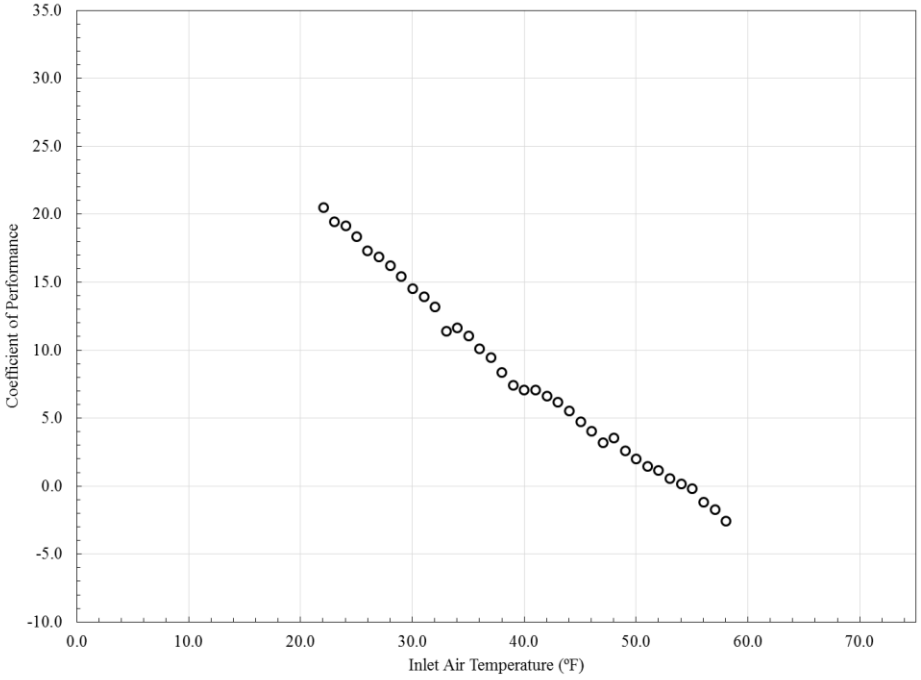


Figure 171: Coefficient of performance for the under slab EAHX based on inlet temperature for US-Exp 1

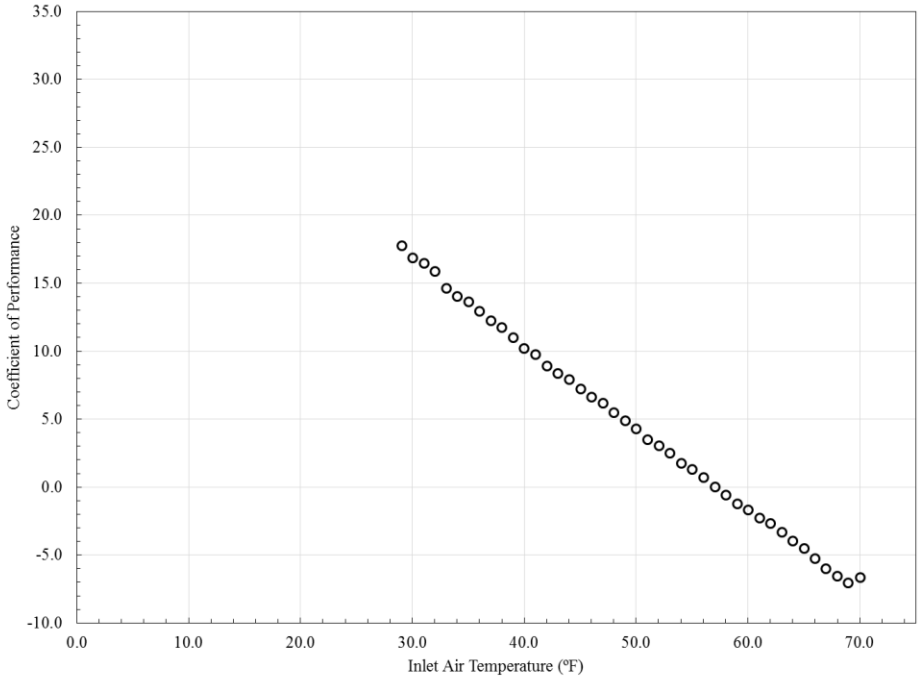


Figure 172: Coefficient of performance for the under slab EAHX based on inlet temperature for US-Exp 2

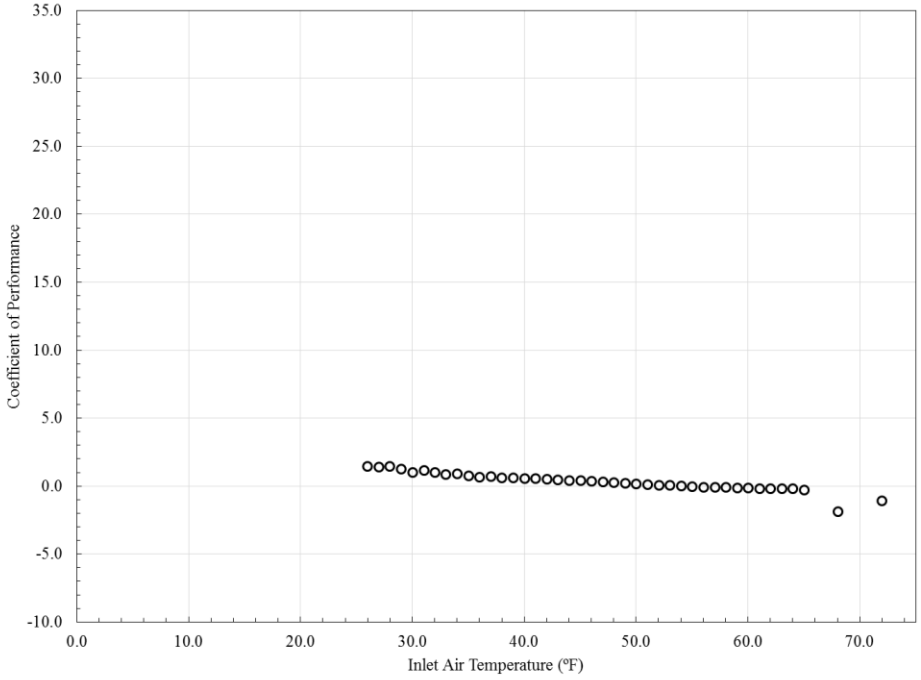


Figure 173: Coefficient of performance for the under slab EAHX based on inlet temperature for US-Exp 4

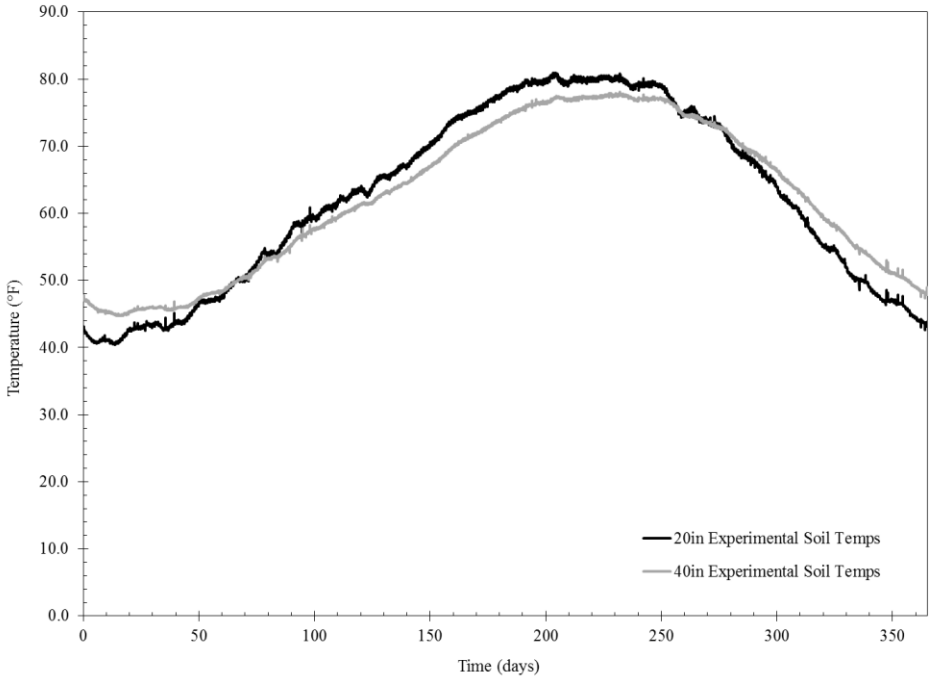


Figure 174: Albuquerque, New Mexico – observed ground temperatures at 20 inch and 40 inch depths (taken from Los Lunas PMC site outside of Albuquerque, NM) [71]

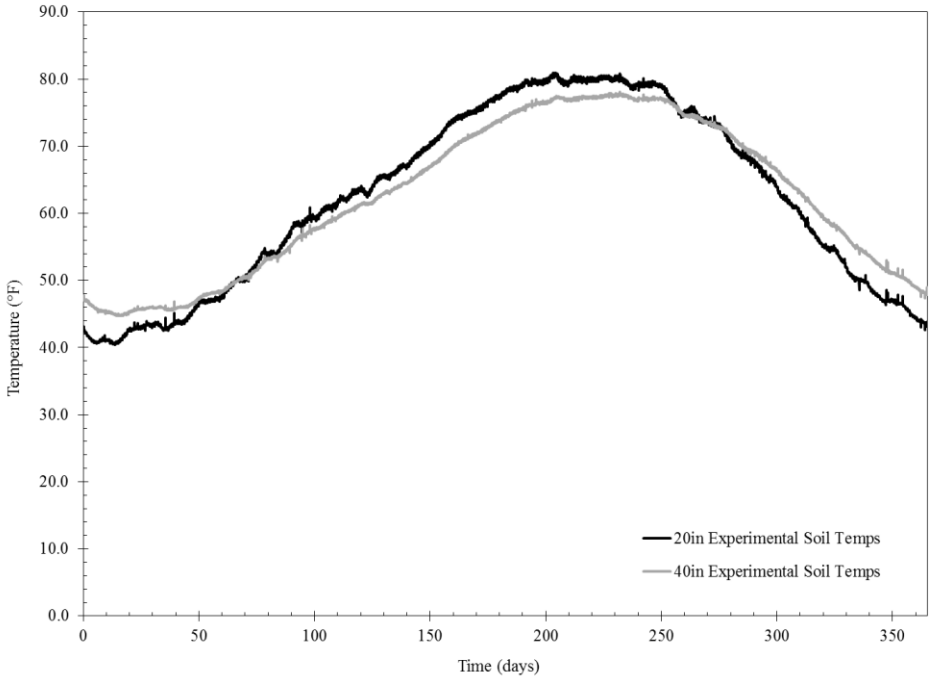


Figure 175: Amarillo, Texas – observed ground temperatures at 20 inch and 40 inch depths (taken from Bushland site outside of Amarillo, TX) [71]

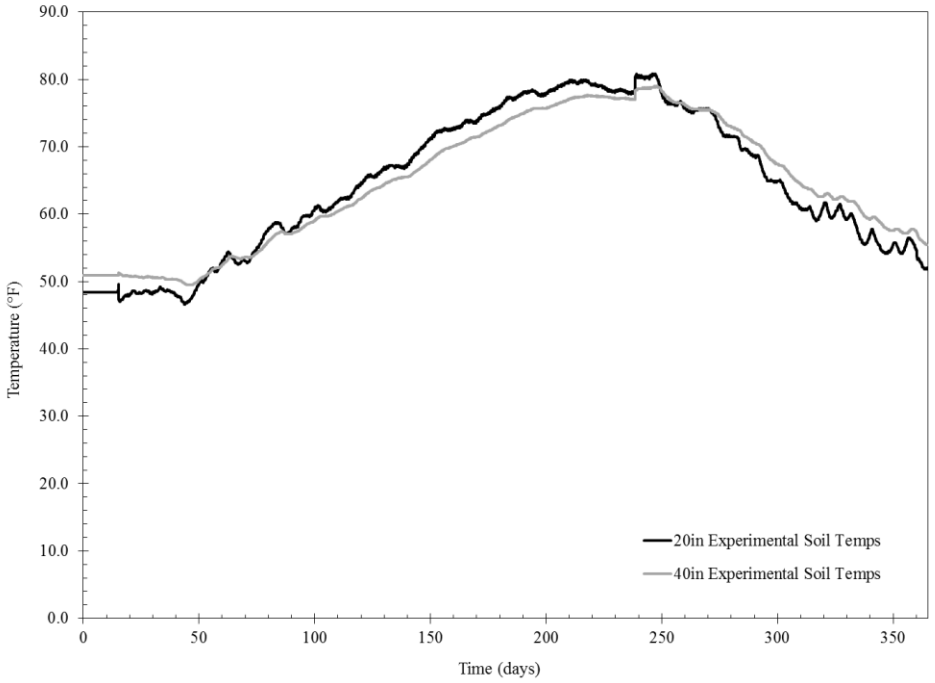


Figure 176: Athens, Georgia – observed ground temperatures at 20 inch and 40 inch depths (taken from Watkinsville site outside of Athens, GA) [71]

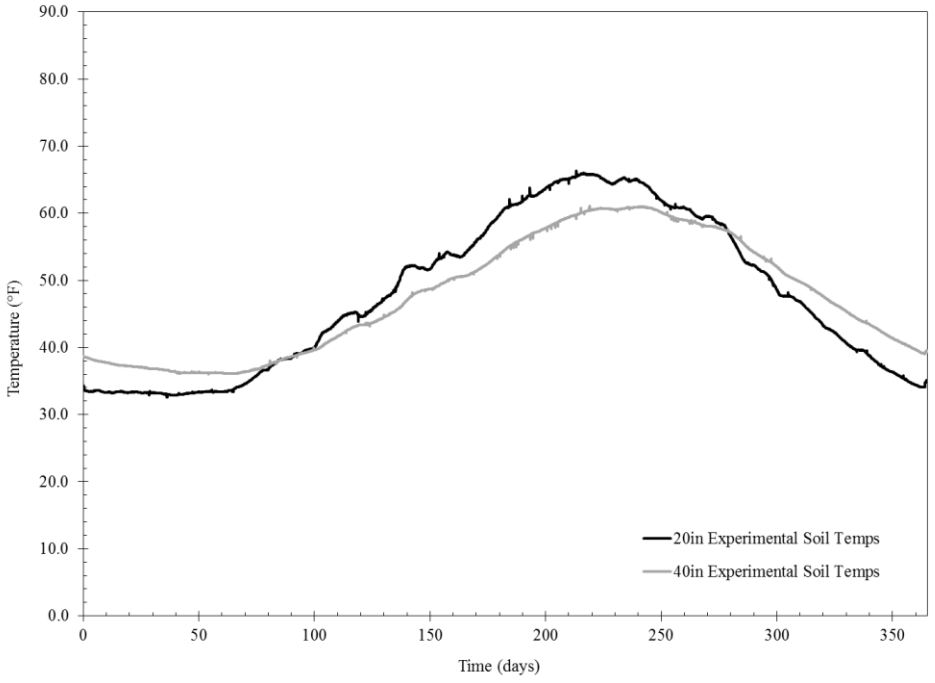


Figure 177: Bozeman, Montana – observed ground temperatures at 20 inch and 40 inch depths (taken from Table Mountain site outside of Bozeman, MT) [71]

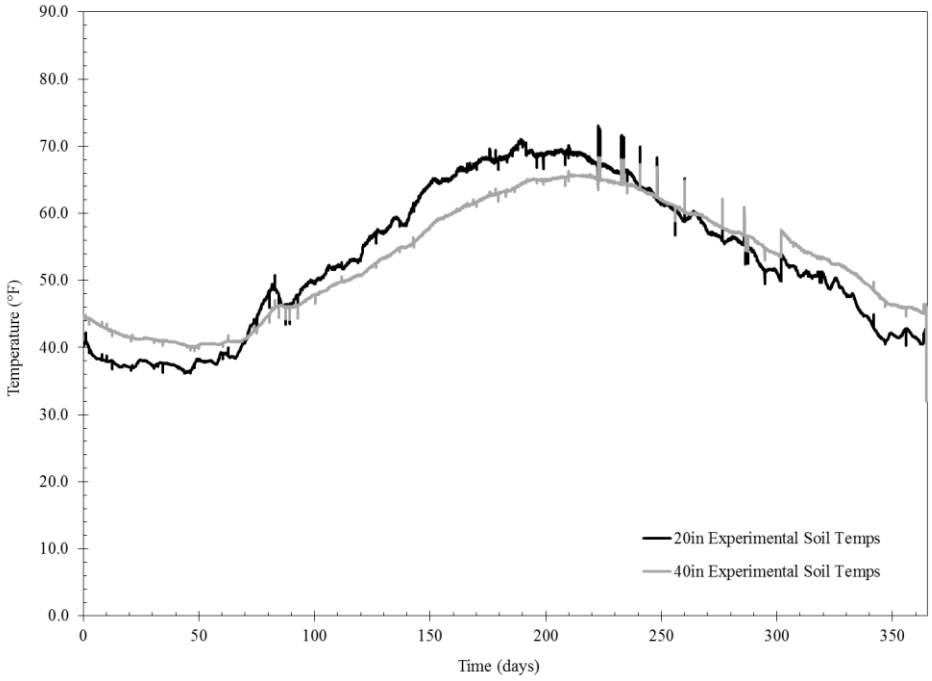


Figure 178: Columbus, Ohio – observed ground temperatures at 20 inch and 40 inch depths (taken from Moly Caren site outside of Columbus, OH) [71]

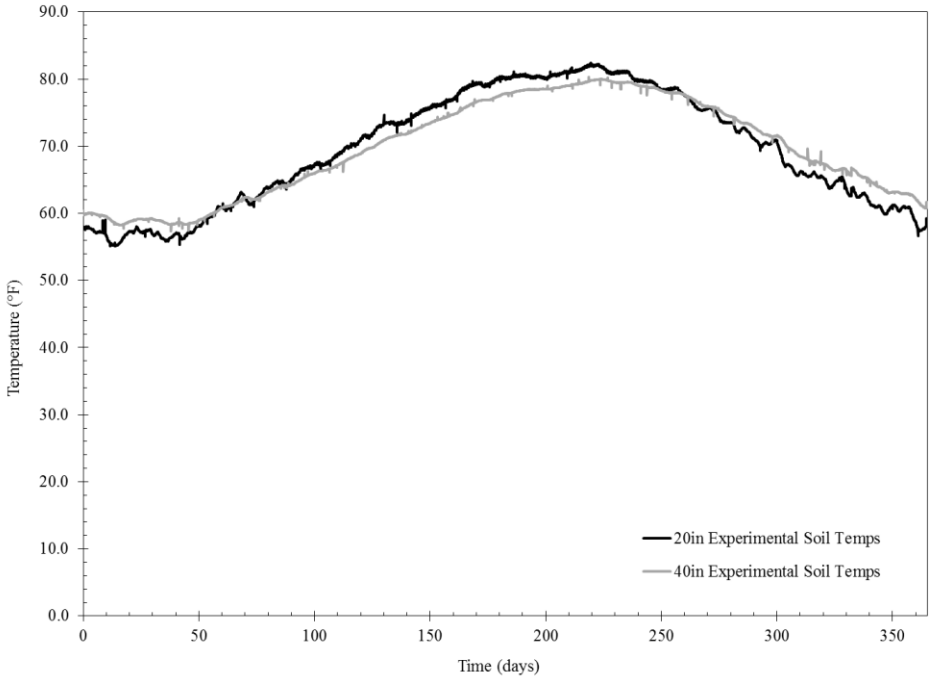


Figure 179: Houston, Texas – observed ground temperatures at 20 inch and 40 inch depths (taken from Prairie View #1 site outside of Houston, TX) [71]

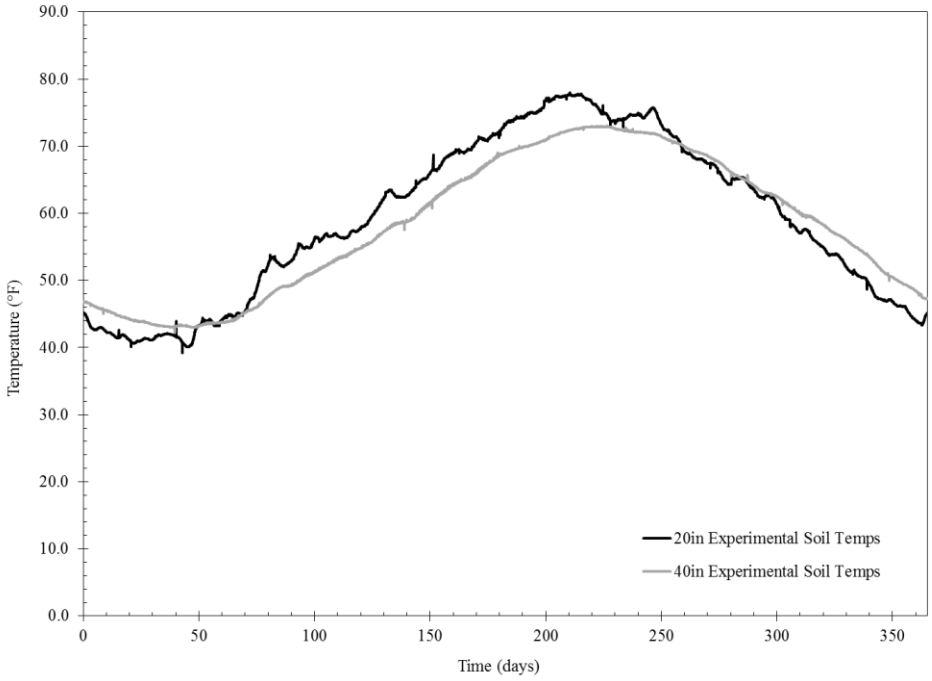


Figure 180: Kansas City, Missouri – observed ground temperatures at 20 inch and 40 inch depths (taken from Powell Gardens site outside of Kansas City, MO) [71]

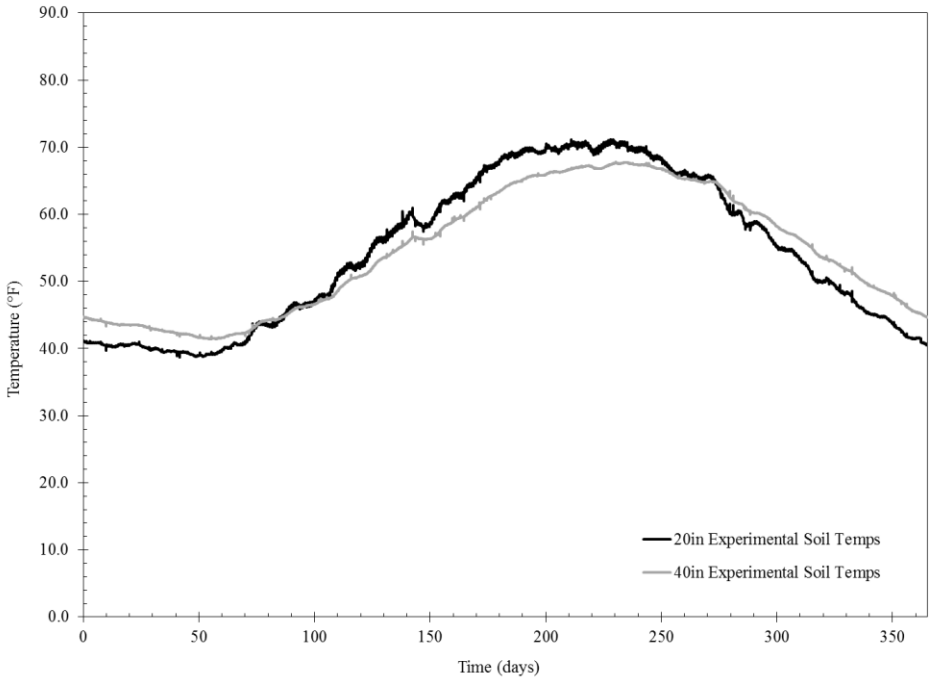


Figure 181: Las Vegas, Nevada – observed ground temperatures at 20 inch and 40 inch depths (taken from Pine Nut site outside of Las Vegas, NV) [71]

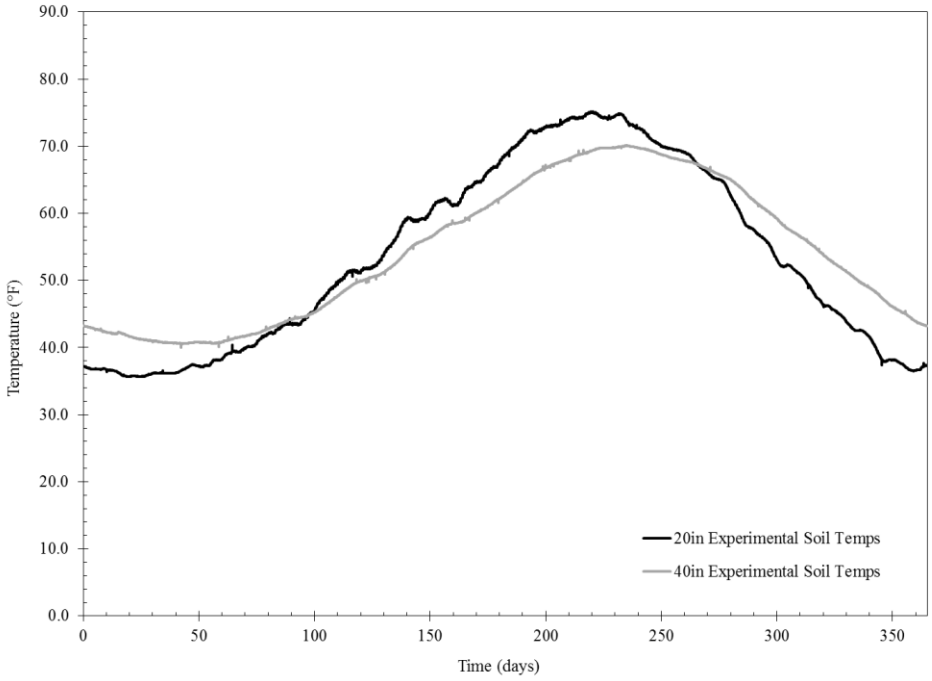


Figure 182: Moses Lake, Washington – observed ground temperatures at 20 inch and 40 inch depths (taken from Lind site outside of Moses Lake, WA) [71]

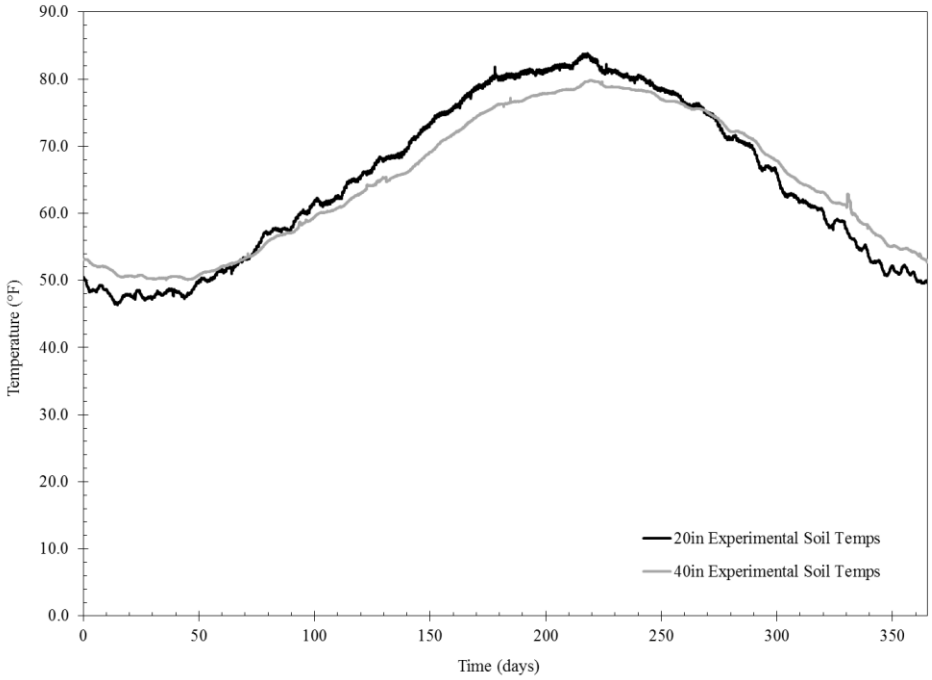


Figure 183: Pine Bluff, Arkansas – observed ground temperatures at 20 inch and 40 inch depths (taken from UAPB Campus-PB site outside of Pine Bluff, AR) [71]

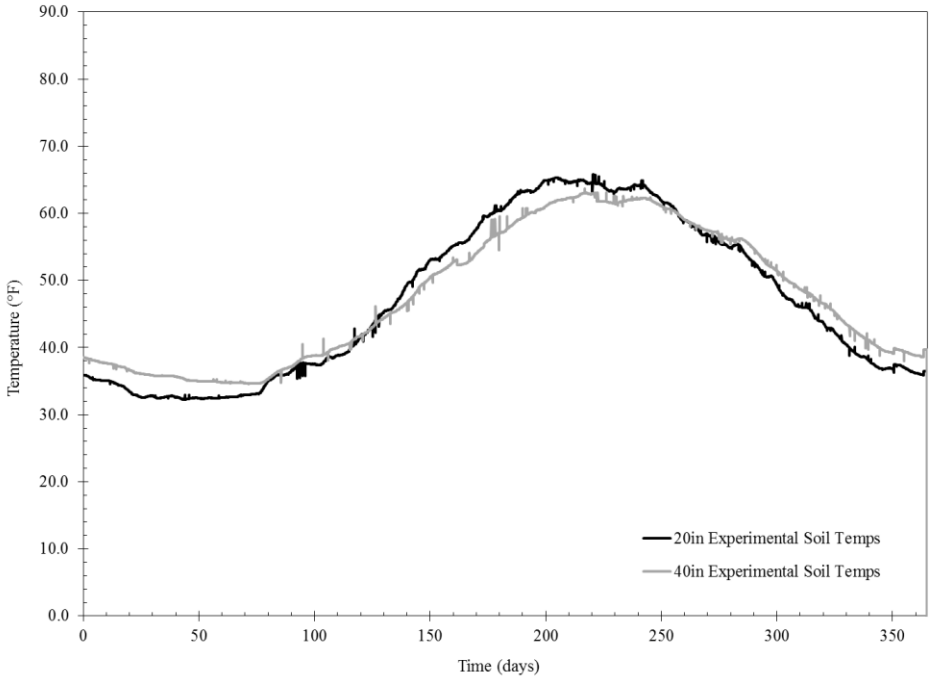


Figure 184: Saint Cloud, Minnesota – observed ground temperatures at 20 inch and 40 inch depths (taken from Crescent Lake site outside of Saint Cloud, MN) [71]

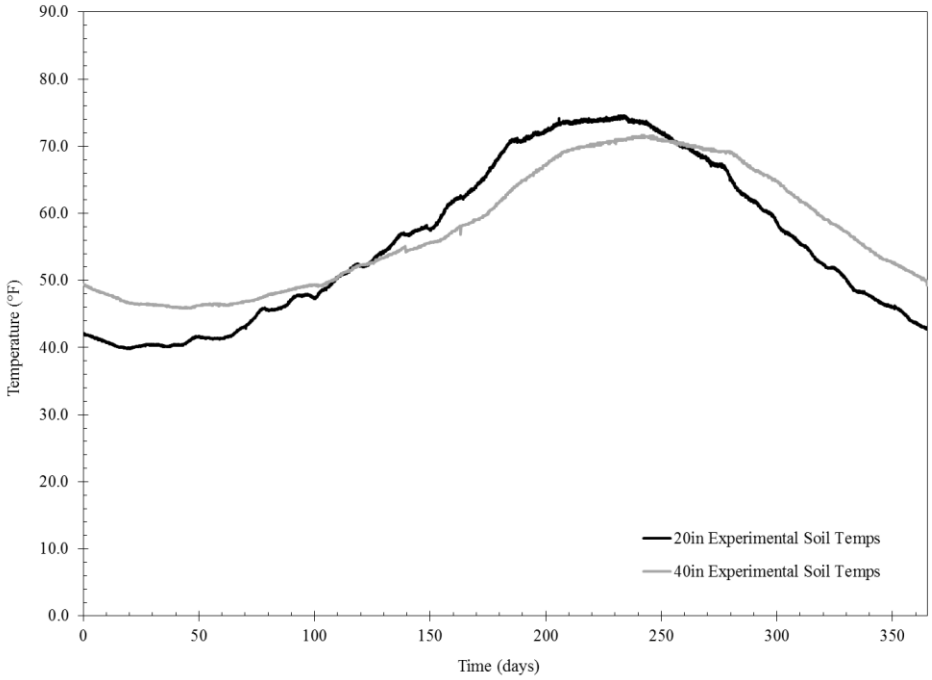


Figure 185: Salt Lake City, Utah – observed ground temperatures at 20 inch and 40 inch depths (taken from Grantsville site outside of Salt Lake City, UT) [71]

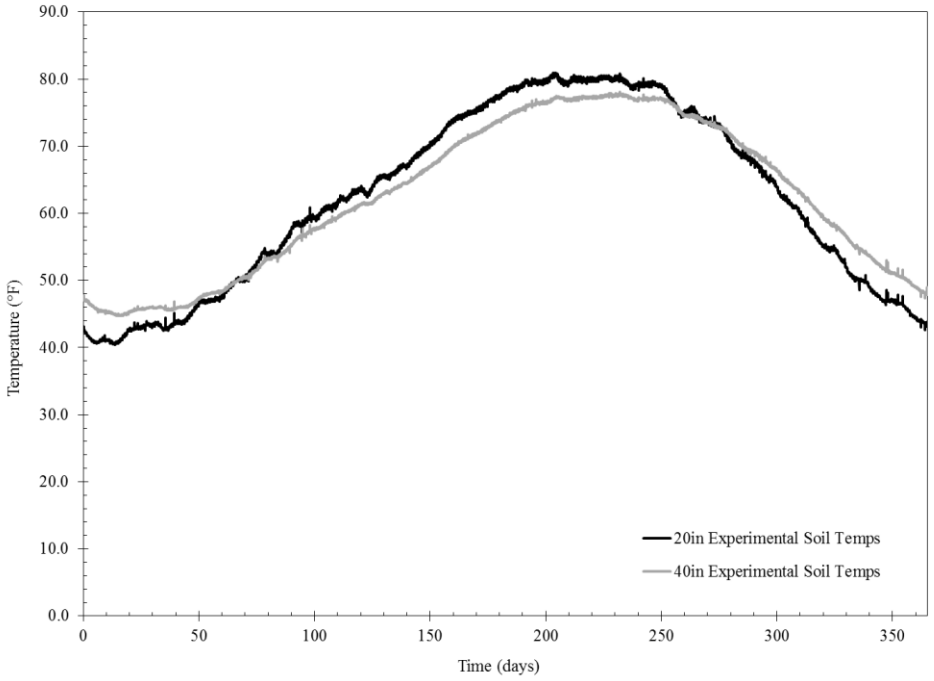


Figure 186: Sioux Falls, South Dakota – observed ground temperatures at 20 inch and 40 inch depths (taken from EROS Data Center site outside of Sioux Falls, SD) [71]

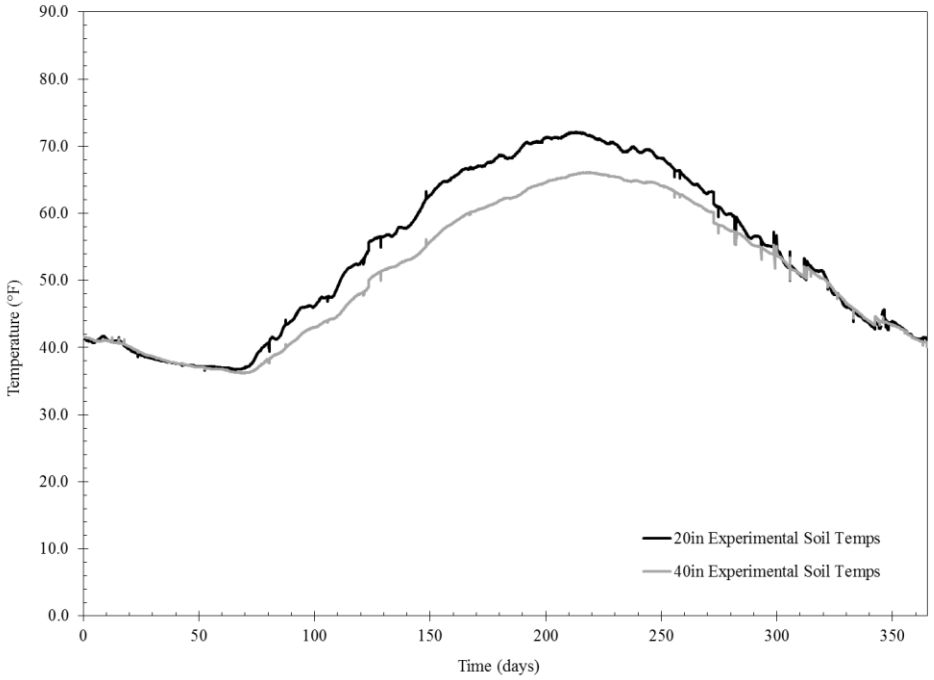


Figure 187: State College, Pennsylvania – observed ground temperatures at 20 inch and 40 inch depths (taken from EROS Data Center site outside of Sioux Falls, SD) [71]

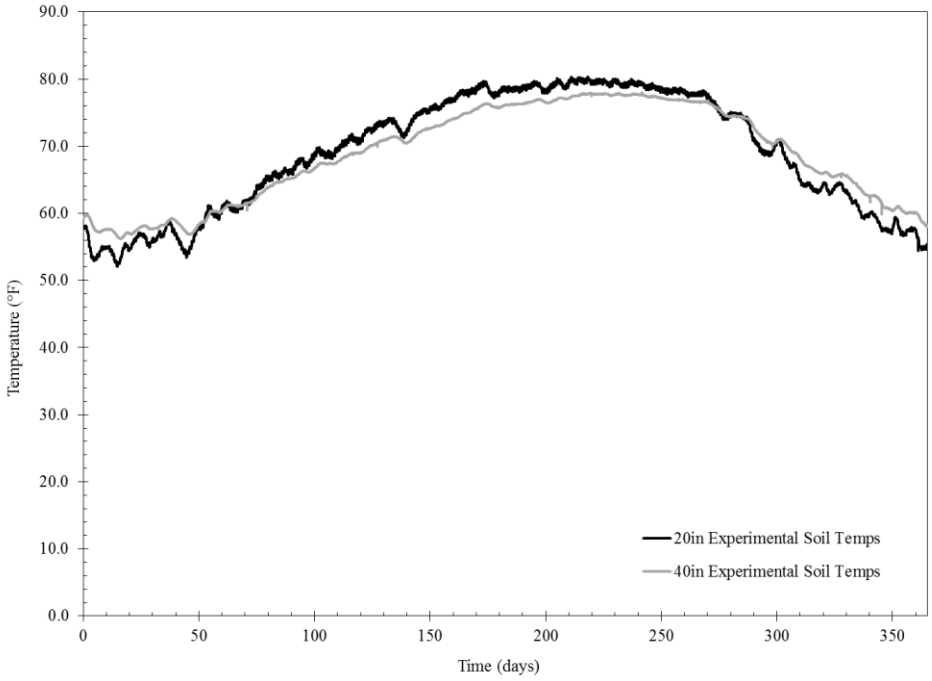


Figure 188: Tallahassee, Florida – observed ground temperatures at 20 inch and 40 inch depths (taken from Wakulla site outside of Tallahassee, FL) [71]

APPENDIX B

LOCATION WEATHER DATA AND CURVE FITS

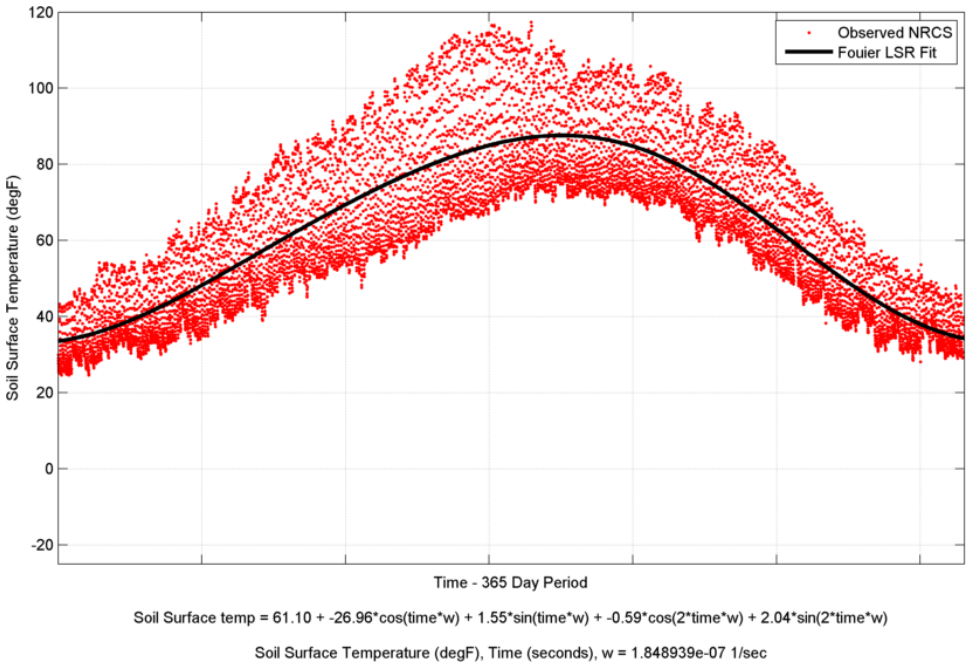


Figure 189: Albuquerque, New Mexico – Least-squares curve fit to observed soil surface temperatures using four term Fourier series

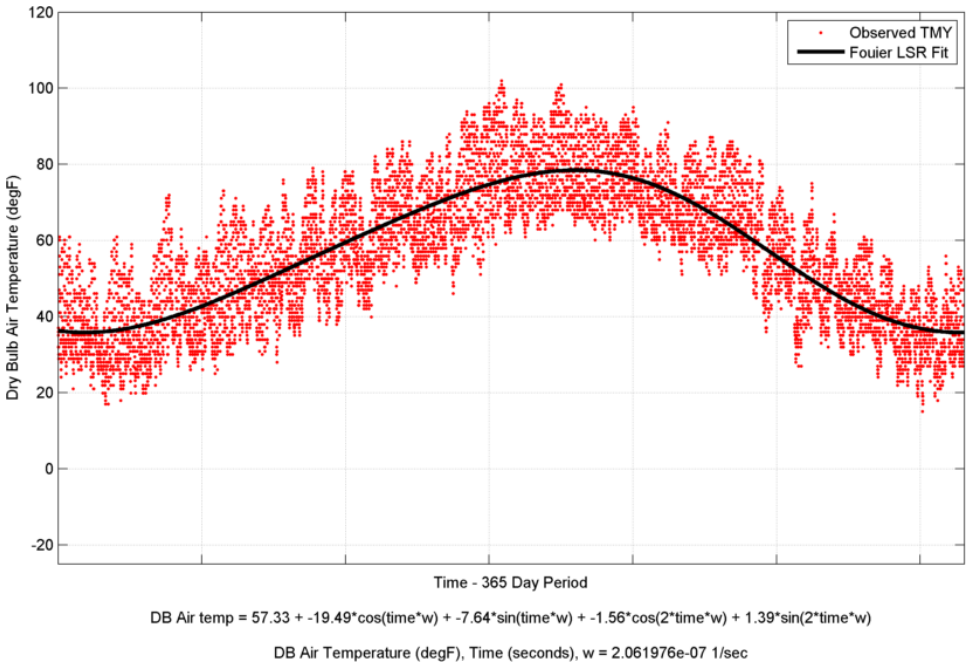


Figure 190: Albuquerque, New Mexico – Least-squares curve fit to dry bulb air temperatures from a typical meteorological year (TMY) using four term Fourier series

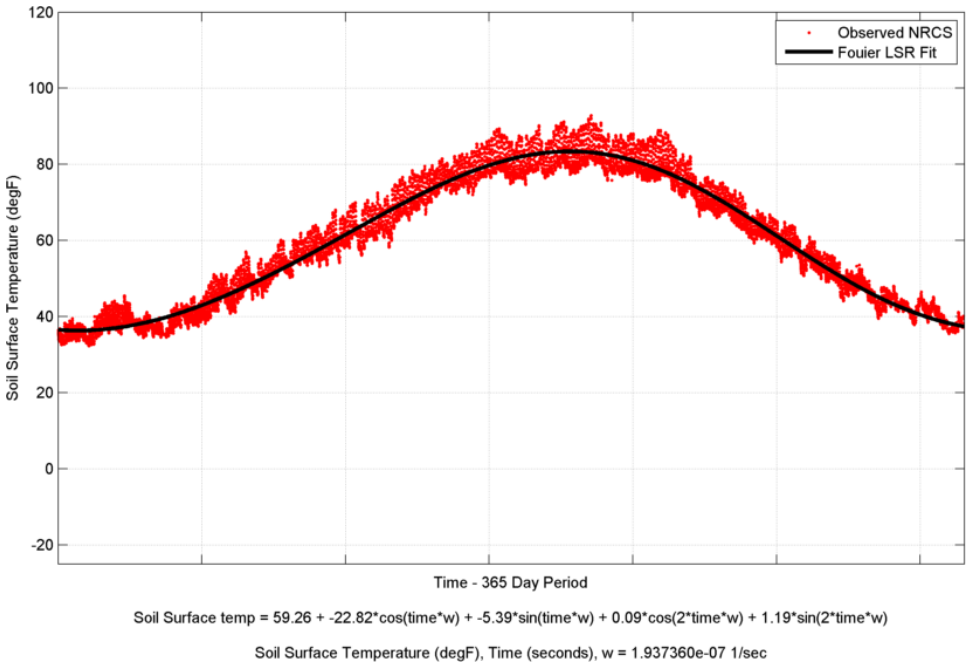


Figure 191: Amarillo, Texas – Least-squares curve fit to observed soil surface temperatures using four term Fourier series

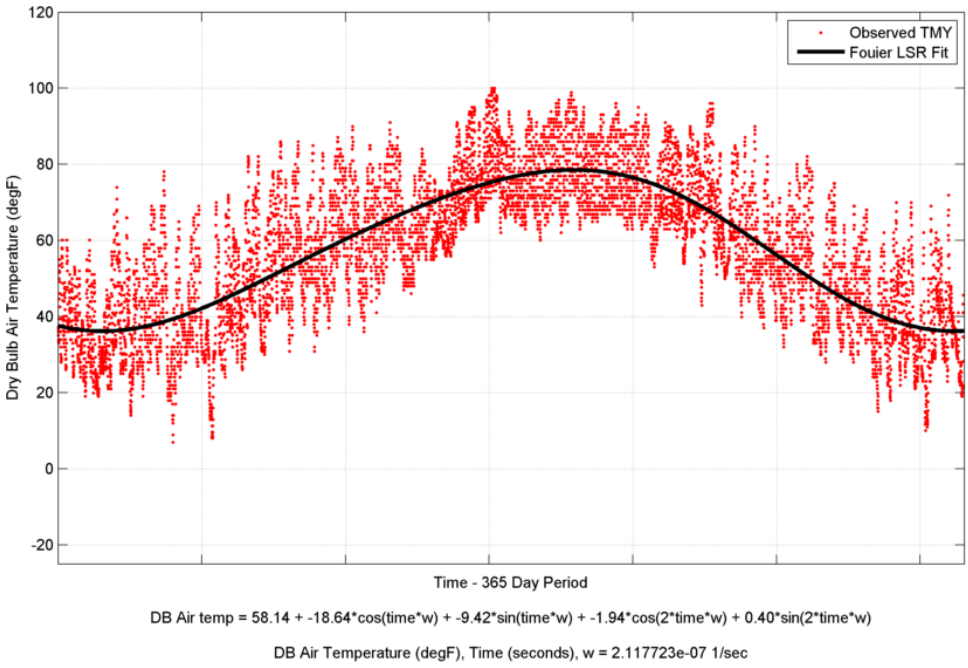


Figure 192: Amarillo, Texas – Least-squares curve fit to dry bulb air temperatures from a typical meteorological year (TMY) using four term Fourier series

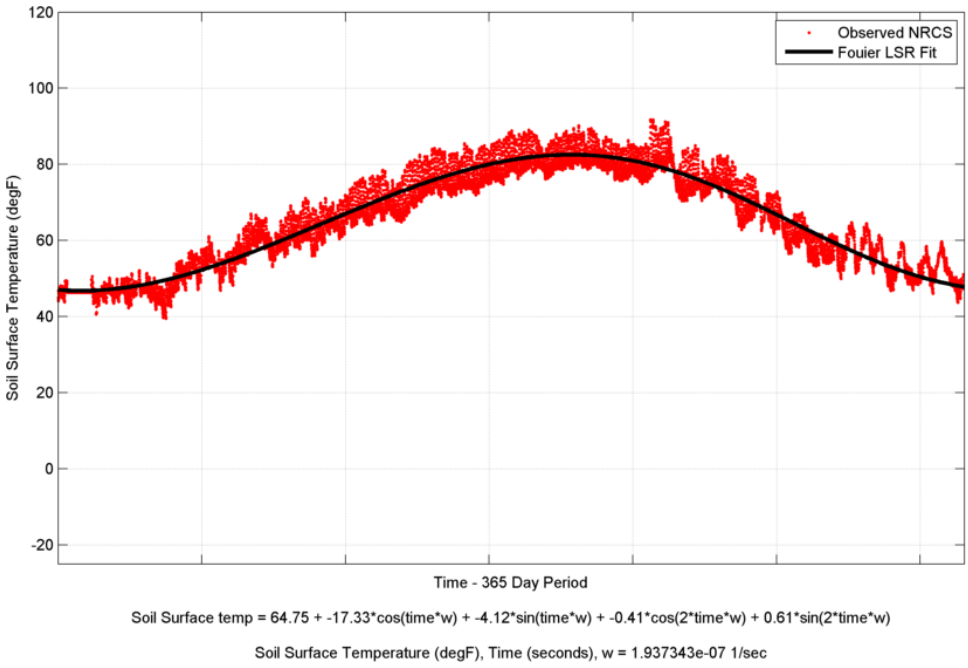


Figure 193: Athens, Georgia – Least-squares curve fit to observed soil surface temperatures using four term Fourier series

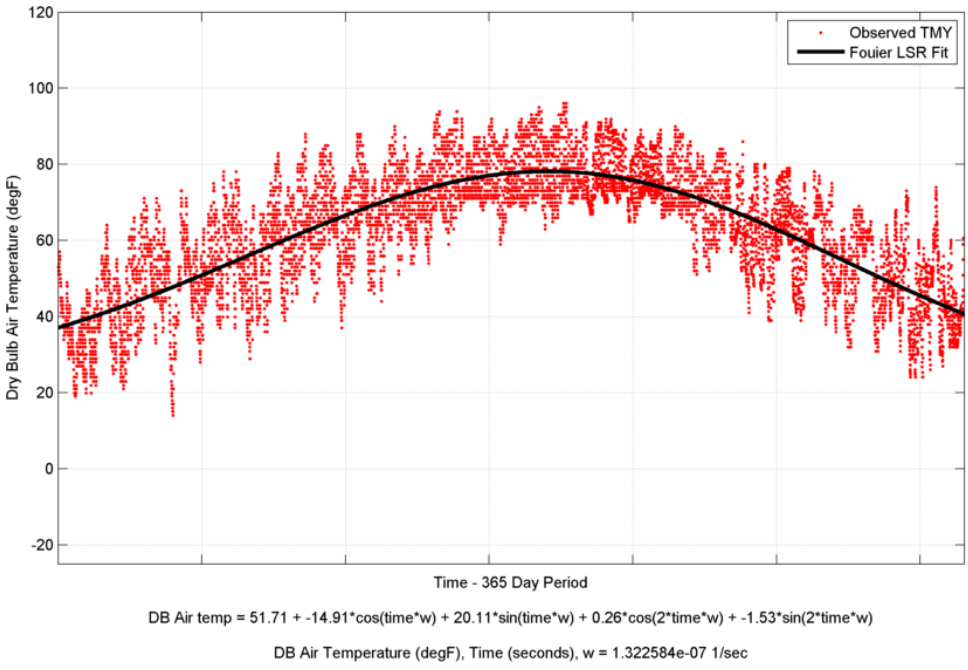


Figure 194: Athens, Georgia – Least-squares curve fit to dry bulb air temperatures from a typical meteorological year (TMY) using four term Fourier series

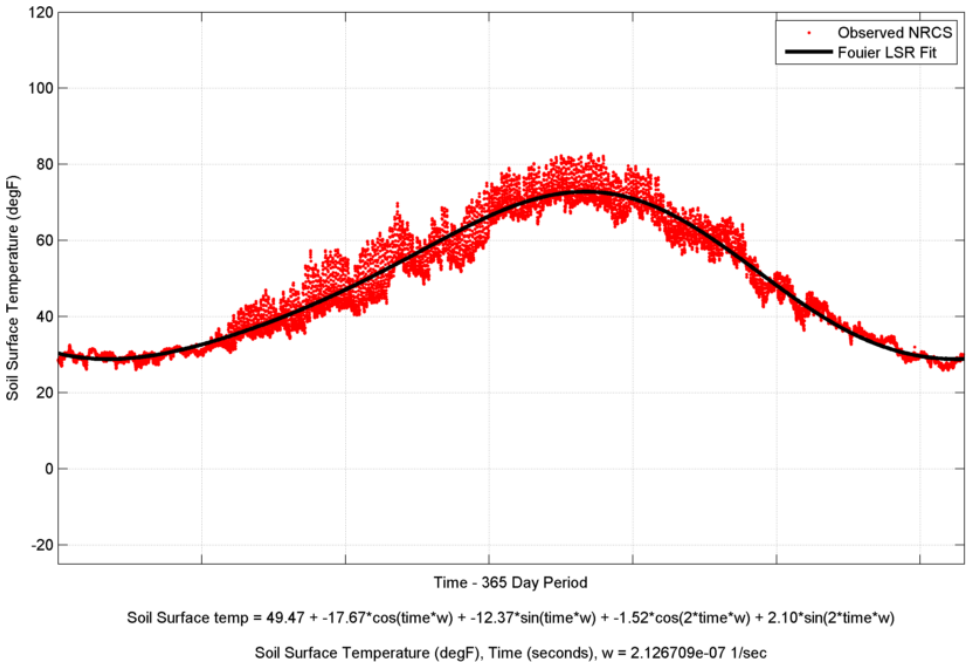


Figure 195: Bozeman, Montana– Least-squares curve fit to observed soil surface temperatures using four term Fourier series

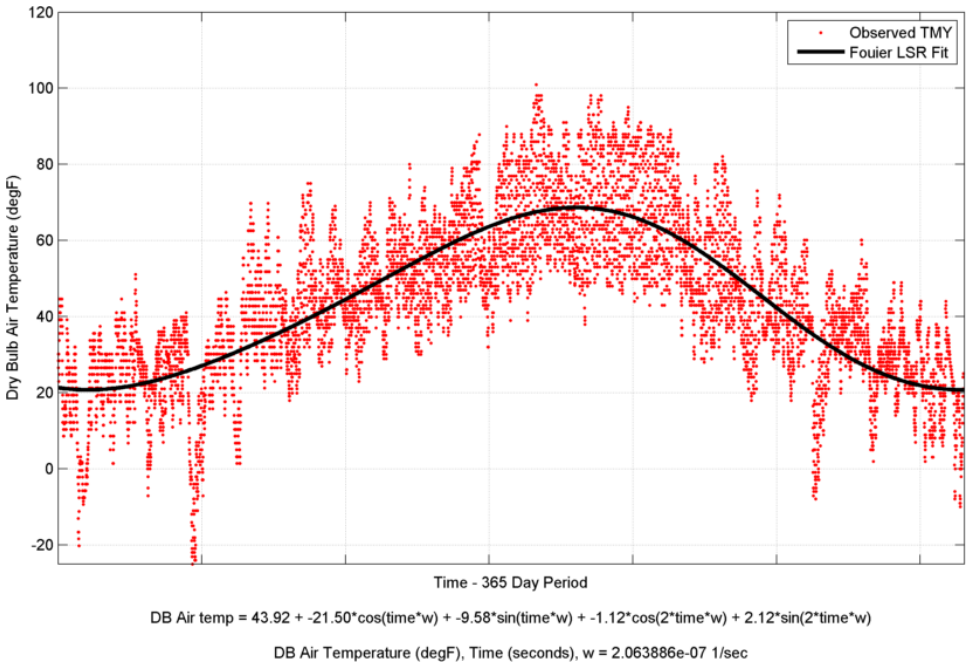


Figure 196: Bozeman, Montana – Least-squares curve fit to dry bulb air temperatures from a typical meteorological year (TMY) using four term Fourier series

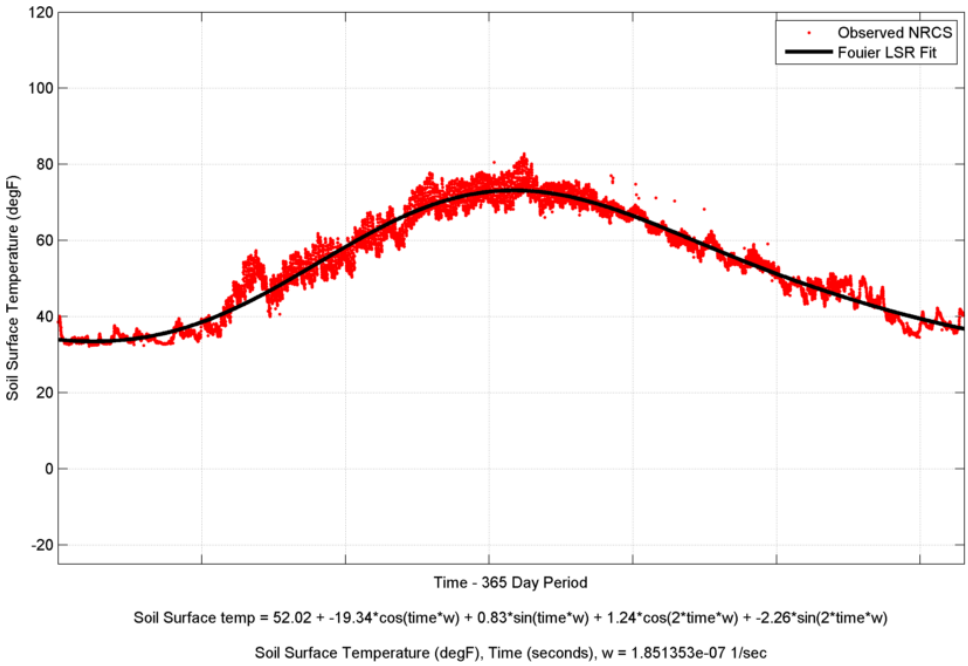


Figure 197: Columbus, Ohio – Least-squares curve fit to observed soil surface temperatures using four term Fourier series

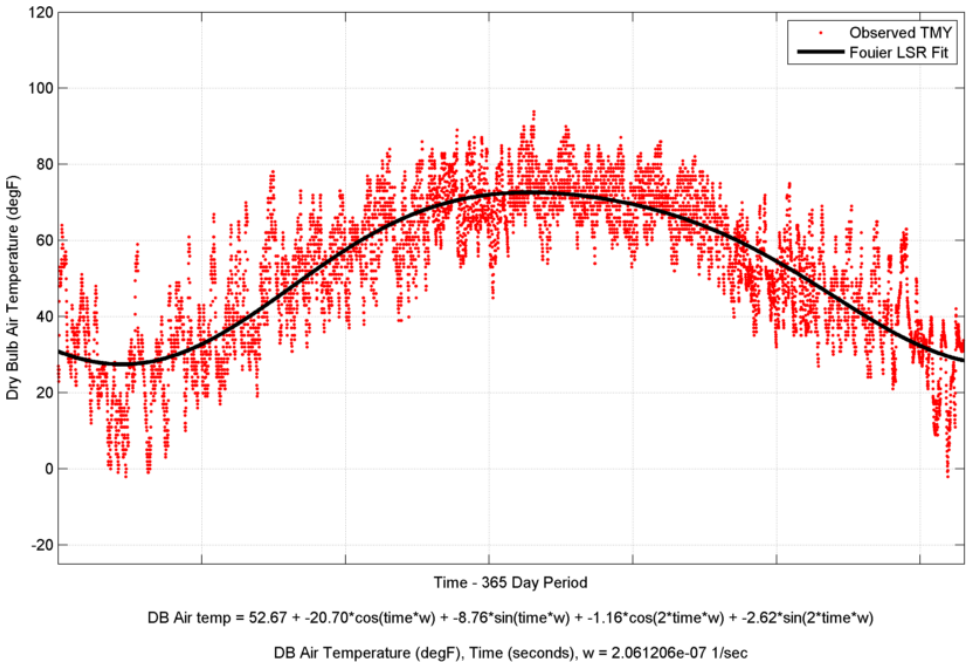


Figure 198: Columbus, Ohio – Least-squares curve fit to dry bulb air temperatures from a typical meteorological year (TMY) using four term Fourier series

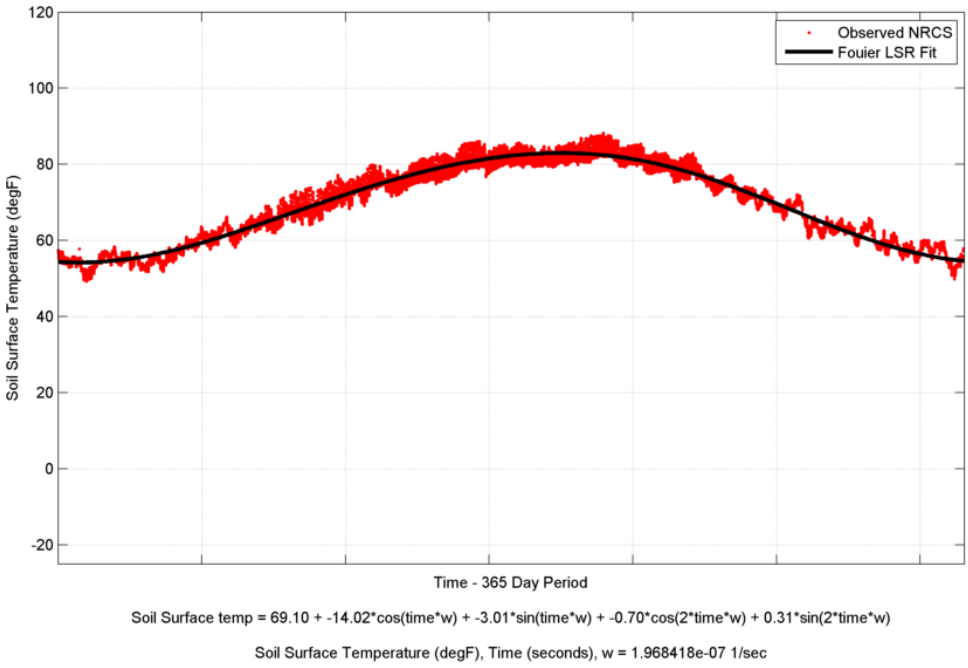


Figure 199: Houston, Texas – Least-squares curve fit to observed soil surface temperatures using four term Fourier series

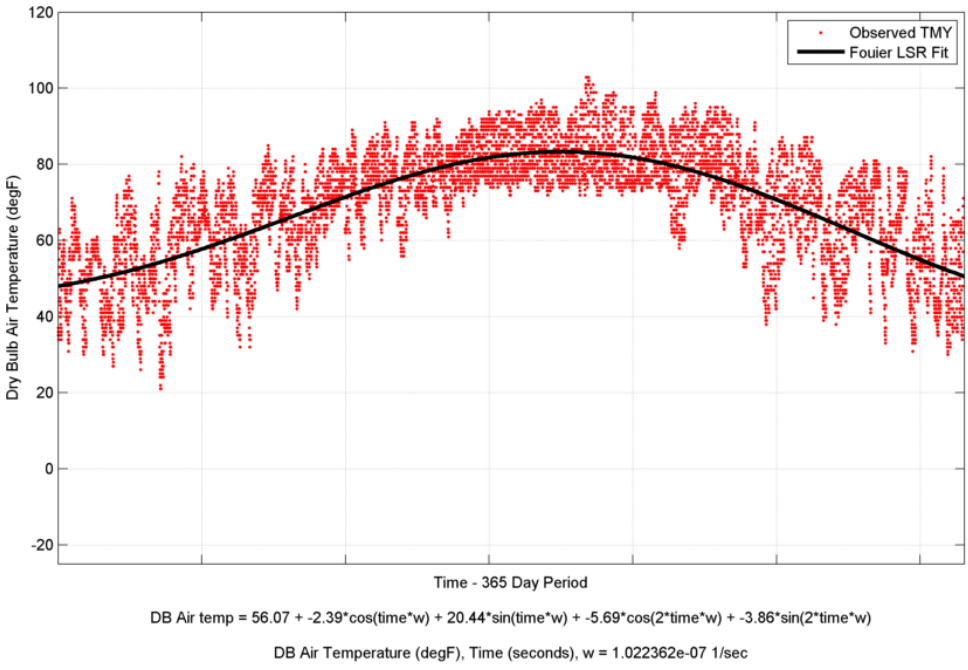


Figure 200: Houston, Texas – Least-squares curve fit to dry bulb air temperatures from a typical meteorological year (TMY) using four term Fourier series

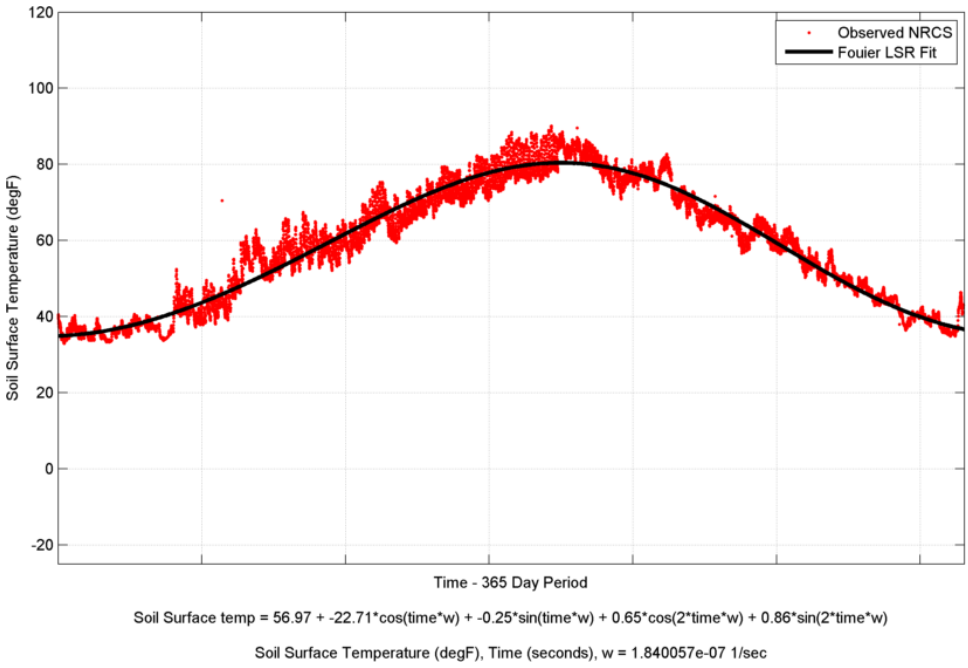


Figure 201: Kansas City, Missouri – Least-squares curve fit to observed soil surface temperatures using four term Fourier series

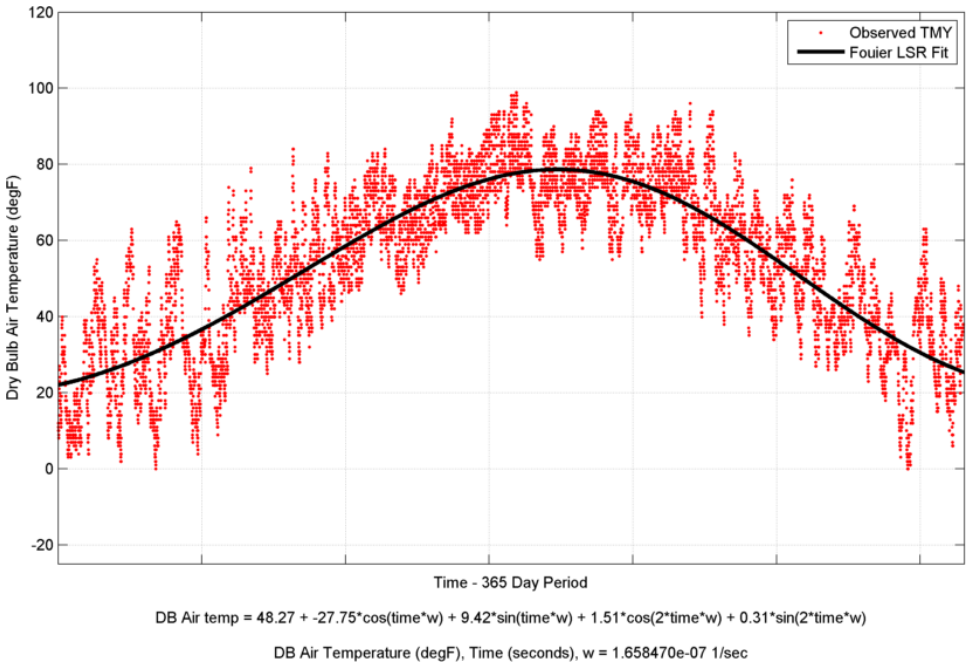


Figure 202: Kansas City, Missouri – Least-squares curve fit to dry bulb air temperatures from a typical meteorological year (TMY) using four term Fourier series

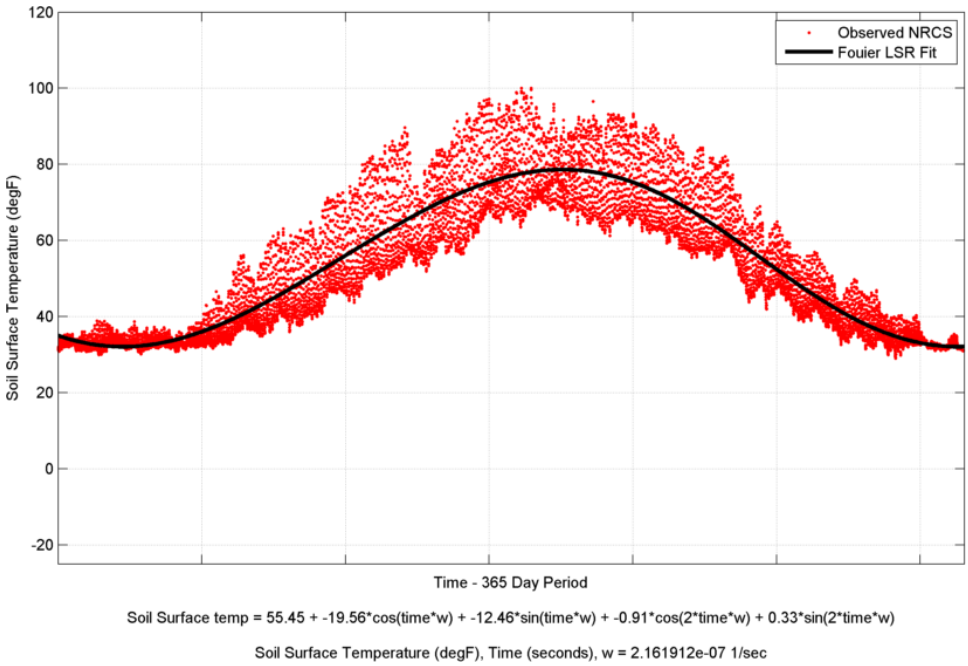


Figure 203: Las Vegas, Nevada – Least-squares curve fit to observed soil surface temperatures using four term Fourier series

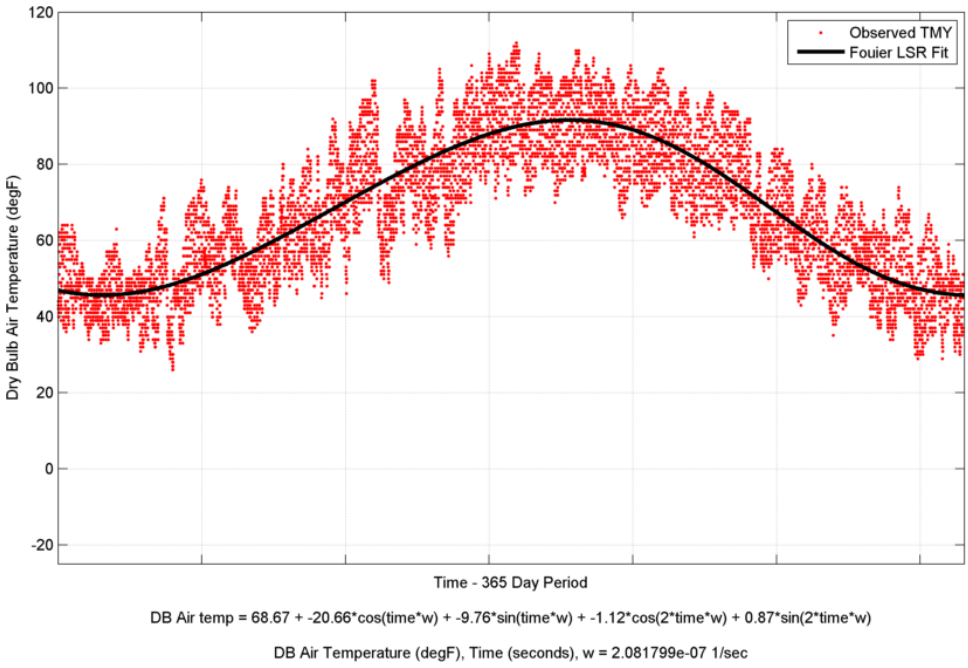


Figure 204: Las Vegas, Nevada – Least-squares curve fit to dry bulb air temperatures from a typical meteorological year (TMY) using four term Fourier series

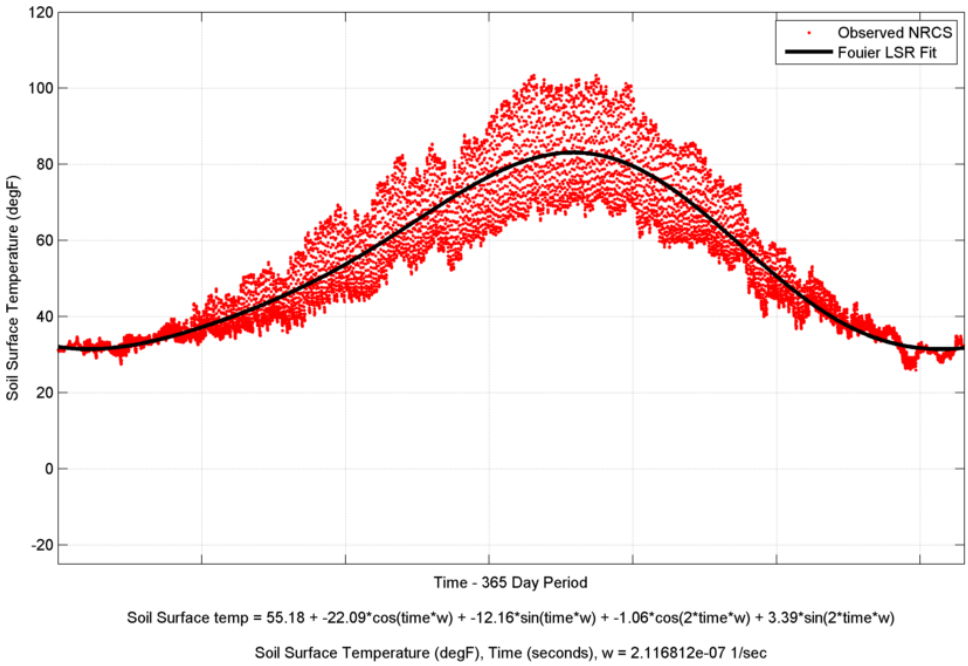


Figure 205: Moses Lake, Washington – Least-squares curve fit to observed soil surface temperatures using four term Fourier series

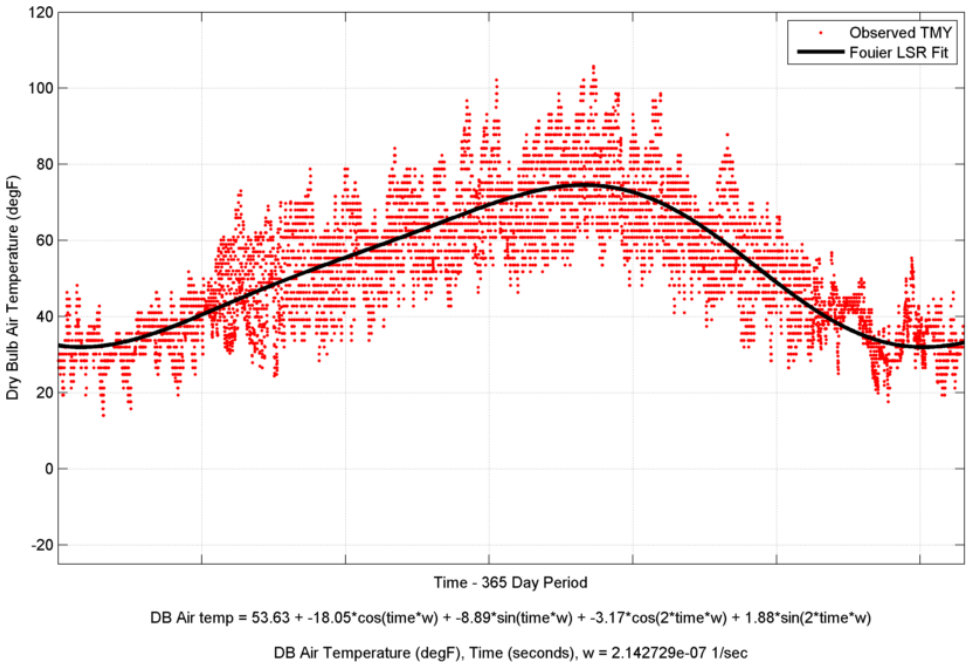


Figure 206: Moses Lake, Washington – Least-squares curve fit to dry bulb air temperatures from a typical meteorological year (TMY) using four term Fourier series

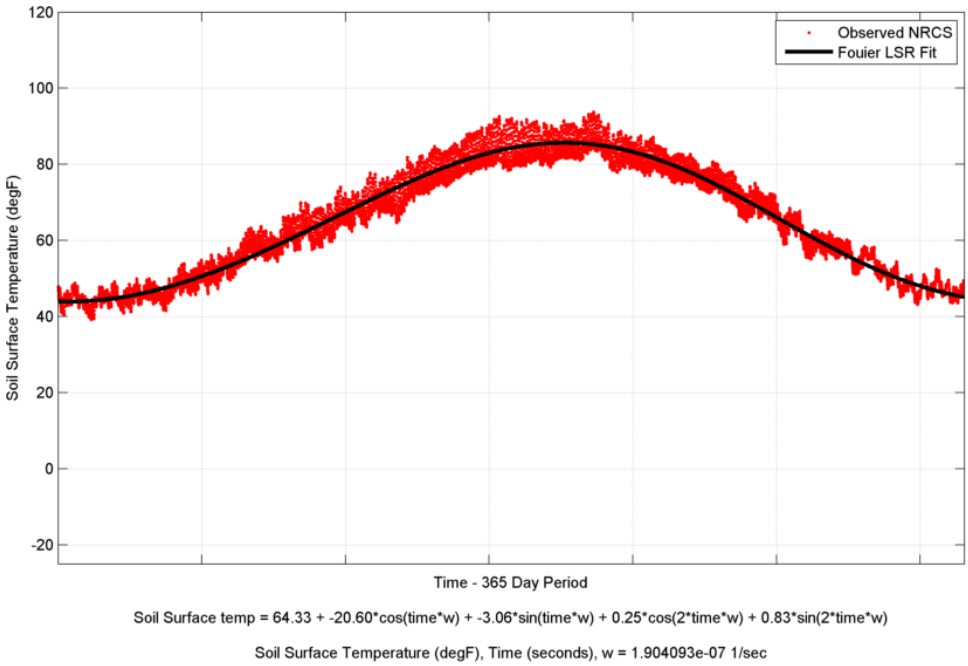


Figure 207: Pine Bluff, Arkansas – Least-squares curve fit to observed soil surface temperatures using four term Fourier series

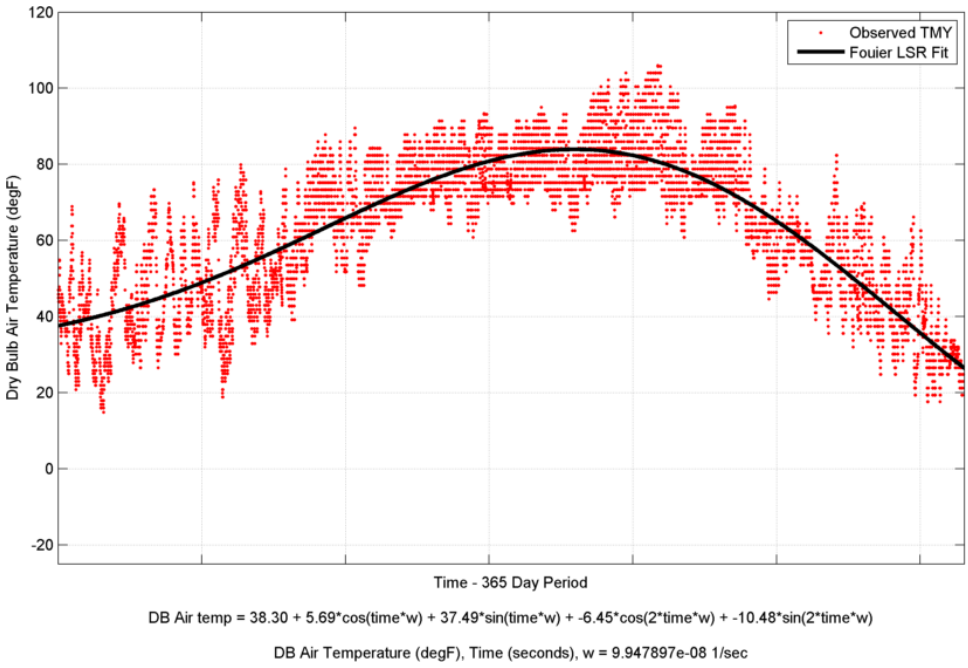


Figure 208: Pine Bluff, Arkansas – Least-squares curve fit to dry bulb air temperatures from a typical meteorological year (TMY) using four term Fourier series

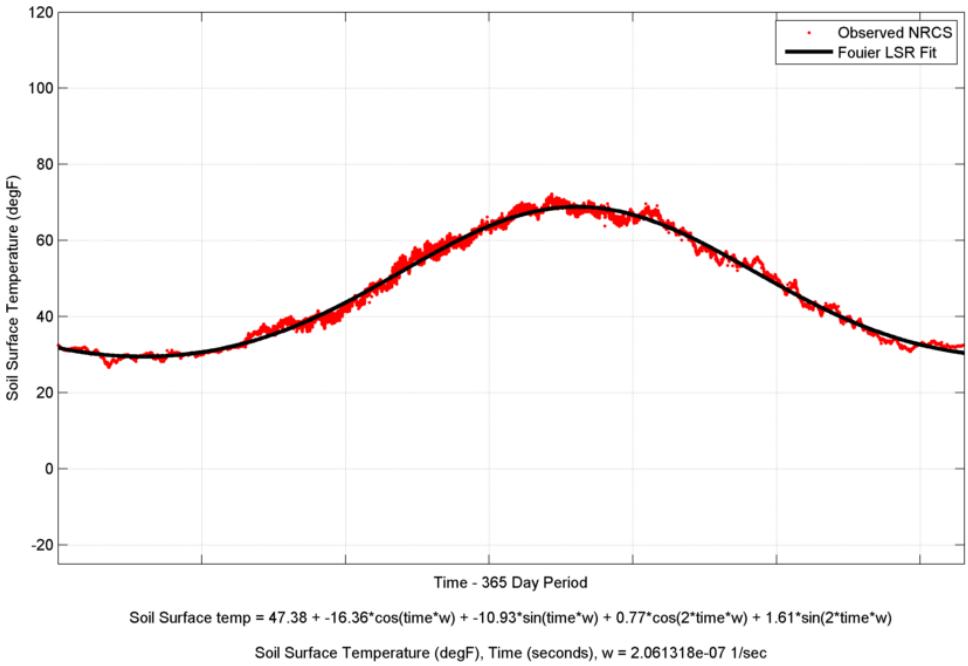


Figure 209: Saint Cloud, Minnesota – Least-squares curve fit to observed soil surface temperatures using four term Fourier series

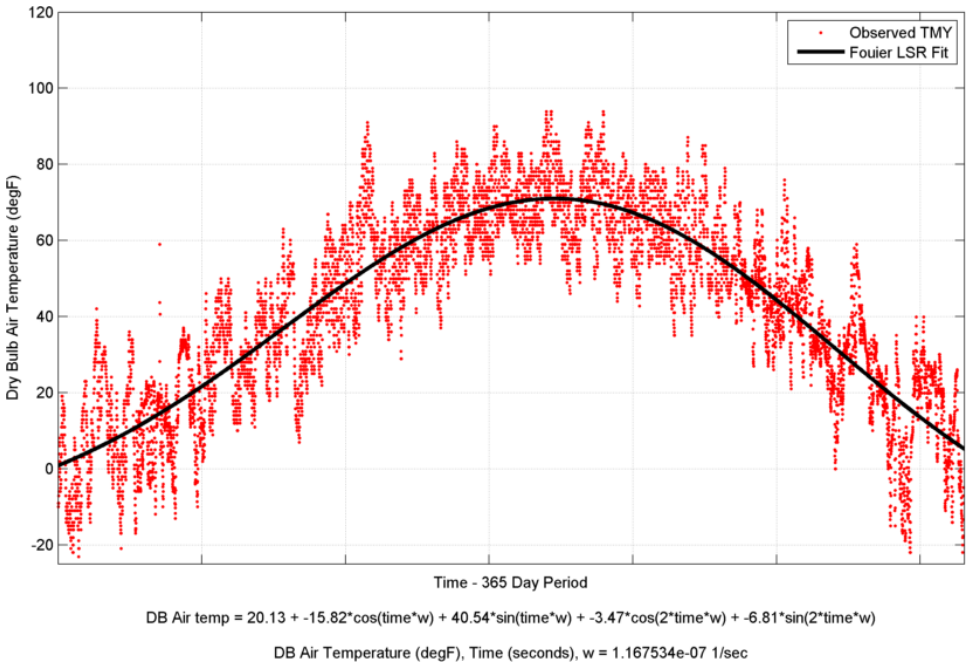


Figure 210: Saint Cloud, Minnesota – Least-squares curve fit to dry bulb air temperatures from a typical meteorological year (TMY) using four term Fourier series

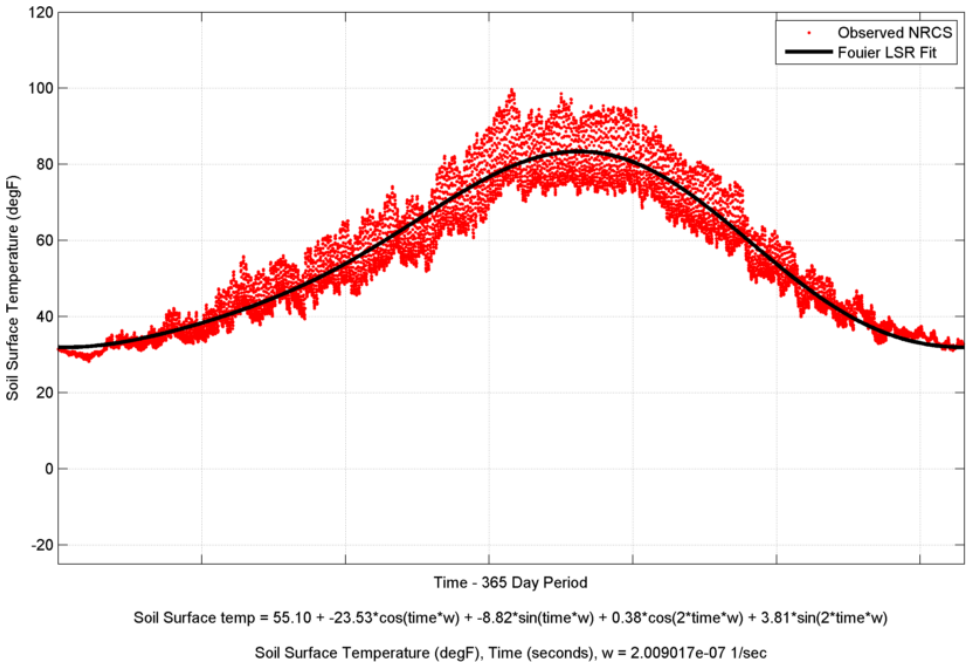


Figure 211: Salt Lake City, Utah – Least-squares curve fit to observed soil surface temperatures using four term Fourier series

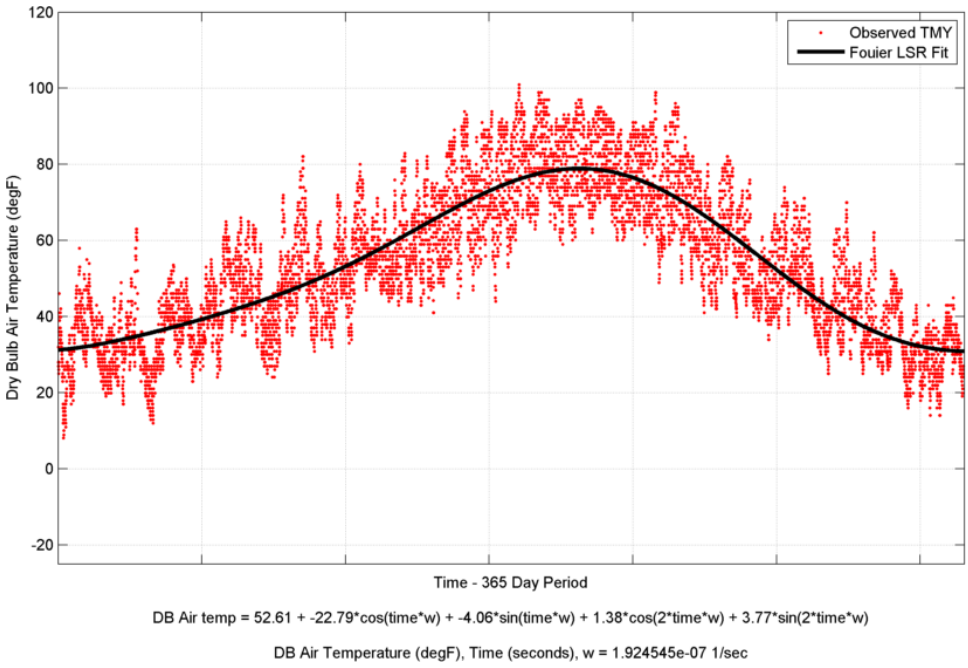


Figure 212: Salt Lake City, Utah – Least-squares curve fit to dry bulb air temperatures from a typical meteorological year (TMY) using four term Fourier series

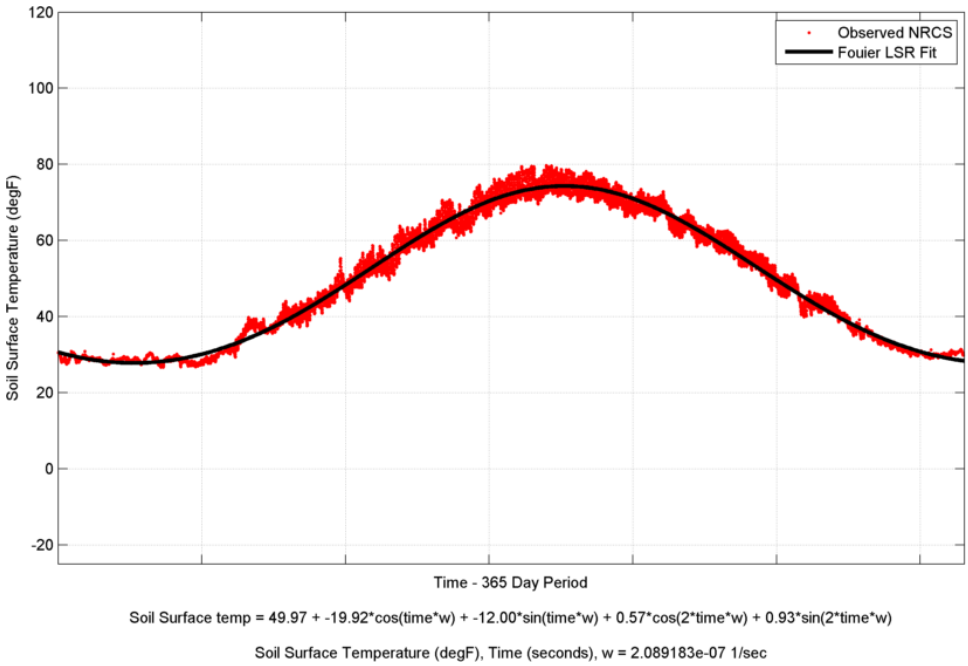


Figure 213: Sioux Falls, South Dakota – Least-squares curve fit to observed soil surface temperatures using four term Fourier series

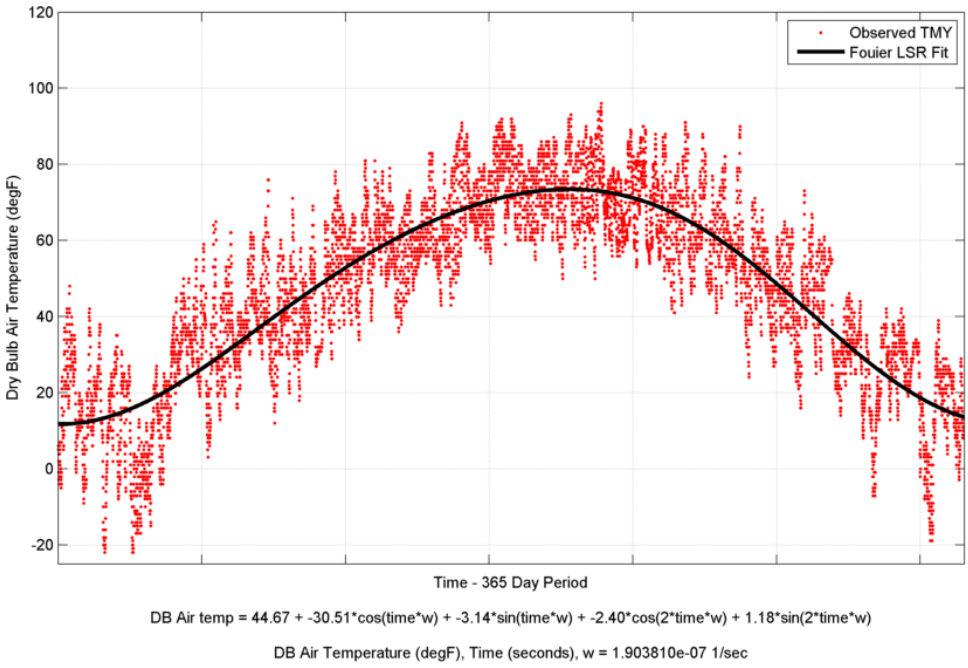


Figure 214: Sioux Falls, South Dakota – Least-squares curve fit to dry bulb air temperatures from a typical meteorological year (TMY) using four term Fourier series

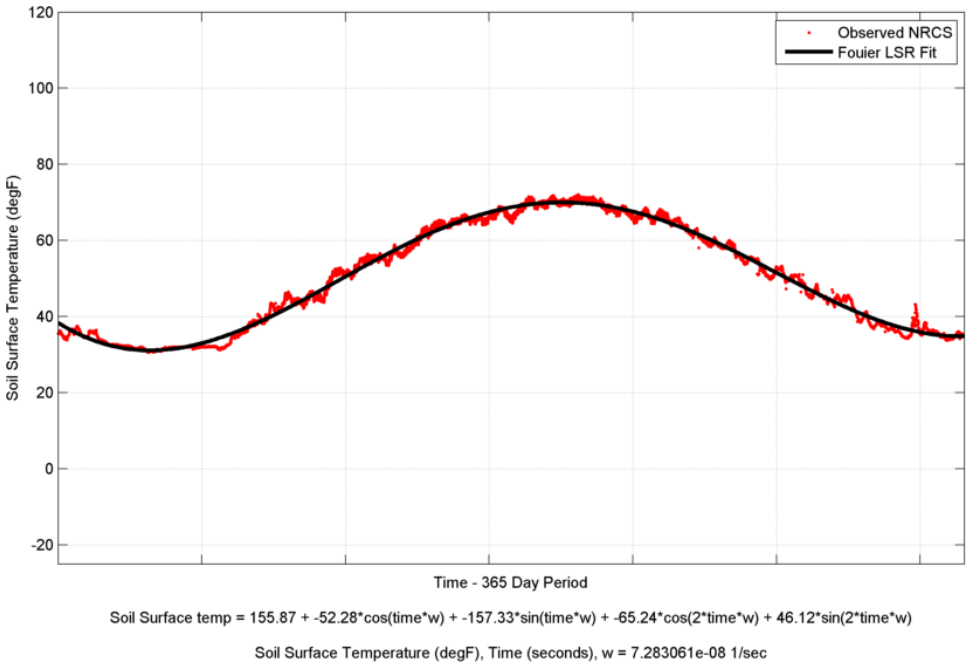


Figure 215: State College, Pennsylvania – Least-squares curve fit to observed soil surface temperatures using four term Fourier series

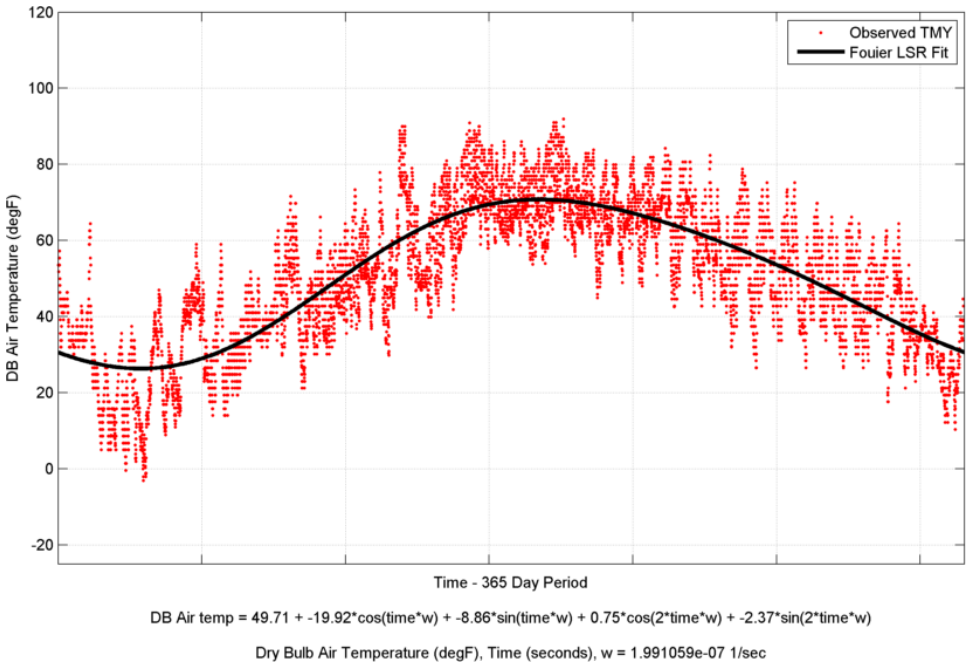


Figure 216: State College, Pennsylvania – Least-squares curve fit to dry bulb air temperatures from a typical meteorological year (TMY) using four term Fourier series

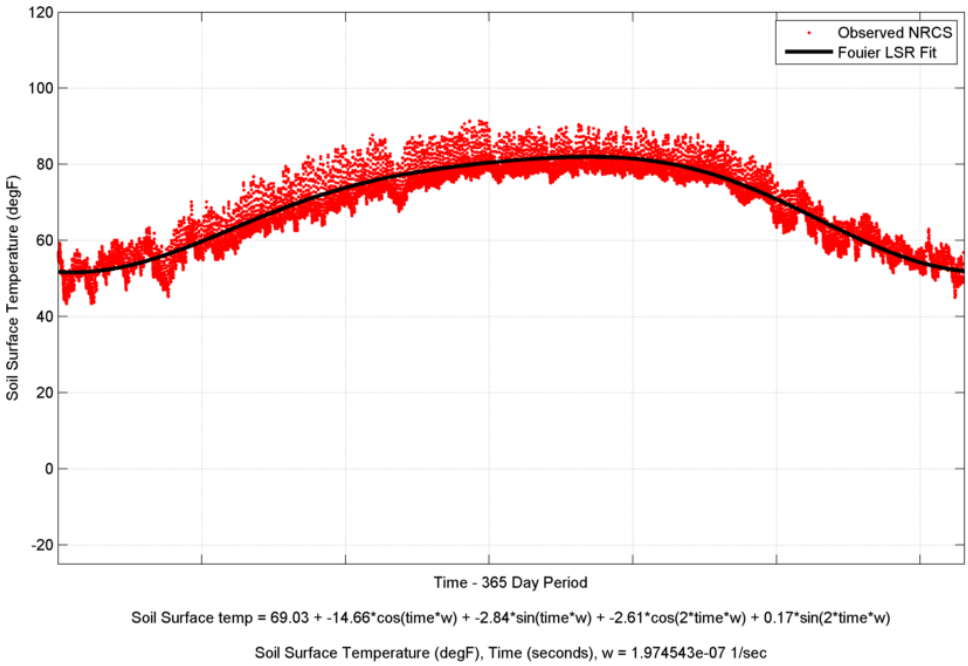


Figure 217: Tallahassee, Florida – Least-squares curve fit to observed soil surface temperatures using four term Fourier series

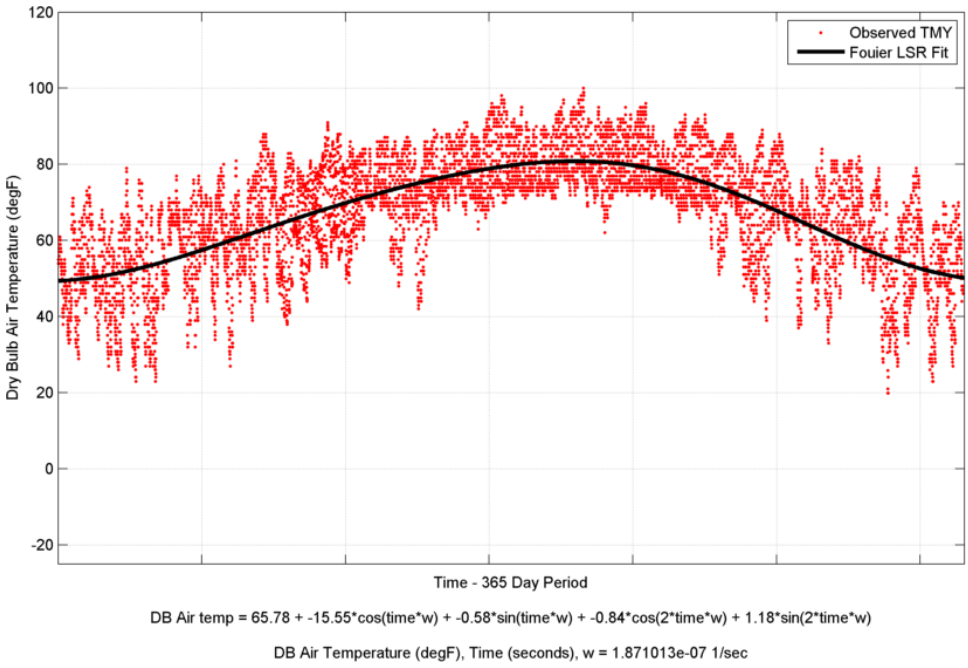


Figure 218: Tallahassee, Florida – Least-squares curve fit to dry bulb air temperatures from a typical meteorological year (TMY) using four term Fourier series

APPENDIX C

ESTIMATED SOIL SURFACE HEAT FLUX

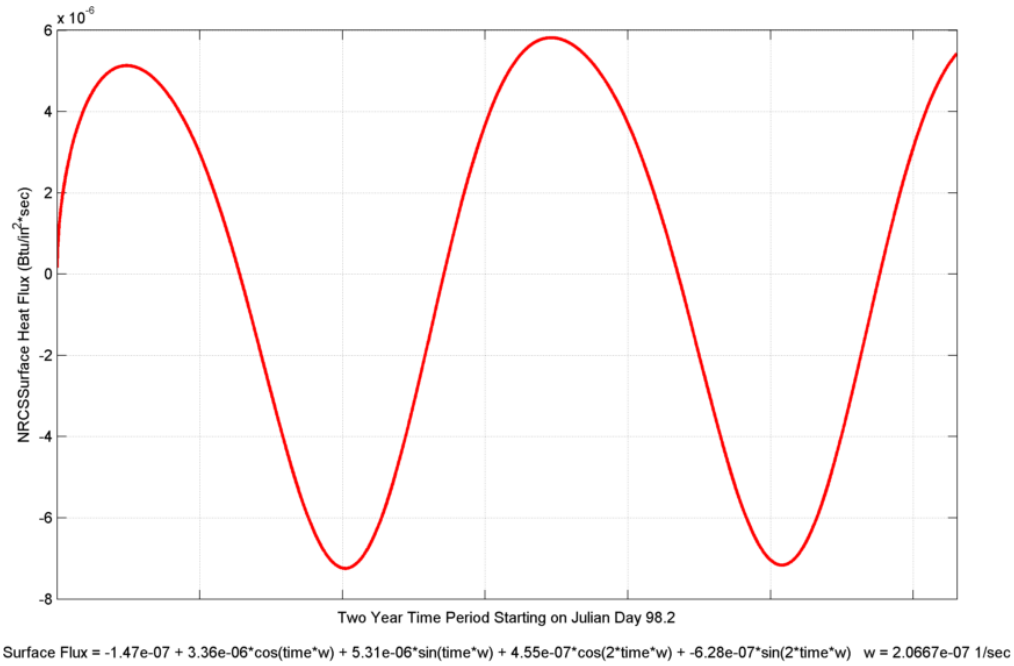


Figure 219: Albuquerque, New Mexico – estimated soil surface heat flux function using the NRCS soil surface temperatures over a two year period starting on Julian day 98.2

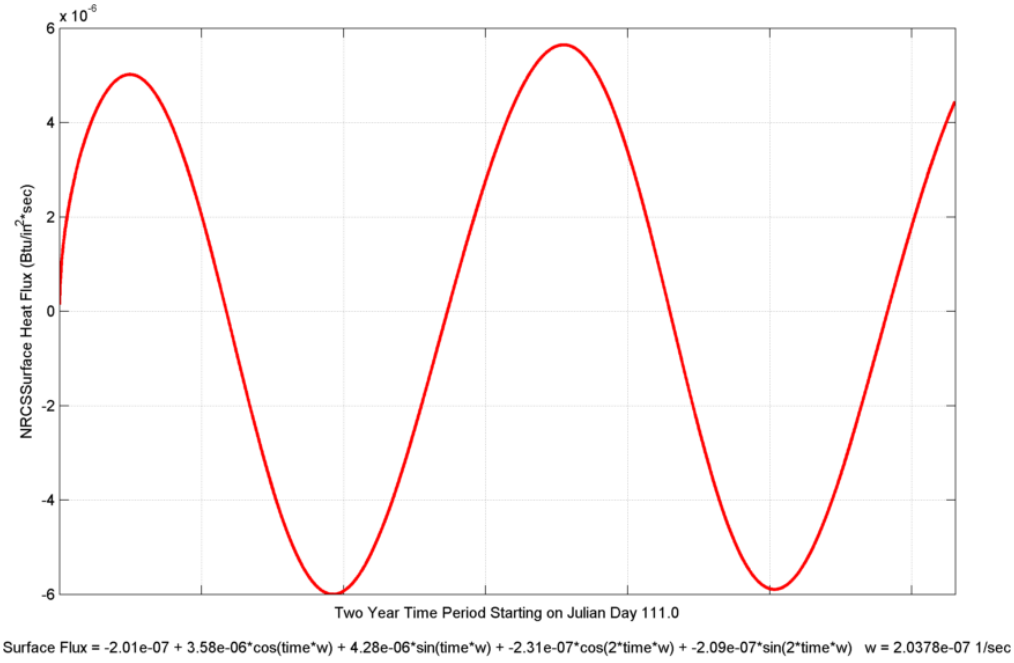


Figure 220: Amarillo, Texas – estimated soil surface heat flux function using the NRCS soil surface temperatures over a two year period starting on Julian day 111

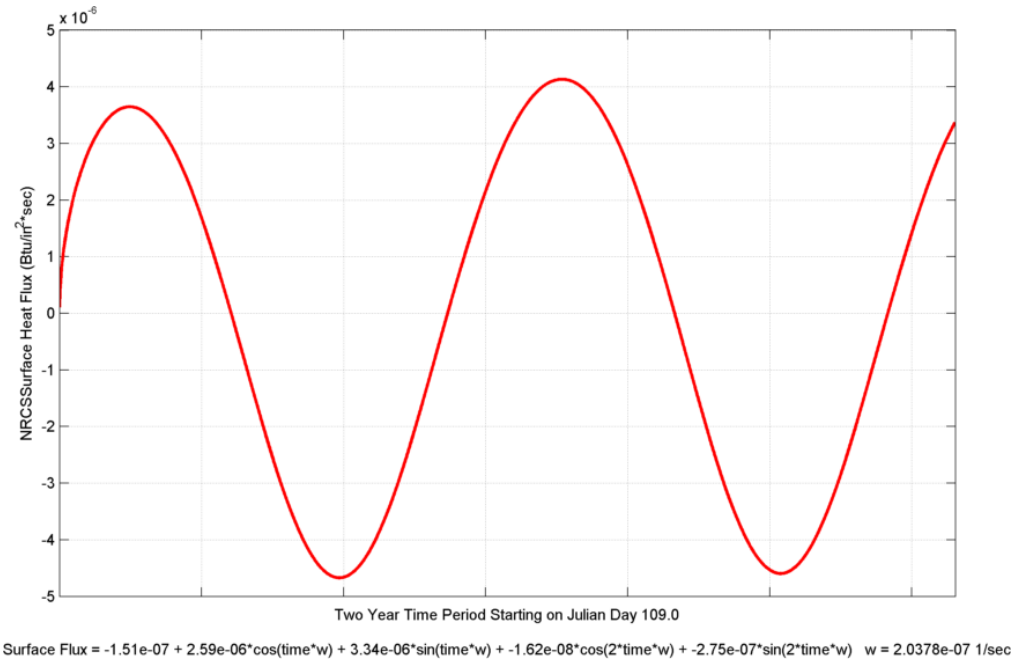


Figure 221: Athens, Georgia – estimated soil surface heat flux function using the NRCS soil surface temperatures over a two year period starting on Julian day 109

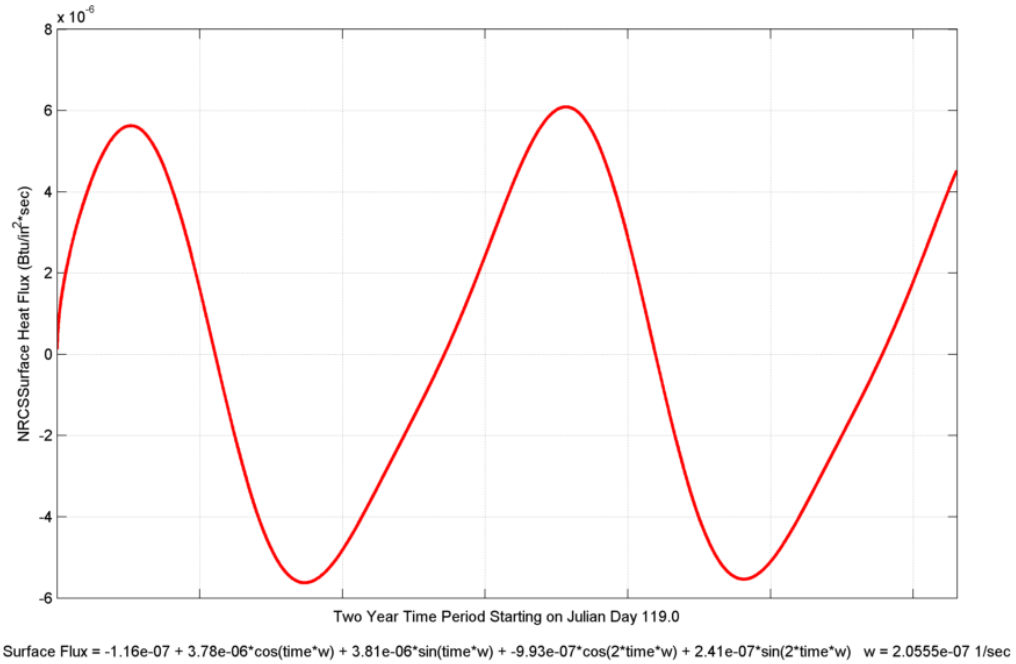


Figure 222: Bozeman, Montana – estimated soil surface heat flux function using the NRCS soil surface temperatures over a two year period starting on Julian day 119

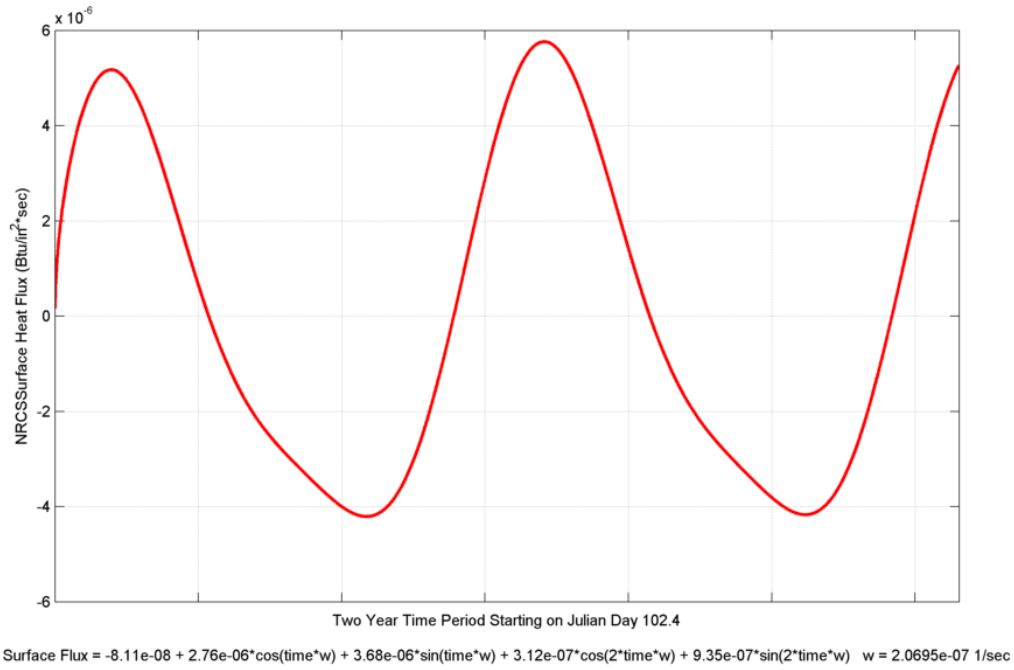


Figure 223: Columbus, Ohio – estimated soil surface heat flux function using the NRCS soil surface temperatures over a two year period starting on Julian day 102.4

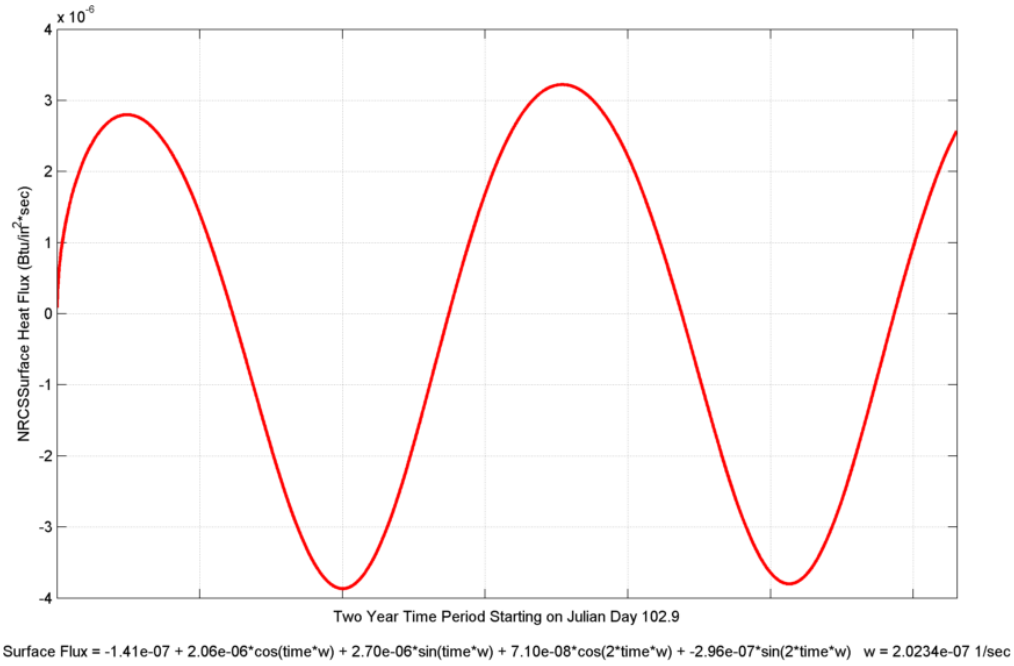


Figure 224: Houston, Texas – estimated soil surface heat flux function using the NRCS soil surface temperatures over a two year period starting on Julian day 102.9

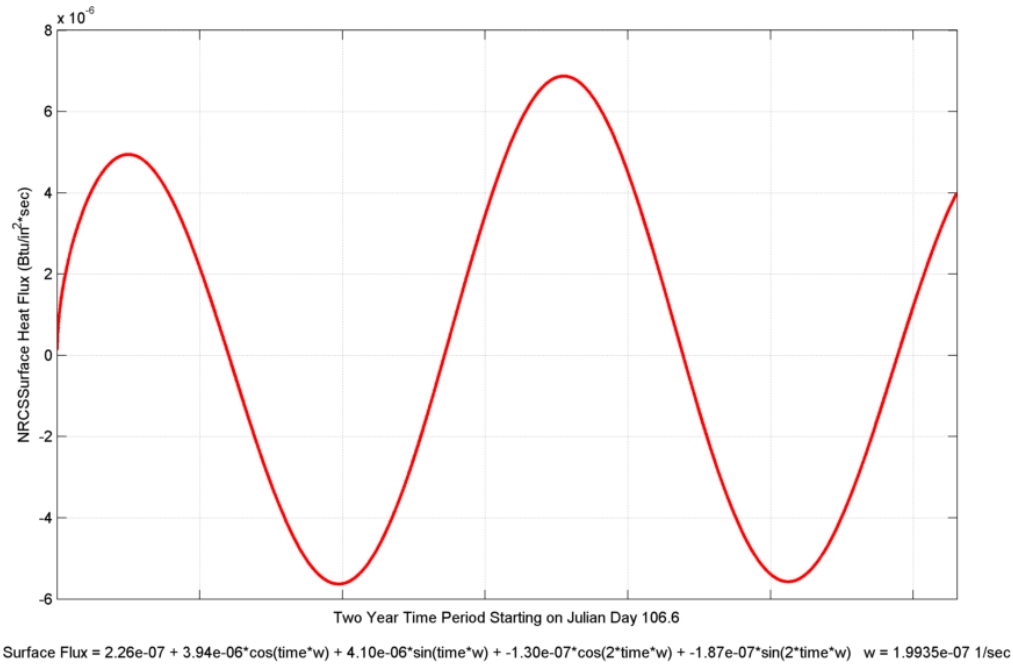


Figure 225: Kansas City, Missouri– estimated soil surface heat flux function using the NRCS soil surface temperatures over a two year period starting on Julian day 106.6

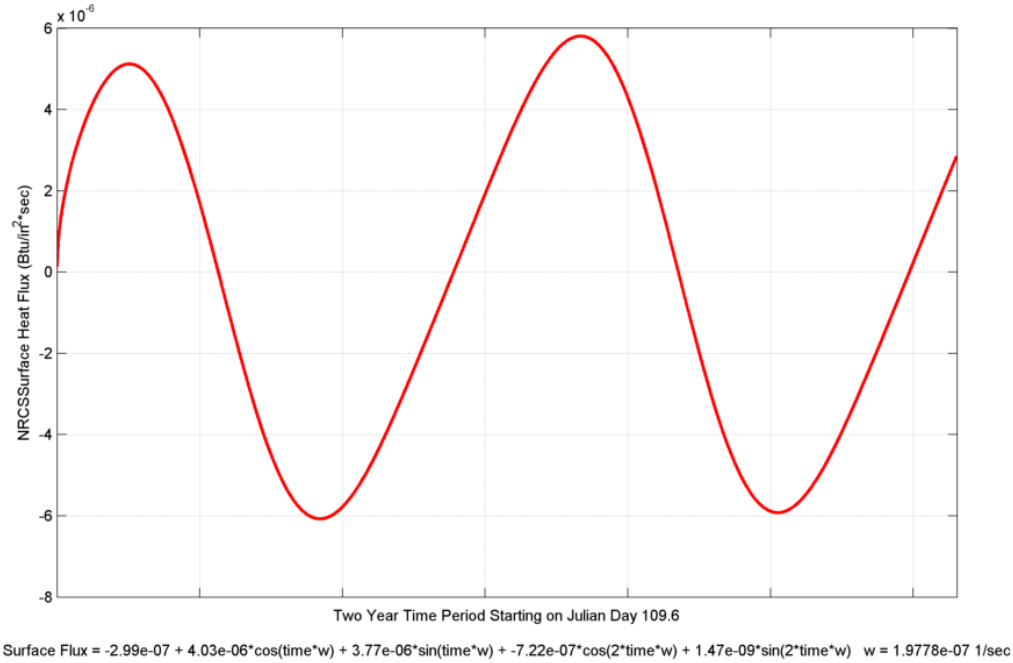


Figure 226: Las Vegas, Nevada – estimated soil surface heat flux function using the NRCS soil surface temperatures over a two year period starting on Julian day 109.6

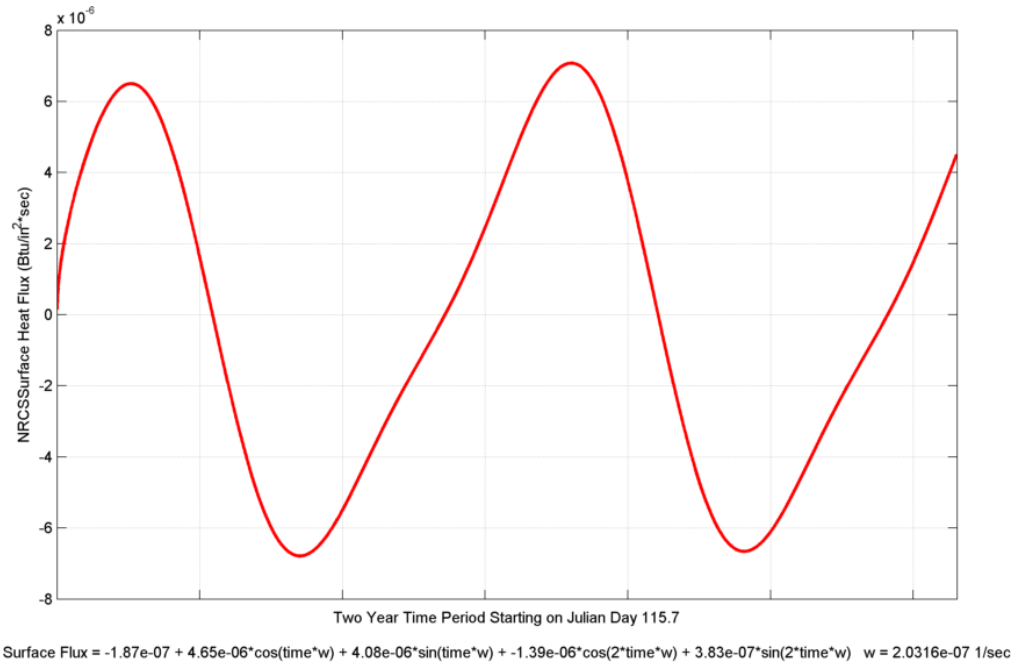


Figure 227: Moses Lake, Washington– estimated soil surface heat flux function using the NRCS soil surface temperatures over a two year period starting on Julian day 115.7

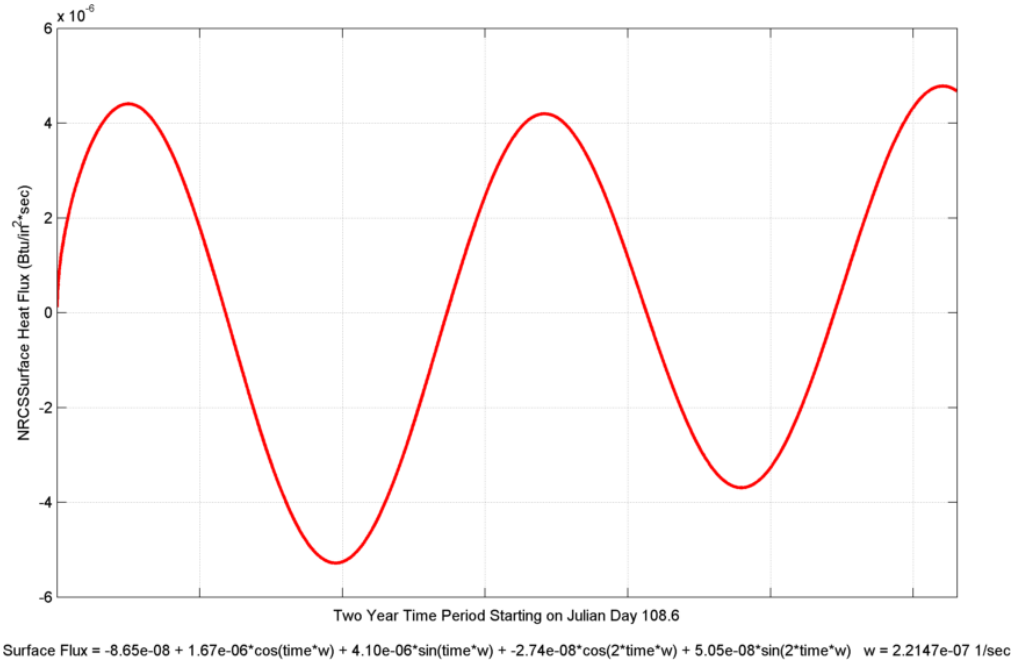


Figure 228: Pine Bluff, Arkansas – estimated soil surface heat flux function using the NRCS soil surface temperatures over a two year period starting on Julian day 108.6

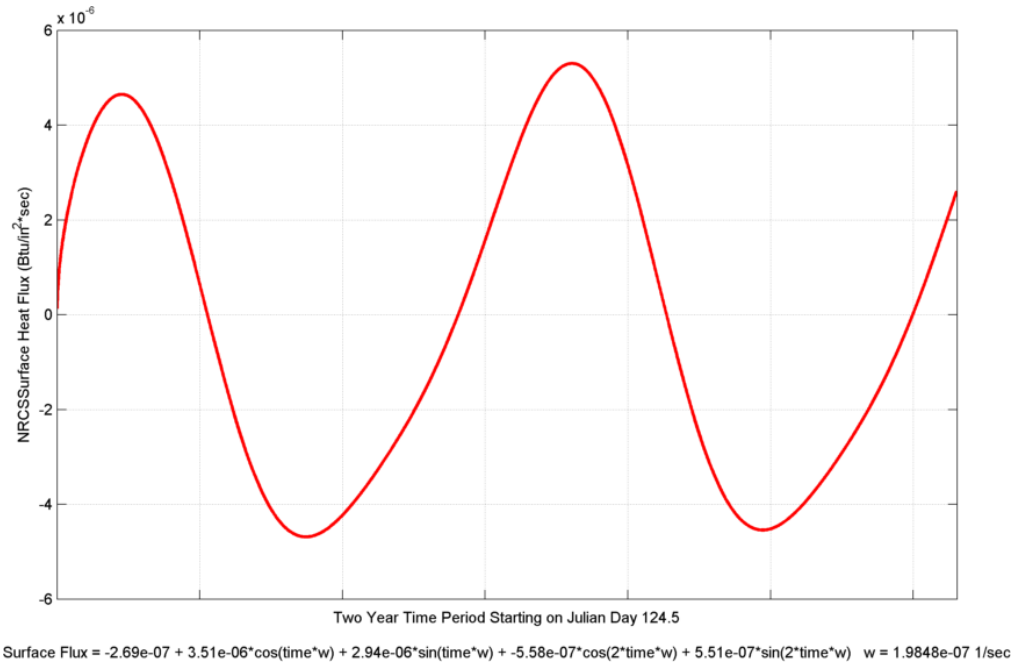


Figure 229: St. Cloud, Minnesota – estimated soil surface heat flux function using the NRCS soil surface temperatures over a two year period starting on Julian day 124.5

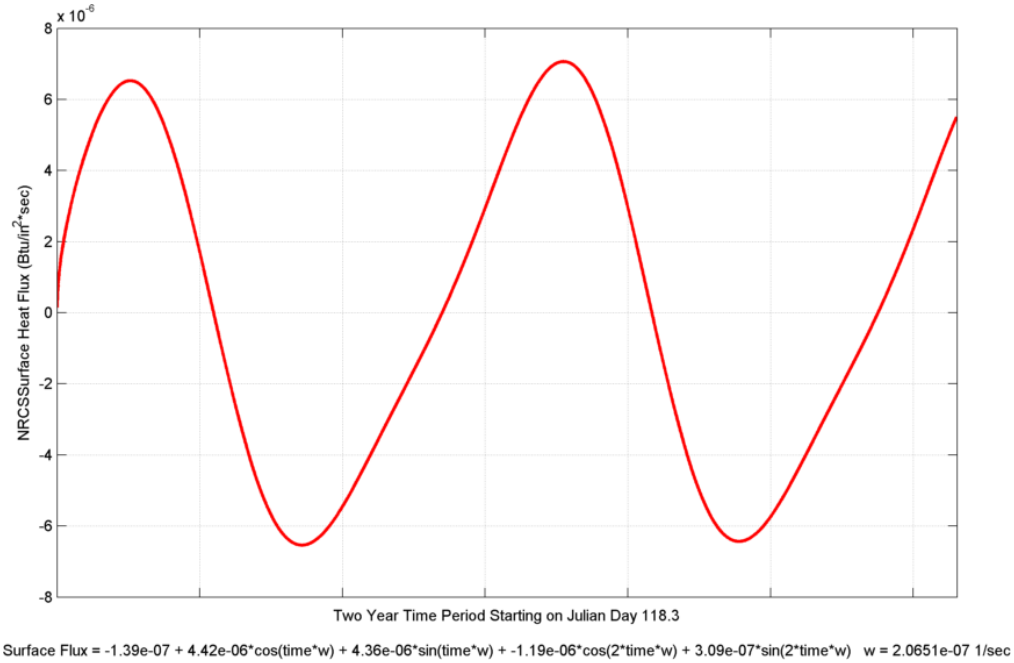


Figure 230: Salt Lake City, Utah – estimated soil surface heat flux function using the NRCS soil surface temperatures over a two year period starting on Julian day 118.3

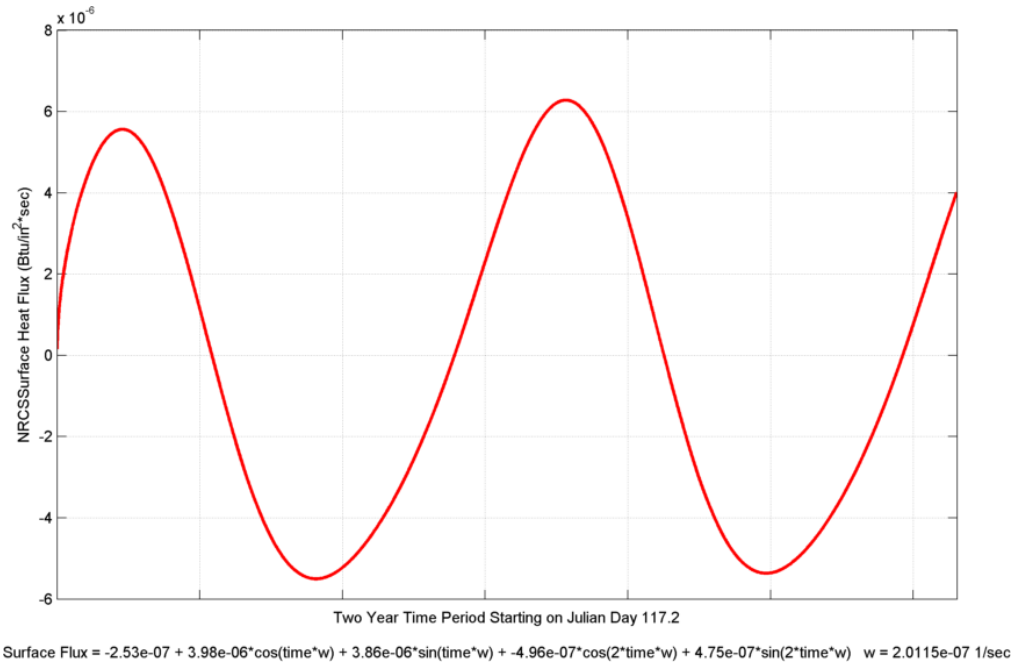


Figure 231: Sioux Falls, South Dakota– estimated soil surface heat flux function using the NRCS soil surface temperatures over a two year period starting on Julian day 117.2

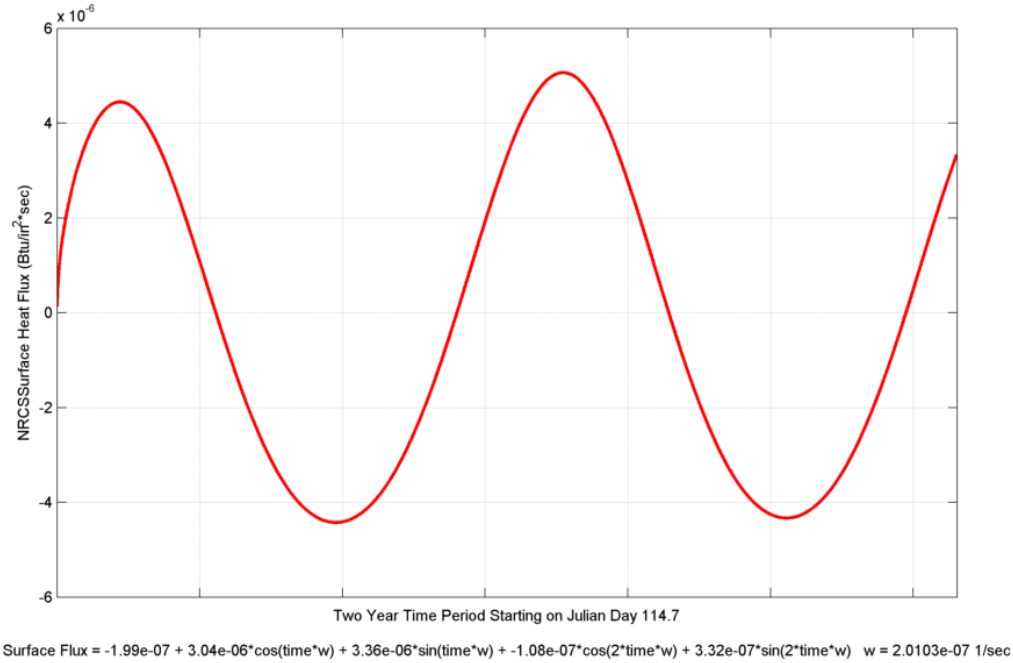


Figure 232: State College, Pennsylvania – estimated soil surface heat flux function using the NRCS soil surface temperatures over a two year period starting on Julian day 114.7

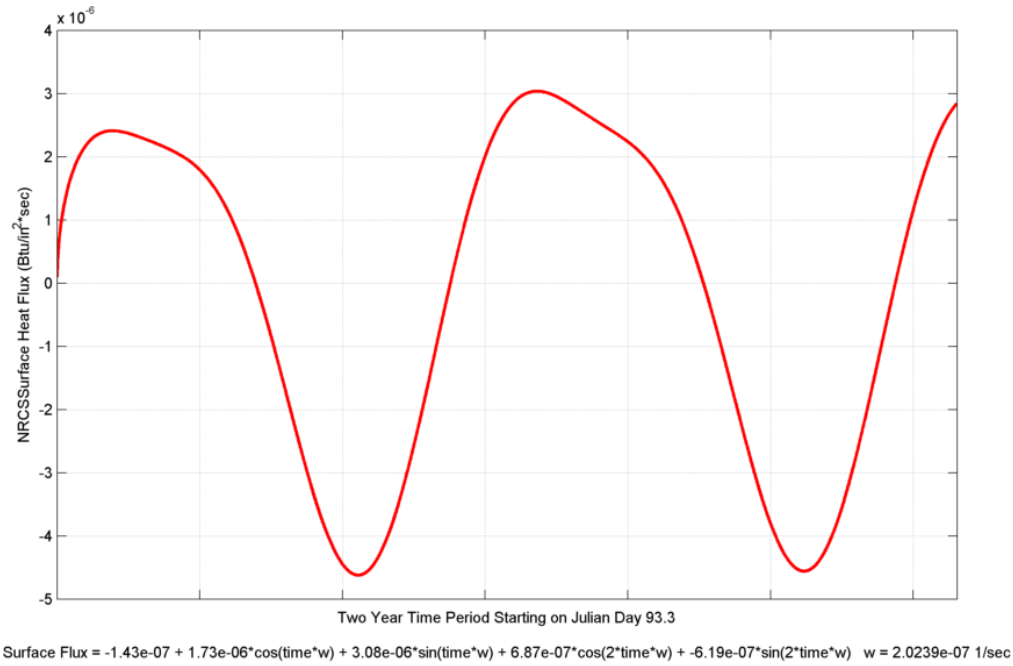


Figure 233: Tallahassee, Florida – estimated soil surface heat flux function using the NRCS soil surface temperatures over a two year period starting on Julian day 93.3

APPENDIX D

UNDER YARD SOIL TEMPERATURES

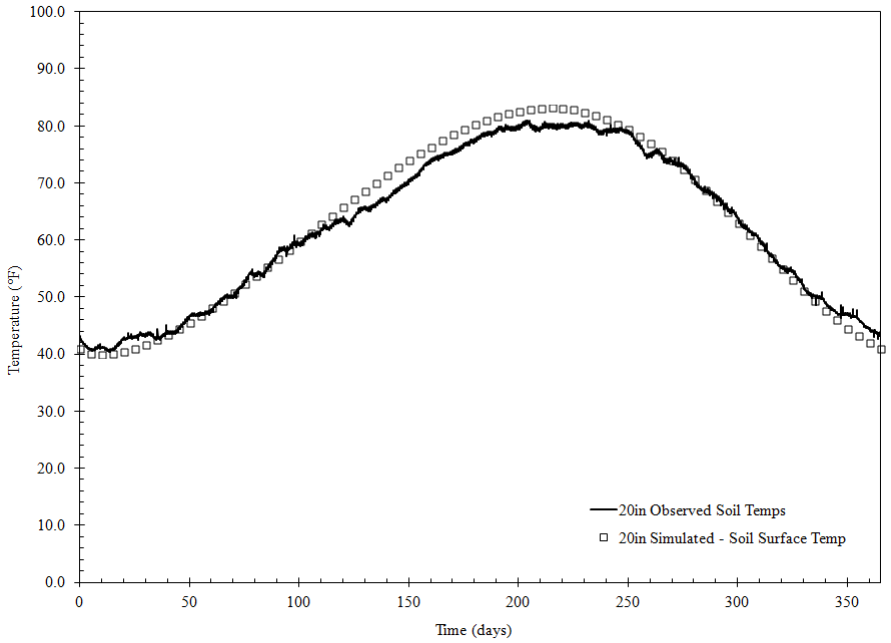


Figure 234: Albuquerque, New Mexico – 20 inch observed vs. simulated Green's Function soil temperatures – observed surface soil temperature boundary condition

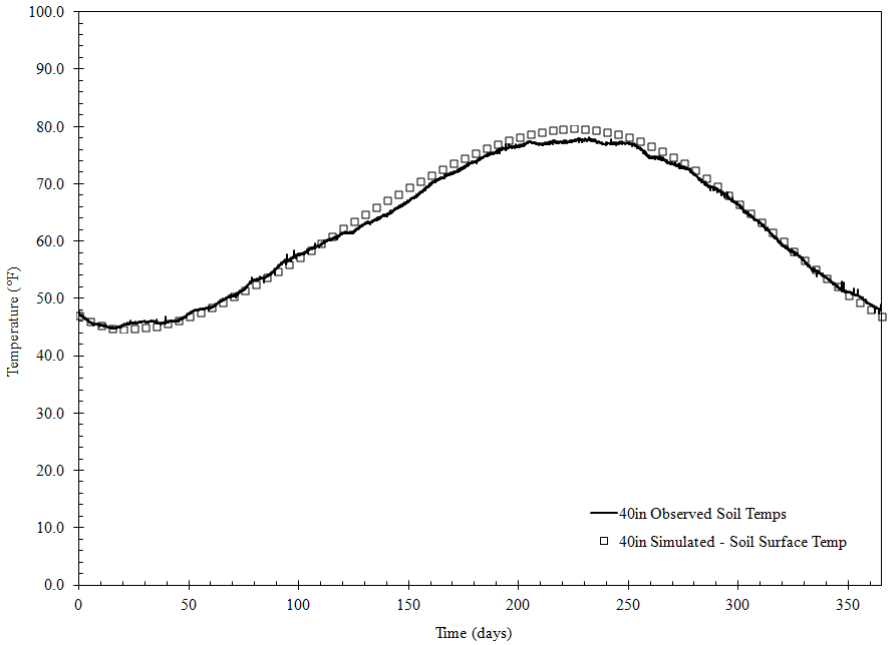


Figure 235: Albuquerque, New Mexico – 40 inch observed vs. simulated Green's Function soil temperatures – observed surface soil temperature boundary condition

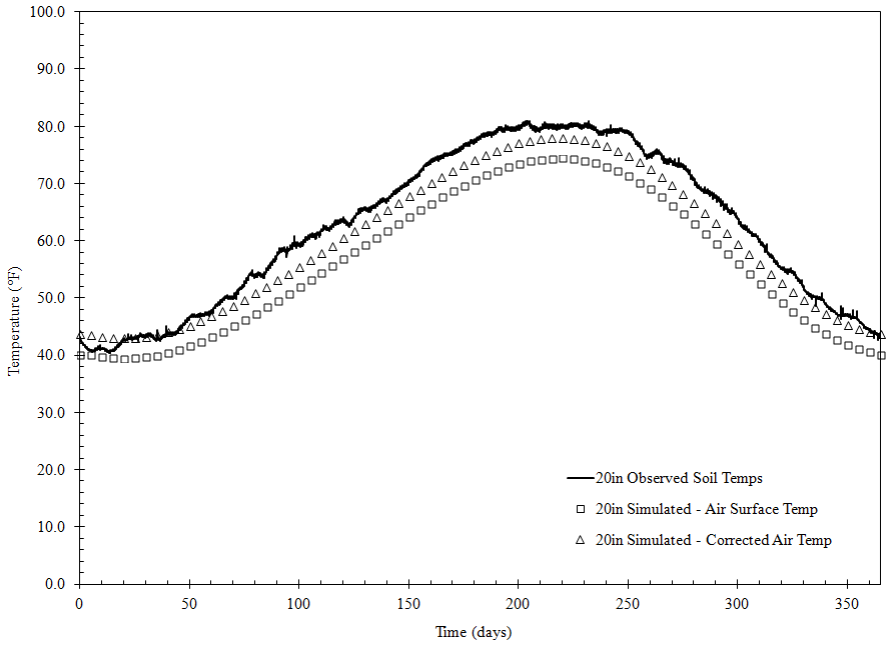


Figure 236: Albuquerque, New Mexico – 20 inch observed vs. simulated Green's Function soil temperatures – typical meteorological year (TMY) and corrected TMY surface air temperature boundary conditions

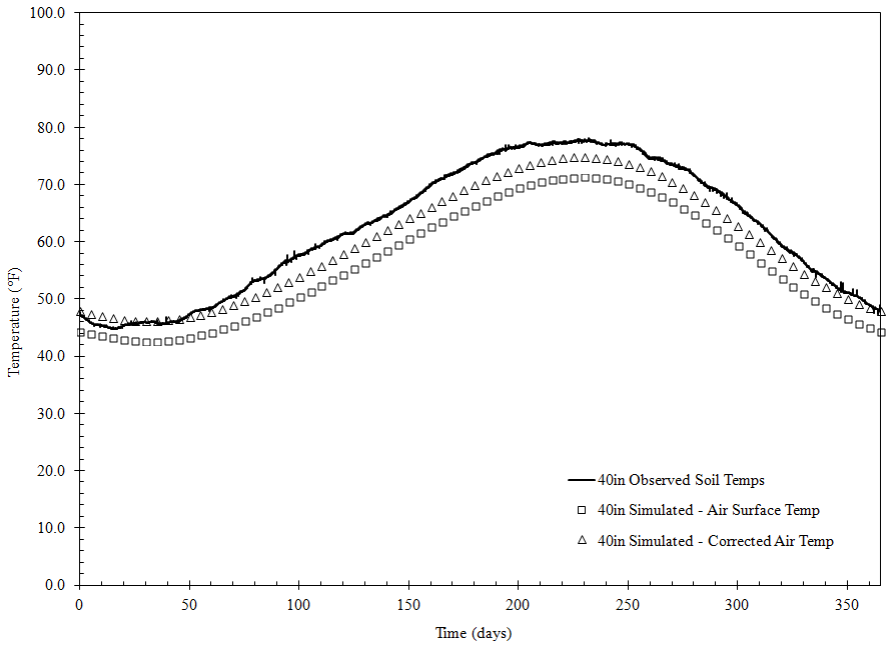


Figure 237: Albuquerque, New Mexico – 40 inch observed vs. simulated Green's Function soil temperatures – typical meteorological year (TMY) and corrected TMY surface air temperature boundary conditions

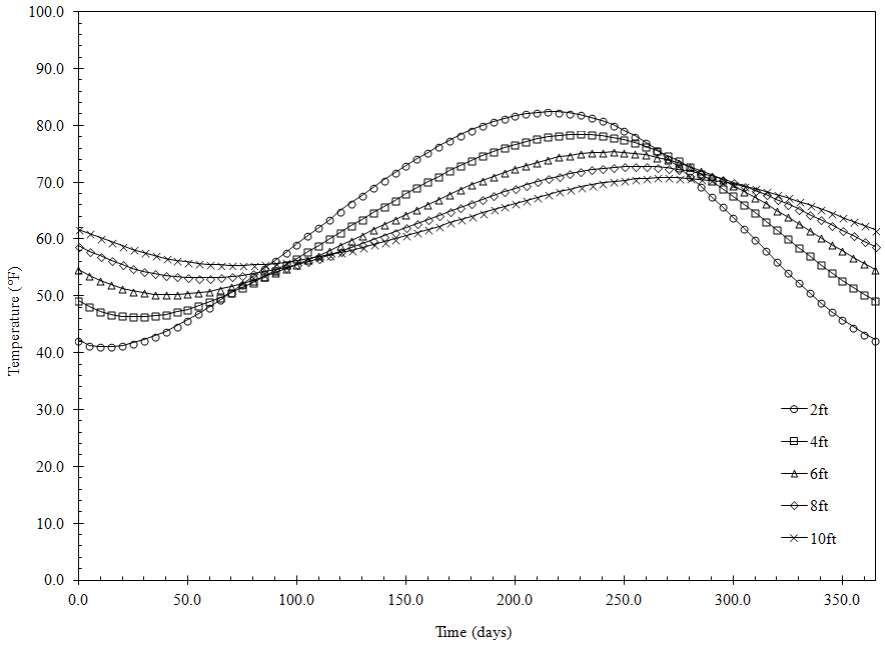


Figure 238: Albuquerque, New Mexico – simulated Green's Function soil temperatures at various depths– observed surface soil temperature boundary condition

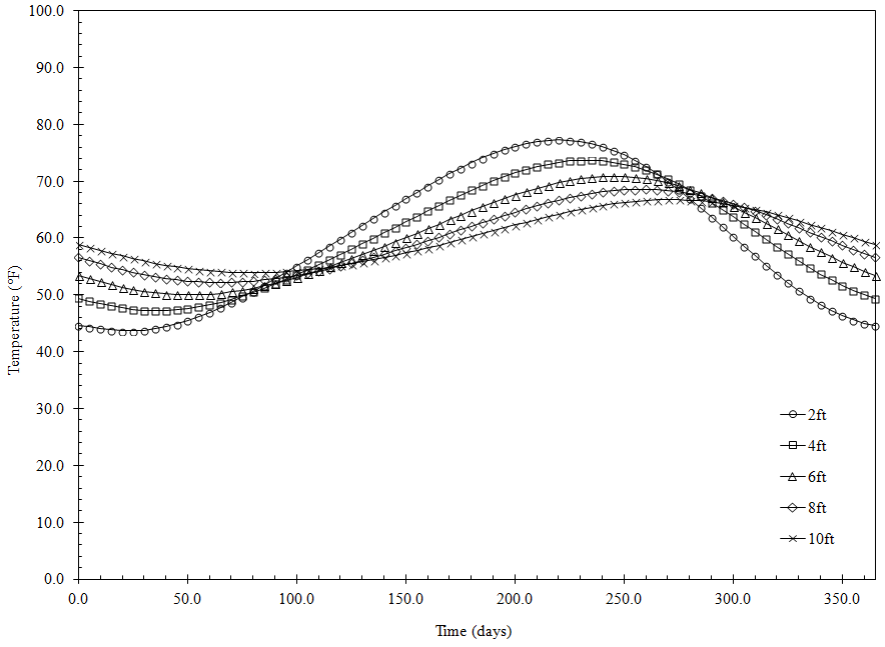


Figure 239: Albuquerque, New Mexico – simulated Green's Function soil temperatures at various depths – corrected TMY surface air temperature boundary condition

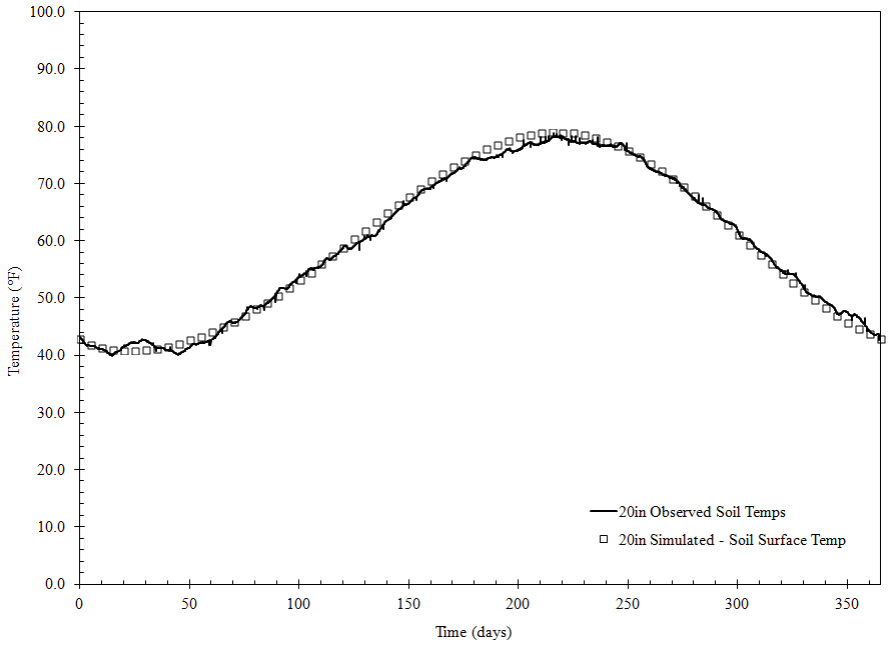


Figure 240: Amarillo, Texas – 20 inch observed vs. simulated Green's Function soil temperatures – observed surface soil temperature boundary condition

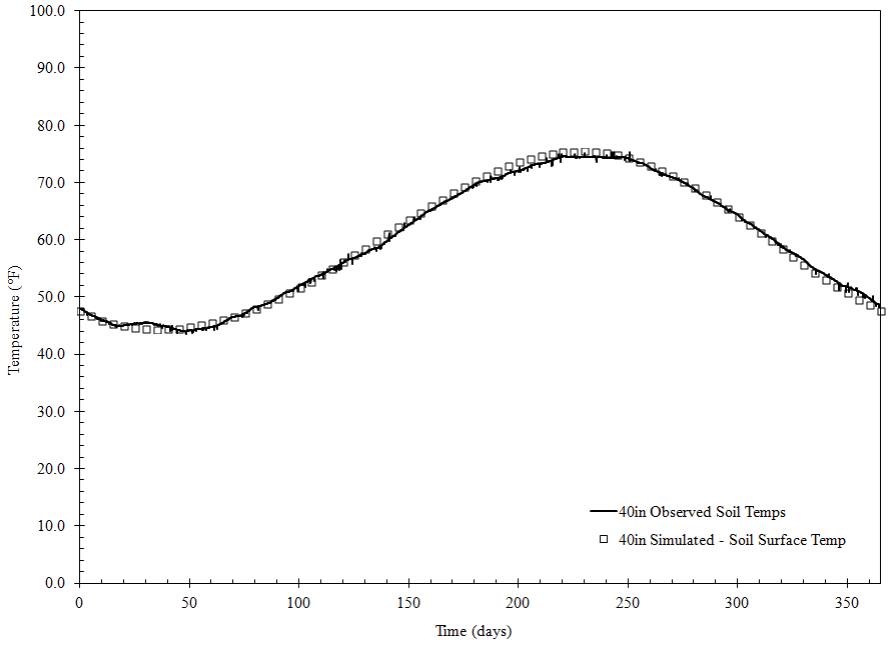


Figure 241: Amarillo, Texas – 40 inch observed vs. simulated Green's Function soil temperatures – observed surface soil temperature boundary condition

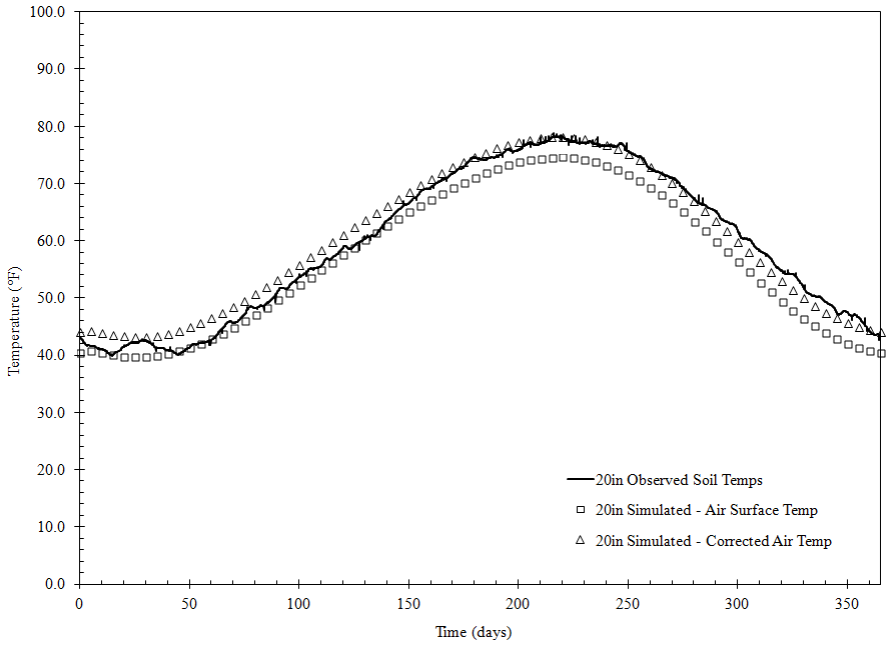


Figure 242: Amarillo, Texas – 20 inch observed vs. simulated Green's Function soil temperatures – typical meteorological year (TMY) and corrected TMY surface air temperature boundary conditions

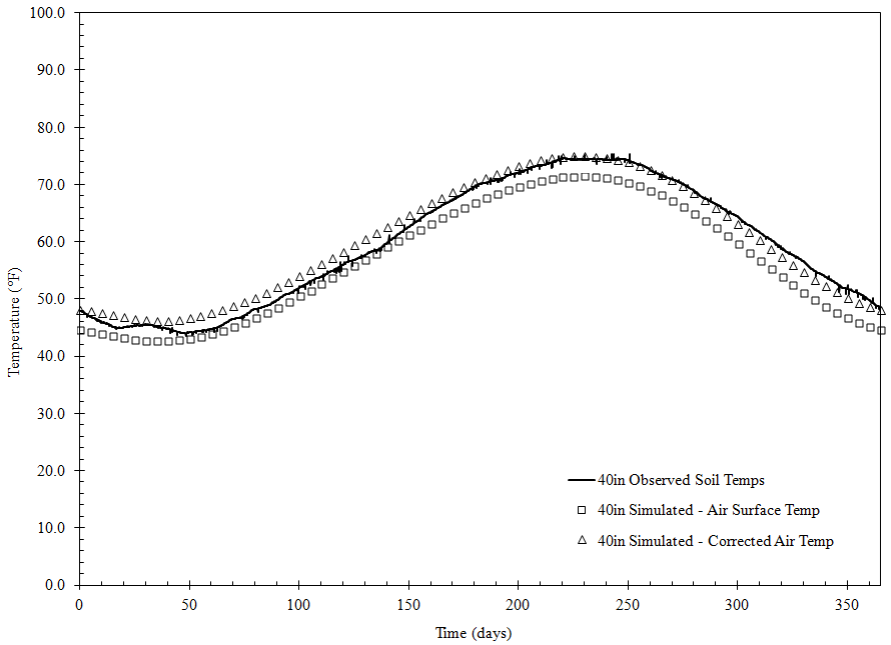


Figure 243: Amarillo, Texas – 40 inch observed vs. simulated Green's Function soil temperatures – typical meteorological year (TMY) and corrected TMY surface air temperature boundary conditions

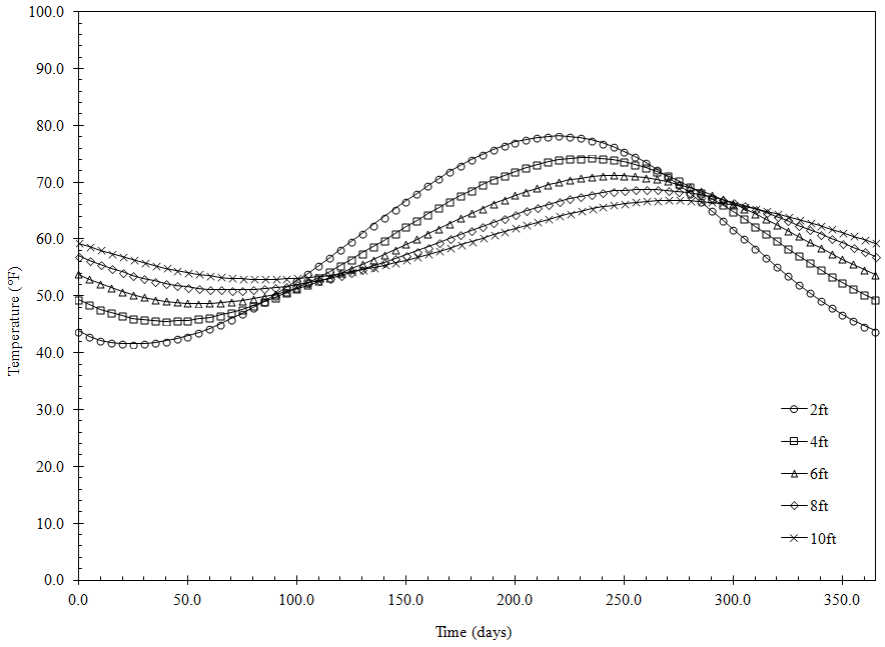


Figure 244: Amarillo, Texas – simulated Green's Function soil temperatures at various depths– observed surface soil temperature boundary condition

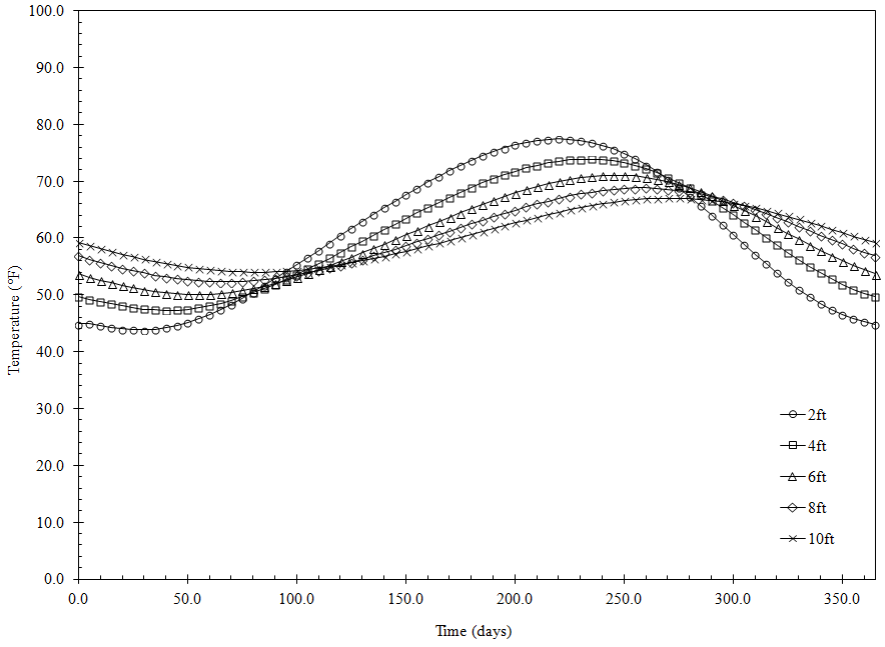


Figure 245: Amarillo, Texas – simulated Green's Function soil temperatures at various depths – corrected TMY surface air temperature boundary condition

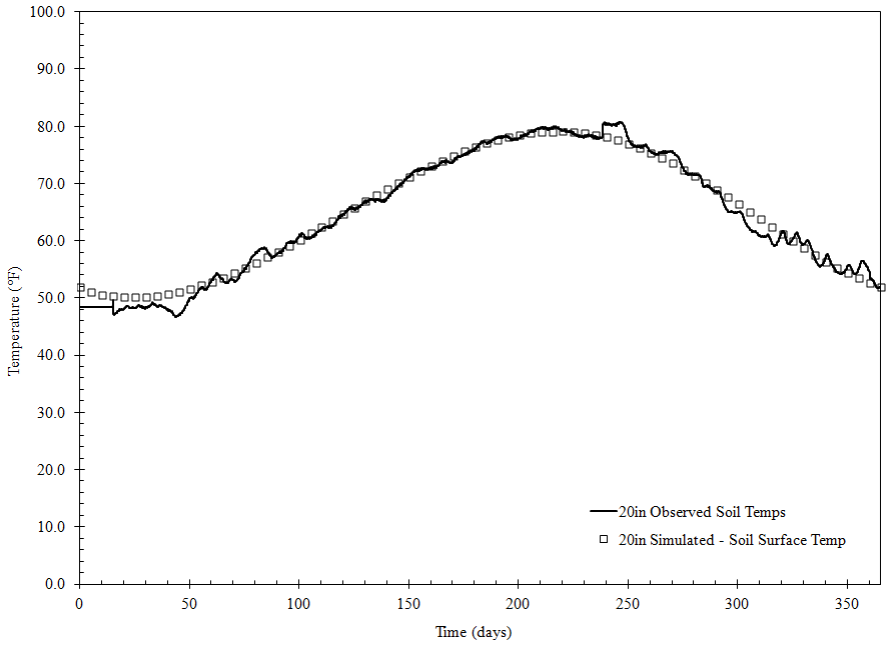


Figure 246: Athens, Georgia – 20 inch observed vs. simulated Green's Function soil temperatures – observed surface soil temperature boundary condition

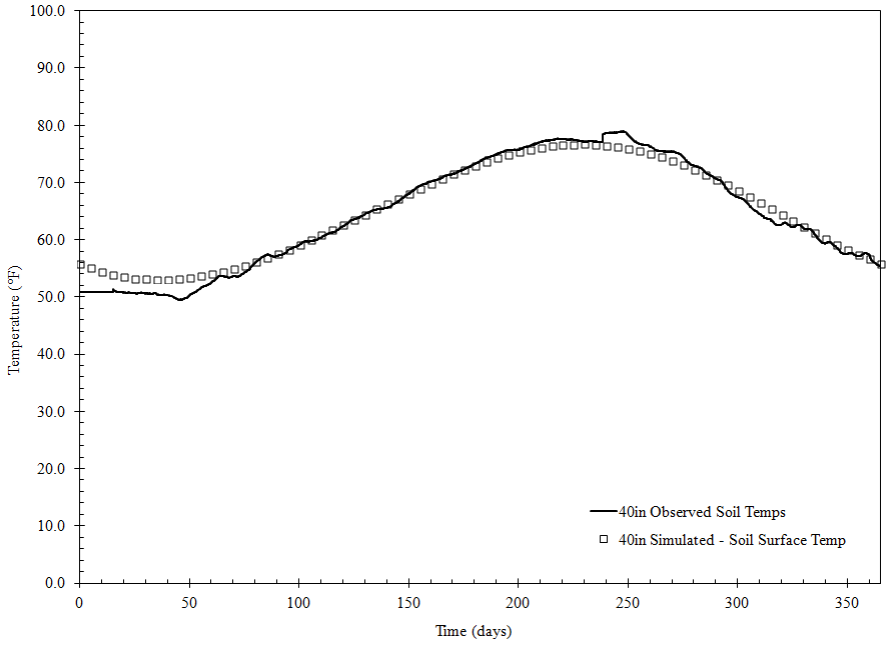


Figure 247: Athens, Georgia – 40 inch observed vs. simulated Green's Function soil temperatures – observed surface soil temperature boundary condition

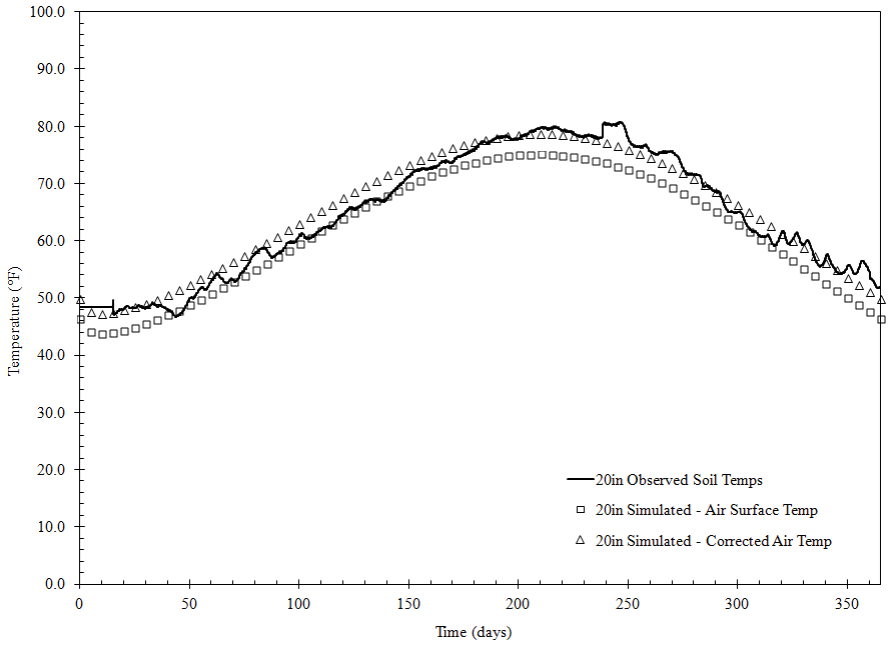


Figure 248: Athens, Georgia – 20 inch observed vs. simulated Green's Function soil temperatures – typical meteorological year (TMY) and corrected TMY surface air temperature boundary conditions

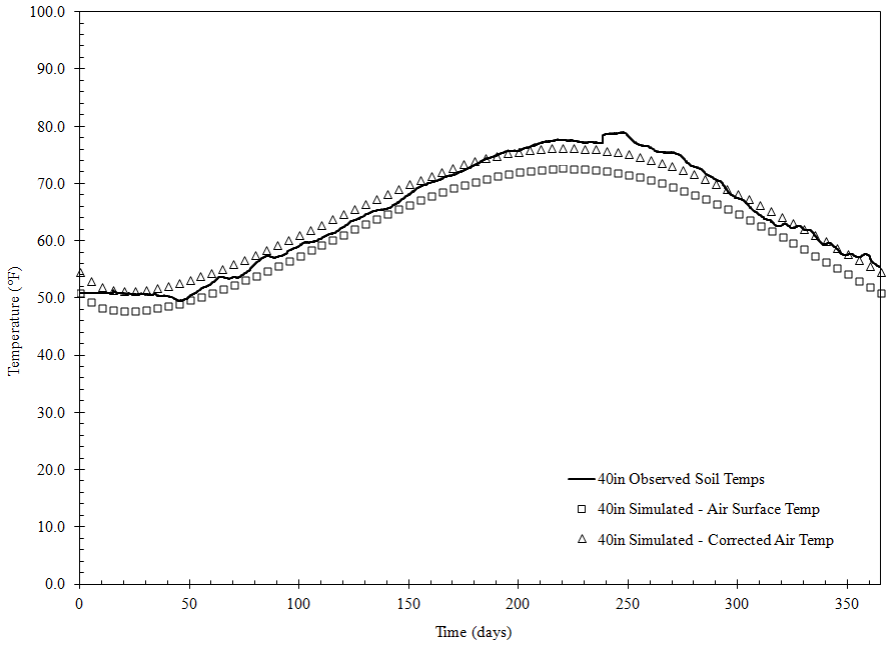


Figure 249: Athens, Georgia – 40 inch observed vs. simulated Green's Function soil temperatures – typical meteorological year (TMY) and corrected TMY surface air temperature boundary conditions

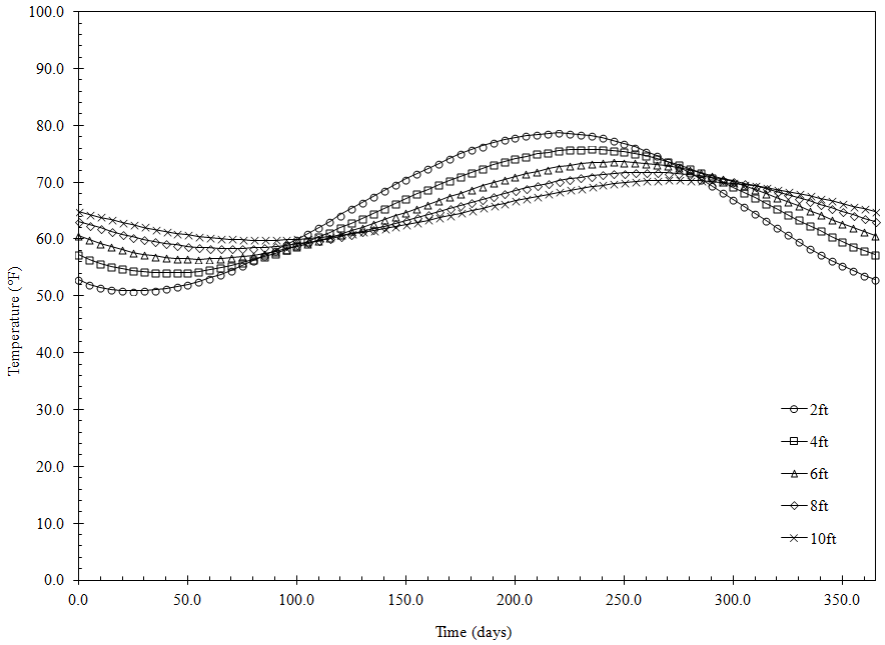


Figure 250: Athens, Georgia – simulated Green's Function soil temperatures at various depths– observed surface soil temperature boundary condition

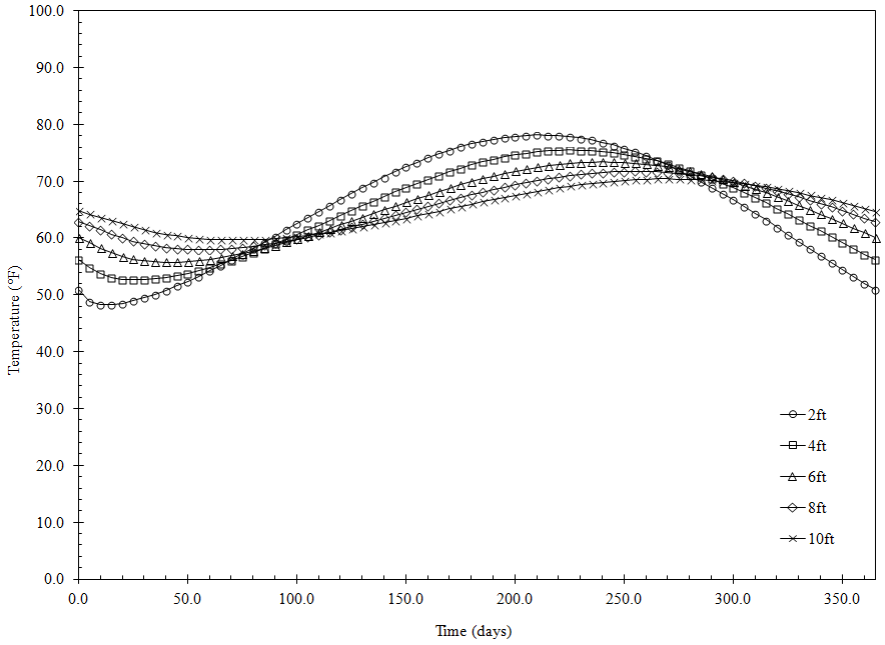


Figure 251: Athens, Georgia – simulated Green's Function soil temperatures at various depths – corrected TMY surface air temperature boundary condition

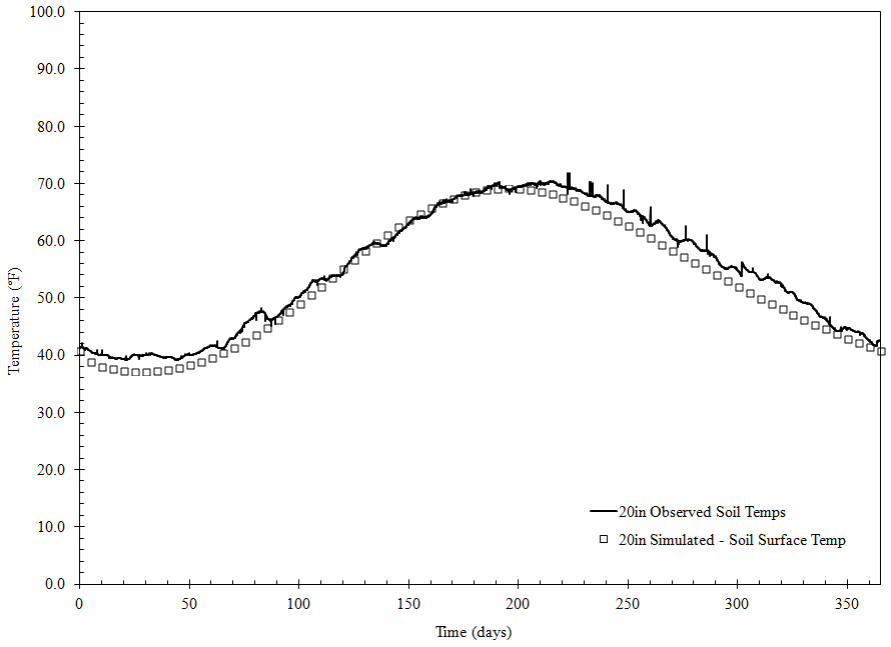


Figure 252: Columbus, Ohio – 20 inch observed vs. simulated Green's Function soil temperatures – observed surface soil temperature boundary condition

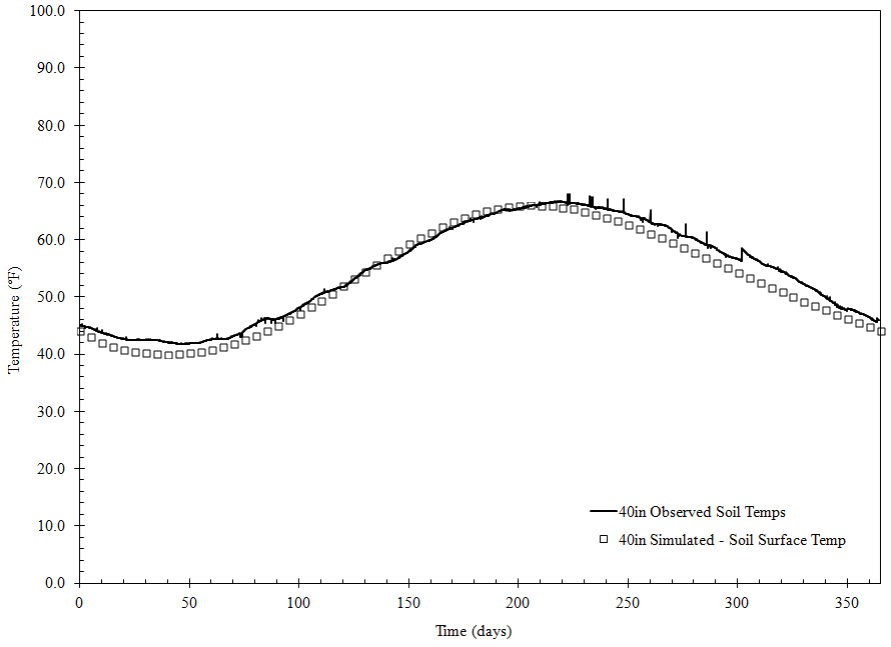


Figure 253: Columbus, Ohio – 40 inch observed vs. simulated Green's Function soil temperatures – observed surface soil temperature boundary condition

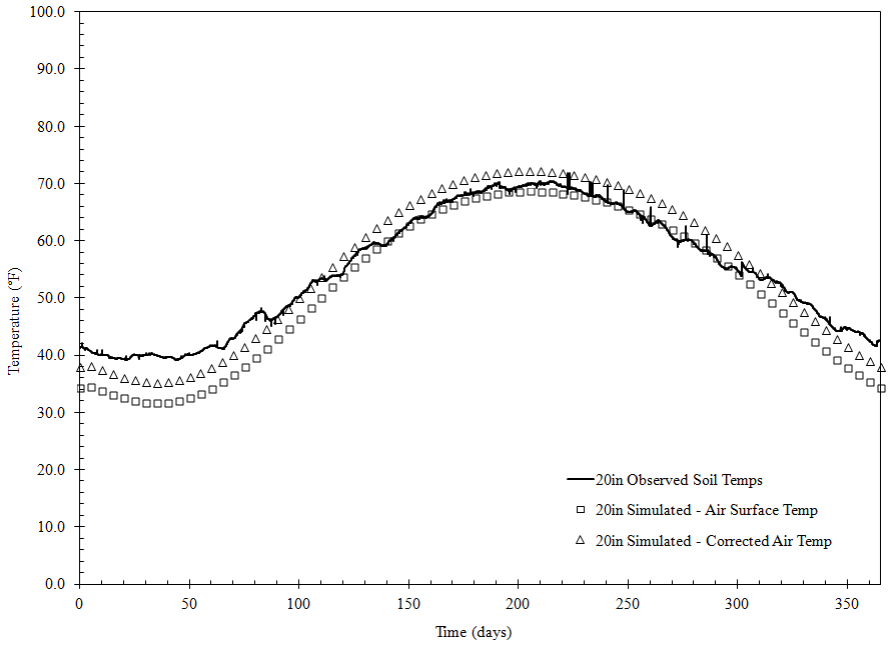


Figure 254: Columbus, Ohio – 20 inch observed vs. simulated Green's Function soil temperatures – typical meteorological year (TMY) and corrected TMY surface air temperature boundary conditions

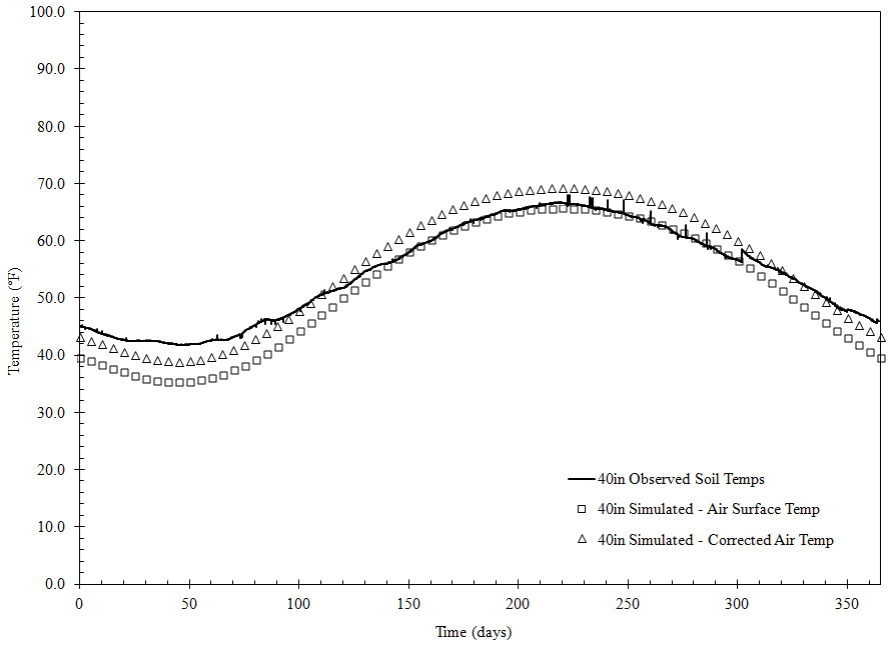


Figure 255: Columbus, Ohio – 40 inch observed vs. simulated Green's Function soil temperatures – typical meteorological year (TMY) and corrected TMY surface air temperature boundary conditions

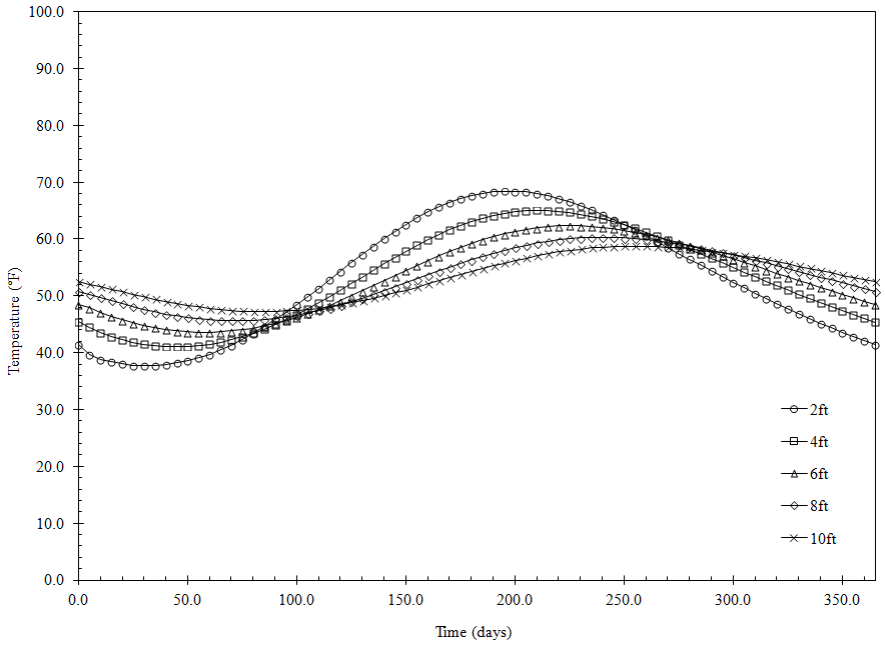


Figure 256: Columbus, Ohio – simulated Green's Function soil temperatures at various depths– observed surface soil temperature boundary condition

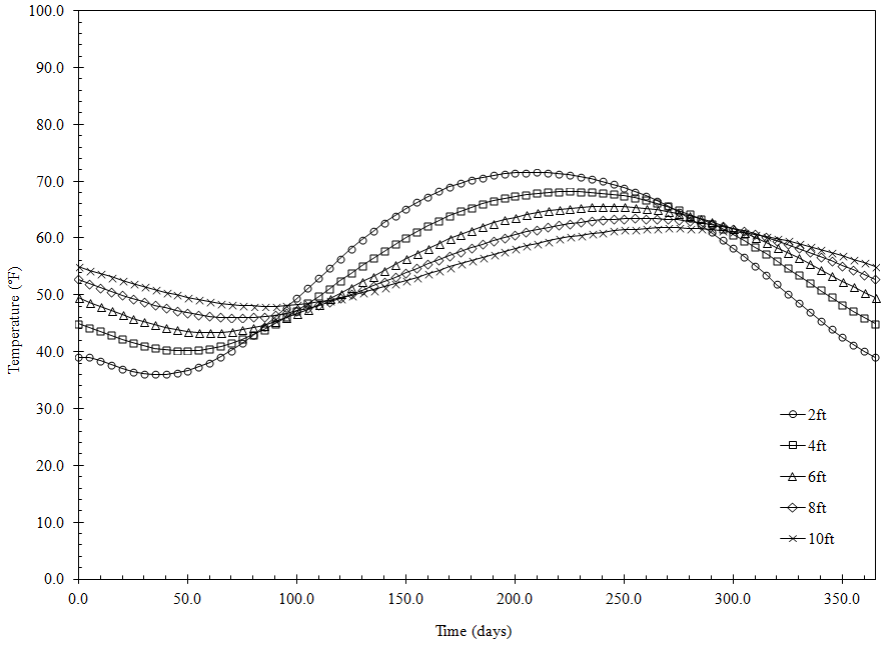


Figure 257: Columbus, Ohio – simulated Green's Function soil temperatures at various depths – corrected TMY surface air temperature boundary condition

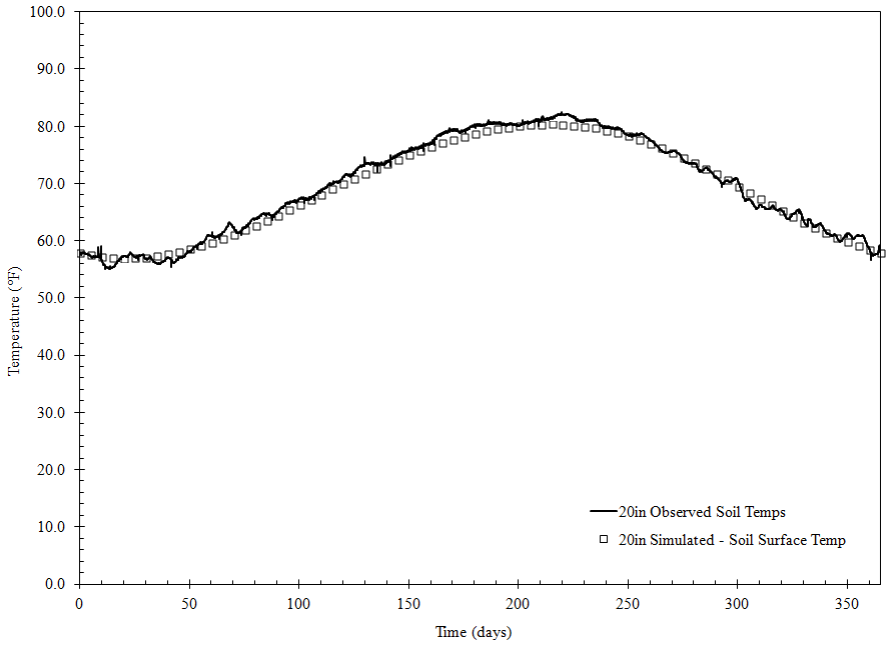


Figure 258: Houston, Texas – 20 inch observed vs. simulated Green's Function soil temperatures – observed surface soil temperature boundary condition

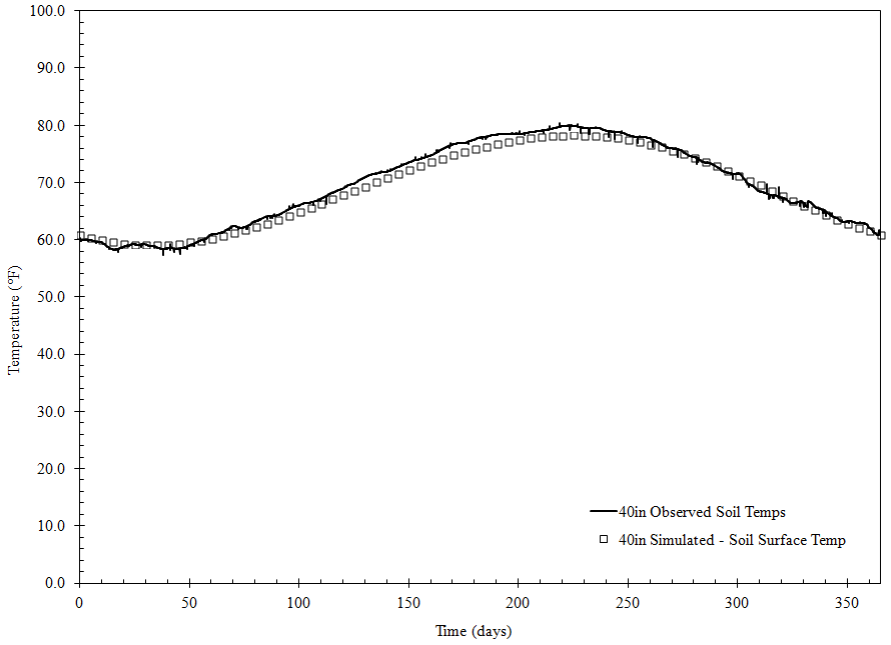


Figure 259: Houston, Texas – 40 inch observed vs. simulated Green's Function soil temperatures – observed surface soil temperature boundary condition

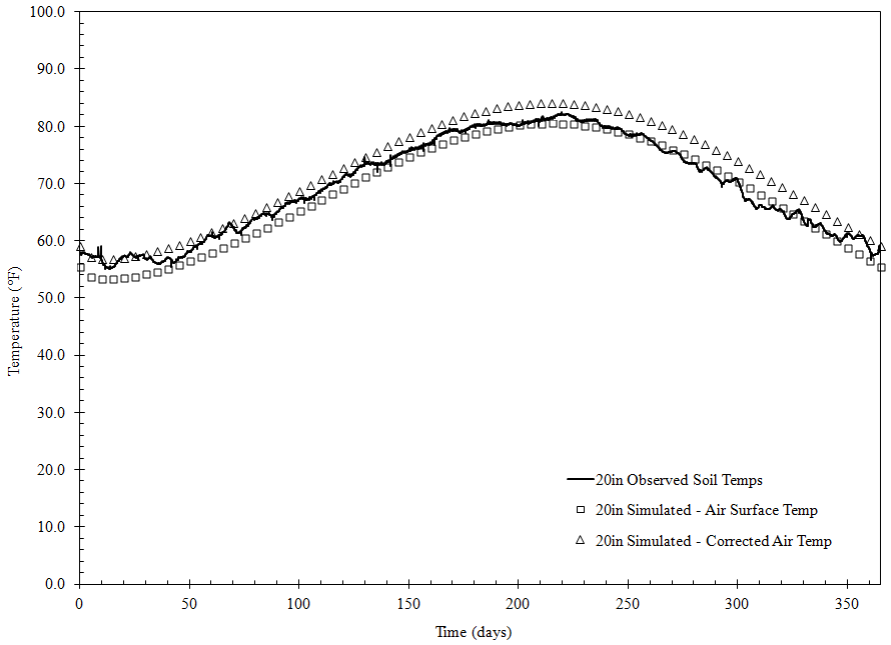


Figure 260: Houston, Texas – 20 inch observed vs. simulated Green's Function soil temperatures – typical meteorological year (TMY) and corrected TMY surface air temperature boundary conditions

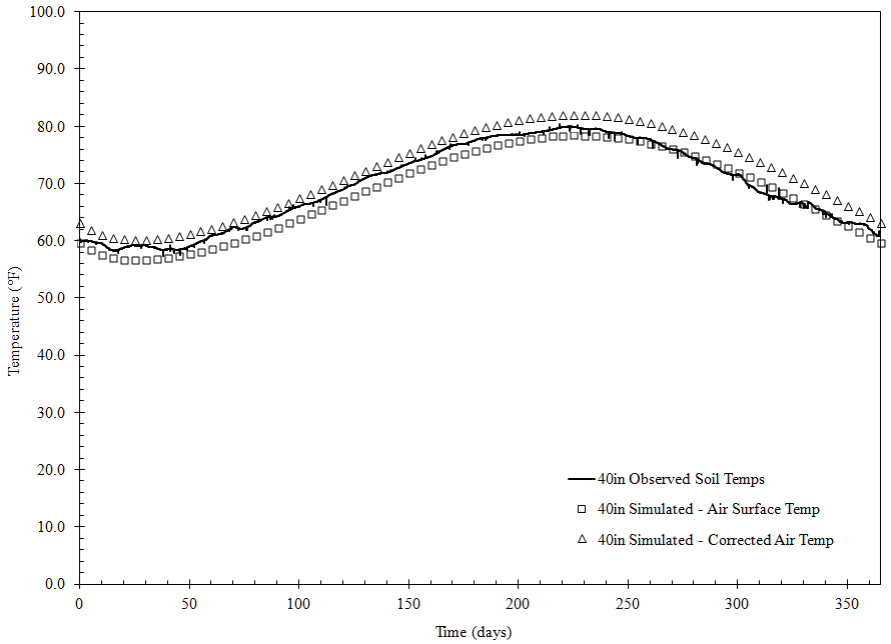


Figure 261: Houston, Texas – 40 inch observed vs. simulated Green's Function soil temperatures – typical meteorological year (TMY) and corrected TMY surface air temperature boundary conditions

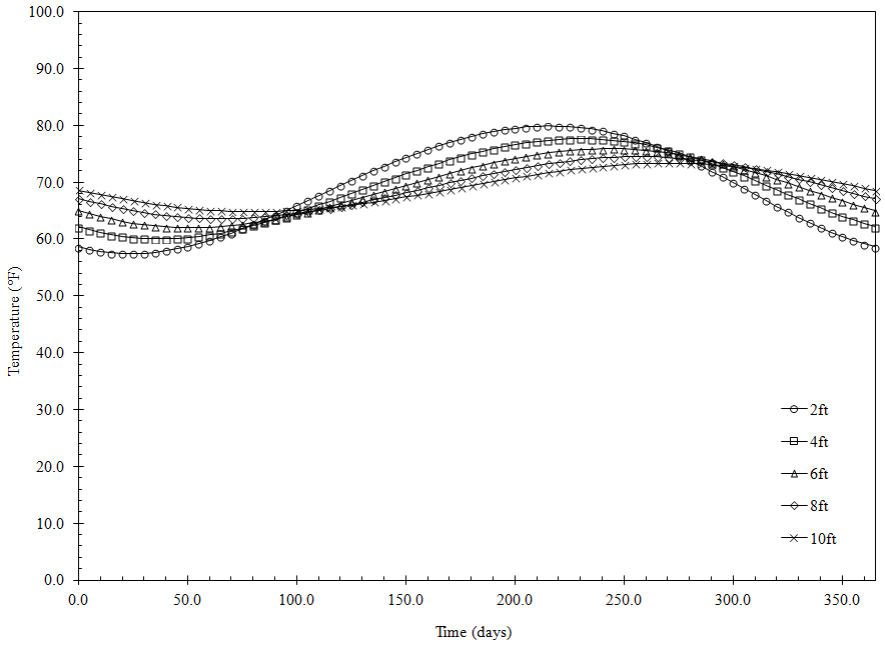


Figure 262: Houston, Texas – simulated Green's Function soil temperatures at various depths– observed surface soil temperature boundary condition

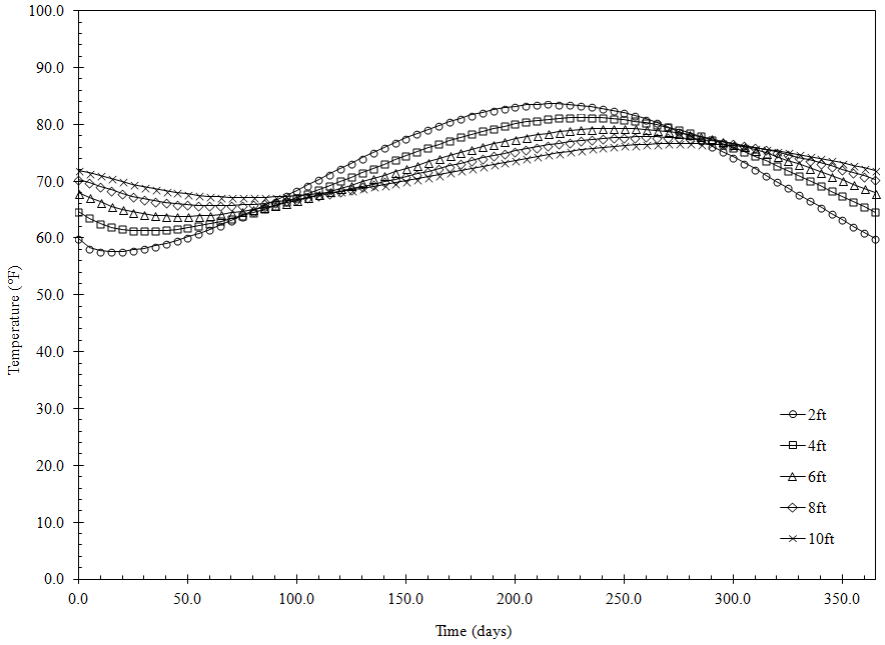


Figure 263: Houston, Texas – simulated Green's Function soil temperatures at various depths– corrected TMY surface air temperature boundary condition

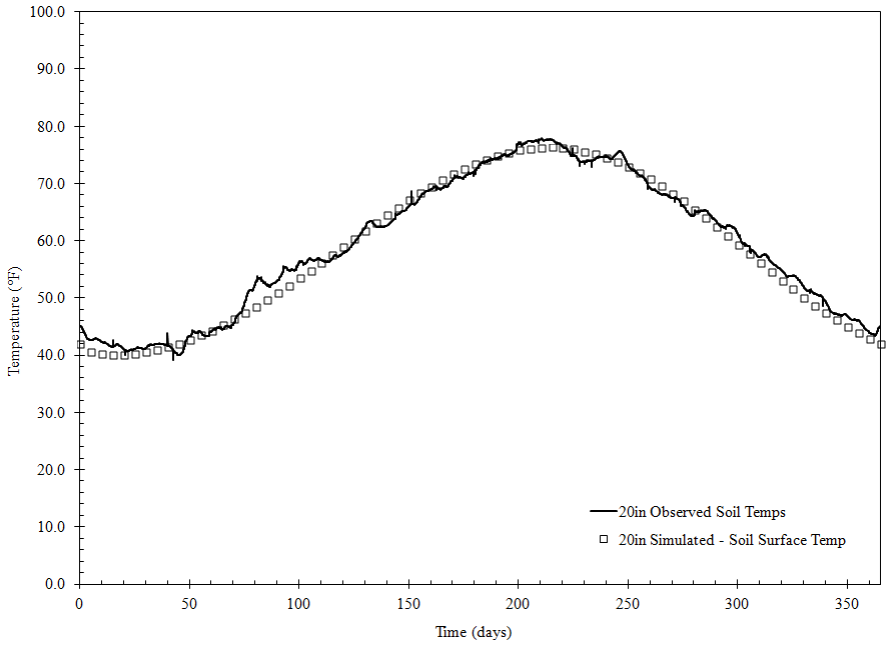


Figure 264: Kansas City, Missouri – 20 inch observed vs. simulated Green's Function soil temperatures – observed surface soil temperature boundary condition

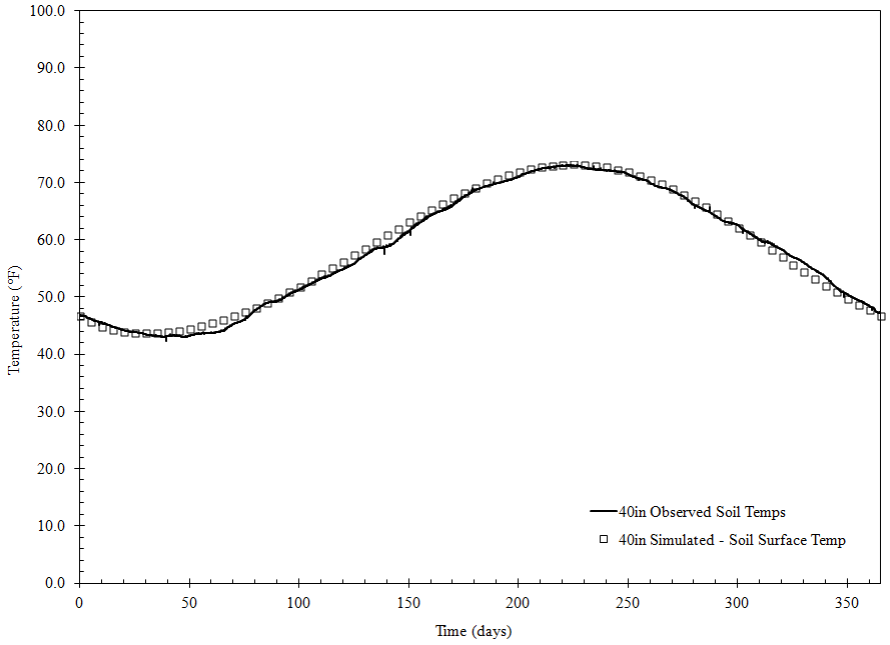


Figure 265: Kansas City, Missouri – 40 inch observed vs. simulated Green's Function soil temperatures – observed surface soil temperature boundary condition

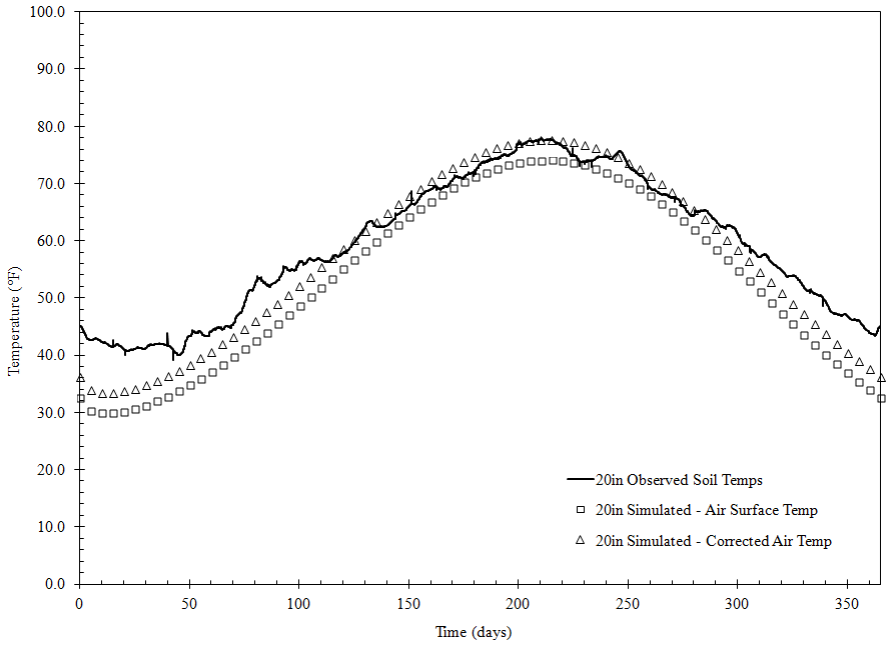


Figure 266: Kansas City, Missouri – 20 inch observed vs. simulated Green's Function soil temperatures – typical meteorological year (TMY) and corrected TMY surface air temperature boundary conditions

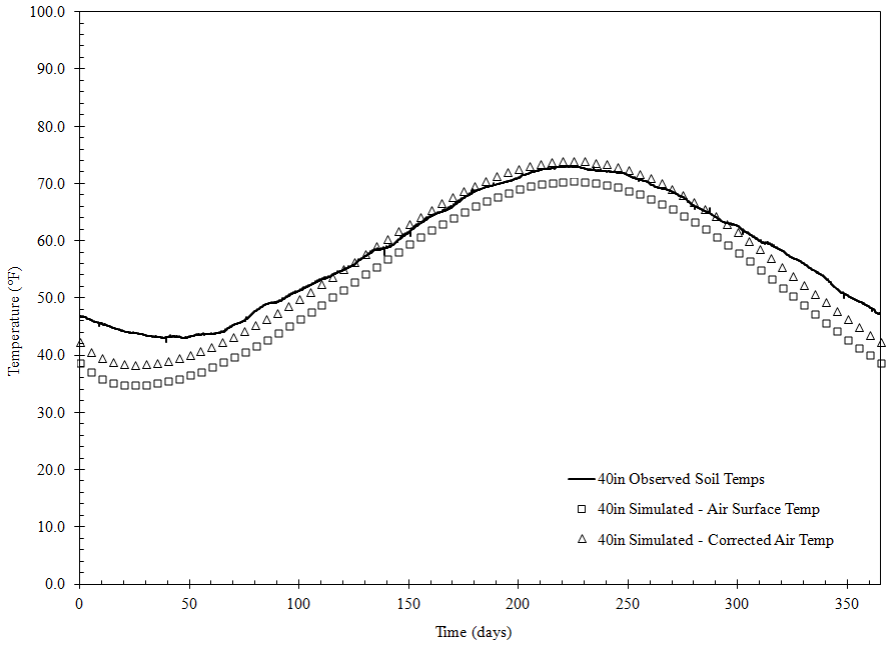


Figure 267: Kansas City, Missouri – 40 inch observed vs. simulated Green's Function soil temperatures – typical meteorological year (TMY) and corrected TMY surface air temperature boundary conditions

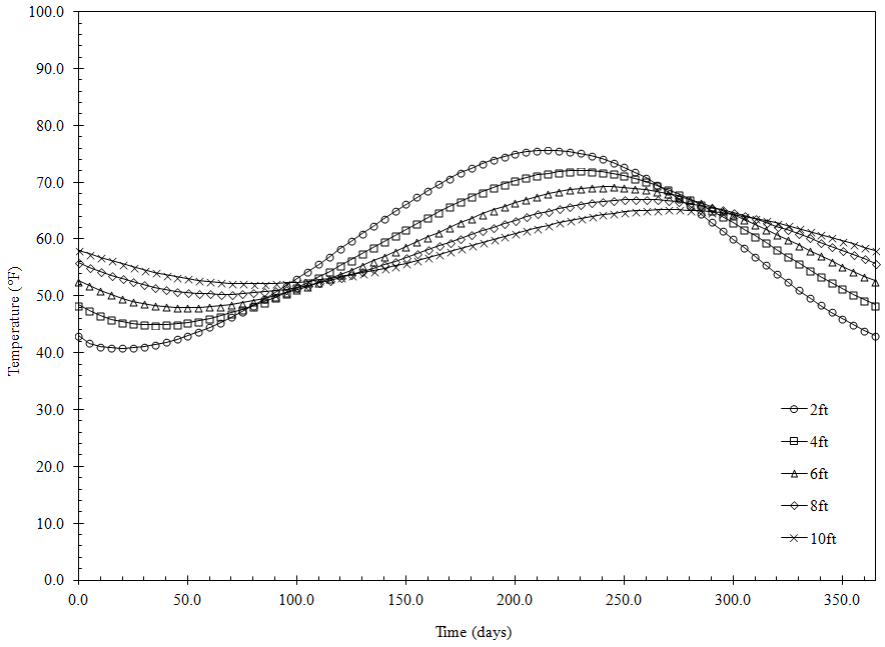


Figure 268: Kansas City, Missouri – simulated Green's Function soil temperatures at various depths– observed surface soil temperature boundary condition

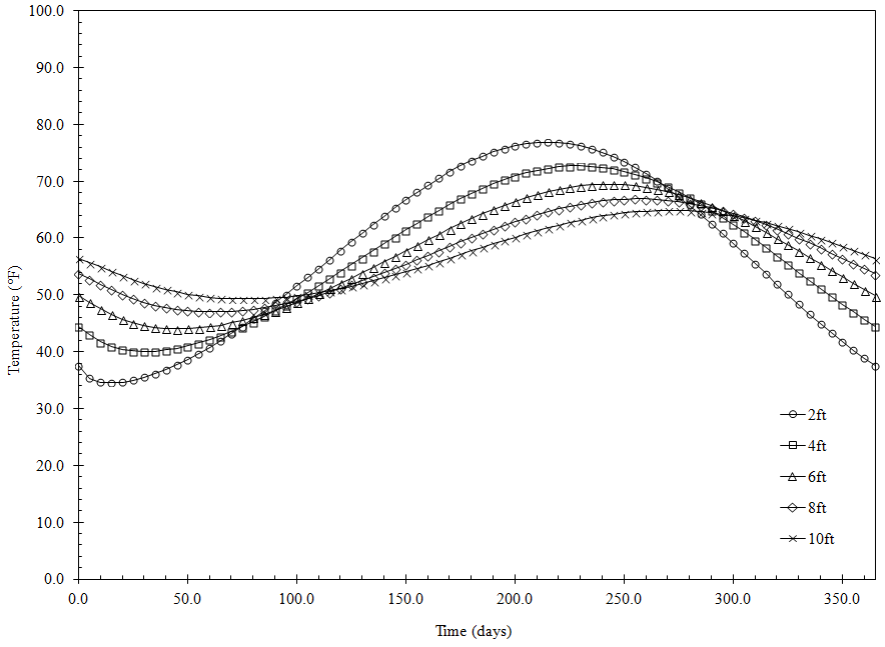


Figure 269: Kansas City, Missouri – simulated Green's Function soil temperatures at various depths – corrected TMY surface air temperature boundary condition

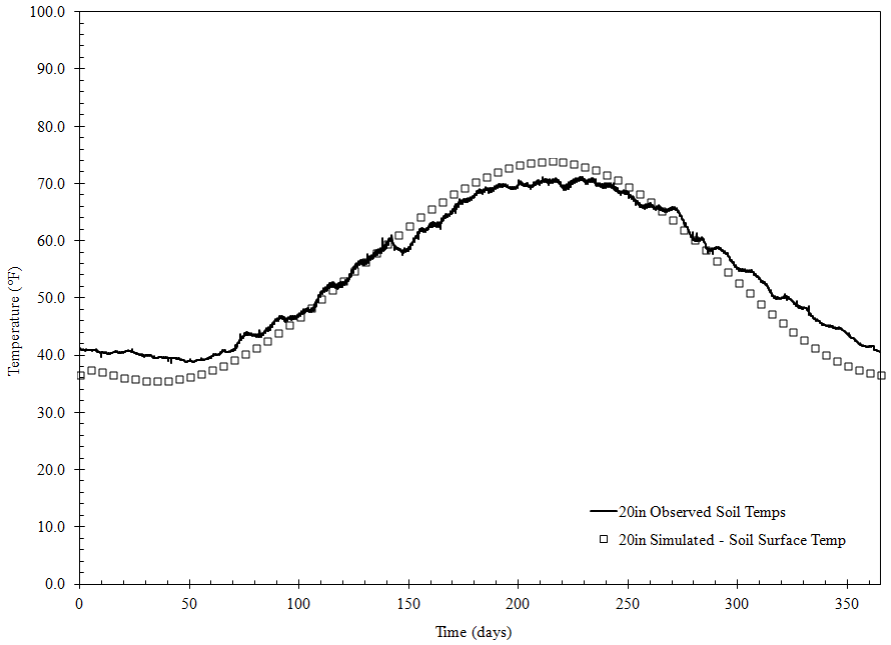


Figure 270: Las Vegas, Nevada – 20 inch observed vs. simulated Green's Function soil temperatures – observed surface soil temperature boundary condition

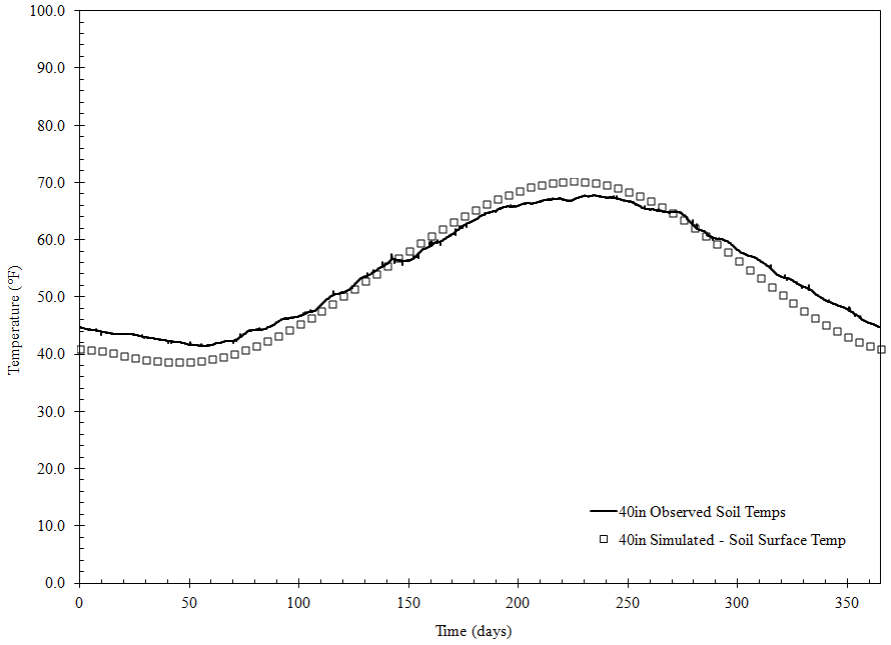


Figure 271: Las Vegas, Nevada – 40 inch observed vs. simulated Green's Function soil temperatures – observed surface soil temperature boundary condition

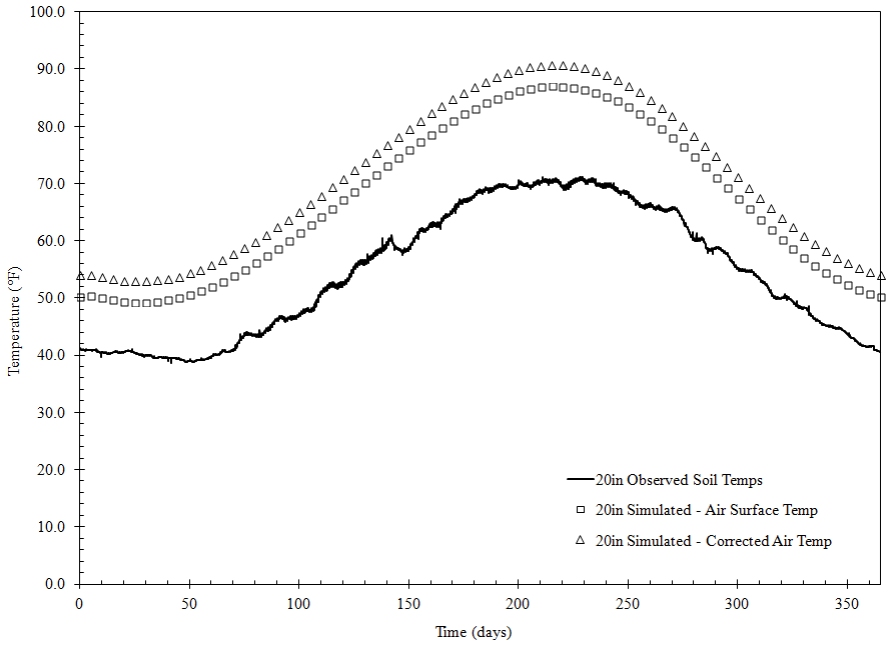


Figure 272: Las Vegas, Nevada – 20 inch observed vs. simulated Green's Function soil temperatures – typical meteorological year (TMY) and corrected TMY surface air temperature boundary conditions

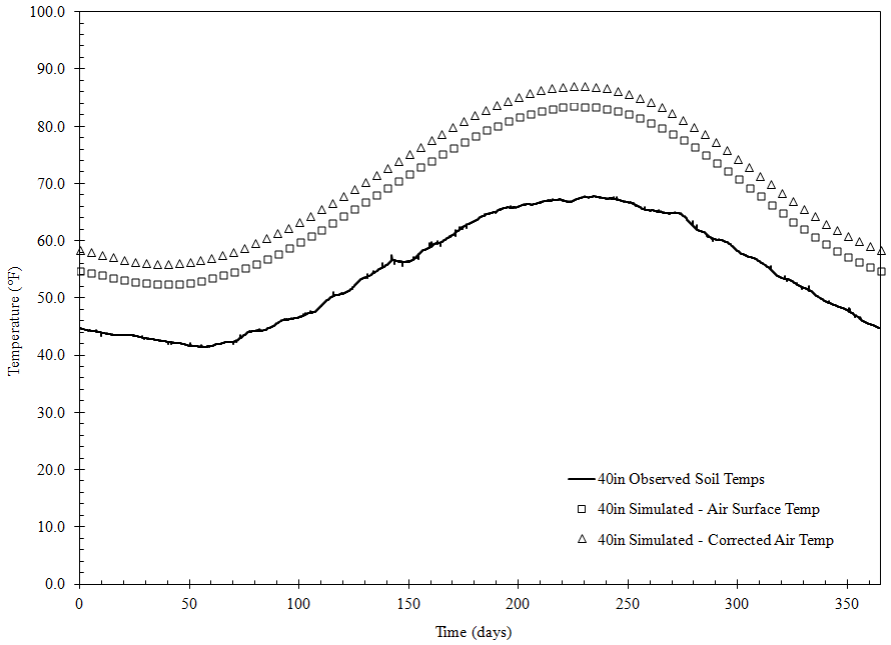


Figure 273: Las Vegas, Nevada – 40 inch observed vs. simulated Green's Function soil temperatures – typical meteorological year (TMY) and corrected TMY surface air temperature boundary conditions

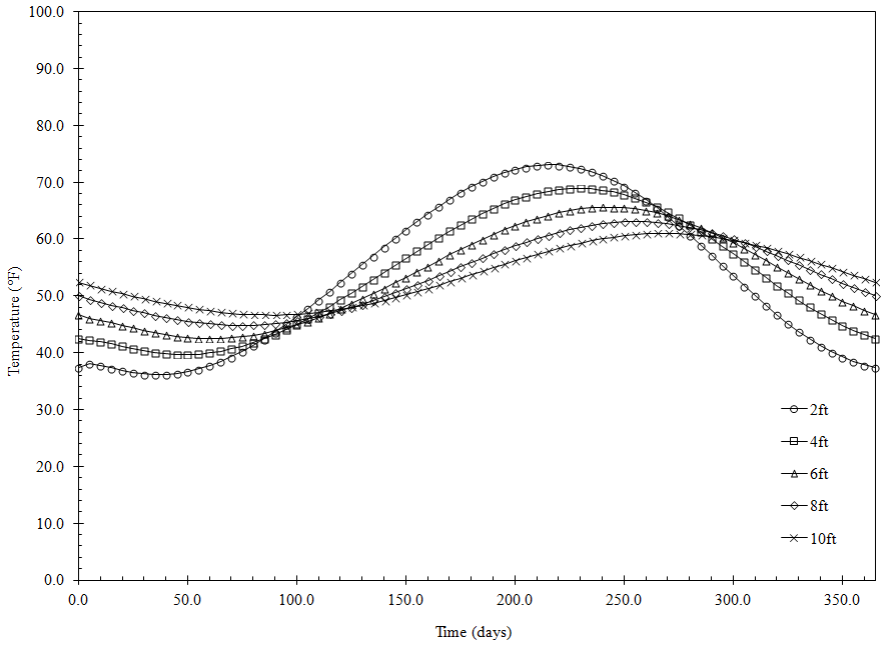


Figure 274: Las Vegas, Nevada – simulated Green's Function soil temperatures at various depths– observed surface soil temperature boundary condition

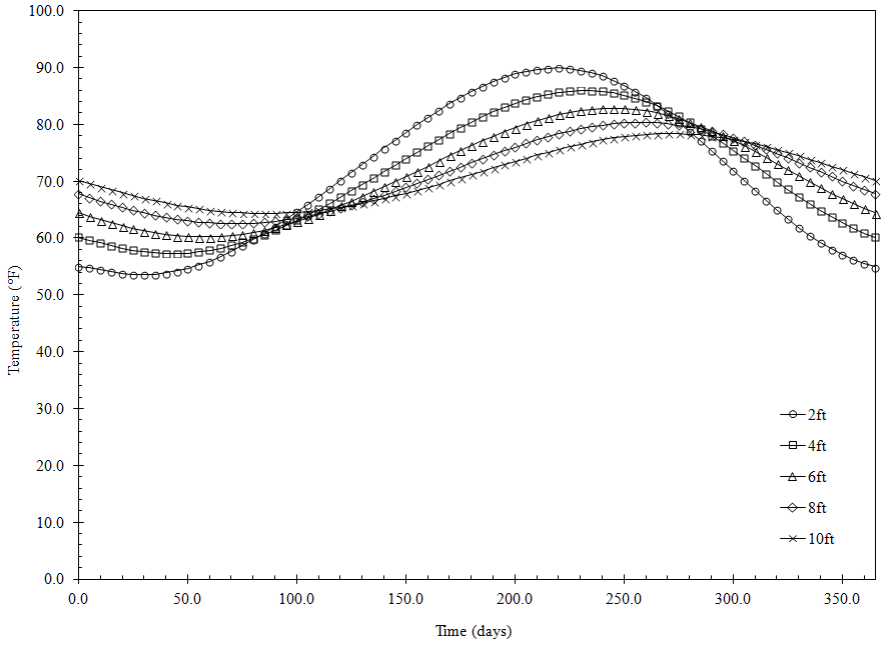


Figure 275: Las Vegas, Nevada – simulated Green's Function soil temperatures at various depths – corrected TMY surface air temperature boundary condition

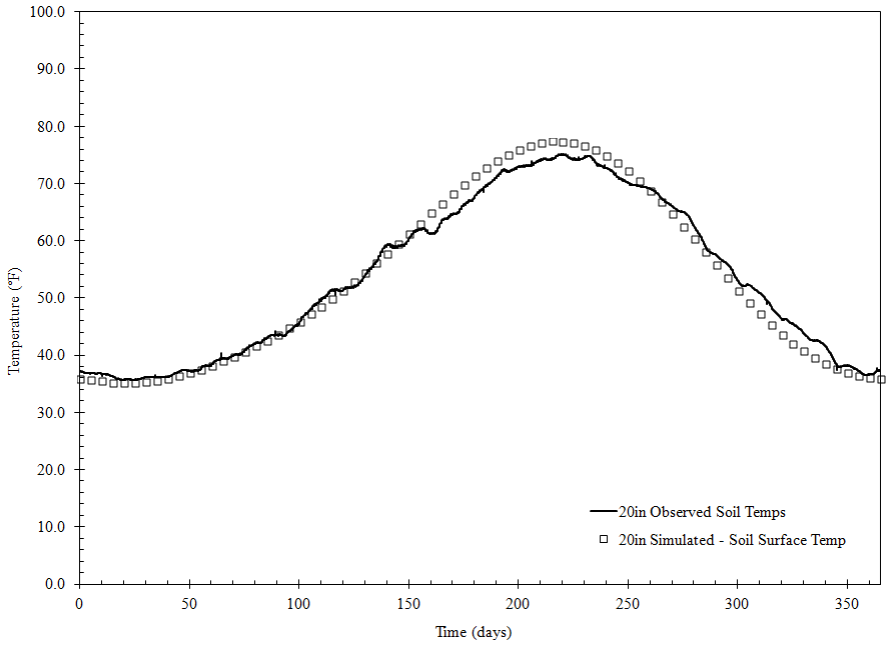


Figure 276: Moses Lake, Washington – 20 inch observed vs. simulated Green's Function soil temperatures – observed surface soil temperature boundary condition

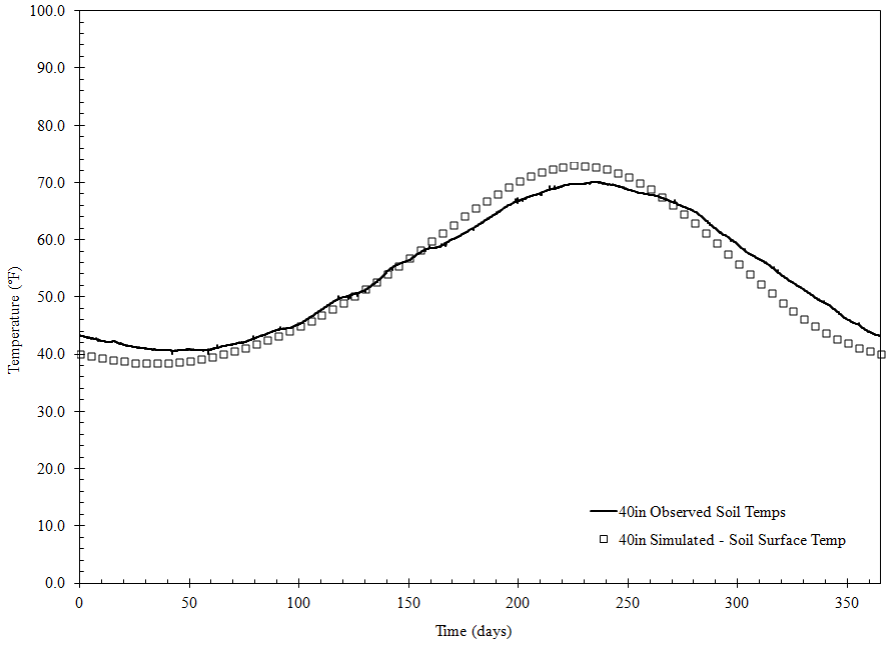


Figure 277: Moses Lake, Washington – 40 inch observed vs. simulated Green's Function soil temperatures – observed surface soil temperature boundary condition

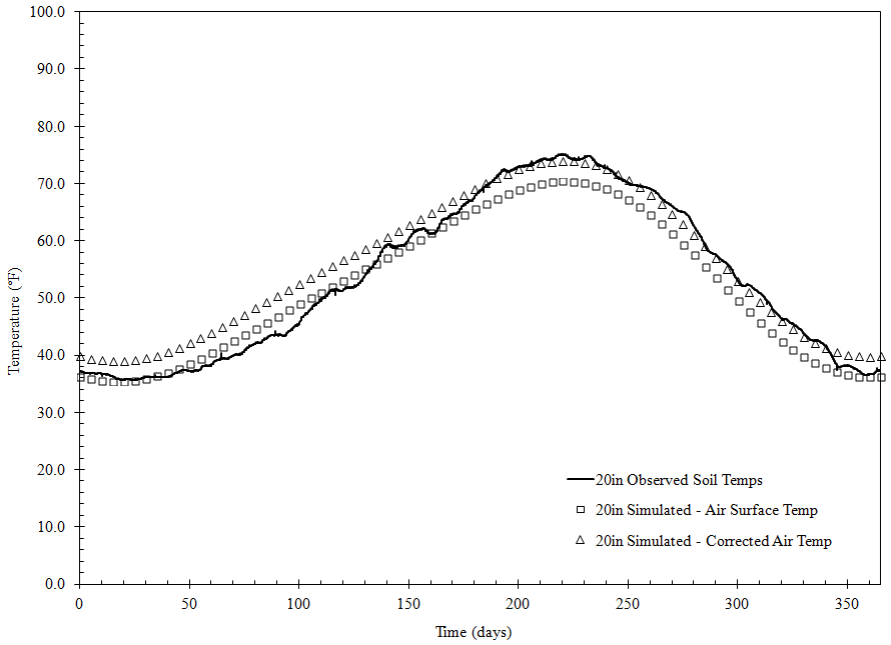


Figure 278: Moses Lake, Washington – 20 inch observed vs. simulated Green's Function soil temperatures – typical meteorological year (TMY) and corrected TMY surface air temperature boundary conditions

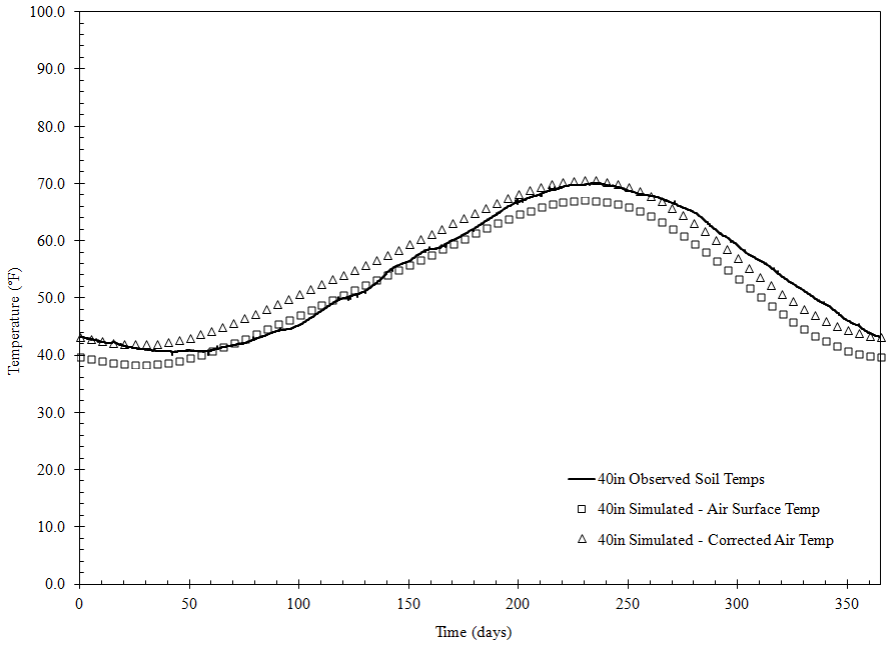


Figure 279: Moses Lake, Washington – 40 inch observed vs. simulated Green's Function soil temperatures – typical meteorological year (TMY) and corrected TMY surface air temperature boundary conditions

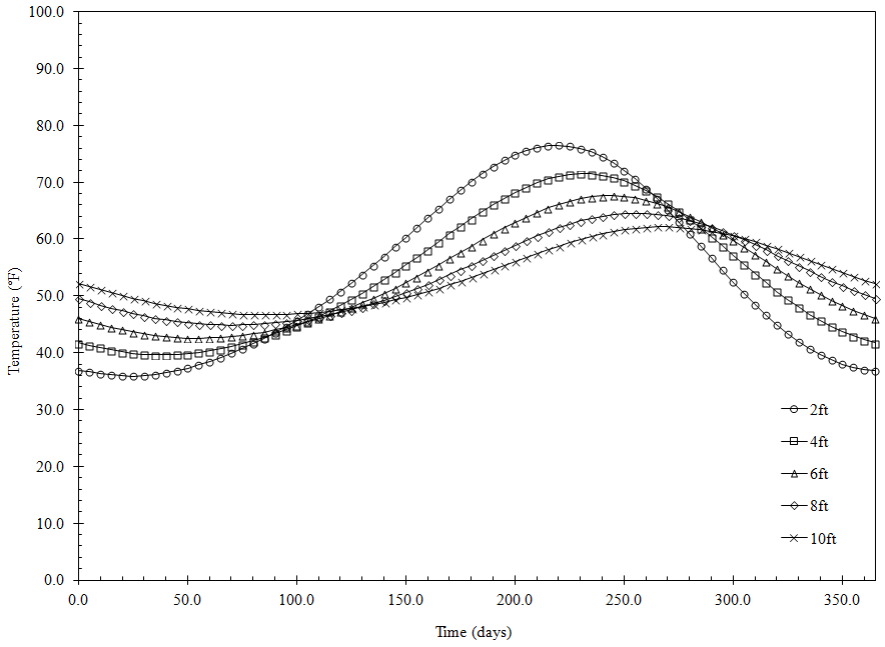


Figure 280: Moses Lake, Washington – simulated Green's Function soil temperatures at various depths– observed surface soil temperature boundary condition

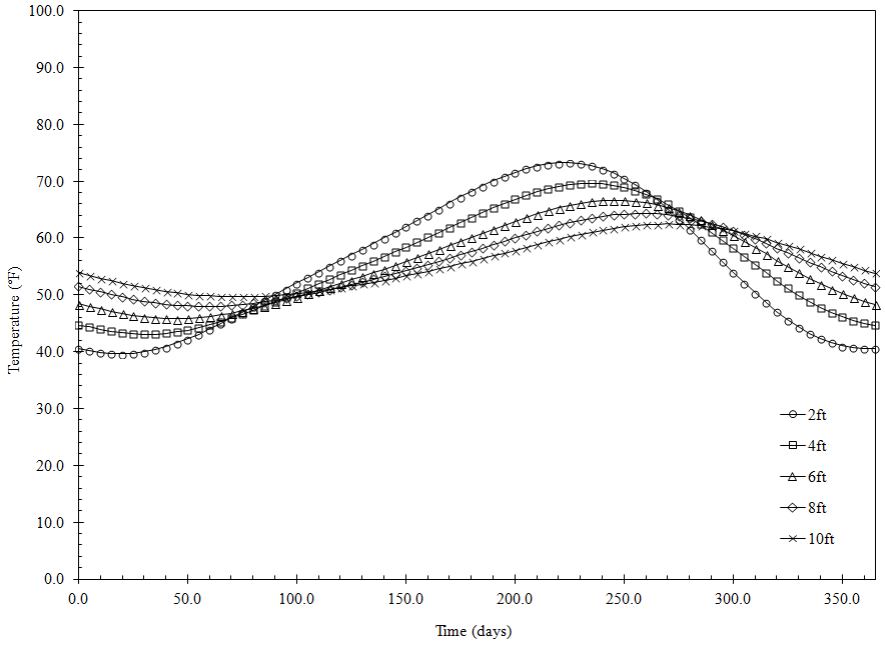


Figure 281: Moses Lake, Washington – simulated Green's Function soil temperatures at various depths – corrected TMY surface air temperature boundary condition

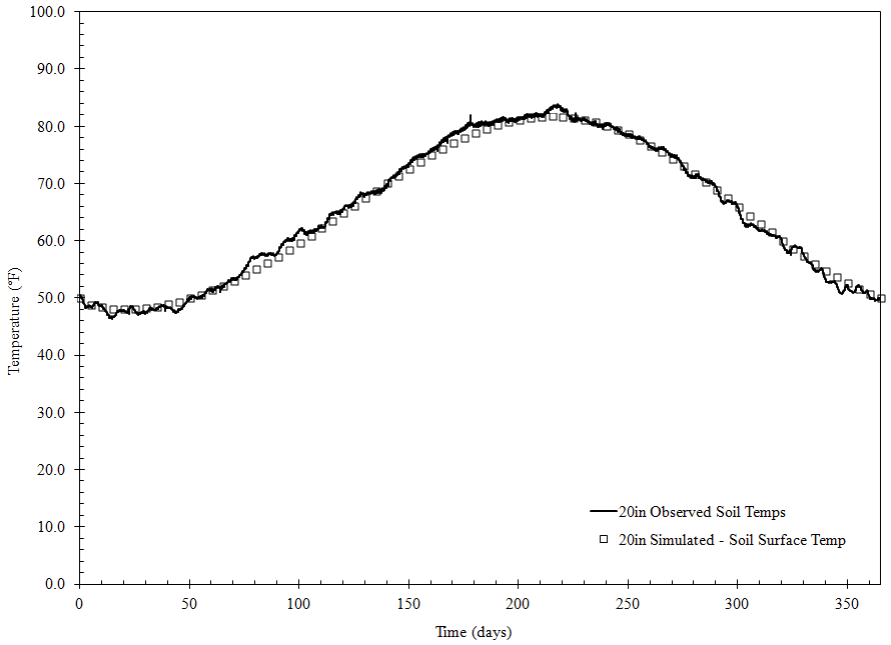


Figure 282: Pine Bluff, Arkansas – 20 inch observed vs. simulated Green's Function soil temperatures – observed surface soil temperature boundary condition

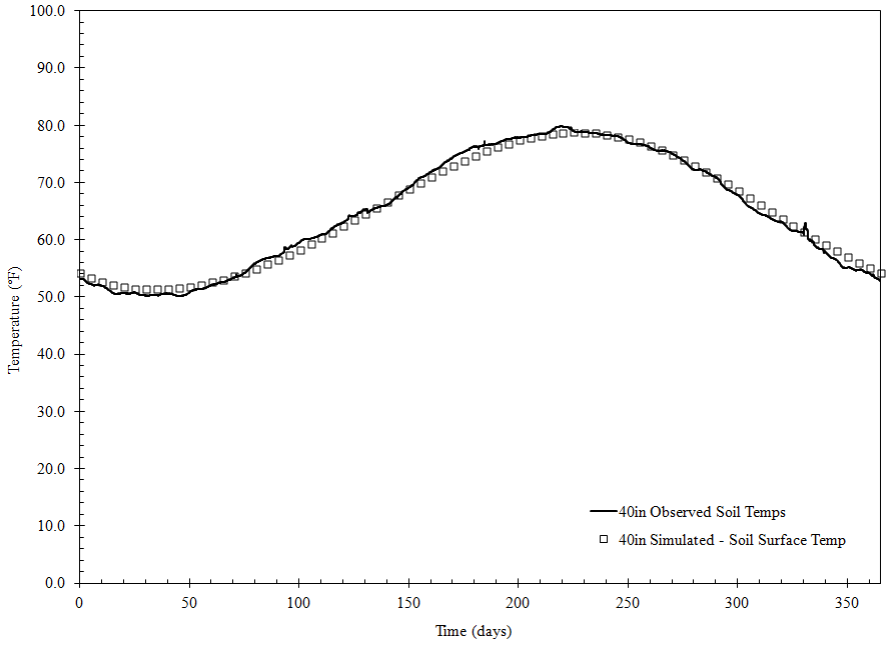


Figure 283: Pine Bluff, Arkansas – 40 inch observed vs. simulated Green's Function soil temperatures – observed surface soil temperature boundary condition

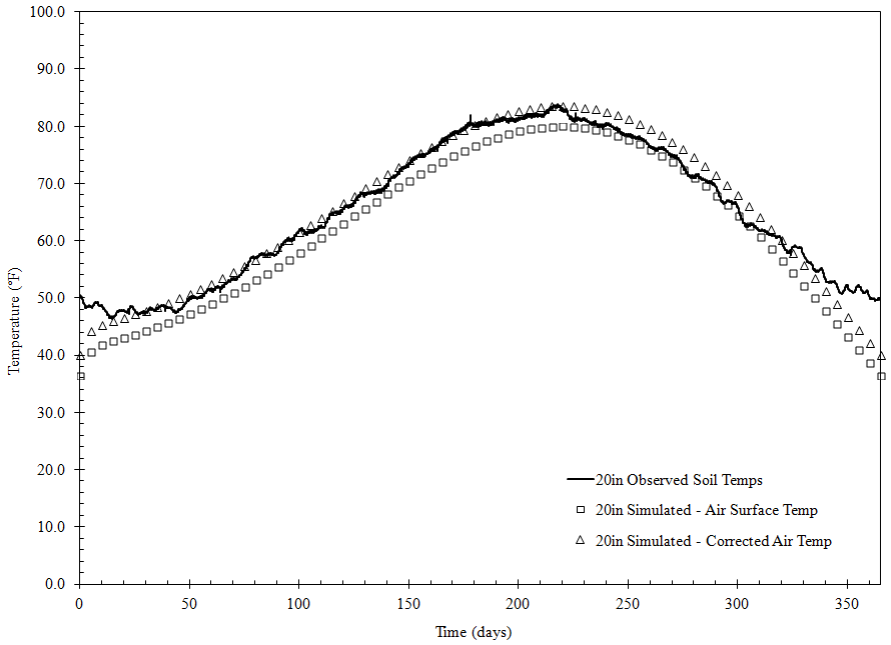


Figure 284: Pine Bluff, Arkansas – 20 inch observed vs. simulated Green's Function soil temperatures – typical meteorological year (TMY) and corrected TMY surface air temperature boundary conditions

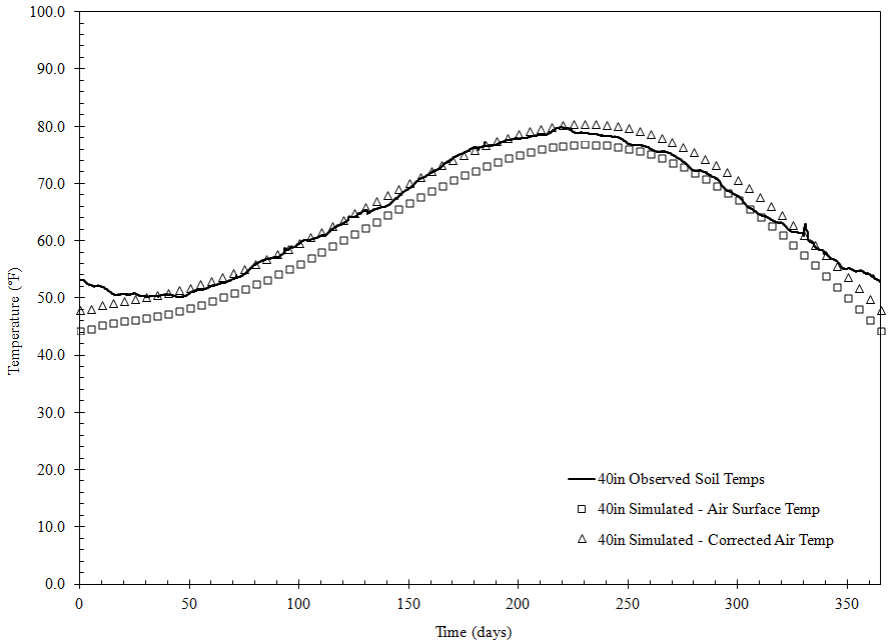


Figure 285: Pine Bluff, Arkansas – 40 inch observed vs. simulated Green's Function soil temperatures – typical meteorological year (TMY) and corrected TMY surface air temperature boundary conditions

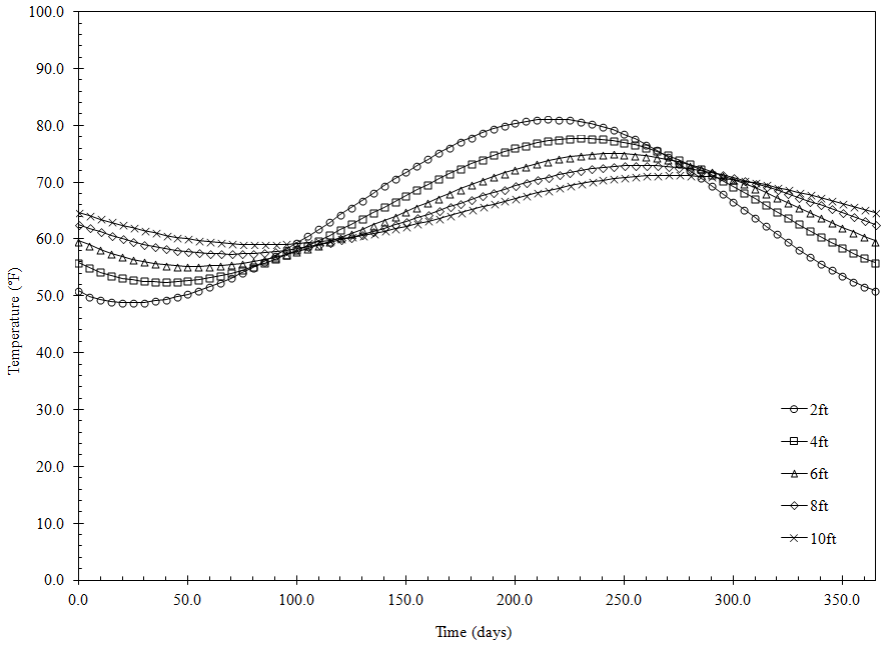


Figure 286: Pine Bluff, Arkansas – simulated Green's Function soil temperatures at various depths– observed surface soil temperature boundary condition

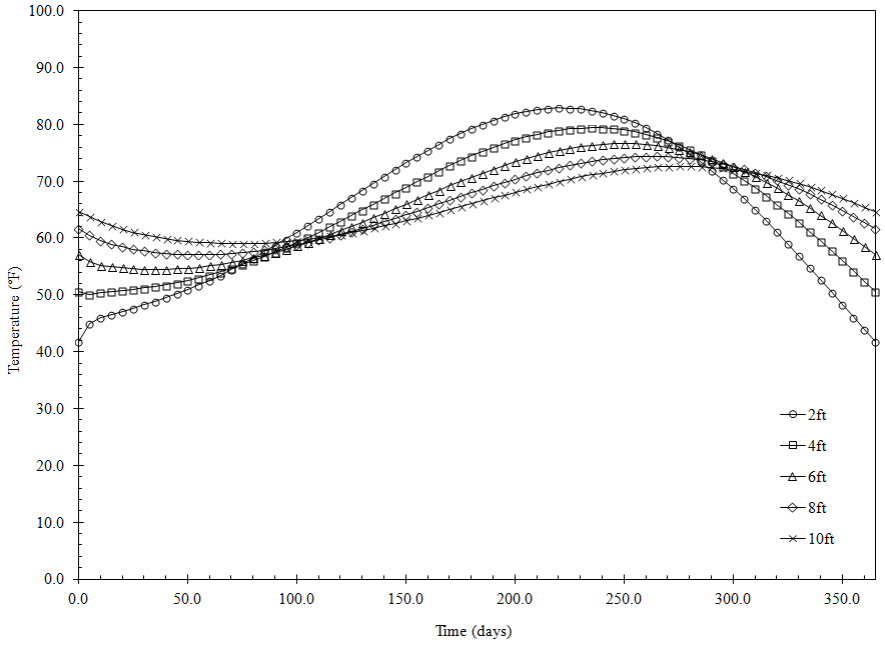


Figure 287: Pine Bluff, Arkansas – simulated Green's Function soil temperatures at various depths – corrected TMY surface air temperature boundary condition

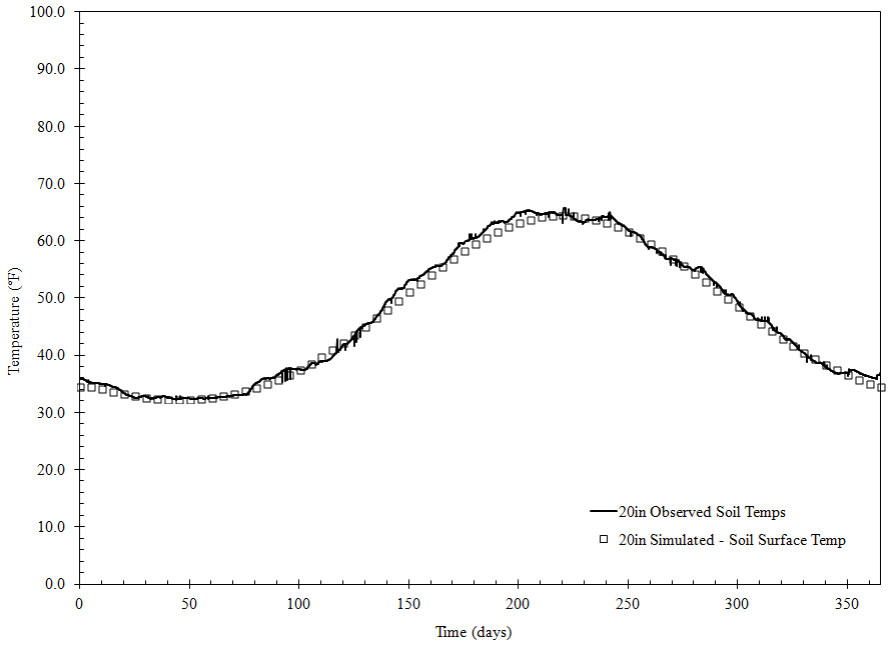


Figure 288: Saint Cloud, Minnesota – 20 inch observed vs. simulated Green's Function soil temperatures – observed surface soil temperature boundary condition

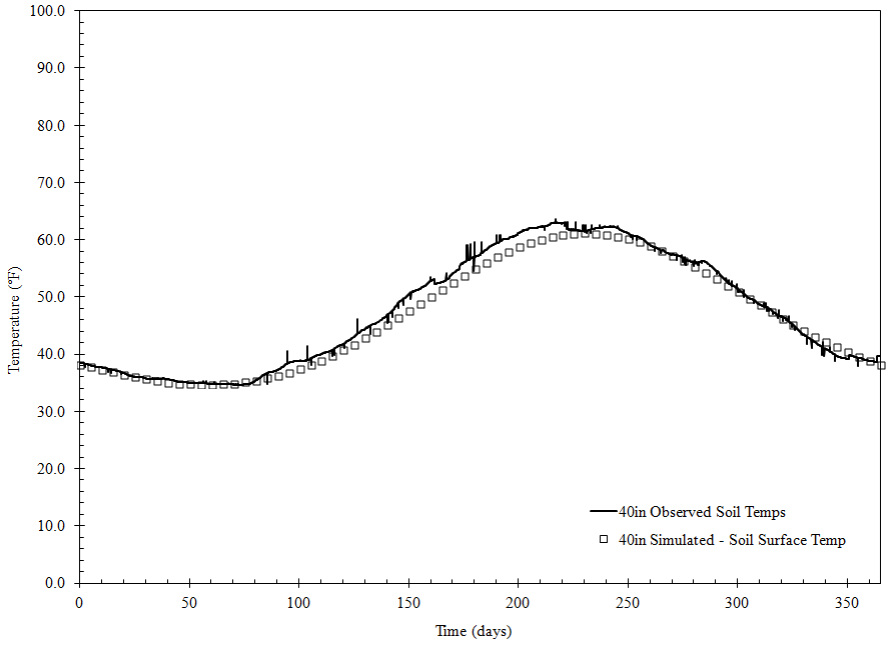


Figure 289: Saint Cloud, Minnesota – 40 inch observed vs. simulated Green's Function soil temperatures – observed surface soil temperature boundary condition

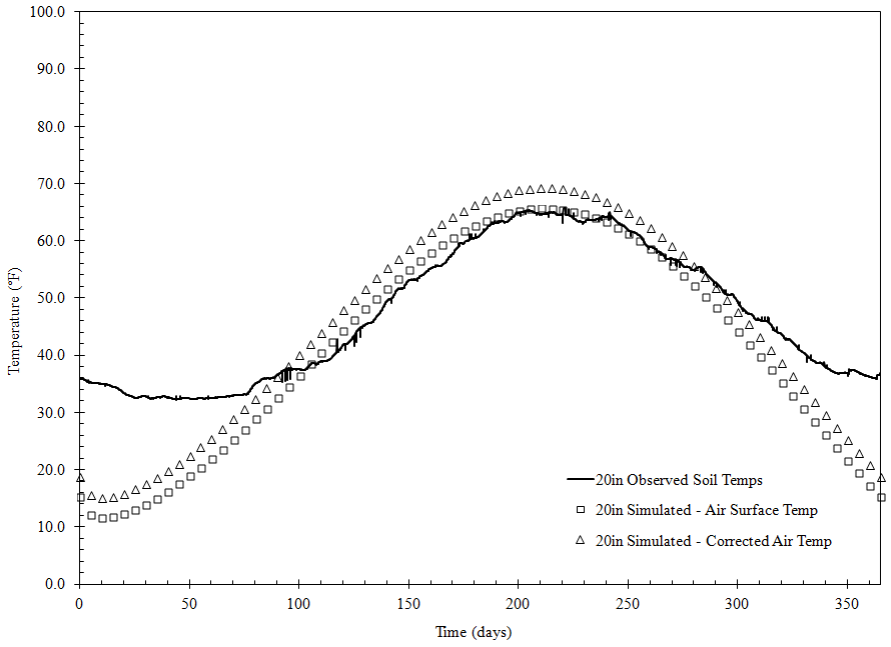


Figure 290: Saint Cloud, Minnesota – 20 inch observed vs. simulated Green's Function soil temperatures – typical meteorological year (TMY) and corrected TMY surface air temperature boundary conditions

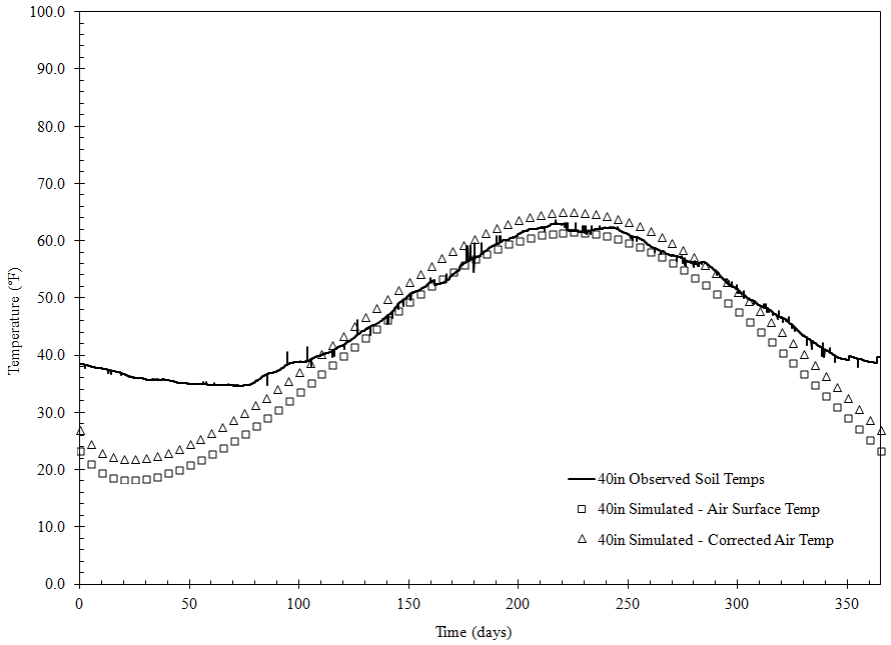


Figure 291: Saint Cloud, Minnesota – 40 inch observed vs. simulated Green's Function soil temperatures – typical meteorological year (TMY) and corrected TMY surface air temperature boundary conditions

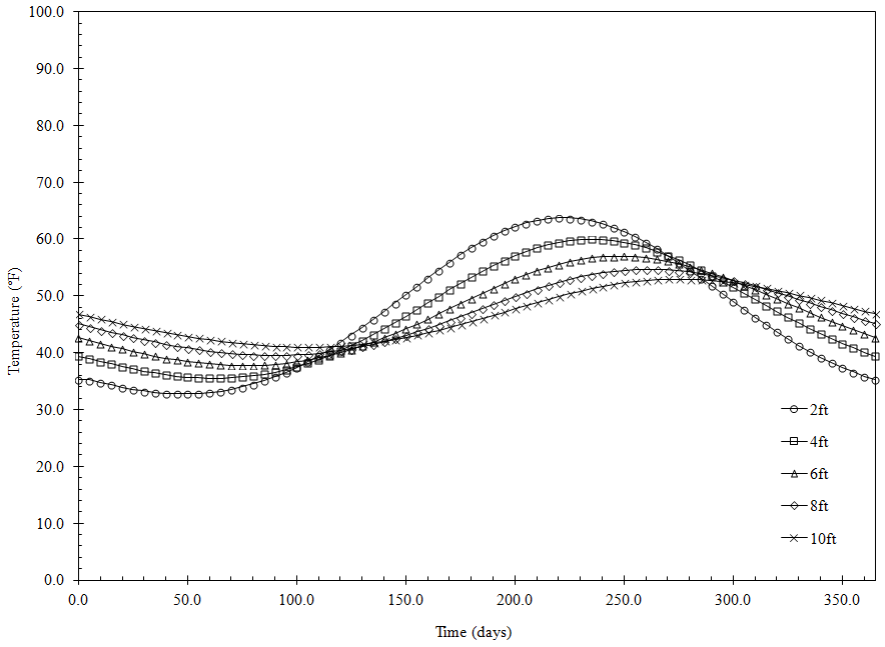


Figure 292: Saint Cloud, Minnesota – simulated Green's Function soil temperatures at various depths– observed surface soil temperature boundary condition

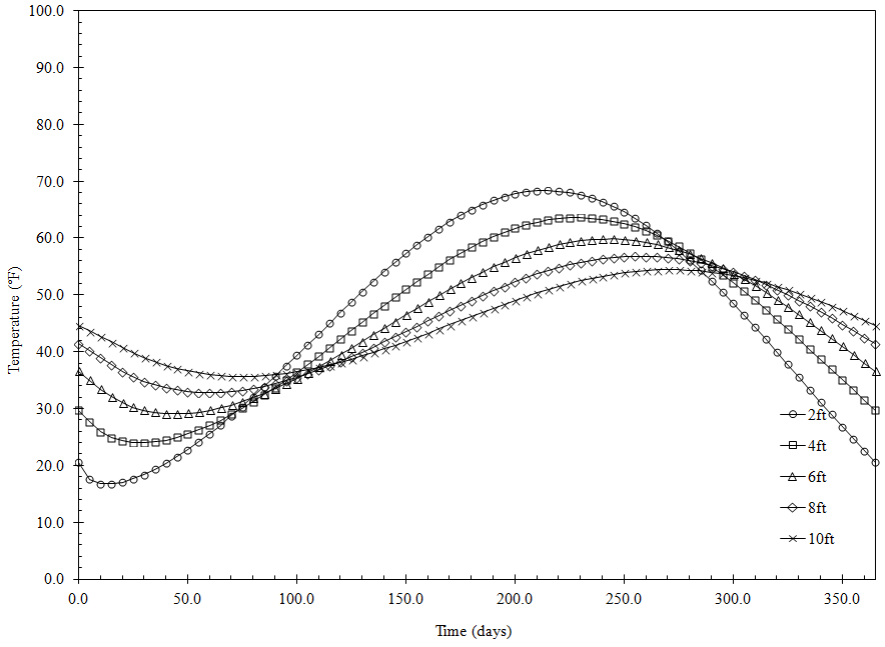


Figure 293: Saint Cloud, Minnesota – simulated Green's Function soil temperatures at various depths – corrected TMY surface air temperature boundary condition

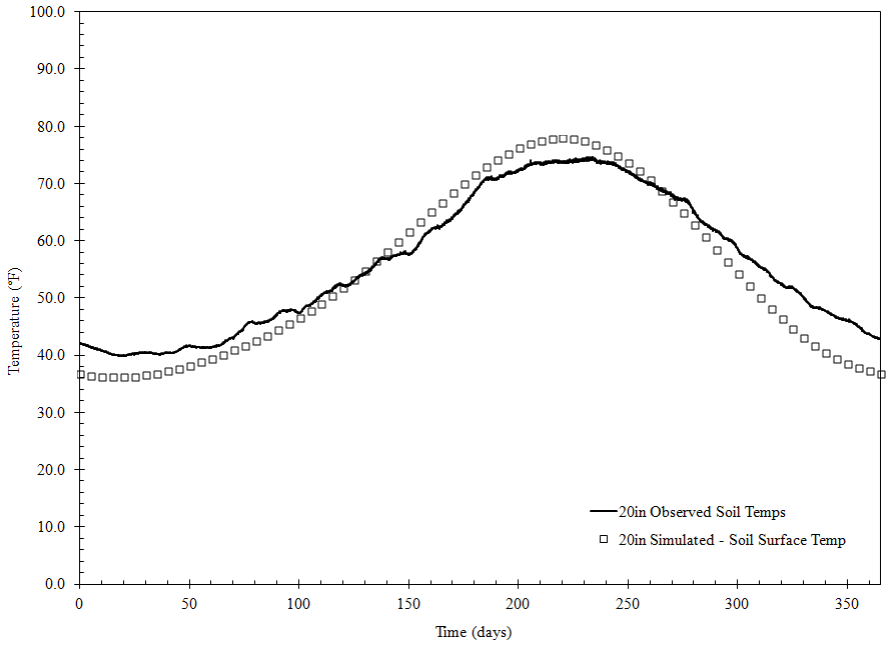


Figure 294: Salt Lake City, Utah – 20 inch observed vs. simulated Green's Function soil temperatures – observed surface soil temperature boundary condition

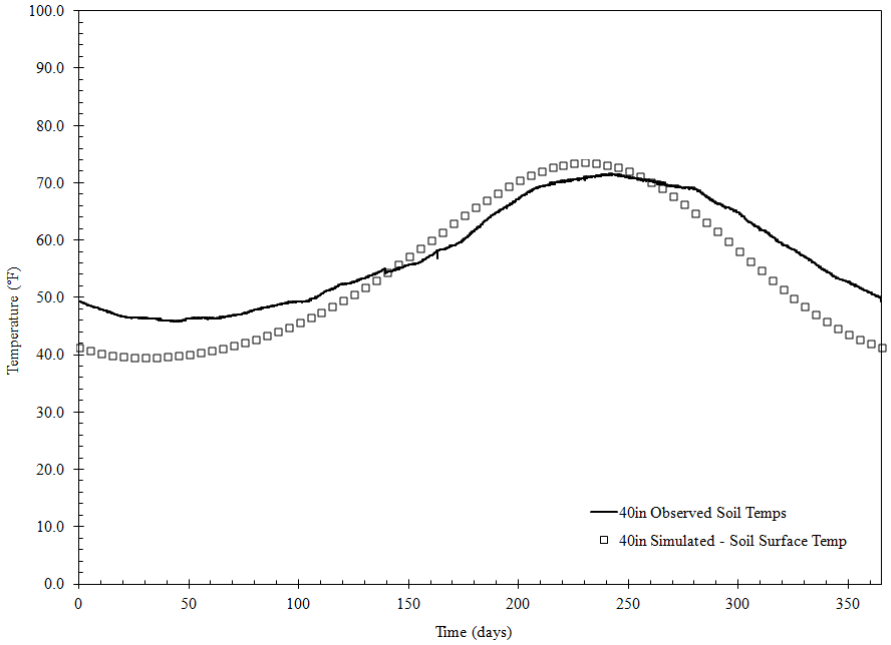


Figure 295: Salt Lake City, Utah – 40 inch observed vs. simulated Green's Function soil temperatures – observed surface soil temperature boundary condition

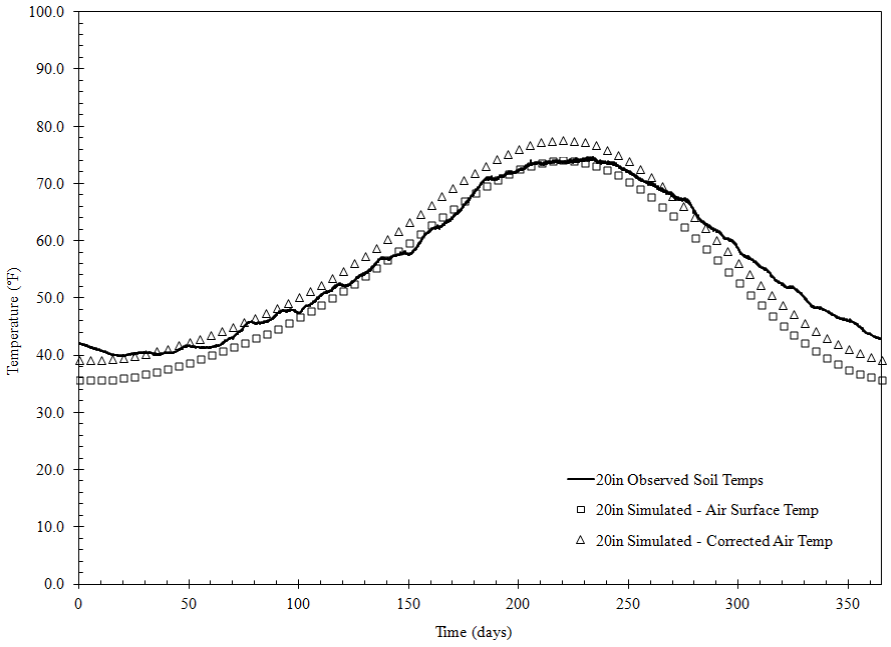


Figure 296: Salt Lake City, Utah – 20 inch observed vs. simulated Green's Function soil temperatures – typical meteorological year (TMY) and corrected TMY surface air temperature boundary conditions

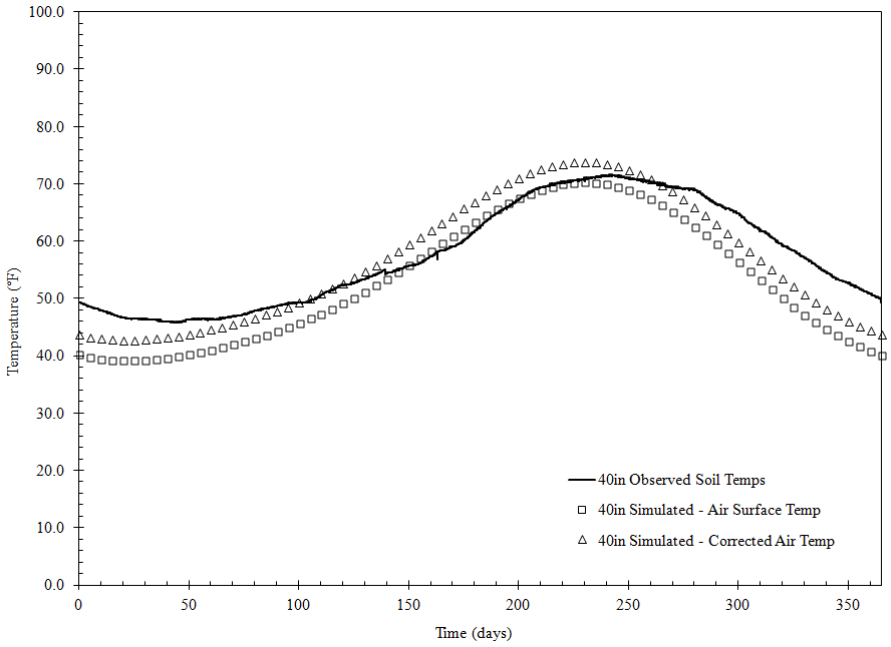


Figure 297: Salt Lake City, Utah – 40 inch observed vs. simulated Green's Function soil temperatures – typical meteorological year (TMY) and corrected TMY surface air temperature boundary conditions

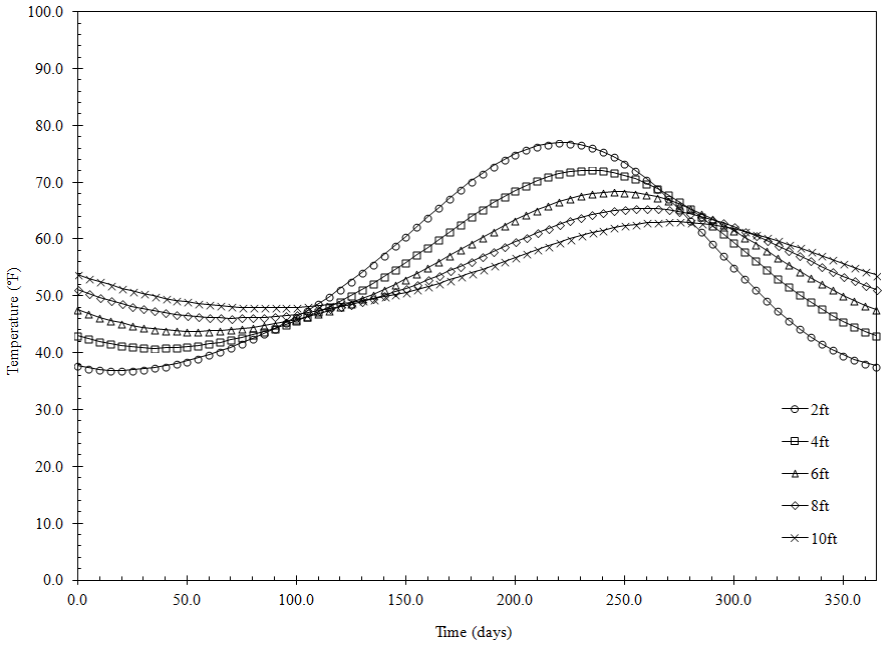


Figure 298: Salt Lake City, Utah – simulated Green's Function soil temperatures at various depths– observed surface soil temperature boundary condition

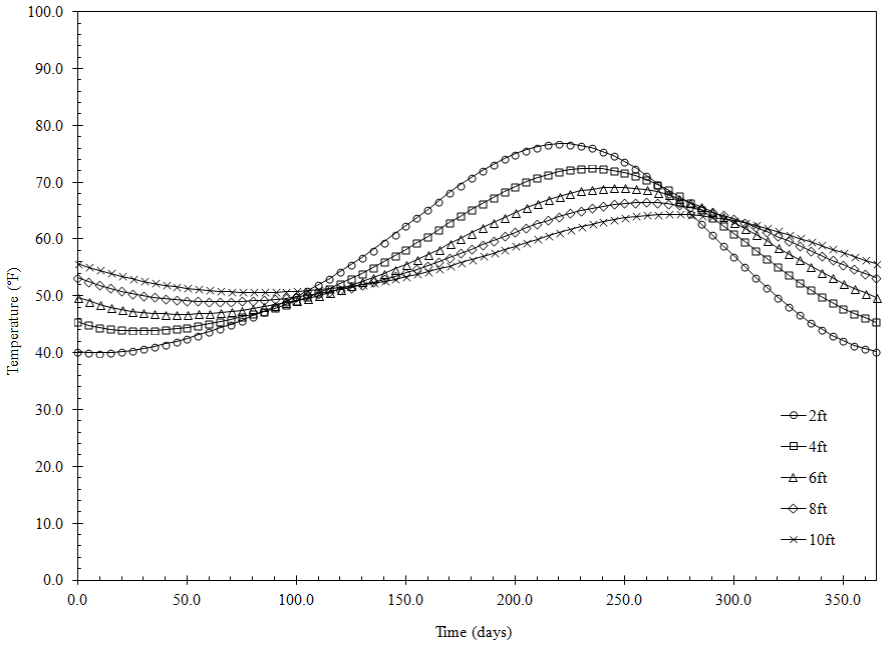


Figure 299: Salt Lake City, Utah – simulated Green's Function soil temperatures at various depths – corrected TMY surface air temperature boundary condition

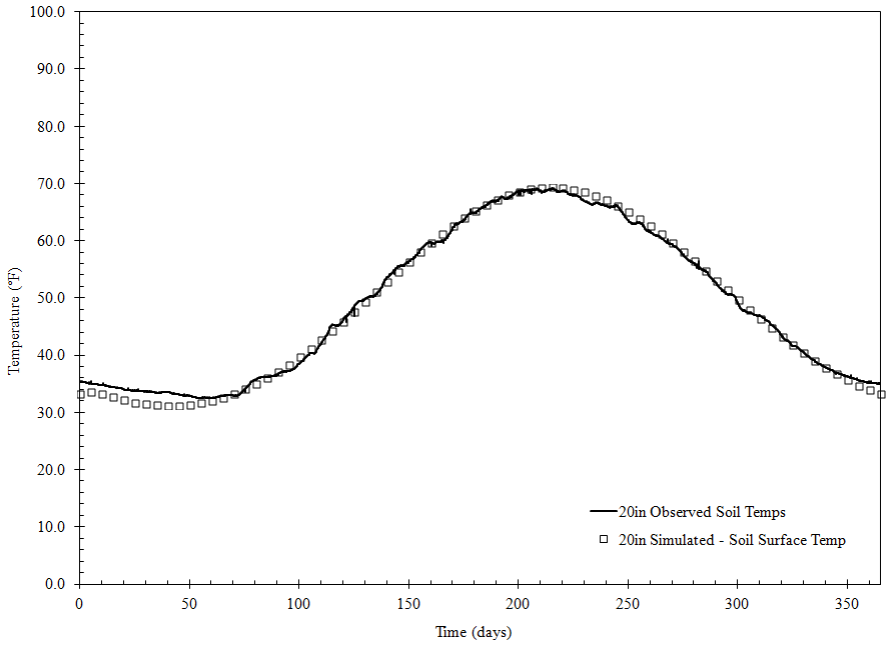


Figure 300: Sioux Falls, South Dakota – 20 inch observed vs. simulated Green's Function soil temperatures – observed surface soil temperature boundary condition

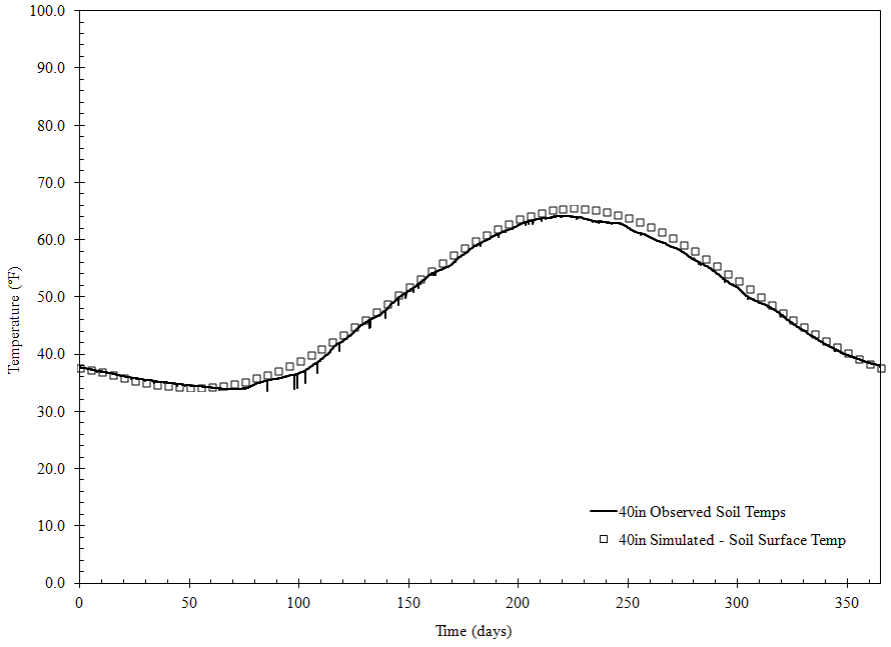


Figure 301: Sioux Falls, South Dakota – 40 inch observed vs. simulated Green's Function soil temperatures – observed surface soil temperature boundary condition

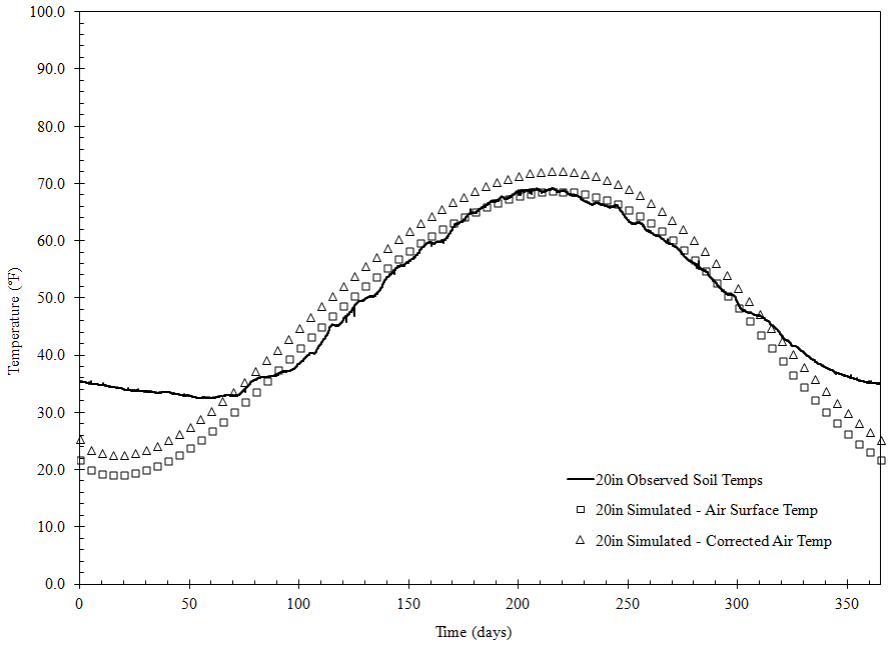


Figure 302: Sioux Falls, South Dakota – 20 inch observed vs. simulated Green's Function soil temperatures – typical meteorological year (TMY) and corrected TMY surface air temperature boundary conditions

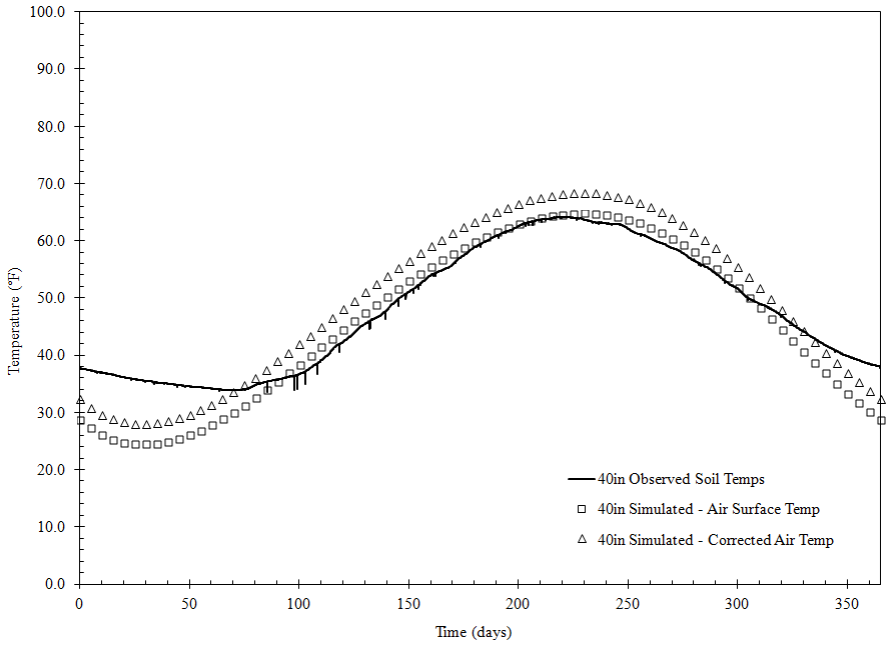


Figure 303: Sioux Falls, South Dakota – 40 inch observed vs. simulated Green's Function soil temperatures – typical meteorological year (TMY) and corrected TMY surface air temperature boundary conditions

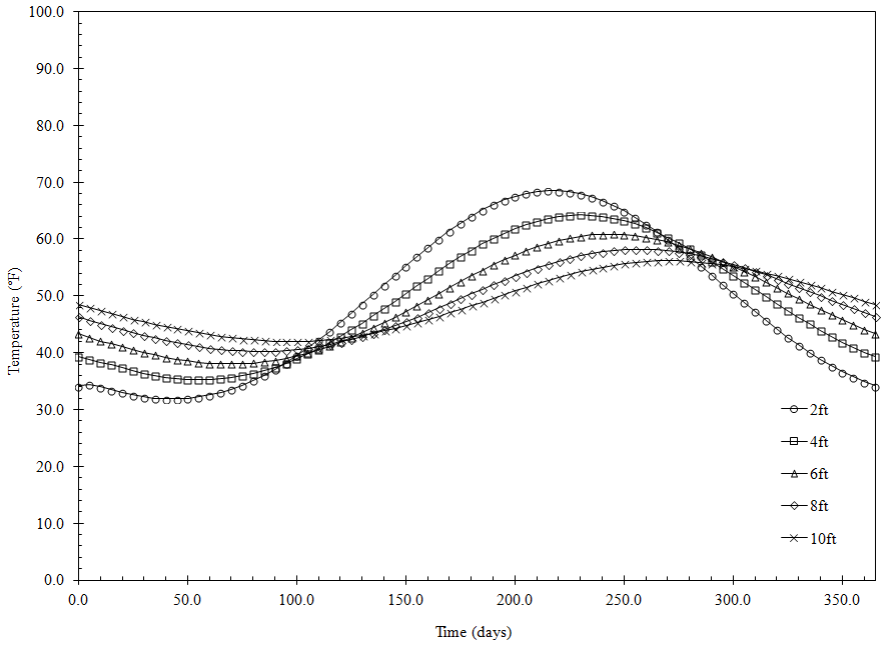


Figure 304: Sioux Falls, South Dakota – simulated Green's Function soil temperatures at various depths– observed surface soil temperature boundary condition

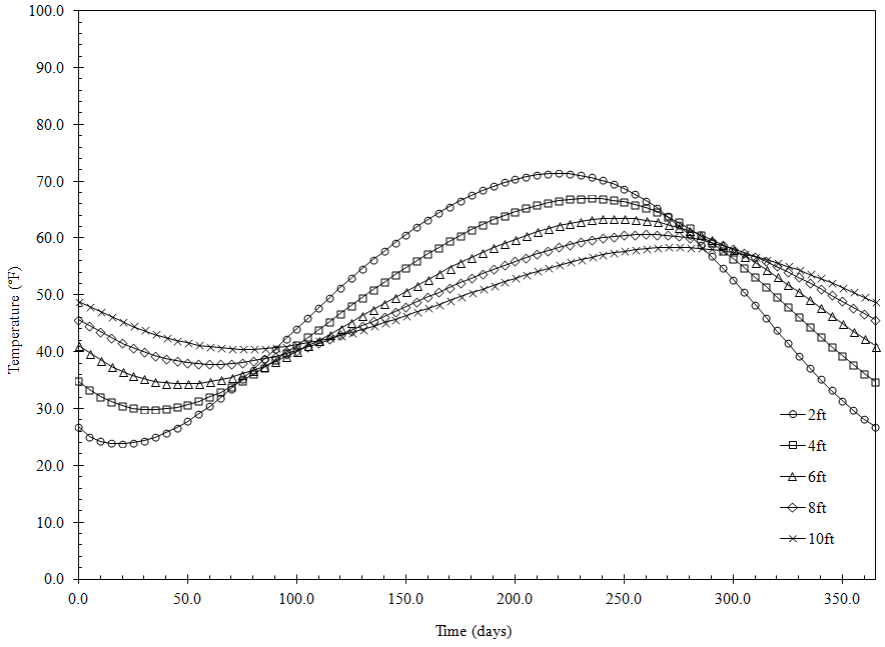


Figure 305: Sioux Falls, South Dakota – simulated Green's Function soil temperatures at various depths – corrected TMY surface air temperature boundary condition

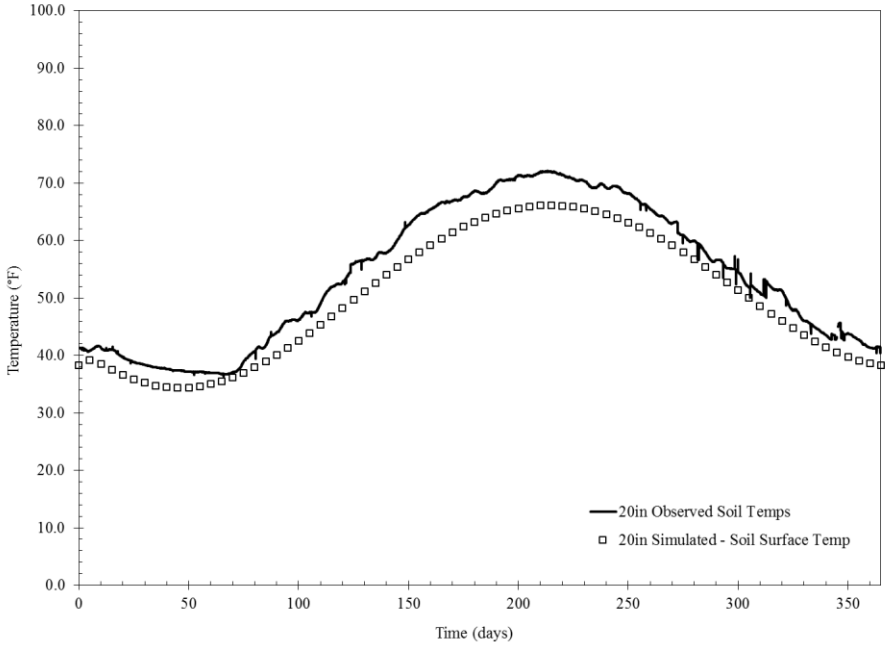


Figure 306: State College, Pennsylvania – 20 inch observed vs. simulated Green's Function soil temperatures – observed surface soil temperature boundary condition

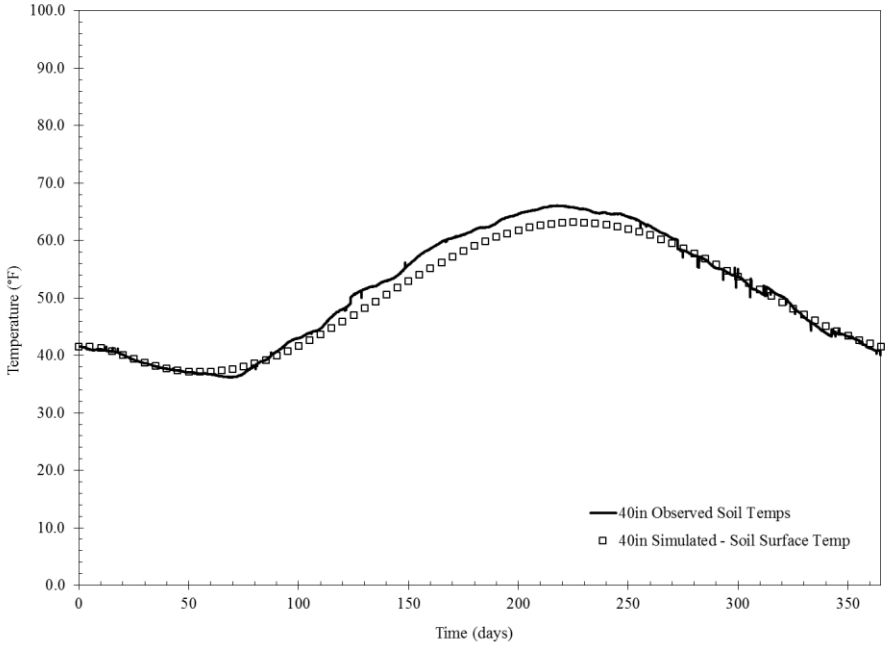


Figure 307: State College, Pennsylvania – 40 inch observed vs. simulated Green's Function soil temperatures – observed surface soil temperature boundary condition

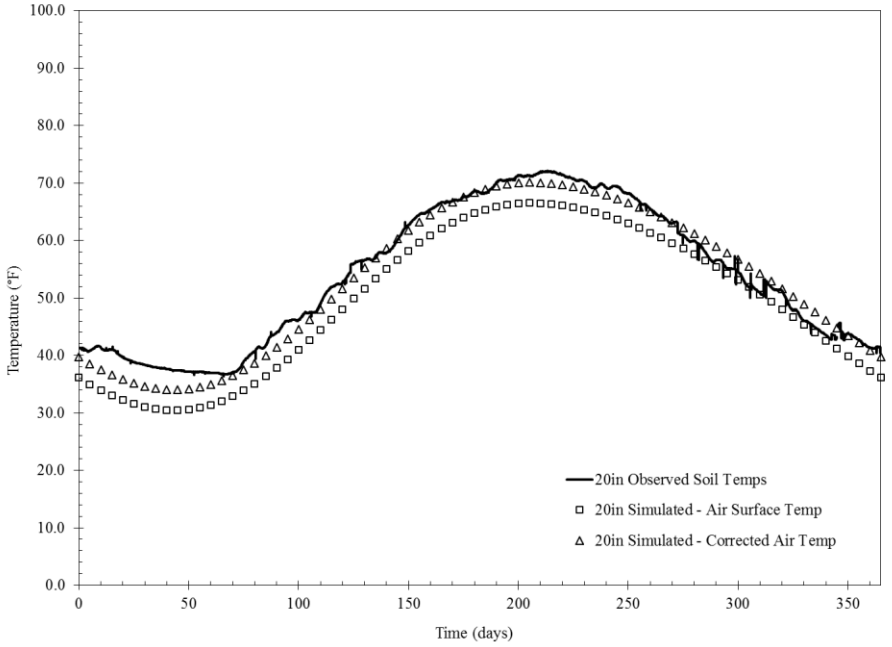


Figure 308: State College, Pennsylvania – 20 inch observed vs. simulated Green's Function soil temperatures – typical meteorological year (TMY) and corrected TMY surface air temperature boundary conditions

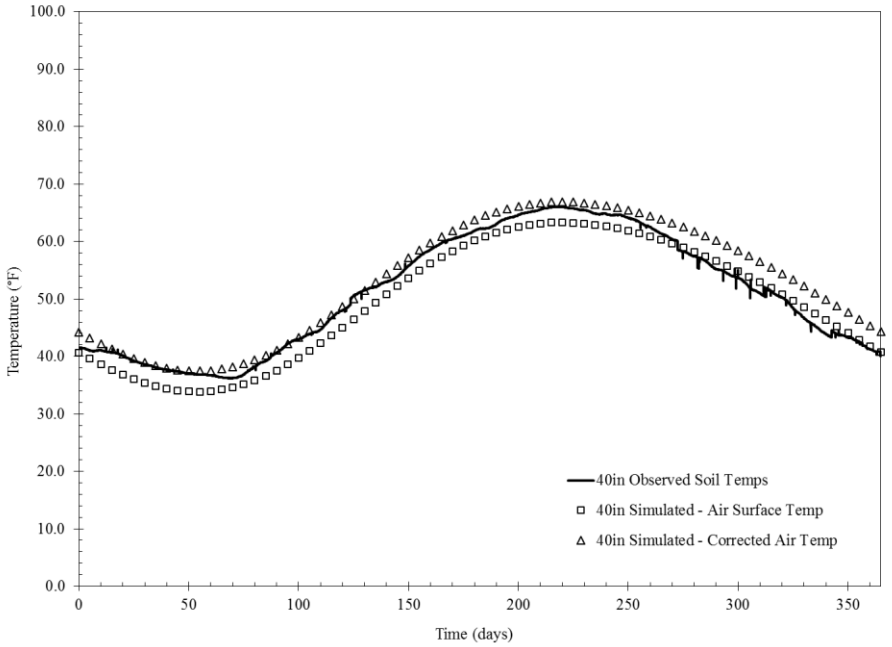


Figure 309: State College, Pennsylvania – 40 inch observed vs. simulated Green's Function soil temperatures – typical meteorological year (TMY) and corrected TMY surface air temperature boundary conditions

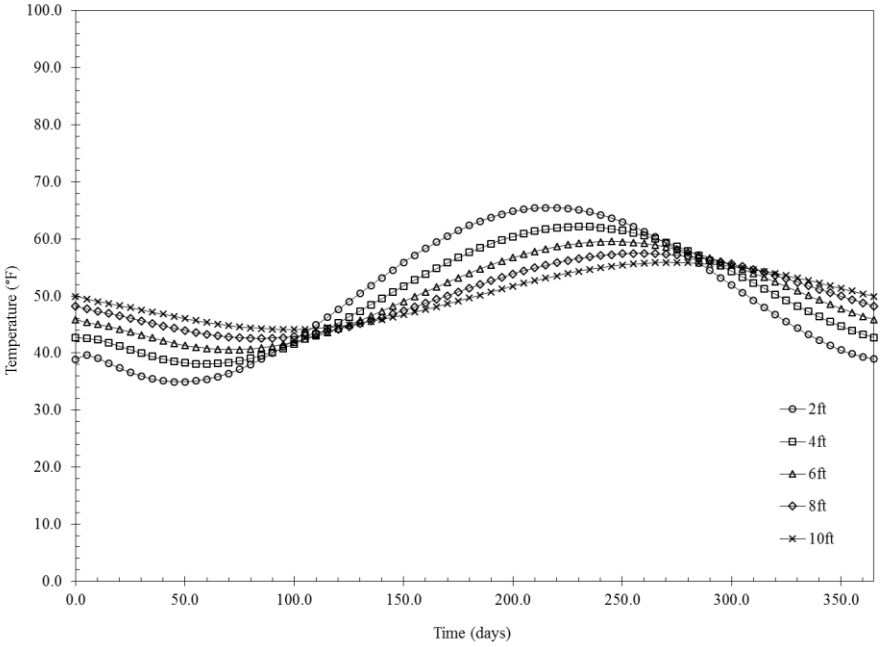


Figure 310: State College, Pennsylvania – simulated Green's Function soil temperatures at various depths– observed surface soil temperature boundary condition

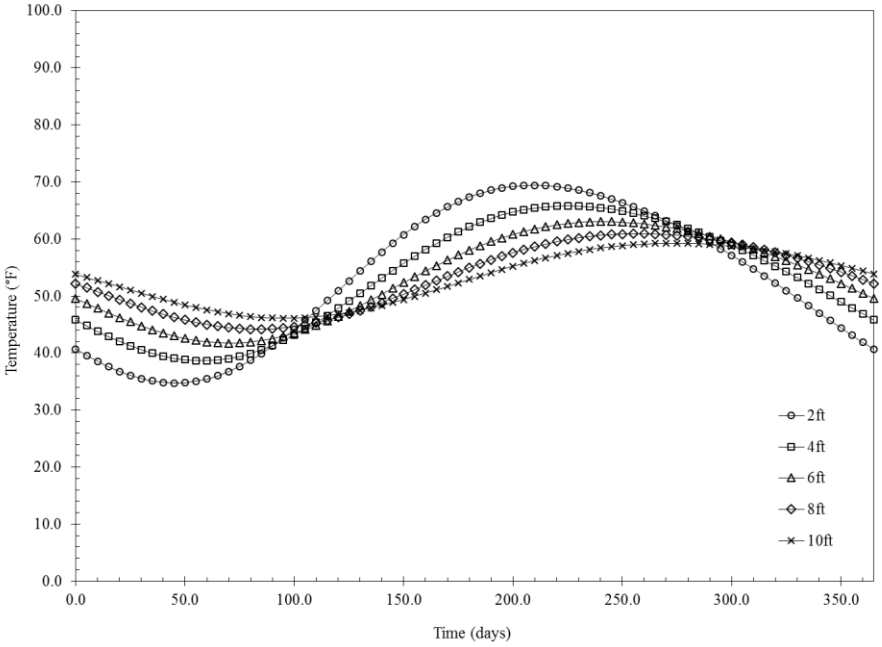


Figure 311: State College, Pennsylvania – simulated Green's Function soil temperatures at various depths – corrected TMY surface air temperature boundary condition

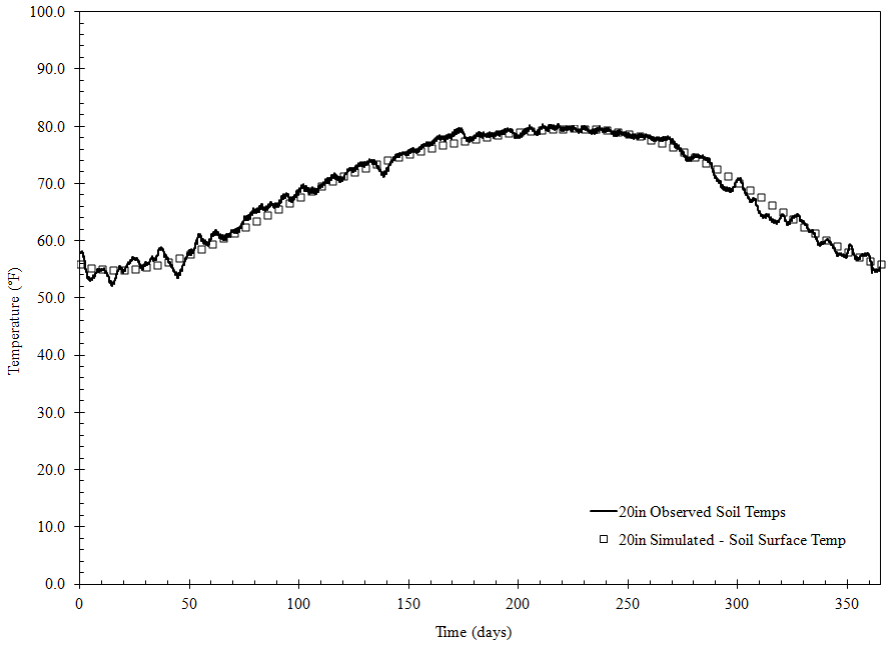


Figure 312: Tallahassee, Florida – 20 inch observed vs. simulated Green's Function soil temperatures – observed surface soil temperature boundary condition

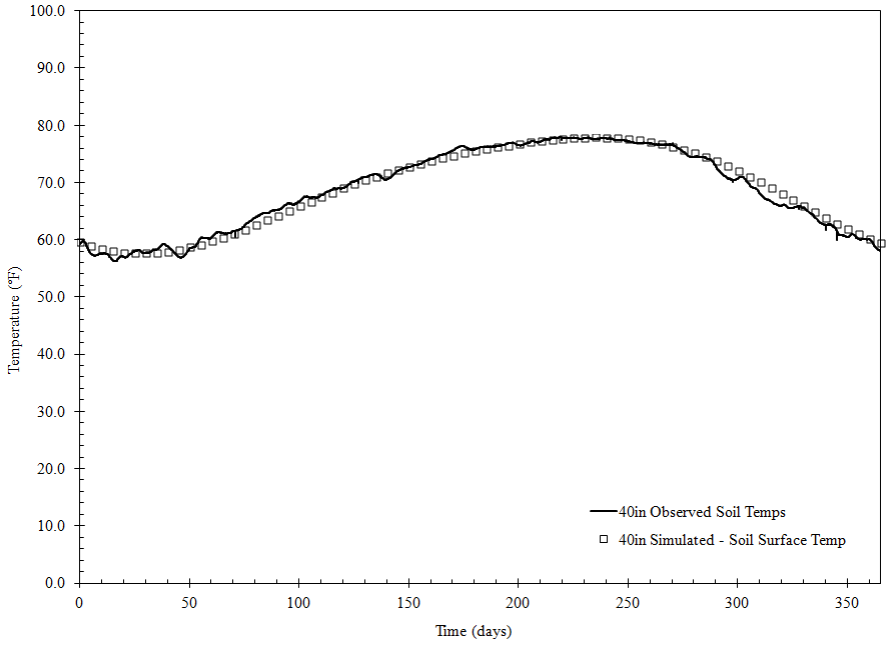


Figure 313: Tallahassee, Florida – 40 inch observed vs. simulated Green's Function soil temperatures – observed surface soil temperature boundary condition

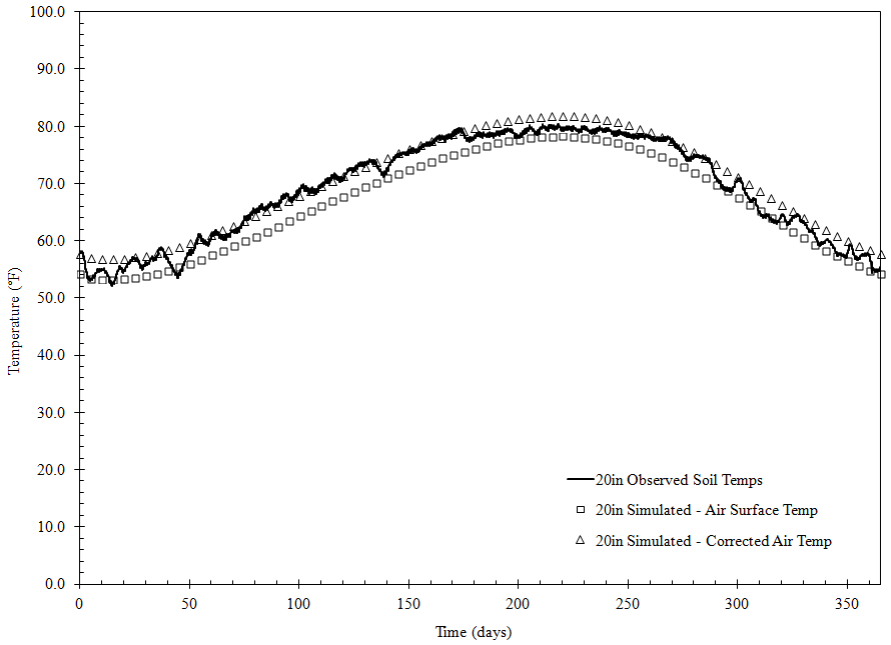


Figure 314: Tallahassee, Florida – 20 inch observed vs. simulated Green's Function soil temperatures – typical meteorological year (TMY) and corrected TMY surface air temperature boundary conditions

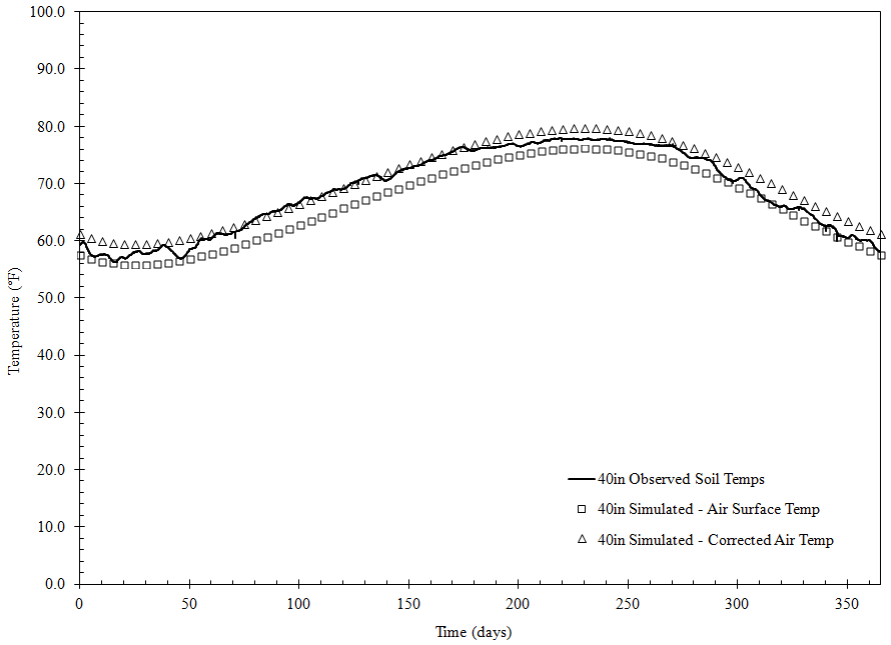


Figure 315: Tallahassee, Florida – 40 inch observed vs. simulated Green's Function soil temperatures – typical meteorological year (TMY) and corrected TMY surface air temperature boundary conditions

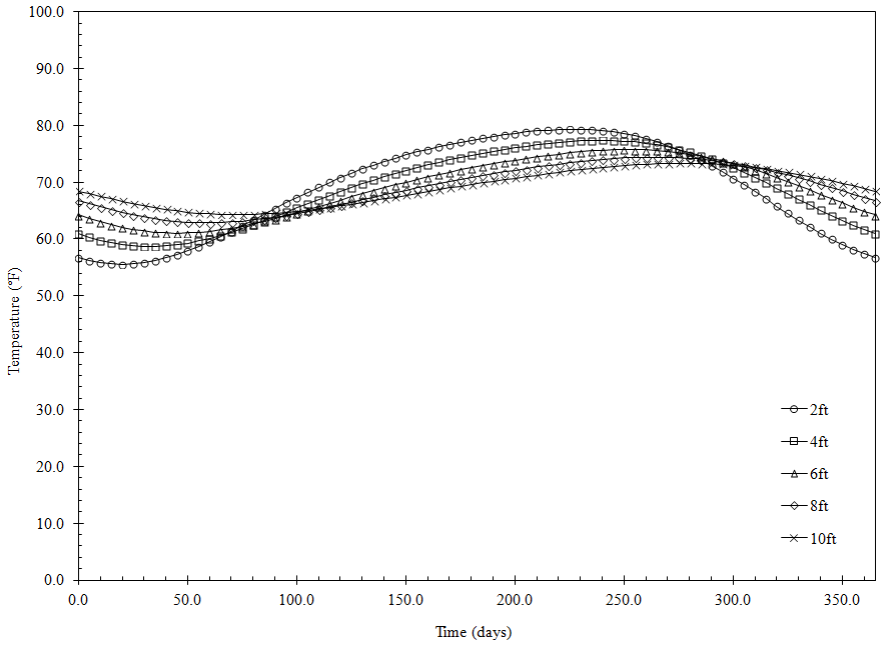


Figure 316: Tallahassee, Florida – simulated Green's Function soil temperatures at various depths– observed surface soil temperature boundary condition

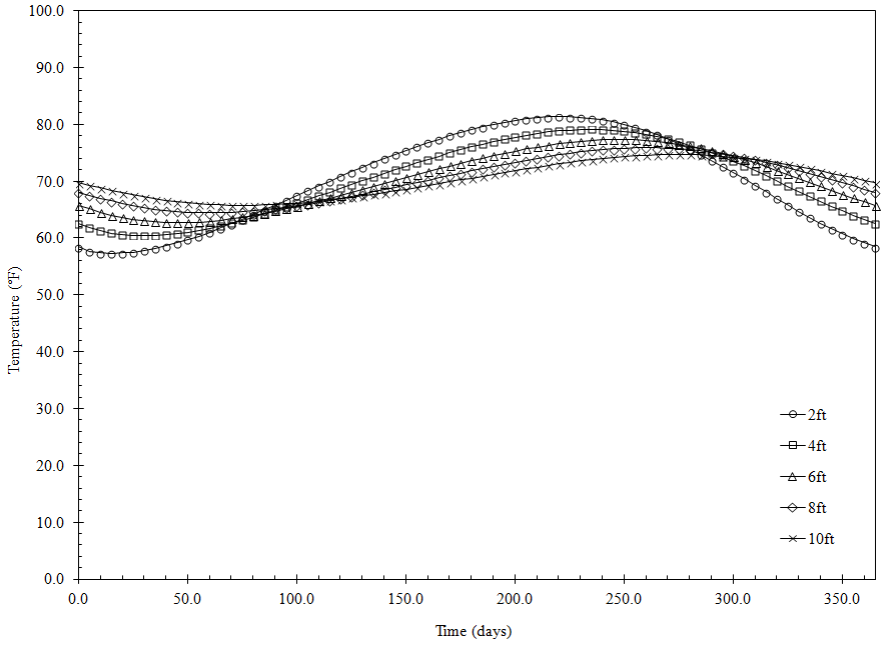


Figure 317: Tallahassee, Florida – simulated Green's Function soil temperatures at various depths – corrected TMY surface air temperature boundary condition

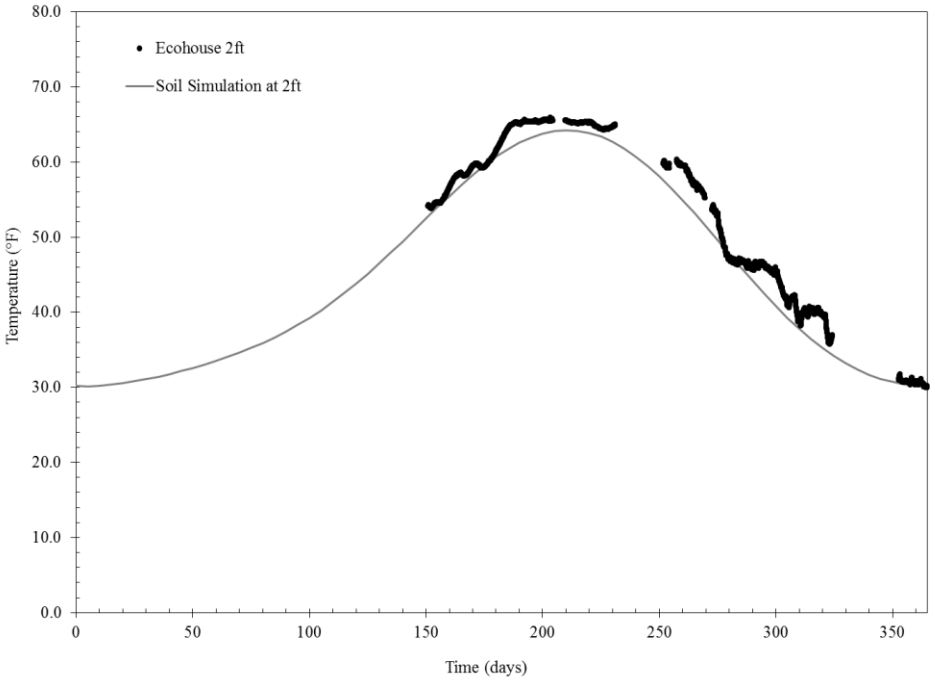


Figure 318: Observed vs. simulated soil temperatures at 2ft depth for the REHAU® Montana Ecosmart House project using the Ecohouse surface temperature BC

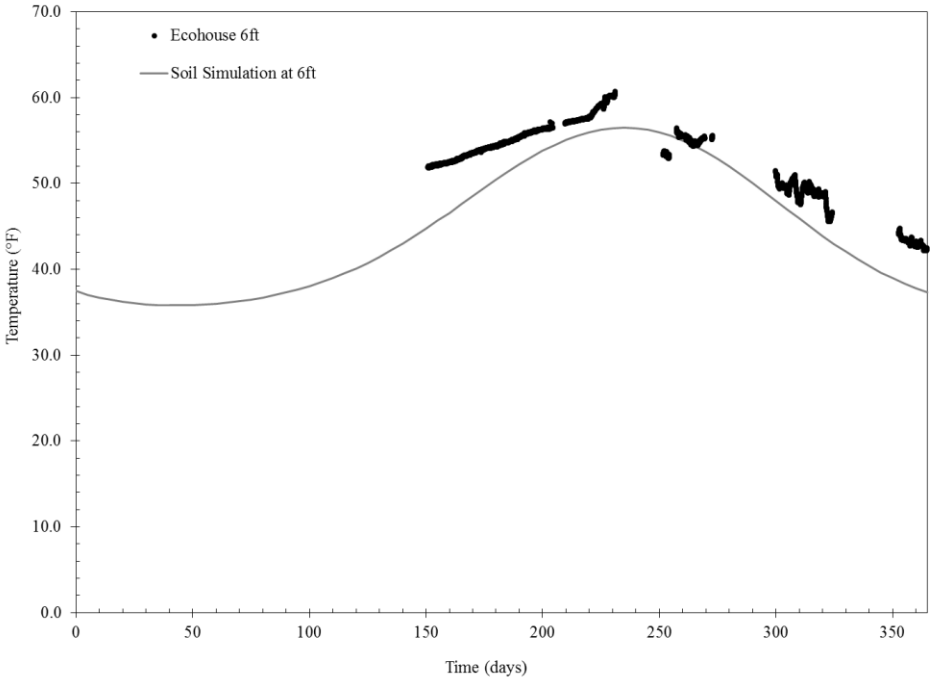


Figure 319: Observed vs. simulated soil temperatures at 6ft depth for the REHAU® Montana Ecosmart House project using the Ecohouse surface temperature BC

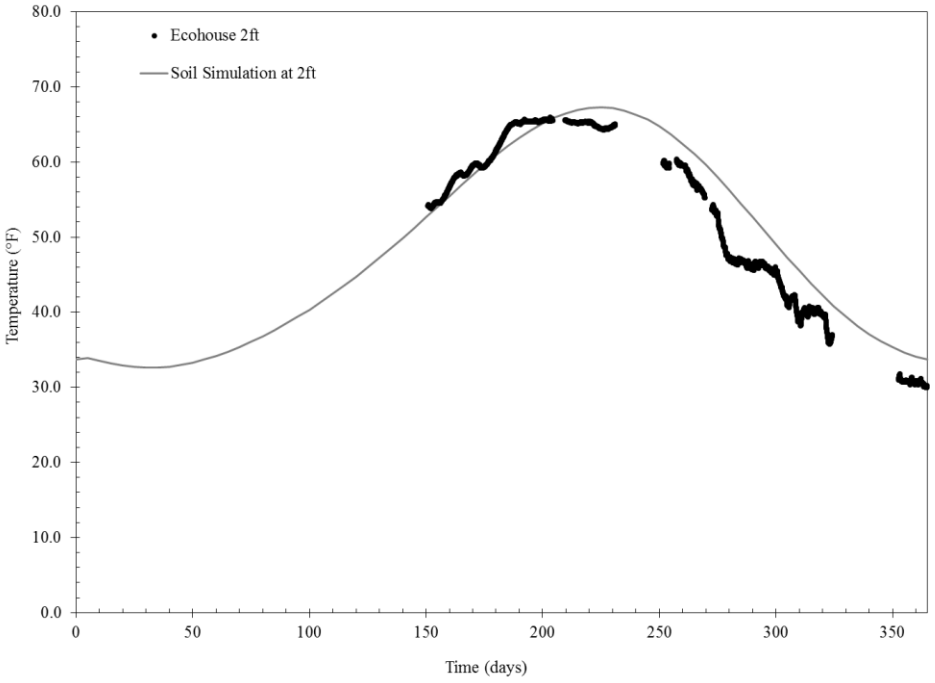


Figure 320: Observed vs. simulated soil temperatures at 2ft depth for the REHAU® Montana Ecosmart House project using the NRCS Table Mtn surface temperature BC

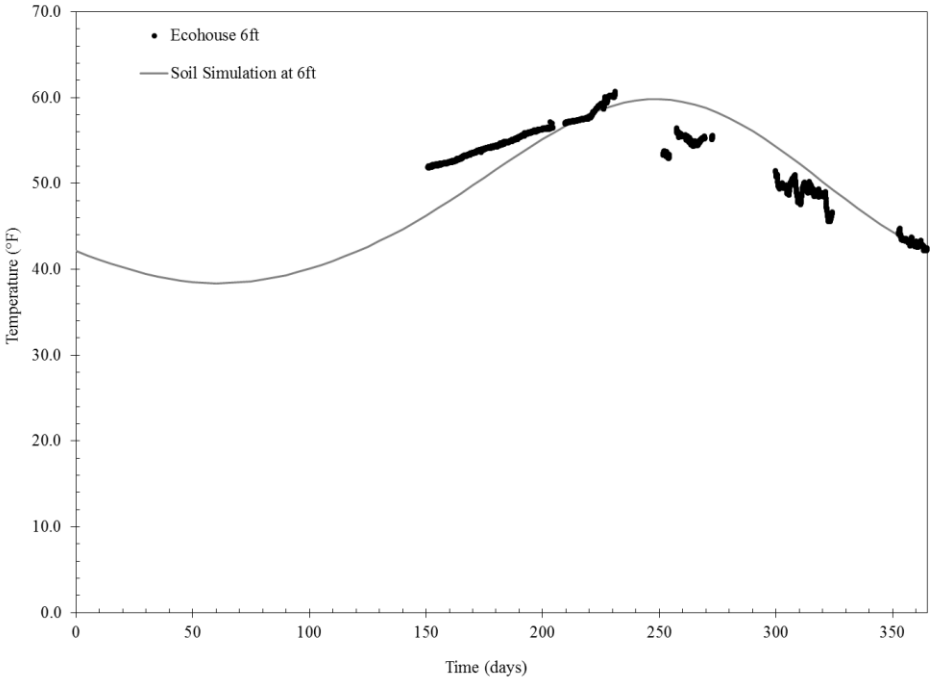


Figure 321: Observed vs. simulated soil temperatures at 6ft depth for the REHAU® Montana Ecosmart House project using the NRCS Table Mtn surface temperature BC

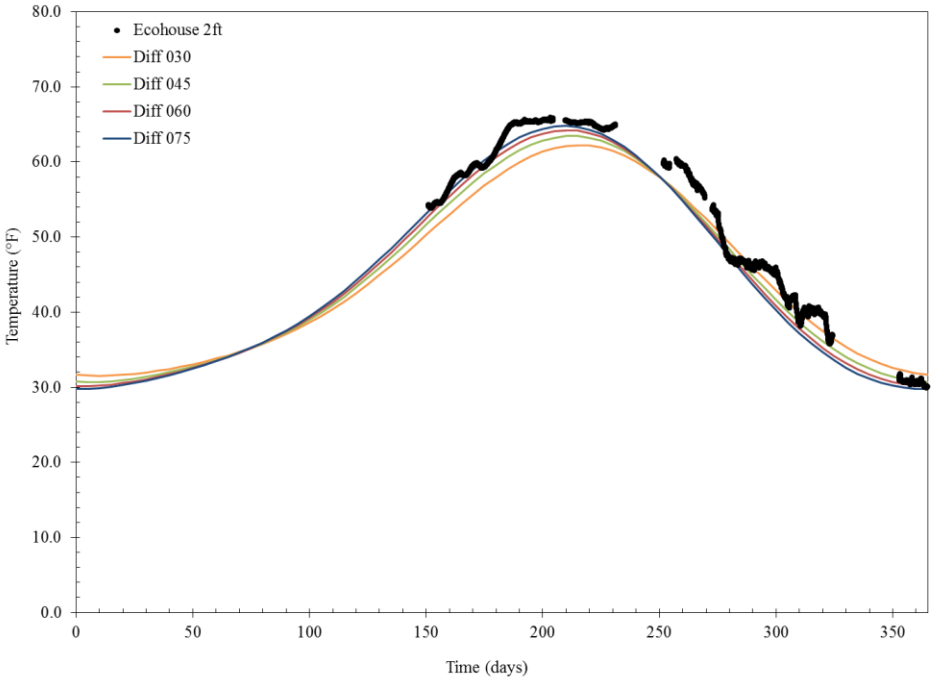


Figure 322: Diffusivity calibration for the REHAU® Montana Ecosmart House soil simulations at 2ft depth

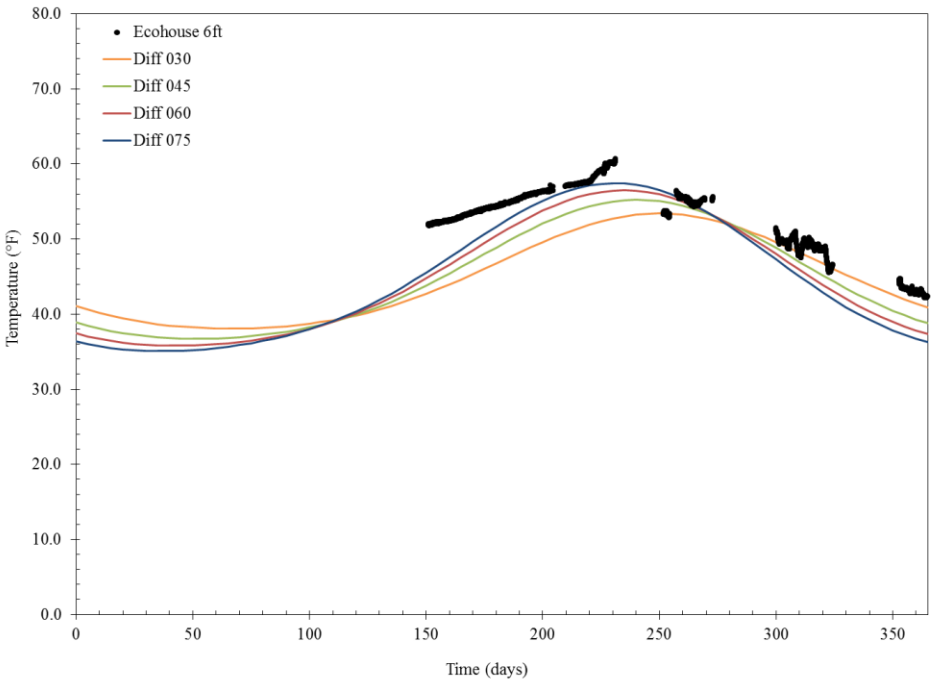


Figure 323: Diffusivity calibration for the REHAU® Montana Ecosmart House soil simulations at 6ft depth

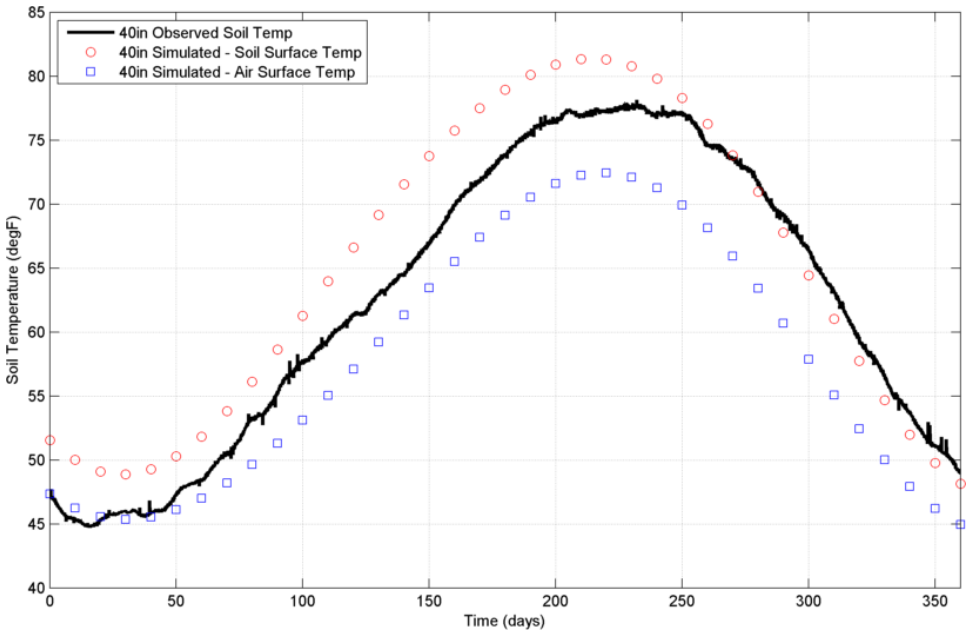


Figure 324: Albuquerque, New Mexico – 40 inch observed vs. simulated soil temperatures using the surface flux boundary condition derived from both soil surface and air surface temperatures

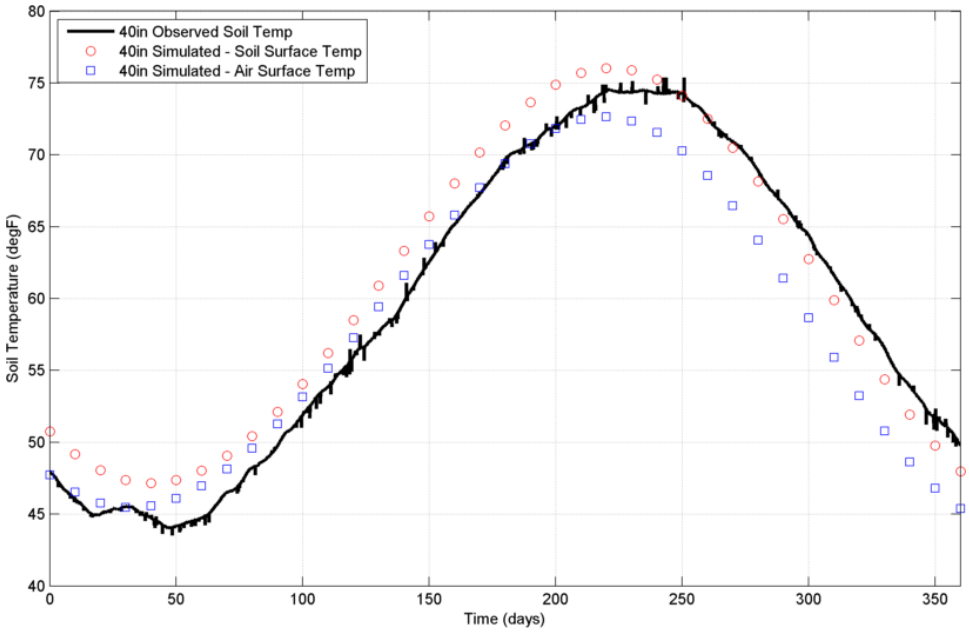


Figure 325: Amarillo, Texas – 40 inch observed vs. simulated soil temperatures using the surface flux boundary condition derived from both soil surface and air surface temperatures

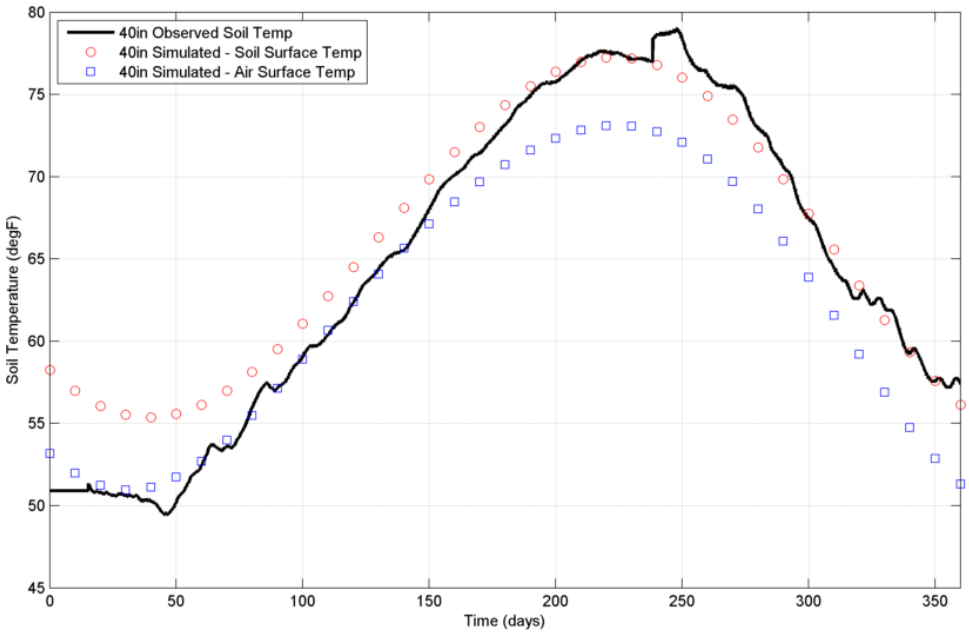


Figure 326: Athens, Georgia – 40 inch observed vs. simulated soil temperatures using the surface flux boundary condition derived from both soil surface and air surface temperatures

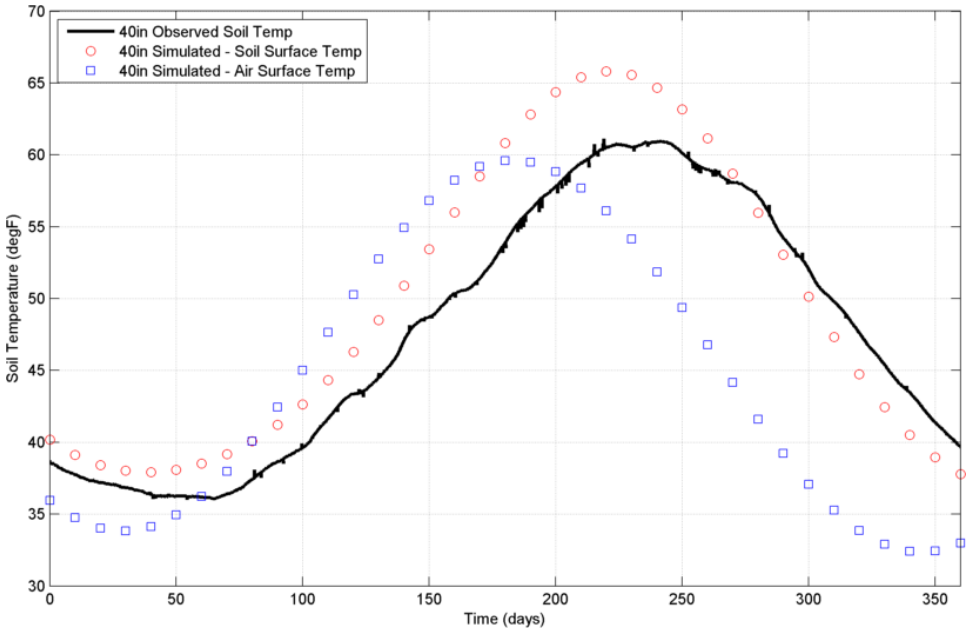


Figure 327: Bozeman, Montana – 40 inch observed vs. simulated soil temperatures using the surface flux boundary condition derived from both soil surface and air surface temperatures

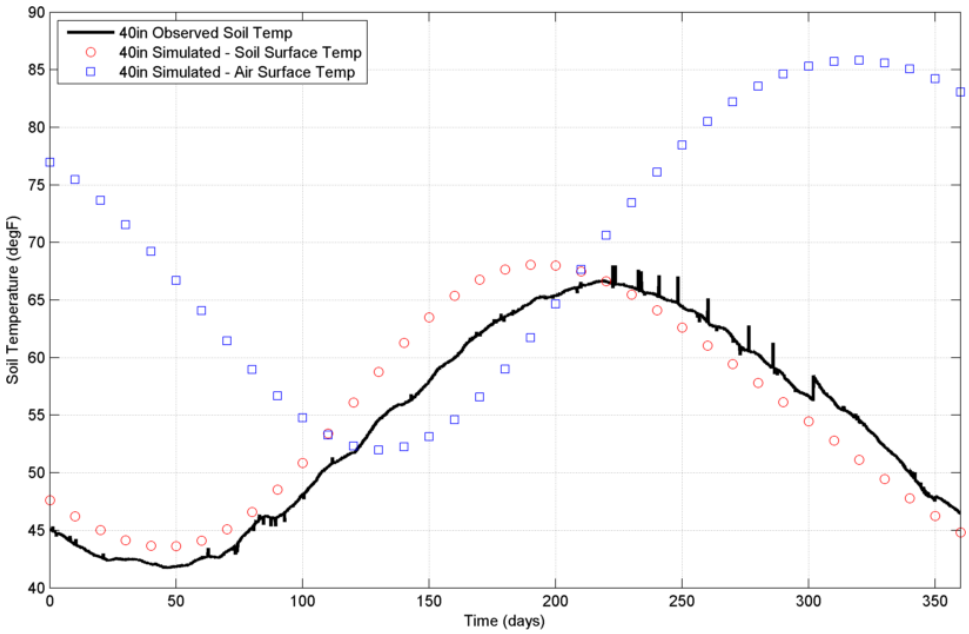


Figure 328: Columbus, Ohio – 40 inch observed vs. simulated soil temperatures using the surface flux boundary condition derived from both soil surface and air surface temperatures

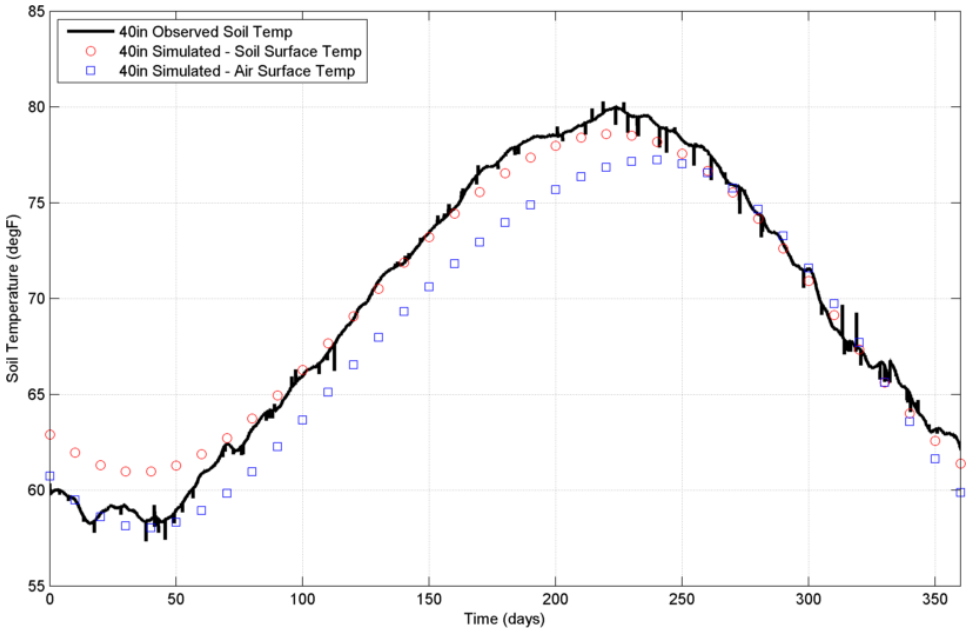


Figure 329: Houston, Texas – 40 inch observed vs. simulated soil temperatures using the surface flux boundary condition derived from both soil surface and air surface temperatures

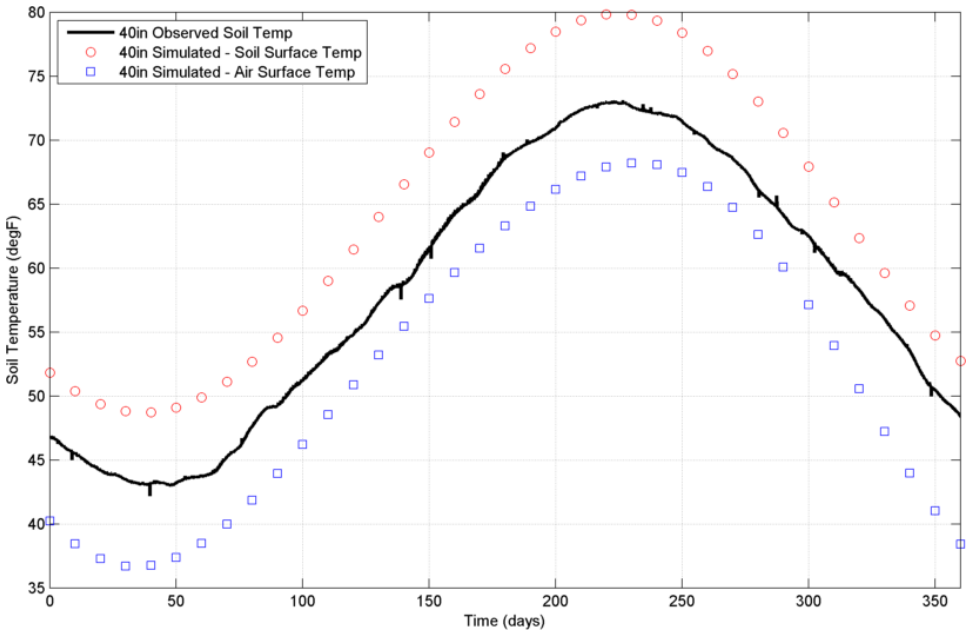


Figure 330: Kansas City, Missouri – 40 inch observed vs. simulated soil temperatures using the surface flux boundary condition derived from both soil surface and air surface temperatures

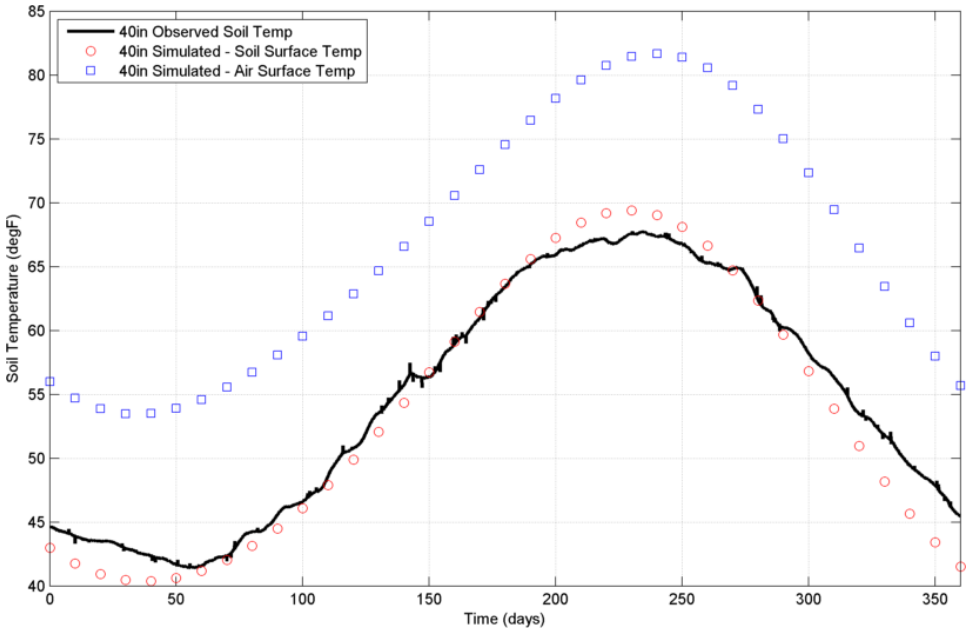


Figure 331: Las Vegas, Nevada – 40 inch observed vs. simulated soil temperatures using the surface flux boundary condition derived from both soil surface and air surface temperatures

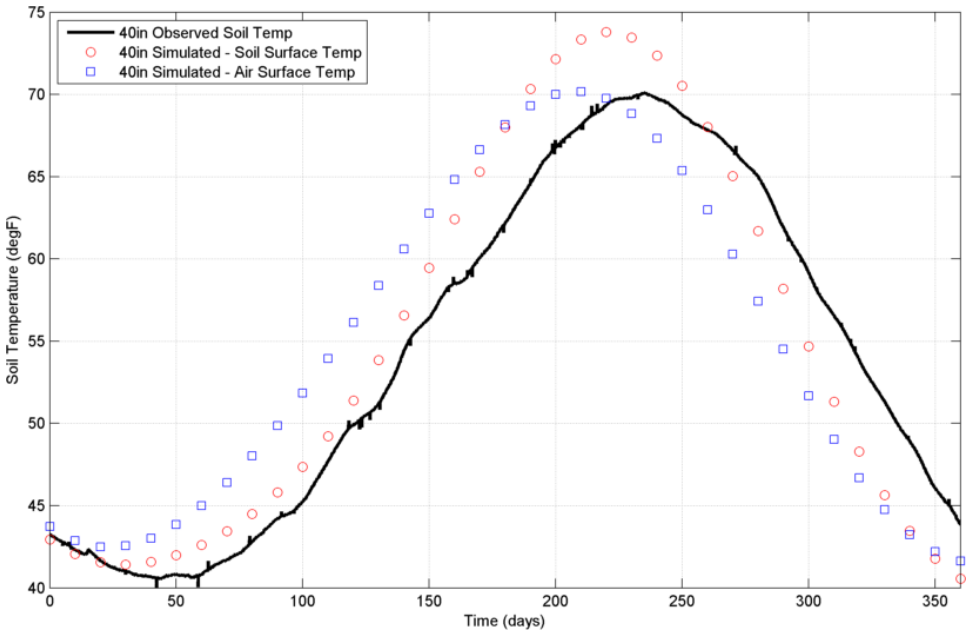


Figure 332: Moses Lake, Washington – 40 inch observed vs. simulated soil temperatures using the surface flux boundary condition derived from both soil surface and air surface temperatures

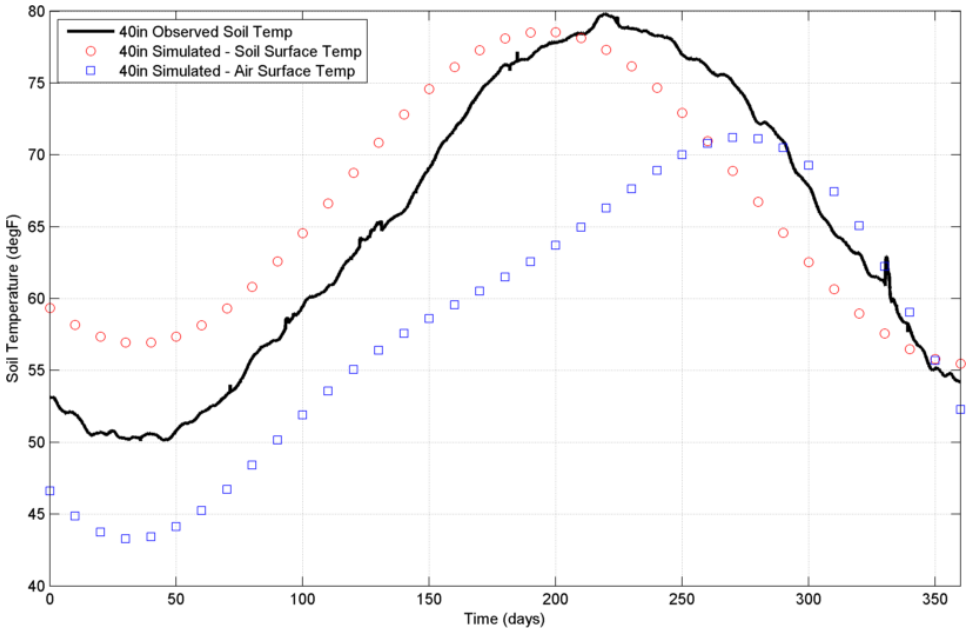


Figure 333: Pine Bluff, Arkansas – 40 inch observed vs. simulated soil temperatures using the surface flux boundary condition derived from both soil surface and air surface temperatures

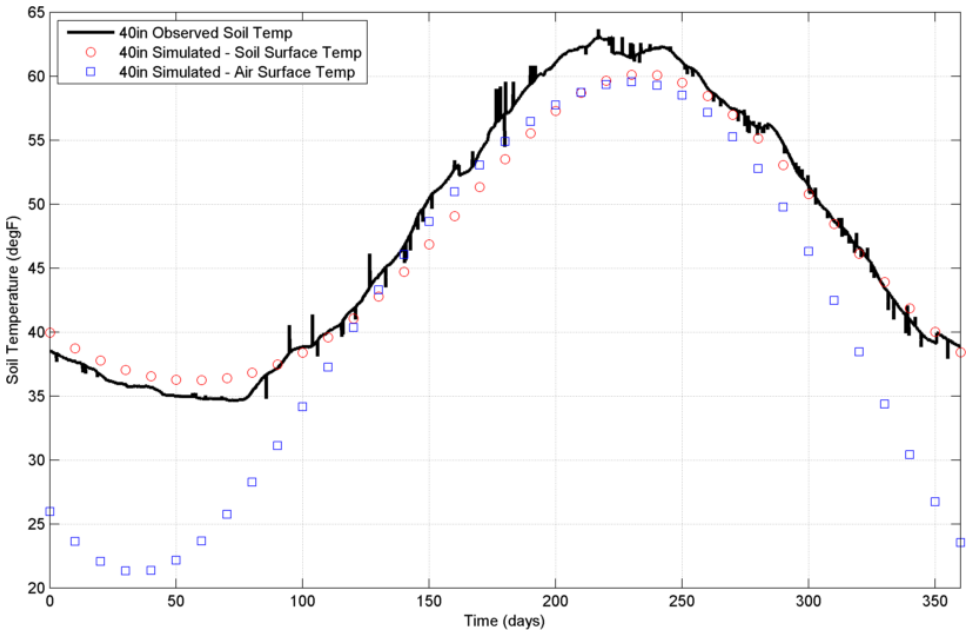


Figure 334: St. Cloud, Minnesota – 40 inch observed vs. simulated soil temperatures using the surface flux boundary condition derived from both soil surface and air surface temperatures

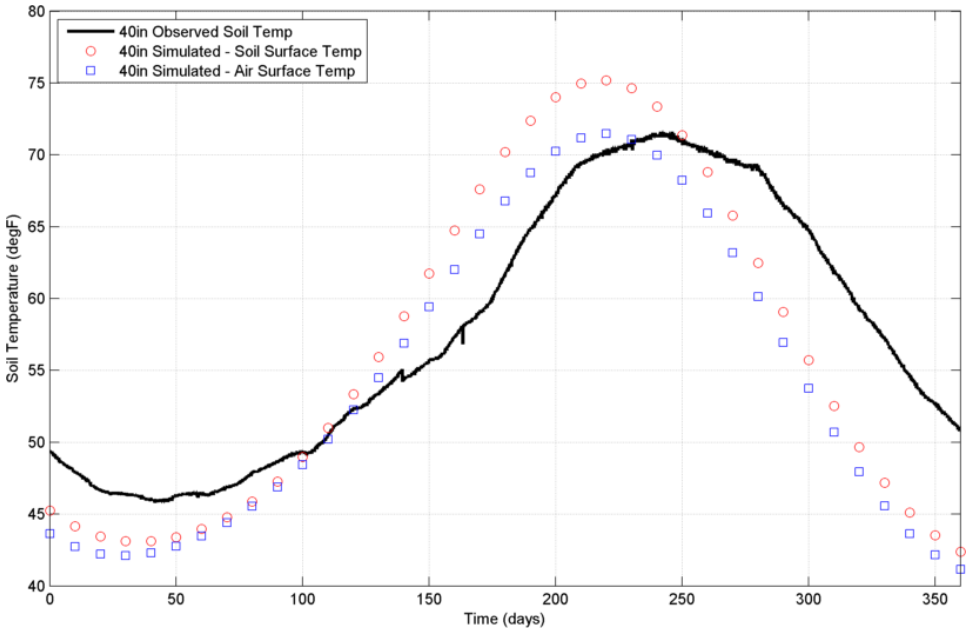


Figure 335: Salt Lake City, Utah – 40 inch observed vs. simulated soil temperatures using the surface flux boundary condition derived from both soil surface and air surface temperatures

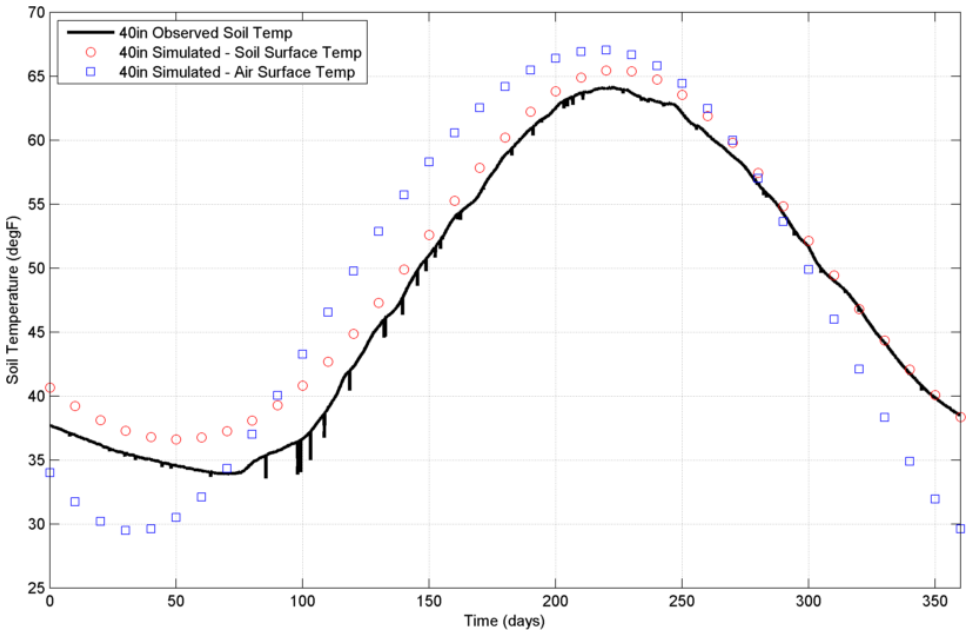


Figure 336: Sioux Falls, South Dakota – 40 inch observed vs. simulated soil temperatures using the surface flux boundary condition derived from both soil surface and air surface temperatures

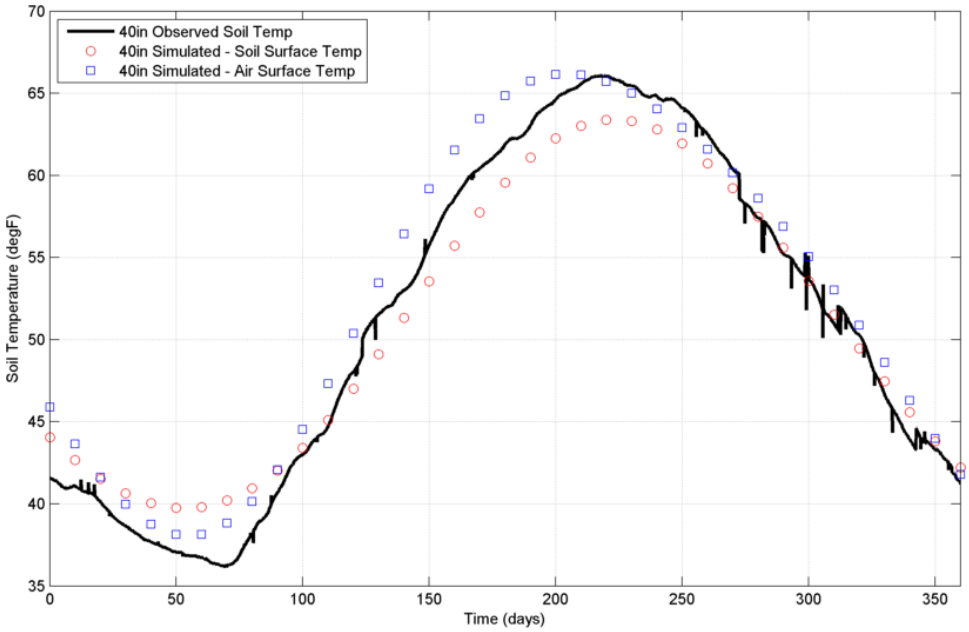


Figure 337: State College, Pennsylvania – 40 inch observed vs. simulated soil temperatures using the surface flux boundary condition derived from both soil surface and air surface temperatures

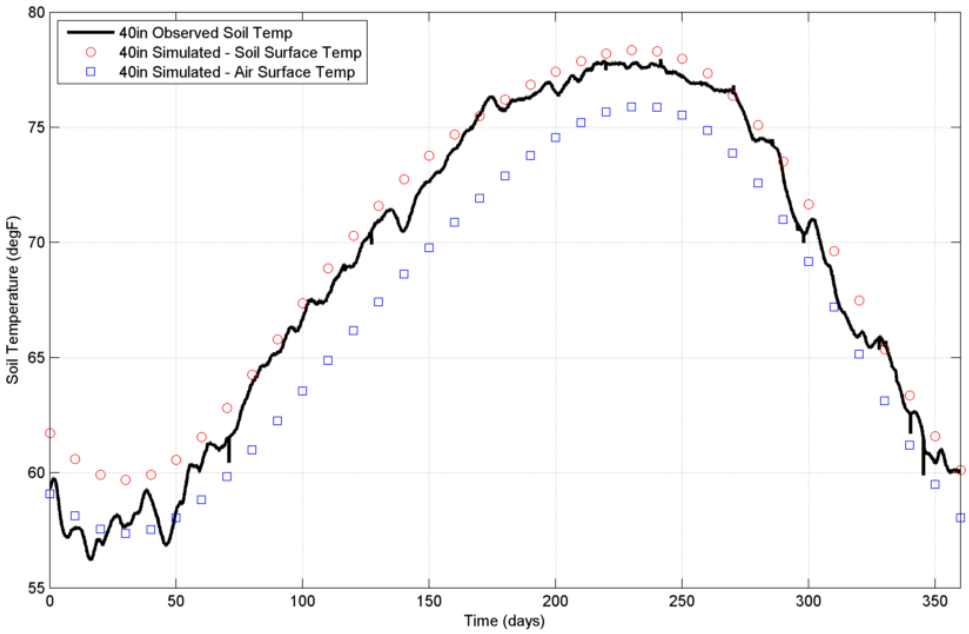


Figure 338: Tallahassee, Florida – 40 inch observed vs. simulated soil temperatures using the surface flux boundary condition derived from both soil surface and air surface temperatures

APPENDIX E

PERIODIC FOUNDATION HEAT LOSS FUNCTIONS

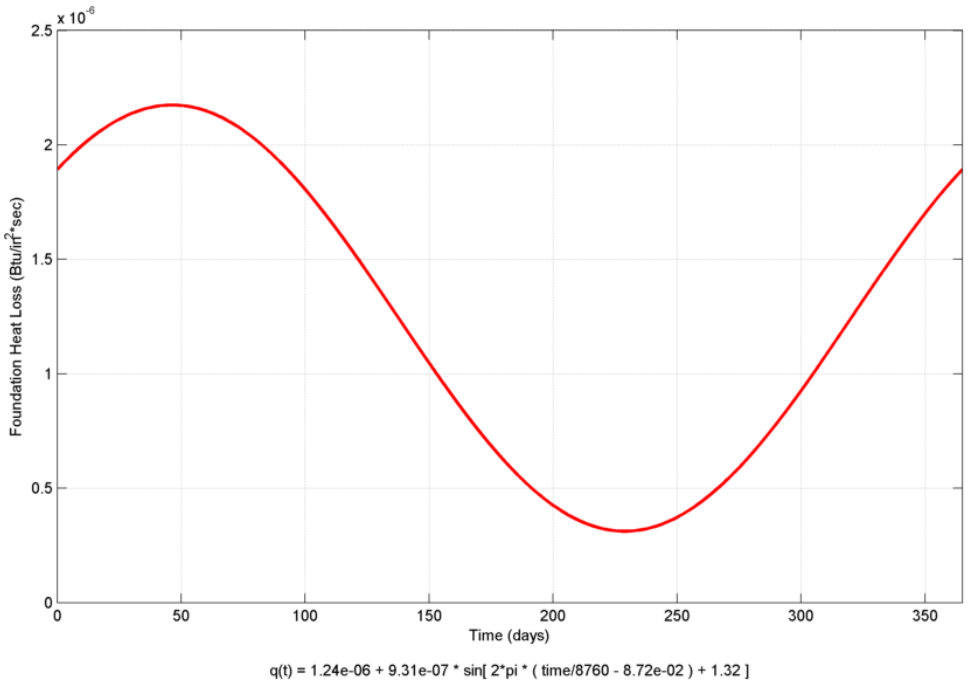


Figure 339: Albuquerque, New Mexico– example foundation heat loss function for 40 by 40 foot on grade slab

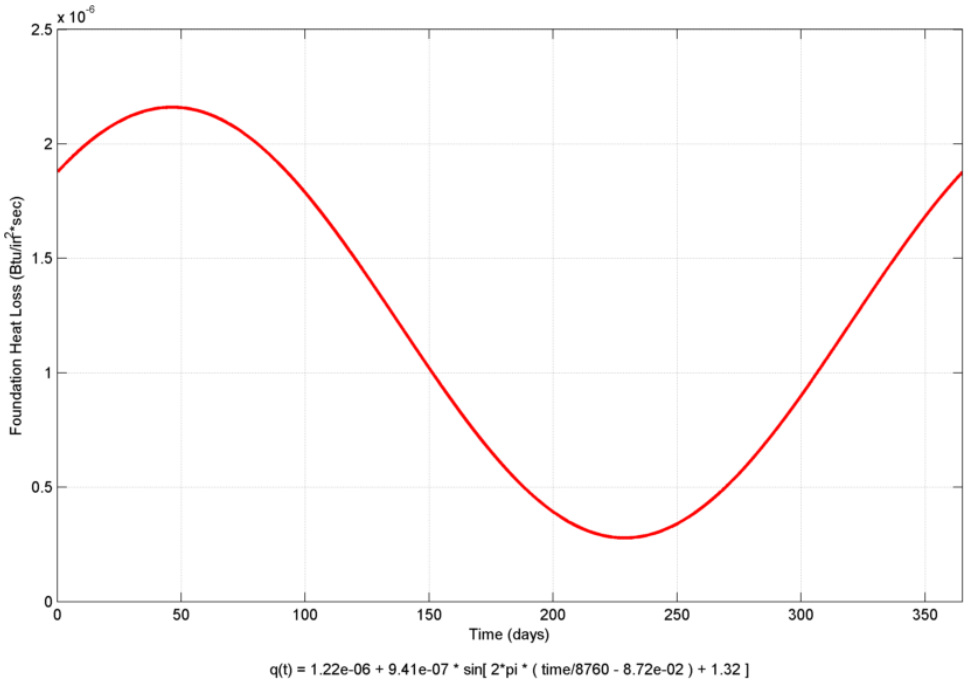


Figure 340: Amarillo, Texas– example foundation heat loss function for 40 by 40 foot on grade slab

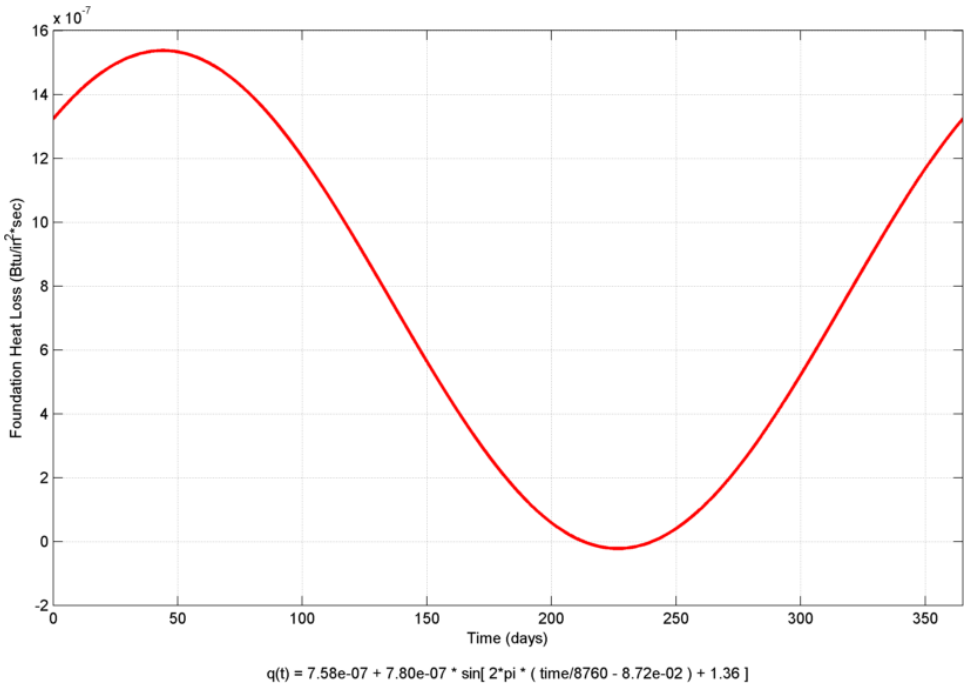


Figure 341: Athens, Georgia– example foundation heat loss function for 40 by 40 foot on grade slab

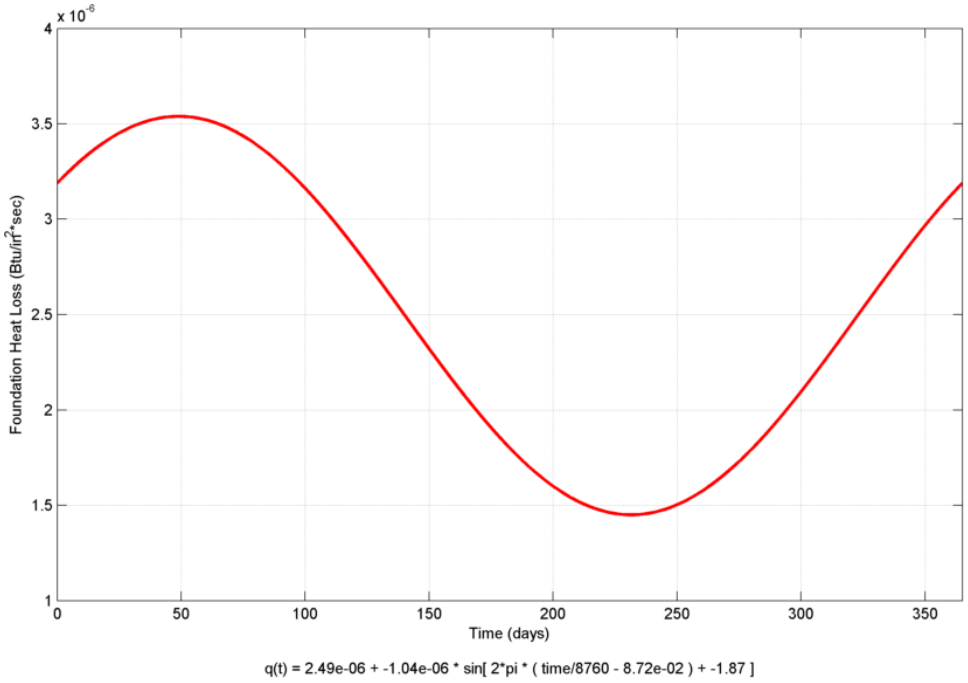


Figure 342: Bozeman, Montana – example foundation heat loss function for 40 by 40 foot on grade slab

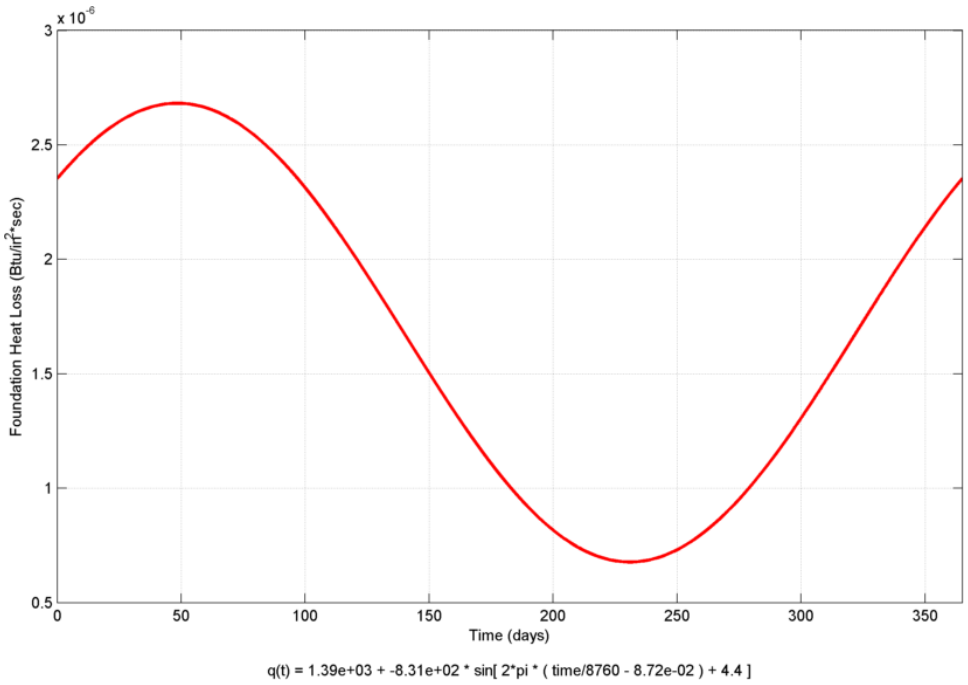


Figure 343: Columbus, Ohio – example foundation heat loss function for 40 by 40 foot on grade slab

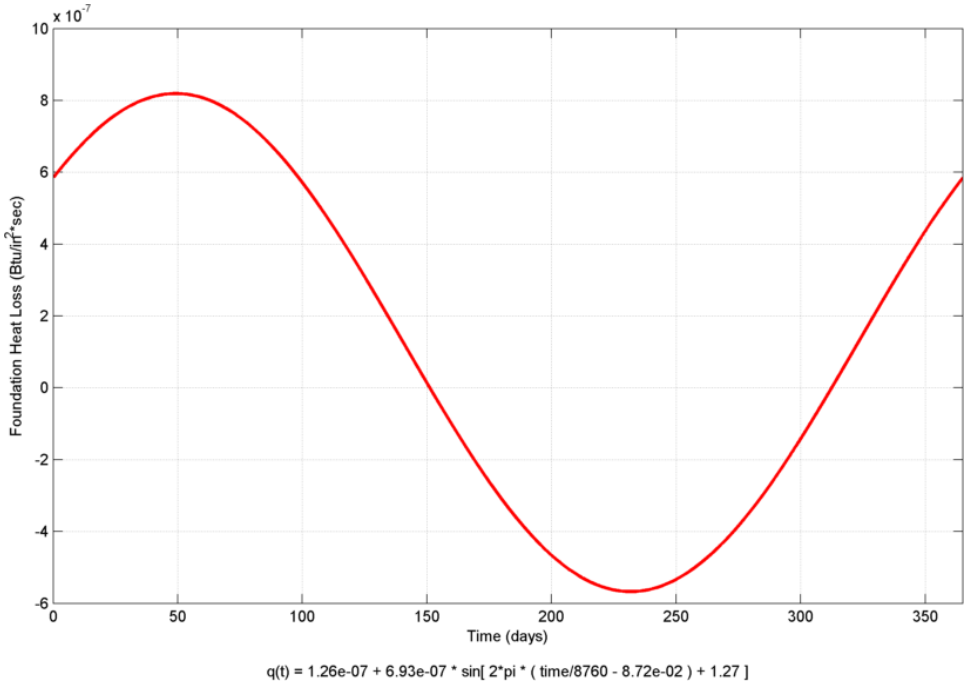


Figure 344: Houston, Texas – example foundation heat loss function for 40 by 40 foot on grade slab

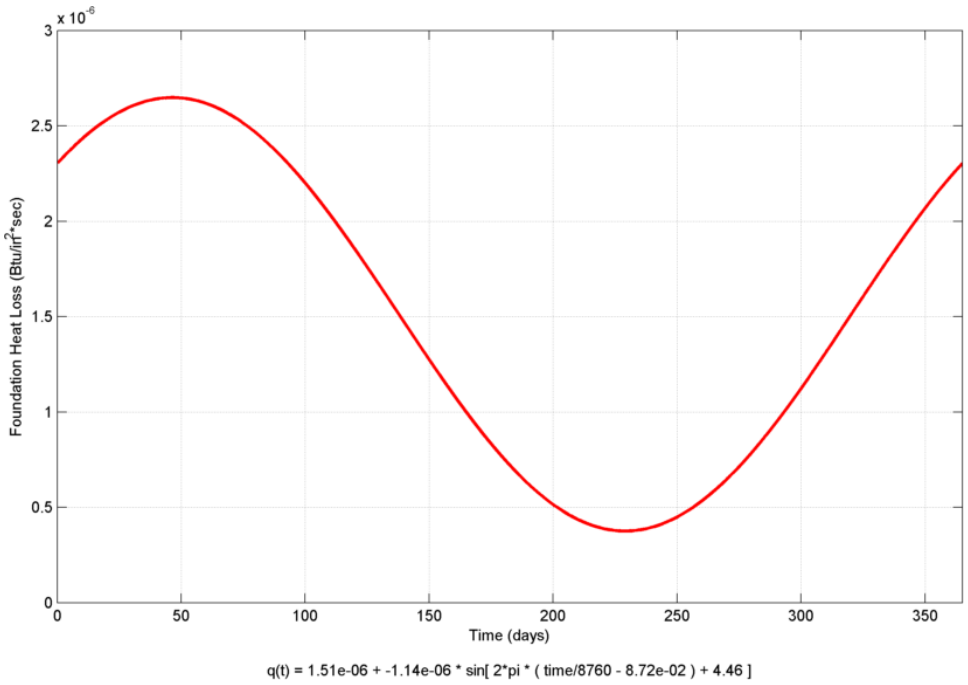


Figure 345: Kansas City, Missouri – example foundation heat loss function for 40 by 40 foot on grade slab

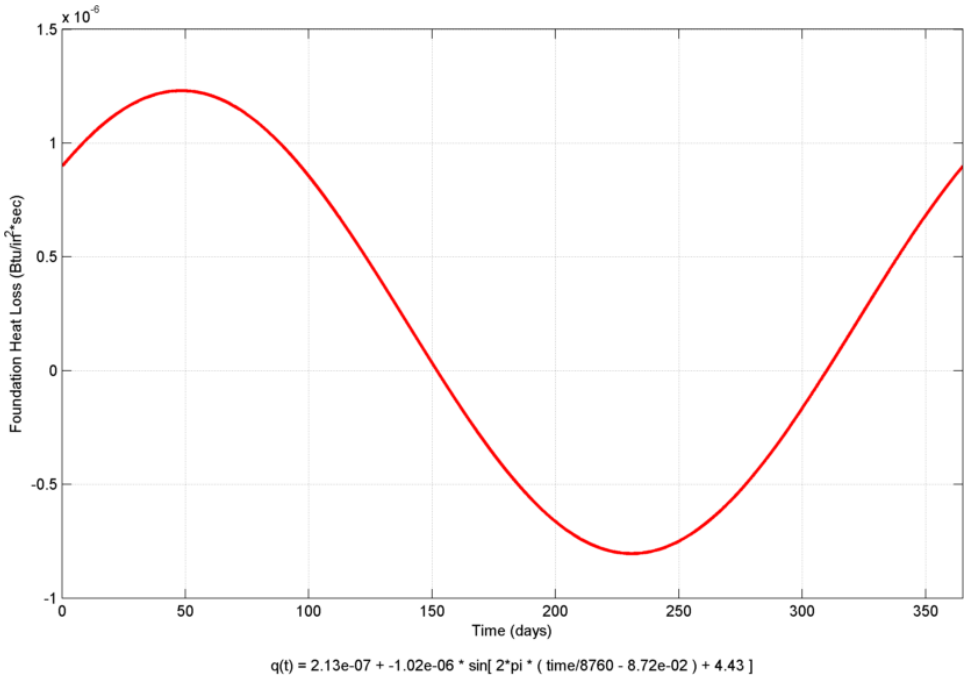


Figure 346: Las Vegas, Nevada – example foundation heat loss function for 40 by 40 foot on grade slab

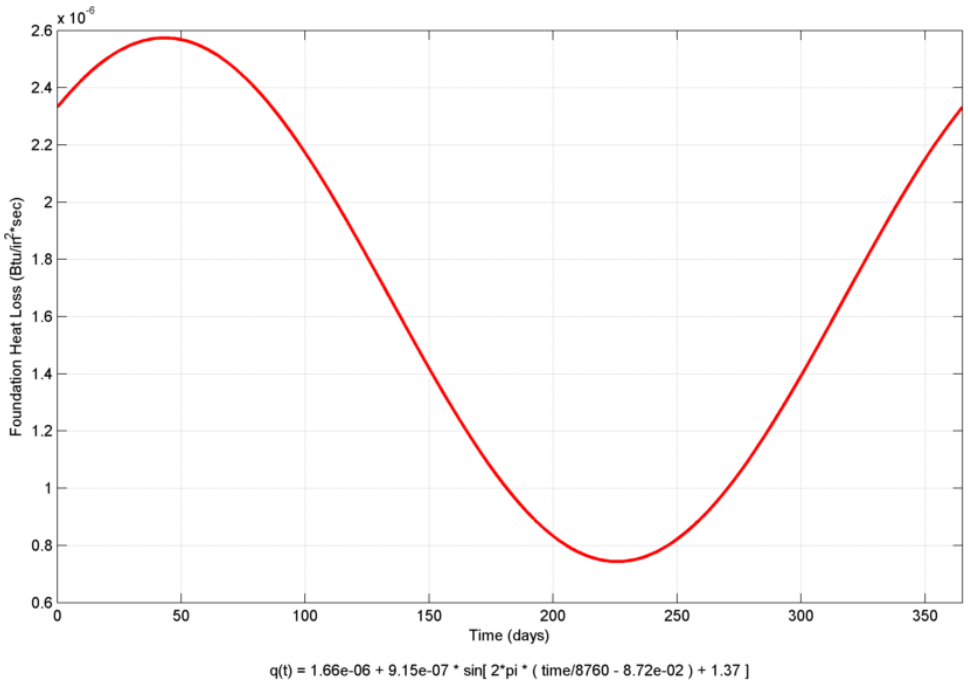


Figure 347: Moses Lake, Washington – example foundation heat loss function for 40 by 40 foot on grade slab

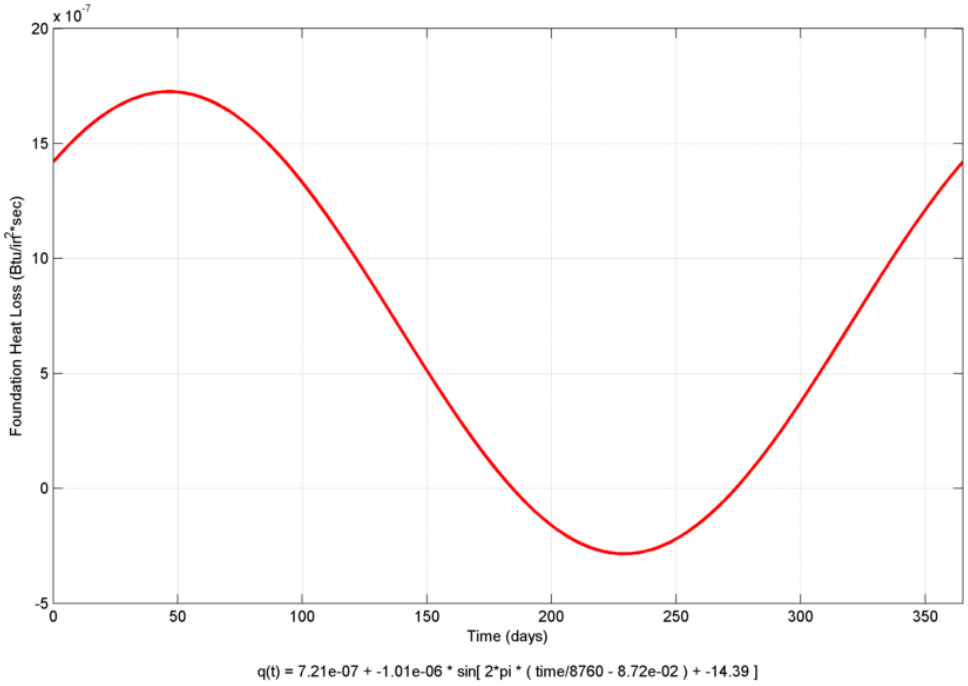


Figure 348: Pine Bluff, Arkansas – example foundation heat loss function for 40 by 40 foot on grade slab

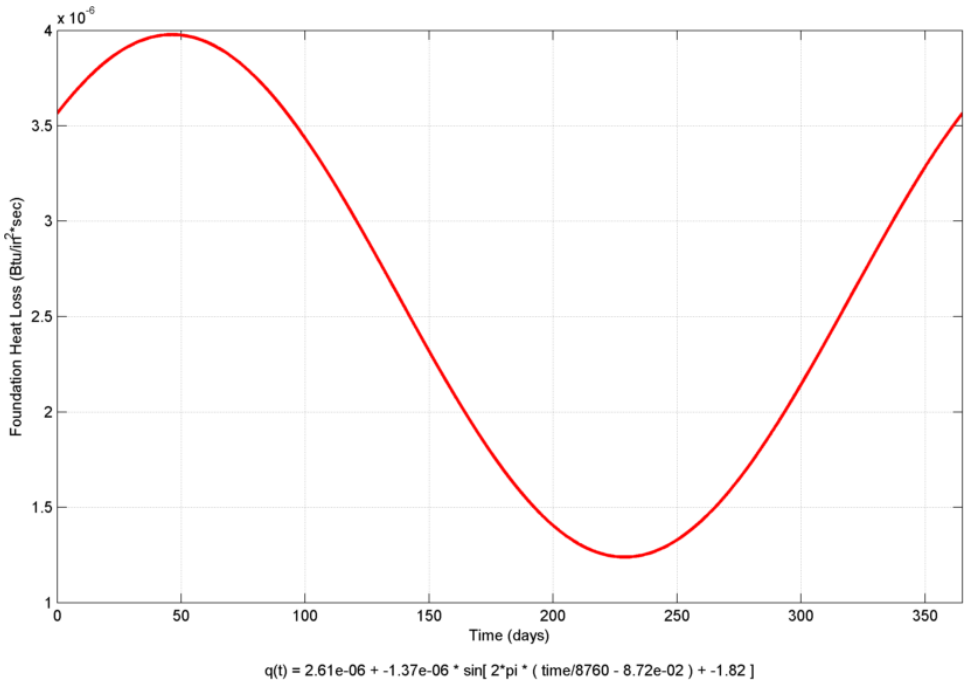


Figure 349: Saint Cloud, Minnesota – example foundation heat loss function for 40 by 40 foot on grade slab

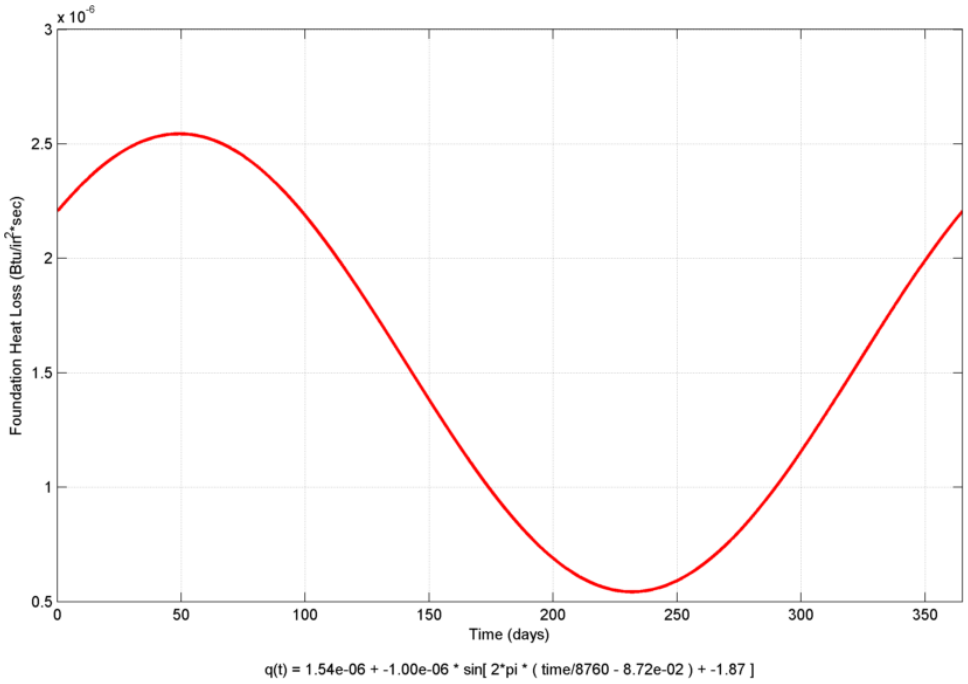


Figure 350: Salt Lake City, Utah – example foundation heat loss function for 40 by 40 foot on grade slab

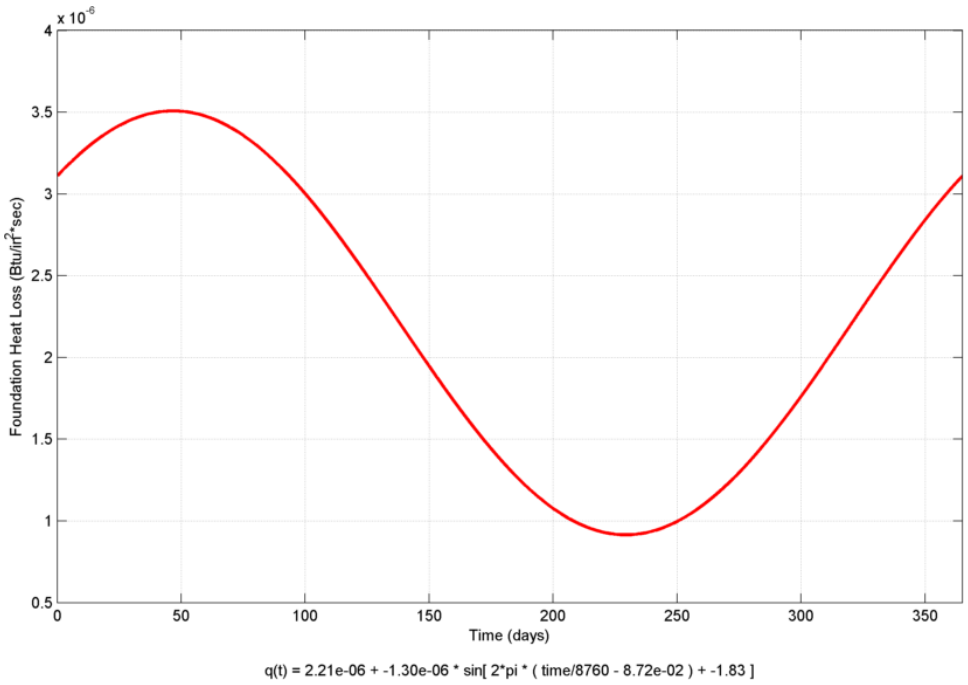


Figure 351: Sioux Falls, South Dakota – example foundation heat loss function for 40 by 40 foot on grade slab

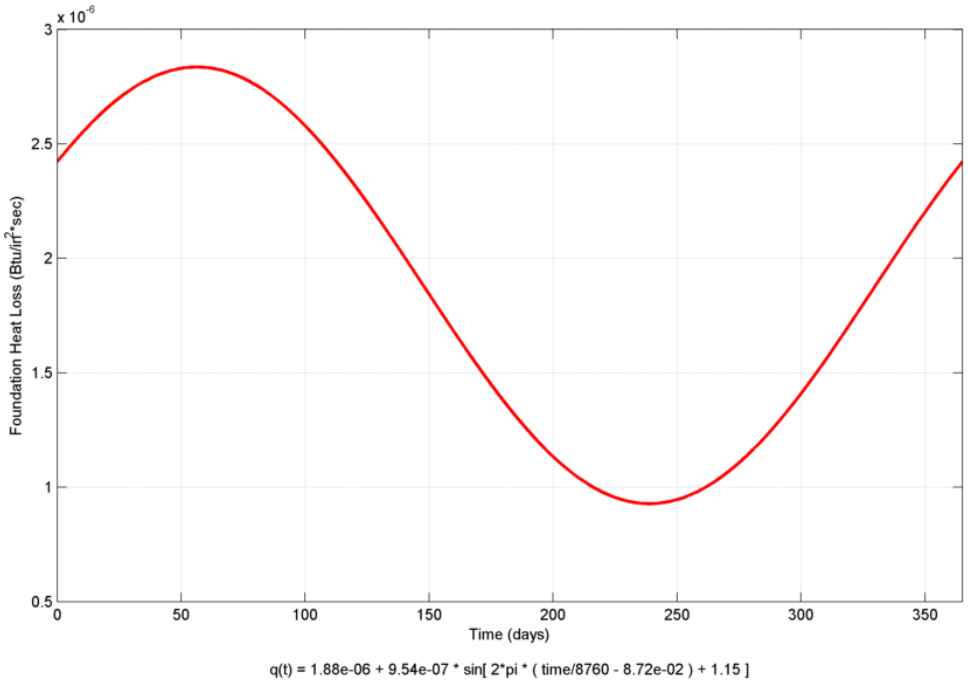


Figure 352: State College, Pennsylvania – example foundation heat loss function for 40 by 40 foot on grade slab

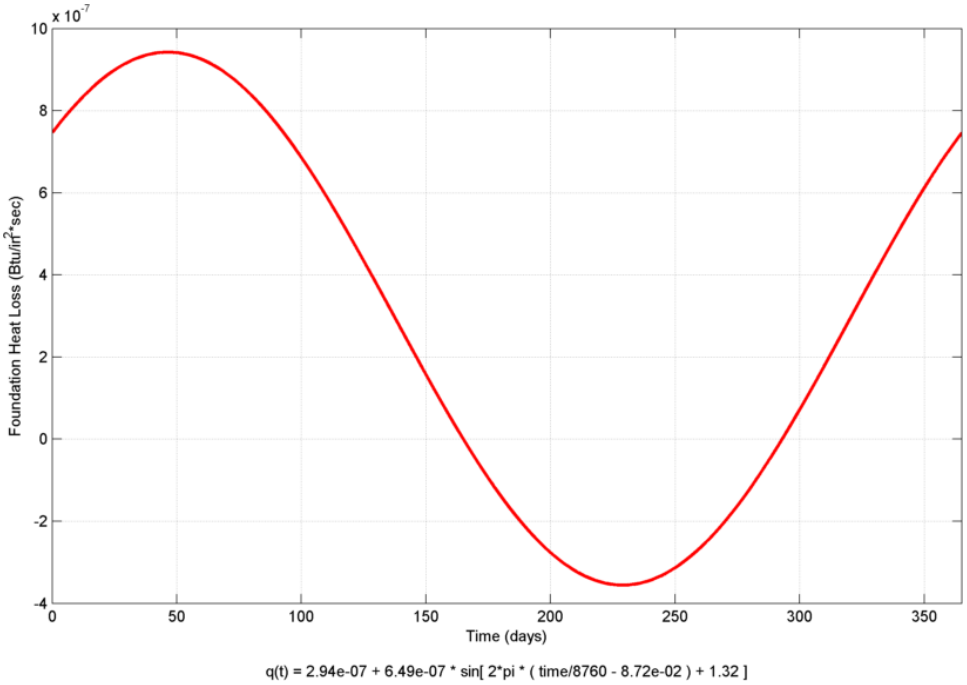


Figure 353: Tallahassee, Florida – example foundation heat loss function for 40 by 40 foot on grade slab

APPENDIX F

SOIL TEMPERATURE DISTRIBUTIONS BELOW ON GRADE SLABS

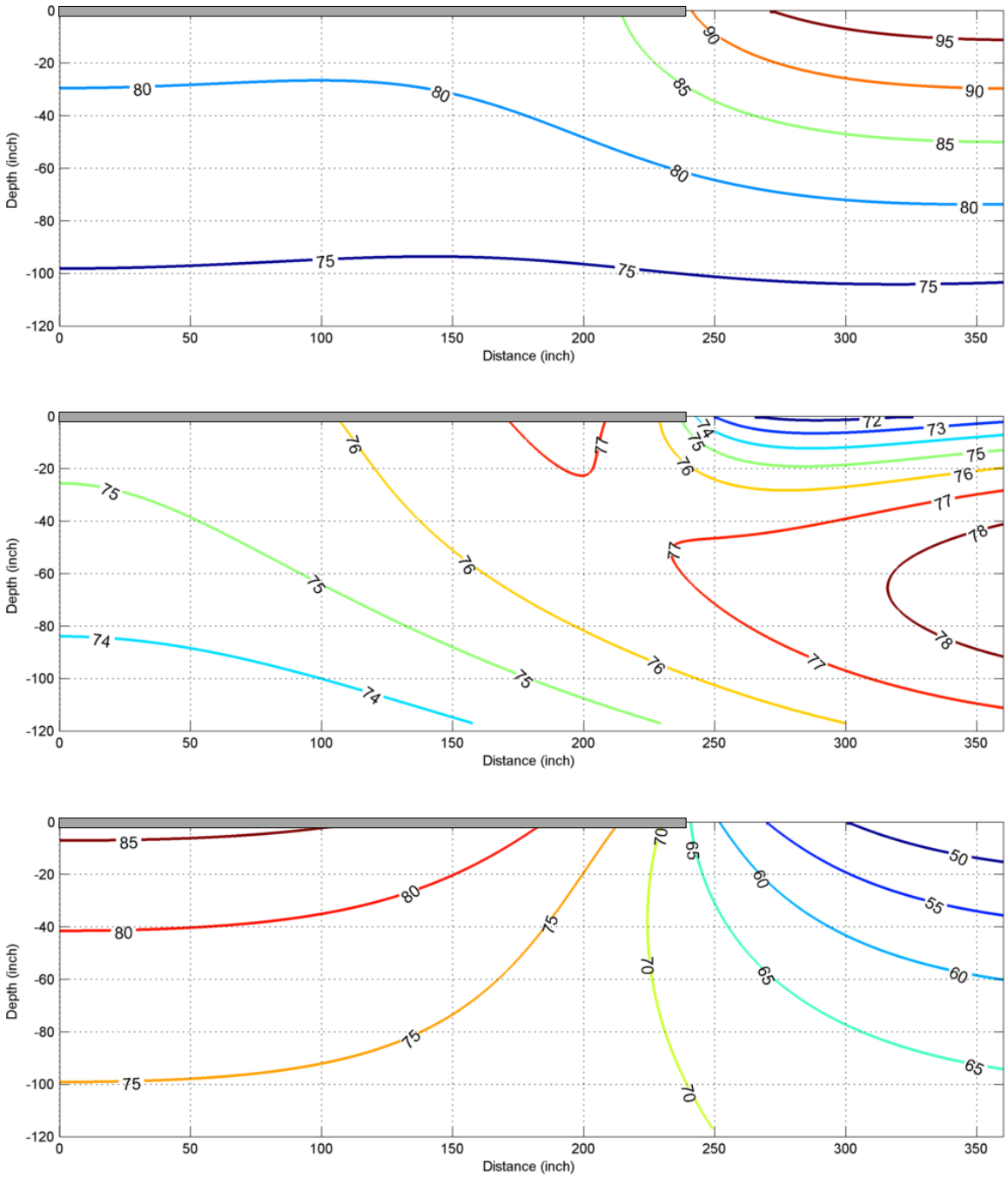


Figure 354: Albuquerque, New Mexico– soil temperature distribution for non-radiant slab at 180 days (top), 270 days (middle), and 360 days (bottom) starting from January 1st for a slab length of 40 feet

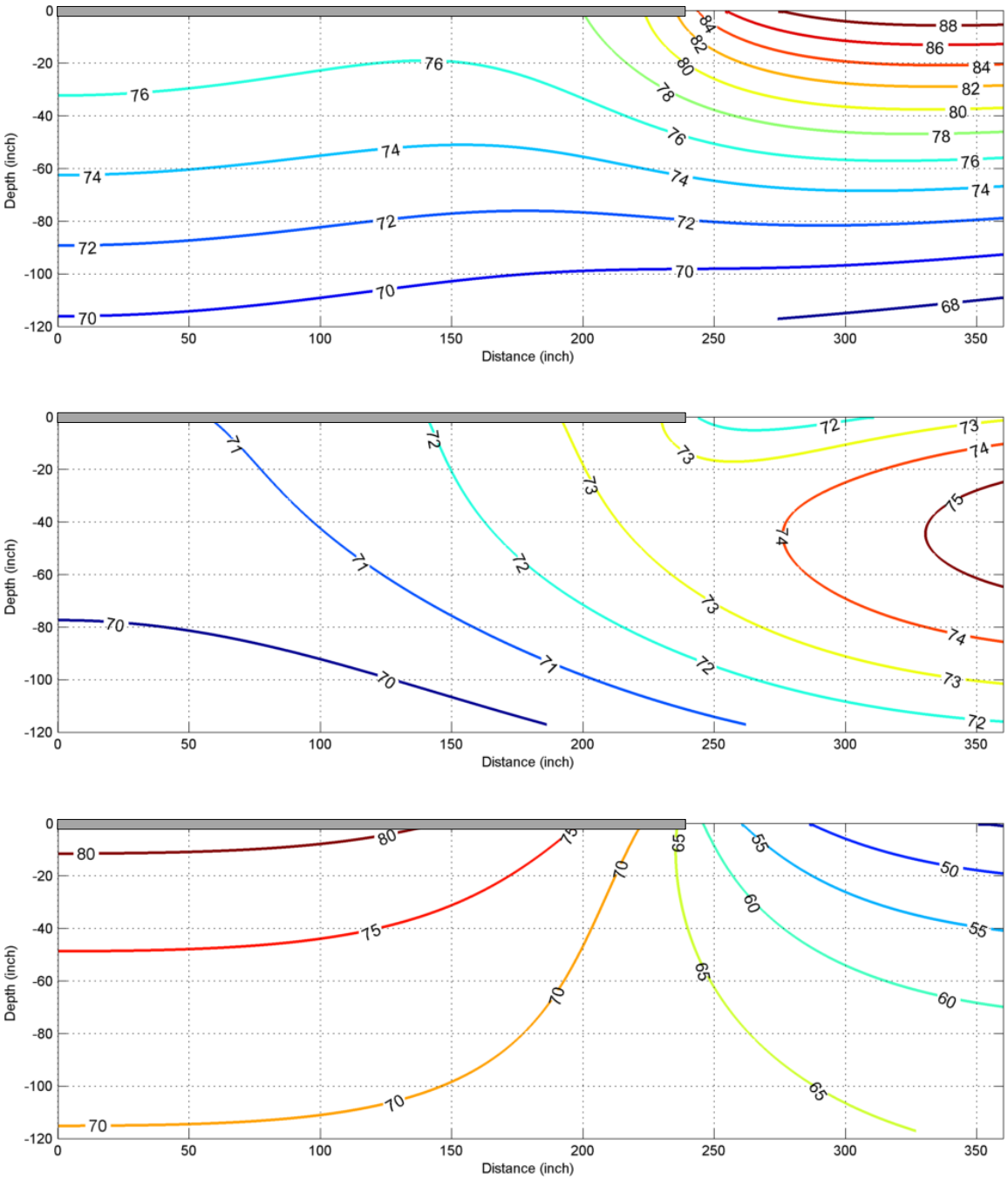


Figure 355: Amarillo, Texas – soil temperature distribution for non-radiant slab at 180 days (top), 270 days (middle), and 360 days (bottom) starting from January 1st for a slab length of 40 feet

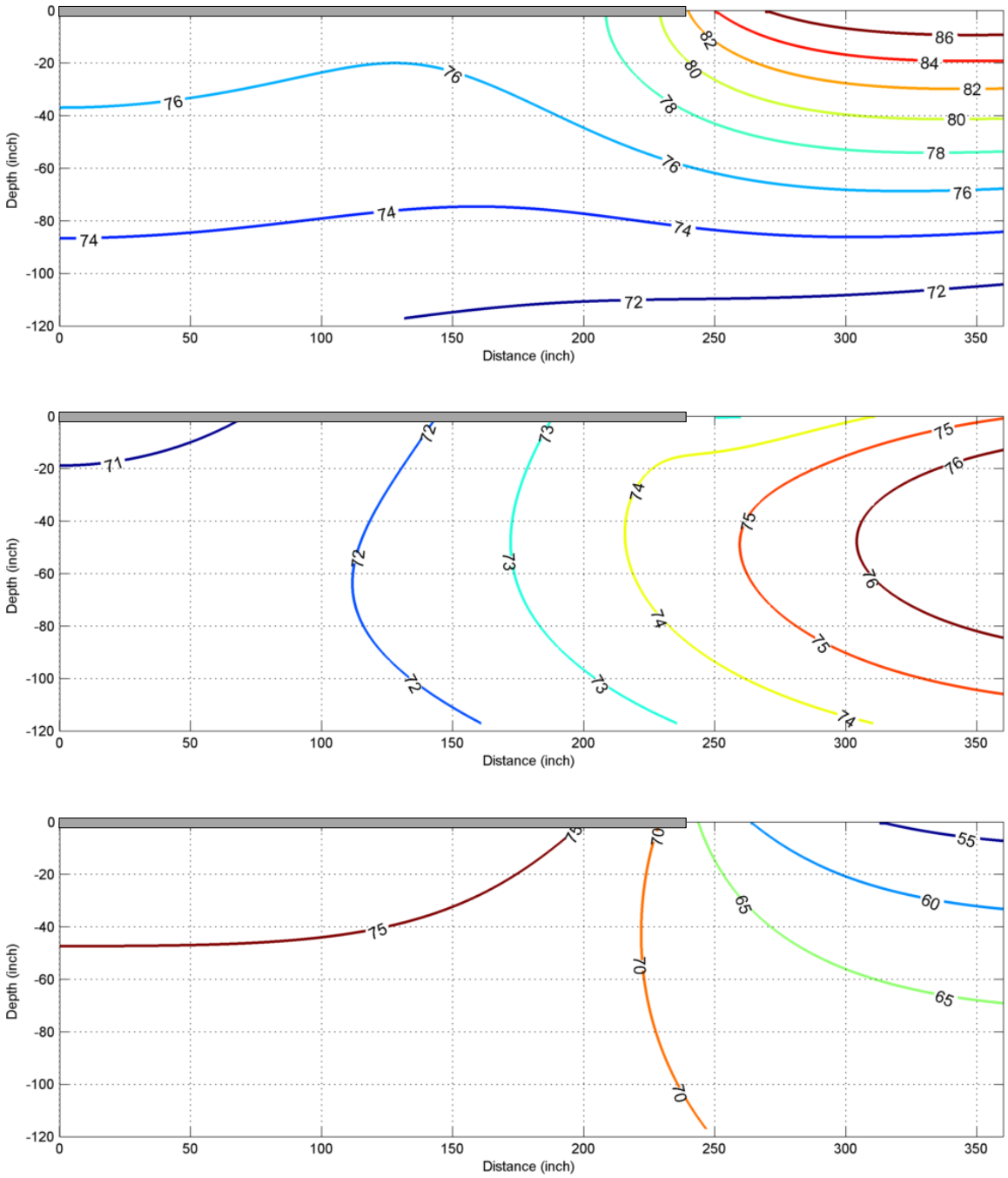


Figure 356: Athens, Georgia – soil temperature distribution for non-radiant slab at 180 days (top), 270 days (middle), and 360 days (bottom) starting from January 1st for a slab length of 40 feet

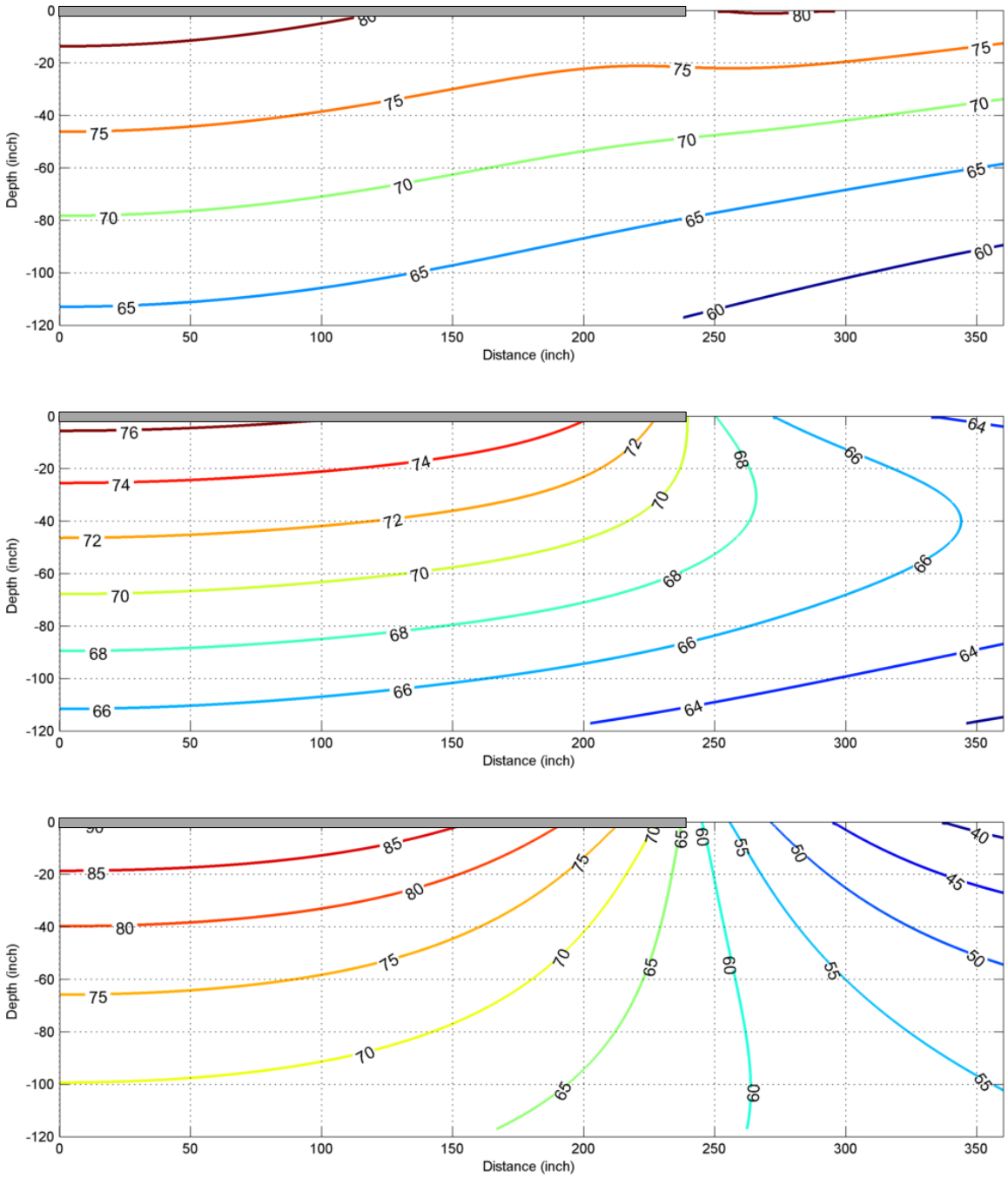


Figure 357: Bozeman, Montana– soil temperature distribution for non-radiant slab at 180 days (top), 270 days (middle), and 360 days (bottom) starting from January 1st for a slab length of 40 feet

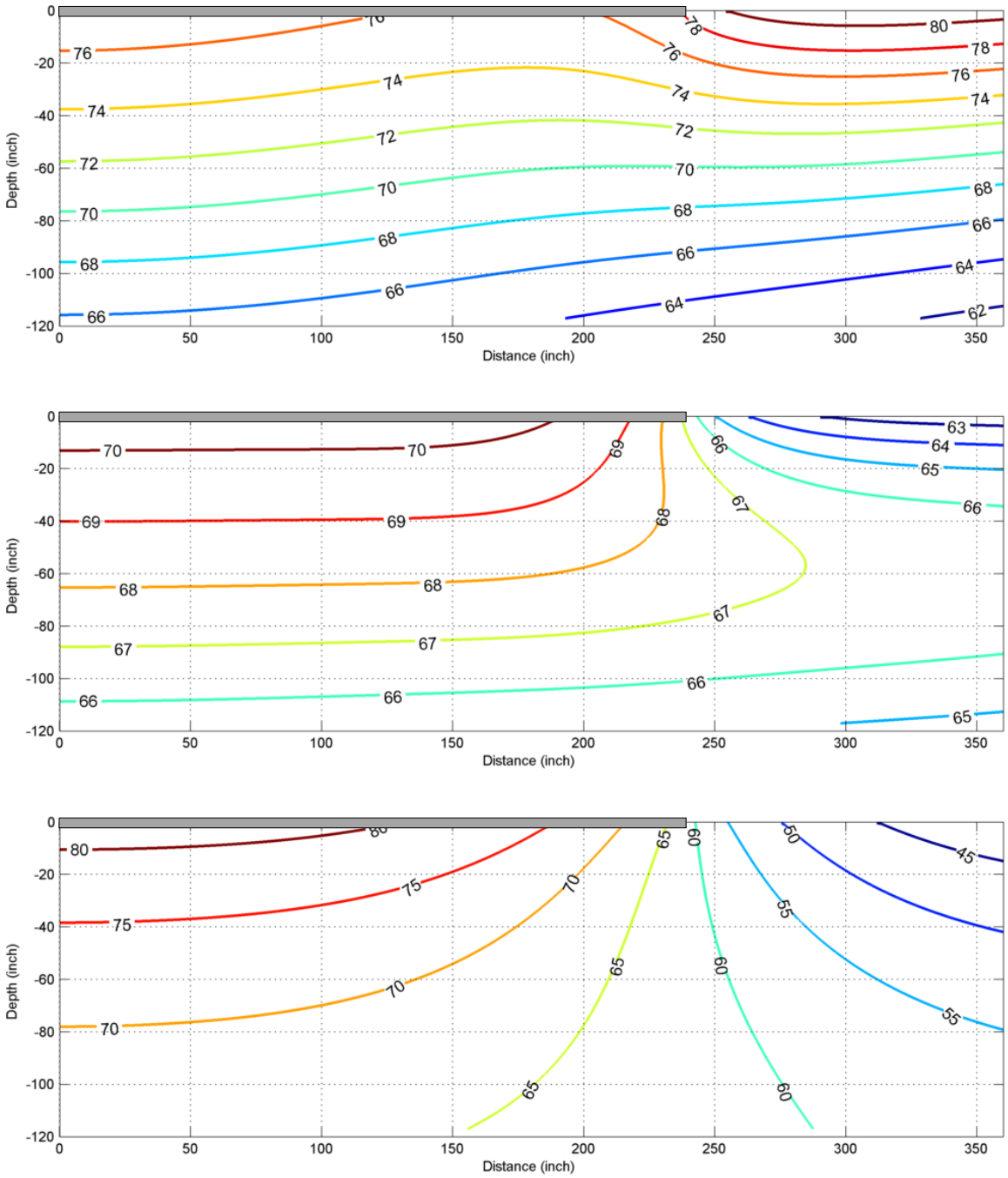


Figure 358: Columbus, Ohio – soil temperature distribution for non-radiant slab at 180 days (top), 270 days (middle), and 360 days (bottom) starting from January 1st for a slab length of 40 feet

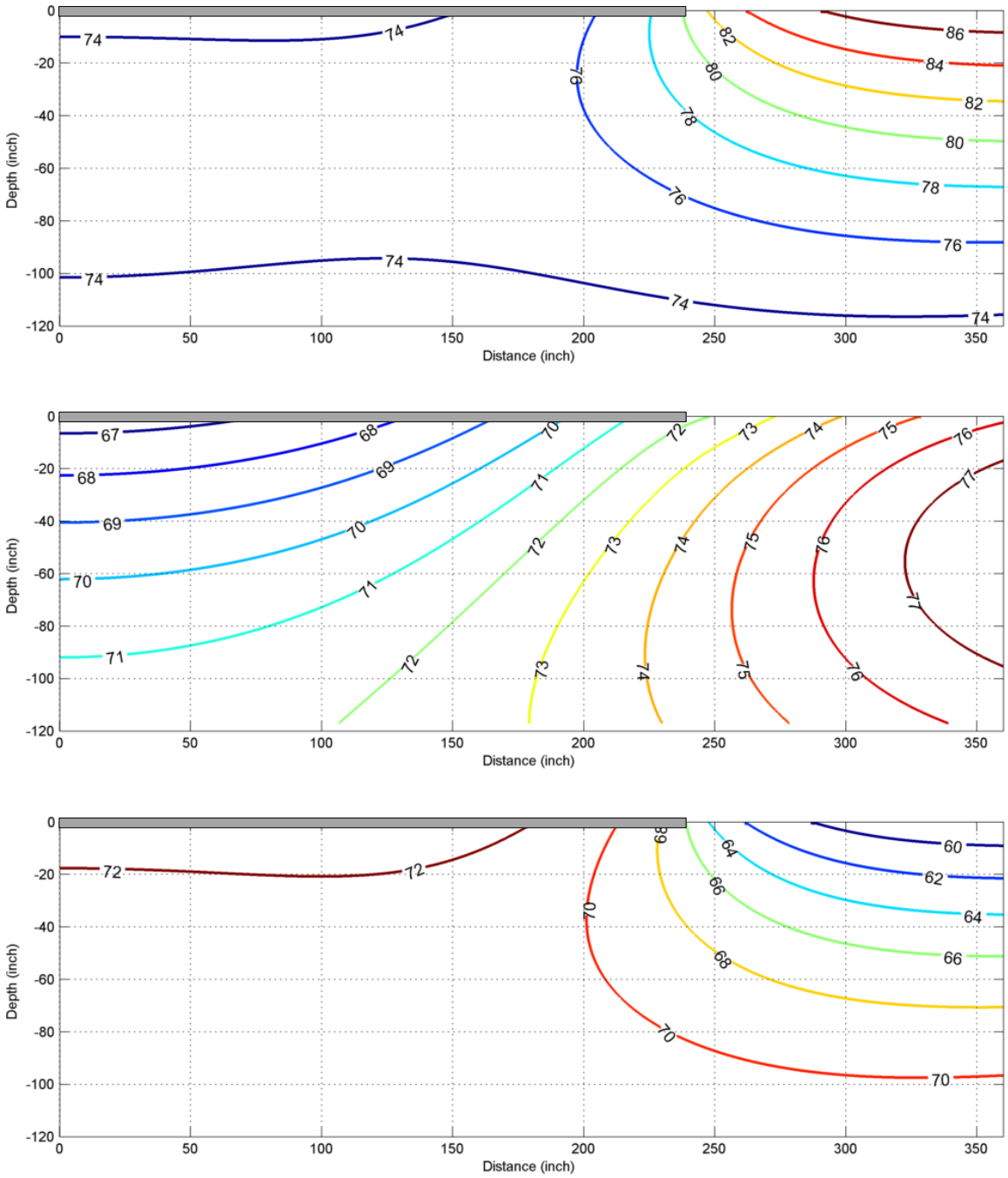


Figure 359: Houston, Texas – soil temperature distribution for non-radiant slab at 180 days (top), 270 days (middle), and 360 days (bottom) starting from January 1st for a slab length of 40 feet

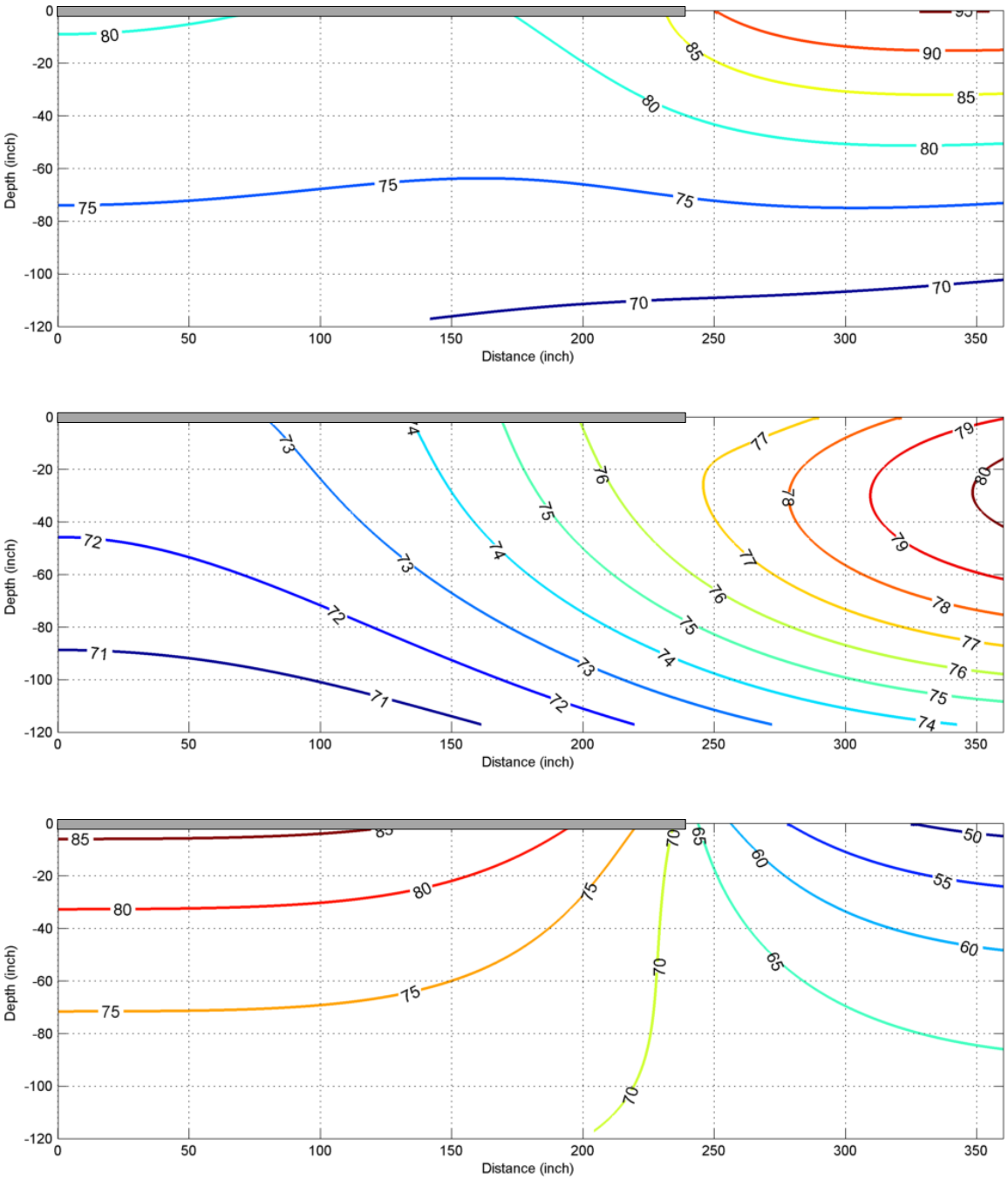


Figure 360: Kansas City, Missouri – soil temperature distribution for non-radiant slab at 180 days (top), 270 days (middle), and 360 days (bottom) starting from January 1st for a slab length of 40 feet

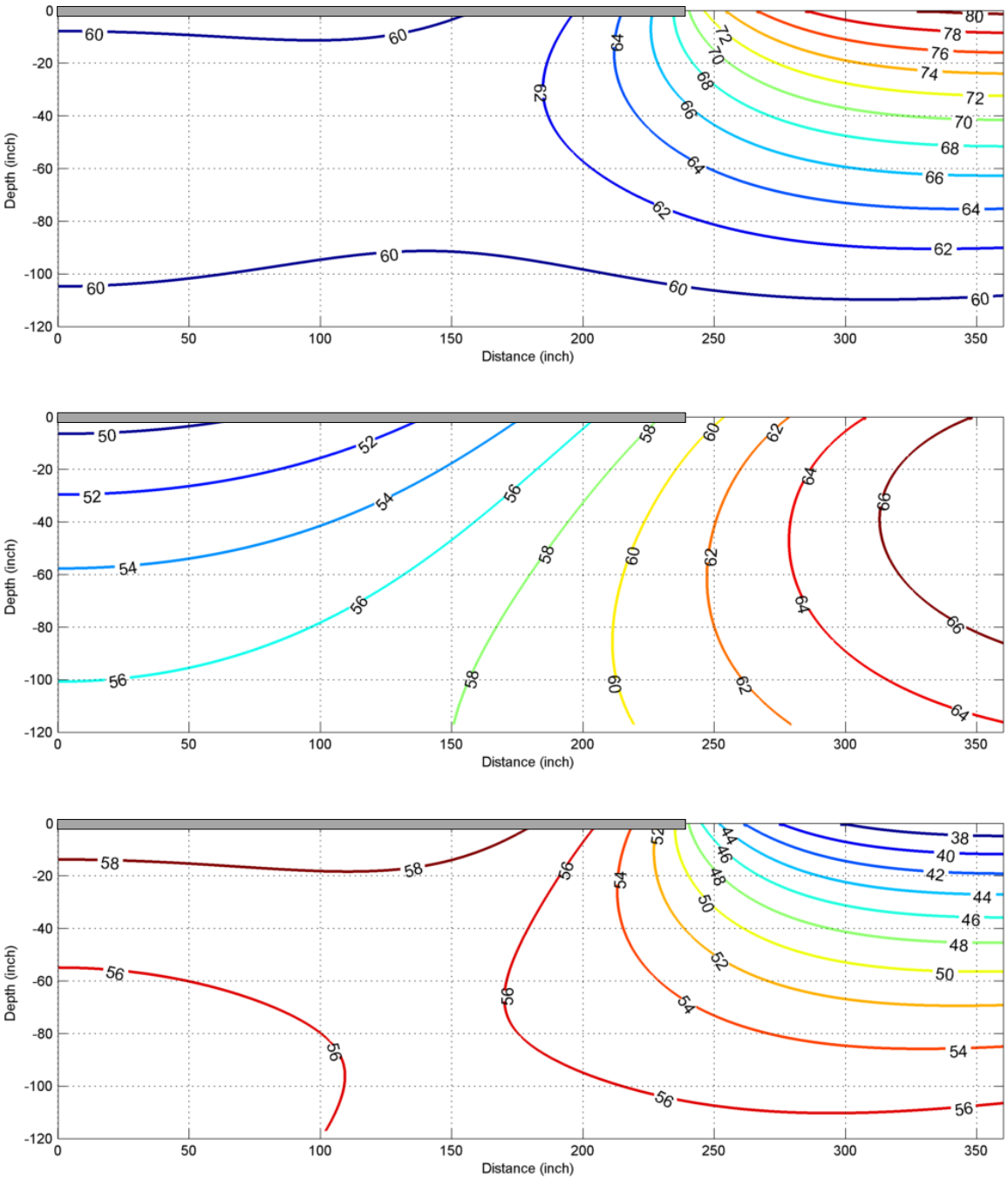


Figure 361: Las Vegas, Nevada – soil temperature distribution for non-radiant slab at 180 days (top), 270 days (middle), and 360 days (bottom) starting from January 1st for a slab length of 40 feet

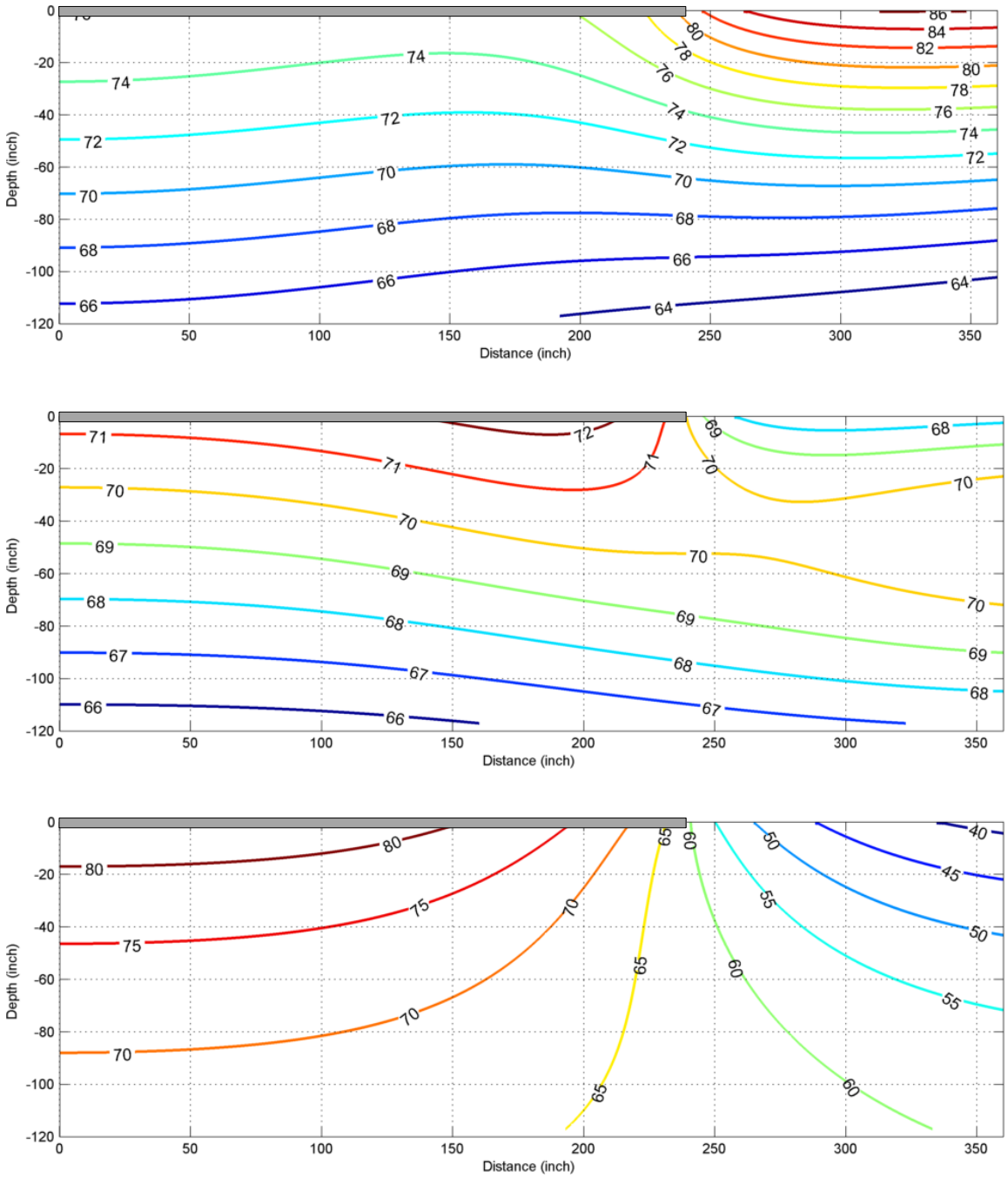


Figure 362: Moses Lake, Washington – soil temperature distribution for non-radiant slab at 180 days (top), 270 days (middle), and 360 days (bottom) starting from January 1st for a slab length of 40 feet

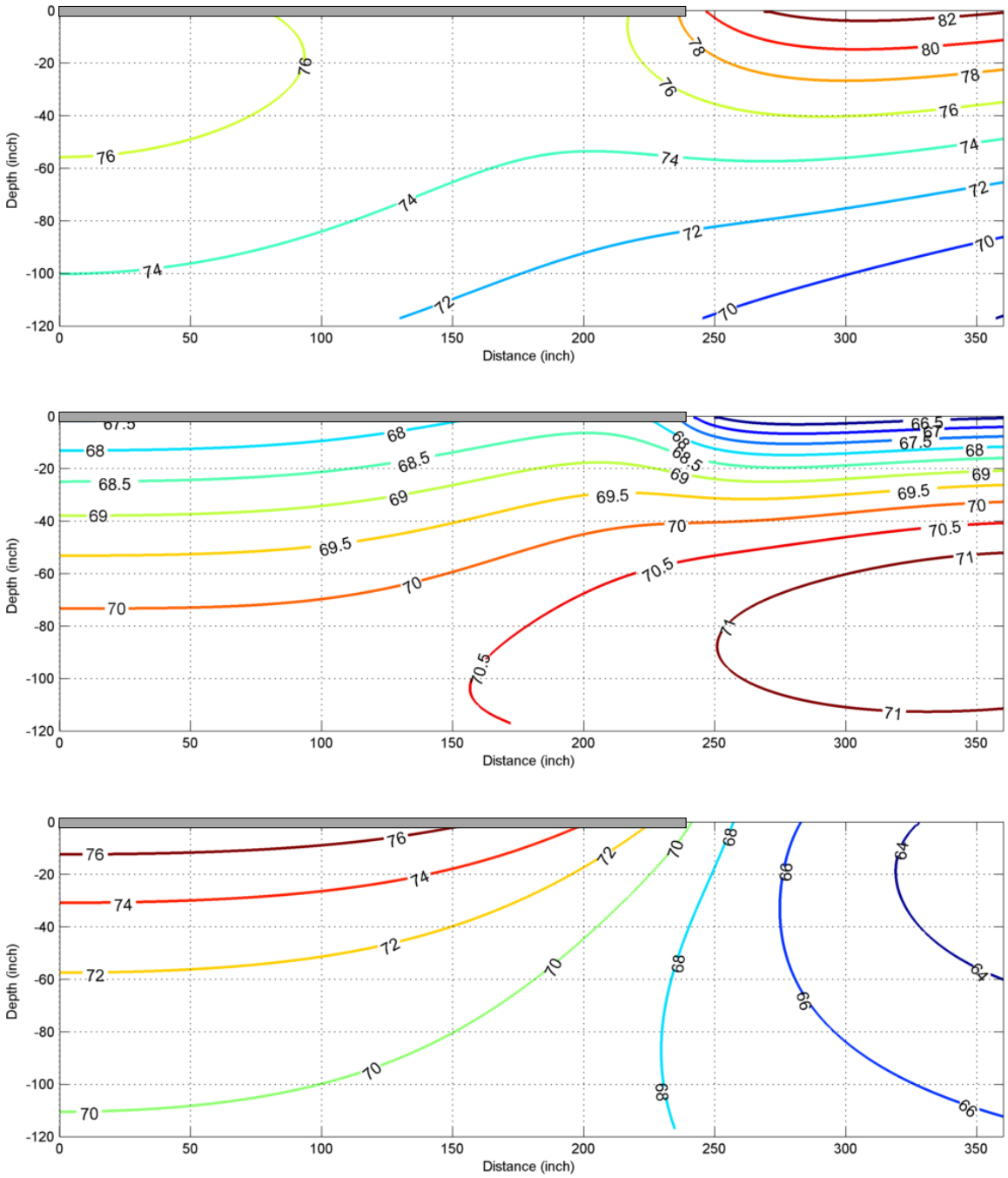


Figure 363: Pine Bluff, Arkansas – soil temperature distribution for non-radiant slab at 180 days (top), 270 days (middle), and 360 days (bottom) starting from January 1st for a slab length of 40 feet

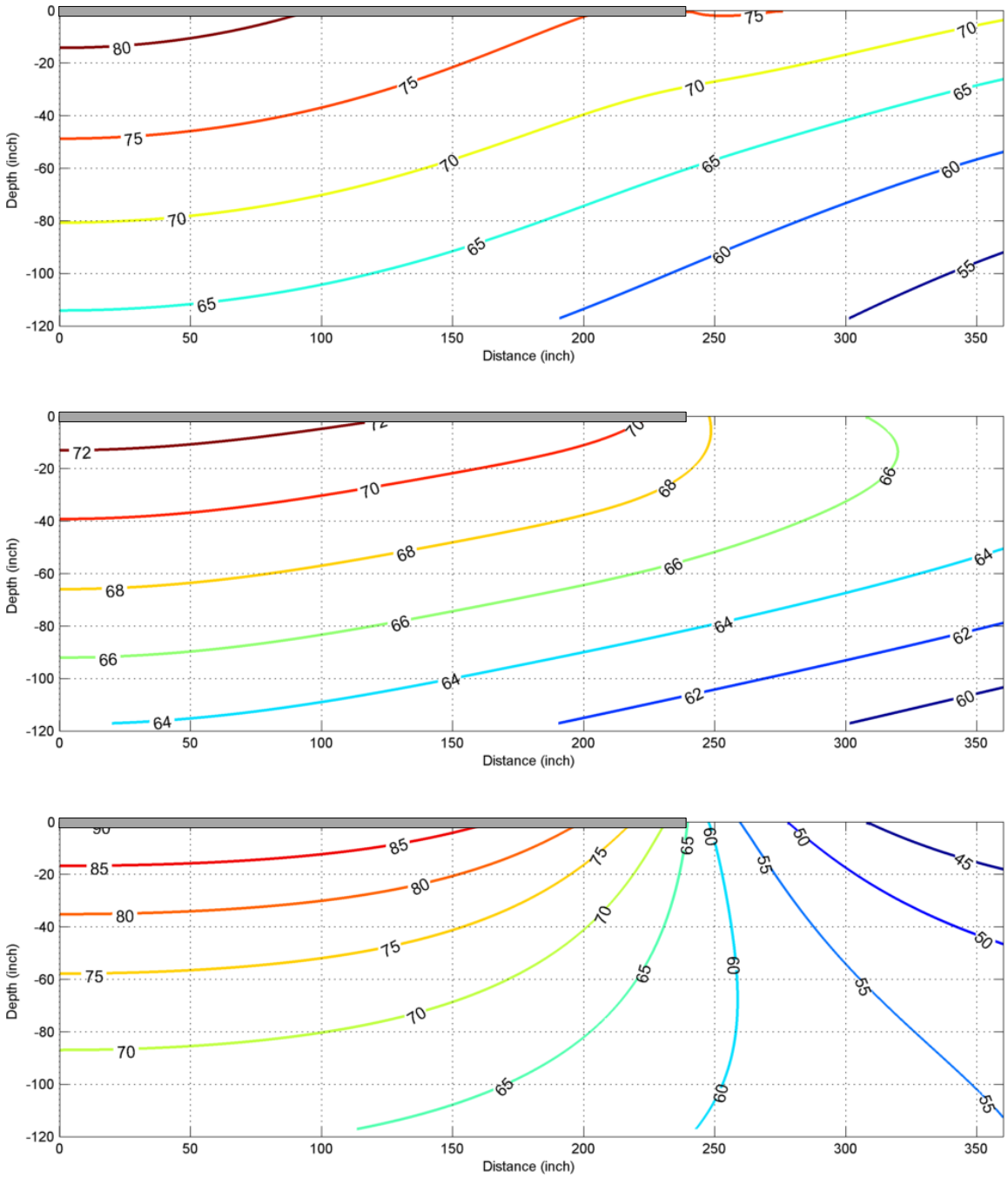


Figure 364: Saint Cloud, Minnesota – soil temperature distribution for non-radiant slab at 180 days (top), 270 days (middle), and 360 days (bottom) starting from January 1st for a slab length of 40 feet

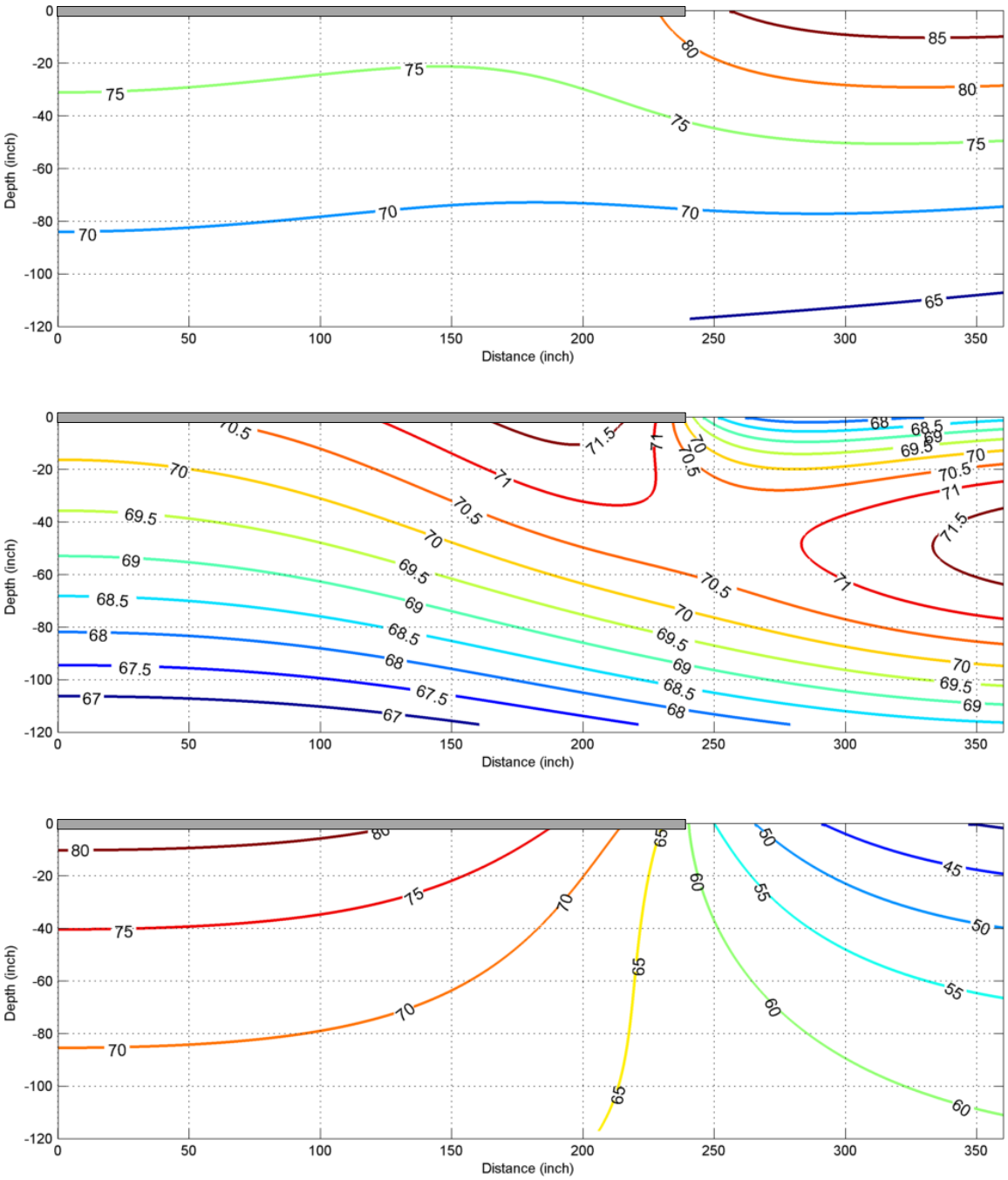


Figure 365: Salt Lake City, Utah – soil temperature distribution for non-radiant slab at 180 days (top), 270 days (middle), and 360 days (bottom) starting from January 1st for a slab length of 40 feet

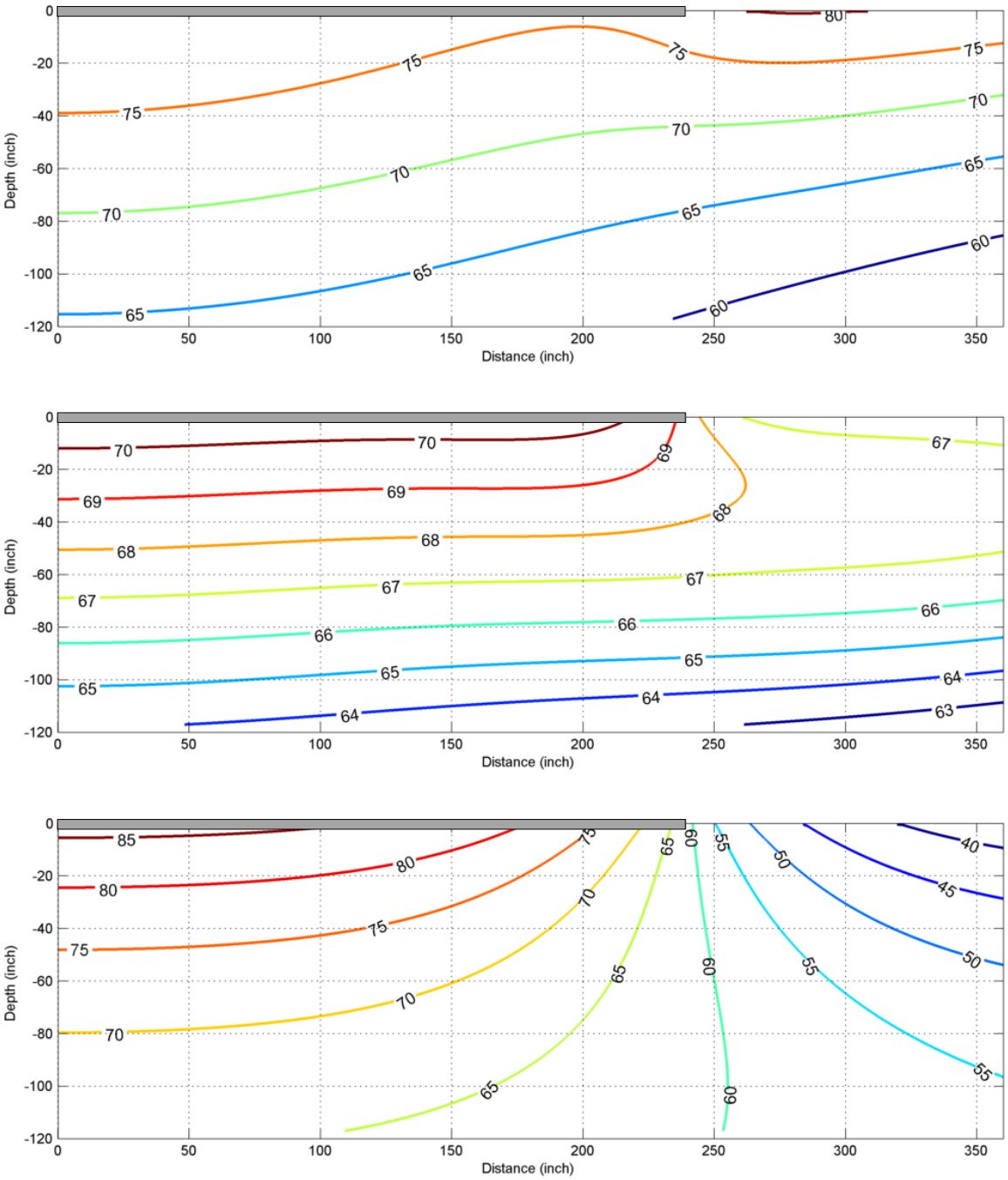


Figure 366: Sioux Falls, South Dakota – soil temperature distribution for non-radiant slab at 180 days (top), 270 days (middle), and 360 days (bottom) starting from January 1st for a slab length of 40 feet

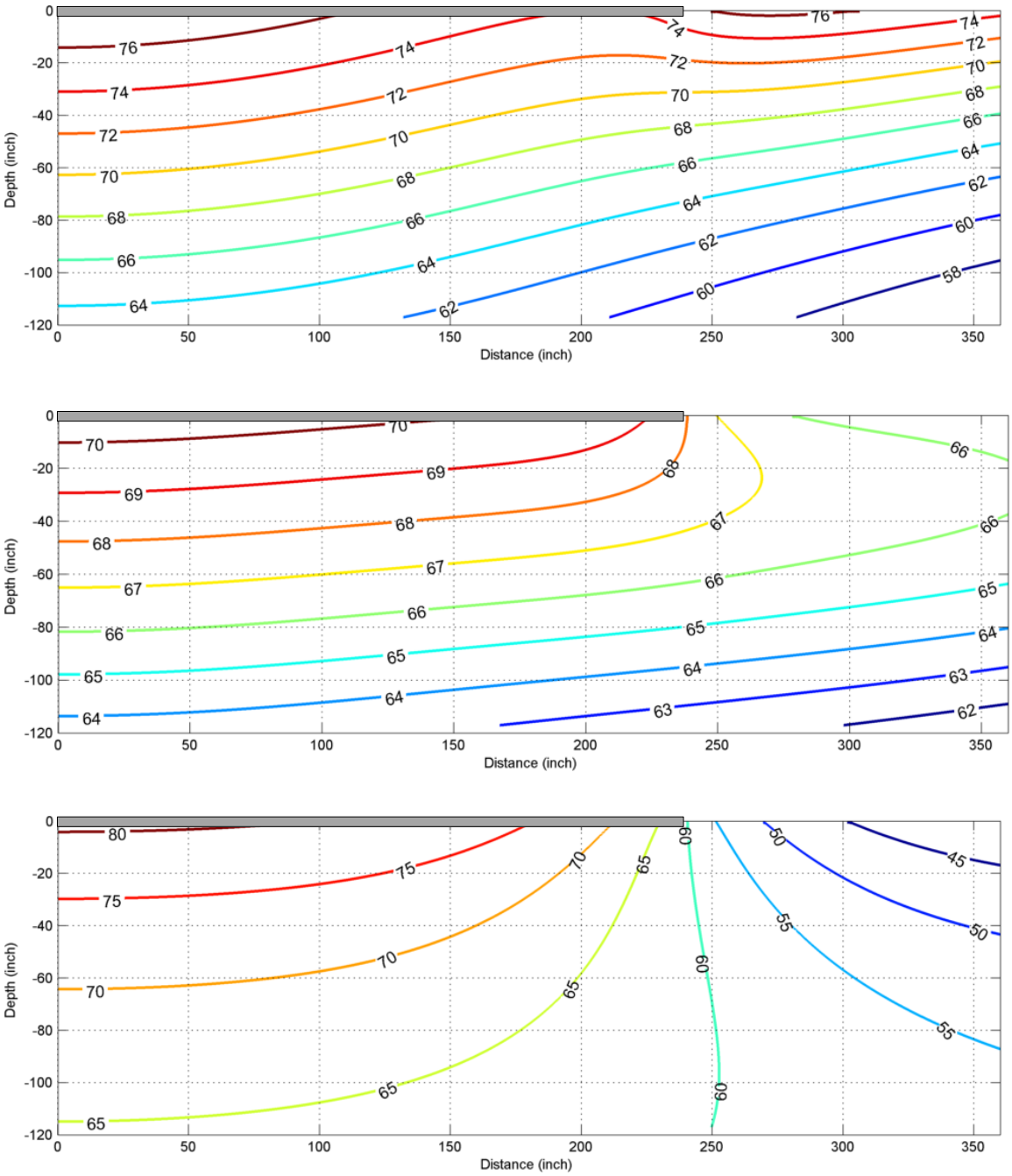


Figure 367: State College, Pennsylvania – soil temperature distribution for non-radiant slab at 180 days (top), 270 days (middle), and 360 days (bottom) starting from January 1st for a slab length of 40 feet

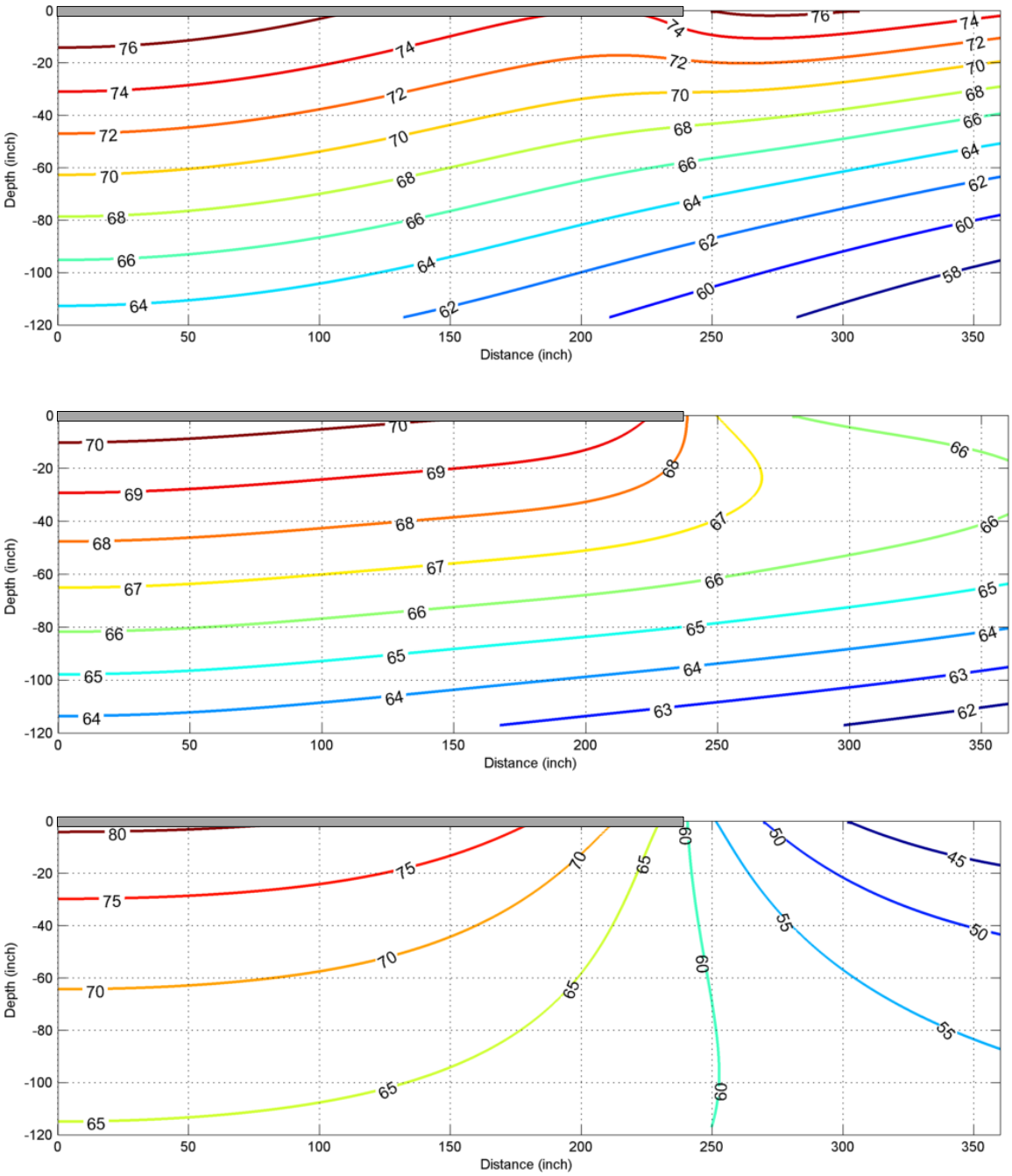


Figure 368: Tallahassee, Florida – soil temperature distribution for non-radiant slab at 180 days (top), 270 days (middle), and 360 days (bottom) starting from January 1st for a slab length of 40 feet

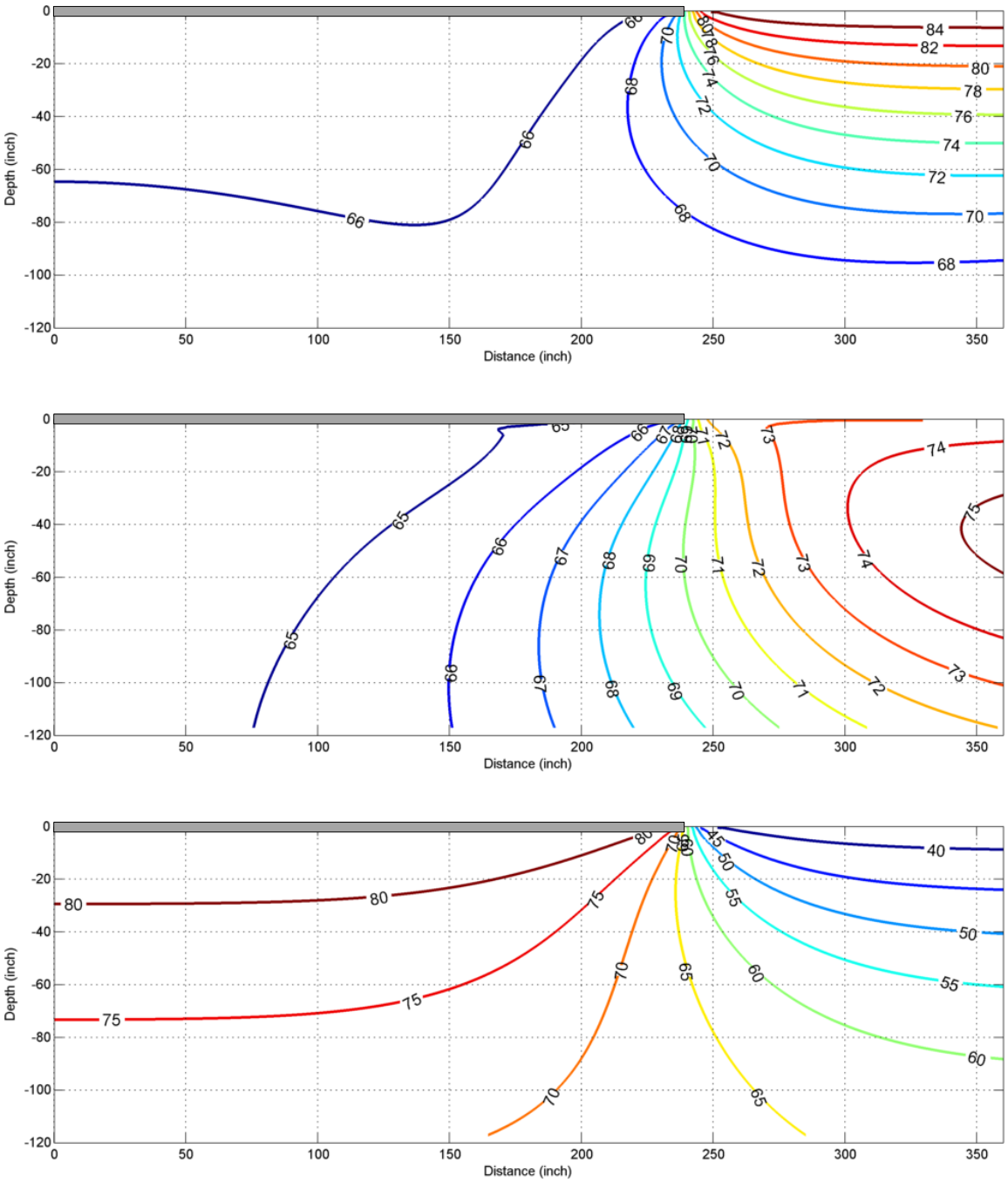


Figure 369: Albuquerque, New Mexico – soil temperature distribution for radiant slab at 180 days (top), 270 days (middle), and 360 days (bottom) starting from January 1st for a slab length of 40 feet

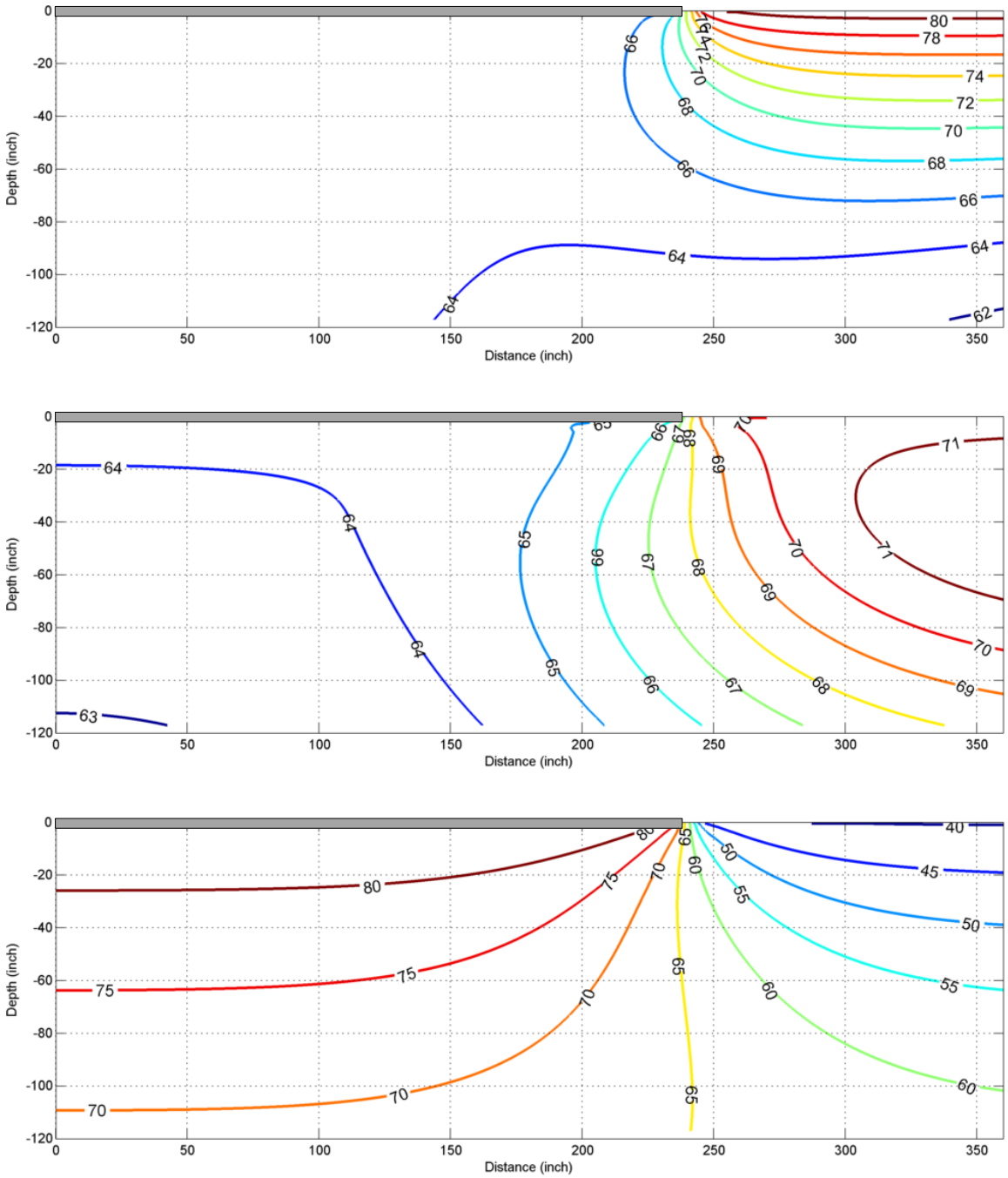


Figure 370: Amarillo, Texas – soil temperature distribution for radiant slab at 180 days (top), 270 days (middle), and 360 days (bottom) starting from January 1st for a slab length of 40 feet

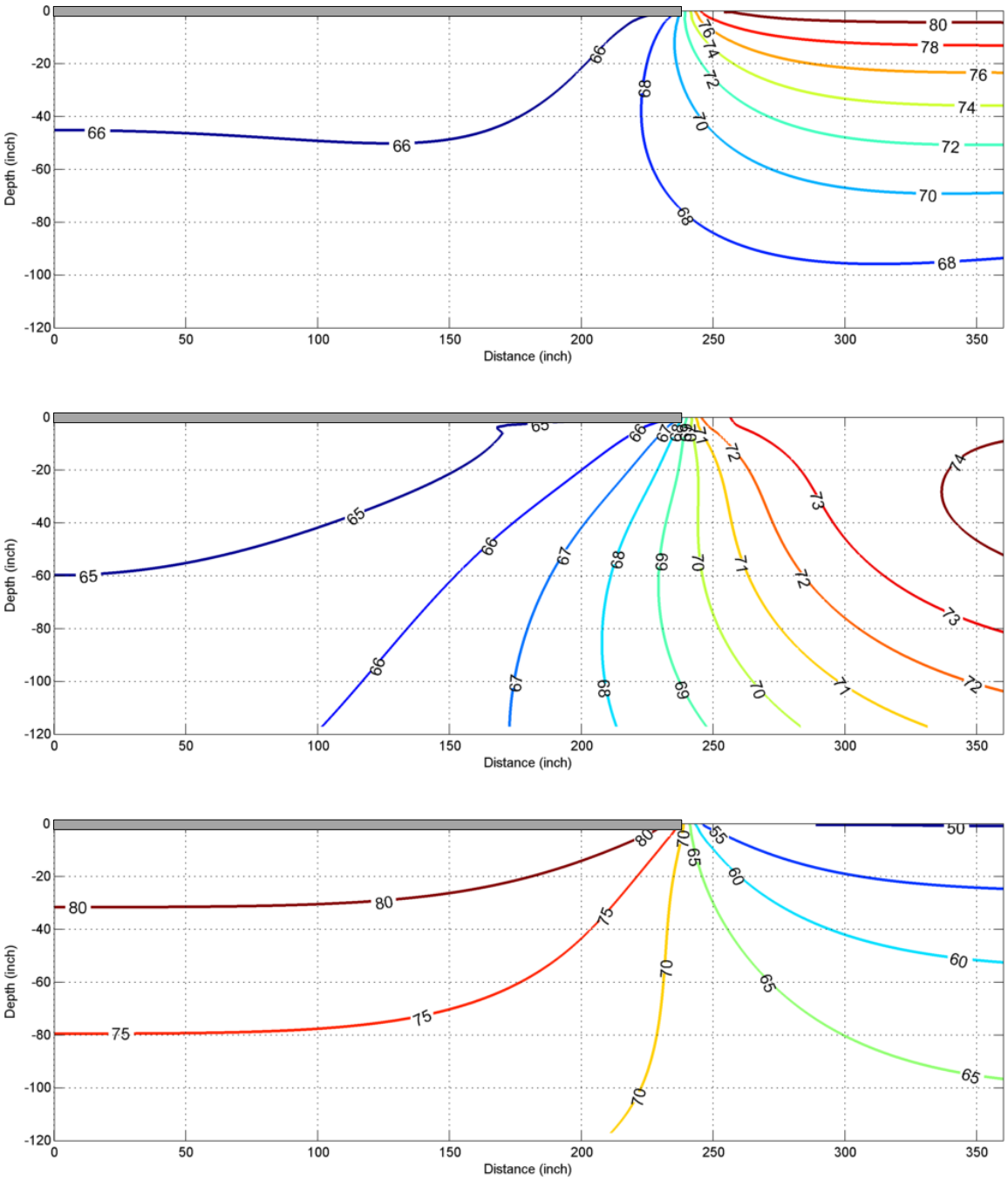


Figure 371: Athens, Georgia – soil temperature distribution for radiant slab at 180 days (top), 270 days (middle), and 360 days (bottom) starting from January 1st for a slab length of 40 feet

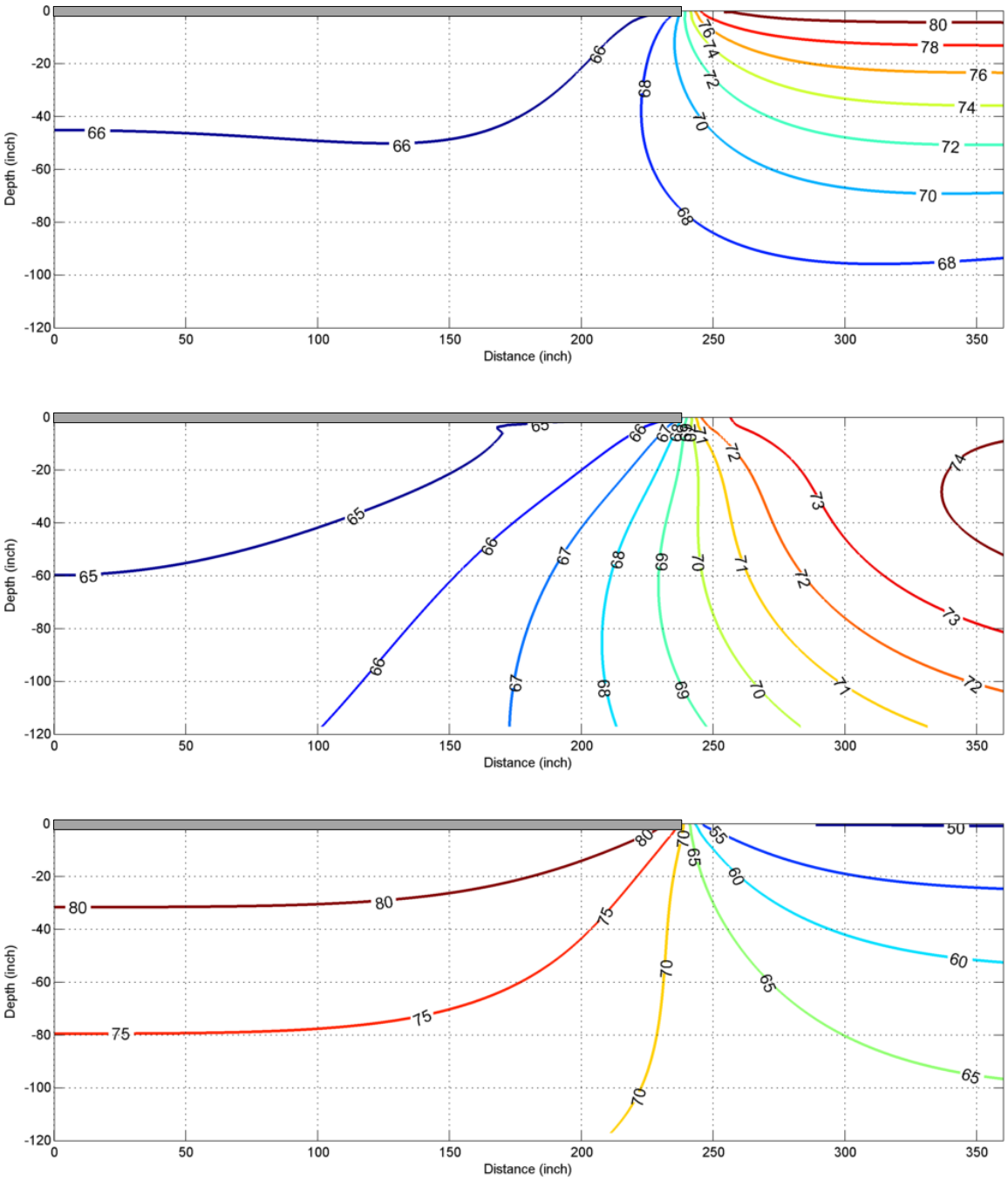


Figure 372: Bozeman, Montana – soil temperature distribution for radiant slab at 180 days (top), 270 days (middle), and 360 days (bottom) starting from January 1st for a slab length of 40 feet

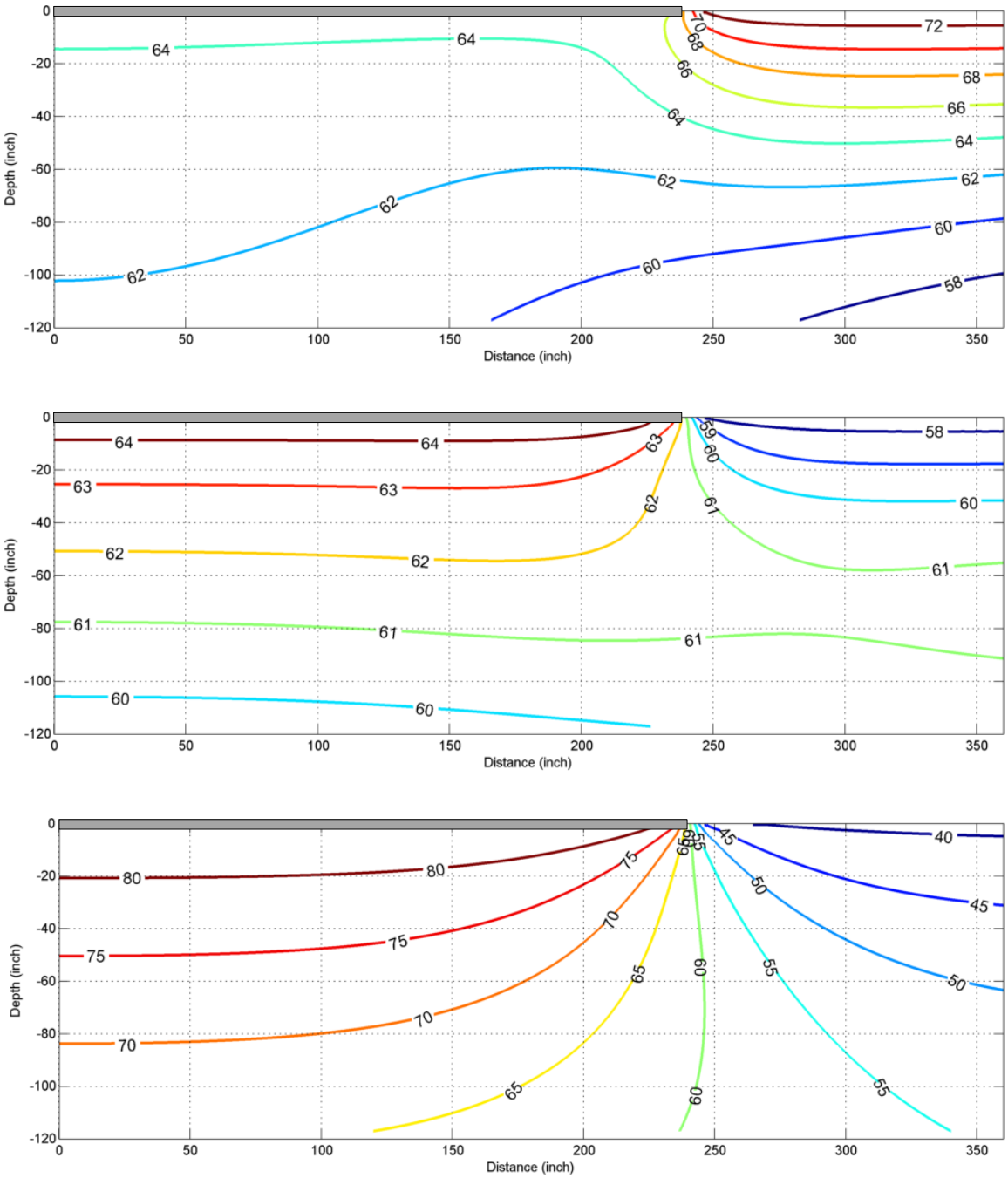


Figure 373: Columbus, Ohio – soil temperature distribution for radiant slab at 180 days (top), 270 days (middle), and 360 days (bottom) starting from January 1st for a slab length of 40 feet

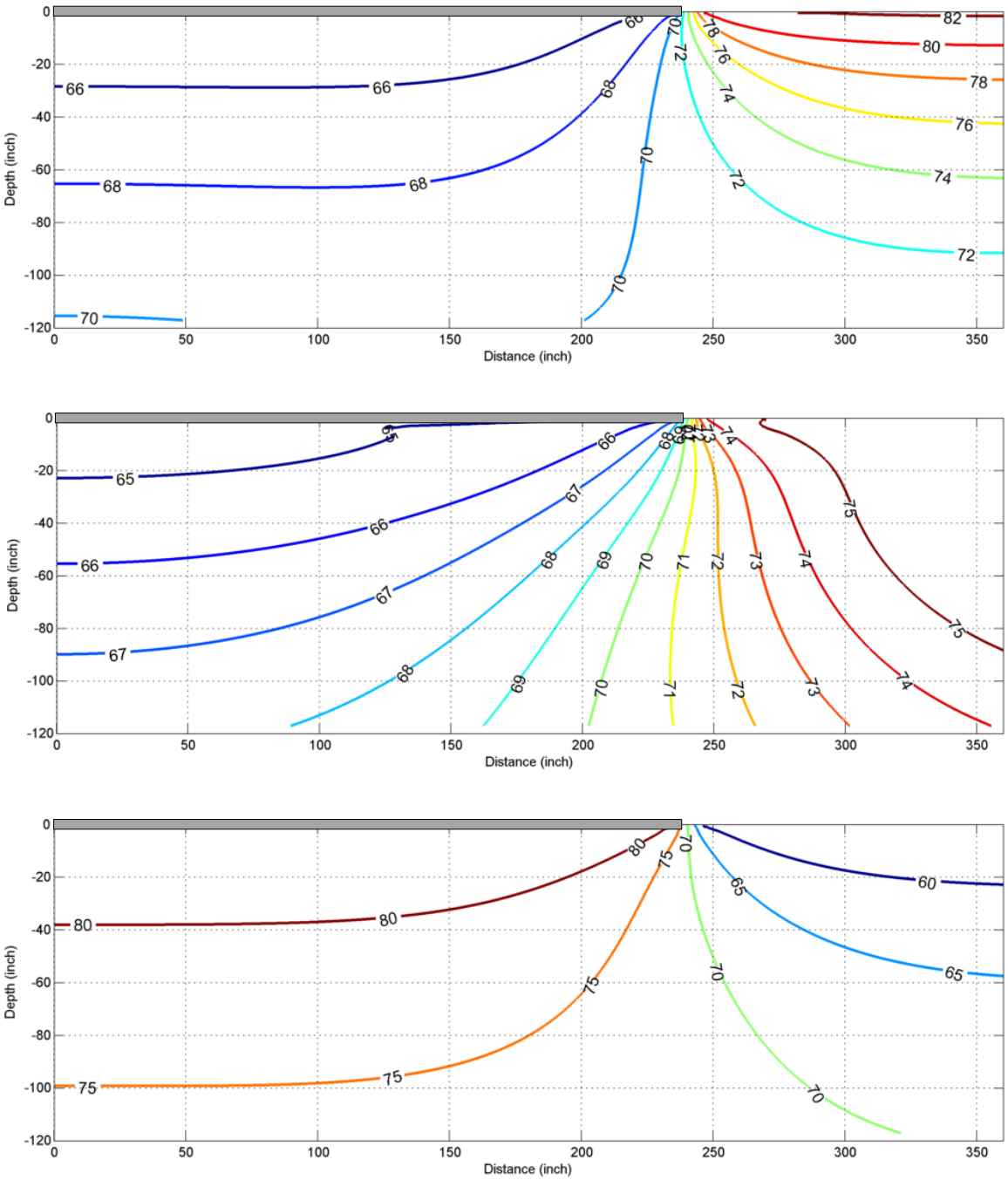


Figure 374: Houston, Texas – soil temperature distribution for radiant slab at 180 days (top), 270 days (middle), and 360 days (bottom) starting from January 1st for a slab length of 40 feet

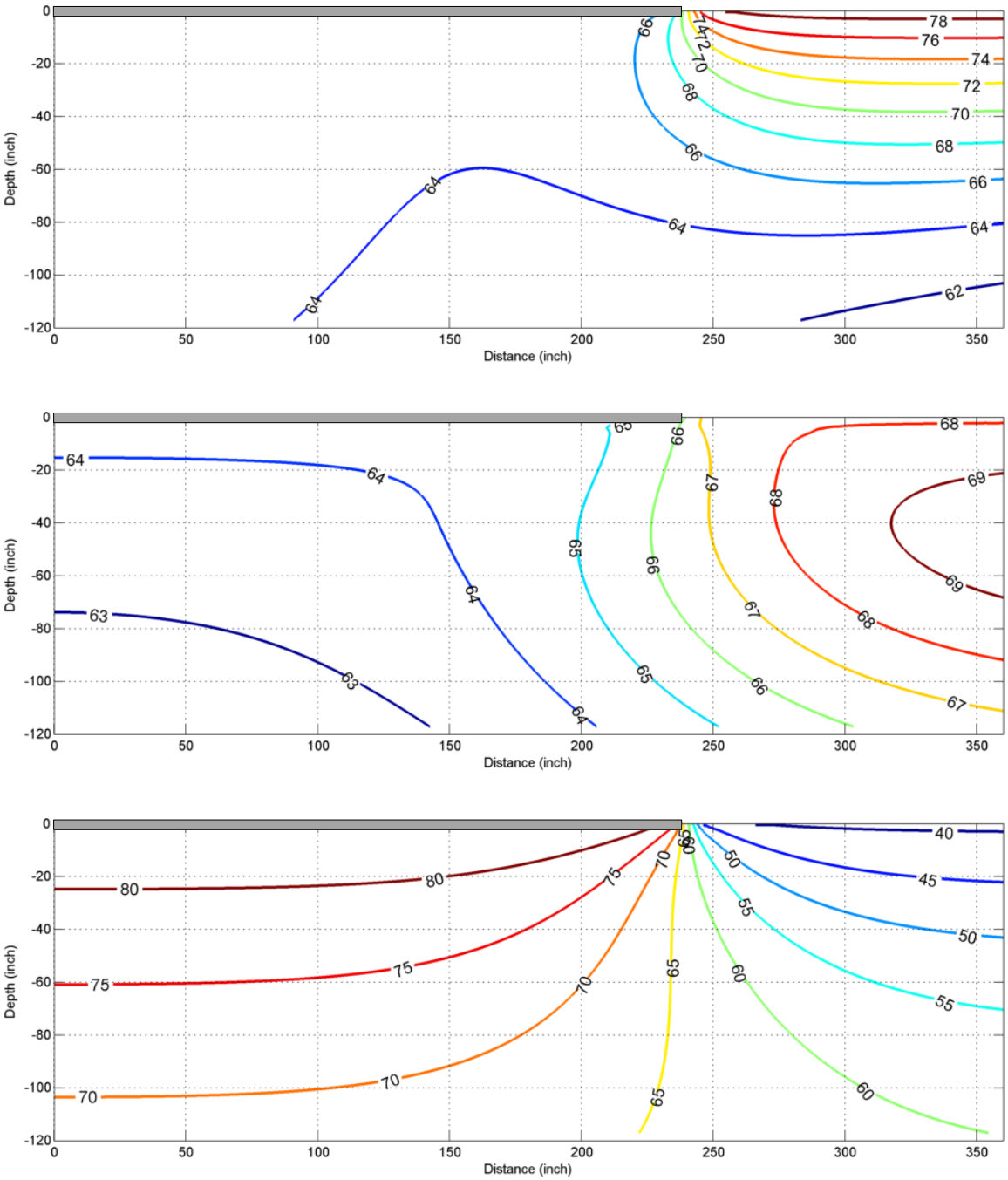


Figure 375: Kansas City, Missouri – soil temperature distribution for radiant slab at 180 days (top), 270 days (middle), and 360 days (bottom) starting from January 1st for a slab length of 40 feet

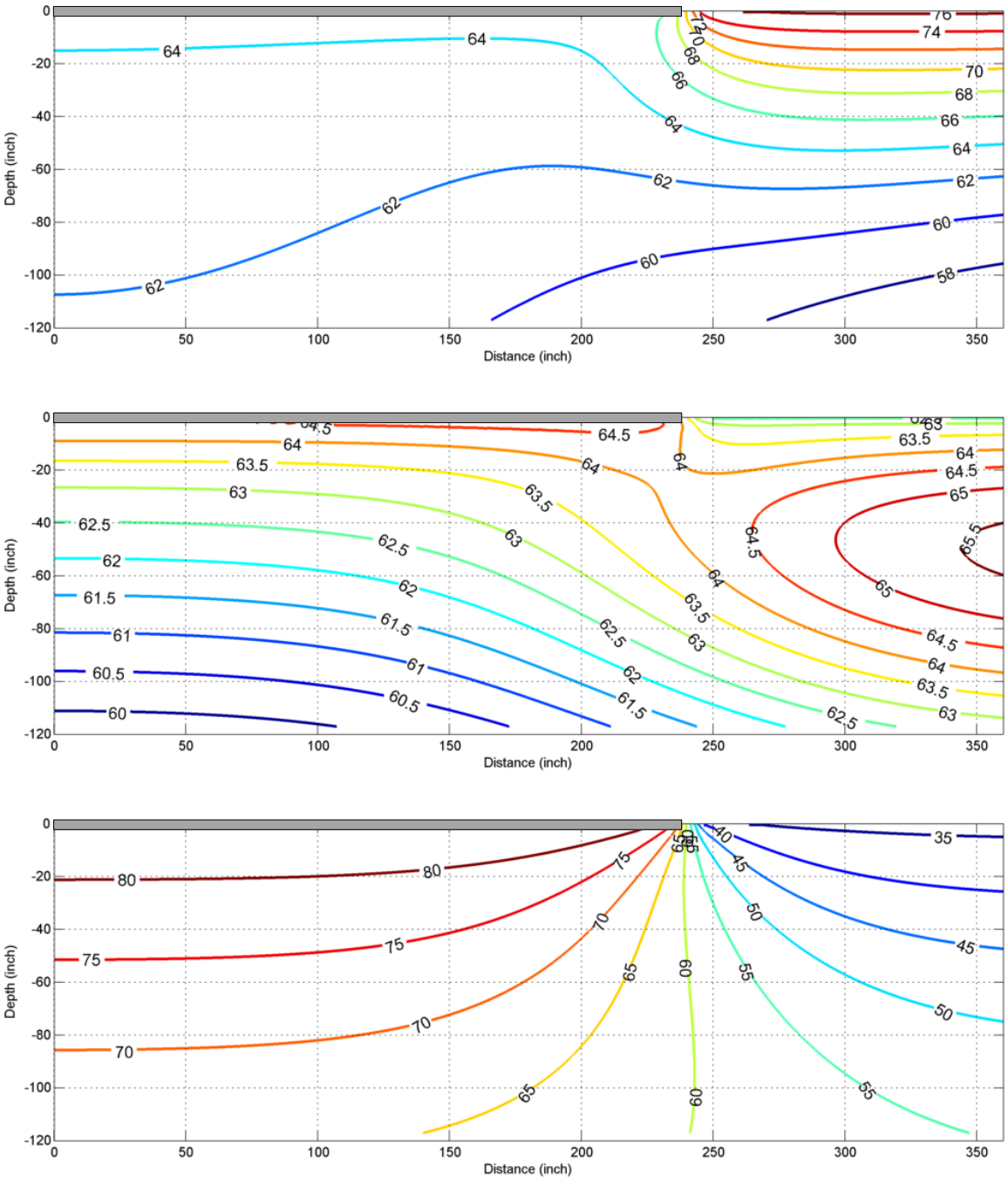


Figure 376: Las Vegas, Nevada – soil temperature distribution for radiant slab at 180 days (top), 270 days (middle), and 360 days (bottom) starting from January 1st for a slab length of 40 feet

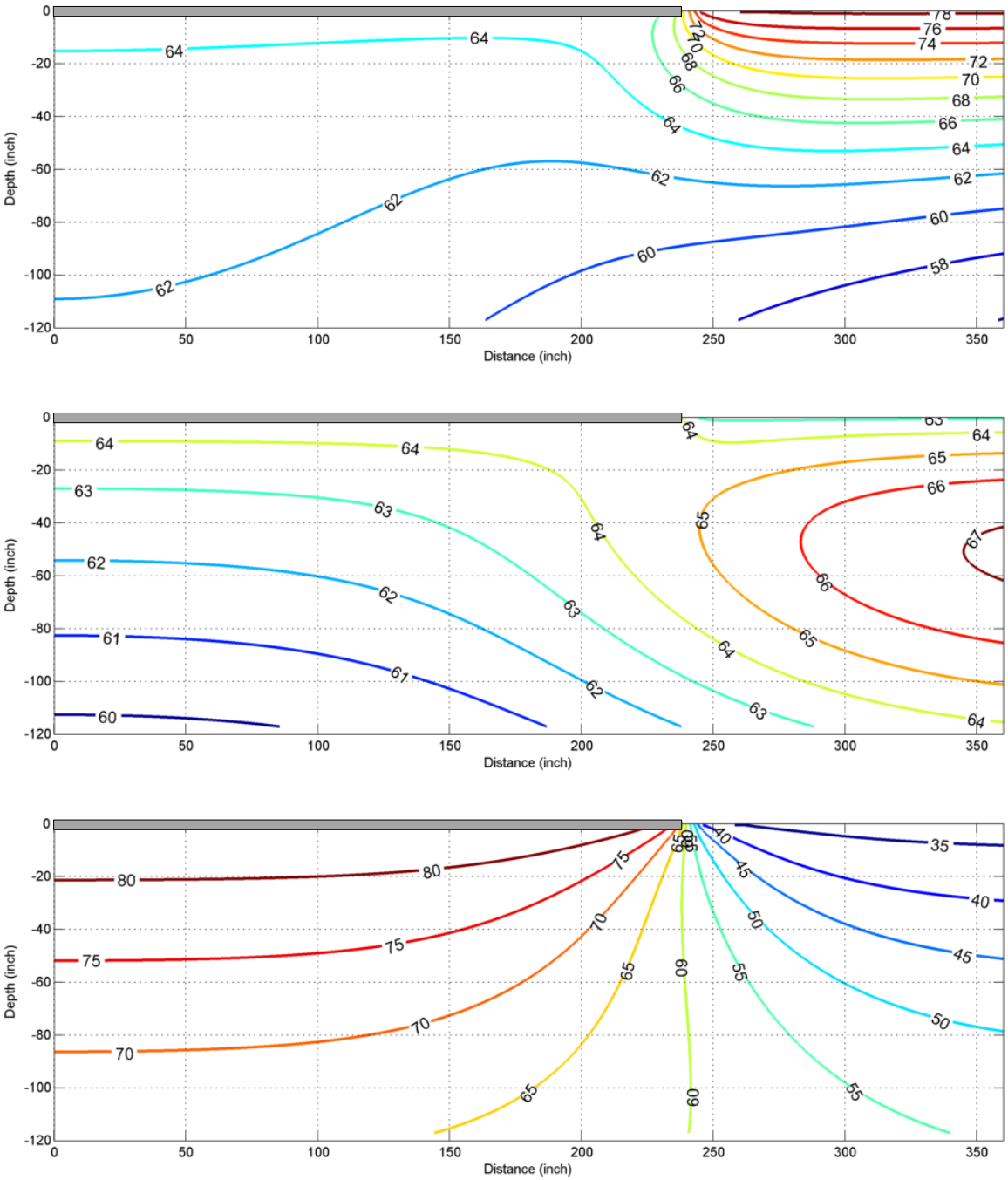


Figure 377: Moses Lake, Washington – soil temperature distribution for radiant slab at 180 days (top), 270 days (middle), and 360 days (bottom) starting from January 1st for a slab length of 40 feet

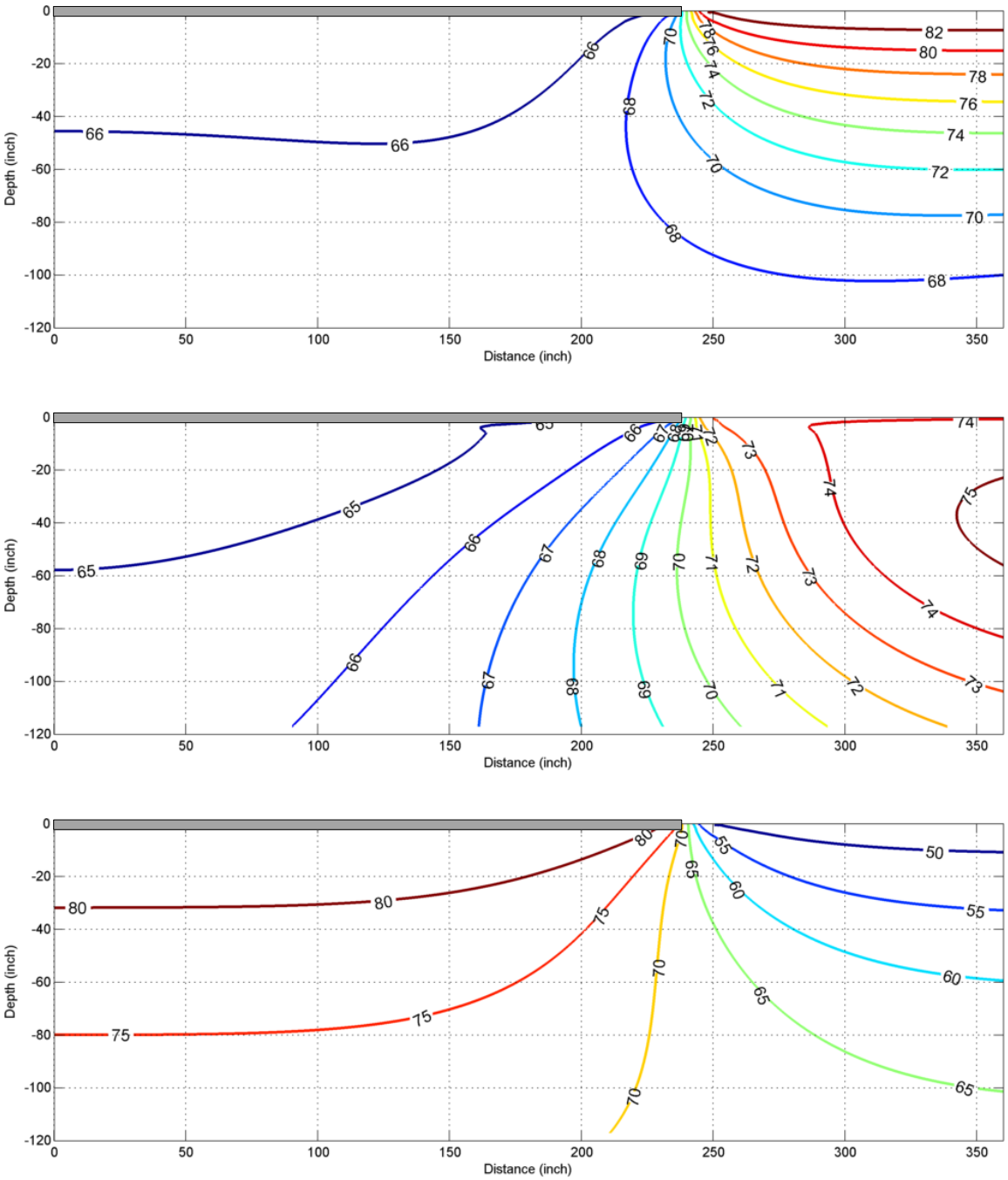


Figure 378: Pine Bluff, Arkansas – soil temperature distribution for radiant slab at 180 days (top), 270 days (middle), and 360 days (bottom) starting from January 1st for a slab length of 40 feet

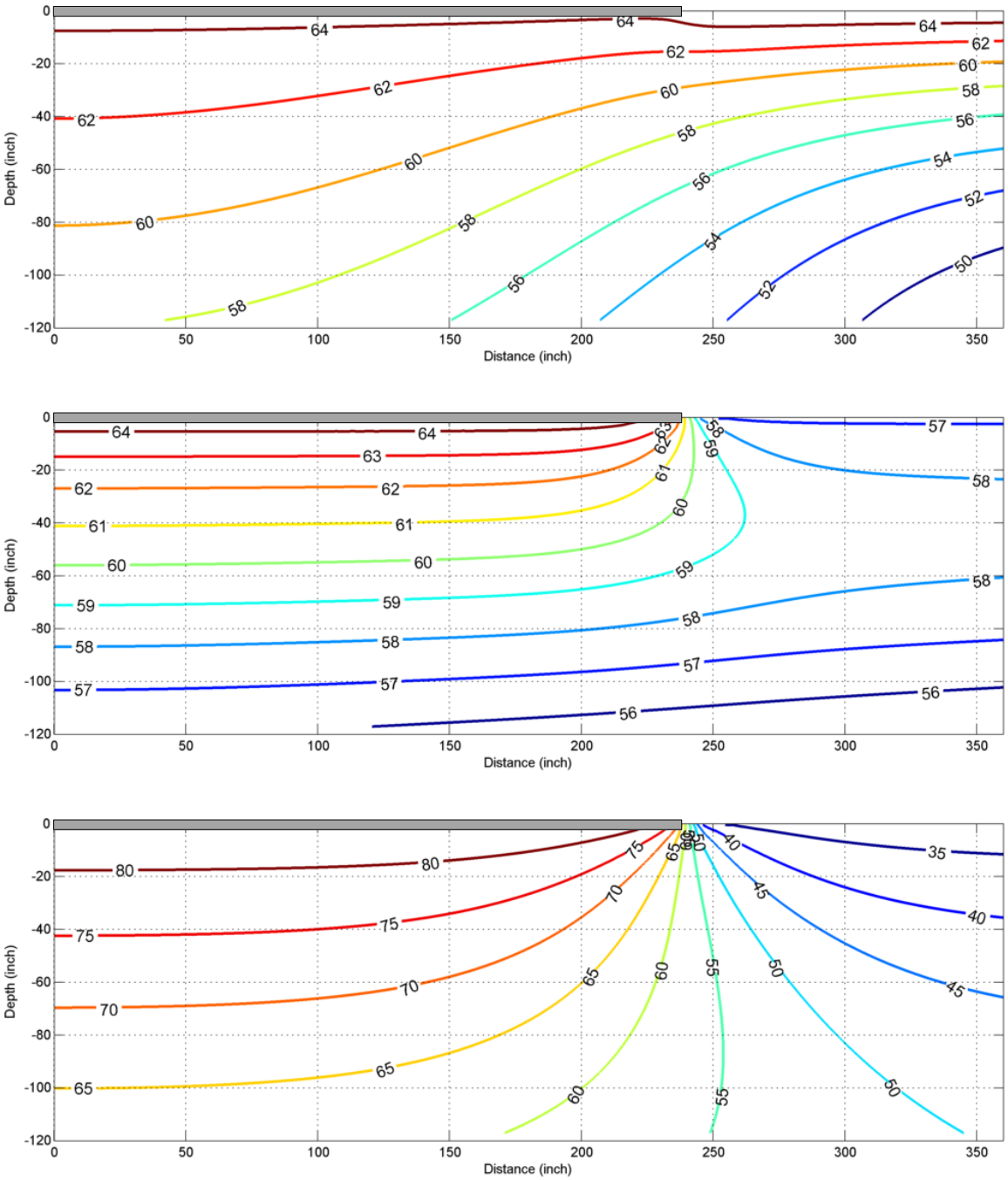


Figure 379: Saint Cloud, Minnesota – soil temperature distribution for radiant slab at 180 days (top), 270 days (middle), and 360 days (bottom) starting from January 1st for a slab length of 40 feet

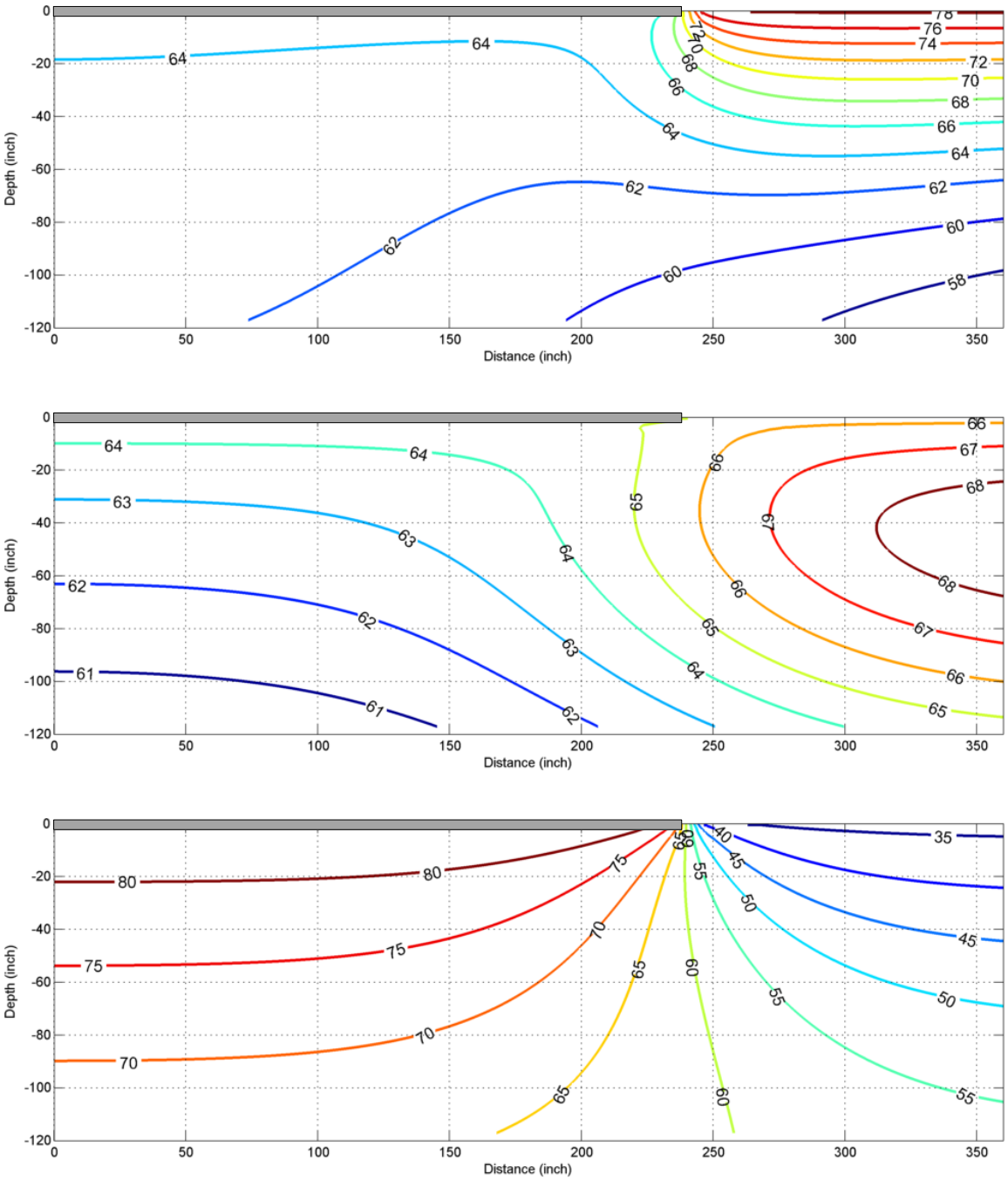


Figure 380: Salt Lake City, Utah – soil temperature distribution for radiant slab at 180 days (top), 270 days (middle), and 360 days (bottom) starting from January 1st for a slab length of 40 feet

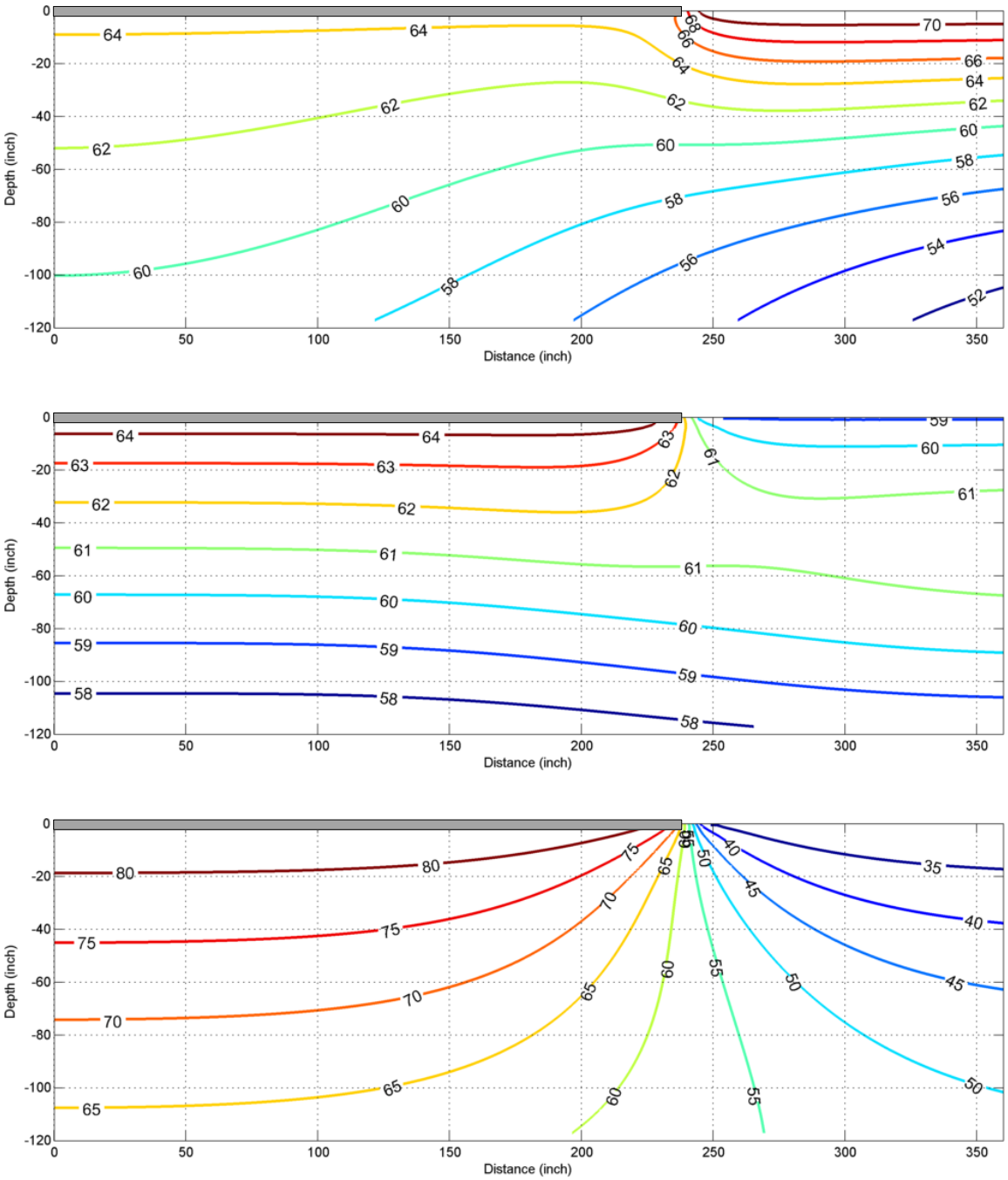


Figure 381: Sioux Falls, South Dakota – soil temperature distribution for radiant slab at 180 days (top), 270 days (middle), and 360 days (bottom) starting from January 1st for a slab length of 40 feet

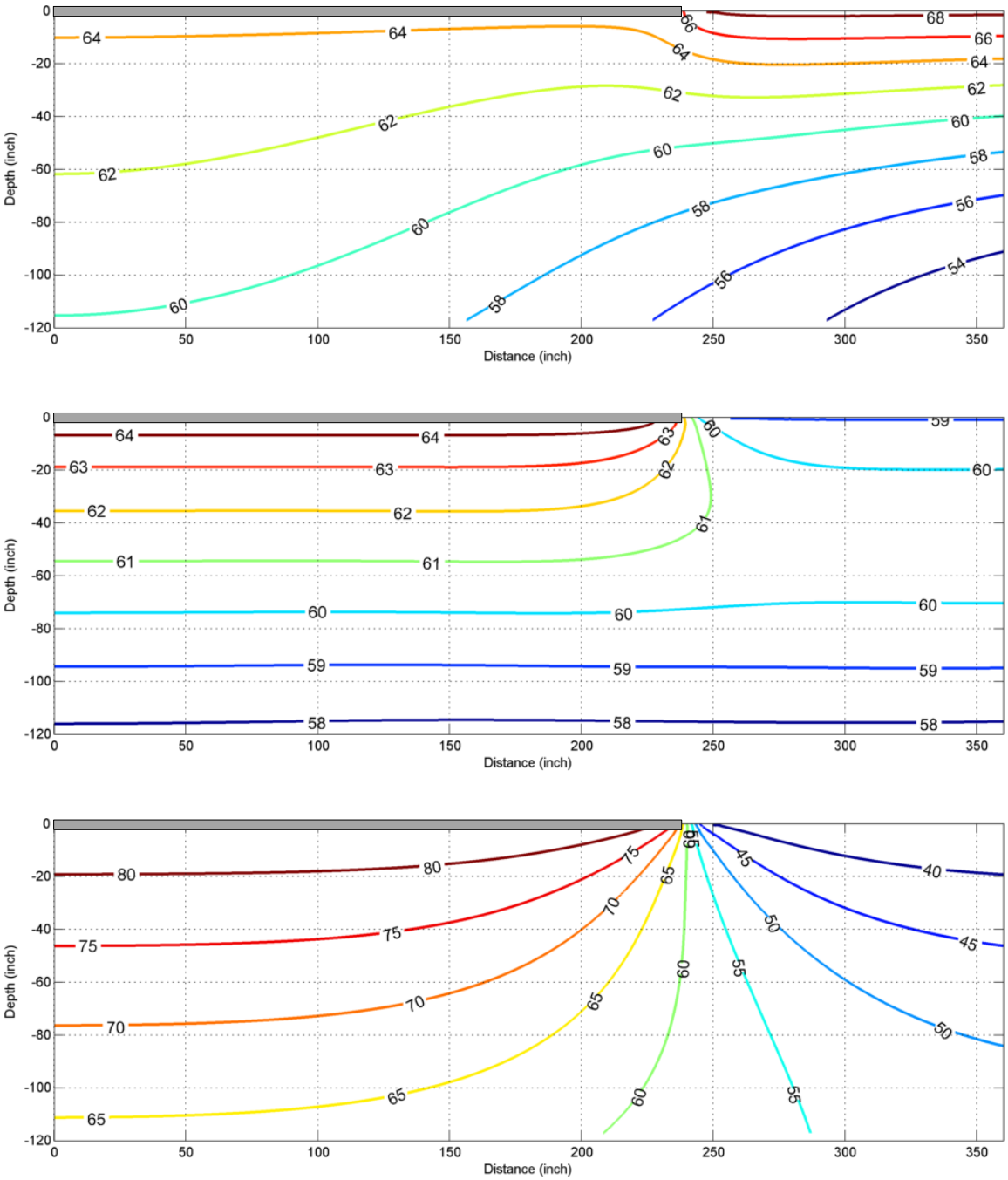


Figure 382: State College, Pennsylvania – soil temperature distribution for radiant slab at 180 days (top), 270 days (middle), and 360 days (bottom) starting from January 1st for a slab length of 40 feet

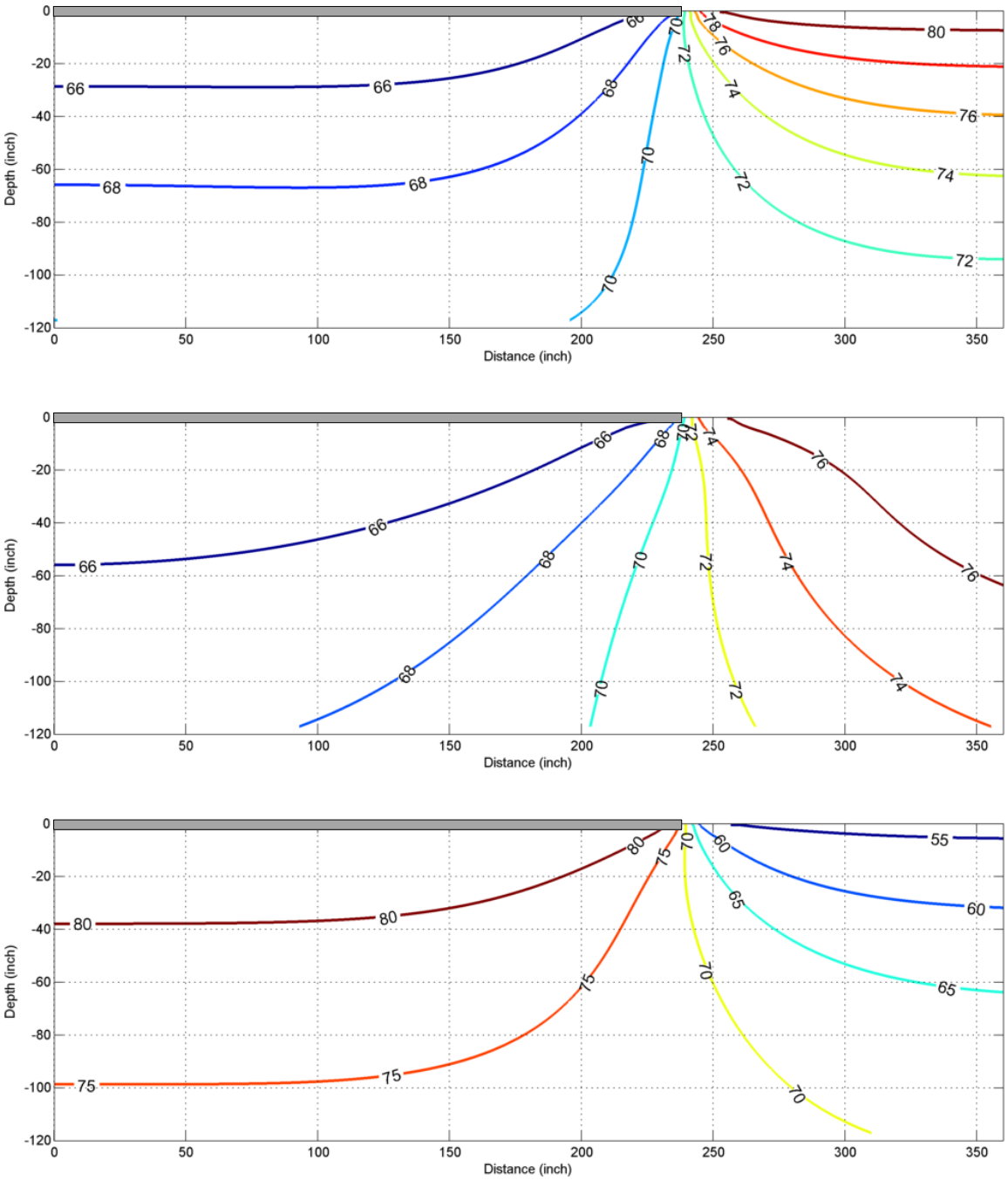


Figure 383: Tallahassee, Florida – soil temperature distribution for radiant slab at 180 days (top), 270 days (middle), and 360 days (bottom) starting from January 1st for a slab length of 40 feet

APPENDIX G

EXAMPLE PROGRAMS

Time Refinement Program

```
function [ t_refined ] = TimeRefinement( t_range,diff,tol,domain,TR )
%TIMEREFINEMENT - The purpose of this program is to determine the refined
%time for the EAHX simulation based on domain size, soil properties, and
%desired end time of the simulation.  Very small Green's Functions do not
%contribute to the final temperature distribution, and this program will
%prevent those small values from being calculated.  It is strongly
%encouraged to have some understanding of how GF values behave with time
%before using this program. The 1-D semi-infinite solid example from the
%Earth-Air Heat Exchanger Simulation Using Green's Functions chapter is
%used in this example as the demonstration.

%INPUTS
%   t_range - time range for simulation (days)
%   diff - soil thermal diffusivity (ft^2/day)
%   tol - tolerance level for the GF value cutoff
%   domain - input array of domain size and distribution spacing (ft)
%   TR - execute time refinement ('Yes' or 'No')

%OUTPUTS
%   t_refined - refined time value (days)


d_x = domain(1);
delx = domain(2);
d_y = domain(3);
dely = domain(4);


x_dim = d_x/delx+1;
y_dim = d_y/dely+1;
GF = zeros(y_dim,x_dim);


%  This is for 1-D simulations
if d_x == 0;
    d_x = delx;
else
end


tau = 0;
tol_check = 0;


if strcmp(TR,'Yes') == 1

    while tol_check <= tol
```

```
        tau = tau + 1;
        i=0;j=0;


        for x = delx : delx : d_x
            j=j+1;
            for y = dely : dely : d_y

                 i=i+1;

                 GF(i,j) = ( y / ( (4*pi)^0.5 * (diff*(t_range-tau))^1.5 ) )* ...
                         exp( (-(y)^2) / (4*diff*(t_range-tau)) );

            end
        end


        tol_check = max(max(GF));

        if tau > t_range
            error('Picked too high of a tolerance, never reaches it')
        else
        end


    end

else
end


if tau == 1
    display('Tolerance was reached immediatly')
    tau = 0;
else
end


t_refined = t_range - tau;
```

Published with MATLAB® R2012b

Base Solution Generation Programs

```
function [ ] = BaseSolutionGeneration(
d_x,delx,d_y,dely,diff,k,t_range,t_step,db_size,tol,TR )
%BASESOLUTIONGENERATION - this function creates the Base Solution Data base
%for use in the Numeric Integration program.  The inputs define properties,
%domain, and time range of data base.  Included in this program is the Time
%Refinement program.  Based on the selected tolerance, this program will
%reset the time range to the approperiate value.
%
%INPUTS
%   d_y - maximum depth of 1-D domain in y-direction (ft)
%   dely - distance between temperature distribution points (ft)
%   diff - diffusivity of soil (ft^2/day)
%   k - thermal conductivity of soil (Btu/hr*ft*degF)
%   t_range - maximum time for any expected simulation (days)
%   t_step - minimum time step for any epxeted simulation (minutes)
%   db_step - size of data blocks (days)
%   tol - minimum value for Time Refinement program to keep GFs (1/ft^2)
%   TR - time refinement 'Yes' or 'No'

format compact


%   Y DOMAIN DIMENSIONS AND GRID SPACING (FT)
[ domain ] = AnalysisDomain( d_x,delx,d_y,dely );


%   TIME REFINEMENT PROGRAM
[ t_refined ] = TimeRefinement( t_range,diff,tol,domain,TR );


%   PUT ALL PROPERTIES INTO ARRAY
[ prop,prop_base ] = PropertyArray( diff,k,t_range,t_refined,t_step,db_size );


%   CREATE NEW DIRECTORY TO SAVE FUNDAMENTAL SOLUTION FILES
[ cur_dir,save_dir ] = Directories( prop );


%   SAVE NOTES FROM INTEGRATION
IntNotes( cur_dir,save_dir,prop,prop_base,domain );


%   RUN FUNDAMENTAL SOLUTION GENERATION
ExampleBSG( cur_dir,save_dir,prop_base,domain,db_size,TR )


end
```

Published with MATLAB® R2012b

```
function [ domain ] = AnalysisDomain( d_x,delx,d_y,dely )
%DOMAIN - changes the domain values to inches and saves them as an array.
%
%OUTPUTS
%   d_y - maximum depth of 1-D domain in y-direction (in)
%   dely - distance between temperature distribution points (in)


d_x = d_x*12;
delx = delx*12;
d_y = d_y*12;
dely = dely*12;


domain = [d_x,delx,d_y,dely];


end
```

Published with MATLAB® R2012b

```
function [ cur_dir,save_dir ] = Directories( prop )
%DIRECTORIES - this function organizes files during batch runs.  Each
%   diffusivity, conductivity, and convective coefficient value will have
%   when applicable will have an independent directory in the Base Solution
%   Data Base.  This code will create that directory.


diff = prop(1);
k = prop(2);


%   Find the current directory
cur_dir = cd;


%   1nd level directory - thermal properties
L1_therm = sprintf('ExampleBSG_diff%d_k%d',diff,k);
mkdir(L1_therm);
cd(cur_dir);


save_dir = sprintf('%s\\%s',cur_dir,L1_therm);
```

```
end
```

Published with MATLAB® R2012b

```
function [ ] = ExampleBSG( cur_dir,save_dir,prop_base,domain,db_size,TR )
%UNTITLED7 Summary of this function goes here
%   Detailed explanation goes here

if strcmp(TR,'Yes') == 1
    t_range = prop_base(4);
else
    t_range = prop_base(3);
end

t_step = prop_base(5);


%   INITIALIZE COUNTER AND FILESIZE
counter = 1; file_size = 0; FundArray = 1;


for t = 0 : t_step : t_range


    if counter == file_size + 1


        %   SAVE DATA BLOCKS
        SaveDataBlock( t,cur_dir,save_dir,t_range,t_step,counter,FundArray )


        %   INITIALIZE A NEW DATA BLOCK
        [ FundArray,FundZero,file_size ] = InitDataBlock( t_step,db_size,domain );


        counter = 1;


    else
    end


    if t == t_range

        %   CALCULATES FUNDAMENTAL SOLUTION FOR TIME ZERO
        Y10_TimeZero( FundZero,prop_base,domain,1,cur_dir,save_dir );
```

```
    else

        %   CALCULATES FUNDAMENTAL SOLUTIONS
        [ FundArray ] = Y10( FundArray,t,t_range,counter,prop_base,domain );

    end


    if t == t_range
        counter = 1;
    else
        counter = counter + 1;
    end


end


end
```

Published with MATLAB® R2012b

```
function [ FundArray,FundZero,file_size ] = InitDataBlock( t_step,db_size,domain )
%INITDATABLOCK - The array is initialized with zeros to start.  This is to
%speed loops and troubleshooting (if zeros show up in array).  It will also
%determine the size of the time dimension for one day of data and pass that
%out as file size, and reset counter to zero.


x_high = domain(1);
delx = domain(2);
y_high = domain(3);
dely = domain(4);


t_dim = (db_size*24*3600)/t_step;   %Want a 24 hr block of data
x_dim = x_high/delx+1;
y_dim = y_high/dely+1;

FundArray = zeros(y_dim,x_dim,t_dim);
FundZero = zeros(y_dim,x_dim);
file_size = size(FundArray,3);


end
```

Published with MATLAB® R2012b

```
function [ ] = IntNotes( cur_dir,save_dir,prop,prop_base,domain )
%INTNOTES - saves the domain and property values for later reference if
%needed.


cd(save_dir);
save('IntNotes','prop','prop_base','domain' );
cd(cur_dir);


end
```

Published with MATLAB® R2012b

```
function [ prop,prop_base ] = PropertyArray( diff,k,t_range,t_refined,t_step,db_size )
%PROPERTYARRAY - This function converts input values into base units and
%saves them in arrays for later use.
%
%OUTPUTS
%   d_y - maximum depth of 1-D domain in y-direction (in)
%   dely - distance between temperature distribution points (in)
%   diff - diffusivity of soil (in^2/sec)
%   k - thermal conductivity of soil (Btu/sec*in*degF)
%   t_range - maximum time for any expected simulation (seconds)
%   t_step - minimum time step for any epxeted simulation (seconds)


prop = [diff;
       k;
       t_range;
       t_refined;
       t_step;
       db_size];



diff = diff*(144/86400);
k = k / 43200;
t_range = t_range*24*3600;
t_refined = t_refined*24*3600;
t_step = t_step*60;
db_size = db_size*24*3600;


prop_base = [diff;
            k;
            t_range;
            t_refined;
```

```
            t_step
            db_size];


end
```

Published with MATLAB® R2012b

```
function [ ] = SaveDataBlock( t,cur_dir,save_dir,t_range,t_step,counter,FundArray )
%SAVEDATABLOCK - saves the current data block when full of GF values.  This
%data block is set to save daily.  The data block is labeled with the start
%and end times it contains in seconds.


if FundArray == 1


else


    upper = (t_range - t) + ( (counter-1) * t_step);
    lower = upper - (t_step * (counter-2));


    cd(save_dir);
    file_name = sprintf('ExampleBSG_%d-%d',upper,lower);
    save(file_name,'FundArray');
    cd(cur_dir);


end


end
```

Published with MATLAB® R2012b

```
function [ FundArray ] = Y10( FundArray,t,t_range,counter,prop_base,domain )
%X10_TIMEZERO - caculates the zero time GF values for all domain values.
%Recall GF are undefined at time equal to zero.  This function uses a time
%close to zero instead of zero.


diff = prop_base(1);
k = prop_base(2);
```

```
x_high = domain(1);
delx = domain(2);
y_high = domain(3);
dely = domain(4);


for x = 0 : delx : x_high
    for y = 0 : dely : y_high


        x_dum = x/delx+1;
        y_dum = y/dely+1;


        GY10 = ( y / ( (4*pi)^0.5 * (diff*(t_range-t))^1.5 ) )* ...
                exp( (-(y)^2) / (4*diff*(t_range-t)) );


        FundArray(y_dum,x_dum,counter) = GY10;


    end
end


end
```

Published with MATLAB® R2012b

```
function [ ] = Y10_TimeZero( FundZero,prop_base,domain,t_zero, ...
    cur_dir,save_dir )
%X10_TIMEZERO - caculates the zero time GF values for all domain values.
%Recall GF are undefined at time equal to zero.  This function uses a time
%close to zero instead of zero.


diff = prop_base(1);
k = prop_base(2);


x_high = domain(1);
delx = domain(2);
y_high = domain(3);
dely = domain(4);


%   REFORMAT TIME TO BE NEAR ZERO
t_range = t_zero;
```

```
t = 0;


for x = 0 : delx : x_high
    for y = 0 : dely : y_high


        x_dum = x/delx+1;
        y_dum = y/dely+1;


        GY10 = ( y / ( (4*pi)^0.5 * (diff*(t_range-t))^1.5 ) )* ...
                exp( (-(y)^2) / (4*diff*(t_range-t)) );


        FundZero(y_dum,x_dum) = GY10;


    end
end


%   SAVE ZERO TIME FILE
cd(save_dir);
file_name = 'ExampleBSG_0';
save(file_name,'FundZero');
cd(cur_dir)


end
```

Published with MATLAB® R2012b

Numerical Integration Program

```
function [ temp_dist ] = BSG_Calc(diff,k,t_range,t_step,location,TR )
%BSG_CALC - is the Numeric Integration program.  This function takes data
%from the Base Solution Generation data base and climatic conditions to
%calculate temperature distributions.
%
%INPUTS
%   diff - diffusivity of soil (ft^2/day)
%   k - thermal conductivity of soil (Btu/hr*ft*degF)
%   t_range - maximum time for any expected simulation (days)
%   t_step - minimum time step for any epxeted simulation (minutes)
%   location - location for climatic conditions input as a string
%   TR - time refinement option 'Yes' or 'No'
```

```
format compact
day = 0;


%   FILE LOCATIONS
[ cur_dir,surfBC_loc,fund_loc ] = CalcDir( diff,k );


%   TIME CONVERSION TO SECONDS
%   input units( days, minutes ), output units( seconds, seconds)
[ t_range,t_step,t_diff ] = RefineTime( t_range,t_step,cur_dir,fund_loc,TR );


%   PRELIMINARY CALCULATIONS AND ARRAY INTIALIZATION
[ fund_size,int_step,t_step_fund,db_size,h_int,diff,k  ] = SoluSetup(
cur_dir,fund_loc,t_step,t_range );
[ soil_int ] = InitArrays( cur_dir,fund_loc );


%   FOURIER SERIES FIT TO WEATHER OR GROUND SURFACE TEMPERATURES
%   input units( strng), output units( degF )
% [ soil_coeff,Tm_NRCS ] = SurfaceBC_CurveFit( surfBC_loc,cur_dir,location,'NRCS','No' );



%   FUNDAMENTAL FILE SELECTON LOOP

for t_minus_tau = t_range : -db_size : db_size


    %   LOAD FUNDAMENTAL SOLUTION DATA BLOCK
    [ FundArray ] = LoadDataBlock( fund_loc,cur_dir,t_minus_tau,t_step_fund,db_size );


    %   NUMERIC INTEGRATION LOOP
    for t = 1 : int_step : fund_size - 1


        %   APPLY BOUNDARY CONDITION
        [ f_tau ] = BCFit( soil_coeff,t,t_range,t_minus_tau,t_step,t_diff );


        %   NUMERICAL INTEGRATION BASED ON TRAPEZOID RULE
        [ soil_int ] = NumInt( soil_int,FundArray,t,t_minus_tau,t_range,f_tau );


    end
    clear FundArray f_tau

    day = 1 + day;
```

```
end


%   ADD THE ZERO TIME STEP
[ f_tau ] = BCFit( soil_coeff,0,t_range,0,0,t_diff );
[ soil_int ] = ZeroNumInt( soil_int,fund_loc,cur_dir,f_tau );


%   FINISH NUMERIC INTEGRATION BY MULTIPLYING BY CONSTANTS
temp_dist = diff * h_int * soil_int;


end
```

Published with MATLAB® R2012b

```
function [ f_tau ] = BCFit( coeff,t,t_range,t_minus_tau,t_step,t_diff )
%BCFIT - calculates the boundary conditions contribution f(tau) for each
%time step in the numerical integration.  The coefficients of the fourier
%series were calculated earlier in the curve_fit function.


%   CHANGE TIME FROM T-TAU TO TAU FOR USE IN THE BOUNDARY CONDTION
tau_day = t_range - t_minus_tau + t_diff;
tau = tau_day + (t-1)*t_step;


%  RESET FOURIER SERIES FOR EVERY 365 DAY PERIOD
year = fix(tau/31536000);
tau = tau - year*31536000;


%   FOURIER SERIES FIT TO SPECIFIED WEATHER DATA
omg = coeff(size(coeff));
f_tau = coeff(1) + coeff(2)*cos(tau*omg) + coeff(3)*sin(tau*omg) + ...
    coeff(4)*cos(2*tau*omg) + coeff(5)*sin(2*tau*omg);
%+ a(3)*cos(3*tau*omg) + b(3)*sin(3*tau*omg) + a(4)*cos(4*tau*omg) + b(4)*sin(4*tau*omg);


end
```

Published with MATLAB® R2012b

```
function [ cur_dir,surfBC_loc,fund_loc ] = CalcDir( diff,k )
%CALCDIR - creates paths to where the BSG data base and climatic conditions
%are stored.
```

```
cur_dir = pwd;

surfBC_loc = 'J:\Google Drive\PhD Research\Locations_TMY_NRCSData';
fund_loc = sprintf('K:\\PhD
Research_TBDrive\\GFFundSoluGen_DataBase\\ExampleBSG_diff%d_k%d',diff,k);

end
```

Published with MATLAB® R2012b

```
function [ soil_int ] = InitArrays( cur_dir,fund_loc )
%INITARRAYS - initializes the data array to the summed integration values.


%   LOAD INTEGRATION NOTES FROM FUNDAMENTAL PROGRAM
cd(fund_loc);
load('IntNotes','domain');
cd(cur_dir);


x_high = domain(1);
delx = domain(2);
y_high = domain(3);
dely = domain(4);


%   INITIALIZE THE NUMERIC INTEGRATION AND INITIAL CONDITION ARRAYS
x_dim = x_high/delx+1;
y_dim = y_high/dely+1;
soil_int = zeros(y_dim,x_dim);


end
```

Published with MATLAB® R2012b

```
function [ FundArray ] = LoadDataBlock( fund_loc,cur_dir,t_minus_tau,t_step_fund,db_size
)
%LOADDATABLOCK - loads a data block from the BSG data base.  The data block
%is determined by the current upper and lower time limits.


%   FIND TIMES FOR CURRENT DATA  BLOCK
upper = t_minus_tau;
```

```
lower = upper - db_size + t_step_fund;


%   LOAD THE FUNDAMENTAL ARRAY FOR THIS TIME AND BOUNDARY CONDITION
cur_block = sprintf('ExampleBSG_%d-%d.mat',upper,lower);
cd(fund_loc)
load(cur_block);
cd(cur_dir)


end
```

Published with MATLAB® R2012b

```
function [ num_int ] = NumInt( num_int,FundArray,t,t_minus_tau,t_range,f_tau )
%NUMINT - sums the individual numeric integration values together.  It
%takes the current fundamental solution times the boundary condtion.


%   MULTIPLY BOUNDARY CONDITION BY FUNDAMENTAL SOLUTION
if t_minus_tau == t_range  && t == 1
    func = 0.5*f_tau * FundArray(:,:,t);
else
    func = f_tau * FundArray(:,:,t);
end

num_int = num_int + func;


end
```

Published with MATLAB® R2012b

```
function [ t_range,t_step,t_diff ] = RefineTime( t_range,t_step,cur_dir,fund_loc,TR )
%REFINE_TRANGE - replaces the specified time for the temperature
%distribution if it is larger than the refined time from the Base Solution
%Generation.  This will keep the Numeric Integration program from iterating
%GF values that do not contribute to temperature distribution.


if strcmp(TR,'Yes')


    cd(fund_loc);
    load('IntNotes','prop');
    cd(cur_dir);
```

```
    t_refined = prop(4);


    if t_range > t_refined

        t_diff = t_range - t_refined;
        t_range = t_refined;

    else
        t_diff = 0;
    end


else
end


t_range = t_range*24*3600;
t_step = t_step*60;
t_diff = t_diff*24*3600;


end
```

Published with MATLAB® R2012b

```
function [ fund_size,int_step,t_step_fund,db_size,h_int,diff,k ] = SoluSetup(
cur_dir,fund_loc,t_step,t_range )
%SOLUSETUP - performs several preliminary calculations for the numeric
%integration.  These include the multiplication constants h and N for the
%trapezoidal rule.


%   LOAD INTEGRATION NOTES FROM FUNDAMENTAL PROGRAM
cd(fund_loc);
load('IntNotes','prop_base');
cd(cur_dir);
diff = prop_base(1);
k = prop_base(2);
db_size = prop_base(6);
t_step_fund = prop_base(5);


%   FIND SIZE OF THE FUNDAMENTAL SOLUTION ARRAYS
fund_size = db_size/t_step_fund;


%   FIND THE STEP SIZE FOR INTEGRATION LOOP
int_step = t_step/t_step_fund;
```

```
%   FIND THE NUMBER OF INTERVALS IN THE NUMERICAL INTEGRATION
N = t_range/t_step + 1;


%   DEFINE H FOR TRAPEZOIDAL RULE
h_int = (t_range - 0) / (N - 1);


end
```

Published with MATLAB® R2012b

```
function [ num_int ] = ZeroNumInt( num_int,fund_loc,cur_dir,f_tau,BCtype )
%ZERONUMINT - adds the zero time step to the numeric integration.  The
%fundamental solution functions are underfined at t-tau = 0.  So have to
%evaluate them close to zero, but not at zero.


cur_file = 'ExampleBSG_0';

%   This loads variable "KFund_array"
cd(fund_loc)
load(cur_file);
cd(cur_dir)

%   Multiply boundary condition and fundamental solution
func = 0.5 * f_tau * FundZero;

num_int = num_int + func;


end
```

Published with MATLAB® R2012b